

DESY-22-045, IFT-UAM/CSIC-22-028,
KEK Preprint 2021-61, PNNL-SA-160884,
SLAC-PUB-17662
January 2023

The International Linear Collider: Report to Snowmass 2021

THE ILC INTERNATIONAL DEVELOPMENT TEAM AND THE ILC COMMUNITY

ABSTRACT

The International Linear Collider (ILC) is on the table now as a new global energy-frontier accelerator laboratory taking data in the 2030's. The ILC addresses key questions for our current understanding of particle physics. It is based on a proven accelerator technology. Its experiments will challenge the Standard Model of particle physics and will provide a new window to look beyond it. This document brings the story of the ILC up to date, emphasizing its strong physics motivation, its readiness for construction, and the opportunity it presents to the US and the global particle physics community.

Alexander Aryshev¹, Ties Behnke², Mikael Berggren², James Brau³, Nathaniel Craig⁴, Ayres Freitas⁵, Frank Gaede², Spencer Gessner⁶, Stefania Gori⁷, Christophe Grojean^{2,8}, Sven Heinemeyer⁹, Daniel Jeans¹, Katja Kruger², Benno List², Jenny List², Zhen Liu¹⁰, Shinichiro Michizono¹, David W. Miller¹¹, Ian Moulton¹², Hitoshi Murayama^{13,14,15}, Tatsuya Nakada¹⁶, Emilio Nanni⁶, Mihoko Nojiri^{1,15}, Hasan Padamsee¹⁷, Maxim Perelstein¹⁷, Michael E. Peskin⁶, Roman Poeschl¹⁸, Sam Posen¹⁹, Aidan Robson²⁰, Jan Strube²¹, Taikan Suehara²², Junping Tian²³, Maxim Titov²⁴, Marcel Vos²⁵, Andrew White²⁶, Graham Wilson²⁷, Kaoru Yokoya¹, Aleksander Filip Zarnecki²⁸ (**Editors**)

Ichiro Adachi¹, Kaustubh Agashe²⁹, Tatjana Agatonovic Jovin³⁰, Hiroaki Aihara²³, Wolfgang Altmannshofer⁷, Daniele Alves³¹, Justin Anguiano²⁷, Ken-Ichi Aoki³², Masato Aoki¹, Toshihiro Aoki¹, Yumi Aoki³³, Yasuo Arai¹, Hayato Araki¹, Haruka Asada³⁴, Kento Asai³⁵, Shoji Asai²³, David Attie²⁴, Howard Baer³⁶, Jonathan Bagger³⁷, Yang Bai³⁸, Ian Bailey³⁹, Ricardo Barrue⁴⁰, Rainer Bartoldus⁶, Emanuela Barzi¹⁹, Matthew Basso⁴¹, Lothar Bauerdick¹⁹, Sebastian Baum⁴², Alain Bellerive⁴³, Sergey Belomestnykh¹⁹, Jorge Berenguer Antequera⁴⁴, Jakob Beyer², Pushpalatha Bhat¹⁹, Burak Bilki^{45,46}, Kevin Black³⁸, Kenneth Bloom⁴⁷, Geoffrey Bodwin⁴⁸, Veronique Boisvert⁴⁹, Fatma Boran^{45,50}, Vincent Boudry⁵¹, Radja Boughezal⁴⁸, Antonio Boveia⁵², Ivanka Bozovic-Jelisavcic³⁰, Jean-Claude Brient⁵¹, Stanley Brodsky⁶, Laurent Brunetti¹⁸, Karsten Buesser², Eugene Bulyak⁵³, Philip N. Burrows⁵⁴, Graeme C. Burt³⁹, Yunhai Cai⁶, Valentina Cairo⁵⁵, Peter Cameron⁵⁶, Anadi Canepa¹⁹, Francesco Giovanni Celiberto^{57,58}, Enrico Cenni²⁴, Zackaria Chacko²⁹, Iryna Chaikovska¹⁸, Mattia Checchin¹⁹, Lisong Chen⁵, Thomas Y. Chen⁵⁹, Hsin-Chia Cheng⁶⁰, Gi-Chol Cho⁶¹, Brajesh Choudhary⁶², Jim Clarke⁶³, James Cline⁶⁴, Raymond Co¹⁰, Timothy Cohen³, Paul Colas²⁴, Chris Damerell⁶⁵, Arindam Das⁶⁶, Sridhara Dasu³⁸, Sally Dawson⁵⁶, Jorge de Blas⁶⁷, Carlos Henrique de Lima⁴³, Aldo Deandrea⁶⁸, Klaus Dehmelt⁶⁹, Jean Delaysen⁷⁰, Marcel Demarteau⁷¹, Dmitri Denisov⁵⁶, Radovan Dermisek⁷², Angel Dieguez⁷³, Takeshi Dohmae¹, Jens Dopke⁶⁵, Katharina Dort⁵⁵, Yong Du⁷⁴, Bohdan Dudar², Bhaskar Dutta⁷⁵, Juhi Dutta⁷⁶, Ulrich Einhaus², Eckhard Elsen², Motoi Endo¹, Grigory Eremeev¹⁹, Engin Eren², Jens Erler⁷⁷, Eric Esarey¹⁴, Lisa Everett³⁸, Angeles Faus Golfe¹⁸, Marcos Fernandez Garcia⁷⁸, Brian Foster⁵⁴, Nicolas Fourches²⁴, Mary-Cruz Fouz⁷⁹, Keisuke Fujii¹, Junpei Fujimoto¹, Esteban Fullana Torregrosa²⁵, Kazuro Furukawa¹, Takahiro Fusayasu⁸⁰, Juan Fuster²⁵, Serguei Ganjour²⁴, Yuanning Gao⁸¹, Naveen Gaur⁶², Rongli Geng⁷¹, Howard Georgi⁸², Tony Gherghetta¹⁰, Steven Goldfarb⁸³, Joel Goldstein⁸⁴, Dorival Goncalves⁸⁵, Julia Gonski⁵⁹, Tomas Gonzalo⁸⁶, Takeyoshi Goto¹, Toru Goto¹, Norman Graf⁶, Joseph Grames⁸⁷, Paul Grannis⁶⁹, Lindsey Gray¹⁹, Alexander Grohsjean², Jiayin Gu⁸⁸, Yalcin Guler⁸⁹, Phillip Gutierrez³⁶, Junji Haba¹, Howard Haber⁷, Joseph Haley³⁶, John Hallford^{2,90}, Koichi Hamaguchi²³, Tao Han⁵, Kazuhiko Hara⁹¹, Daisuke Harada⁹², Koji Hashimoto⁹³, Katsuya Hashino⁸¹, Masahito Hayashi⁹⁴, Gudrun Heinrich⁹⁵, Keisho Hidaka⁹⁶, Takeo Higuchi¹⁵, Fujio Hinode⁹⁷, Zenro Hioki¹, Minoru Hirose⁹³, Nagisa Hiroshima⁹⁸, Junji Hisano³⁴, Wolfgang Hollik⁹⁹, Samuel Homiller⁸², Sungwoo Hong^{11,48}, Anson Hook²⁹, Yasuyuki Horii³⁴, Hiroki Hoshina²³, Ivana Hristova⁶⁵, Katri Huitu¹⁰⁰, Yoshifumi Hyakutake¹⁰¹, Toru Iijima³⁴, Katsumasa Ikematsu⁹⁷, Anton Ilderton¹⁰², Kenji Inami³⁴, Adrian Irlles²⁵, Akimasa Ishikawa¹, Koji Ishiwata³², Hayato Ito¹, Igor Ivanov¹⁰³, Sho Iwamoto¹⁰⁴, Toshiyuki Iwamoto²³, Masako Iwasaki¹⁰⁵, Yoshihisa Iwashita¹⁰⁶, Haoyi Jia³⁸, Fabricio Jimenez Morales⁵¹,

Prakash Joshi³³, Sunghoon Jung¹⁰⁷, Goran Kacarevic³⁰, Michael Kagan⁶, Mitsuru Kakizaki⁹⁸,
 Jan Kalinowski²⁸, Jochen Kaminski¹⁰⁸, Kazuyuki Kanaya⁹¹, Shinya Kanemura⁹³,
 Hayato Kanno¹⁰⁶, Yuya Kano³⁴, Shigeru Kashiwagi⁹⁷, Yukihiko Kato¹⁰⁹, Nanami Kawada⁹⁷,
 Shin-ichi Kawada², Kiyotomo Kawagoe²², Valery Khoze¹¹⁰, Hiromichi Kichimi¹, Doojin Kim⁷⁵,
 Teppei Kitahara³⁴, Ryuichiro Kitano¹, Jan Klamka²⁸, Sachio Komamiya¹¹¹, K. C. Kong²⁷,
 Taro Konomi¹, Katsushige Kotera⁹³, Emi Kou¹⁸, Ilya Kravchenko⁴⁷, Kiyoshi Kubo¹,
 Takayuki Kubo¹, Takuya Kumaoka⁹¹, Ashish Kumar¹, Nilanjana Kumar⁶², Jonas Kunath⁵¹,
 Saumyen Kundu¹¹², Hiroshi Kunitomo¹⁰⁶, Masakazu Kurata¹, Masao Kuriki¹¹³,
 Alexander Kusenko^{15,114}, Theodota Lagouri¹¹⁵, Andrew J. Lankford¹¹⁶,
 Gordana Lastovicka-Medin¹¹⁷, Francois Le Diberder¹⁸, Claire Lee¹¹⁷, Matthias Liepe¹⁷,
 Jacob Linacre⁶⁵, Zachary Liptak¹¹³, Shivani Lomte³⁸, Ian Low^{48,118}, Yang Ma⁵, Hani Maalouf¹¹⁹,
 David MacFarlane⁶, Brendon Madison²⁷, Thomas Madlener², Tomohito Maeda¹²⁰, Paul Malek²,
 Sanjoy Mandal²⁵, Thomas Markiewicz⁶, John Marshall¹²¹, Aurélien Martens¹⁸,
 Victoria Martin¹⁰², Martina Martinello¹⁹, Celso Martinez Rivero⁷⁸, Nobuhito Maru¹⁰⁵,
 John Matheson⁶⁵, Shigeki Matsumoto¹⁵, Hiroyuki Matsunaga¹, Yutaka Matsu²³,
 Kentarou Mawatari¹²², Johnpaul Mbagwu²⁷, Peter McIntosh⁶³, Peter McKeown²,
 Patrick Meade⁶⁹, Krzysztof Mekala²⁸, Petra Merkel¹⁹, Satoshi Mihara¹, Víctor Miralles^{25,123},
 Marcos Miralles López²⁵, Go Mishima⁹⁷, Satoshi Mishima¹, Bernhard Mistlberger⁶,
 Alexander Mitov¹²⁴, Kenkichi Miyabayashi¹²⁵, Akiya Miyamoto¹, Gagan Mohanty¹²⁶,
 Laura Monaco¹²⁷, Myriam Mondragon¹²⁸, Hugh E. Montgomery⁸⁷, Gudrid Moortgat-Pick²,
 Nicolas Morange¹⁸, María Moreno Llácer²⁵, Stefano Moretti^{65,129}, Toshinori Mori²³,
 Toshiyuki Morii¹³⁰, Takeo Moroi²³, David Morrissey¹³¹, Benjamin Nachman¹⁴, Kunihiro Nagano¹,
 Jurina Nakajima³³, Eiji Nakamura¹, Shinya Narita¹²², Pran Nath¹³², Timothy Nelson⁶,
 David Newbold⁶⁵, Atsuya Niki²³, Yasuhiro Nishimura¹³³, Eisaku Nishiyama¹³⁴,
 Yasunori Nomura¹³, Kacper Nowak²⁸, Mitsuaki Nozaki¹, María Teresa Núñez Pardo de Vera²,
 Inês Ochoa⁴⁰, Masahito Ogata⁹⁸, Satoru Ohashi¹⁰⁶, Hikaru Ohta¹, Shigemi Ohta¹,
 Norihito Ohuchi¹, Hideyuki Oide¹³⁵, Nobuchika Okada¹³⁶, Yasuhiro Okada¹, Shohei Okawa¹³⁷,
 Yuichi Okayasu¹, Yuichi Okugawa^{18,97}, Toshiyuki Okugi¹, Takemichi Okui^{1,138},
 Yoshitaka Okuyama¹, Mathieu Omet¹, Tsunehiko Omori¹, Hiroaki Ono¹³⁹, Tomoki Onoe²²,
 Wataru Ootani²³, Hidetoshi Otono²², Shuhei Ozawa⁹⁸, Simone Pagan Griso¹⁴,
 Alessandro Papa^{140,141}, Rocco Paparella¹⁴², Eun-Kyung Park⁹⁸, Gilad Perez¹⁴³,
 Abdel Perez-Lorenzana¹⁴⁴, Yvonne Peters¹⁴⁵, Frank Petriello^{48,118}, Jónatan Piedra⁷⁸,
 Freddy Poirier¹⁸, Werner Porod¹⁴⁶, Christopher Potter³, Alan Price¹⁴⁷, Yasser Radkhorrani²,
 Laura Reina¹³⁸, Jürgen Reuter², Francois Richard¹⁸, Sabine Riemann¹⁴⁸, Robert Rimmer⁸⁷,
 Thomas Rizzo⁶, Tania Robens⁹², Roger Ruber⁸⁷, Alberto Ruiz Jimeno⁷⁸, Takayuki Saeki¹,
 Ipsita Saha¹⁵, Tomoyuki Saito²³, Makoto Sakaguchi¹⁰¹, Tadakatsu Sakai³⁴, Yasuhiro Sakaki¹,
 Kodai Sakurai⁹⁵, Riccardo Salvatico²⁷, Fabrizio Salvatore¹⁴⁹, Yik Chuen San¹⁷, Pearl Sandick¹⁵⁰,
 Tomoyuki Sanuki⁹⁷, Kollassery Swathi Sasikumar⁹⁹, Oliver Schaefer², Ruth Schäfer¹⁵¹,
 Uwe Schneekloth², Thomas Schoerner-Sadenius², Carl Schroeder¹⁴, Philip Schuster⁶,
 Ariel Schwartzman⁶, Reinhard Schwienhorst¹⁵², Felix Sefkow², Yoshihiro Seiya¹⁰⁵,
 Motoo Sekiguchi¹⁵³, Kazuyuki Sekizawa¹⁵⁴, Katsumi Senyo¹⁵⁵, Hale Sert¹⁵⁶, Daniele Sertore¹⁴²,
 Ronald Settles⁹⁹, Qaisar Shafi¹⁵⁷, Tetsuo Shahdara¹, Barmak Shams Es Haghi¹⁵⁰,
 Ashish Sharma¹⁵⁸, Jessie Shelton¹⁵⁹, Claire Shepherd-Themistocleous⁶⁵, Hiroto Shibuya³²,
 Tetsuo Shidara¹, Takashi Shimomura¹⁶⁰, Tetsuo Shindou¹⁶¹, Yutaro Shoji¹⁶², Jing Shu⁷⁴,

Ian Sievers⁵⁵, Frank Simon⁹⁹, Rajeev Singh¹⁶³, Yotam Soreq¹⁶⁴, Marcel Stanitzki²,
 Steinar Stapnes⁵⁵, Amanda Steinhebel³, John Stupak³⁶, Shufang Su¹⁶⁵, Fumihiko Suekane⁹⁷,
 Akio Sugamoto⁶¹, Yuji Sugawara¹⁶⁶, Satoru Sugimoto¹, Yasuhiro Sugimoto¹,
 Hiroaki Sugiyama¹⁶⁷, Yukinari Sumino⁹⁷, Raman Sundrum²⁹, Atsuto Suzuki¹⁶⁸, Shin Suzuki⁹⁸,
 Maximilian Swiatlowski¹³¹, Tim M P. Tait¹¹⁶, Shota Takahashi¹, Tohru Takahashi¹¹³,
 Tohru Takeshita¹⁶⁹, Michihisa Takeuchi⁹³, Yosuke Takubo¹, Tomohiko Tanabe¹⁶⁸,
 Philip (Flip) Tanedo¹⁷⁰, Morimitsu Tanimoto¹⁵⁴, Shuichiro Tao²², Xerxes Tata¹⁷¹,
 Toshiaki Tauchi¹, Geoffrey Taylor⁸³, Takahiro Terada¹⁷², Nobuhiro Terunuma¹, Jesse Thaler¹⁷³,
 Alessandro Thea⁶⁵, Finn Tillinger¹⁵¹, Jan Timmermans¹⁷⁴, Kohsaku Tobioka^{1,138},
 Kouichi Toda¹⁶⁷, Atsushi Tokiyasu⁹⁷, Takashi Toma³², Julie Torndal², Mehmet Tosun⁴⁵,
 Yu-Dai Tsai¹¹⁶, Shih-Yen Tseng²³, Koji Tsumura²², Douglas Tuckler⁴³, Yoshiki Uchida²²,
 Yusuke Uchiyama²³, Daiki Ueda²³, Fumihiko Ukegawa⁹¹, Kensei Umemori¹, Junji Urakawa¹,
 Claude Vallee¹⁷⁵, Roberto Vega¹⁷⁶, Liliana Velasco¹⁷⁷, Silvia Verdú-Andrés⁵⁶, Caterina Vernieri⁶,
 Anna Vilá⁷³, Ivan Vila Alvarez⁷⁸, Joost Vosseveld¹⁷⁸, Raghava Vsrms¹⁷⁹, Natasa Vukasinovic³⁰,
 Doreen Wackerroth¹⁸⁰, Moe Wakida³⁴, Liantao Wang¹¹, Masakazu Washio¹¹¹,
 Takashi Watanabe¹⁶¹, Nigel Watson¹⁸¹, Gordon Watts¹⁸², Georg Weiglein², James D. Wells¹⁸³,
 Marc Wenskat², Susanne Westhoff¹⁵¹, Glen White⁶, Ciaran Williams¹⁸⁰, Stephane Willocq¹⁸⁴,
 Matthew Wing⁹⁰, Alasdair Winter¹⁸¹, Marc Winter¹⁸, Yongcheng Wu⁸⁵, Keping Xie⁵, Tao Xu¹⁶²,
 Zijun Xu⁶, Vyacheslav Yakovlev¹⁹, Shuei Yamada¹, Akira Yamamoto^{1,55}, Hitoshi Yamamoto^{25,97},
 Kei Yamamoto¹¹³, Yasuchika Yamamoto¹, Masato Yamanaka¹⁰⁵, Satoru Yamashita²³,
 Masahiro Yamatani¹⁸⁵, Naoki Yamatsu²², Shigehiro Yasui¹³³, Takuya Yoda¹⁰⁶, Ryo Yonamine¹,
 Keisuke Yoshihara¹⁸⁶, Masakazu Yoshioka^{97,122,168}, Tamaki Yoshioka²², Fukuko Yuasa¹,
 Keita Yumino¹, Dirk Zerwas¹⁸, Ya-Juan Zheng²⁷, Jia Zhou¹⁸⁴, Hua Xing Zhu¹⁸⁷,
 Mikhail Zobov¹⁸⁸, Fabian Zomer²⁴

While many of the authors above contributed substantially to the writing of this report, authorship here mainly represents an endorsement of the goals that this report puts forward. This endorsement is not exclusive of other Higgs factory proposals. If you would like to add your name in support, please visit <https://agenda.linearcollider.org/event/9135/>.

- ¹KEK, Tsukuba, JAPAN
- ²Deutsches Elektronen-Synchrotron DESY, GERMANY
- ³University of Oregon, Eugene, OR USA
- ⁴University of California, Santa Barbara, CA USA
- ⁵University of Pittsburgh, Pittsburgh, PA USA
- ⁶SLAC National Accelerator Laboratory, Menlo Park, CA USA
- ⁷University of California, Santa Cruz CA USA
- ⁸Humbolt University, Berlin, GERMANY
- ⁹Universidad Autónoma de Madrid, SPAIN
- ¹⁰University of Minnesota, Minneapolis, MN USA
- ¹¹University of Chicago, Chicago, IL USA
- ¹²Yale University, New Haven, CT USA
- ¹³University of California, Berkeley, CA USA
- ¹⁴Lawrence Berkeley National Laboratory, Berkeley, CA USA
- ¹⁵Kavli IPMU, University of Tokyo, Kashiwa, JAPAN
- ¹⁶EPFL, Lausanne SWITZERLAND
- ¹⁷Cornell University, Ithaca NY USA
- ¹⁸IJCLab, Université Paris-Saclay, Orsay FRANCE
- ¹⁹Fermi National Accelerator Laboratory, Batavia, IL USA
- ²⁰University of Glasgow, Glasgow UK
- ²¹Pacific Northwest National Laboratory, Richland, WA USA
- ²²Kyushu University, Fukuoka JAPAN
- ²³University of Tokyo, Tokyo, JAPAN
- ²⁴CEA Saclay, Gif sur Yvette, FRANCE
- ²⁵IFIC, CSIC-University of Valencia, Valencia, SPAIN
- ²⁶University of Texas, Arlington, TX USA
- ²⁷University of Kansas, Lawrence, KS
- ²⁸University of Warsaw, Warsaw POLAND
- ²⁹University of Maryland, College Park, MD USA
- ³⁰University of Belgrade, Belgrade, SERBIA
- ³¹Los Alamos National Laboratory, Los Alamos, NM USA
- ³²Kanazawa University, Kanazawa, JAPAN
- ³³Sokendai, KEK, Tsukuba, JAPAN
- ³⁴Nagoya University, Nagoya, JAPAN
- ³⁵Saitama University, Saitama, JAPAN
- ³⁶University of Oklahoma, Norman, OK USA
- ³⁷John Hopkins University, Baltimore, MD USA
- ³⁸University of Wisconsin, Madison, WI USA
- ³⁹Lancaster University, Lancaster, UK
- ⁴⁰LIP Laboratório, Lisbon, PORTUGAL
- ⁴¹University of Toronto, Toronto, ON CANADA
- ⁴²Stanford University, Stanford, CA USA
- ⁴³Carleton University, Ottawa, ON CANADA
- ⁴⁴University of Cordoba, Cordoba, SPAIN
- ⁴⁵Beykent University, Istanbul, TURKEY
- ⁴⁶University of Iowa, Iowa City, IA USA
- ⁴⁷University of Nebraska, Lincoln NE USA
- ⁴⁸Argonne National Laboratory, Lemont, IL USA
- ⁴⁹Royal Holloway University, London, UK
- ⁵⁰Cucurova University, Adana, TURKEY
- ⁵¹Institut Polytechnique de Paris, Palaiseau, FRANCE
- ⁵³Karazin National University, Kharkiv, UKRAINE

- ⁵⁴Oxford University, Oxford, UK
- ³⁹Lancaster University, Lancaster, UK
- ⁵⁵CERN, Geneva, SWITZERLAND
- ⁵⁶Brookhaven National Laboratory, Upton, NY USA
- ⁵⁷ECT*, Trento, ITALY
- ⁵⁸INFN-TIFPA Trento, Trento, ITALY
- ⁵⁹Columbia University, New York, NY USA
- ⁶⁰University of California, Davis, CA USA
- ⁶¹Ochanomizu University, Tokyo, JAPAN
- ⁶²University of Delhi, New Delhi, INDIA
- ⁶³Daresbury Laboratory, Daresbury, UK
- ⁶⁴McGill University, Montreal, QC CANADA
- ⁶⁵Rutherford Appleton Laboratory, Chilton, UK
- ⁶⁶Hokkaido University, Sapporo, JAPAN
- ⁶⁷Universidad de Granada, Granada, SPAIN
- ⁶⁸IP2I Lyon, Villeurbanne, FRANCE
- ⁶⁹SUNY Stony Brook, Stony Brook, NY USA
- ⁷⁰Old Dominion University, Norfolk, VA USA
- ⁷¹Oak Ridge National Laboratory, Oak Ridge TN USA
- ⁷²Indiana University, Bloomington, IN USA
- ⁷³University of Barcelona, Barcelona, SPAIN
- ⁷⁴Chinese Academy of Sciences, Beijing CHINA
- ⁷⁵Texas A&M University, College Station, TX USA
- ⁷⁶University of Hamburg, Hamburg, GERMANY
- ⁷⁷University of Mainz, Mainz, GERMANY
- ⁷⁸IFCA, CSIC-University of Cantabria, Santander, SPAIN
- ⁷⁹CIEMAT, Madrid, SPAIN
- ⁸⁰Saga University, Saga, JAPAN
- ⁸¹Peking University, Beijing, CHINA
- ⁸²Harvard University, Cambridge, MA USA
- ⁸³University of Melbourne, Melbourne, AUSTRALIA
- ⁸⁴University of Bristol, Bristol, UK
- ⁸⁵Oklahoma State University, Stillwater, OK USA
- ⁸⁶Aachen University, Aachen GERMANY
- ⁸⁷Thomas Jefferson National Accelerator Facility, Newport News, VA USA
- ⁸⁸Fudan University, Shanghai, CHINA
- ⁸⁹Konya Technical University, Konya, TURKEY
- ⁹⁰University College London, London, UK
- ⁹¹University of Tsukuba, Tsukuba, JAPAN
- ⁹²Rudjer Boskovic Institute, Zagreb, CROATIA
- ⁹³Osaka University, Osaka JAPAN
- ⁹⁴Osaka Institute of Technology, Osaka JAPAN
- ⁹⁵Karlsruhe Institute of Technology, Karlsruhe, GERMANY
- ⁹⁶Tokyo Gakugei University, Tokyo, JAPAN
- ⁹⁷Tohoku University, Sendai, JAPAN
- ⁹⁸Toyama University, Toyama, JAPAN
- ⁹⁹Max Planck Institute, Munich, GERMANY
- ¹⁰⁰Helsinki Institute of Physics, Helsinki, FINLAND
- ¹⁰¹Ibaraki University, Mito, JAPAN
- ¹⁰²University of Edinburgh, Edinburgh, UK
- ¹⁰³Sun Yat Sen University, Zhuhai, CHINA
- ¹⁰⁴Eötvös Loránd University, Budapest, HUNGARY
- ¹⁰⁵Osaka City University, Osaka, JAPAN
- ¹⁰⁶Kyoto University, Kyoto, JAPAN

- ¹⁰⁷Seoul National University, Seoul, SOUTH KOREA
- ¹⁰⁸University of Bonn, Bonn, GERMANY
- ¹⁰⁹Kindai University, Higashiosaka, JAPAN
- ¹¹⁰Durham University, Durham, UK
- ¹¹¹Waseda University, Tokyo, JAPAN
- ¹¹²Birla Institute of Technology and Science, Pilani, INDIA
- ¹¹³Hiroshima University, Hiroshima, JAPAN
- ¹¹⁴University of California, Los Angeles, CA USA
- ¹¹⁵University of Witwatersrand, Johannesburg, SOUTH AFRICA
- ¹¹⁶University of California, Irvine CA USA
- ¹¹⁷University of Montenegro, Podgorica, MONTENEGRO
- ¹¹⁸Northwestern University, Evanston, IL USA
- ¹¹⁹Lebanese University, Beirut, LEBANON
- ¹²⁰Nihon University, Tokyo, JAPAN
- ¹²¹University of Warwick, Coventry, UK
- ¹²²Iwate University, Morioka, JAPAN
- ¹²³INFN, Rome, ITALY
- ¹²⁴University of Cambridge, Cambridge, UK
- ¹²⁵Nara Women's University, Nara, JAPAN
- ¹²⁶Tata Institute of Fundamental Research, Mumbai, INDIA
- ¹²⁷INFN, Milan, ITALY
- ¹²⁸Universidad Nacional Autónoma Mexico, Mexico City, MEXICO
- ¹²⁹Southampton University, Southampton, UK
- ¹³⁰Kobe University, Kobe, JAPAN
- ¹³¹TRIUMF, Vancouver, BC CANADA
- ¹³²Northeastern University, Boston, MA USA
- ¹³³Keio University, Tokyo, JAPAN
- ¹³⁴Tohoku ILC Promotion Council, Sendai, JAPAN
- ¹³⁵Tokyo Institute of Technology, Tokyo, JAPAN
- ¹³⁶University of Alabama, Tuscaloosa, AL USA
- ¹³⁷University of Victoria, Victoria, BC CANADA
- ¹³⁹Nippon Dental University, Niigata, JAPAN
- ¹⁴⁰Università della Calabria, Cosenza, ITALY
- ¹⁴¹INFN Cosenza, Cosenza, ITALY
- ¹⁴²INFN-LASA, Milan, ITALY
- ¹⁴³Weizmann Institute, Rehovot, ISRAEL
- ¹⁴⁴CINVESTAV, Mexico City, MEXICO
- ¹⁴⁵University of Manchester, Manchester, UK
- ¹⁴⁶University of Würzburg, Würzburg, GERMANY
- ¹⁴⁷University of Siegen, Siegen, GERMANY
- ¹⁴⁸Deutsches Elektronen-Synchrotron DESY, Zeuthen, GERMANY
- ¹⁴⁹University of Sussex, Brighton, UK
- ¹⁵⁰University of Utah, Salt Lake City, UT USA
- ¹⁵¹University of Heidelberg, Heidelberg, GERMANY
- ¹⁵²Michigan State University, Lansing, MI USA
- ¹⁵³Kokushikan University, Tokyo, JAPAN
- ¹⁵⁴Niigata University, Niigata, JAPAN
- ¹⁵⁵Yamagata University, Yamagata, JAPAN
- ¹⁵⁶Istanbul University, Istanbul, TURKEY
- ¹⁵⁷University of Delaware, Newark, DE USA
- ¹⁵⁸Indian Institute of Technology, Madras, INDIA
- ¹⁵⁹University of Illinois, Champaign, IL USA
- ¹⁶⁰Miyazaki University, Miyazaki, JAPAN
- ¹⁶¹Kogakuin University, Tokyo, JAPAN

- ¹⁶²Hebrew University, Jerusalem, ISRAEL
- ¹⁶³Institute of Nuclear Physics, Krakow, POLAND
- ¹⁶⁴Technion - Israel Institute of Technology, Haifa, ISRAEL
- ¹⁶⁵University of Arizona, Tucson, AZ USA
- ¹⁶⁶Ritsumeikon University, Kyoto, JAPAN
- ¹⁶⁷Toyama Prefectural University, Toyama, JAPAN
- ¹⁶⁸Iwate Prefectural University, Takizawa, JAPAN
- ¹⁶⁹Shinsu University, Nagano, JAPAN
- ¹⁷⁰University of California, Riverside, CA USA
- ¹⁷¹University of Hawaii, Honolulu, HI USA
- ¹⁷²Institute for Basic Science, Daejeon, SOUTH KOREA
- ¹⁷³Massachusetts Institute of Technology, Cambridge, MA USA
- ¹⁷⁴NIKHEF, Amsterdam, NETHERLANDS
- ¹⁷⁵Florida State University, Tallahassee, FL USA
- ¹⁷⁶Aix Marseille Univ, CNRS/IN2P3, CPPM, Marseille, FRANCE
- ¹⁷⁷Southern Methodist University, Dallas, TX USA
- ¹⁷⁸CQUEST, Sogang University, Seoul, SOUTH KOREA
- ¹⁷⁹University of Liverpool, Liverpool, UK
- ¹⁸⁰Indian Institute of Technology Bombay, Mumbai, INDIA
- ¹⁸¹SUNY Buffalo, Buffalo, NY USA
- ¹⁸²University of Birmingham, Birmingham, UK
- ¹⁸³University of Washington, Seattle, WA USA
- ¹⁸⁴University of Michigan, Ann Arbor, MI USA
- ¹⁸⁵University of Massachusetts, Amherst, MA USA
- ¹⁸⁶Institute of Space and Astronautical Science, Sagami-hara, JAPAN
- ¹⁸⁷Iowa State University Ames, IA USA
- ¹⁸⁸Zhejiang University, Zhejiang, CHINA
- ¹⁸⁹INFN, Frascati, ITALY

Contents

1	Introduction	23
1.1	Context for the ILC	23
1.2	Outline	25
2	Outline of the ILC Physics Case	27
3	Route to the ILC	31
3.1	International Development Team	33
3.2	ILC Pre-Lab	34
3.3	ILC Laboratory	38
3.4	Timeline for ILC Detectors	38
4	ILC Accelerator	41
4.1	ILC accelerator design	41
4.1.1	Design evolution since the TDR	43
4.1.2	Superconducting RF Technology	45
4.1.3	Accelerator design	55
4.1.4	Operation at the Z -pole	65
4.1.5	Civil engineering and site	67
4.1.6	Green ILC	69
4.1.7	ILC cost and schedule	75
4.2	ILC staging up to 1 TeV	77
4.2.1	Introduction	77

4.2.2	Parameters	78
4.2.3	Luminosity upgrade	78
4.2.4	Energy upgrade	79
4.2.5	Positron source	81
4.2.6	RTML	81
4.2.7	Beam Delivery System (BDS)	81
4.2.8	Polarization upgrade	82
4.2.9	Summary	82
4.3	R&D program on superconducting RF	82
4.3.1	Gradient status for the ILC baseline 250 GeV	83
4.3.2	High Gradient (45 MV/m) SRF for upgrade paths to 1 TeV	85
4.3.3	Toward 60 MV/m - advanced shape cavities	87
4.3.4	Nb ₃ Sn	92
4.4	ILC Accelerator technical preparation plan	95
4.5	Opportunities for US contributions	102
4.5.1	Superconducting linac	102
4.5.2	Electron and positron sources	104
4.5.3	Damping ring, beam delivery system, and beam dump	104
4.5.4	Summary	104
5	General Aspects of the ILC Physics Environment	105
5.1	Key Standard Model processes	105
5.2	Energy and luminosity	111
5.3	Beam polarization	112
5.4	Control of luminosity, beam energy and polarization	115
5.4.1	Luminosity measurement	115
5.4.2	Beam energy measurement	116
5.4.3	Polarization measurement	117
6	ILC Detectors	121

6.1	Detector requirements for the physics program	121
6.2	The ILD Detector	123
6.2.1	Concept of the ILD Detector	123
6.2.2	ILD vertexing system	125
6.2.3	ILD tracking system	126
6.2.4	ILD calorimeter- and muon system	128
6.2.5	ILD detector integration and costing	130
6.2.6	Future developments of the ILD detector	131
6.2.7	Science with ILD	132
6.2.8	Integration of ILD into the experimental environment	133
6.2.9	The ILD Concept Group	135
6.2.10	Conclusion and outlook	135
6.3	The SiD Detector	136
6.3.1	Detector description and capabilities	136
6.3.2	Silicon-based tracking	136
6.3.3	Vertex detector	137
6.3.4	Main tracker	139
6.3.5	Main calorimeters	140
6.3.6	Forward calorimeters	142
6.3.7	Magnet coil	142
6.3.8	Muon system	143
6.3.9	The machine-detector interface	143
6.3.10	R&D issues for the SiD design	143
6.4	New Technologies for ILC Detectors	145
6.4.1	Introduction	145
6.4.2	Low-mass support structures for Silicon trackers	146
6.4.3	Integrated micro-channel cooling	147
6.4.4	Dual read-out calorimetry	147
6.4.5	Crystal electromagnetic calorimetry	148

6.4.6	Liquid Argon calorimetry	148
6.4.7	Digital pixel calorimetry	149
6.4.8	Low gain avalanche detectors	150
6.4.9	New sensor technologies for highly compact electromagnetic calorimeters	151
6.4.10	Single crystal sapphire sensors for charged particle detection	152
6.4.11	Other novel sensor technologies	155
6.4.12	Gaseous RICH detector for particle ID at ILC	157
7	ILC Detector Simulation	159
7.1	ILC Fast Simulation Frameworks	159
7.1.1	DELPHES for ILC	159
7.1.2	SGV	160
7.2	ILCSoft framework	161
7.2.1	Simulation models	161
7.2.2	Event reconstruction	161
7.3	ILC SM Background Samples	162
7.3.1	Event generation	162
7.3.2	Beam induced background	162
7.3.3	Event Samples and data formats	163
8	ILC Physics Measurements at 250 GeV	165
8.1	Higgs – conventional decays	165
8.1.1	Zh cross-section and Higgs mass	167
8.1.2	Hadronic decays	167
8.1.3	Leptonic decays	169
8.1.4	Electroweak boson decays	169
8.1.5	CP properties	170
8.2	Higgs – exotic decays	170
8.3	Triple gauge couplings	174
8.4	Precision QCD	177

9	ILC Precision Electroweak Measurements	187
9.1	Introduction	187
9.2	Radiative Return to the Z	188
9.3	Di-fermion production	193
9.3.1	Di-fermion production at general CM energies	194
9.3.2	Di-fermion production at the Z pole	196
9.4	W and Z boson masses	197
9.4.1	Measurement of m_W	198
9.4.2	Measurement of m_Z and Γ_Z	202
9.5	W boson branching fractions	202
10	ILC Physics Measurements at 350, 500, and 1000 GeV	205
10.1	Top quark	205
10.1.1	Top quark mass	205
10.1.2	Boosted top quarks	209
10.1.3	Top quark electroweak couplings	209
10.1.4	Searches for FCNC interactions of the top quark	212
10.2	Higgs	212
10.2.1	WW fusion	212
10.2.2	Higgs self-coupling	213
10.2.3	Top quark Yukawa coupling	216
10.3	Triple gauge couplings	217
10.4	Quark and lepton pair-production	219
10.4.1	Full simulation studies	219
10.4.2	Z' limits	220
10.4.3	Indirect WIMP search	221
10.5	New Particle Searches – TeV Scale	221
10.5.1	SUSY	223
10.5.2	New scalars	227

10.5.3	WIMP dark matter	228
10.5.4	Heavy neutrinos	230
10.6	New particle searches – Dark Sector	234
11	ILC Fixed-Target Program	239
11.1	The physics of light Dark Sectors	239
11.2	ILC Facilities for fixed-target experiments	241
11.3	Dark Sector particle searches	243
11.4	Experiments on strong-field QED	246
12	Precision Tests of the Standard Model	249
12.1	Precision Standard Model theory for ILC	249
12.2	Standard Model Effective Field Theory	250
12.3	A practical SMEFT analysis for ILC	253
12.4	Expectations for the practical SMEFT fit	256
12.5	Expectations for the Higgs self-coupling	257
13	Big Physics Questions Addressed by ILC	261
13.1	Can the Standard Model be exact to very high energies?	261
13.2	Why is there more matter than antimatter?	264
13.3	What is the dark matter of the universe?	265
13.4	What is the energy scale of new physics?	267
13.5	Why is electroweak symmetry broken?	270
14	ILC and Models of Physics Beyond the Standard Model	273
14.1	ILC and dark matter	273
14.2	ILC and supersymmetry	275
14.2.1	Direct SUSY particle production	275
14.2.2	Observation of SUSY effects on the Higgs boson	278
14.3	ILC and composite Higgs fields	278
14.4	ILC and flavor	280

14.5	Mass Reach of Precision Higgs Measurements	281
14.6	The Higgs Inverse Problem	283
15	Long-Term Future of the ILC Laboratory	287
15.1	Physics opportunities for a multi-TeV collider	288
15.2	Physics opportunities for a multi-10 TeV collider	295
15.3	Very high gradient superconducting RF	297
15.4	Very high gradient normal conducting accelerators	304
15.5	Plasma, laser, and structure wakefield accelerators	311
16	Conclusions	315

Summary of the Report by Snowmass 2021 Topical Group

This report is a contributed paper written for the Snowmass 2021 study of the future of US particle physics. It is intended to be a reference document on all aspects of the proposed International Linear Collider (ILC), an electron-positron collider spanning the range of center of mass energies from the Z pole to 1 TeV. Although the report is written specifically from the viewpoint of the ILC project, much of the information we have gathered applies equally well to other Higgs factory proposals. Connections to other Snowmass Frontiers are discussed. To make this information more useful, we reference it here according to the Snowmass 2021 organization.

General

- **All:** A summary of the report and of the ILC physics case is presented in Chapters 1 and 2. The current status of the ILC and its potential realization in Japan is presented in Chapter 3. A general orientation to ILC physics and experimentation is presented in Chapter 5.

Energy Frontier

- **EF01:** Material on the ILC study of the Higgs boson is presented in Chapters 8 and 10, particularly in Secs. 8.1, 8.2, and 10.2. The ILC expectations for the precision of Higgs boson couplings are explained in Chapter 12.
- **EF02:** Material on the implications of the study of the Higgs boson and tests of Beyond-Standard-Model scenarios is presented in Secs. 8.1 and 8.2, and in Chapter 14.
- **EF03:** Material on study of heavy quarks at the ILC is presented in Secs. 9.3 and 10.1.
- **EF04:** Material on precision electroweak measurements at the ILC is presented in Chapter 9 and material on precision theory for the ILC and the interpretation of ILC data using Standard Model Effective Field theory is presented in Chapter 12.
- **EF05:** Material on precision QCD at the ILC is presented in Sec. 8.4.
- **EF08:** Material on searches for supersymmetric particles and extended Higgs sectors at the ILC is presented in Sec. 10.5 and 14.2.
- **EF09:** Material on ILC searches for a wide variety of Beyond-Standard-Model theories, including searches for new particles and decays and precision probes, is presented in Secs. 8.2, 10.1, 10.4, 10.5, 10.6, and Chapters 11 and 14.
- **EF10:** Material on the ILC searches for particles of dark matter and dark sectors is presented in Secs. 10.5, 10.6, 11.3, and 14.1.

Neutrino Physics Frontier

- **NF01:** Material on searches for TeV-mass particles appearing in models of neutrino mass is presented in Sec. 10.5.

Rare Processes and Precision Measurements

- **RF06:** Material on searches for dark sector particles in the ILC fixed target program is presented in Chapter 11.

Cosmic Frontier

- **RF06:** Material on the ILC searches for particles of dark matter and dark sections is presented in Secs. 10.5, 10.6, 11.3, and 14.1.

Theory Frontier

- **TF02:** Material on use of Effective Field Theory in the interpretation of ILC data is presented in Chapter 12.
- **TF06:** Material on the precision theory for ILC is presented in Secs. 8.4 and 12.1.
- **TF07:** Material on the theoretical interpretation of ILC results is presented in Chapters 13 and 14.
- **TF06:** Material on precision theory for ILC is presented in Secs. 8.4 and 12.1.
- **TF11:** Material on searches for TeV-mass particles appearing in models of neutrino mass is presented in Sec. 10.5.

Accelerator Frontier

- **AF03:** Material on the ILC accelerator design and R&D on ILC accelerator technologies is presented in Chapter 4.
- **AF04:** Material on extensions of the ILC to multi-TeV energies is presented in Chapter 15.
- **AF06:** Material on advanced accelerator technologies for the ILC laboratory is presented in Secs. 15.4 and 15.5.
- **AF07:** Material on many aspects of ILC accelerator technology is presented in Chapters 4 and 15. Material on the measurement of energy, luminosity, and beam polarization at the ILC is presented in Section 5.4.

Instrumentation Frontier

- **IF02 - IF07, IF09:** The ILD and SiD detectors proposed for the ILC are described as integrated concepts in Chapter 6. Material on new proposed technologies is presented in Section 6.4. The material here cuts across the various Instrumentation topical groups.

Community Engagement Frontier

- **CommF07:** Material on sustainable accelerator laboratory design and “Green ILC” is presented in Sec. 4.1.6.

Chapter 1

Introduction

The ILC is a proposed next-generation e^+e^- collider. It starts with $\sqrt{s} = 250$ GeV as the Higgs factory. The precision study of the Higgs boson is the next major goal in collider physics; the ILC will reach important benchmarks in the measurement of the Higgs boson couplings. Such high precision measurements will provide guidance to the next energy scale for future facilities. At the same time, the ILC provides numerous searches for new physics with monophoton or invisible and exotic Higgs decays, for example into a light dark sector. It can host ancillary experiments with beam dump and/or near IP detectors to search for long-lived and invisible particles. It is technologically mature with a well-understood cost that is about the same as the LHC. The linear design allows further phases at higher as well as lower energies. The ILC can have a dedicated run at the Z resonance, improving the measurement of the precision electroweak observables by an order of magnitude. Its length can be extended to reach the $t\bar{t}$ threshold and open $t\bar{t}$ as well as $t\bar{t}H$ production at 500–550 GeV. The site was specifically chosen to allow for an upgrade up to 1 TeV with the same technology, for the Higgs self-coupling measurement and many new physics searches. Superconducting RF cavity technology has ample room for improvements, allowing for even a 3–4 TeV collider in the same tunnel. Future technologies such as plasma wakefield or dielectric laser accelerators could reach the tens of TeV energy range.

This report is intended to be a comprehensive sourcebook on the ILC, discussing plans for the accelerator, the experimentation, and the physics analyses and also the physics context and theoretical implications of the ILC measurements. We hope that it will be useful to those who would like to better understand or evaluate the ILC proposal. Also, since the physics programs of all proposed Higgs factories are closely aligned, most of our physics discussion will also be helpful in understanding the physics prospects for all facilities of this type.

1.1 Context for the ILC

We first describe the context for the ILC as it has evolved over half a century of development in particle physics.

The need for a linear collider was recognized already in the 1960's given the energy loss due to unavoidable synchrotron radiation from beams in circular colliders. To achieve power-efficient acceleration, the development of superconducting radio frequency (SCRF) cavities started in earnest in the 1980's. Over four decades, intensive research and development achieved much higher acceleration gradients and reduced the costs of SCRF by more than an order of magnitude. SCRF provides better tolerances compared to room-temperature klystron-based designs, and was chosen as the ILC technology in 2005 by the International Technology Recommendation Panel chaired by Barry Barish. The International Committee for Future Accelerators, a body created by the International Union of Pure and Applied Physics in 1976 to facilitate international collaboration in the construction and use of accelerators for high energy physics, recommended the launch of the Global Design Effort (GDE) to produce a Technical Design Report (TDR) for the ILC as an international project. The GDE successfully produced the TDR in 2013 with a purposely site-independent design [1, 2, 3, 4, 5].

There is also a long history of discussions on the scientific merit for the ILC. The energy scale of the weak interaction, which makes the Sun burn and allows the synthesis of the chemical elements, was pointed out to be around 250 GeV in 1933 by Enrico Fermi. The need to reach this energy scale has been obvious since then, though the precise target energy was not clear. Early discussions for linear colliders called for 1000 GeV as a safe choice for guaranteed science output. The GDE focused on 500 GeV for the study of the Higgs boson based on the precision electroweak data of early 2000's. It was only in 2012 that the Higgs boson was discovered at the Large Hadron Collider (LHC) at CERN. This provided a clear target energy for the ILC at 250 GeV. In the same year, the Japanese Association of High-Energy Physicists (JAHEP) issued a report expressing interest in hosting the ILC in Japan with 250 GeV center-of-momentum energy as its first phase. The European Strategy for Particle Physics updated in 2013 highlighted “*the ILC, based on superconducting technology, will provide a unique scientific opportunity at the precision frontier.*” This was followed by the report of the US Prioritization Panel for Particle Physics Projects (P5) that listed “*Use the Higgs boson as a new tool for discovery*” as the first among the science drivers for particle physics and stated “*As the physics case is extremely strong, all (funding) Scenarios include ILC support*”.

Intense discussions ensued worldwide on how to realize the ILC. The Japanese government instituted a multitude of committees looking into the scientific and societal merit of hosting the ILC in Japan as well as its technological feasibility and costs. The US government encouraged Japan to host the ILC, with letters from the Secretary of Energy and the Deputy Secretary of State to Japanese Ministers. The 2020 update of the European Strategy for Particle Physics stated “*An electron-positron Higgs factory is the highest-priority next collider*” and added “*The timely realisation of the electron-positron International Linear Collider (ILC) in Japan would be compatible with this strategy and, in that case, the European particle physics community would wish to collaborate.*” Following this update, ICFA created the International Development Team (IDT) in August 2020 to prepare for the creation of prelab towards the realization of the ILC. The IDT is hosted by KEK, the national laboratory for high-energy accelerators in Japan.

Since its launch, the IDT has collected information, worked with ICFA, interacted with the community, consulted the funding agencies, to formulate what is required of the ILC Pre-Lab. The Pre-Lab is envisioned to be a four-year process, finalizing the Engineering Design Report for the ILC in a site-specific fashion for the Kitakami mountain range in northern Japan, forging agreements

among international partners, and recommending specific experiments for the ILC.

1.2 Outline

This report will update the information contained in the documents prepared by the ILC for the European Strategy for Particle Physics. Those documents include a comprehensive review of the ILC up to 2019 [6] and a review of the ILC capabilities for precision measurement [7]. A comprehensive bibliography for the ILC, up to mid-2020, can be found in [8].

The outline of this report is the following: Chapter 2 will present the most important points of the physics case for the ILC. In Chapter 3, we will present the status of the current plan to realize the ILC in Japan.

Chapter 4 will present the current state of the ILC accelerator design, including details of the various ILC energy stages up to a CM energy of 1 TeV. This chapter will also discuss the prospects for extension of the ILC to even higher energies and other issues for ILC accelerator R&D. It will conclude with a discussion of the opportunities and tentative plans for US contributions to the ILC accelerator.

Chapter 5 will review the basic aspects of the physics environment of the ILC—the major physics processes, the plan for stage-by-stage improvement in the energy and luminosity, and the key role played in the experimental program by electron and positron beam polarization.

Chapter 6 will describe the ILC detectors. We will begin with descriptions of the two current proposed detectors ILD and SiD, including the expected measurement capabilities and issues for which further R&D is needed. The chapter will conclude with a survey of new technologies that offer the promise of further improvements in the detector capabilities. Chapter 7 will describe the simulation framework used in studying the detector capabilities and projecting the measurement accuracy of physical observables.

Chapter 8 will describe the planned physics measurements at a CM energy of 250 GeV. These include measurements on the Higgs boson and the W boson, measurements of 2-fermion production, the ILC program in precision QCD, and descriptions of a number of relevant new particle searches.

Chapter 9 will describe the ILC program in precision electroweak measurements. This includes improvements of the precision electroweak parameters of the Z boson, both at 250 GeV through the radiative return reaction $e^+e^- \rightarrow \gamma Z$ and through a dedicated program of running at the Z resonance. It also includes high-precision measurements of the W boson mass and width and improved measurements of these properties for the Z boson.

Chapter 10 will describe the planned physics measurements at CM energies of 350 GeV and above, up to 1 TeV. The topics here include the ILC program of precision measurements of the top quark, the completion of the measurement of the Higgs boson profile, including the measurements of the Higgs self-coupling and the top quark Yukawa coupling, and the ultimate capabilities of the ILC in triple gauge boson couplings and new particle searches.

Chapter 11 will describe the fixed-target program that the intense, high-energy electron and

positron beams of the ILC will make available.

Chapters 12-14 will address the interpretation of the ILC measurements. Chapter 12 will begin with a review of the status of precision SM theory for ILC processes. It will then discuss the network of tests of the SM available at the ILC. This chapter will present a unified description of these tests using Standard Model Effective Field Theory (SMEFT), reviewing the conceptual basis of this approach and demonstrating its power in providing a unified interpretation of the full set of ILC experimental measurements. Chapter 13 will present a theoretical context for the expectation that the ILC will discover deviations from the SM predictions and the relation of such deviations to the most important question now being asked in particle physics. Chapter 14 will bring these two lines of analysis together, quantifying the ability of the ILC to overturn the SM and to provide evidence of the more correct underlying model for particle physics.

Finally, Chapter 15 will lay out some possible futures for the ILC laboratory with accelerators at still higher energies offering multi-TeV and multi-10-TeV electron, positron, and photon collisions.

Chapter 2

Outline of the ILC Physics Case

The physics motivation for constructing the ILC is very strong. The flagship program of the ILC is the study of the Higgs boson at a much higher level of precision than will be possible at the LHC. The ILC will also carry out precision measurements of the other heavy and still-mysterious particle in the Standard Model (SM), the top quark. It will carry out a program of specific searches for postulated new particles in regions that are very difficult for the LHC to access. Beyond these specific targets, the ILC will greatly improve the level of our understanding of the full set of electroweak processes in the region up to its final CM energy. In the context of Standard Model Effective Field Theory (SMEFT), these measurements will work together to strongly challenge the Standard Model. In this chapter, we will introduce each of these points and prepare the ground for a more detailed discussion later in this report.

We begin with the 125 GeV Higgs boson. This particle is the centerpiece of the SM, yet still we know little about it. From the LHC experiments, we now know that the couplings of the Higgs boson agree with those predicted in the SM, at the level of 20% accuracy for the major decay modes. However, this is not nearly sufficient to distinguish the minimal SM description of the Higgs boson from those of competing models. According to SMEFT, the deviations of Higgs couplings from SM predictions are parametrically of the order of m_h^2/M^2 , where M is the mass scale of additional new particles. Given the constraints from particle searches at the LHC, these deviations are expected to be at most of order 5-10%, and, to claim discovery of new physics, the deviations must be measured with high significance. This calls for a dedicated program to measure the full suite of couplings of the Higgs boson, and to push the precision of those measurements to the 1% level and below. This requires an e^+e^- collider such as the ILC.

The ILC is well-positioned to carry out this program of measuring the complete profile of the Higgs boson couplings. At 250 GeV, the ILC accesses the reaction $e^+e^- \rightarrow Zh$, producing about half a million Higgs bosons, each tagged by a recoil Z boson at the lab energy of 110 GeV. Looking in the opposite hemisphere, we will measure all of the branching ratios of the Higgs boson down to values of order 10^{-4} . These include 10 different modes of Higgs decay predicted in the SM, and also, possibly, invisible, partially-invisible, flavor changing, and other exotic modes of Higgs decay. By counting recoil Z bosons, we will obtain an absolute measurement of the cross section

for $e^+e^- \rightarrow Zh$, which can then be translated into absolute normalizations of the various partial widths.

At the second stage of the ILC at 500 GeV, the W fusion reaction $e^+e^- \rightarrow \nu\bar{\nu}h$ opens up. This reaction offers an event sample of about 1 million Higgs boson events in which the only visible signals in the event are from Higgs decay. This will not only allow new measurements to complement the 250 GeV data but also improved understanding of such issues as $h \rightarrow b\bar{b}/gg/c\bar{c}$ separation, angular distributions in $h \rightarrow WW^*$, and CP violation tests in $h \rightarrow \tau^+\tau^-$. The combination of the 250 and 500 GeV programs will give high confidence in any deviations from the SM detected in the Higgs boson data.

Running at 500 GeV and above also gives access to two important Higgs couplings that cannot be probed directly in Higgs decays, the Higgs coupling to $t\bar{t}$ and the Higgs self-coupling. Our studies of the ILC capabilities at 1 TeV predict truly archival measurements of these quantities, with errors below 2% and 10%, respectively.

Different models of new physics beyond the SM affect the various Higgs couplings differently. Since the ILC program can determine each Higgs coupling of the large set available, individually and without ambiguity, it will provide a pattern of deviations from the predictions of the SM that can distinguish different hypotheses about the underlying model.

The ILC program of experimental measurements on the Higgs boson will be described in Chapters 8 and 10 of this report, and the interpretation of these measurements will be discussed in some detail in Chapters 12 and 14.

The 500 GeV ILC will also give an excellent opportunity for the measurement of the mass and properties of the top quark. The mass of the top quark will be determined from the position of the sharp threshold in $e^+e^- \rightarrow t\bar{t}$. The threshold shape is determined by the short-distance top quark mass, so that the mass defined in this way, which is needed for high-precision predictions in and beyond the SM, is determined from the data without ambiguity. At e^+e^- colliders, the electroweak form factors of the top quark, which contain crucial information about the role of the top quark in electroweak symmetry breaking, determine the primary top quark pair production cross section. Thus, very high precision measurements of these form factors are possible. The ILC program of measurements on the top quark will be discussed in Chapter 10 of this report.

Beyond these SM particles, the ILC has the potential to access new particles predicted in models beyond the SM. The LHC experiments have given powerful access to proposed new particles with couplings to QCD, but their capability to discover particles with only electroweak couplings is limited. All LHC searches come with caveats concerning the sizes of electroweak cross sections, the expected decay patterns, the amount of missing energy, and other features. Searches at the ILC will allow these caveats to be eliminated, giving access to systems with large missing energy and other challenging features, in particular, to supersymmetry partners of the Higgs boson and to dark matter in models with compressed spectra. These issues will be described in Sections 8 and 10 of this report.

The ILC will dramatically improve the precision of our understanding of electroweak reactions. For example, the reaction $e^+e^- \rightarrow W^+W^-$ has strong dependence on both initial- and final-

state polarizations. At the ILC, we will have beam polarization in the initial state and complete reconstruction of the final state, allowing us to dissect the structure of the triple-gauge-boson coupling. The reactions $e^+e^- \rightarrow f\bar{f}$ allow searches for additional electroweak resonances that access the 10-TeV mass range and are flavor- and helicity-specific. The study of radiative-return events ($e^+e^- \rightarrow \gamma Z$) at 250 GeV will already improve our precision knowledge of Z -fermion couplings beyond that obtained at LEP. A dedicated ILC “Giga- Z ” run at the Z resonance ($5 \times 10^9 Z$ s) will improve the precision of most electroweak observables by more than an order of magnitude. These measurements and others are described in Chapters 8, 9, and 10.

The simplicity of hadronic final states in e^+e^- annihilation also allows not only higher precision tests of QCD but also new observables that give insight into features such as jet substructure that have come to light at the LHC. This new program of QCD measurements will be described in Chapter 8.

The ILC will also make available the most intense and highest-energy electron and positron beams for beam dump and dedicated fixed-target experiments to search for light weakly-interacting particles. This program will be described in Chapter 11.

These measurements are very powerful already when they are considered separately, but they take on increased power when they are combined in a coherent way to stress-test the SM. This becomes particularly clear when the full set of SM tests is analyzed using SMEFT. In this approach, corrections to the SM are described by contributions to an effective Lagrangian from operators of dimension 6 and higher invariant under the well-tested SM gauge symmetries. There is only one Lagrangian; its higher-dimension operators generally contribute to many electroweak reactions and so receive an array of experimental constraints. We will describe this method in detail and give examples of its powerful use in Chapter 12.

There is one more important point that we should make concerning the program of measurements of the ILC. The goal of testing the SM is not simply to improve the error bars. It is widely appreciated that the Standard Model of particle physics, though it is very successful in describing the results of experiments, is not adequate as a complete theory of elementary particles. The goal of the ILC experiments must be to *prove that the SM is incomplete*, and, even more, to show the path to a better understanding of nature.

One way to demonstrate the inadequacy of the SM is to discover a new resonance that the SM does not account for. This was the primary goal of the LHC experiments. So far, no such resonance has appeared. There is still considerable room to discover a new resonance at the HL-LHC, but that window is closing. It is important to open a new, complementary window, and this is what the ILC’s capability for precision tests of the SM will make available.

It is not straightforward, though, to demonstrate a deviation from the SM through precision measurements. First, of all, the deviation must be observed with high statistical significance. Second, the possible systematic uncertainties that could mimic the deviation must be under complete control. This calls for multiple cross-checks on the sources of uncertainty and, if possible, measurements with different sources of systematic uncertainty that can be compared. Finally, the view provided by precision measurements cannot be one-dimensional; rather, it should be part of a collective program that has the power to show a pattern of discrepancies. In the best case, a pattern

of well-established deviations from the SM can point to a common origin and thus indicate the nature of the true underlying theory.

The experimental program of the ILC is well-equipped to address these points. The general simplicity and cleanliness of e^+e^- annihilation provides an excellent starting point in the quest for precision. This environment allows the construction of detectors with high segmentation and very low material budget, allowing collider event measurements of unprecedented quality. In the energy region of the ILC, electroweak cross sections have a large and well-understood dependence on beam polarization. With the two signs for each of the electron and positron beam polarizations, the ILC will provide four distinct event samples, each with a distinct combination of physics process. By comparing these samples, we can determine detector performance and measure important backgrounds from data. As we have noted above for the Higgs boson program, changes in the center of mass energy can also bring in new physics processes that access and cross-check the variables targeted in precision measurements. The enabling features of the ILC experimental environment will be discussed in Chapter 5. The capabilities of detectors for the ILC and strategies for further improvement will be discussed in Chapter 6. Throughout the succeeding chapters, we will show these elements at work to ensure the high quality of the ILC measurements.

The ILC thus offers a new approach to the discovery of physics beyond the SM, one of great capability and robustness. These experiments must be carried out. They have the power to lead us to a new stage in our understanding of fundamental physics.

Chapter 3

Route to the ILC

This chapter will describe the organization, schedule, and prospects for the ILC as we currently understand these as of March 1, 2022. The future plans for the ILC organization are subject to decisions by ICFA in the coming years. In future versions of this report, we will update this section as required.

The worldwide community of particle physicists pursued the dream of realizing a high-energy e^+e^- linear collider since 1960s. By the end of 20th century, it was clear that such a machine can be built only as an international project because of its scale. The International Committee for Future Accelerators (ICFA) launched the serious effort to come up with a worldwide proposal in November 2003 [9], first by creating International Technology Recommendation Panel (ITRP). Under the chairmanship of Barry Barish from Caltech, the ITRP recommended [10] that the L-band superconducting RF cavity based on niobium is favored over the warm X-band copper-based cavity. ICFA unanimously endorsed this choice at its meeting in August 2004 in Beijing. This marked the beginning of the International Linear Collider (ILC) project.

ICFA launched the Global Design Effort (GDE) [11] in March 2005, with Barry Barish as the director, to produce a technical design for the ILC following the technology decision. Barish was assisted by three regional directors, Michael Harrison (Americas), Kaoru Yokoya (Asia), and Brian Foster (Europe). The design effort was specifically site unspecific, and the GDE was truly an international effort with more than 2000 scientists from more than 300 institutions in 49 countries. It aimed for a center-of-momentum energy of $\sqrt{s} = 500$ GeV, with expandability up to 1 TeV. It concluded its mission with the publication of the Technical Design Report (TDR) in June 2013 [12]. The site was left for a bid from interested countries.

It was a fortunate coincidence that the discovery of the Higgs boson was announced on July 4, 2012, a year before the publication of the TDR. Given its mass of 125 GeV, it became clear that an e^+e^- linear collider would be a perfect machine for the precision study of the Higgs boson. ICFA decided to launch a new organization named Linear Collider Collaboration (LCC), with a Linear Collider Board (LCB) as an oversight body, to follow the GDE and coordinate coordinate global research and development efforts for two next-generation particle physics colliders: the ILC, and the

Compact Linear Collider (CLIC) that published its Conceptual Design Report in 2012. The mission of the LCB and LCC was to promote constructing a linear collider as a global project. Members of the collaboration included approximately 2000 accelerator and particle physicists, engineers and other scientists from around the world. ICFA appointed Sachio Komamiya as the chair of the LCB and Lyn Evans as the director of the LCC. Evans was joined by three associate directors, Mike Harrison for the ILC, Steinar Stapnes for CLIC, and Hitoshi Yamamoto for Physics and Detectors, the deputy director Hitoshi Murayama, and three regional directors, Akira Yamamoto (Asia), Brian Foster (Europe), Harry Weerts (Americas), officially starting the LCC in March 2013 with a mandate for three years. The mandate was extended in December 2016, with Harrison replaced by Shichiro Michizono and Yamamoto by Jim Brau. The chair was succeeded by Tatsuya Nakada (EPFL). In October 2017, the LCC published a report [13] describing the machine parameters and cost for a 250 GeV machine as the first stage.

Before the launch of the LCC, the Japanese Association of High-Energy Physicists (JAHEP) issued a report in October 2012 [14], expressing interest in hosting the ILC in Japan with 250 GeV center-of-momentum energy as its first phase, followed by an upgrade to 500 GeV, maintaining the extendability to 1 TeV. This report marked the beginning of an international discussion to build the ILC with Japan as its potential host in mind, and the LCC put an emphasis on adopting the TDR to a site in Japan.

In parallel, the European Strategy for Particle Physics updated in 2013 highlighted “*the ILC, based on superconducting technology, will provide a unique scientific opportunity at the precision frontier.*” This was followed by the report of the US Prioritization Panel for Particle Physics Projects (P5) that listed “*Use the Higgs boson as a new tool for discovery*” as the first among the science drivers for particle physics and stated “*As the physics case is extremely strong, all (funding) Scenarios include ILC support*”.

To implement such vision for the ILC, KEK organized the International Working Group that published its report in October 2019 [15]. It laid out a framework for cost sharing. Civil engineering will be a responsibility of the Host State. Accelerator components will be provided by all Member States. Construction of conventional facilities will be managed by the ILC Laboratory, and the Host State will provide a significant part of the conventional facilities. The operational cost should be shared among Member States, and the way of sharing should be agreed upon before the construction begins. In addition, it proposed a preparatory laboratory (Pre-Lab) would be established based on a mutual understanding of the laboratories around the world and with the consent of their respective governmental authorities. The Pre-Lab would coordinate the preparatory tasks needed before the construction of the ILC. The Pre-Lab would also assist the inter-governmental negotiations, which are expected to take place in parallel. KEK will play a central role as the host laboratory of the Pre-Lab. After an inter-governmental agreement on the ILC, the Pre-Lab is expected to transition to a full ILC Laboratory. The ILC Laboratory will be responsible for the construction and operation of the ILC accelerator complex.

The Japanese government officially expressed interest in the ILC project at the meeting of the LCB, with the participation of members of the International Committee for Future Accelerators (ICFA), in March 2019 held at the University of Tokyo [16]. However, it stayed short of expressing interest in hosting the ILC. In February 2020, the Japanese government repeated its position

in the joint LCB-ICFA meeting held at SLAC in February 2020. In the same year, the 2020 update of the European Strategy for Particle Physics stated “*An electron-positron Higgs factory is the highest-priority next collider*” and added “*The timely realisation of the electron-positron International Linear Collider (ILC) in Japan would be compatible with this strategy and, in that case, the European particle physics community would wish to collaborate.*” It should also be noted that more than a hundred Diet members express interest in hosting the ILC in Japan, as well as the local politicians in the area of the proposed site.

Given all these developments, ICFA in August 2020, launched the International Development Team (IDT) [17, 18], replacing the LCC and the LCB, “*as the first step towards the preparatory phase of the ILC project, with a mandate to make preparations for the ILC Pre-Lab in Japan*” by the end of 2021.

3.1 International Development Team

The mission of the IDT [19] is to “*make preparations for the ILC Pre-Lab in Japan, as the first step of the preparation phase of the ILC project.*” ICFA appointed Tatsuya Nakada as the chair of the IDT hosted by KEK. The Executive Board (EB) also includes three regional representatives Steinar Stapnes (Europe), Andy Lankford (Americas), Geoffrey Taylor (Asia-Pacific), in addition to chairs of working groups. Each working group has a large number of scientists involved from around the world as can be seen from the websites linked below.

Nakada chairs both the EB and the Working Group 1 (WG1) [20] whose mission is to carry out, together with the Executive Board, the key tasks of developing the function and organizational structure for the ILC Pre-Lab and to support the preparation of scenarios for contributions with national and regional partners. Current members are Paul Collier (CERN), Bruce Dunham (SLAC), Eckhard Elsen (DESY), Brian Foster (Oxford), Juan Fuster (Valencia), Stuart Henderson (Jefferson Lab), Reiner Kruecken (TRIUMF), Joe Lykken (Fermilab), Maksym Titov (Saclay), and Satoru Yamashita (UTokyo).

The Working Group 2 (WG2) [21] is responsible for the accelerator design chaired by Shinichiro Michizono. WG2 is responsible for the preparation of the work plan of the ILC Pre-Lab. There are four subgroups: (1) Superconducting RF Technology (SRF), (2) Damping Rings (DR) / Beam Delivery System (BDS) / Dump, (3) Sources, (4) Civil Engineering. The four subgroups of WG2 are charged to discuss the technical preparation plan and possible schedule and international sharing at the Pre-Lab.

The Working Group 3 (WG3) [22] is responsible for the physics and detector activities chaired by Hitoshi Murayama. WG3 aims to raise awareness and interest in the ILC development and expand the community, support newcomers to get involved in physics and detector studies, encourage new ideas for experimentations at the ILC. The WG3 Steering Group consists of the coordinator (WG3 Chair), two deputy coordinators, subgroup conveners, and additional members of the Steering Group. The Physics Potential and Opportunities Subgroup [23] has many conveners for specific subjects.

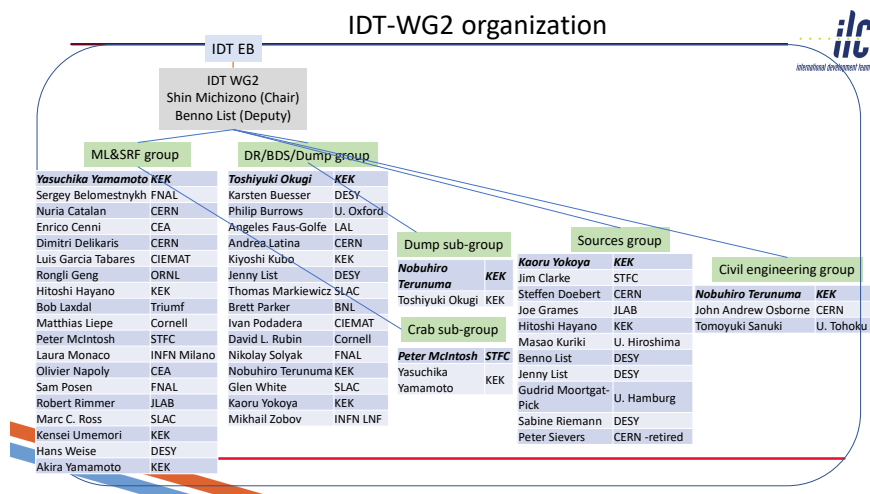


Figure 3.1: The current organization of the IDT WG2.

The IDT organized the ILC workshop on Potential Experiments (ILCX2021). At this workshop, it discussed expansion of the scope of the ILC facility beyond the collider experiments for the precision Higgs physics to include [24]:

- potential beam-dump experiments, fixed-target experiments, forward and off-axis detectors, to search for dark matter, long-lived particles, axion, etc,
- simulating Hawking radiation with strong QED that combines the ILC beam with powerful laser,
- nuclear physics applications for studies of pentaquarks, tetraquarks, electron-nucleus scattering,
- industrial applications with neutrons and muons from the beam dump such as studying soft error in self-driving automobiles, archeology, and non-destructive inspection of cargos,
- hard X-ray free electron laser for biological, medical, and material science,
- the Green ILC concept to recover spent energy of the beams for other purposes.

3.2 ILC Pre-Lab

The IDT put out a [proposal](#) for the ILC Pre-Lab [25] on June 1, 2021, to fulfill its mandate. It proposes a four-year Pre-Lab phase of the ILC for five purposes:

- Completion of technical preparations and production of engineering design documents for the accelerator complex.

WG3 Organisation and mandates

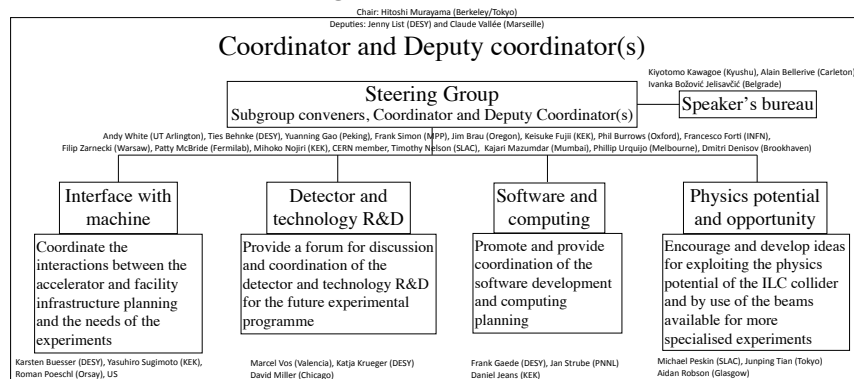


Figure 3.2: The current organization of the IDT WG3.

- Compilation of design studies and documentation of the civil engineering and site infrastructure work, and of the environmental impact assessment.
- Community guidance to develop the ILC physics programme that will fully exploit its potential.
- Provision of information to national authorities and to Japanese regional authorities to facilitate development of the ILC Laboratory.
- Coordination of outreach and communication work.

The proposed framework consists of mostly in-kind contribution from various laboratories around the world. The Pre-Lab is envisioned to be a legal entity in Japan to coordinate the activities with support from KEK and Japanese universities.

The MEXT Minister Koichi Hagiuda responded to a question during a session of the Diet budget committee concerning the ILC on February 25, 2021. A possible translation of his remark is

I am all in favor of building this facility in Japan, but it would require an international cooperation. If the proposal is to spend approximately two hundred million dollars for the preparatory phase, without a clear outlook (to fund the whole ILC project based on international cost sharing), I find it difficult to see how Japanese public would support such a spending. I believe it is imperative to obtain a broad support from both domestic and international communities as a prerequisite.

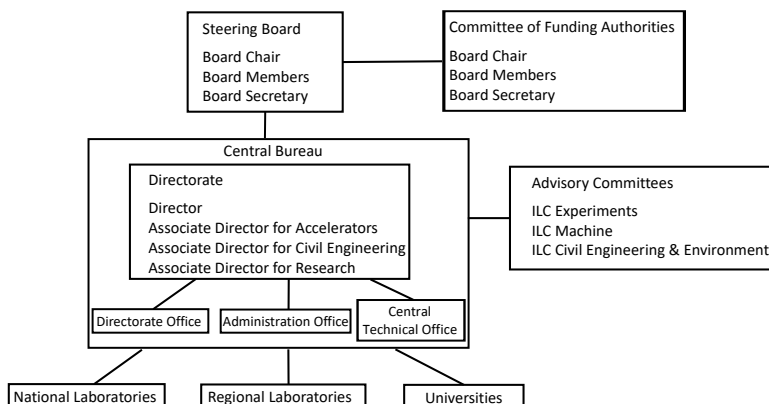


Figure 3.3: The proposed organization of the ILC Pre-Lab.

This remark detailed the push to launch the ILC Pre-Lab in Japan. KEK consulted MEXT to prepare a budget request for the ILC Pre-Lab in June 2021 but did not receive an encouragement. KEK in the end decided not to submit a budget request.

On the other hand, MEXT decided to constitute a second phase of the advisory panel to review the progress towards the realization of the ILC since the panel met three years earlier. The panel started its activity in July 2021, and concluded the process in February 2022.

The final report from the panel, also available in English [26], is summarised by KEK [27]:

1. The panel recognizes the academic significance of particle physics and the importance of the research activities, including that of a Higgs factory, and understands the value of international collaborative research. However, the panel found that it is still premature to proceed into the ILC Pre-Lab phase, which is coupled with an expression of interest to host the ILC by Japan as desired by the research community proposing the project.
2. Given the increasing strain in the financial situation of the related countries, the panel recommends the ILC proponents to reflect upon this fact and to reevaluate the plan. They should reexamine the approach towards a Higgs factory in a global manner taking into account the progress in the various studies such as the Future Circular Collider (FCC) and ILC.
3. The panel recommends that the development work in the key technological issues for the next-generation accelerator should be carried out by further strengthening the international collaboration among institutes and laboratories, shelving the question of hosting the ILC.
4. For realizing a very large project such as the ILC, cultivating a framework where the related countries can exchange information on their situations and discuss required steps would be important.
5. The panel recommends that the research community should continue efforts to expand the

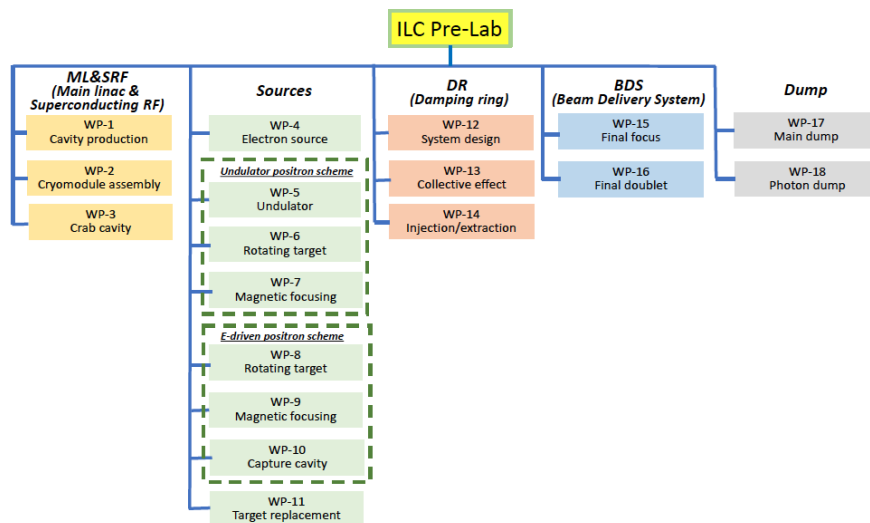


Figure 3.4: The proposed Work Packages of the ILC Pre-Lab.

broad support from various stakeholders in Japan and abroad by building up trust and mutual understanding through bi-directional communication with the people concerned.

The panel recognizes clearly the importance of particle physics, in particular a Higgs factory. Although the launch of the ILC Pre-Lab is judged to be premature, the report recommends the development work on the key technological issues, and points out the importance of building up an environment for discussion among governments on the ILC project.

In March 2022, the IDT EB is submitted a proposal to ICFA to continue its effort towards the ILC Pre-Lab under certain conditions. There has to be a substantial increase of funding from MEXT for “the development work in the key technological issues” to form an international collaboration based on MoUs among the laboratories. Since the Japanese government has not expressed interest in hosting the ILC in Japan, site-specific studies are excluded at this moment. Yet an expanded work on technology development based on international collaboration would advance a major part of the work envisaged for the Pre-Lab. In parallel, international discussions need to be developed in such a way that the Pre-Lab as originally envisioned will start in the 2024–2025 time frame. The site-specific study can commence only after the launch of the Pre-Lab.

At its meeting in March 2022, ICFA decided to prolong the mandate of the IDT by one year with a statement: “In particular, the IDT will work to further strengthen international collaboration among institutes and laboratories, and to expand the broad support from various stakeholders. ICFA will monitor developments over the next year to assess the availability of resources and progress in international discussions.”

Following the statement by ICFA, the IDT has identified time-critical issues in the work packages from the Pre-Lab proposal. Collaborative efforts between KEK and laboratories world-wide are being prepared to address them, and these will be formalized by MoUs. In Japan, discussion is advancing between KEK and MEXT for a substantial budget increase, for the Japanese Fiscal

Year 2023 starting in April 2023, for the development of ILC-related technologies. Once this is approved, it is expected that the support will continue. The IDT is also preparing to launch an international expert panel to start a general discussion on a global project for a large accelerator facility such as the ILC. Although the panel members are from the particle physics community, the discussion will proceed in close contact with government authorities. It is also planned to have occasional extended panel meetings inviting the government authorities to attend. This is to ensure that the conclusions will be commonly understood by the government authorities. Once this is done for the general discussion on the global project, the panel will proceed to the ILC-specific issues. The second step should lead to the starting of the Pre-Lab and governmental negotiation for the ILC construction. It is planned to have a substantial progress for the first step by the end of 2022. These two IDT activities are seen positively by MEXT and are supported by the Federation of Diet Members in Japan. It is hoped that the P5 process will observe these developments during its deliberations and take them into account in its final recommendations in early 2023.

3.3 ILC Laboratory

Once the Pre-Lab is launched and finishes the Engineering Design Report, and secures an overall agreement to fund the ILC project as a whole, the ILC Laboratory will be launched. Some ideas for the ILC Laboratory have been developed by the GDE/LCB [28] and the KEK International Working Group [15]. The overall framework for the ILC laboratory will be revisited by the IDT international expert panel in the second phase. The final decision on the laboratory structure and governance will be decided in the negotiation among the governments participating in the ILC construction.

It is envisioned that the ILC construction would take about nine years with an additional year of commissioning. This would require a stable organization to maintain steady funding and human resources from all participating countries.

3.4 Timeline for ILC Detectors

The originally envisioned timeline for the IDT and Pre-Lab is shown in Fig. 3.5.

We do not know when the process will begin to create the Pre-Lab, and unfortunately the schedule is uncertain and delayed. But once it does begin, it leaves rather little time for the standard process of Expression of Interest (EoI), Letters of Interest (LoI), and the actual proposal for experiments at the ILC.

Clearly, it is crucial for all potential experimental proposals to stay up-to-date with the developing technology and science case, to be ready when the opportunity arises.

Timeline for the ILC experiments

2021	IDT calls for EoI Necessary R&D for EoI
2022	----- Assumed start of Pre-lab -----
2022	EoI presentation Necessary R&D for Lol
2023	Lol submission and presentation Continuation of R&D Selection process by the ILCC
2024	ILCC recommendation on the first set of the projects to proceed toward TP Necessary R&D for TP
2025	TP submission and presentation of the first set of experiments Continuation of R&D Selection process by the ILCC
2026	----- Assumed start of ILC-lab -----
2026-27	ILCC recommendation for the first set of experiments to proceed toward TDRs
2027	ILC-lab approval of the first set of experiments and request to proceed toward TDRs

- Funding agencies will not provide dedicated ILC detector R&D funds before the Pre-lab being established.
- For some EoIs, R&D would be needed to make Lols.
→ driving the timing for the Lol submission
- Selection process starts with the Lols.
→ driving the timing for the Lol decision
- Experiments are formally approved based on TPs.
- The ILC-lab is needed for approvals.
- Availability of resources is part of the approval criteria.
→ driving the timing for the TP decision
- These considerations are for the initial set of experiments. There could be more experiments proposed at later time.

IDT-EB 21/12/2020

Figure 3.5: The originally envisioned timeline for the Pre-Lab and ILC detectors.

Chapter 4

ILC Accelerator

4.1 ILC accelerator design

The International Linear Collider (ILC) is a 250 GeV (extendable up to 1 TeV) linear e^+e^- collider, based on 1.3 GHz superconducting radio-frequency (SCRF) cavities. It is designed to achieve a luminosity of $1.35 \cdot 10^{34} \text{ cm}^{-2}\text{s}^{-1}$ and provide an integrated luminosity of 400 fb^{-1} in the first four years of running. The electron beam will be polarized to 80 %, and positrons with 30 % polarization will be provided if the undulator based positron source concept is employed.

Its parameters have been set by physics requirements first outlined in 2003, updated in 2006, and thoroughly discussed over many years with the physics user community. After the discovery of the Higgs boson it was decided that an initial energy of 250 GeV provides the opportunity for a precision Standard Model and Higgs physics programme at a reduced initial cost [29]. Some relevant parameters are given in Table 4.1. This design evolved from two decades of R&D, described in Sec. 1, an international effort coordinated first by the GDE under ICFA mandate and since 2013 by the Linear Collider Collaboration (LCC).

The design of the ILC accelerator is governed by the goal of high power-efficiency. The overall power consumption of the accelerator complex during operation is 111 MW at 250 GeV and is limited to 300 MW at 1 TeV, which is about 70 % more than today's peak power consumption of CERN [31]. This is achieved by the use of SCRF technology for the main accelerator, which offers a high RF-to-beam efficiency through the use of superconducting cavities, operating at 1.3 GHz, where high-efficiency klystrons are commercially available. At accelerating gradients of 31.5 to 35 MV/m this technology offers high overall efficiency and reasonable investment costs, even considering the cryogenic infrastructure needed for the operation at 2 K.

The underlying TESLA technology is mature, with a broad industrial base throughout the world, and is in use at a number of free electron laser facilities that are in operation (FLASH [32, 33] and European XFEL [34] at DESY, Hamburg), under construction (LCLS-II [35] at SLAC, Stanford) or in preparation (SHINE [36, 37] in Shanghai) in the three regions Asia, Americas, and Europe that contribute to the ILC project. In preparation for the ILC, Japan and the U.S. have founded a

Quantity	Symbol	Unit	Initial	\mathcal{L} Upgrade	Z pole	Upgrades
Centre of mass energy	\sqrt{s}	GeV	250	250	91.2	500
Luminosity	\mathcal{L}	$10^{34} \text{cm}^{-2} \text{s}^{-1}$	1.35	2.7	0.21/0.41	1.8/3.6
Polarization for e^-/e^+	$P_-(P_+)$	%	80(30)	80(30)	80(30)	80(30)
Repetition frequency	f_{rep}	Hz	5	5	3.7	5
Bunches per pulse	n_{bunch}	1	1312	2625	1312/2625	2625
Bunch population	N_e	10^{10}	2	2	2	2
Linac bunch interval	Δt_b	ns	554	366	554/366	366
Beam current in pulse	I_{pulse}	mA	5.8	8.8	5.8/8.8	8.8
Beam pulse duration	t_{pulse}	μs	727	961	727/961	961
Average beam power	P_{ave}	MW	5.3	10.5	1.42/2.84*	10.5/21
RMS bunch length	σ_z^*	mm	0.3	0.3	0.41	0.3
Norm. hor. emitt. at IP	$\gamma\epsilon_x$	μm	5	5	6.2	5
Norm. vert. emitt. at IP	$\gamma\epsilon_y$	nm	35	35	48.5	35
RMS hor. beam size at IP	σ_x^*	nm	516	516	1120	474
RMS vert. beam size at IP	σ_y^*	nm	7.7	7.7	14.6	7.7
Luminosity in top 1%	$\mathcal{L}_{0.01}/\mathcal{L}$		73%	73%	99%	58.3%
Beamstrahlung energy loss	δ_{BS}		2.6%	2.6%	0.16%	4.5%
Site AC power	P_{site}	MW	111	128	94/115	173/215
Site length	L_{site}	km	20.5	20.5	20.5	31

Table 4.1: Summary table of the ILC accelerator parameters in the initial 250 GeV staged configuration and possible upgrades. A 500 GeV machine could also be operated at 250 GeV with 10 Hz repetition rate, bringing the maximum luminosity to $5.4 \cdot 10^{34} \text{cm}^{-2} \text{s}^{-1}$ [30]. *): For operation at the Z-pole additional beam power of 1.94/3.88 MW is necessary for positron production.

collaboration for further cost optimisation of the TESLA technology. In recent years, new surface treatment technologies utilising nitrogen during the cavity preparation process, such as the so-called nitrogen infusion technique, have been developed at Fermilab, with the prospect of achieving higher gradients and lower loss rates with a less expensive surface preparation scheme than assumed in the TDR (see Sec. 4.3).

When the Higgs boson was discovered in 2012, the Japan Association of High Energy Physicists (JAHEP) made a proposal to host the ILC in Japan [38, 39]. Subsequently, the Japanese ILC Strategy Council conducted a survey of possible sites for the ILC in Japan, looking for suitable geological conditions for a tunnel up to 50 km in length (as required for a 1 TeV machine), and the possibility to establish a laboratory where several thousand international scientists can work and live. As a result, the candidate site in the Kitakami region in northern Japan, close to the larger cities of Sendai and Morioka, was found to be the best option. The site offers a large, uniform granite formation with no currently active faults and a geology that is well suited for tunnelling. Even in the great Tohoku earthquake in 2011, underground installations in this rock formation were essentially unaffected [40], which underlines the suitability of this candidate site.

This section starts with a short overview of the changes of the ILC design between the publication of the TDR in 2013 and today, followed by a description of the SCRF technology, and a description of the overall accelerator design and its subsystems. Thereafter, possible upgrade options are laid out, the Japanese candidate site in the Kitakami region is presented, and costs and schedule of the accelerator construction project are shown.

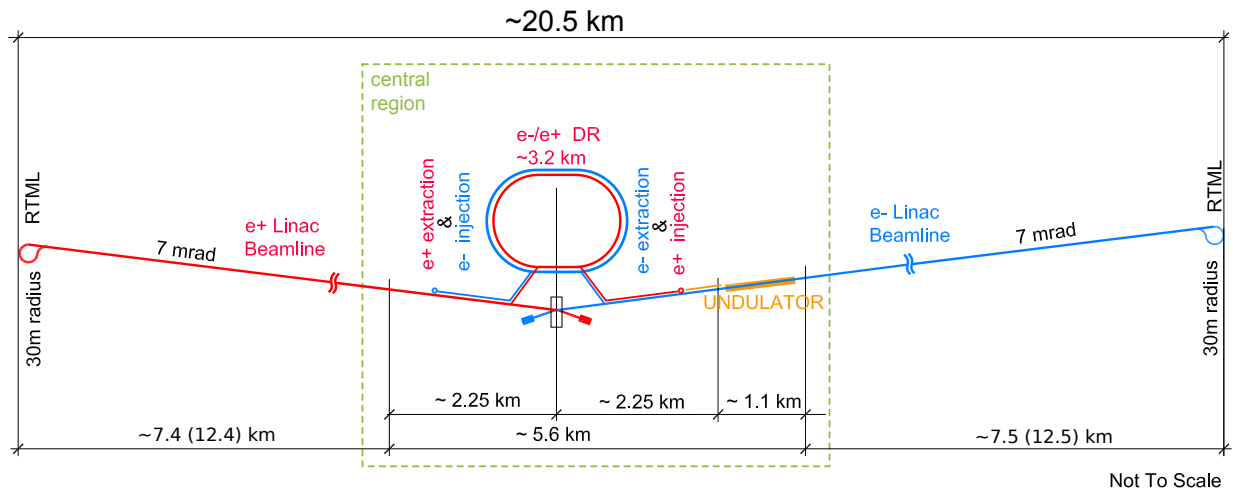


Figure 4.1: Schematic layout of the ILC in the 250 GeV staged configuration.

4.1.1 Design evolution since the TDR

Soon after the discovery of the Higgs boson, the TDR for the ILC accelerator was published in 2013 [3, 4] after 8 years of work by the Global Design Effort (GDE). The TDR design was based

on the requirements set forth by the ICFA mandated parameters committee [41]:

- a centre-of-mass energy of up to 500 GeV,
- tunability of the centre-of-mass energy between $\sqrt{s} = 200$ GeV and 500 GeV,
- a luminosity sufficient to collect 500 fb^{-1} within four years of operation, taking into account a three-year ramp up. This corresponds to a final luminosity of 250 fb^{-1} per year and an instantaneous luminosity of $\mathcal{L} = 2 \cdot 10^{34} \text{ cm}^{-2} \text{ s}^{-1}$,
- an electron polarization of at least 80 %,
- the option for a later upgrade to energies up to 1 TeV.

The accelerator design presented in the TDR met these requirements at an estimated construction cost of 7,982 MILCU for a Japanese site, plus 22.9 Mh (million hours) of labor in participating institutes [4, Sec. 15.8.4]. Costs were expressed in ILC Currency Units, ILCU, where 1 ILCU corresponds to 1 US\$ at 2012 prices.

In the wake of the Higgs discovery and the JAHEP proposal to host the ILC in Japan [38, 39], plans were made for a lower cost facility operating at $\sqrt{s} = 250$ GeV near the maximum of the $e^+e^- \rightarrow Zh$ cross section. A revised plan based on the TDR [4, Sect. 12.5] and subsequent analyses [42] was made for a machine with 125 GeV polarized beams and a luminosity of $\mathcal{L} = 1.35 \cdot 10^{34} \text{ cm}^{-2} \text{ s}^{-1}$, capable of delivering about 200 fb^{-1} per year, or 400 fb^{-1} within the first four years of operation.

Several other changes of the accelerator design have been approved by the ILC Change Management Board since 2013, in particular:

- The free space between the interaction point and the edge of the final focus quadrupoles (L^*) was unified between the ILD and SiD detectors [43], facilitating a machine layout with the best possible luminosity for both detectors.
- A vertical access shaft to the experimental cavern was foreseen [44], allowing a CMS-style assembly concept for the detectors, where large detector parts are built in an above-ground hall while the underground cavern is still being prepared.
- The shield wall thickness in the Main Linac tunnel was reduced from 3.5 to 1.5 m [45], leading to a significant cost reduction. This was made possible by dropping the requirement for personnel access during beam operation of the main linac.
- Power ratings for the main beam dumps, and intermediate beam dumps for beam aborts and machine tuning, were reduced to save costs [46].
- A revision of the expected horizontal beam emittance at the interaction point at 125 GeV beam energy, based on improved performance expectations for the damping rings and a more thorough scrutiny of beam transport effects at lower beam energies, lead to an increase of the luminosity expectation from 0.82 to $1.35 \cdot 10^{34} \text{ cm}^{-2} \text{ s}^{-1}$ [47].

- The active length of the positron source undulator has been increased from 147 to 231 m to provide sufficient intensity at 125 GeV beam energy [48].

These changes contributed to an overall cost reduction, risk mitigation, and improved performance expectation.

Several possibilities were evaluated for the length of the initial tunnel. Options that include building tunnels with the length required for a machine with $\sqrt{s} = 350$ GeV or 500 GeV, were considered. In these scenarios, an energy upgrade would require the installation of additional cryomodules (with RF and cryogenic supplies), but little or no civil engineering activities. In order to be as cost effective as possible the final proposal endorsed by ICFA [49] does not include these empty tunnel options.

While the length of the main linac tunnel was reduced, the beam delivery system and the main dumps are still designed to allow for an energy upgrade up to $\sqrt{s} = 1$ TeV.



Figure 4.2: A 1.3 GHz superconducting niobium nine-cell cavity.

4.1.2 Superconducting RF Technology

The heart of the ILC accelerator consists of the two superconducting Main Linacs that accelerate both beams from 5 to 125 GeV. These linacs are based on the TESLA technology: beams are accelerated in 1.3 GHz nine-cell superconducting cavities made of niobium and operated at 2 K (Fig. 4.2). These are assembled into cryomodules comprising nine cavities or eight cavities plus a quadrupole/corrector/beam position monitor unit, and all necessary cryogenic supply lines (Fig. 4.3). Pulsed klystrons supply the necessary radio frequency power (High-Level RF HLRF) to the cavities by means of a waveguide power distribution system and one input coupler per cavity.

This technology was primarily developed at DESY for the TESLA accelerator project that was proposed in 2001. Since then, the TESLA technology collaboration [50] has been improving this technology, which is now widely used around the world. As discussed in Section 4.3, the TESLA technology is based on a history of superconducting accelerator projects of more than 50 years, starting in the 1970s with the Illinois Microtron Superconducting Linac and the Stanford Superconducting Accelerator. Today, a large number of superconducting accelerators such as CEBAF at Jefferson Lab, SNS at Oak Ridge Laboratory, or FRIB at Michigan State University, to name just a few U.S. facilities, are in operation, demonstrating the success of this approach.



Figure 4.3: An ILC type cryomodule. ©Rey.Hori/KEK.

The quest for high gradients

The single most important parameter for the cost and performance of the ILC is the accelerating gradient g . The TDR baseline value is an average gradient $g = 31.5 \text{ MV/m}$ for beam operation, with a $\pm 20\%$ gradient spread between individual cavities. Recent progress in R&D for high gradient cavities raises the hope to increase the gradient by 10% to $g = 35 \text{ MV/m}$, which would reduce the total cost of the 250 GeV accelerator by about 6%. To achieve the desired gradient in beam operation, the gradient achieved in the low-power vertical test (mass production acceptance test) is specified 10% higher to allow for operational gradient overhead for low-level RF (LLRF) controls, as well as some degradation during cryomodule assembly (few MV/m). Section 4.3 discusses the evolution of achievable gradients have evolved over the past 50 years, and the prospects for further improvements.

Gradient impact on costs: To the extent that the cost of cavities, cryomodules and tunnel infrastructure is independent of the achievable gradient, the investment cost per GeV of beam energy is inversely proportional to the average gradient achieved. This is the reason for the enormous cost saving potential from higher gradients. This effect is partially offset by two factors: the energy stored in the electromagnetic field of the cavity, and the dynamic heat load to the cavity from the electromagnetic field. These grow quadratically with the gradient for one cavity, and therefore linearly for a given beam energy. The electromagnetic energy stored in the cavity must be replenished by the RF source during the filling time that precedes the time when the RF is used to accelerate the beam passing through the cavity; this energy is lost after each pulse and thus reduces the overall efficiency and requires more or more powerful modulators and klystrons. The overall cryogenic load is dominated by the dynamic heat load from the cavities, and thus operation at higher gradient requires larger cryogenic capacity. Cost models that parametrise these effects indicate that the minimum of the investment cost per GeV beam energy lies at 50 or more GeV, depending on the relative costs of tunnel, SCRF infrastructure and cryo plants, and depending on the achievable Q_0 [51]. Thus, the optimal gradient is significantly higher than the value of approximately 35 MV/m that is currently realistic; this emphasises the relevance of achieving higher

gradients.

It should be noted that in contrast to the initial investment, the operating costs rise when the gradient is increased, and this must be factored into the cost model. The reason for this is that the energy stored in the cavity, which is lost after each pulse, as well as the heat generated in the cavity walls rise with the square of the gradient, thus leading to a rise of electricity need with gradient that is linear to first order.

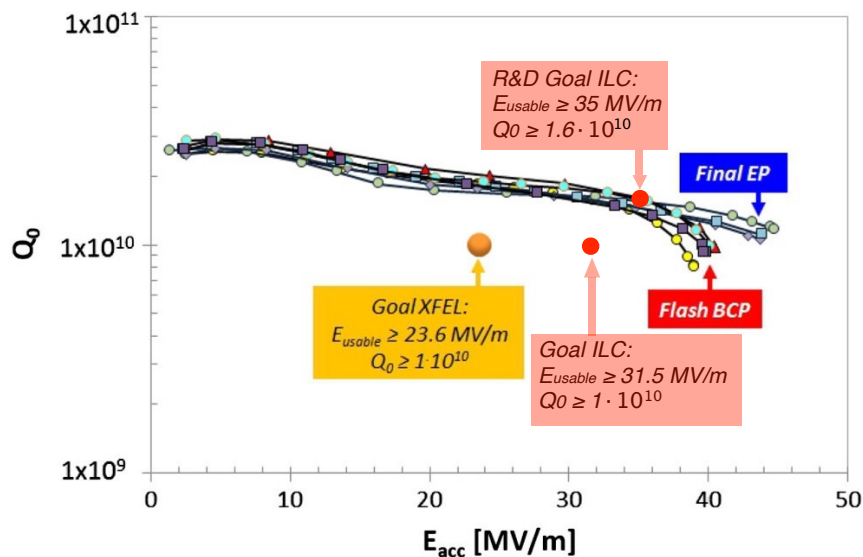


Figure 4.4: Examples of the $Q_0(E_{acc})$ curves of some of the best cavities, either treated at RI using “EP final”, or at EZ using “BCP flash.” [52, Fig. 19]. RI employs a production process that closely follows the ILC specifications, with a final electropolishing step. The ILC gradient / Q_0 goals are overlaid.

Results from European XFEL cavity production: The production and testing of 831 cavities for the European XFEL [52, 53] provides the biggest sample of cavity production data so far. Cavities were acquired from two different vendors, Research Instruments (RI) and Zanon Research (EZ). RI employed a production process with a final surface treatment closely following the ILC specifications, including a final electropolishing (EP) step, while EZ used buffered chemical polishing (BCP). The European XFEL specifications asked for a usable gradient of 23.6 MV/m with a $Q_0 \geq 1 \cdot 10^{10}$ for operation in the cryomodule; with a 10 % margin this corresponds to a target value of 26 MV/m for the performance in the vertical test stand for single cavities. Figure 4.4 shows the Q_0 data versus accelerating gradient of the best cavities received, with several cavities reaching more than 40 MV/m, significantly beyond the ILC goal, already with Q_0 values that approach the target value $1.6 \cdot 10^{10}$ that is the goal of future high-gradient R&D.

European XFEL production data, in particular from vendor RI, provide excellent statistics for the cavity performance as received from the vendors, as shown in Fig. 4.5. For vendor RI, the yield

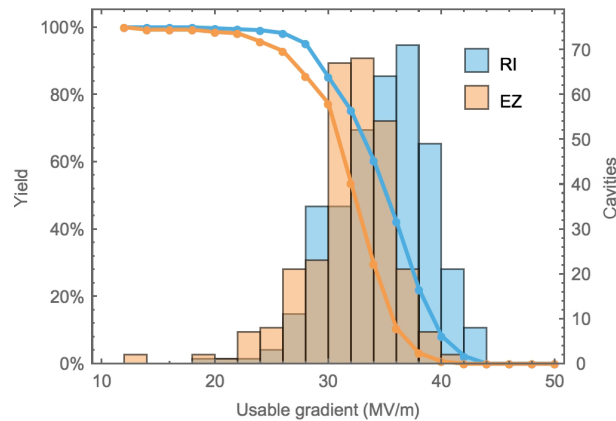


Figure 4.5: Distribution and yield of the “as received” maximum gradient of cavities produced for the European XFEL, separated by vendor [53, Fig. 33]. Vendor RI employs a production process that closely follows the ILC specifications, with a final electro polishing step.

for cavities with a maximum gradient above 28 MV/m is 85%, with an average of 35.2 MV/m for the cavities that pass the cut.

Since the European XFEL performance goal was substantially lower than the ILC specifications, cavities with gradient below 28 MV/m, which would not meet ILC specifications, were not generally re-treated for higher gradients, limiting our knowledge of the effectiveness of re-treatment for large gradients. Still, with some extrapolation it is possible to extract yield numbers applicable to the ILC specifications [54].

The European XFEL data indicate that after re-treating cavities with gradients outside the ILC specification of $35 \text{ MV/m} \pm 20\%$, *i.e.*, below 28 MV/m, a yield of 94% for a maximum gradient above 28 MV/m can be achieved, with an average value of 35 MV/m, meeting the ILC specification. Taking into account limitations from Q_0 and the onset of field emission, the usable gradient is lower. This gives a 82 (91)% yield and an average usable gradient of 33.4 MV/m after up to one (two) re-treatments. The re-treatment and testing rate is significantly higher than assumed in the TDR, but the European XFEL experience shows that re-treatment can mostly be limited to a simple high-pressure rinse (HPR) rather than an expensive electropolishing step.

Overall, the European XFEL cavity production data demonstrate that it is possible to mass-produce cavities meeting the ILC specifications as laid out in the TDR with the required performance and yield.

Choice of RF frequency

The choice of operating frequency is a balance between the higher cost of larger, lower-frequency cavities and the increased cost at higher frequency associated with the lower sustainable gradient from the increased surface resistivity. The optimum frequency is in the region of 1.5 GHz, but

during the early R&D on the technology, 1.3 GHz was chosen due to the commercial availability of high-power klystrons at that frequency.

Cavities

The superconducting accelerating cavities for the ILC are nine-cell structures made out of high-purity niobium (Fig. 4.2), with an overall length of 1.25 m and an active length of 1.038 m. Cavity production starts from niobium ingots which are forged and rolled into 2.8 mm thick niobium sheets that are individually checked for defects by an eddy current scan and optical inspection [3]. Cavity cells are produced by deep-drawing the sheets into half cells, 18 of which are joined by electron beam welding with two end groups to form the whole structure. This welding process is one of the most critical and cost-intensive steps of the cavity manufacturing procedure. Utmost care must be taken to avoid irregularities, impurities and inclusions in the weld itself, and deposition of molten material at the inner surface of the cavity that can lead to field emission.

After welding, the inner surface of the cavity must be prepared. The process is designed to remove material damage incurred by chemical procedures during the fabrication process, chemical residues from earlier production steps, hydrogen in the bulk niobium from earlier chemical processing, and contamination from particles. In a last step, the cavity is closed to form a hermetically sealed structure ready for transport. The treatment steps involve a series of rinses with ethanol or high pressure water, annealing in a high purity vacuum furnace at 800° C and 120° C, and electropolishing or buffered chemical polishing. The recipe for the surface preparation has been developed over a long time. Still, it remains subject to optimisation, since it is a major cost driver for the cavity production and largely determines the overall performance and yield of the cavities. In particular the electropolishing steps are complicated and costly, as they require complex infrastructure and highly toxic chemicals. An important advantage of nitrogen infusion and other novel surface treatment processes (see Sec. 4.3.2) is that the final electropolishing step is omitted.

Careful quality control during the production process is of high importance. At the European XFEL, several quality controls were conducted by the manufacturer during production, with non-conformities reported to the institute responsible for the procurement, where a decision was made whether to accept or reject a part [52]. With this “build to print” approach, in which the manufacturer guarantees that a precise production process will be followed but does not guarantee a specific performance, procurement costs are reduced, because the manufacturer does not carry, and does not charge for, the performance risk.

Upon reception from the manufacturer, cavities are tested in a vertical cryostat (“vertical test”), where Q_0 is measured as a function of the gradient. Cavities that fall below the specified gradient goal are re-treated by an additional (expensive) electropolishing step or a comparatively simple high-pressure rinse. After retreatment, the vertical test is repeated.

Re-treatment and tests constitute a major cost driver in cavity production. For the ILC TDR, it was assumed that 25 % of the cavities would fall below the 28 MV/m gradient threshold and undergo re-treatment and a second vertical test. European XFEL data from RI that followed the ILC production recipe indicate that 15 % to 37 % of the cavities fall below 28 MV/m, depending on

whether the maximum or the “usable” achieved gradient is considered [54].

After successful testing, prior to installation in the cryomodule, cavities are equipped with a magnetic shield and the frequency tuner, which exerts mechanical force on the cavity to adjust the resonant frequency to the frequency of the external RF field [4, Sect. 3.3].

Power coupler

The power coupler transfers the radio frequency (RF) power from the waveguide system to the cavity. In the ILC, a coupler with a variable coupling coefficient is employed; this is realised using a movable antenna. Another role of the coupler is to separate the cavity vacuum from the atmospheric pressure in the waveguide, and to insulate the cavity at 2 K from the surrounding room temperature. Thus, the coupler has to fulfill a number of demanding requirements: transmission of high RF power with minimal losses and no sparking, vacuum tightness and robustness against window breaking, and minimal heat conductivity. As a consequence, the coupler design is highly complex, with a large number of components and several critical high-tech manufacturing steps.

The baseline coupler design was originally developed in the 1990s for the TESLA Test Facility (TTF, now FLASH) at DESY, and has since been modified by a collaboration of LAL and DESY for use in the European XFEL. About 840 of these couplers (depicted in Fig. 4.6) were fabricated by three different companies for the European XFEL [55], where 800 are now in operation. A lot of experience has been gained from this production [56].

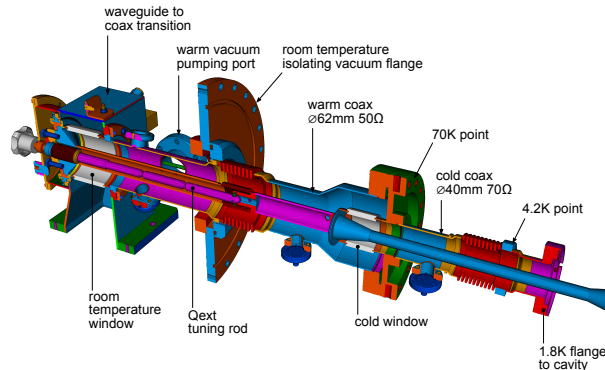


Figure 4.6: An European XFEL type coupler.

Cryomodules

To facilitate transportation, installation and operation, 8 or 9 cavities are integrated into a 12.6 m long cryomodule (Fig. 4.3), which houses the cavities, thermal insulation, and all necessary supply tubes for liquid and gaseous helium at 2 – 80 K temperature.

Nine of these cryomodules are connected in the tunnel to form a cryostrring with a common liquid

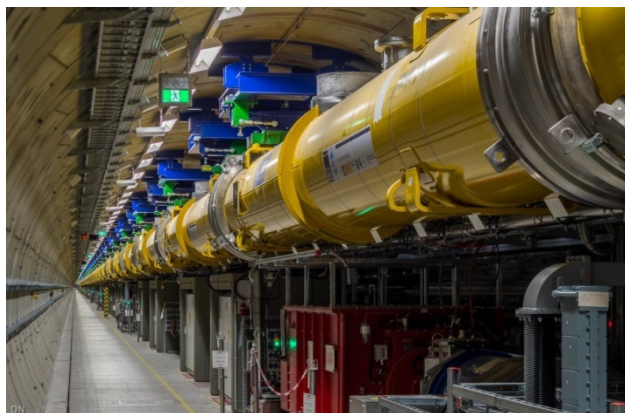


Figure 4.7: View of installed cryomodules in the tunnel of the European XFEL [57].

helium supply. RF for one such string is provided by two klystrons. No separate helium transfer line is necessary, as all helium transport lines are integrated within the modules. A quadrupole / beam position monitor / corrector magnet unit is mounted instead of the 9th cavity in every third module. Figure 4.7 shows installed cryomodules in the tunnel of the European XFEL [57].

Cryomodule assembly requires a dedicated facility with large clean rooms, especially trained, experienced personnel, and thorough quality control [58]. The cryomodules are certified for liquid helium pressure of up to 2 bar. Thus they must conform to the applicable pressure vessel codes, which brings with it very stringent documentation requirements for all pressure bearing parts [59].

For the European XFEL project, 103 cryomodules were produced at production rate is close to the rate envisaged for a possible European contribution of 300 cryomodules to a 250 GeV ILC in Japan.

While the design gradient for European XFEL accelerator modules of 23.6 MV/m is significantly lower than the aim of 31.5–35 MV/m for the ILC, a number of cryomodules have been built around the world that come close to or reach the ILC TDR specification of 31.5 MV/m: An European XFEL prototype module at DESY reached 30 MV/m [60], Fermilab has demonstrated cryomodule operation at the ILC specification of 31.5 MV/m [61], and KEK has reported stable pulsed operation of a cryomodule at 36 MV/m [62].

Figure 4.8 shows the average cavity gradients per cryomodule for the European XFEL serial-production cryomodules [63]. In the tests, the gradients were limited administratively to 31 MV/m; the true maxima might be higher. For almost all of the modules, the cavity gradients are significantly above the European XFEL specification of 23.6 MV/m.

Plug-compatible design

In order to allow various designs of sub-components from different countries and vendors to work together in the same cryomodule, a set of interface definitions has been internationally agreed upon.

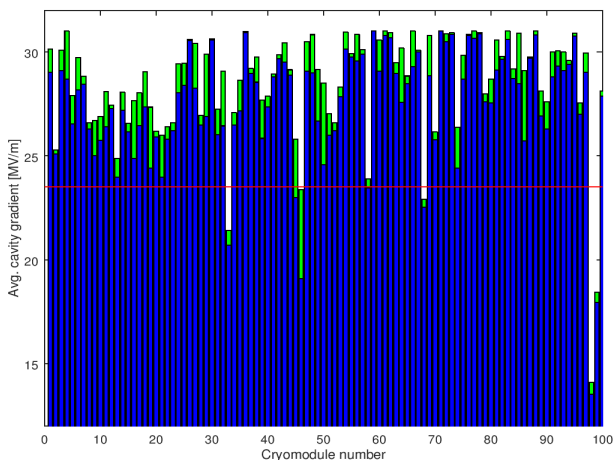


Figure 4.8: Average of the operating (blue) and maximum (green) gradient for cavities in each European XFEL serial-production cryomodule. The specification of 23.6 MV/m is marked by a red line [63]. Modules 98 and 99 were assembled from the lowest-performing cavities.

This “plug-compatible” design ensures that components are interchangeable between modules from different regions and thus reduces the cost risk. Corresponding interface definitions exist for the cavity, the fundamental-mode power coupler, the mechanical tuner and the helium tank. The “S1Global” project [64] has successfully built a single cryomodule from several cavities equipped with different couplers and tuners, demonstrating the viability of this concept.

High-level radio-frequency

The high-level radio-frequency (HLRF) system provides the RF power that drives the accelerating cavities. The system comprises modulators, pulsed klystrons, and a waveguide power distribution system.

Modulators: The modulators provide the short, high-power electrical pulses required by the pulsed klystrons from a continuous supply of electricity. The ILC design foresees the use of novel, solid state Marx modulators. These modulators are based on a solid-state switched capacitor network, where capacitors are charged in parallel over the long time between pulses, and discharged in series during the short pulse duration, transforming continuous low-current, low voltage electricity into short high-power pulses of the required high voltage of 120 kV at a current of 140 A, over 1.65 ms. Such Marx modulators have been developed at SLAC [65] and successfully tested at KEK [66]. However, long-term data about the required large mean time between failures (MTFB) are not yet available.

Klystrons: The RF power to drive the accelerating cavities is provided by 10 MW L-band multi-beam klystrons. Devices meeting the ILC specifications were initially developed for the TESLA project, and later for the European XFEL. They are now commercially available from two vendors (Thales and Toshiba), both of which provided klystrons for the European XFEL. The ILC specifications ask for a 65 % efficiency (drive beam to output RF power), which are met by the existing devices.

Recently, the High Efficiency International Klystron Activity (HEIKA) collaboration [67, 68] has been formed that investigates novel techniques for high-efficiency klystrons. Taking advantage of modern beam dynamic tools, methods such as the Bunching, Alignment and Collecting (BAC) method [69] and the Core Oscillation Method (COM) [70] (Fig. 4.9) have been developed that promise increased efficiencies up to 90 % [71]. One advantage of these methods is that it is possible to increase the efficiency of existing klystrons by equipping them with a new electron optics, as was demonstrated retrofitting an existing tube from VDBT, Moscow. This increased the output power by almost 50 % and its efficiency from 42 % to 66 % [72].

To operate the ILC at an increased gradient of 35 MV/m would require that the maximum klystron output power is increased from 10 to 11 MW. It is assumed that this will be possible by applying the results from this R&D effort to high-efficiency klystrons.

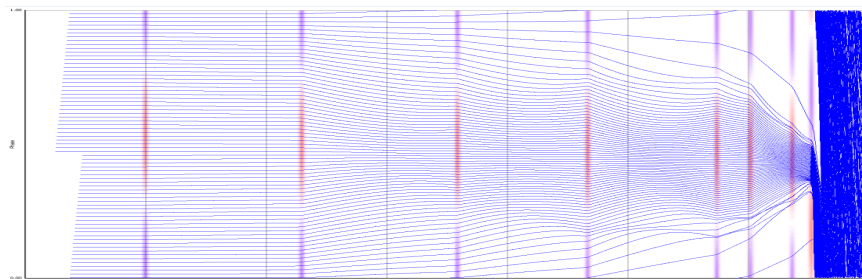


Figure 4.9: Electron phase profile of an 800 MHz klystron employing the Core Oscillation Method (COM) [70].

Local Power-Distribution System (LPDS): In the baseline design, a single RF station with one modulator and klystron supplies RF to 39 cavities, which corresponds¹ to 4.5 cryomodules [4, Sec. 3.6.4]. Then 2 klystrons drive a 9 cryomodule cryo-string unit. The power is distributed by the LPDS, a system of waveguides, power dividers and loads. All cavities from a 9-cavity module and half of a 8-cavity module are connected in one LPDS, and three such LPDS units are connected to one klystron. This arrangement allows an easy refurbishment such that a third klystron can be added to a cryo-string, increasing the available power per cavity by 50 % for a luminosity upgrade (cf. Sec. 4.2.3).

¹Out of three cryomodules, two have nine cavities and one has eight plus a quadrupole, which amounts to 26 cavities for a three cryomodule unit. Three such units share a cryogenic supply and are connected to two klystrons, see Sect. 4.1.3.

The LPDS design must provide a cost-effective solution for the distribution of the RF power with minimal losses, and at the same time provide the flexibility to adjust the power delivered to each cavity by at least $\pm 20\%$ to allow for the specified spread in maximum gradient. The LPDS design therefore contains remotely controlled, motor-driven Variable Power Dividers (VPD), phase shifters, and H-hybrids that can distribute the power with the required flexibility. This design allows one to optimise the power distribution during operation, based on the cavity performance in the installed cryomodule, and thus to get the optimum performance out of the system. It does not require a measurement of the individual cavity gradients after the module assembly, and is thus compatible with the ILC production scheme, where only a fraction of the cryomodules are tested. This is a notable difference from the scheme employed at the European XFEL, where 100% of the modules were tested, and the power distribution for each module was tailored to the measured cavity gradients, saving investment costs for the LPDS but making the system less flexible.

Cryogenics

The operation of the large number of superconducting cryomodules for the main linacs and the linacs associated with the sources requires a large-scale supply of liquid helium. The cryomodules operate at 2 K and are cooled with superfluid helium, which at 2 K has a vapor pressure of about 32 mbar.

The accelerator is supplied with liquid helium by several cryogenic plants [4, Sec. 3.5] of a size similar to those in operation at CERN for the LHC, at Fermilab, and DESY, with a cooling capacity equivalent to about 19 kW at 4.5 K. The 2 K and 4.5 K helium refrigerators are located in an underground access hall [73] that is connected to the surface, where the helium compressors, gas tanks and further cryogenic infrastructure are located. The total helium inventory is approximately 310,000 liquid liters or about 41 metric tonnes, about one third of the LHC's helium inventory. A factor 2 more helium is needed for 500 GeV operation.

Series production and industrialisation

Due to the construction of the European XFEL, the industrial basis for the key SCRF components is broad and mature. In all three regions (Europe, America, Asia), several vendors for cavities have been qualified for ILC type cavities, and provided cost estimates in the past. RF couplers have also been successfully produced by European and American vendors for the European XFEL and LCLS-II projects.

ILC/TESLA type cryomodules have been built in laboratories around the world (DESY, CEA in Europe, FNAL and JLAB in America, KEK in Asia). Series production has been established in America at Fermilab and JLAB for LCLS-II. The largest series production was conducted by CEA in France [74, 58], again for the European XFEL, with the assembly of 103 cryomodules in total by an industrial partner under the supervision of CEA personnel, with a final throughput of one cryomodule produced every four working days.

ILC type pulsed 10 MW klystrons are commercially available from two vendors in Japan and

Europe.

4.1.3 Accelerator design

Electron and positron sources

The electron and positron sources are designed to produce 5 GeV beam pulses with a bunch charge that is 50% higher than the design bunch charge of 3.2 nC ($2 \cdot 10^{10}$ e), in order to have sufficient reserve to compensate any unforeseen inefficiencies in the beam transport. In the baseline design, both sources produce polarized beams with the same time structure as the main beam, *i.e.*, 1312 bunches in a 727 μ s long pulse.

The electron source design [4] is based on the SLC polarized electron source, which has demonstrated that the bunch charge, polarization and cathode lifetime parameters are feasible. The long bunch trains of the ILC do require a newly developed laser system and powerful preaccelerator structures, for which preliminary designs are available. The design calls for a Ti:sapphire laser impinging on a photocathode based on a strained GaAs/GaAsP superlattice structure, which will produce electron bunches with an expected polarization of 85%, sufficient for 80% beam polarization at the interaction point, as demonstrated at SLAC [75].

The positron source poses a larger challenge.

In the baseline design, hard circularly polarized photons are produced in a helical undulator driven by the main electron beam. These are converted to e^+e^- pairs in a target of 1 m diameter rotating at 100 m/s. Positrons are captured in a flux concentrator or a quarter wave transformer, accelerated to 400 MeV in two normal conducting preaccelerators followed by a superconducting accelerator very similar to the main linac, before they are injected into the damping rings at 5 GeV. The positrons inherit a longitudinal polarization of 30% from the circularly polarized photons. The positron polarization thus achieved is 30%. The E-166 experiment at SLAC has successfully demonstrated this concept [76], albeit at intensities much lower than foreseen for the ILC. Technological challenges of the undulator source concept are the target heat load, the radiation load in the flux concentrator device, and the dumping of the high intensity photon beam remnant.

As an alternative, an electron-driven positron source concept has been developed. In the electron-driven scheme, a 3 GeV electron beam from a dedicated normal conducting linac produces positrons in a rotating target. The electron drive beam, being independent from the main linac, has a completely different time structure. Positrons are produced in 20 pulses at 300 Hz with 66 bunches each. With this scheme, it takes about 67 ms to produce the positrons needed for a single Main Linac pulse with its 1312 bunches, compared to 0.8 ms for the undulator source. This different time structure spreads the heat load on the target over a longer time, allowing a target rotation speed of only 5 m/s rather than 100 m/s, which reduces the engineering complexity of the target design, in particular the vacuum seals of the rotating parts. Although not free from its own engineering challenges, such as the high beam loading in the normal conducting cavities, the electron driven design is currently considered to be a low risk design that is sure to work.

Aside from the low technical risk, the main advantage of the electron driven design is the

independence of positron production and electron main linac operation, which is an advantage for accelerator commissioning and operation in general. In particular, electron beam energies below 120 GeV for operation at the Z resonance or the WW threshold would be no problem. The undulator source, on the other hand, offers the possibility to provide beams at the maximum repetition rate of 10 Hz given by the damping time in the damping rings of 100 ms, whereas the electron driven scheme is limited to 6 Hz due to the additional 66 ms for positron production. The main difference between the concepts is the positron polarization offered by the undulator source, which adds significantly to the physics capabilities of the machine. The physics implications of positron polarization is discussed later in the report, in Sec. 5.3.

Both concepts have been reviewed recently [48] inside the ILC community, with the result that both source concepts appear viable, with no known show stoppers, but they require some more engineering work. The decision on the choice will be taken once the project has been approved, based on the physics requirements, operational aspects, and technological maturity and risks.

Beam polarization and spin reversal At the ILC, the electron beam and potentially the positron beam are longitudinally polarized at the source, *i.e.*, the polarization vector is oriented parallel or antiparallel to the beam direction. Whenever a longitudinally polarized beam of energy E_{beam} is deflected by an angle θ_{bend} , the polarization vector undergoes a precession through an angle $\theta_{\text{pol}} = \gamma a \theta_{\text{bend}}$ [77], with the Lorentz factor $\gamma = E_{\text{beam}}/m_e$ and the electron's anomalous magnetic moment $a = (g - 2)/2$. To preserve the longitudinal beam polarization during the long transport from the source through the damping rings to the start of the main linac, which involves many horizontal bends, the beam polarization vector is rotated into the transverse plane, perpendicular to the damping ring plane, before the beam is transferred to the damping rings, and rotated back to a longitudinal direction by a set of spin rotators at the end of the RTML (see Sec. 4.1.3). Through the use of two rotators, it is possible to bring the polarization vector into any desired direction, and compensate any remaining net precession between these spin rotators and the interaction point, so that any desired longitudinal or transverse polarization at the IP can be provided.

To control systematic effects, fast helicity reversal is required. This is helicity reversal of each beam independently, on a pulse to pulse basis, which must be achieved without a change of the magnetic fields of the spin rotator magnets. For the electron beam, a fast helicity reversal is possible through a flip of the cathode laser polarization. For the undulator-based positron source, the photon polarization is given by the undulator field. Two parallel sets of spin rotators in front of the damping rings are used that rotate the polarization vector either to the $+y$ or $-y$ direction. With this scheme, fast kickers can select a path through either of the two spin rotators and thus provide a fast spin reversal capability [77, 78].

Damping rings

The ILC includes two oval damping rings of 3.2 km circumference, sharing a common tunnel in the central accelerator complex. The damping rings reduce the horizontal and vertical emittance of

the beams by almost six orders of magnitude² within a time span of only 100 ms, to provide the low emittance beams required at the interaction point. Both damping rings operate at an energy of 5 GeV.

The damping rings' main objectives are

- to accept electron and positron beams at large emittance and produce the low-emittance beams required for high-luminosity production.
- to dampen the incoming beam jitter to provide highly stable beams.
- to delay bunches from the source and allow feed-forward systems to compensate for pulse-to-pulse variations in parameters such as the bunch charge.

Compared to today's fourth generation light sources, the target value for the normalized beam emittance ($4 \mu\text{m}/20 \text{ nm}$ for the normalised horizontal / vertical beam emittance) is low, but not a record value, and it is thus considered to be a realistic goal.

The main challenges for the damping ring design are to provide

- a sufficient dynamic aperture to cope with the large injected emittance of the positrons.
- a low equilibrium emittance in the horizontal plane.
- a very low emittance in the vertical plane.
- a small damping time constant.
- damping of instabilities from electron clouds (for the positron DR) and fast ions (for the electron DR).
- a small (3.2 – 6.4 ns) bunch spacing, requiring very fast kickers for injection and ejection.

Careful optimization has resulted in a TME (Theoretical Minimum Emittance) style lattice for the arcs that balances a low horizontal emittance with the required large dynamic aperture [4, Chap. 6]. Recently, the horizontal emittance has been reduced further by lowering the dispersion in the arcs through the use of longer dipoles [47]. The emittance in the vertical plane is minimised by careful alignment of the magnets and tuning of the closed orbit to compensate for misalignments and field errors, as demonstrated at the CESR-TA facility [79].

The required small damping time constant requires large synchrotron radiation damping, which is provided by the insertion of 54 wigglers in each ring. This results in an energy loss of up to 7.7 MV per turn and up to 3.3 MW RF power to store the positron beam at the design current of 390 mA. This actually exceeds the average beam power of the accelerated positron beam, 2.6 MW at a 250 GeV.

²The normalized vertical emittance of the positrons is reduced from $\gamma\epsilon_y \approx 8 \text{ mm}$ to 20 nm.

Electron cloud (EC) and fast ion (FI) instabilities limit the overall current in the damping rings to about 400 – 800 mA, where the EC limit that affects the positrons is assumed to be more stringent. These instabilities arise from electrons and ions being attracted by the circulating beam towards the beam axis. A low base vacuum pressure of 10^{-7} Pa is required to limit these effects to the required level. In addition, gaps between bunch trains of around 50 bunches are required in the DR filling pattern, which permits the use of clearing electrodes to mitigate EC formation. These techniques have been developed and tested at the CESR-TA facility [80]

In the damping rings, the bunch separation is only 6.4 ns (3.2 ns for a luminosity upgrade to 2625 bunches). Extracting individual bunches without affecting their emittance requires kickers with rise/fall times of 3 ns or less. Such systems have been tested at ATF [81].

The damping ring RF system will employ superconducting cavities operating at half the Main Linac frequency (650 MHz). Klystrons and accelerator modules can be scaled from existing 500 MHz units in operation at CESR and KEK [4, Sec. 6.6].

Low emittance beam transport: ring to Main Linac (RTML)

The Ring to Main Linac (RTML) system [4, Chap. 7] is responsible for transporting and matching the beam from the Damping Ring to the entrance of the Main Linac. Its main objectives are

- transport of the beams from the Damping Rings at the center of the accelerator complex to the upstream ends of the Main Linacs,
- collimation of the beam halo generated in the Damping Rings,
- rotation of the spin polarization vector from the vertical to the desired angle at the IP (typically, in longitudinal direction).

The RTML consists of two arms for the positrons and the electrons. Each arm comprises a damping ring extraction line transferring the beams from the damping ring extraction into the main linac tunnel, a long low emittance transfer line (LTL), the turnaround section at the upstream end of each accelerator arm, and a spin rotation and diagnostics section.

The long transport line is the largest, most costly part of the RTML. The main challenge is to transport the low emittance beam at 5 GeV with minimal emittance increase, and in a cost-effective manner, considering that the total length of both arms is about 14 km for the 250 GeV machine.

In order to preserve the polarization of the particles generated in the sources, their spins are rotated into a vertical direction (perpendicular to the Damping Ring plane) before injection into the Damping Rings. A set of two rotators [82] employing superconducting solenoids allows to rotate the spin into any direction required.

At the end of the RTML, after the spin rotation section and before injection into the bunch compressors (which are considered part of the Main Linac, not the RTML [83]), a diagnostics section allows measurement of the emittance and the coupling between the horizontal and vertical plane. A skew quadrupole system is included to correct for any such coupling.

A number of circular fixed-aperture and rectangular variable-aperture collimators in the RTML provide betatron collimation at the beginning of the LTL, in the turn around and before the bunch compressors.

Bunch compressors and Main Linac



Figure 4.10: Artist's rendition of the ILC Main Linac tunnel. The shield wall in the middle has been removed. ©Rey.Hori/KEK.

At the heart of the ILC are the two Main Linacs, which accelerate the beams from 5 to 125 GeV. The linac tunnel, as depicted in Figs. 4.10 and 4.11, has two parts, separated by a shield wall. One side (on the right in Fig. 4.10) houses the beamline with the accelerating cryomodules as well as the RTML beamline hanging on the ceiling. The other side contains power supplies, control electronics, and the modulators and klystrons of the High-Level RF system. The concrete shield wall (indicated as a dark-grey strip in in Fig. 4.10) has a thickness of 1.5 m [45]. The shield wall allows access to the electronics, klystrons and modulators during operation of the klystrons with cold cryomodules, protecting personnel from X-ray radiation emanating from the cavities caused by dark currents. Access during beam operation, which would require a wall thickness of 3.5 m, is not possible.

The first part of the Main Linac is a two-stage bunch compressor system [4, Sec. 7.3.3.5], each consisting of an accelerating section followed by a wiggler. The first stage operates at 5 GeV, with no net acceleration, the second stage accelerates the beam to 15 GeV. The bunch compressors reduce the bunch length from 6 to 0.3 mm.

After the bunch compressors, the Main Linac continues for about 6 km with a long section consisting entirely of cryomodules, bringing the beam to 125 GeV.

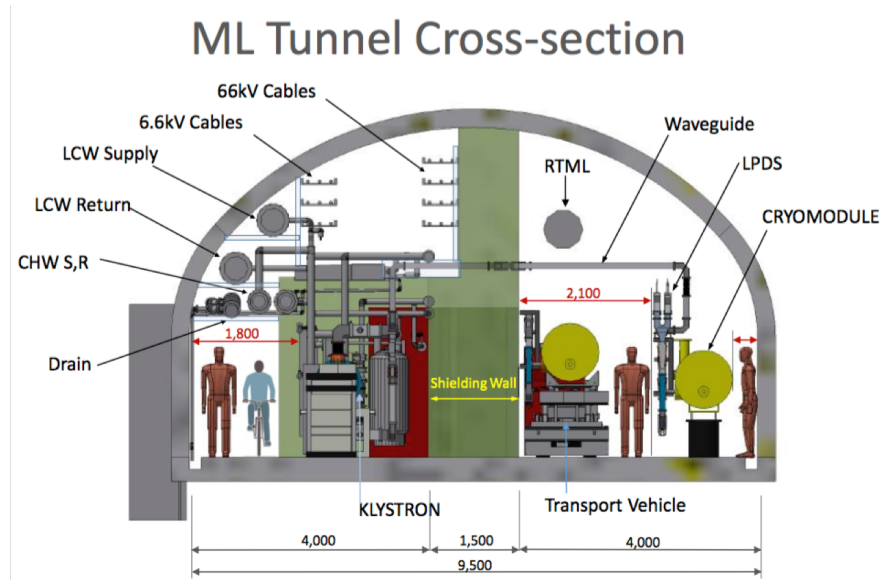


Figure 4.11: Cross section through the Main Linac tunnel.

RF distribution: Each cryomodule contains 9 cavities, or for every third module, 8 cavities and a package with a superconducting quadrupole, corrector magnets, and beam position monitor. Nine such modules, with a total of 78 cavities, are powered by 2 klystrons and provide 2.54(2.82) GeV at a gradient of 31.5(35) MV/m. Table 4.2 gives an overview over the units that form the linacs. The waveguide distribution system allows an easy refurbishment to connect a third klystron for a luminosity upgrade. The 50 % RF power increase would allow 50 % higher current through smaller bunch separation, and longer beam pulses because of a reduced filling time, so that the number of bunches per pulse and hence the luminosity can be doubled, while the RF pulse duration of 1.65 ms stays constant.

Cryogenic supply: A 9 module unit forms a cryo string, which is connected to the helium supply line with a Joule-Thomson valve. All helium lines are part of the cryomodule, obviating the need for a separate helium transfer line. Up to 21 strings with 189 modules and 2.4 km total length can be connected to a single plant; this is limited by practical plant sizes and the gas–return header pressure drop.

Cost reduction from larger gradients: Figure 4.12 shows the layout of the cryogenic supply system for the 250 GeV machine. At the top, the situation is depicted for the gradient of 31.5 MV/m with a quality factor of $Q_0 = 1.0 \cdot 10^{10}$, as assumed in the TDR [4]. In this case, the access points PM±10 would house two cryogenic plants, each supplying up to 189 cryomodules or an equivalent cryogenic load. In this configuration 6 large plants in the access halls plus 2 smaller plants in the central region would be needed. The bottom picture shows the situation for a gradient of 35 MV/m with $Q_0 = 1.6 \cdot 10^{10}$, as could be expected from successful R&D. The increased gradient

Unit	Comprises	Length	Voltage
Cavity	1.038 m active length	1.25 m	32.6 / 36.2 MV
Cryomodule	$8^{2/3}$ cavities	12.65 m	282 / 314 MV
RF Unit	4.5 cryomodules	58.2 m	1.27 / 1.41 GV
Cryostring	2 RF units	116.4 m	2.54 / 2.82 GV
Cryounit	up to 21 cryostrings	2454 m	53.4 / 39.3 GV

Table 4.2: Units that make up the main linacs. The voltage takes into account that the beam is 5° shifted in phase (“off crest”) for longitudinal stability, and is given for an average gradient of 31.5/35 MV/m. A RF unit is powered by one klystron, each cryostring is connected by a valve box to the liquid helium supply, and a cryounit is supplied by one cryogenic plant. Total lengths include additional space between components. Cryomodules comprise 9 or 8 cavities, in a 2 : 1 mixture, resulting in $8^{2/3}$ cavities per cryomodule on average.

would allow reduction of the total number of cryomodules by roughly 10% from 987 to 906. The increased quality factor would reduce the dynamic losses such that 4 cryo plants would provide sufficient helium.

In general, the accelerator is designed to make good use of any anticipated performance gain from continued high gradient R&D, in the case that raising the gradient is seen to be beneficial from an economical point of view, without incurring unwanted technology risk.

Beam delivery system and machine detector interface

The Beam Delivery System (BDS) transports the e^+/e^- beams from the end of the main linacs, focuses them to the required small beam spot at the Interaction Point (IP), brings them into collision, and transports the spent beams to the main dumps [4, Chap. 8]. The main functions of the BDS are

- measuring the main linac beam parameters and matching it into the final focus.
- protecting beamline and detector from mis-steered beams ³.
- removing large amplitude (beam-halo) and off-momentum particles from the beam to minimize background in the detector.
- accurately measuring the key parameters energy and polarization before and after the collisions.

The BDS must provide sufficient diagnostic and feedback systems to achieve these goals.

The BDS is designed such that it can be upgraded to a maximum center-of-mass energy of 1 TeV; components such as the beam dumps, that are not cost drivers for the overall project but

³On the electron side, the protective fast beam abort system is actually located upstream of the positron source undulator.

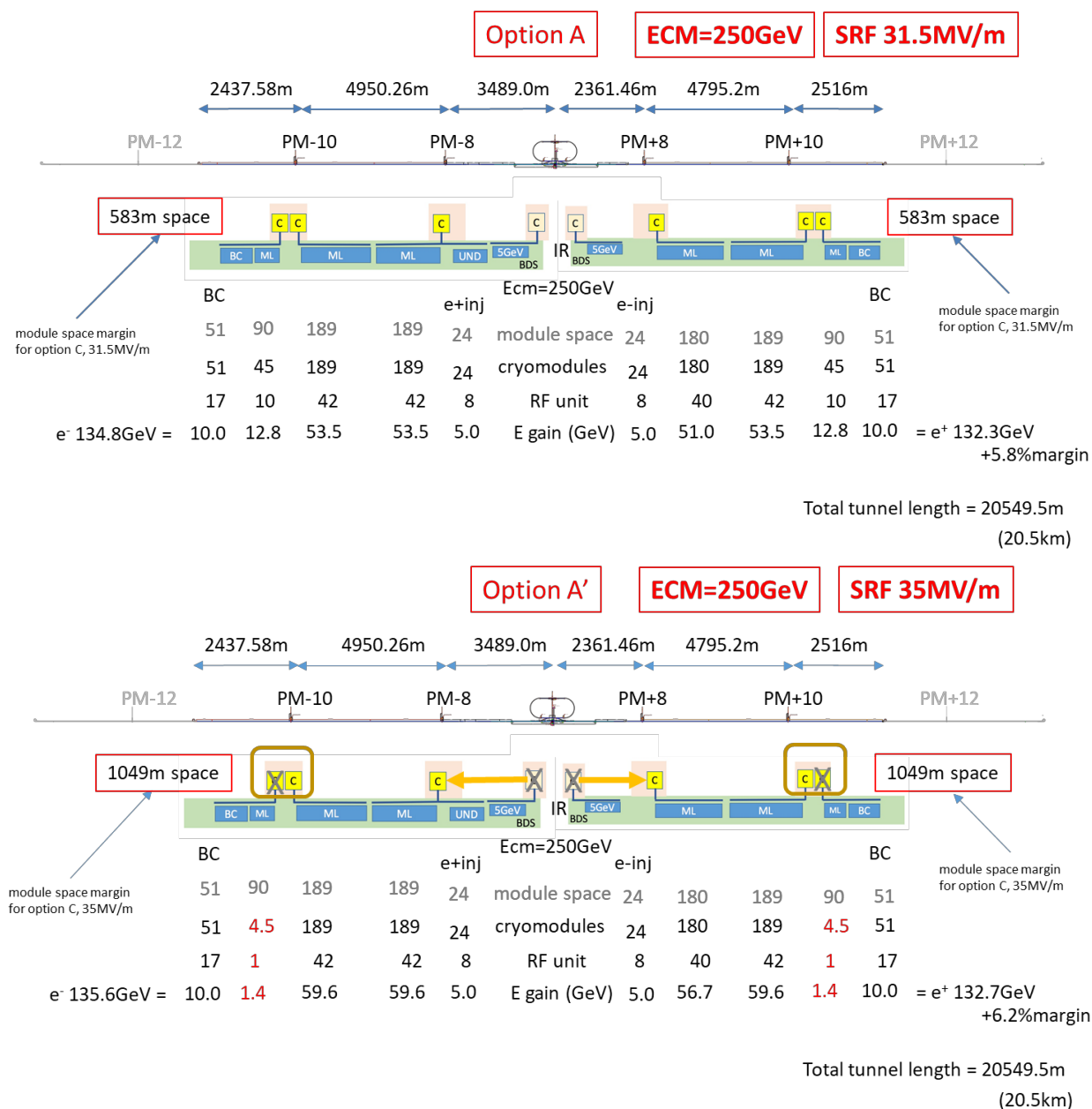


Figure 4.12: Cryogenic layout for a gradient of 31.5 MV/m (top) and 35 MV/m (bottom) [29]. “Module space” indicates how many cryomodules can be physically installed, “cryomodules” and “RF unit” indicates the number of actually installed modules and klystrons (one klystron per 4.5 cryomodules). “E gain” indicates the energy gain in GeV. “BC”, “ML”, “e+ inj”, “e- inj” and “UND” refer to the sections with need for liquid helium: bunch compressor, main linac, 5GeV boosters in the positron and electron source, and the positron source undulator section, respectively. PM±8, 10, 12 refer to access hall locations, “C” to cryo plants; meter numbers on top indicate the length of the corresponding section.

would be cumbersome to replace later, are dimensioned for the maximum beam energy from the beginning. In other places, such as the energy collimation dogleg, those components necessary for 125 GeV beam operation are installed and space for a later upgrade is reserved.

Overall, the BDS is 2254 m long from the end of the main linac (or the undulator and target bypass insert of the positron source on the electron side, respectively) to the IP.

Diagnostics and collimation section: The BDS starts with a diagnostics section, where emittance, energy and polarization are measured and any coupling between the vertical and horizontal planes is corrected by a set of skew quadrupoles. The energy measurement is incorporated into the machine protection system and can, *e.g.*, extract off-momentum bunches caused by a klystron failure in the main linac that would otherwise damage the machine or detector. An emergency dump [46] is dimensioned such that it can absorb a full beam pulse at 500 GeV, sufficient for 1 TeV operation.

The diagnostics section is followed by a collimation system, which first removes beam halo particles (betatron collimation). Then, off-momentum particles are removed. In this energy collimation section, sufficient dispersion must be generated by bending the beam in a dogleg, while avoiding excessive synchrotron radiation generation in dispersive regions that leads to an increase of the horizontal emittance. This emittance dilution effect grows as E_{beam}^6 at constant bending radius for the normalised emittance, and determines the overall length of the energy collimation section for a maximum 500 GeV beam energy to about 400 m.

Final focus with feedback system and crab cavities: The final focus system demagnifies the beam to the required spot size of $516 \times 7.7 \text{ nm}^2$ by means of a final quadrupole doublet. Even the relatively small energy spread of $\approx 0.1\%$ leads to a significant spread of the focal length of the doublet and requires a correction to achieve the desired beam size, which is realised by a local chromaticity correction scheme [84].

To bring the beams to collision with the necessary nanometer accuracy requires a continuous compensation of drift and vibration effects. Along the ILC, the pulse length and bunch separation (727 μs and 554 ns, respectively) are large enough to allow corrections between pulses as well as within a bunch train (intratrain feedback). Beam-beam offsets of a fraction of the beam size lead to a measurable deflection of the outgoing beams, and these measurements are used to feed fast stripline kickers that stabilize the beam. Finally, the 3.9 GHz crab cavities close to the interaction point are incorporated that rotate the bunches to compensate for the 14 mrad beam crossing angle [4, Sect. 8.9].

Test results from ATF2: The Accelerator Test Facility 2 (ATF2) was built at KEK in 2008 as a test bench for the ILC final focus scheme [3, Sec. 3.6]. Its primary goals were to achieve a 37 nm vertical beam size at the interaction point (IP), and to demonstrate beam stabilisation at the nanometer level [85, 86]. After scaling for the different beam energies (ATF2 operates at $E_{\text{beam}} = 1.3 \text{ GeV}$), the 37 nm beam size corresponds to the TDR design value of $\sigma_y^* = 5.7 \text{ nm}$ at 250 GeV beam energy. As Fig. 4.13 shows, this goal has been reached within 10% [87] by the

successive application of various correction and stabilisation techniques, validating the final focus design, in particular the local chromaticity correction [88].

The fifth generation FONT5 feedback system [89] for the ILC and CLIC has also been tested at the ATF2, where a beam stabilisation to 41 nm has been demonstrated, in excellent agreement with the predicted one given the incoming bunch jitter and bunch-to-bunch correlation [90].

Since November 2016, intensity-dependence effects on the ATF2 beam size have been studied extensively. They show a degradation of the beam size with increasing intensity that is compatible with the effect of wakefields. Simulations and experiments in ATF2 show that the effect is not important when scaled to ILC, and could be mitigated by including a dedicated “wakefield knob” in the routine tuning procedure.

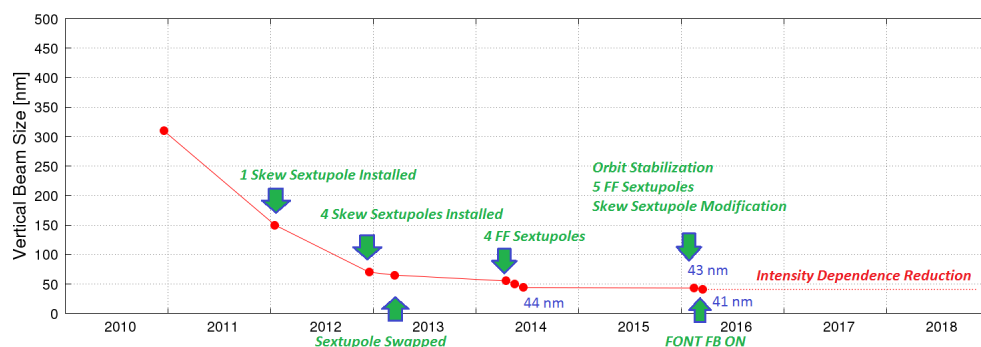


Figure 4.13: Beamsizes achieved at the Accelerator Test Facility 2 (ATF2) as a function of time [91]. The latest result (41 nm [87]) is within 10 % of the goal beam size of 37 nm.

Machine detector interface (MDI): The ILC is configured to have two detectors that share one interaction point, with one detector in data taking position at any time, in a so-called “push–pull” operation [3, Sec. 8.4]. Both detectors are mounted on movable platforms that allow an exchange of the detectors within approximately 24 hours.

In the push–pull scheme, the innermost final focus quadrupole “QD0”, a slim, superconducting magnet package combined with a sextupole for local chromaticity correction, is installed within the detectors. The other part of the final focus doublet (“QF1”) is located outside the detector on a bridge, and does not move with the detector. Since the TDR, the free space L^* between interaction point and the QD0 edge has been harmonised to a common value of $L^* = 4.1$ m [43], which facilitates the design of a final focus optics that delivers optimal and equal performance to both detectors.

The detectors are located in an underground cavern. In contrast to the TDR design, it is foreseen to have a large vertical access shaft [44], which permits a CMS–style detector installation concept, in which the detectors are assembled in large modules in a surface hall and lowered into the hall by means of a gantry crane capable of lowering pieces that weigh up to 4000 t. As the CMS experience shows, this concept significantly reduces the schedule risk associated with the

experimental hall, since the cavern needs to be available for detector installation only one or two years prior to commissioning.

Main dump: The main beam dumps [4, Sect. 8.8] are rated for a maximum beam power of 17 MW [46], enough for a 1 TeV upgrade of the accelerator. The main dump design is based on the successful SLAC 2.2 MW beam dump [92]. It utilises water at 10 bar pressure (to prevent boiling) as the absorber medium. The main engineering challenges lie in the safe recombination of the produced oxyhydrogen gas and in the safe containment and disposal of radioisotopes, in particular tritium and ^7Be produced from spallation processes. The entry window is another component that must be carefully designed.

Measurement of beam energy, luminosity, and beam polarization: This paragraph gives a brief overview on the BDS components which serve the measurements of beam energy, luminosity, and beam polarization. These measurements and their combination with additional information from e^+e^- collision data will be discussed in more detail in Sec. 5.4.

Two energy spectrometers, one located 700 m upstream of the IP, the other 55 m downstream, provide independent and complementary measurements of the beam energy with an accuracy of 100 ppm [93].

The luminosity is measured to 10^{-3} accuracy from low angle Bhabha scattering in the luminosity calorimeters of the main collider experiments, typically covering polar angles from 30 to 90 mrad. Additional calorimeters (BeamCal) in the region 5 to 30 mrad provide a fast signal that is sensitive to the beam sizes and offsets of the colliding beam, and that can thus be used for their tuning, as part of an intra-beam feedback system.

Beam polarization is measured by means of Compton scattering [94]: electrons that scatter off green or infrared light laser photons lose enough energy that they can be detected in a spectrometer; their momentum spectrum is used to fit the beam polarization [95]. Two such polarimeters are located 1800 m upstream and 150 m downstream of the IP, which allows to interpolate the precise polarization at the IP and control the systematics, including effects from precession of the polarization vector by transverse fields and depolarizing effects in the interaction, which lead to a sizeable variation of the polarization within the bunch during the collision. Each polarimeter will measure the local polarization up to a relative scale uncertainty of 0.25%, whose impact on physics measurements will be largely mitigated by extracting the luminosity-weighted average polarisation values from the e^+e^- collision data themselves. It is expected that uncorrectable point-to-point uncertainties will be one to even two orders of magnitude smaller, dominated by residual variations in the beam conditions.

4.1.4 Operation at the Z -pole

The TDR described the design of ILC for the energy range between 200 GeV and 500 GeV with possible upgrade to 1 TeV. The project starts with 250 GeV as the Higgs factory. However, once the ILC for 250 GeV is built, it is still possible to operate it below the lowest of these energy regions—in

particular at the Z pole at a center-of-mass energy of 91.2 GeV. Of course, the luminosity will be lower than at 250 GeV.

The first issue for the Z -pole operation is positron production. Since the electron beam of energy 45.6 GeV cannot produce sufficient number of positrons by the undulator scheme, another electron beam (125 GeV) dedicated to positron production is necessary. This is achieved by operating the e^- part of the accelerator at twice the repetition frequency, with alternating beams for positron production and for physics collisions. In this scheme the maximum repetition frequency of collision allowed by the AC power system of ILC250 turns out to be 3.7 Hz. Thus, the machine operation cycle is as follows:

1. Create 5 GeV electron beam (1312 bunches) and store it in DR for $1/(2 \times 3.7 \text{ Hz}) = 135 \text{ ms}$.
2. Extract the electron beam from DR, accelerate it to 125 GeV in the electron main linac, let it go through the undulator, create positron beam, accelerate the positron beam to 5 GeV and store it in the positron DR for 135 ms.
3. Create the next 5 GeV electron beam and store it in DR for 135 ms in parallel with step 2.
4. Extract the electron/positron beams from each DR, accelerate to 45.6 GeV in the electron/positron main linacs and collide them.

This one cycle takes $2 \times 135 \text{ ms} = 270 \text{ ms} = 1/3.7 \text{ Hz}$. The spent electron beam after step 2 is transported to the special beam dump (designed for up to 8 MW).

In this scenario the positron main linac is operated at 3.7 Hz, whereas the electron main linac is at 7.4 Hz, one pulse accelerates electrons to 125 GeV at the full gradient (31.5 MV/m) and the next pulse to 45.6 GeV at a gradient of 8.76 MV/m by adopting reduced klystron power⁴.

The time for damping in DR is 135 ms, shorter than the 200 ms of standard 5 Hz operation. This is feasible because the power system of DR can accept up to 10 Hz.

There are many issues to be considered in addition to above such as

- Required wiggler strength in DR and re-evaluation of the dynamic aperture
- Beam dynamics in the low-gradient main linac under alternating gradient (31.5 and 8.76 MV/m) operation mode. (Orbit correction for colliding beam only).
- Tight horizontal collimation depth due to large geometric emittance. Momentum band-width of the BDS system (a longer bunch length of 0.41 mm is adopted to reduce the beam energy spread).

⁴For the latter low energy pulse one might imagine accelerating the beam to 45.6 GeV at full gradient and turning off the power in the rest of the linac. This would have the advantage of better beam dynamics in the linac and a consequently smaller emittance at the end of the linac. However this scheme does not work with the baseline accelerator design because it is not possible to detune quickly the cavities in the rest of the electron linac as needed to avoid beam loading. Implementation of such a full gradient low energy pulse would need a dedicated rest-of-linac bypass for the electron beamline.

- The wakefield effects in BDS due to low energy and long bunch.
- Beam-beam interaction with large disruption parameter ($D_y \approx 32$).

These issues are discussed in detail in [96].

The relevant parameters are listed in Tab. 4.1. The luminosity is estimated to be $2.05 \times 10^{33}/\text{cm}^2/\text{s}$ with 1312 bunches per pulse and $4.1 \times 10^{33}/\text{cm}^2/\text{s}$ with twice the number of bunches. The expected beam polarization is the same as in the 250 GeV case, i.e. $> 80\%$ for electrons and $\sim 30\%$ for positrons.

In the case that the e-driven positron source is adopted instead of the undulator source, simple 5 Hz operation is possible as at 250 GeV and, therefore, the luminosity would be higher by a factor 5/3.7, i.e. $2.8 \times 10^{33}/\text{cm}^2/\text{s}$ with 1312 bunches. In this case, the positron beam would not be polarized.

In summary, Z-pole operation of the ILC is possible with similar performance for both positron source concepts under discussion.

4.1.5 Civil engineering and site

In 2014, the ILC Strategy Council announced the result of its candidate site evaluation for the best possible ILC site in Japan [97]. The evaluation was conducted by a number of Japanese experts from universities and industry, and reviewed by an international committee. It considered technical as well as socio-environmental aspects, and concluded that the candidate site in the Kitakami region is best suited for the ILC.

The site (Fig. 4.15) is located in the Japan's northern Tohoku region, not far from Sendai with its international airport, in the prefectures of Iwate and Miyagi. The closest cities are Ichinoseki, Oshu, and Kitakami, which all offer Shinkansen (bullet train) access to Sendai and Tokyo. The closest harbour is in the city of Kesen-Numa. The coastal region in this area was severely hit by the great Tohoku earthquake in 2011. Both prefectures are supportive of the ILC project and view it as an important part of their strategy to recover from the earthquake disaster.

The Kitakami site was largely selected because of its excellent geological condition. The proposed ILC trajectory lies in two large, homogeneous granite formations, the Hitokabe granite in the north and Senmaya granite to the south. The site provides up to 50 km of space, enough for a possible 1 TeV upgrade or more, depending on the achievable accelerating gradient. Extensive geological surveys have been conducted in the area, including boring, seismic measurements, and electrical measurements [99], as shown in Fig. 4.14. The surveys show that the rock is of good quality, with no active seismic faults in the area.

Earthquakes are frequent throughout Japan, and the accelerator and detectors need proper supports that isolate them from vibrations during earthquakes and micro tremors [100]. Proven technologies exist to cope with all seismic events, including magnitude 9 earthquakes such as the great Tohoku earthquake.

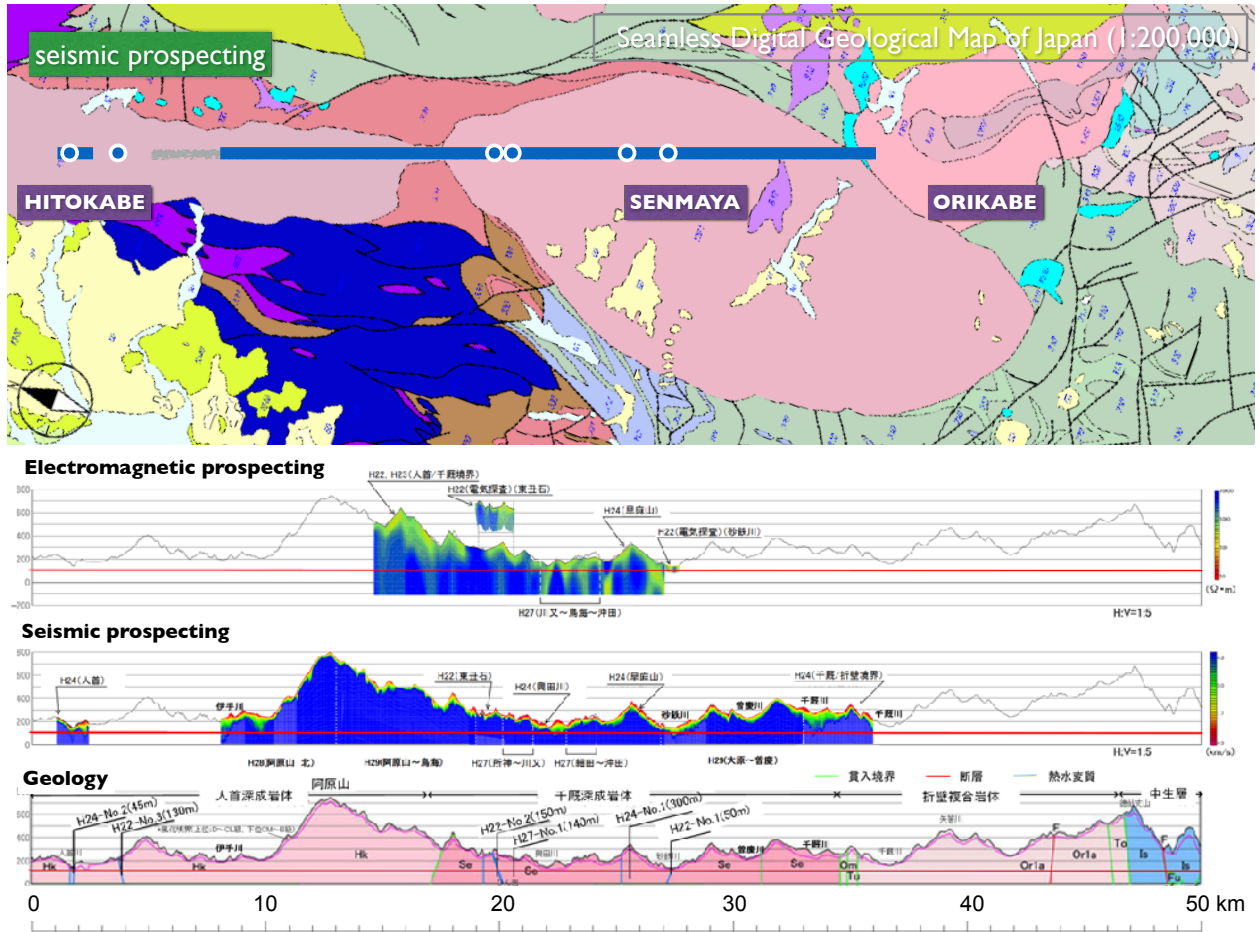


Figure 4.14: Geological situation at the Kitakami site.

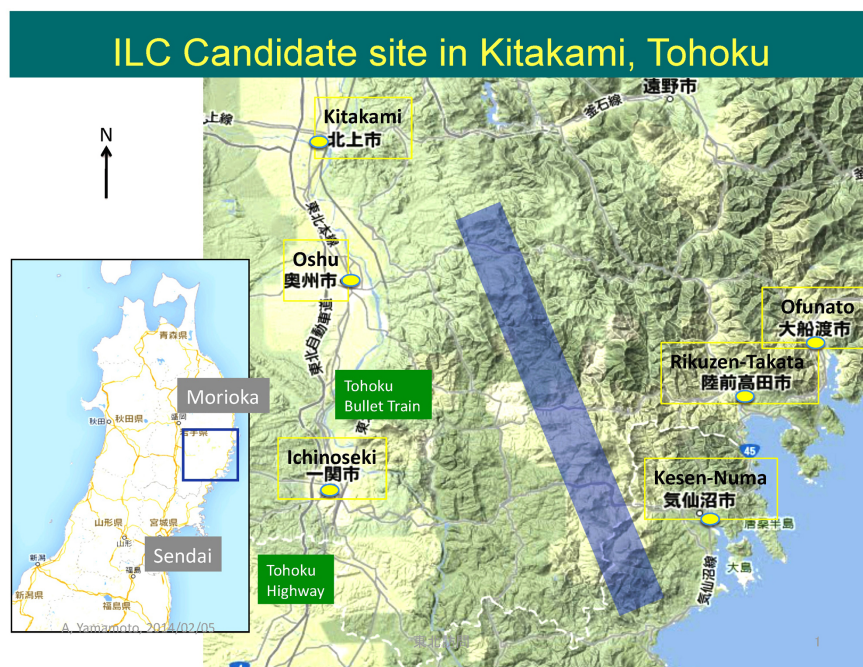


Figure 4.15: The Kitakami candidate site for the ILC [98].

Vibration measurements taken during the construction of a road tunnel show that accelerator operation would be possible during the excavation of a tunnel for an energy upgrade [101].

4.1.6 Green ILC

<https://www.overleaf.com/project/5feb77d659085f27f0653fa4>

The design of the ILC is based on Superconducting RF technology, which is more efficient than the normal conducting technology in terms of the energy consumption. However, still the total energy consumption of ILC is 111 MW at 250-GeV initial phase, 163 MW at 500-GeV phase and 300 MW at 1-TeV phase as shown in Table 4.1. These values are comparable to the energy consumption of the LHC but still large in absolute terms. The world is moving to carbon-neutrality as a goal, and this should apply also to the major laboratories of particle physics. This being so, the reduction of energy consumption and the usage of sustainable energy, and thus the efficient and sustainable design of the ILC, are crucial issues that must be addressed, especially to cooperate with the local community in the regions of the ILC site in Japan. For this purpose, the Advanced Accelerator Association (AAA) in Japan, consisting of members from both industry and academia, organized the "Green-ILC Working Group (WG)". The Green-ILC WG collaborates with the international team of the ILC. Its activities include studies on the efficient design of ILC components, accelerator sub-systems, the overall system design, and even an ILC city hosting the laboratory campus. The ILC team has been continuously communicating with the local community of the ILC Kitakami



Figure 4.16: Schematic for the concept of Green ILC.

site about its carbon-neutrality policy. In addition, Green ILC activities have been contributing to the ICFA panel on sustainable colliders and accelerators. Because the available resources within ILC group are limited, we are cooperating with industry, the local community of ILC Kitakami site, and ICFA for mutually beneficial activities in this area.

History of Green ILC activities

The Green ILC activity was triggered by three presentations from the ILC group at the 2nd Workshop on Energy Sustainable Science at Research Infrastructure (2nd ESSRI WS) in October 2013, in which the strategy of Green ILC, aiming at the sustainable and efficient design of the ILC, was presented [102, 103, 104]. At that time, the vision of Green ILC was put forward, as reflected in the schematic illustration shown in Fig. 4.16. Soon after 2nd ESSRI WS (2013), a session including four presentations was organized for Green ILC in the LCWS2013 workshop in Tokyo in November 2013. In February 2014, the Green-ILC WG (WG) was organized under the Advanced Accelerator Association Promoting Science and Technology (AAA), an association of 102 corporate organizations from industry and 41 institutional organizations from academia [105]. The proposals and discussions of the Green-ILC WG have been summarized in the Green-ILC WG

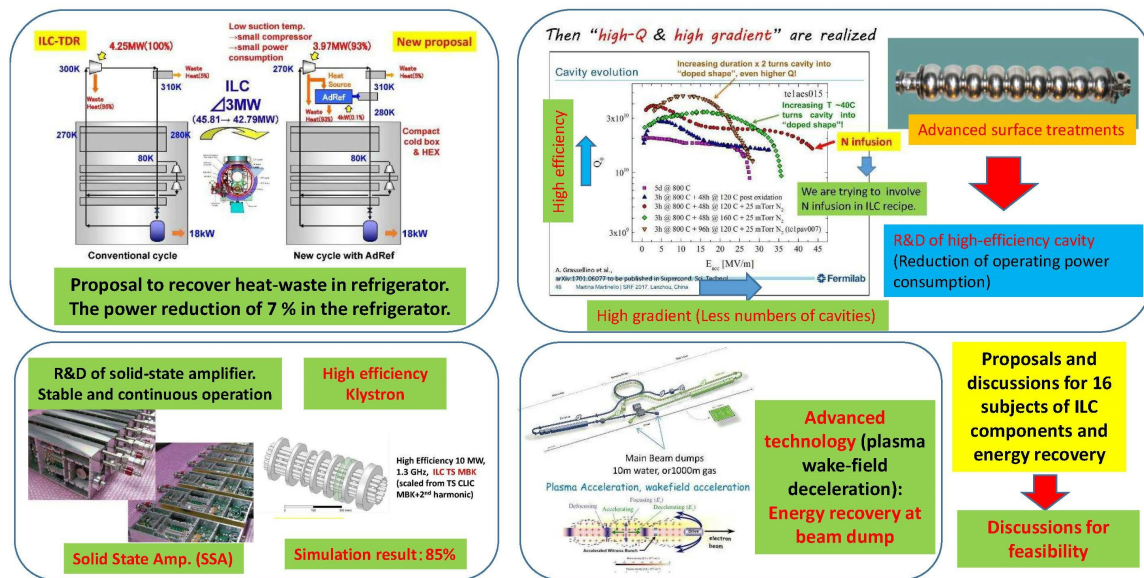


Figure 4.17: Illustrations of R&D for high-efficiency components of the ILC. Upper left: a proposal for efficient refrigerator, Lower left: proposals for a high efficiency power source; Upper right: examples of high-Q and high-gradient cavities; Lower right: a proposal for a beam dump with wake field deceleration.

Report-2016 [106], which includes papers on green accelerators in the world, green components for the ILC, energy recovery and storage for the ILC, and plans for a Green ILC city. Most recently, the ILC team has been discussing relevant issues with the community of the ILC Kitakami-site through the Tohoku ILC Project Development Center [107], which was established in August 2020. The Green ILC WG has also been contributing to the ICFA panel on sustainable colliders and accelerators since this was initiated in 2015 [108].

R&D and proposals of components for Green ILC

In the Green-ILC WG and in recent Linear Collider workshops, we have discussed various subjects for the efficient and sustainable design of the ILC. Figure 4.17 illustrates some of the results that have been presented.

The upper left-hand box of Fig. 4.17 shows an examples of an efficient refrigerator proposed by a company at the Green-ILC meeting of the AAA [106]. The waste heat from the refrigerator is recovered in the heat circuit and reused, and the power consumption is reduced by 7% in total compared to the refrigerator design of described in the ILC TDR.

The lower left-hand box of Fig. 4.17 shows examples of R&D on efficient power sources for the ILC, a Solid State Amplifier (SSA) and high-efficiency klystron [109]. The usage of SSA in ILC has

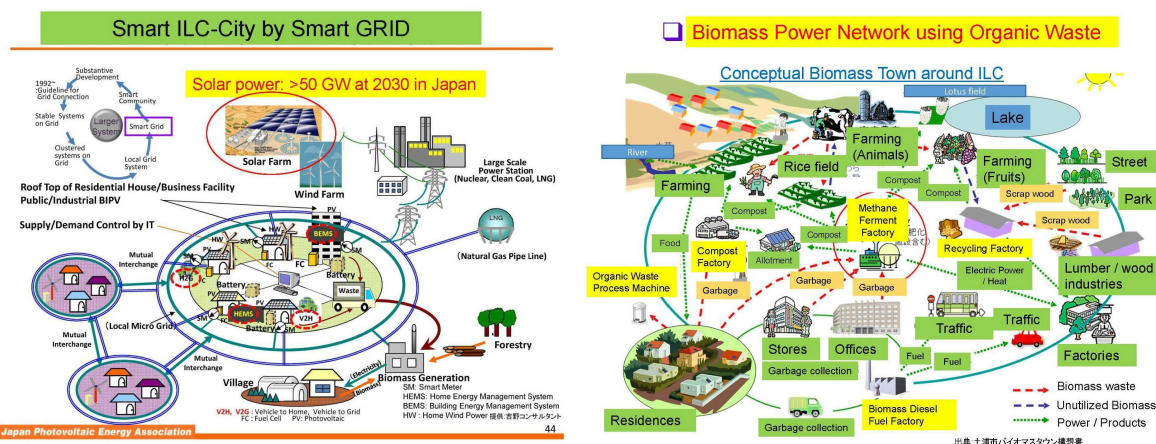


Figure 4.18: Proposals for a smart power grid (left) and biomass power network (right) for the ILC city.

historically been difficult because of its high cost, but recently the cost of SSA has been decreasing rapidly. The power source design with SSA for ILC might become feasible within a few years. If the SSA is used in the ILC, a quick and hot swap of SSA modules is possible. This will lead to a high mean time between failures and a short mean time to repair in the ILC operation. Because the refrigerator of the ILC would operate continuously even in the stand-by mode during repair, this will contribute to the reduction of the power consumption of the ILC. Recent development of a new klystron technology [110] and the availability of modern computer tools will allow us to boost the efficiency of the L-band klystron from around 65% in existing ILC commercial tubes to almost 85% in the new design. The fabrication of prototype klystrons to realize this new technology is under study now.

The upper right-hand box of Fig. 4.17 shows plots of Q vs. E_{acc} for SRF cavities after applying various advanced surface treatments [111, 112]. Some advanced surface treatments are found to provide high Q and high E_{acc} at the same time. The LCLS-II project [35] has applied a nitrogen-doping surface treatment to realize high Q at gradients somewhat lower than those of ILC. The technology of high Q and high gradient might be introduced into the design of the ILC once the yield rate for these surface treatments in mass production has been studied systematically. The ILC design using such high-gradient cavities will reduce the length of the linac, thus reducing both the construction cost and the energy consumption in the ILC operation.

The lower right-hand box of Fig. 4.17 shows a proposal for a new beam dump design using the technology of wake-field deceleration [113, 114]. The beam dump of the ILC, including its cooling water system, is a high radiation area and must be heavily shielded. The concept of wake-field deceleration of the beam can reduce the radiation level of the beam dump dramatically, even enough that it is feasible to recover the heat energy of beam dump through cooling water. This technology is not confirmed yet, but it might resolve a common problem of the beam dump for all accelerators and contribute to their sustainability.

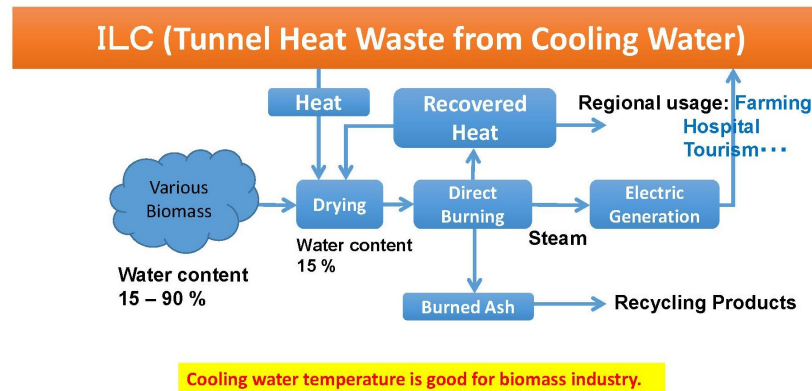


Figure 4.19: A proposal to use the waste heat of ILC tunnel for drying biomass.

Proposal for the operation of Green ILC

A proposal for the reduction and modulation of energy consumption by the ILC by scheduling its operation modes was discussed in the Green ILC session of the ILCX2021 workshop [109]. The energy consumption of ILC varies depending on the operation mode, which switches among modes such as full beam operation, reduced beam, standby, and stop (repair). The various modes can be scheduled according to the available regenerative energy resources and demand for electric power in the region of the ILC site. Variations of the demand of electric power with the season and time of day can also be taken into account. Moreover, the power consumption of ILC can be modulated by the use of pre-chilled water and/or liquid helium. If we consider the optimum scheduling of ILC operations to minimize and modulate the power consumption, this will contribute to both the efficient and sustainable operation of the ILC and to improved use of electric power in the local area that surrounds it.

R&D and proposals for a Green ILC city

The Green-ILC WG discussed the design of an ILC city that includes the ILC Laboratory campus. If the ILC is realized in Japan, it is likely that the ILC Laboratory and a surrounding new ILC city will be built near the ILC machine. In that case, the city will be newly constructed, and so advanced concepts for an efficient and sustainable city might be introduced. Fig. 4.18 shows some concepts and proposals for a smart power grid (left) and a biomass power network (right) for the ILC city [106].

In the smart power grid, solar power farms and biomass power stations are included. The ILC machine would be connected to the smart grid and the operation modes of ILC would be organized in concert with its daily schedule of energy production. The biomass power network for the ILC city would include methane fermentation, biomass diesel fuel production, and scrap wood recycling factories. Biomass would be collected through the network, and various kinds of energy would

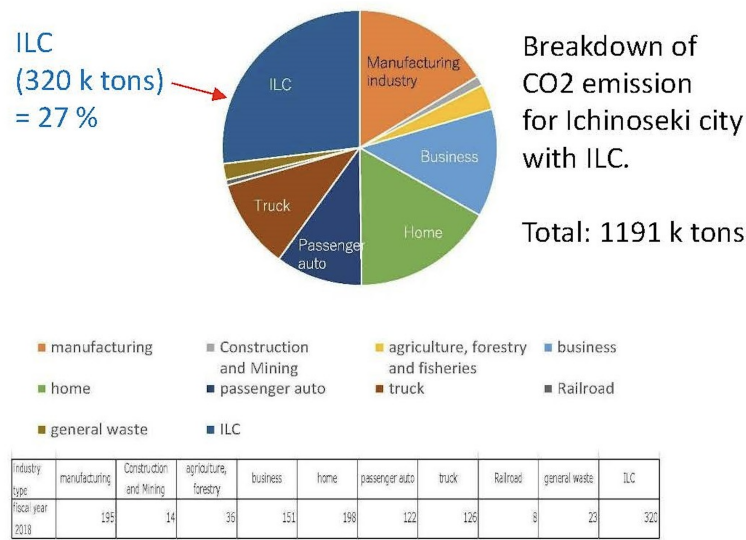


Figure 4.20: Breakdown of total CO₂ emission in Ichinoseki city, including the contribution from the ILC Laboratory.

be produced by biomass and distributed to residents, offices, buildings, facilities, and factories. The electric power produced by the biomass power network would be provided to the smart grid network. The ILC machine would also contribute to the biomass power network by the use of waste heat from the ILC tunnel, as shown in Fig. 4.19. The recycling of waste heat from cooling water in the ILC tunnel has been proposed by a company that uses such waste heat to dry biomass. Then energy can be produced as electricity and heat by burning the biomass [106].

Cooperation with ICFA international panel on sustainable colliders and accelerators

The ICFA international panel on sustainable colliders and accelerators started in 2015 [108]. The panel started with 20 members, of whom 2 were from the ILC group. The ICFA panel has been discussing and promoting strategy and coordination for sustainable colliders and accelerators, energy efficient accelerator concepts, energy efficient and sustainable accelerator technologies, and energy management of large research facilities, with networking across the laboratories. It has also been providing close and active communications among various projects and regions. Green ILC activities have been contributing to the ICFA panel from its beginning. Because available resources in the ILC team are limited, we are cooperating with the ICFA panel in mutually beneficial studies of these issues.

Studies and proposals for organization of the local area around the ILC Kitakami-site in Japan

Because the ILC will be a major user of energy and source of atmospheric CO₂, we have a responsibility to work with the local community to mitigate this and bring the plan for the ILC Laboratory as close to carbon-neutrality as possible. As explained above, the ILC team is in close communication on this issue with local authorities through the Tohoku ILC Project Development Center [107]. Currently, the ILC is expected to emit 320 kilotons of CO₂ per year, compared to 871 kilotons of CO₂ emitted in 2018 by Ichinoseki City, the closest city to the ILC Kitakami site; see Fig. 4.20. Forests in this local area can absorb about 300 kilotons/year. It then is feasible for the ILC Laboratory, working with local authorities, to shape its planning to offset these losses [109, 115]. In particular: (1) The ILC community should develop energy-saving technologies and not only apply them to the ILC, but also give them back to society. (2) The ILC community should cooperate with the community of the area to increase the percentage of renewable energy in the area. (3) The ILC Laboratory should integrate into its construction plan a program of sound management of the local forestry industry to increase the absorption of CO₂.

The ILC Laboratory has much expertise to bring to bear on the wise use of energy resources and sustainable energy policies, and we can also draw on insights from and collaborations with the broader scientific community. We consider it a priority to work with members of the local community not only to make the ILC more green, but also to assist the transition to greener policies in the region that hosts the ILC Laboratory.

4.1.7 ILC cost and schedule

For the Technical Design Report, the construction cost of the ILC accelerator was carefully evaluated from a detailed, bottom-up, WBS (Work Breakdown Structure)-based cost estimation [4, Sect. 15]. The TDR estimate distinguishes two cost categories: Value accounts for materials and supplies procured from industry and is given in ILCU (ILC Currency Unit, where 1 ILCU = 1 US\$ in 2012 prices), and Labor accounts for work performed in the participating institutions and is given in person-hours or person-years⁵.

The Value of acquired goods reflects its worth in the local currency of the purchasing institution. Therefore, conversion of Value between currencies is performed based on Purchasing Power Parities (PPP), which are regularly evaluated and published by the OECD [116, 117], rather than currency exchange rates. The PPP values reflect local price levels and thus depend on the type of goods and the country, but fluctuate significantly less than currency exchange rates. Therefore, conversions from ILCU to other currencies cannot not be made on the basis of exchange rates to the U.S. dollar, but on PPP values.

The TDR estimate covers the cost of the accelerator construction, assumed to last 9 years plus one year of commissioning. It includes the cost for the fabrication, procurement, testing, installation, and commissioning of the whole accelerator, its components, and the tunnels, buildings

⁵One person-year corresponds to 1700 working hours.

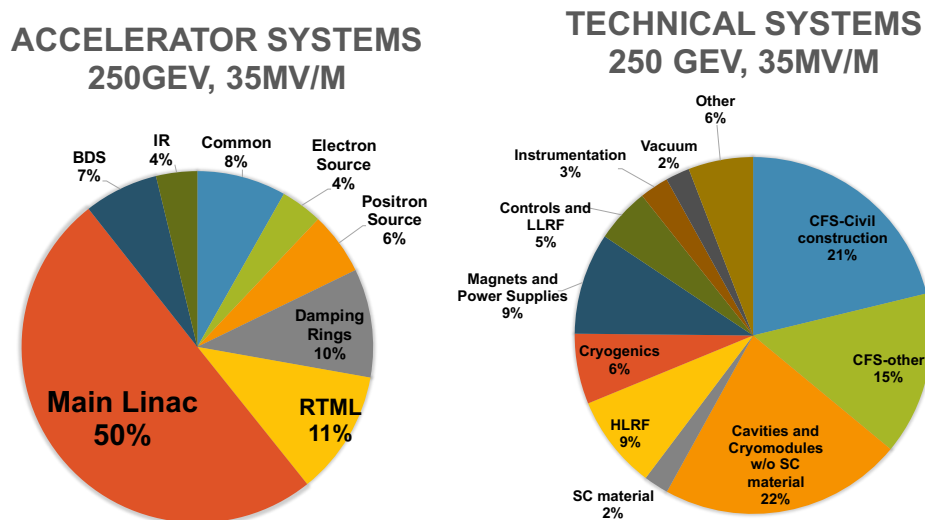


Figure 4.21: Breakdown of Value costs into accelerator systems (left) and technical systems (right) for the 250 GeV ILC accelerator, assuming that cost reduction measures are successful and a gradient of 35 MV/m can be reached.

etc., and the operation of a central laboratory at the site over the construction period. It does not, however, cover costs during the preparation phase preceding the start of construction work (“ground breaking”), such as design work, land acquisition, infrastructure (roads, electricity, water) for the site.

Based on the TDR cost estimate, an updated cost estimate was produced for the 250 GeV accelerator. This updated cost estimate includes the cumulative effect of the changes to the design since the TDR (see Sect. 4.1.1), and evaluates the cost for the reduced machine by applying appropriate scaling factors to the individual cost contributions of the TDR cost estimate.

The resulting Value estimate for the ILC accelerator at 250 GeV is 4,780 – 5,260 MILCU [29] in 2012 prices, where the lower number assumes a cavity gradient of 35 MV/m, while the higher number is based on the TDR number of 31.5 MV/m. In addition, 17,165 kh (thousand person-hours) are required of institutional Labor.

In 2018, the ILC Advisory Panel of the Japanese Ministry of Education, Culture, Sports, Science and Technology (MEXT) concluded its review of the ILC [118]. For this review, costs were evaluated in Japanese Yen in 2017 prices, taking into account the local inflation for goods and construction costs. For the purpose of this estimate, also the Labor costs were converted to Yen to yield 119.8 G¥, resulting in a total range of the accelerator construction cost of 635.0 – 702.8 G¥, where the range covers uncertainties in the civil construction costs (18 G¥) and of the gradient (49.8 G¥). For the this estimate, conversion rates of 1 US\$ = 100 JP¥ and 1 € = 1.15 US\$ were assumed.

Operation costs of the accelerator and the central laboratory are estimated to be 36.6 – 39.2 G¥

(about 318 – 341 M€) per year.

4.2 ILC staging up to 1 TeV

4.2.1 Introduction

The requirements for ILC physical characteristics [6] define a continuous range of center-of-mass energy from 92 GeV (Z -pole [119]) to 500 GeV with the possibility of additional upgrading to a center-of-mass energy of 1 TeV. The GDE has focused on providing a reliable design and cost estimation for the 200 – 500 GeV base machine. The design is a price-performance optimized solution for a given energy range. The center-of-mass energy of 250 GeV can be realized with a straight machine 20 km long, and the energy of 500 GeV can be achieved if it is expanded to 30 km. To be as cost-effective as possible, the final ILC proposal [120] approved by ICFA does not include empty tunnel options for future upgrades. Despite the fact that the length of the main tunnel of the linear accelerator has been reduced, the beam delivery system and main dumps are designed to allow for an energy upgrade up to 1 TeV.

The development of accelerator structures with higher acceleration gradients can lead to a significant increase in energy while maintaining a compact infrastructure. To date, significant progress has been made in the development of structures with a gradient well above the 31.5 MV/m required for the ILC, and even above the 45 MV/m as required for the 1 TeV ILC [121, 122]. In the longer term, structures with an alternative shape or with a thin-film Nb₃Sn coating or multilayer coating can significantly improve the performance of linear particle accelerators [123, 124]. Newer acceleration schemes can achieve even higher gradients as discussed in Sect. 4.3. Finally, the emergence of acceleration schemes based on plasma wake field acceleration or other advanced concept could open up the ILC energy regime up to 30 TeV. Thus, the ILC laboratory has the potential to support a higher energy electron-positron collider. The ability to increase energy levels makes the Linear Collider a very flexible tool, allowing in response to a new discoveries at the LHC. There are several options for upgrading the ILC in terms of energy, luminosity and beam polarization.

The level of detail of the staging and upgrade scenarios is significantly less mature than the baseline. In particular, the TeV upgrade parameters and associated conceptual design represent a relatively simple and straightforward scaling of the base machine based on assumptions about higher achievable operating parameters for SCRF technology with an average acceleration gradient of 45 mV/m with $Q_0 = 2 \times 10^{10}$. Achieving these values requires further research and development beyond the basic technology. It is anticipated that this R&D will continue in parallel with both construction and operation of the base machine, so that the expansion of the core linear accelerators required to increase particle energy will benefit from improved technology. In addition, accelerator research and development should continue to dramatically increase particle collision energy in preparation for future experimental efforts that may indicate the existence of new particles and new phenomena at higher energy.

Both luminosity enhancement and low-energy staging are based on existing technology and do

not require additional research and development. For upgrades to TeV energies, a design approach that has minimal impact on the operation of the ILC is desired. The two sets of parameters presented for upgrading to TeV (the so-called low and high beamstrahlung) were obtained after careful consideration of the physical impact.

It should be emphasized that the flexibility in the choice of beam parameters remains one of the key advantages of the ILC. It can be adjusted whenever new ideas and discoveries either from (HL-) LHC or from the ILC itself set new requirements.

4.2.2 Parameters

Table 4.1 shows the main ILC parameter sets for center-of-mass energy of 250 GeV and of 500 GeV, the luminosity upgrade of these, and a possible set of parameters for the energy 1 TeV. The parameters for the first stage of the 250 GeV machine are identical to the baseline parameters set for this energy.

4.2.3 Luminosity upgrade

The ILC luminosity can be improved by increasing the luminosity per bunch (or by the charge of the bunch) or by increasing the number of bunches per second [125]. Increasing the brightness per bunch requires a smaller vertical beam size, which can be achieved by tighter focusing and / or lower beam emittance. However, this approach invariably involves high perturbation of the beam, resulting in the risk of luminosity loss due to improper beam steering. Thus, a very accurate feedback system is required. The ILC design also allows the number of bunches to collide per second to be increased by doubling the number of bunches per pulse and possibly increasing the pulse repetition rate. Doubling the number of bunches per pulse from the base number of 1312 to 2625 will require a decrease in the time separation between bunches from 554 ns to 366 ns, which will lead to an increase in the beam current from 5.8 mA to 8.8 mA, which will require installation of 50% more klystrons and modulators. Since the RF pulse duration of 1.65 ms will not change, the cryogenic load will also not change. The beam pulse duration increases from 714 μ s to 961 μ s. The choice of the distance between bunches is consistent with both the harmonic number of the damping ring and the duration of the RF pulse of the main linear accelerator. Doubling the number of bunches would double the beam current in the damping rings. For a positron ring, this may exceed the limitations associated with the electron cloud instability. To reduce this risk, the damping ring tunnel is large enough to accommodate a third damping ring so that the positron current can be distributed over the two rings. Basic schematics for electron and positron sources are specified to produce more bunches needed for upgrades. RTML, and in particular the SCRF RF linear accelerator sections for beam compressors - are already compatible with a large number of bunches.

The pulse repetition rate is 5 Hz in the base configuration. However, when ILC for the center-of-mass energy 500 GeV is built and it is operated at 250 GeV, the repetition rate can be increased up to 10 Hz so as to further double the luminosity. The RF and the wiggler magnet systems of the damping rings can be reinforced so that the beams can be damped within 100 ms. The klystrons in

the bunch compressors and the main linacs can be operated at 10 Hz. The wall plug power system and the cryogenics of the main linacs can accept this mode because the accelerating gradient is low. The positron source must be improved for higher target heat load. Thus, the luminosity at 250 GeV can be increased to $5.4 \times 10^{34} \text{ cm}^{-2}\text{s}^{-1}$ with 2625 bunches per pulse and 10 Hz.

The invasive nature of the additional cryogenic power installation requires a shutdown, during which all additional RF power supply must be installed. This will also include additional water cooling and the required wall plug power, although pipe sizes are already specified for the additional baseline load and do not need upgrades. In particular, the 25% increase in cryogenic load (mainly due to high power coupler losses and HOM losses due to higher current) is within the base specification. All beam position monitors (and other instruments) are compatible with shorter beam spacing. Beam dynamics problems (multi-bunch effects) are also acceptable, and high power couplers and HOM couplers/absorbers are specified in the baseline for higher beam currents.

4.2.4 Energy upgrade

An obvious advantage of a linear collider is the possibility of an energy upgrade. In principle, the main linear accelerator can be expanded with the cost that is proportional to added length (i.e. added beam energy) with some additional costs of moving the turnarounds and compressors. Additional costs arise if the beam delivery system (BDS), including the beam dumps, has to be expanded to cope with the increased beam energy. The current ILC BDS is designed to be easily modified to operate at center-of-mass energies up to 1 TeV at minimal cost. Depending on the actual gradient achieved during the construction of the ILC, maximum 162 cryomodules can be installed in previously unoccupied space in the tunnel reserved for the timing constraint in addition to those required to reach 250 GeV, which will increase the center of mass energy by approximately 50 GeV to about 300 GeV, and two additional cryogenic plants may need to be installed. Further increases in energy will require the expansion of the tunnel. As noted above, an accelerator with a total length of at least 50 km can be placed on the Kitakami site, which is more than enough for center-of-mass energy of 1 TeV. Any expansion of the accelerator system can be accomplished by adding new cryomodules at the low energy (upstream) ends of the accelerator without the need to move already installed modules.

The upgrade can take place in two phases: a preparation phase, when the accelerator is still running and producing data, and an installation phase, when the accelerator stops. During the preparation phase, the necessary components will be purchased and manufactured, in particular cryomodules, klystrons and modulators. At the same time, civil engineering will continue to excavate new access tunnels, underground halls and the main tunnel. Recent research shows that the level of vibration caused by tunneling will allow construction of tunnel extensions close to the existing ones without impacting machine operation [126], minimizing the required shutdown time. During the installation phase, the newly built tunnels will be connected to the existing ones, the beam lines at the turnarounds and wiggler sections of the bunch compressors will be dismantled, and new cryomodules and a new turnaround and bunch compressors will be installed. In parallel, any necessary changes can be made to the positron source and the final focus of the machine. Since the cryomodules would be ready for installation at the beginning of the shutdown period, it is

anticipated that the shutdown could be limited to about a year for an energy upgrade

The choice of beam parameters and luminosity increase for the 1 TeV upgrade is also based on direct scaling from a set of base parameters, but more limited by additional considerations related to higher energy and average beam power:

1. The total wall plug power required for the modified machine must be below some realistic limit (assumed to be 300 MW);
2. The beam current and pulse duration must be compatible with injectors, damping rings and the main linear accelerator of the basic design;
3. Energy losses due to beamstrahlung should be acceptable, and the maximum pair-production angle should be limited at the maximum luminosity per bunch crossing.

Limiting the total wall plug power requires reducing the repetition rate from 5 Hz to 4 Hz, while the need to maintain the RF pulse length in the original main linear accelerator at approximately 1.6 ms and the choice of the damping ring harmonic number limits the number of bunches to 2450. The limits of beamstrahlung depend on physics, therefore, for the study of physical and detector groups, a set of parameters with high beamstrahlung radiation with $\delta_{BS} \sim 10\%$ and, accordingly, a higher luminosity $5.11 \times 10^{34} \text{ cm}^{-2}\text{s}^{-1}$ was proposed. The parameter set is based on the reduced charge of one bunch (1.7×10^{10}), shorter bunch length ($250\mu\text{m}$ and $225\mu\text{m}$ for low and high δ_{BS} , respectively), and increased horizontal beam size for controlling beamstrahlung and pair-production angle, while the vertical beta function at the interaction point (IP) is further reduced to increase the luminosity per bunch crossing [127]. The bunch lengths and IP beta functions are within the range of bunch compressor and final focusing systems.

Increasing the beam energy will require the expansion of the main SCRF linear accelerators to provide an additional 250 GeV per beam. The beam current for the 1 TeV upgrade (7.6 mA) is higher than the baseline (5.8 mA) but less than that for luminosity upgrade (8.8 mA) for 500 GeV design, suggesting some level of modification. Assuming the luminosity upgrade is the first to occur; the injectors (sources and damping rings) will be reused unchanged. Compressor sections along with the RTML will be moved to the beginning of the extended linear accelerators. It is also necessary to lengthen the 5 GeV long-transfer line from the damping ring to the turn-around. The beam delivery system will require the installation of additional dipoles to provide the required higher integrated field strength. The cost and schedule of the upgrade is entirely dependent on the expansion of the main linear accelerators. One of the key cost considerations is the choice of an accelerating gradient. Ongoing R&D for high gradient SCRF is expected to continue in parallel with the construction and operation of the base machine. With this in mind, it is assumed that when the linear accelerator technology is upgraded, a higher gradient and quality factor are incorporated. The actual choice of these options will clearly depend on the state-of-the-art at the time of the upgrade. However, for the purposes of this discussion, an average acceleration gradient of 45 MV/m with $Q_0 = 2 \times 10^{10}$ will be assumed. Using the existing baseline linear accelerator with bunch compressors described in [4, Sec. 7.3.3.5], main linac weak quadrupole magnets for the 15-25 GeV energy range, and normal FODO lattice for 25-125 GeV beam energy, there are four key consequences for the upgrade:

1. The beam current and pulse length must be compatible with the existing RF installation and cryogenic refrigeration capacity.
2. The extension part of the main linac tunnel and the turn around must be ready for bunch compressors and a weak quadrupole section relocation.
3. The new, higher accelerating gradient SRF cavities should be installed.
4. The rest of the original linear accelerator will use the FoFoDoDo lattice as opposed to the basic FoDo lattice, which will result in weaker focusing and larger beta function values. Simulation of the beam dynamics showed that the growth of the vertical emittance can be kept within acceptable limits.

4.2.5 Positron source

The undulator-based positron source must be compatible with the initial energy of the electron beam of 500 GeV. The solution is to replace the baseline helical undulator with a shorter one, with a longer period and a smaller field. The upgraded undulator will provide a photon beam similar to the baseline so that the same target and capture device can be used without modification [128]. One of the important considerations is the opening angle of photons, which is halved for higher beam energy; this makes collimating photons for polarization more challenging. Currently, a conservative estimate of 20% polarization is considered acceptable, but higher values may be possible, provided that a suitable solution is found for collimating photons with a smaller aperture [129]. The baseline design geometry of the target-bypass dogleg for the high-energy electron beam already accommodates the 500 GeV beam transport with a few percent horizontal emittance growth [130], although additional dipole magnets will need to be installed. The electron-driven positron source is compatible with Energy upgrade as it is.

4.2.6 RTML

The two-stage compressor system will need to be “relocated” to a new location upstream. This scenario assumes that a new two-stage compressor will be installed, as well as a new turnaround and an extended transport line. Also, during the shutdown for the final installation of the warm wiggler base sections and cryomodules, the most upstream sections of the main linear accelerator will be updated as discussed in the “Energy upgrade” subsection. The original turnaround will be disconnected and bypassed by a new long transport line. It is likely that the space between the original and the upgraded linac will also be used for additional diagnostic and dump systems, including an emergency extraction dump to protect the machine, similar to the one found at the linac exit (BDS entrance).

4.2.7 Beam Delivery System (BDS)

The BDS geometry (length and average bend radius) is already compatible with the transport of a 500 GeV beam with an acceptable increase in the emittance generated by synchrotron radiation

[128]. Additional dipoles are required (as well as appropriate power supplies and cooling) to be installed in drift spaces provided in the base grid. The main high power dumps have already been designed for higher average beam powers to avoid the need to replace them during modernization (dumps will become radioactive after several years of operation).

4.2.8 Polarization upgrade

It is assumed that at center-of-mass energies up to 500 GeV, ILC beams will have at least 80% of the electron polarization at IP in combination with a positron polarization of 30% for an undulator positron source. At 1 TeV, the positron polarization will reach at least 20%.

At beam energies above 125 GeV, the flux of undulator photons increases rapidly. Photon polarization is maximal at zero angle of radiation emission; it reduces and even inverts at large angles. Thus, collimation of the excess photon flux at large radiation angles increases the net polarization. Thus, as an upgrade option, 60% polarization of positrons at IP can be possible at a center-of-mass energy of 500 GeV with the addition of a photon collimator.

The design of the accelerator includes sets of spin rotators, which allow to choose any desired direction of the polarization vectors at the IP. The baseline running scenario considers data taking with longitudinal polarization configurations as default, but data sets with transverse polarization could be added as upgrades.

4.2.9 Summary

These chapters examined incremental upgrade and upgrade options other than the 500 GeV baseline scheme and demonstrates the greater design flexibility and capabilities of the ILC installation. The basic design already contains the possibility to simply increase luminosity by doubling the average beam power (50% increase in average RF power). The parameters and scope of future upgrades to center-of-mass energy of 1 TeV were presented, based on the expansion of the main linear accelerators with minimal impact on the existing (baseline) machine. The construction of the extended machine, in principle, could proceed in parallel with the physical launch, with minimal interruption for connecting the baseline and modernized linear accelerators and the subsequent commissioning of the machine. The physical parameters (luminosity) for retrofitting to TeV energies represent a compromise between the physical requirements of the beam-beam (limiting bremsstrahlung and pair-production angle) and the desire to limit the total required wall plug power to about 300 MW.

4.3 R&D program on superconducting RF

The technology for the ILC at 250 GeV is "shovel-ready". The TDR was completed some time ago. The technology has been demonstrated and industrialized. A large-scale prototype (the European XFEL) has been installed, and in operation. New large scale facilities—LCLS-II, ESS, PIP-II, and SHINE—are soon to be commissioned or under construction. Extensive SRF infrastructure exists

worldwide for cavity fabrication, surface treatment, clean assembly, cold testing, and cryomodule assembly. Major SRF facilities are available at DESY, CERN, INFN, Saclay, Orsay, INFN, KEK, JLAB, Cornell, Fermilab, MSU, and at several industries around the world. New infrastructure is becoming available for upcoming projects such as for ESS in Europe, and PAPS in China. New industries in S. Korea, China and Japan are rapidly growing familiar with SRF technology.

The decade 2010–2020 has brought enormous progress to the physics, technology and applications of SRF cavities as will be presented in the following Sections. Here we summarize some of the highlights. Unprecedented high Q values have been attained up to $E_{acc} = 20\text{--}30$ MV/m. These advances were achieved by novel surface preparation techniques, such as nitrogen doping, cold-electropolishing, and 300 C baking, along with special cavity cool-down procedures to eliminate the residual resistance contribution from trapped DC magnetic flux. These recent accomplishments have translated into significant increases (by a factor of $> 2\text{--}3$) in the efficiency of CW particle accelerators (e.g., LCLS-II at SLAC) operated at medium accelerating fields of about 20 MV/m.

On the high gradient frontier, most relevant for ILC, new treatments of Nitrogen-Infusion and two-step baking (75/120 C) have paved the way for gradients near 50 MV/m. Applying these advanced treatments to improved shape cavities developed earlier holds the prospect of gradients close to 60 MV/m. A radical step of replacing the standing wave TESLA type structure with a Travelling Wave structure will open the door to gradients of 70 MV/m by lowering the peak surface fields. But much development work will be needed to reach these exceptional levels.

In Section 4.1.2, we have described the evolution of superconducting RF technology up to the present and explained the robustness of the ILC plan for operation at a nominal gradient of 31.5 MeV/m. However, superconducting RF technology continues to move forward. To reduce the cost of the 250 GeV ILC, to reduce the cost of the upgrade to 500 GeV, and to propose affordable designs for the ILC at 1 TeV and beyond, it is important to continue to improve this technology to achieve gradients as high as possible in cavities that can be produced reliably by industry. In this section, we will describe the R&D program to improve the gradient of superconducting RF cavities. The improvements that we describe here go beyond the baseline ILC design, but we expect that they will be brought into play as the ILC evolves to higher energy. The far-future application of extremely high-gradient superconducting RF to take the ILC beyond 1 TeV will be described in Sec. 15.3.

4.3.1 Gradient status for the ILC baseline 250 GeV

Figure 4.22 shows the steady progress in single and multicell cavity gradients [131] over the last 3+ decades coming from high purity, high Residual Resistivity Ratio (RRR) Nb, electropolishing, 800 C furnace treatment for H removal, 100‘atm. high pressure water rinsing (HPR) for removal of field emission particulates, and final baking at 120‘C for removal of the high field Q-slope. These procedures establish a standard ILC cavity preparation and treatment recipe from which cavity gradients of 35 MV/m are expected, as observed from the European XFEL production run. More than 40 ‘‘best’’ cavities from the European XFEL production run showed 40–45 MV/m [132], as shown in Fig. 4.23. At DESY, two large grain 9-cell cavities reached 45 MV/m [133].

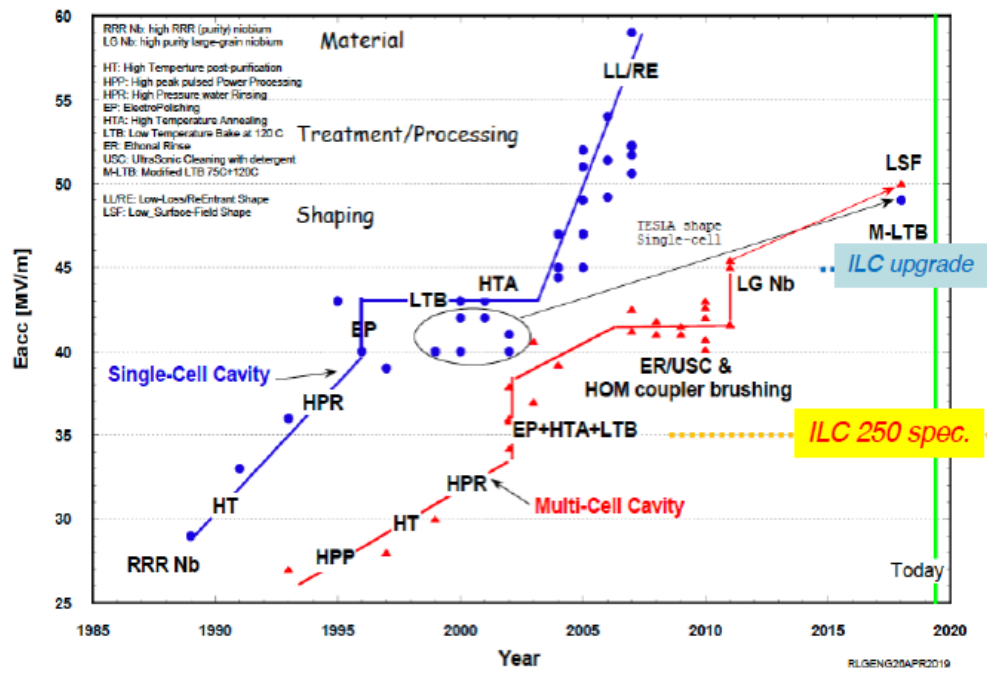


Figure 4.22: Steady progress in single and multi-cell cavity gradients over 3+ decades [131].

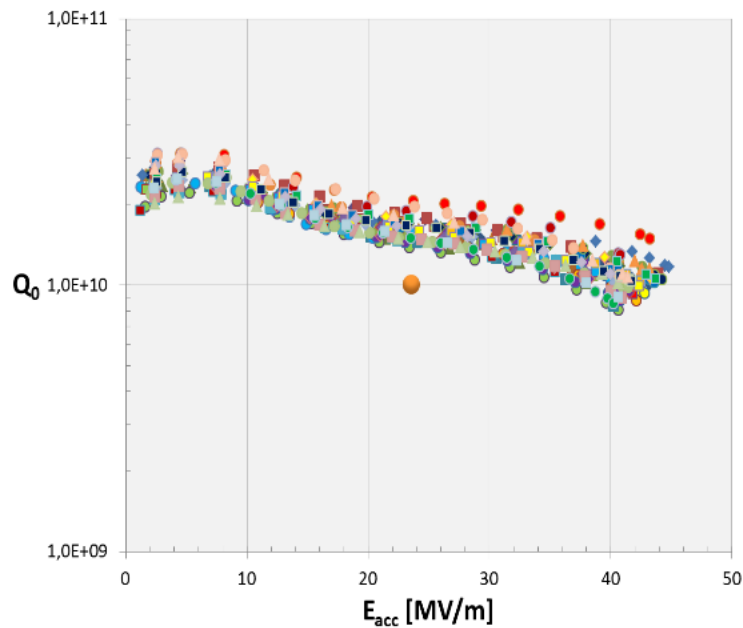


Figure 4.23: 9-cell test results from DESY on > 40 cavities produced and treated by Research Instruments (RI) [132].

Key areas of further development over the last 5 years have been for higher Q values at medium gradients (16–22 MV/m) for CW operation with the invention of new techniques of Nitrogen doping [134, 135]. Nitrogen doping for high Q has already been applied to the construction of a large (4–8 GeV) new accelerator, LCLS-II, and its high energy upgrade LCLS-II-HE. For LCLS-II, more than 300 cavities in more than 35 cryomodules, have been delivered to SLAC, and most of these are already installed. For LCLS-II-HE, ten 1.3 GHz 9-cell N-doped cavities have reached average 3.5×10^{10} at 25.7 MV/m.

Further improvements can be expected from impressive developments [136] that show $Q = 5 \times 10^{10}$ at 30 MV/m by baking at 300 C (mid-T baking) to dissolve the natural oxide (and other surface layers) into the bulk, but not exposing the cavity to air or water before RF measurements. It is interesting to note how the Q rises with field, as seen for N-doping (Fig. 4.24(a)). After exposure to air, followed by HPR, the Q dropped to 2×10^{10} at 30 MV/m. Surface analysis of similarly treated samples show a Nitrogen peak at a few nm below the surface, suggesting that N is present at the surface and has diffused into the Nb to give the doping effect. IHEP in China followed up on these encouraging results with several 9-cell TESLA cavities with successful results [137], as shown in Fig. 4.24(b). After mid-T (300 C) furnace bake, and HPR, all the 9-cell cavities demonstrate high Q in the range of 3.5 – 4.4×10^{10} at the gradient between 16–24 MV/m, as shown in Fig. 4.24(b). These cavities have all exceeded the specification of LCLS-II HE (2.7×10^{10} at 21MV/m). KEK is also pursuing the mid-T baking option. After mid-T baking and high pressure water rinsing, single cell cavities reach Q values of 5×10^{10} at 16 MV/m and quench fields of 20–25 MV/m [138].

4.3.2 High Gradient (45 MV/m) SRF for upgrade paths to 1 TeV

Section 4.2 discusses ILC energy upgrade paths from 250 GeV to 380 GeV (Top Factory), 500 GeV and 1000 GeV. For the 1000 GeV upgrade (Scenario B), the 2013 ILC TDR uses a gradient of 45 MV/m with $Q_0 = 2 \times 10^{10}$ for the additional linac from 500 GeV to 1000 GeV. The SRF parameters are chosen on the forward-looking assumptions of advances in SRF technology derived from R&D which will continue in parallel to both construction and operation of ILC 250 GeV to 1000 GeV. Such extrapolations in SRF performance are reasonably based on expectations from proof-of-principle results already in hand. As discussed further below, single cell cavities with improved treatment reach 49 MV/m, and single cell cavities with improved shapes that reach 52–59 MV/m.

Nitrogen Infusion

On the high gradient frontier (with higher Q 's), the invention of Nitrogen infusion [122], stemming from Nitrogen-doping, demonstrates gradients of 40–45 MV/m as shown in Fig. 4.25, and compared to the performance of cavities prepared with the standard ILC recipe. JLAB has shown success with infusion [139], but KEK [140] and DESY [141] have found the technique to be sensitive to the quality of the infusion furnace, and difficult to implement.

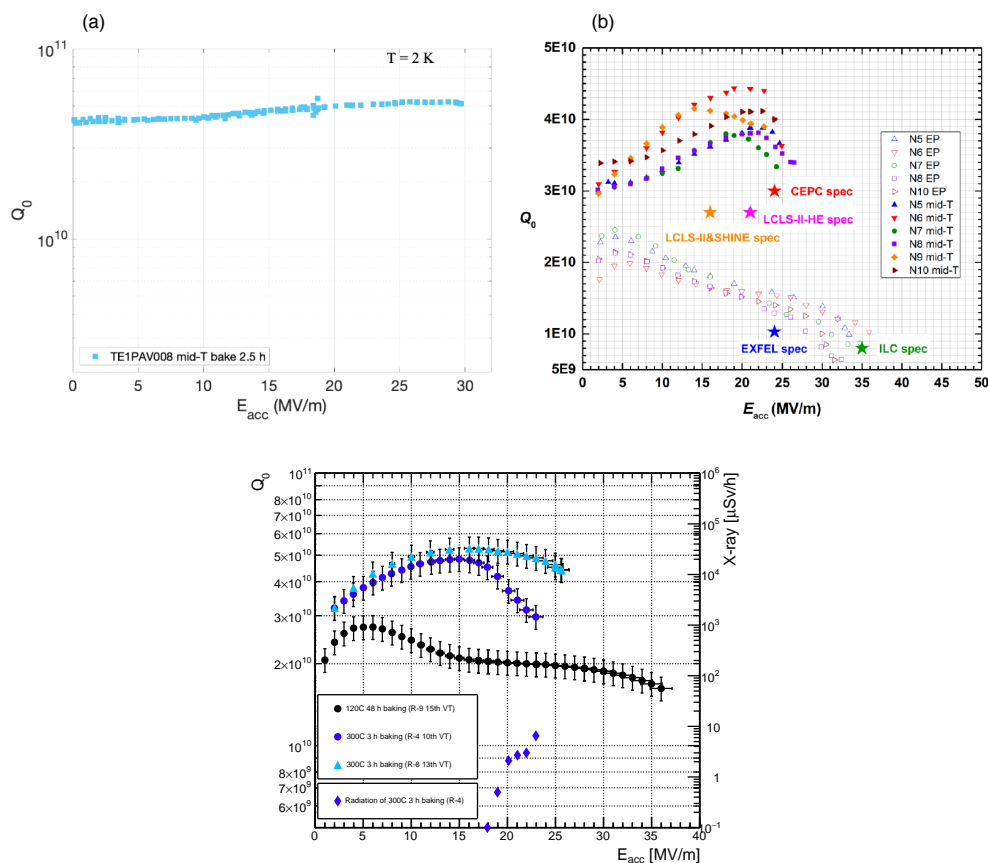


Figure 4.24: (a) $Q = 5 \times 10^{10}$ at 30 MV/m by baking at 300 C to dissolve the natural oxide (and other surface layers) into the bulk, but not exposing the cavity to air or water before RF measurements; (b) IHEP (China) results on mid-T baking for 9-cell cavities compared to results on the same cavities with the standard ILC treatment [137]; (c) 300 C baking results from KEK on single cell cavities after high pressure water rinsing. Standard ILC treatment results are also included.

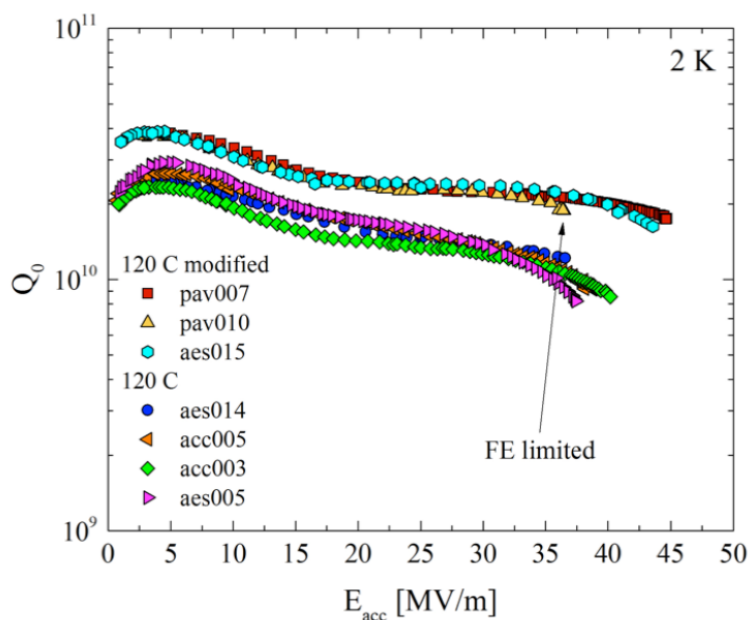


Figure 4.25: Comparison of the performance of several 1-cell cavities from N-infusion with cavities prepared by the standard ILC recipe of EP and 120 C baking.

Two-Step Baking and Cold Electropolishing

In another new development, extraordinarily high quench fields for 1.3 GHz niobium TESLA-shaped SRF cavities, some near 50 MV/m have been achieved with the 75/120 C bake surface treatment developed at FNAL, as shown in Fig. 4.26(a). Two-Step baking with Cold Electropolishing [121] show gradients in the range of 40–50 MV/m (average 45 MV/m), as depicted in Fig. 4.26(b). Note that 3 cavities that quench below 28 MV/m were found to have physical defects that likely limited the performance.

4.3.3 Toward 60 MV/m - advanced shape cavities

Continuing along the gradient frontier, multicell cavities of Re-entrant (RE) [142, 143], Low-Loss (LL) [144] and ICHIRO [145] shapes (Fig. 4.27(b)) have been introduced to lower H_{pk}/E_{acc} 10 - 20% by rounding the equator to expand the surface area of the high magnetic field region, and by allowing E_{pk}/E_{acc} to rise by about 20%. The Re-entrant shape has an Ω -like profile with $H_{pk}/E_{acc} = 0e/35.4/(MV/m)$, $E_{pk}/E_{acc} = 2.28$ (for 60 mm aperture) as compared to 42.6 Oe/(MV/m) and $E_{pk}/E_{acc} = 2.0$ for the standard TESLA shape (70 mm aperture). The GR/Q value for the re-entrant shape is about 34% higher than the TESLA shape, which reduces cryogenic losses. The 20% increase in E_{pk} makes cavities with the new shapes more susceptible to field emission, but we can expect progress in field emission reduction with cleaner surface preparation developments over the coming decades.

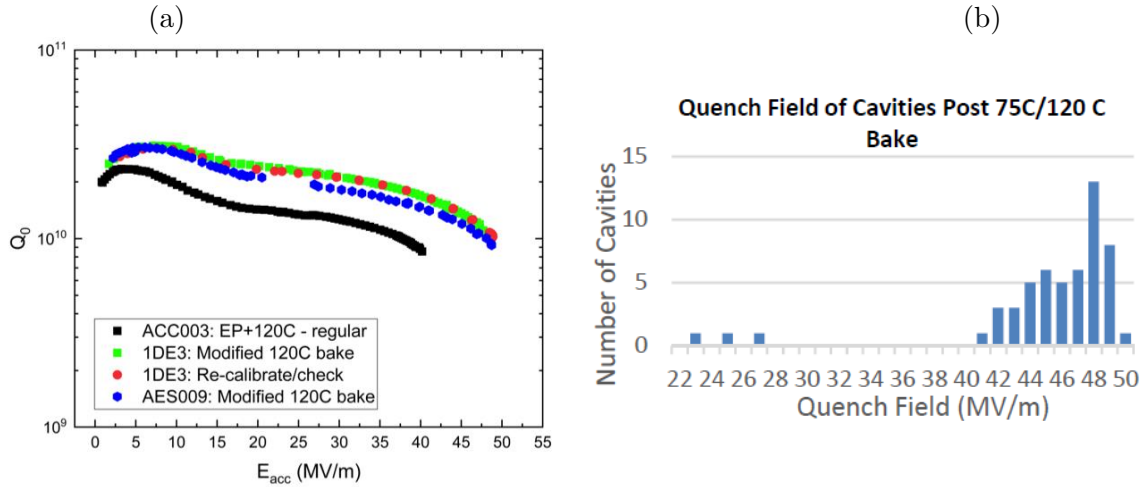


Figure 4.26: (a): Q vs. E curve of 1-cell cavity reaching 49 MV/m from Cold EP/optimized baking (75/120 C) compared to the curve of a cavity prepared by the standard ILC recipe. (b) Histogram of gradients of a large number of single cell cavities prepared by Cold EP/optimized baking (75/120 C).

The motivation in trying the new shape was that quench, governed by H_{pk} , is a hard limit, whereas field emission, governed by E_{pk} , can be improved by better engineering. The Low-Loss shape with 60 mm aperture has $H_{pk}/E_{acc} = 36.1$ Oe/(MV/m), and $E_{pk}/E_{acc} = 2.36$, and a 23% higher GR/Q than the TESLA shape. (Here G stands for the Geometry Factor of the cavity shape, and R/Q is the geometric shunt impedance.) The ICHIRO shape is a variant of the LL shape. A relative newcomer to the advanced shape effort is the LSF shape [146], which is a small refinement of the LL shape. This obtains $H_{pk}/E_{acc} = 37.1$ Oe/(MV/m) without raising E_{pk}/E_{acc} ($= 1.98$). For comparison, the RE shape with 60 mm aperture has $H_{pk}/E_{acc} = 35.4$ Oe/MV/m, and $E_{pk}/E_{acc} = 2.28$.

Many single cell cavities with the advanced shapes were built, prepared with the standard ILC recipe, and tested to demonstrate gradients of 50 – 54 MV/m with Q_0 values above 10^{10} [147, 148], as shown in Fig. 4.27(a). A record field of 54 MV/m at Q about 10^{10} was set by a single cell Re-entrant cavity with 60 mm aperture, and 59 MV/m at Q about 3×10^9 (see Fig. 4.27(c) [149]) for the same cavity. However, the best multi-cell cavities of the new shapes have only reached 42 MV/m [150], mostly due to the dominance of field emission. A 5-cell cavity of the LSF shape recently tested at JLAB showed 50 MV/m gradient in three of the five cells [151] by exciting several modes of the fundamental pass-band.

As we have seen earlier, the newly developed, two-step bake procedure has demonstrated a gradient of 49 MV/m in TESLA shape 1-cell cavities. Combining the two-step bake with one of the advanced shape cavities has the potential of improving the gradients toward 60 MV/m. For example, the Low-Loss shape has the potential for 18% improvement from 49 to 58 MV/m. But no laboratory has attempted such combined efforts as yet.

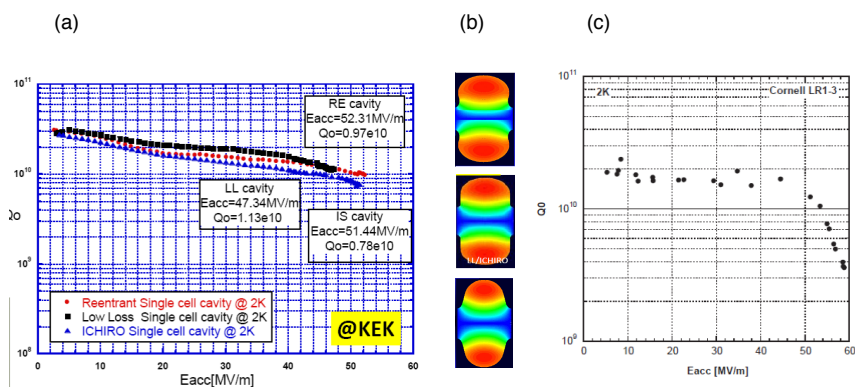


Figure 4.27: (a) Gradients greater than 50 MV/m demonstrated in single cell cavities of various improved shapes. (b) Comparison of RE (top), LL/ICHIRO (middle) and TESLA (bottom) cavity cell shapes. Here, color is magnetic field intensity, red highest, blue lowest. (c) Record gradient near 59 MV/m demonstrated with the RE shape (60 mm aperture).

Depending on the R&D resources available, we can anticipate that 9-cell accelerator structures, using some of the advanced techniques discussed here, could achieve the single-cell levels of 55 MV/m in about 10 years. This estimate is based on the historical time lag seen in Fig 4.22 between 1-cell results and 9-cell results. To reach 70 MV/m in Travelling Wave structures could take another 5–10 years, considering that these are based on the familiar superconductor Nb and considering that first efforts on Travelling Wave cavities have already started.

Cost reduction efforts

The energy upgrades would also benefit from cost saving measures under exploration, such as niobium material cost reduction (15-25%) for sheet production directly from ingots (with large grains), and/or from seamless cavity manufacturing from tubes using hydroforming, or spinning, instead of the expensive machining and electron beam welding procedures now in practice. Cost-reducing avenues for cryomodules [152] are to connect cryomodules in continuous, long strings similar to cryostats for long strings of superconducting magnets, saving the cost for the expensive ends. The elimination of the external cryogenic transfer line by placing all cryogenic supply and return services in the cryomodule also reduce costs, not only directly for the cryogenic components, but also by reducing tunnel space required. Additional cost reductions and efficiency improvements (not included in the TDR 1 TeV estimate) can be also be expected from improved klystron and modulator technology. In Sec. 15.3, we discuss the ILC upgrade path from 1 TeV to 2 TeV based on gradients/ Q of 55 MV/m/ 2×10^{10} obtained by the best new treatments, such as the two-step bake/Cold EP, applied to advanced shape structures, such as the Low-Loss structure, built from Niobium. This section also provides tables summarizing the main parameters of the 2 TeV ILC upgrade path to be compared to CLIC 1.5 TeV and the 70–80 MV/m SRF upgrade paths to 3 TeV. As discussed in Sec. 15.3, we consider the ILC upgrade path from 1 TeV to 3 TeV based on very high gradient SRF opened by R&D underway on two fronts:

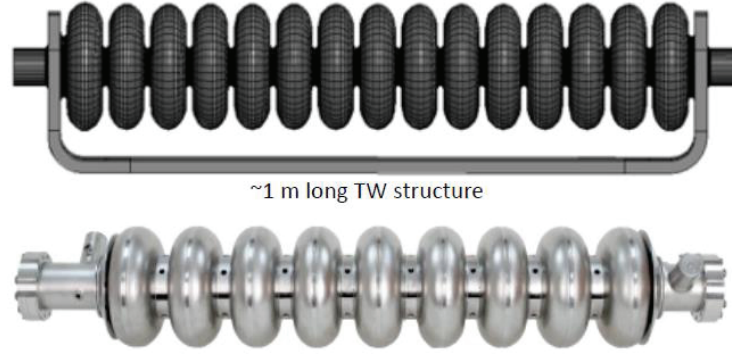


Figure 4.28: The TW structure compared to the one-meter standing-wave ILC structure.

1. Optimized travelling wave (TW) superconducting structures [153, 154, 155] with effective gradients up to 70 MV/m, along with 100% increase in R/Q . This reduces the dynamic heat load by 40% due to increase of GR/Q , where G is the geometry factor of TW structure.
2. 80 MV/m/ 1×10^{10} gradient/ Q potential for Nb₃Sn [155] at 4.2 K, based on extrapolations from high power pulsed measurements on single cell Nb₃Sn cavities.

Travelling wave structures

Travelling wave (TW) structures offer several main advantages compared to standing wave (SW) structures: substantially lower peak magnetic (H_{pk}/E_{acc}), lower peak electric field (E_{pk}/E_{acc}) ratios, together with substantially higher R/Q (for lower cryogenic losses). The emphasis for future design is to lower H_{pk}/E_{acc} , as much as possible, since H_{pk} presents a hard ultimate limit to the performance of Nb cavities via the critical superheating field. But, as Fig 4.28 shows, the TW structure requires twice the number of cells per meter as for the SW structure in order to provide the proper phase advance (about 105 degrees), as well as a feedback waveguide for redirecting power from the end of the structure back to the front end of accelerating structure, which avoids high peak surface fields in the accelerating cells. The feedback requires careful tuning to compensate reflections along the TW ring to obtain a pure traveling wave regime at the desired frequency.

As discussed in Sec. 15.3, to obtain a luminosity comparable to CLIC 3 TeV, the beam bunch charge for the 3 TeV upgrade can be 3 x lower than the bunch charge for 0.5 TeV. Hence it is possible to lower the cavity aperture (from 70 mm to 50 mm) without severe penalty in wake-fields to obtain an overall 48% reduction in H_{pk}/E_{acc} , and factor of 2 gain in R/Q over the TESLA standing wave structure. Accordingly, we examine the impact of 70 MV/m for the 3 TeV ILC upgrade to obtain a luminosity comparable to CLIC 3 TeV. Section 15.3 provides tables summarizing the main parameters of the 70 MV/m ILC upgrade path as compared to CLIC 3 TeV, including capital costs, AC powers, energy spreads and backgrounds at the IP. Modelling and optimization calculations are underway for TW structure optimization [155]. Table 4.3 shows one set of optimized parameters for optimized cell shape, phase advance, and 50 mm aperture that yield $H_{pk}/E_{acc} = 28.8 \text{ Oe}/(\text{MV}/\text{m})$

Optimization	120/200
Phase advance θ , deg	90
A , mm	23.826
B , mm	36.4
a , mm	4.512
b , mm	7.52
E_{pk}/E_{acc}	1.727
B_{pk}/E_{acc} , mT/(MV/m)	2.878
R_{sh}/Q , Ohm/m	2127
α , degrees	90.91
l , mm	31.121
R_{eq} , mm	98.950
v_{gr}/c	0.01831
E_{acc}^* , MV/m	69.5
$E_{acc}^* \cdot 2L$, MV	4.00

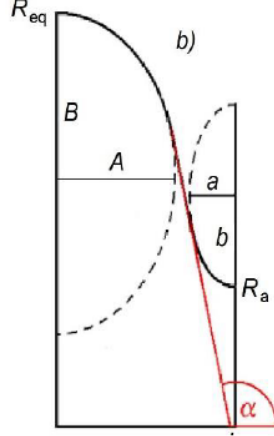


Table 4.3: Parameters of optimized cells with limiting surface fields: $E_{pk} = 120$ MV/m and $B_{pk} = 200$ mT, aperture radius $R_a = 25$ mm. E_{acc} is the accelerating rate when the limiting surface fields are achieved. $2L$ is the cell length = 57.55 mm. An 18-cell structure (1.036 m) will have the nearly same active length as the TESLA structure (1.061 m). (from [143], Table II, column 2).

with $E_{pk}/E_{acc} = 1.73$. Since H_{pk}/E_{acc} is 42.6 Oe/MV/m and $E_{pk}/E_{acc} = 2$ for the TESLA structure, the TW structure has reduced the critical parameter H_{pk}/E_{acc} by 48%! The geometrical parameters for the cell shape are defined in the inset figure accompanying Table 4.3. If results for the best single cell TESLA shape cavities prepared today ($E_{acc} = 49$ MV/m, $H_{pk} = 209$ Oe) can be reached in such a TW structure it will be possible to reach $E_{acc} = 72.5$ MV/m. The 100% R/Q increase lowers the dynamic heat load and cryogenic power needed for high gradients.

The high group velocity in the TW mode also increases the cell-to-cell coupling from 1.8% for the TESLA structure to 2.3%. Thus TW structures have less sensitivity to cavity detuning errors, making tuning easier, despite the larger number of cells. Studies [155] show that the cell shape can be fine tuned to avoid multipacting, without increasing H_{pk} more than 1%. HOM damping is under study. Preliminary results show that the first 10 monopole modes up to 7 GHz show no trapping.

Many significant challenges must still be addressed along the TW development path. High circulating power in the feedback waveguide must be demonstrated. Cavity fabrication and surface processing procedures and fixtures must deal with (roughly) double the number of cells per structure.

First structure fabrication and testing efforts have started for TW cavity development [153, 154]. With the relatively easier BCP treatment only, the first single cell TW cavity (Fig. 4.29(a)) with recirculating waveguide achieved 26 MV/m accelerating gradient, limited by the high field Q-slope, as expected for BCP. This result is very encouraging for a first attempt. A 3-cell Nb TW structure with recirculating waveguide (Fig. 4.29(b)) was designed and fabricated but has not yet been tested.

In Sec. 15.3, we consider the ILC upgrade path from 1 TeV to 3 TeV based on 70 MV/m

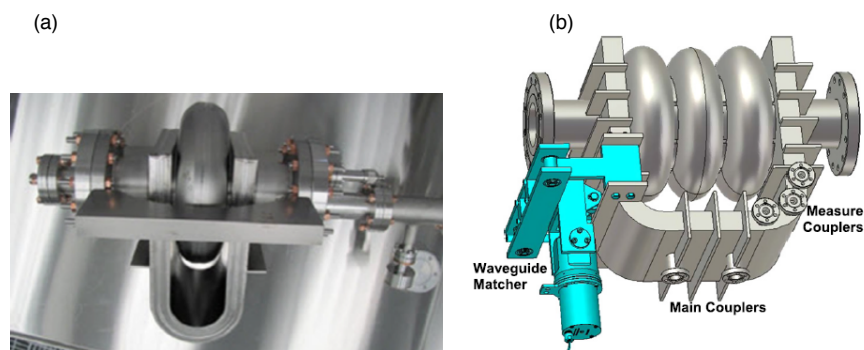


Figure 4.29: (a) 1-cell TW Niobium structure with return waveguide, treated by BCP and tested to reach 26 MV/m. (b) 3-cell TW structure built but not yet tested.

TW Nb cavities and $Q = 3 \times 10^{10}$, to be compared to CLIC 3 TeV. That Section provides tables summarizing the main parameters of the 3 TeV ILC with CLIC 3 TeV.

4.3.4 Nb₃Sn

A15 compounds (a series of inter metallic compounds with the chemical formula A₃B, where A is a transition metal and B can be any element) are intermetallic and brittle in the bulk form, so SRF structures are produced as a thin layer on the inner surface of an already formed structure. Nb₃Sn is the most explored compound, and Nb₃Sn films on a Nb structure give the best results so far [156, 157, 158]. Still, as yet, this does not give as high gradients as pure Nb cavities. The A15 phase is in the composition range of 18–25% Sn. The superconducting properties T_c , Δ , and H_c , depend strongly on the Sn content [159]. Perfect ordering in the stoichiometric phase is achieved close to stoichiometry (at 24.5 at%) where H_{sh} is 420 mT as compared to Nb’s H_{sh} of 220 mT at 0 K [160, 161, 162]. Accordingly, we can expect the upper limit of the gradient to be 400 mT or near 95 MV/m.

Nb₃Sn films a few microns thick can be deposited on the inner surface of Nb cavities by the Sn vapor diffusion process, that is, by exposing the Nb surface to Sn vapor (10^{-3} mbar) in an UHV furnace at temperatures between 1050 C and 1250 C. In general, the Nb₃Sn films produced exhibit good material quality with Sn content of about 25%, T_c of about 18 K, Δ from 2.7 to 3.2 meV [163]. The correct stoichiometry is established by a “phase locking” feedback process [164]. The process is diffusion-limited, resulting in good thickness uniformity over large surface areas [165], and at the same time it produces very clean grain boundaries [166]. Coating results are typically reproducible for the same Nb cavity substrate, but have been seen to vary between different cavities.

Some of the limitations of Nb₃Sn films created through this process arise from the sensitivity of the thermodynamic critical field H_c (and therefore the superheating field) to the exact Sn concentration. For example, a Sn depletion of 3% reduces H_c by 75%. Other difficulties are the high surface roughness at Nb₃Sn grain boundaries possibly causing local field enhancement. Somewhat thinner (1 μ m) layers give smoother surfaces and best results (Fig. 4.30).

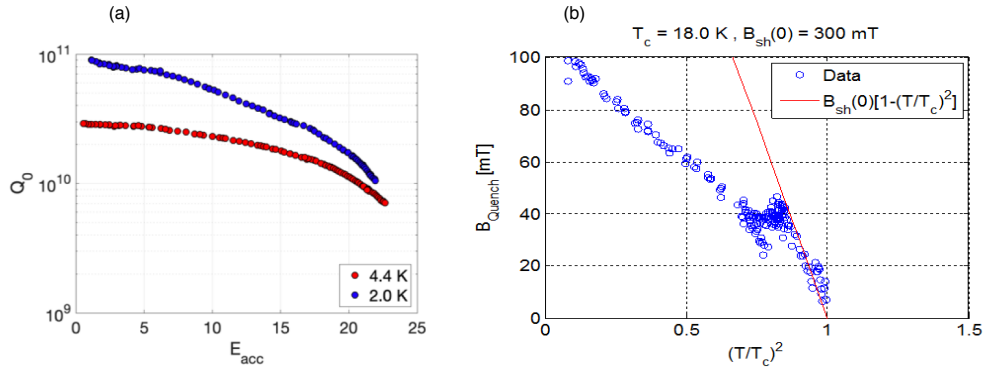


Figure 4.30: (a) Record CW behavior for Nb₃Sn coated with the solid state diffusion method at Fermilab showed $E_{acc} = 23$ MV/m. Excellent performance was obtained by making a smooth thin film about $1 \mu\text{m}$. (b) Measurements of the critical RF field of Nb₃Sn using high power pulsed RF. The high temperature results extrapolate to a maximum surface magnetic field of 300 mT, which would translate to $E_{acc} = 85$ MV/m for a Low-Loss shape cavity.

Since its origin more than 40 years ago, most practitioners of the Sn vapor deposition process have encountered a Q-slope problem and gradient limits [167, 168, 169, 170, 171]. By the late 1990's, 1.5 GHz single and multi-cell Nb cavities coated with Nb₃Sn were investigated up to peak accelerating fields of 15-30 MeV/m. The best case of a flat Q vs E curve out to 23 MV/m has been achieved at Fermilab [156, 157, 158]. The performance at 4.2 K is also very attractive showing $Q_0 > 10^{10}$ at gradient of 18 MV/m. The latest films have smaller surface roughness (by a factor of 2), smaller thickness ($1 \mu\text{m}$ vs $2-3 \mu\text{m}$) and smaller grain size ($0.7 \mu\text{m}$ vs $1.2 \mu\text{m}$). Careful material science is still required to understand and confidently control the Nb₃Sn crystal growth dynamics so as to produce low-loss surfaces.

High power pulsed RF measurements (Fig. 4.30(b)) at Cornell on a Nb₃Sn cavity show encouraging trends for very high gradients [156]. At high temperature ($T > 15$ K), the results track the high superheating field, extrapolating to 300 mT ($E_{acc} \approx 80$ MV/m) at zero temperature. But at lower temperature, thermal limitations take over to limit the highest field to about 100 mT (24MV/m) which is close to the CW result of 22 MV/m.

Theoretical studies [172, 173, 174, 175] and DC critical field measurements [176] suggest that thin layers of high temperature superconductors such as Nb₃Sn or TiN or MgB₂ deposited on the RF surface of Nb cavities could lead to substantially higher gradients than possible with Nb. The phase-space for such new development is quite extensive [176]. We expect that the enthusiasm of the proponents in each area will continue to drive efforts. The road to an accelerating cavity with gradients higher than possible with Nb is likely to be very long.

In Sec. 15.3, which discusses possible ILC upgrade beyond the TDR, we consider the ILC upgrade path from 1 TeV to 3 TeV assuming that the promise of this program can be met. We present designs are based on Nb₃Sn cavities with gradients of 80 MV/m and Q of 1×10^{10} . The discussion there provides tables summarizing the main parameters of the 3 TeV ILC based on this

technology, to be compared to CLIC 3 TeV design, and also discusses the potential benefits from 80 MV/m Nb₃Sn.

There is a second approach to the creation of accelerating cavities based on Nb₃Sn thin films. This is to use a substrate made of an inexpensive and thermally efficient material, Cu or bronze, coating the inner surface with an A15 superconductor such as Nb₃Sn. A machine whose RF structures are made of bulk Cu or bronze operating with the properties of Nb₃Sn would deliver higher gradient and higher temperature of operation and would give some cost reduction with respect to the use of a Nb substrate. The use of a Cu substrate would also take advantage of the long experience and recent advances in the fabrication of Cu accelerating structures.

The strategy of Nb₃Sn on Cu is currently at a very early stage because most funding in the U.S. has been devoted to the Sn vapor deposition process described above. However, there are small efforts in the U.S. and abroad for producing Nb₃Sn on bronze or Cu. There is as yet no actual tested structure with $Q \sim 10^{10}$ and useful accelerating fields.

To deposit Nb₃Sn on the Cu or bronze substrate, the Sn vapor diffusion process described above cannot be used, since Cu melts at 1085°C. But several alternative methods have been developed to solve this problem. One possible method is to directly deposit Nb₃Sn superconducting material, with no heat treatment required. One such method [177] was developed a few years ago within an Italian student program [178]. A different method has been demonstrated by a group at the Technische Universität Darmstadt, which performs direct deposition of Nb₃Sn at 435°C using magnetron sputtering in a co-sputtering mode from two targets [179].

Another, simpler, electroplating technique to coat Nb surfaces with Cu and Sn layers from aqueous solutions and produce Nb₃Sn during a standard heat treatment at 700°C was developed and made reproducible at FNAL in the last few years [180]. The know-how was then transferred to KEK within an U.S.-Japan Science and Technology Cooperation Program in HEP. Critical temperatures of 17.6 to 17.8 K are routinely achieved. The technology is presently used by Akita Kagaku Co. Ltd, a Japanese electroplating company, to coat 3 GHz Nb cavities. This technique can be implemented on Cu surfaces also, after sputtering them with Nb by using a magnetron system. The main challenge of this method is to achieve the required purity in the Nb₃Sn superconducting phase.

Another venue to coat Cu and/or bronze was invented by the Japanese National Institute for Materials Science (NIMS). This process builds upon the A15 superconducting wire technology and also exploits the heat treatment temperature reduction effect of the Cu as the ternary element of the Nb-Sn-Cu phase diagram. In the presence of Cu as the ternary element, the maximum temperature of the heat treatment cycle needed for Nb₃Sn formation is less than 700°C. When Cu is not present in the system, as for instance in the Sn vapor diffusion process, the temperature required from the binary phase diagram is much higher. This temperature difference affects the grain size of the Nb₃Sn phase, in that the grain size through the bronze process is much finer than that achieved in the Sn vapor diffusion process. It is thought that this method would be suitable to use on SRF cavities fabricated by hydro-forming.

Most of these coating methods are scalable to standard SRF cavity cells. More details on these various coating methods, and a discussion of their scaling to standard SRF cavity cells, is presented

in [181]. It seems important to bring one of these methods to the level of development at which the promise of Nb₃Sn on Cu or bronze could be investigated in working SRF cavities. Then it will be possible to attack the issues of surface roughness, purity, and high Q and perhaps to demonstrate the production of cavities with favorable performance, reproducibility, and cost.

4.4 ILC Accelerator technical preparation plan

Although much work has already been done to establish the ILC design and technical readiness, a number of issues remain to be studied to prepare the final design of the ILC. The technical basis for the ILC was fully documented ten years ago in the ILC Technical Design Report and its Addendum [3, 4]. Still, three sets of issues need to be studied anew. First, it is necessary to revisit all of the items to understand whether any updates are called based on more recent R&D results (including the past ten years of SRF cost reduction R&D) and consistency with the ILC staging plan [29]. Second, because the TDR work was done without a specific site in view, issues related to the site must be addressed again for the specific candidate site in the Tohoku region of Japan. Finally, the MEXT advisory panel and the Science Council of Japan have called attention to some remaining technical issues that need to be resolved during the ILC preparation period [182, 183].

The International Development Team (IDT) was established by the International Committee for the Future Accelerators in August 2020 to prepare for establishing the ILC Pre-lab as the first step toward the construction of the ILC in Japan. IDT-WG2 is now identifying the accelerator-related activities for the ILC Pre-lab necessary before starting the construction of the ILC. The ILC Pre-lab activities are expected to continue about 4 years and the principal accelerator activities of the ILC Pre-lab are technical preparations and engineering design and documentation. The deliverables of the Pre-lab accelerator activities, both technical preparations and engineering design and documentation, will be provided as in-kind contributions by member laboratories of the Pre-lab. Overall management of worldwide Pre-lab accelerator activities will be provided by the Associate Director for Accelerators, assisted by the Central Technical Office. Similarly, each technical preparation and engineering design work package will be led by a manager drawn from one of the member laboratories, guided by the domain and common technology managers. The detailed organization chart for Pre-lab accelerator activities will be defined by the Pre-lab Directorate. The ILC Machine Advisory Committee (ILCMAC), in its advisory role to the Associate Director for Accelerators, will monitor technical progress and review the engineering design and documentation. A full description of technical preparation is given in the document “Technical Preparation and Work Packages (WPs) during ILC Pre-lab” [184]. In this section, we will briefly review this plan.

The Work Packages for the technical preparation activities cover the following topics:

- **Main Linac (ML) and SRF production:** Cavity and Cryomodule (CM) global production readiness will be demonstrated through the fabrication of roughly 40 cavities in each of the 3 regions, the requirement of RF performance achieved with $\geq 90\%$ success demonstrated with sufficient statistics by using a part (about a half) of the 40 cavities in each region, and the fabrication of 2 CMs in each of the three regions using 40% of the cavities fabricated.

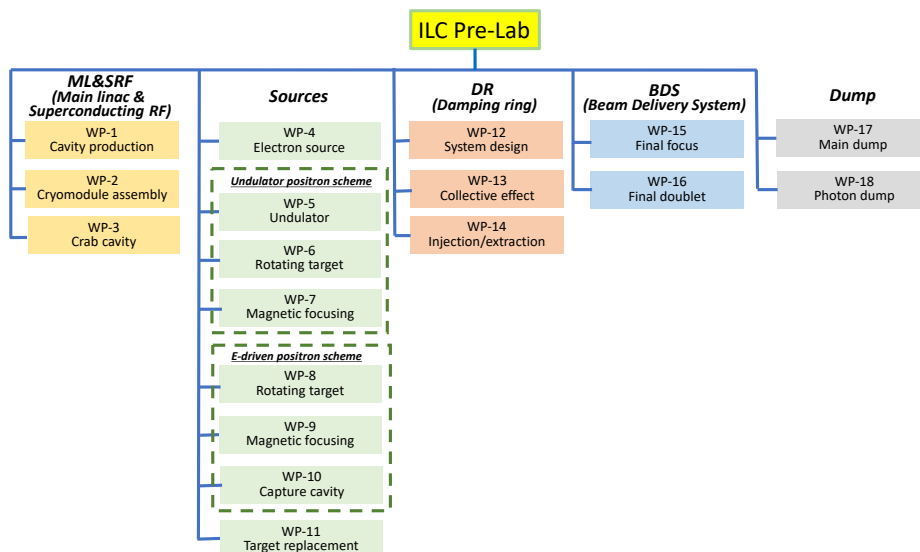


Figure 4.31: Summary of the Work Packages for the technical preparations that will be carried out during the ILC Pre-Lab period.

- ML global integration:** The program of global CM transfer will be conducted to demonstrate that the CM production satisfies high-pressure gas safety (HPGS) regulations, safe transport across oceans, and the qualification of the CM performance after shipping from Europe and the Americas to Japan across the oceans. One of the two CMs in each region will be used for this purpose. We plan to accomplish this goal with two steps. In the first step, if transport-test CMs (fully constructed but not suitable for use in the linac) are available from LCLS-II and/or European XFEL, those will be used to test simple transportation and to gather important information about stress, acceleration, *etc.*, excluding the HPGS regulation process. In the second step, the ILC prototype CM developed during the ILC Pre-lab phase will be shipped to Japan, including the HPGS regulation process and the full CM quality assurance program within the ILC Pre-lab phase period.
- Positron source :** The final design will be selected from either the an undulator-driven or the electron-driven option and its technology readiness will be demonstrated.
- Damping Ring (DR) and Beam Delivery System (BDS):** Readiness of the nanobeam technology for the DR, based on work at the ATF3 and related facilities, and the BDS systems will be demonstrated, particularly including the fast kicker and feedback controls.
- Beam dump:** A system design will be established, including beam window handling, cooling water circulation, and safety assurance.

A total of 18 WPs (3 ML&SRF, 8 Sources, 3 DR, 2 BDS, and 2 Dumps) are proposed as illustrated in Fig. 4.31 and summarized in an extended list below. The classification of some items should be clarified. The crab cavity (WP-3) will be installed in the BDS area, but is classified as

ML&SRF since the crab cavity uses SRF technology. The photon dump (WP-18) will be used for the undulator positron source. However, this WP-18 is classified as dump due to its specialty. The target replacement (WP-11) is a common WP for undulator and e-driven positron sources. These relationships are also shown in Fig. 4.31.

The explicit tasks of the WPs are as follows:

- **WP-1 (ML&SRF):** Cavity Industrial Production Readiness (3×40 Cavities)
 - Cavity industrial production readiness to be demonstrated, including cavities with He tank + magnetic shield for cavity, high-pressure-gas regulation, surface-preparation/heat treatment (HT)/Clean-room work, partly including the 2nd pass, vertical test (VT)
 - Plug compatibility, Nb material, and recipe for surface treatment to be reconfirmed/decided
 - Cavity Production Success yield to be confirmed (before He tank jacketing)
 - Tuner baseline design to be established

Note: Infrastructure for surface treatment, HT, VT, pre-tuning, *etc.*, is the responsibility of each region.

- **WP-2 (ML&SRF):** Cryomodule (CM) Assembly, Global Transfer and Performance Assurance (3×2 CMs)
 - Coupler production readiness to be demonstrated, including preparation/RF processing (3×20 Couplers)
 - Tuner production readiness to be demonstrated, including reliability verification (3×20 Tuners)
 - Superconducting Magnet (SCM: Q+D combined) production readiness to be demonstrated (3×3 SCMs, 1 prototype + 2 in each region)
 - CM production readiness to be demonstrated including high-pressure-gas, vacuum vessel (VV), cold-mass, and assembly (cavity-string, coupler, tuner, SCM, *etc.*)
 - CM test including degradation mitigation (in 2-CM joint work, *etc.*) at assembly site before ready for CM transportation
 - CM Transportation cage and shock damper to be established
 - Ground transportation practice, using mockup-CM
 - Ground transportation test, using production-CM longer than European XFEL
 - Global transport of CM by sea shipment (requiring longer container)
 - Performance assurance test after CM global transport (at KEK)
 - Returning transport of CM back to home country (by sea shipment)

Note: Infrastructure for coupler conditioning: klystron, baking furnace, and associated environment is the responsibility of each region. Also, hub-lab infrastructure for the CM production, assembly, and test is the responsibility of each region.

- **WP-3 (ML&SRF):** Crab Cavity (CC) for BDS (2 CCs + 1 for SRF validation)
 - Decision of installation location with cryogenics/RF location accelerator tunnel
 - Confirmation of the complete CC system specifications
 - Development of CC cavity/coupler/tuner integrated design (ahead of Preliminary CC technology Down-selection)
 - Preliminary CC technology down-selection (2 cavity options)
 - CC Model-work and Prototype production and high-power validation of CC cavity/coupler/tuner integrated system for two primary candidates (ahead of final CC technology Down-selection)
 - Harmonized operation of the two prototype cavities in a vertical test to verify ILC synchronization performance (cryo insert development and commercial optical RF synchronization system)
 - Final CC technology down-selection
 - Preliminary Crab CM design – confirming dressed cavity integration and compliance with beam-line specification
 - Final CM engineering design prior to production
 - Infrastructure for CC development and test in each region
- Further ML&SRF tasks associated with the Pre-Lab program (1 CM)
 - Cavity (incl He tank) production (incl couplers and tuner), magnetic shield for CM, high-pressure gas regulation, EP/HT/Clean work, including VT
 - Input coupler production including preparation/RF processing readiness (excluding klystron, baking furnace, clean room)
 - Prototype CM production including High-pressure gas, vacuum vessel, cold-mass, and assembly (cavity-string, coupler/tuner, SCM and tooling, *etc.*)
 - Prototype CM test including harmonized operation with two cavities
 - Prototype CC-CM transport cage and shock damper design and manufacture
 - Prototype CC-CM transport tests
 - Infrastructure for CM development and testing in each region
- **WP-4 (Sources):** Electron Source
 - Drive laser system
 - HV Photogun
 - GaAs/GaAsP Photocathodes
- **WP-5 (Sources):** Undulator Positron Source
 - Simulation (field errors, masks, alignment)
- **WP-6 (Sources):** Undulator Positron Source rotating target

- Design finalization, partial laboratory test, mock-up design
- Magnetic bearings: performance, specification, test
- Full wheel validation, mock-up
- **WP-7 (Sources):** Undulator Positron Source magnetic focusing system
 - OMD design finalization with yield calculation
 - OMD with fully assembled wheel
- **WP-8 (Sources):** Electron-Driven Positron Source rotating target
 - Target stress calculation with FEM
 - Vacuum seal
 - Target module prototyping
- **WP-9 (Sources):** Electron-Driven Positron Source rotating target
 - Flux concentrator conductor
 - Transmission line
 - Flux concentrator system prototyping
- **WP-10 (Sources):** Electron-Driven Positron Source capture system
 - APS cavity for the capture linac
 - Capture linac beam loading compensation and tuning method
 - Capture linac operation and commissioning
 - Power unit prototyping
 - Solenoid prototyping
 - Capture linac unit prototyping
- **WP-11 (Sources):** Positron Source target maintenance
 - Target Maintenance (a common issue for the undulator and electron-driven sources)
- **WP-12 (Damping Rings):** System Design
 - Optics optimization, simulation of the dynamic aperture with magnet model
 - Magnet design : Normal conducting magnet and SC wiggler
 - Magnet design : Permanent magnet
 - Prototyping of permanent magnet
- **WP-13 (Damping Rings):** Evaluation of collective effects in the ILC damping ring
 - Simulation : Electron cloud instability
 - Simulation : Ion-trapping instability

- Simulation : Fast ion instability (FII)
- System design : Fast FB for FII
- Beam test : Fast FB for FII
- **WP-14 (Damping Rings):** System design of ILC DR injection/extraction kickers
 - Fast kicker: System design of DR and LTR/RTL optics optimization
 - Fast kicker: Hardware preparation of drift fast step recovery diode pulser
 - Fast kicker: System design and prototyping of induction kicker
 - Fast kicker: Long-term stability test at ATF
 - E-driven kicker: System design, including induction kicker development
- **WP-15 (BDS):** System design of ILC final focus beamline
 - ILC-FFS system design: Hardware optimization
 - ILC-FFS system design: Realistic beam line driven / IP design
 - ILC-FFS beam tests: Long-Term stability
 - ILC-FFS beam tests: High-order aberrations
 - ILC-FFS beam tests: R&D complementary studies
- **WP-16 (BDS):** Final doublet design optimization
 - Re-optimization of TDR FF design considering new coil winding technology and IR design advances
 - Assembly of QD0 prototype, connection to Service Cryostat and measurement of warm/cold vibration stability with a sensitivity of a few nanometers
- **WP-17 (Beam Dump):** System design of the main beam dump
 - Engineering design of water flow system
 - Engineering design and prototyping of components; vortex flow in the dump vessel, heat exchanger, hydrogen recombiner
 - Engineering design and prototyping of window sealing and remote exchange
 - Design of the countermeasure for failures / safety system
- **WP-18 (Beam Dump):** System design of the photon dump for the undulator positron source
 - System design and component test of an open-window water dump
 - System design and component test of a graphite dump

The cost and required human resources required for the WPs are estimated in [184]. The values given are initial estimates. The actual numbers will depend on the laboratories that will take the responsibility for the deliverables, so these estimates will be re-evaluated later. Infrastructure associated with the series of items mentioned above will need to be newly prepared and/or improved with each region taking responsibility for implementation and financial support. The technical readiness scoped in each WP needs to be verified through periodical reviews conducted by the ILC Pre-Lab. The ILC technical design will need to be updated reflecting the progress on the WPs, and these updates will be implemented/added to the engineering documents. Stability and tuning issues in some WPs will also need to be coordinated with the start-to-end accelerator design that will be done as part of the "engineering design and documentation" activities of the Pre-Lab. These linkages will be carried out as a part of the ILC Pre-Lab responsibility.

We expect these activities can be completed within a four-year preparation period. We divide the timeline into two categories: "Technical Preparation and Readiness" and "Engineering documentation". Here is a plan showing how the WP activities fit into the timeline, using the SRF and Positron Source work as examples:

Year	Technical preparation	Engineering documentation
1	Continue cost-reduction R&D for SRF cavities Start pre-series production of SRF cavities in cooperation with industry Continue e^+ source development	Start review and update of TDR cost estimates by an international team
2	Complete cost-reduction R&D Determine production yield Start assembling cavities into cryomodules Review e^+ source designs	Conduct a review on the progress for technical work and cost estimation by an internal panel
3	Demonstrate overseas shipment of cryomodules taking all the safety and legal aspects into account Select e^+ source design and start prototyping and cost issues of critical items, <i>e.g.</i> , the e^+ target	Complete cost estimate and conduct internal and external review Complete risk analysis for the technical and cost issues Complete a draft of the Engineering Design Report
4	Evaluate cryomodules after shipment and demonstrate the quality assurance procedure Establish regional organization for the ILC component production Continue prototype work for critical components of the e^+ source, <i>e.g.</i> , the e^+ target	Complete and publish the Engineering Design Report Start producing specification documents and drawings of large items for tendering

Progress in technical preparation activities will be monitored and evaluated through periodic reviews. The activities will be also synchronized with the engineering documentation.

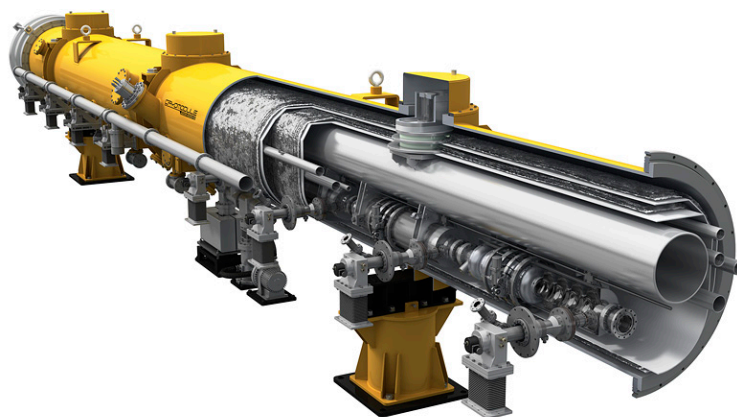


Figure 4.32: Cutaway view of an ILC cryomodule. (Image by Rey Hori [185].)

4.5 Opportunities for US contributions

US laboratories host world-class infrastructure and expertise in technology that is relevant for particle accelerators. This presents a number of opportunities for the US to make important contributions to the ILC accelerator that leverage existing capabilities. These contributions would help the project to go forward and position the US well for strong participation in ILC-based experiments.

4.5.1 Superconducting linac

The superconducting linear accelerator that drives the ILC requires 1000 cryomodules to reach a center of mass energy of 250 GeV. Each cryomodule (see Fig. 4.32) contains 8 or 9 superconducting radiofrequency (SRF) cavities, each about 1 meter long, which generate large amplitude electric fields to accelerate the beam. They also contain liquid-helium-based cryogenics to keep the cavities at 2 K, magnets, RF power couplers, frequency tuners, vacuum valves, and instrumentation. US labs have substantial experience with these sophisticated components from US-based accelerator projects including CEBAF, SNS, LCLS-II, and PIP-II. Large scale production facilities exist at Fermilab and at Jefferson Lab for assembling SRF cryomodules (see Fig. 4.33). These facilities include large cleanrooms for making vacuum connections between cavities while minimizing the risk of generating particulates that can cause field emission, large fixtures for connecting cavity strings to cold masses and inserting cold masses into cryomodules, and equipment for welding, RF diagnostics, and coupler assembly. Fermilab and JLab also have existing cryomodule test facilities, which require 2 K refrigerators, dedicated radiation areas, and RF systems. These facilities have very recently been used for the mass production of cryomodules for LCLS-II, for which the cryomodule design was largely based on ILC. As such the production facilities have already been recently tested with a very relevant system, though ILC would require approximately 5 times as many modules to be produced as the entire production of LCLS-II and its high energy upgrade LCLS-II-HE combined.



Figure 4.33: View of some of the cryomodule assembly facilities at Fermilab (left) and Jefferson Lab (right).

However, the Fermilab and JLab teams would take on the larger production with enthusiasm and experience. The vast majority of the infrastructure is already in place, with some modifications required for the higher throughput required to meet the 1 cryomodule per week target for the Americas region at peak production.

In addition to Fermilab and JLab, there are also SRF facilities at Argonne, Cornell, and FRIB, which are less specialized towards production of ILC-like cryomodules, but could be leveraged for example for cavity treatment. SLAC's expertise in high power RF sources could be leveraged for driving the cavities as well as RF distribution. SLAC is also planning a relevant cryomodule test facility that could be used. LBNL's expertise in low level RF could be leveraged for cavity control, particularly for resonance control at high accelerating gradients.

US expertise can also contribute to advanced performance for ILC cryomodules. Since the 2012 TDR, significant progress has been made in SRF R&D, including new procedures developed by researchers from US labs for reaching high gradients. Some of these developments could be implemented in ILC cryomodules to push performance by 10%, either resulting in fewer cryomodules required to reach the design center of mass energy, or else as a safety margin on top of the nominal energy and beginning towards first energy upgrades. The relevant new technologies include cold electropolishing [186] and the two step bake [121].

Advances from US labs can also contribute to some of the auxiliary systems of the cryomodules. The tuner used in LCLS-II was an evolution of previous designs and is well suited to the short beamtubes of the ILC, while maintaining minimal backlash [187]. The quadrupole magnet used in LCLS-II is also an evolution of previous designs, with conduction cooling and a split design to allow it to be assembled outside of the cleanroom [188]. A system and procedure for plasma processing of SRF cavities was developed at ORNL [189] and later adapted to 9-cell cavities by FNAL [190], which may be useful for reducing effects such as field emission in some cases.

US labs are expected to also play a leading role in developing technologies for energy upgrades to the ILC to reach the 380 GeV-1 TeV energy range beyond the baseline ILC and the multi-TeV energy

range in the future. This includes SRF R&D, such as development of advanced superconductors including Nb₃Sn for cavities [191], advanced geometries [154], and a plasma accelerator that leverage the SRF-based ILC baseline system. For more details on these upgrades, see Sec. 15.

4.5.2 Electron and positron sources

Many US labs have capabilities in sources from their own facilities. The plan for ILC has a positron source, which can be accomplished in different ways. One of these employs superconducting undulators, the other targets, and both subjects can benefit from expertise at a number of US labs.

4.5.3 Damping ring, beam delivery system, and beam dump

US accelerator scientists have extensive experience also in the technologies needed for the damping ring, beam delivery system, and beam dump.

The damping ring is expected to be similar to multiple US facilities, such as the APS upgrade at Argonne, CESR at Cornell, and NSLS-II at Brookhaven.

For beam dynamics and lattice development, researchers at nearly all US labs with accelerators have substantial relevant experience as well as specialized tools and codes such as ACE3P, ELEGANT, and BLAST.

Expertise in superconducting magnets at labs such as FNAL, Berkeley, and BNL can be applied to the magnets needed for the final focus at the interaction point. A similar task is ongoing at US labs for production of magnets for the high luminosity upgrade of the LHC.

For research and development related to plasma-accelerator-based multi-TeV upgrades to ILC, US labs host multiple accelerator facilities that could be used for relevant R&D including AWA at Argonne, FACET at SLAC, ATF at BNL, BELLA at LBL, and FAST at Fermilab.

4.5.4 Summary

The US National Laboratories are anticipating a wide range of contributions to the ILC accelerator. These contributions are synergistic, both from past programs—*i.e.*, they leverage existing infrastructure and expertise in US labs—and for developments for the future—*i.e.*, much of the needed R&D for the US contribution to ILC has application to other accelerator projects that the laboratories are involved in.

By virtue of this, there is a broad interest among all of the US National Laboratories invested in accelerator physics in participating in ILC. In addition to synergies with US labs, there is also synergy with US industry. A substantial part of the US funds for ILC construction will be put towards procurements from US companies for high-tech components that will be used in cryomodules and other accelerator elements.

Chapter 5

General Aspects of the ILC Physics Environment

This chapter gives a general orientation to the physics of the ILC. We will describe the major physics processes that the ILC will allow us to study, and the reactions that appear as backgrounds in the analyses discussed in Chapters 8–10.

We will also call attention to the effects of beam polarization. The reaction cross sections at an e^+e^- collider have direct and strong dependence on the beam polarizations. In the SM, highly relativistic left- and right-handed polarized electrons are essentially different species, with different electroweak quantum numbers. Thus, measurements with different beam polarization measure different reactions, and the comparison of these reaction rates can give direct insight into the physics. Longitudinal polarization is maintained in linear acceleration, so that a highly polarized source of electrons or positrons produces a comparable effect of polarization in collisions. Thus, at linear colliders, beam polarization works as a new tool for discovery, one not available at proton colliders or circular e^+e^- colliders. It plays a large role in the complementarity of the various types of machines.

5.1 Key Standard Model processes

The major reactions at e^+e^- colliders in the center of mass (CM) energy range of 100 GeV to 1 TeV are shown in Fig. 5.1. The typical size of a cross section in e^+e^- annihilation is the point cross section

$$\frac{4\pi\alpha^2}{3E_{CM}^2} = 1.4 \text{ pb} \cdot \left(\frac{250 \text{ GeV}}{E_{CM}} \right)^2, \quad (5.1)$$

This corresponds to the middle region (10^3 fb) of the plots in Fig. 5.1, corresponding, for example, to several million events in a data set of 2 ab^{-1} at 250 GeV. The most important 2-body reactions are enhanced over this value by the strength of the weak interaction couplings g^2/e^2 , color factors, and spin factors. Still, this is a much smaller number of events than is typically collected by a

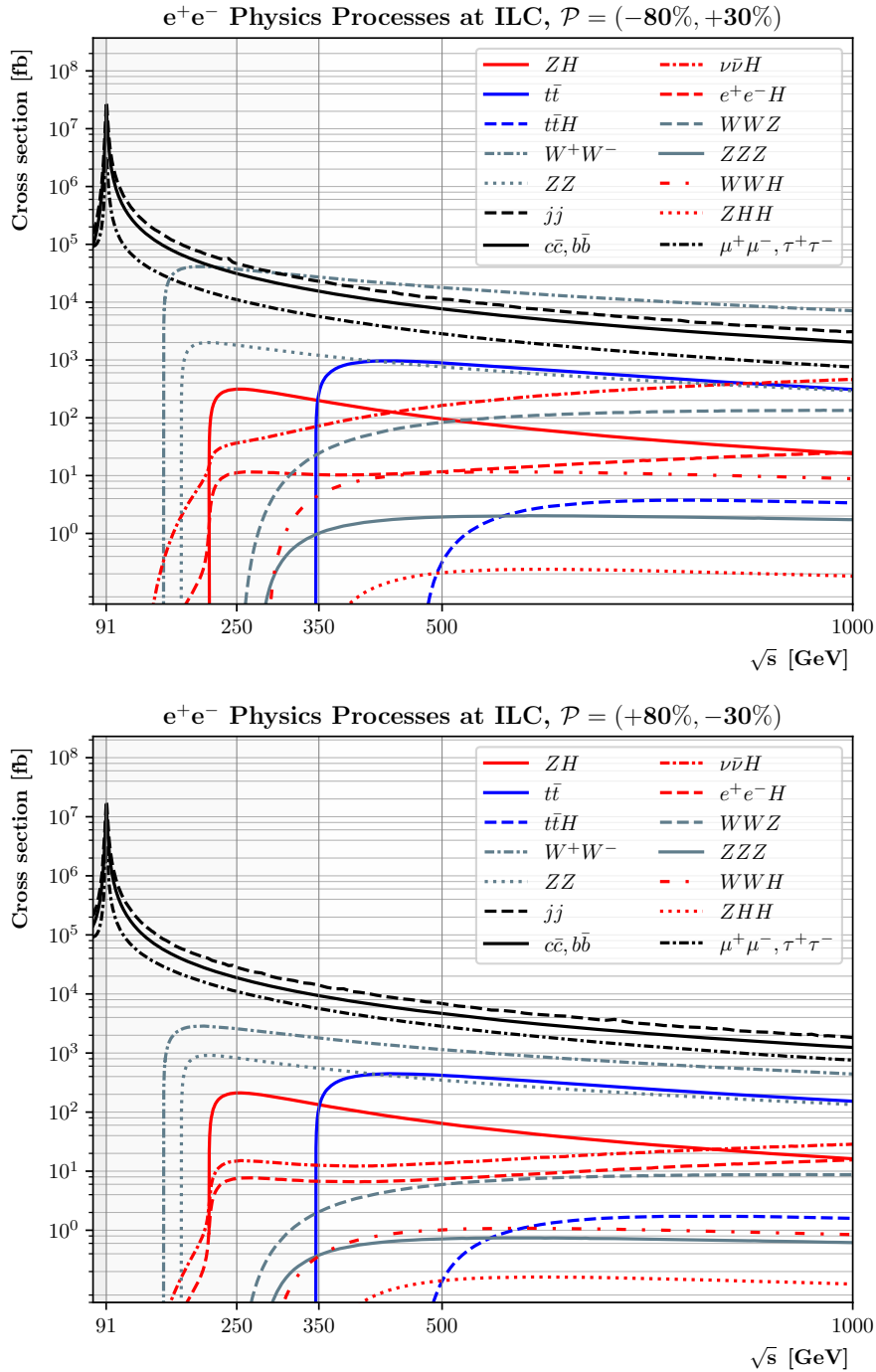


Figure 5.1: Cross sections of the most important Standard Model processes in e^+e^- annihilation in the energy range of the ILC. Initial state radiation is included, and cross section are plotted for reactions in which the annihilation retains $> 90\%$ of the nominal CM energy. The cross sections are shown for predominantly left-handed beam polarization ($-80\%/ +30\%$ for e^-/e^+) (top) and for predominantly right-handed beam polarization ($+80\%/ -30\%$) (bottom). It is instructive to compare the two plots, which have subtle and not-so-subtle differences.

hadron collider experiment. However, these events appear individually in e^+e^- bunch collisions, are essentially free of extra tracks and debris associated with the beams, and are reconstructable with high efficiency over an angular region that extends to within milliradians of the beam directions. The simplicity of typical events allows the use of detector technologies with high degrees of discrimination and precision, as will be discussed in the next chapter.

Since the electron is an elementary particle, the basic parameters of the ILC beams are very well understood. Though the beams contain a distribution of electron and positron energies due to initial state photon radiation and radiation of photons in the beam-beam interaction (“beamstrahlung”), these are minor and computable effects. There is no analogue of the nonperturbative parton distributions needed for the interpretation of cross sections at hadron colliders. Thus, the ILC can carry out measurements of absolutely normalized cross sections at the part-per-mil level, adding a dimension for precision tests of the SM. The beam polarizations can be measured both by dedicated detectors and through SM processes with large cross sections.

Each of the reactions shown in the figure has its own individual role in the program of the ILC. Each reaction gives access to its own set of precision tests of the Standard Model and searches for the effects of new physics. It is important to understand the hierarchy of reactions to understand the important sources of background that enter the various analyses. At an e^+e^- collider, backgrounds from simple QED and QCD processes are readily eliminated. The major backgrounds to processes with the production of heavy particles—within the SM, W , Z , Higgs, and top—are other reactions with heavy SM particles in the final state.

Each reaction also has its own characteristic dependence on beam polarization, as is shown in the figure. This will be an important theme of the discussion in this Chapter.

The simplest reaction in e^+e^- annihilation is that of $e^+e^- \rightarrow f\bar{f}$, where f can be a quark or a lepton. Even for the hadronic reactions, the final state is typically two narrow jets and is easily discriminated from reactions of electroweak bosons. At the tree level in the SM, the differential cross section is very simple. For example, for 100% left-handed polarized beams and $s \gg m_Z^2$, the differential cross sections are

$$\frac{d\sigma}{d\cos\theta} = \frac{\pi\alpha^2}{2s} \left[\left(\frac{1}{2}I_{fL}^3 + \frac{1}{2}Y_{fL} \right)^2 (1 + \cos\theta)^2 + \left(\frac{1}{2}Y_{fR} \right)^2 (1 - \cos\theta)^2 \right], \quad (5.2)$$

where (I_{fL}^3, Y_{fL}) are the electroweak quantum numbers of f_L and $(0, Y_{fR})$ are the electroweak quantum numbers of f_R . Note that the production of the two helicity states of f separates into the two hemispheres. Thus, with two different values for the beam polarization and separate measurement of the forward and backward cross sections, it is possible to probe all four individual helicity amplitudes contributing to this reaction. This provides a powerful and specific probe for new physics, as we will discuss in Sec. 10.4. Bhabha scattering ($e^+e^- \rightarrow e^+e^-$) has a more complex differential cross section, but this reaction is extremely well understood within the SM, leading to its own set of new physics tests.

The reaction $e^+e^- \rightarrow$ hadrons is also an exceptionally clean setting for studies of jets and the measurement of fragmentation functions. The potential ILC contributions to QCD, including new observables sensitive to jet substructure, are described in Sec. 8.4.

The annihilation reaction with the largest cross section in the 250–500 GeV CM energy region is $e^+e^- \rightarrow W^+W^-$. This reaction is forward-peaked, due to the contribution from a diagram with t -channel neutrino exchange. The reaction can be reconstructed in all W decay modes, with the most complex final states having 4 jets. This reaction obtains contributions from diagrams with the triple gauge couplings $WW\gamma$ and WWZ . Because of a cancellation among the SM diagrams required by the unitarity of that theory, the angular distributions and polarization effects in this reaction are exceptionally sensitive to new physics contributions to the triple gauge couplings. These effects are most pronounced in the central and backward W^+W^- production. We will discuss the measurement of these effects in Secs. 8.3 and 10.3. In contrast, the forward production is essentially model-independent. Because the neutrino exchange diagram requires left-handed electrons and right-handed positrons, the forward production has a large polarization asymmetry and so provides a very useful *in situ* measurement of beam polarization.

The other vector boson pair production reactions, $e^+e^- \rightarrow \gamma\gamma, Z\gamma, ZZ$, do not involve triple gauge couplings in the Standard Model. It can be shown that the new physics corrections to these reactions are also suppressed in the description of new physics by Effective Field Theory. Thus, these reactions can provide fundamental test of the Effective Field Theory framework, and, in some cases, tests of general positivity theorems of Quantum Field Theory. We will discuss these issues in Sec. 13.4.

The reaction $e^+e^- \rightarrow \gamma Z$ with the photon almost collinear to the beam direction provides a large source of Z bosons that can be used to probe the Z properties even at CM energies well above the Z resonance. In the ILC run at 250 GeV, we expect to study about 90 million Z bosons in this “radiative return” reaction, leading to an improvement of a factor of 10 in the precision of $\sin^2\theta_w$ even without running at the Z resonance. The study of this reaction will be discussed in Sec. 9.2.

At 250 GeV, the dominant reaction for production of the Higgs boson is $e^+e^- \rightarrow ZH$. This process is expected to produce about half a million Higgs bosons in the 250 GeV run of the ILC, with each Higgs boson tagged by a recoiling Z boson. This will give an excellent setting for the measurement of SM and non-Standard Higgs boson decays. That study will be described in Secs. 8.1 and 8.2.

The ILC also expects a number of reactions with photons in the initial state. The photons arise as virtual photons from initial-state radiation and as real beamstrahlung photons emitted in the beam-beam interaction. For the ILC accelerator parameter sets, these two sources contribute roughly equally to the spectrum of initial photons. Important reactions due to initial-state photons are single W production ($e\gamma \rightarrow W\nu$) and single Z production ($e\gamma \rightarrow Ze$). Reactions with two photons in the initial state include photon annihilation to lepton pairs, quark pairs, and W^+W^- . The single boson production reactions have a role in the precision determination of the W and Z masses, as will be described in Sec. 9.4. All of these processes appear as the major backgrounds to new particle searches involving missing energy, as discussed particularly in Secs. 10.5 and 10.6.

The cross sections for $\gamma\gamma$ production at large angle decrease as $1/s(\gamma\gamma)$. The converse of this statement is that there is a large cross section for $\gamma\gamma$ annihilation to quarks and leptons at the lowest possible CM energies. This leads to an “underlying event” giving a few tracks in each e^+e^- bunch crossing. We find that this background has a negligible effect on our analyses.

At energies above 250 GeV, the initial electrons and positrons can radiate W and Z bosons and these can interact to produce SM and, possibly, new particles by vector boson fusion. The cross sections for these processes rise as $\log(s/m_W^2)$ and so above 500 GeV they become the dominant modes of heavy particle production. The coupling of the electron to the Z is rather small, so the ratio of the ZZ to WW luminosities is

$$\left[\frac{(\frac{1}{2} - \sin^2 \theta_w)^2 + (\sin^2 \theta_w)^2}{\cos^2 \theta_w} / \frac{1}{2} \right]^2 = 1\% \quad (5.3)$$

for unpolarized beams, and even smaller for polarized beams enhanced in the $e_L^- e_R^+$ initial state. Thus, WW fusion plays the dominant role. The most important processes here are WW fusion to a single Z ($e^+e^- \rightarrow \nu\bar{\nu}Z$) and to a single Higgs boson ($e^+e^- \rightarrow \nu\bar{\nu}H$).

The process $e^+e^- \rightarrow \nu\bar{\nu}H$ begins to dominate the $e^+e^- \rightarrow ZH$ process at about 400 GeV. Above this energy, the WW fusion process provides a second, independent data set for the study of Higgs boson couplings. In the WW fusion events, the Higgs boson appears as a heavy, centrally-produced particle with no other visible activity in the event. The fact that the Higgs boson can be produced in two distinct ways at e^+e^- colliders allows cross-checks of any anomalies with the same experimental program. This is another of the special benefits of studying the Higgs boson through e^+e^- annihilation. The study of the Higgs boson in WW fusion will be discussed in detail in Sec. 10.2.1.

The threshold for top quark pair production $e^+e^- \rightarrow t\bar{t}$, occurs in the region around of CM energy of 340–345 GeV. Because the top quark threshold is a very narrow feature, the measurement of the threshold shape can give a very direct and accurate measurement of the top quark mass. At and above the top quark threshold, the ILC can study the couplings of the top quark with high precision. Of special interest are the electroweak couplings of the top quark, which have secondary importance at hadron colliders but provide the primary pair production mechanism at e^+e^- colliders. These couplings can be especially sensitive to new physics corrections, especially in models in which the Higgs boson is composite. There is a significant advantage in measuring these couplings well above threshold, because the axial vector current terms in the top quark vertices are very small near threshold, and because the matching of predictions for the $t\bar{t}$ continuum to the rather different theory of the threshold region introduces extra theory uncertainties. We will discuss all of these issues in Sec. 10.1.

At the highest ILC energies, it is also possible to access multi-Higgs boson production processes. The most important of these are the reactions $e^+e^- \rightarrow ZHH$ and $e^+e^- \rightarrow \nu\bar{\nu}HH$, which depend directly on the Higgs boson self-coupling, and $e^+e^- \rightarrow t\bar{t}H$, which directly measures the Higgs boson coupling to the top quark. We will discuss these analyses in Sec. 10.2.

Thus, each separate ILC reaction has a role to play in challenging the predictions of the SM. Even further, it is best not to interpret the individual processes in isolation from one another. By representing the SM and its possible corrections using Effective Field Theory, the contributions from the different reactions can be brought together and applied in a unified way. The whole set of collider measurements is then more powerful than the simple sum of its parts. We will discuss this strategy of interpreting the ILC measurements in some detail in Chapter 12.

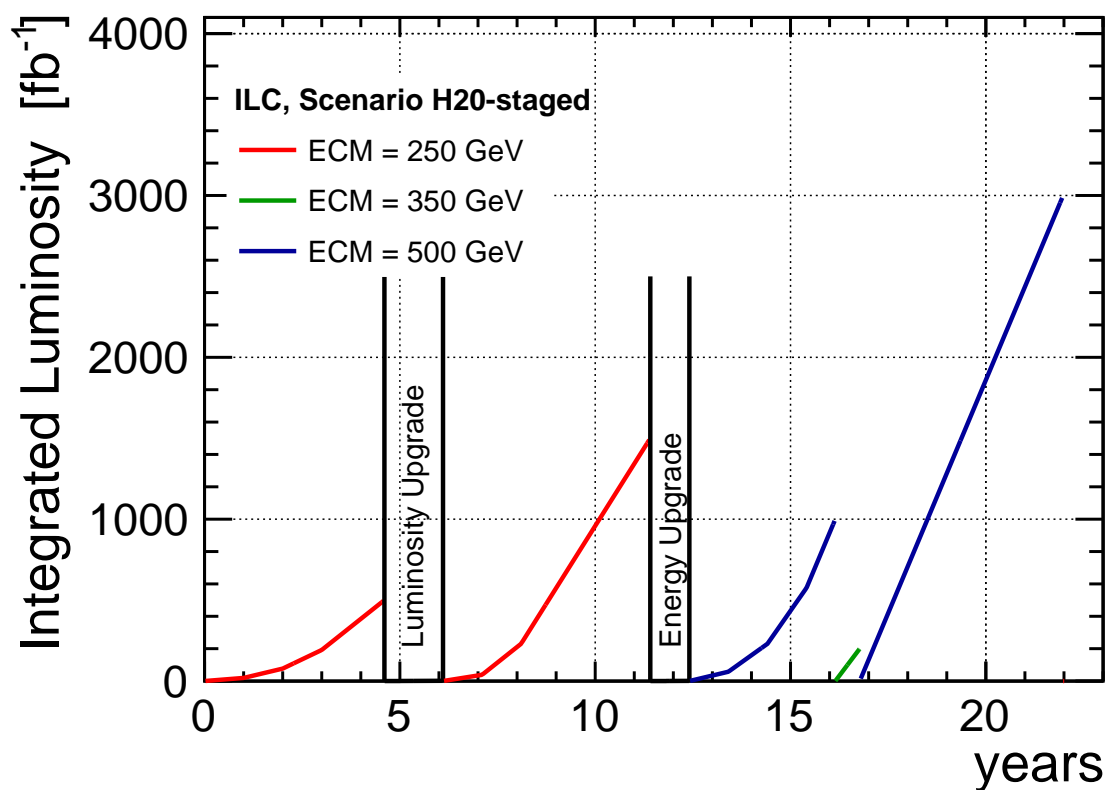


Figure 5.2: The plan for the operation of the ILC through its various stages from 250 GeV to 500 GeV that is used in this report for projections of the physics results expected from the ILC. The details of this program most relevant for physics studies are shown in Table 5.1. The detailed accelerator parameters for each stage are given in Table 4.1. The total length of the program is 22 years. Additional stages at the Z boson resonance and at 1 TeV could be added to this plan. Parameters for these programs are also presented in Table 5.1.

	91 GeV	250 GeV	350 GeV	500 GeV	1000 GeV
$\int \mathcal{L}$ (ab^{-1})	0.1	2	0.2	4	8
duration (yr)	1.5	11	0.75	9	10
beam polarization (e^-/e^+ ; %)	80/30	80/30	80/30	80/30	80/20
(-, -+, +-, ++) (%)	(10,40,40,10)	(5,45,45,5)	(5,68,22,5)	(10,40,40,10)	(10,40,40,10)
δ_{ISR} (%)	10.8	11.7	12.0	12.4	13.0
δ_{BS} (%)	0.16	2.6	1.9	4.5	10.5

Table 5.1: Parameters of the ILC stages most relevant for physics studies. The values given here are those actually used for the results to be quoted in this report. The fourth line gives the fraction of the total running time spent in each of the four possible beam polarization orientations. The fifth and sixth lines give the average energy loss in the electron or positron energy spectrum due to initial state radiation and beamstrahlung, respectively.

5.2 Energy and luminosity

As we have discussed already in Sec. 4.2, the ILC is designed to be upgraded, in stages, in energy and luminosity. Our current plan for the energy and luminosity evolution of the ILC is shown in Fig. 5.2. The parameters of the successive stages that are most important for understanding the physics studies are shown in Table 5.1.

The last lines of the table show the average fractional energy loss to initial state radiation and beamstrahlung. These values reflect the long tails to low energy; for most accepted events, the loss is a few percent.

The ILC will begin with collisions at 250 GeV and a modest design luminosity of $1.35 \times 10^{34} \text{ cm}^{-2}\text{sec}^{-1}$. This luminosity would then be doubled by doubling the number of accelerated bunches per RF pulse, an upgrade that only requires the addition of RF power. In about 11 years, the ILC will have accumulated a total integrated luminosity of 2 ab^{-1} . This will be followed by an energy upgrade, which entails lengthening the linear accelerators to double their energy. We assume the current ILC accelerator parameters for this upgrade, but this will be less costly if higher-gradient superconducting RF cavities are available at that time. The 500 GeV stage will accumulate 4 ab^{-1} of integrated luminosity at 500 GeV, with also 200 fb^{-1} of luminosity near 350 GeV to measure the top quark mass to the level of the theoretical systematic errors.

Two additional runs could be added to this plan. The first is a run at the Z boson resonance, accumulating about 5×10^9 Z bosons. The accelerator parameters for this ‘‘Giga- Z ’’ program have been discussed in Sec. 4.1.4. If this run is done after the installation of RF for the 250 GeV luminosity upgrade, the Z program would take about 1.5 years. The second is a run at 1 TeV, requiring a second lengthening of the linear accelerators. Since the luminosity of a linear collider naturally increases roughly linearly with the center of mass energy, we expect that the 1 TeV operator will accumulate 8 ab^{-1} of integrated luminosity in a 10-year program.

All of this data-taking will benefit from the expected high degree of polarization of the electron beam and the planned polarization of the positron beam. At 1 TeV, where the main object of study

will be the WW fusion reactions, this benefit can be enhanced by choosing to operate predominantly with $e_L^- e_R^+$ -polarized beams.

This plan for the evolution of the ILC is based on a detailed optimization study based on the physics goals, carried out in 2015 [192]. Of course, the plan can be revised according to new developments in particle physics and superconducting RF technology.

5.3 Beam polarization

The ILC design includes beam polarization for both electron and positrons. Beam polarization can be used in experiments in a number of different ways. In this section, we will summarize these and provide the polarization measures appropriate to each case. More details can be found in the individual analysis described below.

The ILC design calls for electron polarization of 80% and positron polarization of 30%. Both signs of the polarization will be available in each run. It is important that the polarization be flipped as often as possible to cancel systematic errors from drifts of detector parameters. For both beams, the polarization can be flipped pseudo-randomly bunch train by bunch train. For the electron beam, this is done at the source by controlling the polarization of the laser used to stimulate electron emission from the cathode. This is similar to the scheme used in the SLD experiment [193] and now applied with very high rate polarization flipping in the JLab program [194, 195]. For the positron beam, the polarization is flipped by spin rotators placed downstream of the helical undulator [78].

The polarization of a beam containing N_L left- and N_R right-handed particles is given by

$$P = \frac{N_R - N_L}{N_L + N_R} \quad (5.4)$$

Then a beam of polarization P contains the fractions of particles of each helicity

$$f_L = \frac{1 - P}{2} \quad f_R = \frac{1 + P}{2} . \quad (5.5)$$

For beams that contain dominantly e_L^- over e_R^- , P is negative and therefore f_L is larger than f_R . The ILC will have four different possible polarization configurations. We will refer to the one with -80% electron polarization and $+30\%$ positron polarization as $-80/+30$ and the other configurations similarly as $-80/-30$, $+80/+30$, and $+80/-30$. For the $-80/+30$ beam configuration, the content in terms of the electron and positron helicity states is

$$f_L(e^-) = 90\% \quad f_R(e^-) = 10\% \quad ; \quad f_R(e^+) = 65\% \quad f_L(e^+) = 35\% , \quad (5.6)$$

so the collisions are dominantly from the $e_L^- e_R^+$ initial state. Since the e_R^- and e_L^- have different $SU(2) \times U(1)$ quantum numbers, each of the four polarization settings is effectively a different scattering experiment. The results of the four experiments can be combined in various ways for different purposes. We describe four of these here.

Cross section asymmetries: Because of helicity conservation in vector boson couplings, e^+e^- annihilation reactions proceed only from the $e_L^-e_R^+$ and $e_R^-e_L^+$ initial helicity combinations. Typically, in annihilation to fermions, the first cross section is larger than the second by about a factor of 2. (Specifically for $e^+e^- \rightarrow ZH$, the $e_L^-e_R^+$ cross section is larger by a factor 1.4.). If we write the two cross sections for 100% polarized initial states as

$$\sigma = \sigma_0(1 \pm \mathcal{A}) \quad (5.7)$$

with $+$ for pure $e_L^-e_R^+$ and $-$ for pure $e_R^-e_L^+$, then the cross section for electron and positron polarizations P_{e^-} and P_{e^+} is

$$\begin{aligned} \sigma(P_{e^-}, P_{e^+}) &= f_L(e^-)f_R(e^+) \sigma_0(1 + \mathcal{A}) + f_R(e^-)f_L(e^+) \sigma_0(1 - \mathcal{A}) \\ &= \left(\frac{1 - P_{e^-}P_{e^+}}{2} \right) \sigma_0 - \left(\frac{P_{e^-} - P_{e^+}}{2} \right) \sigma_0 \mathcal{A}. \end{aligned} \quad (5.8)$$

The asymmetry A between the cross sections with $-+$ and $+-$ polarized beams is then

$$A = -P_{eff} \mathcal{A}, \quad (5.9)$$

with

$$P_{eff} = \frac{P_{e^-} - P_{e^+}}{1 - P_{e^-}P_{e^+}} = \mp 89\% \quad (5.10)$$

for the $-80/+30$ and $+80/-30$ beam configurations, respectively, at the ILC. For this measurement of the intrinsic polarization asymmetry, many sources of systematic uncertainty cancel out, including the absolute luminosity and the absolute detector acceptance. It is necessary that the detector performance be the same for left- and right-handed beams, which is insured if the polarization is flipped rapidly. The measurement of \mathcal{A} does depend strongly on the absolute knowledge of the polarization. As will be discussed in more detail in Sec. 5.4.3, the Compton polarimeters up- and downstream of the IP will monitor the time variations, while the absolute scale of the long-term average polarization values will be directly determined from e^+e^- collision data. Thus, the lion share of the uncertainty will decrease with the size of the data set, down to a floor which is given by the remaining uncorrectable point-to-point fluctuations. These are estimated to be between one and two orders of magnitude smaller than the total polarimeter uncertainty, thus at the level of 10^{-4} .

It is clear already from Eqn. (5.2) that the polarization asymmetry \mathcal{A} gives direct information on the quantum numbers of the particles participating in an e^+e^- annihilation reaction. As we will see in Sec. 12.4, the polarization asymmetry in the reaction $e^+e^- \rightarrow ZH$ also plays an outside role in the global analysis using Effective Field Theory that determines the Higgs boson couplings. It is then remarkable that this quantity can be obtained so precisely using polarized beams.

Cross section enhancements: Another result of Eqn. (5.8) is that, if the physics of a process very much favors the $e_L^-e_R^+$ helicity state, beam polarization gives an enhancement of the effective luminosity. For WW fusion reactions, which appear only from the $e_L^-e_R^+$ initial state, the effective luminosity for $-80/+30$ polarized beams is enhanced from that for unpolarized beams by the factor

$$\mathcal{L}_{eff}/\mathcal{L} = (1 + P_e)(1 - P_p) = 2.3. \quad (5.11)$$

In practice, one should not try to achieve the full promised luminosity enhancement. Each physics process has its own dependence on polarization, and it is also important to reserve some of the luminosity for data on the modes with smaller production cross sections. This is reflected in our choice of the division of polarization modes in line 4 of Table 5.1. The run at the top quark threshold has a quite specific goal, and running with mainly $-80/+30$ polarized beams is optimal for this. At other energies, where the physics program is more general, the fraction of polarizations used should be optimized taking into account also the uses that we will describe next.

Background reduction: Especially for reactions that include neutrinos or other sources of missing energy, the process $e^+e^- \rightarrow W^+W^-$ is a the dominant source of background. It is therefore important that the cross section for $e^+e^- \rightarrow W^+W^-$ is dramatically reduced in the $+80/-30$ initial state. Backgrounds from photon-induced processes such as $\gamma\gamma \rightarrow \ell^+\ell^-$ and single W production are still present in the $-80/-30$ and $+80/+30$ samples, while the annihilation reactions are highly suppressed. This ability to reduce some relevant backgrounds and to directly measure others can be crucial in measuring the rates of these processes precisely or, in the case of particle searches, establishing strong limits.

This is illustrated for a search for dark matter pair production that will be described in Sec. 10.5. Fig. 5.3 shows the results of a simulated search for dark matter pair production $e^+e^- \rightarrow \chi\chi$ at 500 GeV [196]. The analysis assumes no signal and puts a lower limit on an Effective Field Theory mass scale Λ . What concerns us now is the left-hand plot, which includes statistical errors only. The red (short-dash) curve shows the limit from the mixture of polarization states in Table 5.1. The figure shows that almost all of the exclusion comes from the 40% of the run that is collected with the $+80/-30$ beam configuration. However, there is a second half to this story, which is explained below.

Control of systematic uncertainties: With its four configurations for the polarization of the electron and positron beams, the ILC will be carrying out four different experiments simultaneously. These four data samples have very different mixes of physics processes, with e^+e^- annihilation reactions essentially missing from the $-80/-30$ and $+80/+30$ samples while non-annihilation processes remain. However, with rapid polarization flipping, the experiments will be done in the same detector. This allows nuisance parameters associated with detector acceptance and energy response to be measured by comparison of the different samples. The potential systematic uncertainties associated with these parameters can thus be greatly reduced.

As an example of an application of this strategy, look now at the right-hand plot in Fig. 5.3. Nominally, uncertainties from knowledge of the detector would weaken the observed limits, and this effect is visible in the black curve giving the result for unpolarized beams and in the curves for individual polarization states. However, the use of a mix of polarization states, including the nominally unproductive helicity-violating configurations, can be used to evaluate these uncertain detector parameters and retain most of the power of the analysis that included only statistical uncertainties.

In processes subject to smaller systematic uncertainties, an advantage from the enhancement of cross sections is often compensated by the loss of productive luminosity in measuring the samples with helicity-violating polarization configurations. However, the use of positron polarization leads to double the number of individual data sets, adding redundancy and cross-checks. The goal of

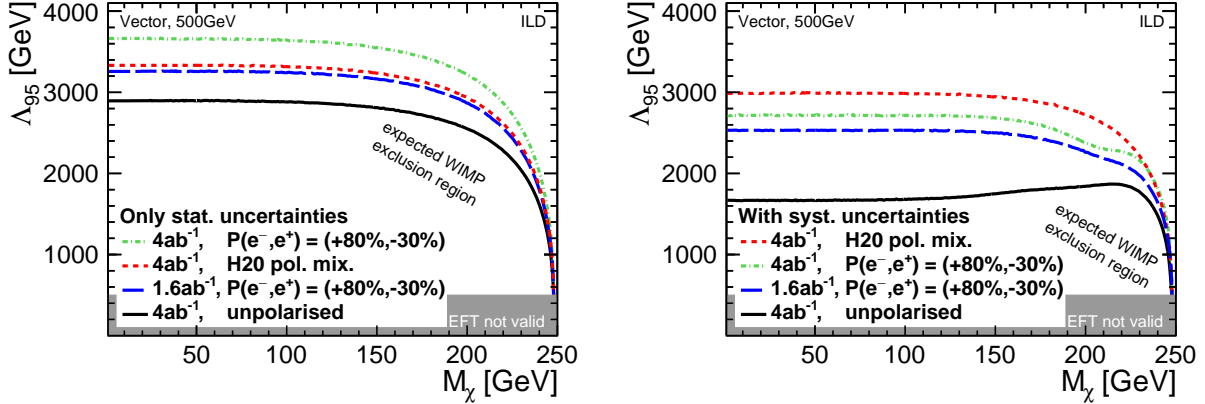


Figure 5.3: Limits on an Effective Field Theory mass scale associated with dark matter particle pair production in e^+e^- annihilation from a search simulation at 500 GeV, showing the dependence of the results on beam polarization, from [196]. Higher limits are better. In both figures, the black curve is an analysis for unpolarized beams, the red (short-dash) curve corresponds to the mixture of polarization states in Table 5.1. Left: analysis with statistical errors only; Right: analysis including both statistical and systematic errors.

the ILC is to demonstrate that the physics of e^+e^- annihilation differs from the predictions of the Standard Model. These checks could prove essential in making that case.

5.4 Control of luminosity, beam energy and polarization

In this section, we will discuss the control of the top-level accelerator parameters—luminosity, beam energy and polarization.

5.4.1 Luminosity measurement

The luminosity will be measured via low-angle Bhabha scattering. The forward regions of the ILC detectors will be equipped with dedicated luminosity calorimeters, described in Sections 6.2.4 and 6.3.6. Recent test beam results obtained with prototype detectors [197] underpin the assumptions on the hardware made in previous detailed simulation studies, which show that the luminosity can be measured to 2.6×10^{-3} and 1.6×10^{-3} at center-of-mass energies of 500 and 1000 GeV, respectively [198]. The energy calibration of the calorimeter contributes to the total uncertainty at the level of 1×10^{-3} . The largest contribution, however, originates from the residual physics backgrounds from $e^+e^- \rightarrow e^+e^-e^+e^-$ and $e^+e^- \rightarrow e^+e^-q\bar{q}$, which in these studies are not corrected for but taken as full-scale contribution to the error budget. Other substantial contributions to the total uncertainty arise from beamstrahlung and ISR, as well as from the electromagnetic deflections of the Bhabhas while they traverse the colliding bunches. It is assumed that these effects can be cor-

rected from simulations. The above numbers include the uncertainty corresponding to a knowledge of the bunch parameters at the 20% level. As will be discussed below, this is a rather conservative assumption. Without the these simulation-dependent corrections, the numbers above would increase by about 50%. At $\sqrt{s} = 250$ GeV, the (uncorrected) effect of the electromagnetic deflection is about twice as large as at 500 GeV, but shrinks to half a per-mil with the simulation-based correction [199]. From the results of this paper and [198], we estimate the luminosity uncertainty at 250 GeV to be less than 4×10^{-3} .

The in-situ determination of the properties of the colliding bunches will be performed by the so-called beam calorimeters (BeamCals); see Secs. 6.2.4 and 6.3.6. Beyond their role as veto taggers for high-energy electrons, the BeamCals record the energy depositions of the enormous numbers e^+e^- pairs created by beamstrahlung. From the pattern of these energy depositions, the relevant parameters of the colliding bunches can be reconstructed, e.g. in terms of number of particles, horizontal and vertical emittances, beam positions and bunch sizes at the IP [200]. For most parameters, precisions of 10% are reached for each bunch crossing in single-parameter analyses. A full multi-parameter analysis would profit from additional information, e.g. from an optional GamCal further down-stream or external constraints on the emittances or bunch charges. The precisions achieved in [200] have been propagated to the luminosity spectrum via GuineaPig [201] in the context of a mono-photon WIMP search [202]. This results in precisions of better than 10% per bin from 200 bunch crossings, showing a clear potential to monitor time-dependences within a bunch train. The long-term average luminosity spectrum can be determined also from Bhabha scattering. This approach has been pioneered for CLIC in [203], reaching a few percent per bin even in the more challenging beam conditions at CLIC. Combining these complementary online and offline methods for monitoring the luminosity spectrum together with accelerator instrumentation data, e.g. from the downstream energy spectrometer, will be an interesting study to pursue in the future.

5.4.2 Beam energy measurement

The beam energy will be monitored upstream and downstream of the e^+e^- interaction point by complementary techniques [93]: the upstream energy spectrometer measures the deflection of the beam in a magnetic chicane with high-resolution beam position monitors, while the downstream spectrometer detects the synchrotron radiation emitted in a chicane in the extraction beamline. Both systems are designed to reach relative precisions of 10^{-4} (100 ppm). The downstream spectrometer can provide information on the beam energy spectrum, complementing the method for beam energy determination described in the previous subsection. Both systems are part of the beam delivery system and the machine-detector interface described in Sec. 4.1.3.

The long-term average center-of-mass energy can be controlled to at least one order of magnitude better from $e^+e^- \rightarrow \mu^+\mu^-(\gamma)$ events. As detailed in [204, 205], the excellent momentum resolution of the detectors proposed for the ILC combined with a calibration to the J/ψ mass will allow a calibration of the center-of-mass energy to a few ppm for the Z pole of the ILC, and to 10 ppm at higher \sqrt{s} .

5.4.3 Polarization measurement

The beam delivery system and the extraction line of the ILC are equipped with laser-Compton polarimeters, providing instantaneous measurements of the beam polarizations at about 1800 m upstream and 150 m downstream of the main e^+e^- interaction point. The expected polarimeter precision of $\delta P/P = 0.25\%$ was presented in Sec. 4.1.3. The decisive polarization values for physics analyses are, however, the luminosity-weighted long-term average values at the interaction point. These will be obtained by combining three main ingredients: the time-resolved polarimeter measurements [95], simulations of the spin transport along the beam delivery system and the extraction line and the beam-beam interaction [206], and a long-term reference scale obtained from the e^+e^- data themselves, predominantly employing physics processes with large left-right asymmetries like W pair production [207, 208, 209]. However, we will argue that for ultimate precision, the polarization values should be included as free (or somewhat pre-constrained) extra parameters in the actual extraction of physics parameters, which will then directly determine the *residual impact* on the physics parameters as well as any possible correlations.

Such an approach has been pioneered in a recent study [210, 211], which employs observables from 2-fermion and 4-fermion processes at $\sqrt{s} = 250$ GeV to constrain the relevant physics parameters (cross-sections, asymmetries, anomalous triple gauge couplings etc) as well as the beam polarizations and parameters modeling the detector acceptance. For the 2-fermion distributions, three additional free parameters allow us to describe deviations from the tree-level helicity amplitudes due to ISR/beamstrahlung (k_0 and Δk in Fig. 5.4) and γ -exchange (ϵ_μ). The study considers various running scenarios of a generic e^+e^- Higgs factory. The results are shown in Fig. 5.4. The orange bars correspond to the standard ILC configuration with both beams polarized and an integrated luminosity of 2 ab^{-1} . It is still a prototype analysis, and as such includes so far only the channels $e^+e^- \rightarrow \mu^+\mu^-$ and $e^+e^- \rightarrow \mu^\pm\nu_\mu jj$, thus the absolute precisions on physics observables should not be taken from Fig. 5.4, but rather from the relevant sections in Chapters 8, 9, and 10. Extrapolating these results to include all relevant final states indicates that the control of all four polarisation values (for electron/positron beams with positive/negative signs) at the level of a few 10^{-4} should be feasible.

The precision of such extractions of the average polarization values from collision data will increase with the size of the data set, thus in particular at the Z pole, the precision will improve further, even without WW processes being available [210]. The final systematic limitation will be the residual point-to-point uncertainties of the polarimeter measurements, which limit the ability to correct for time variations of the polarisations based on the polarimeters. As discussed in Sec. 4.1.3, these uncorrectable point-to-point uncertainties are expected to be between one and two orders of magnitude smaller than the total polarimeter uncertainty, thus at the level of 10^{-4} .

It should be noted that, for ultimate precision physics and a reliable discrimination of genuine deviations from the SM expectations from instrumental effects, any residual polarization in a nominally unpolarized beam, denoted by $P_{e^\pm}^0$ in the figure, must also be included in such global interpretations. This has been realised more than 20 years ago [212] based on SLD experience, and has been revisited more recently in [208] for the ILC and in [213] for the FCCee. As Fig. 5.4(a) shows, these residual polarizations are basically impossible to constrain from collision data beyond the information provided from polarimeters (yellow markers/lines), unless at least part of

the data is taken with non-zero beam polarizations (dark blue bars). The corresponding effect on the 2-fermion physics observables is seen in Fig. 5.4(b), most strikingly in the column showing the initial state asymmetry A_e . If the data are taken with both beams polarized, there is only a tiny residual impact of the finite knowledge on the beam polarizations (the difference between the open cross symbols and the full bars for the orange/dark blue cases), while it is huge in case of electron polarization only (light grey bar). In case of no beam polarisation at all, the set of independent physics observables is reduced, and in particular the initial and final state asymmetries as well as the ϵ parameter which accounts for $Z - \gamma$ -interference effects collapse into one parameter (A_{FB}^μ). Thus, the ability to polarize both beams adds extra physics observables and reduces the impact of systematic uncertainties, as discussed in the previous section.

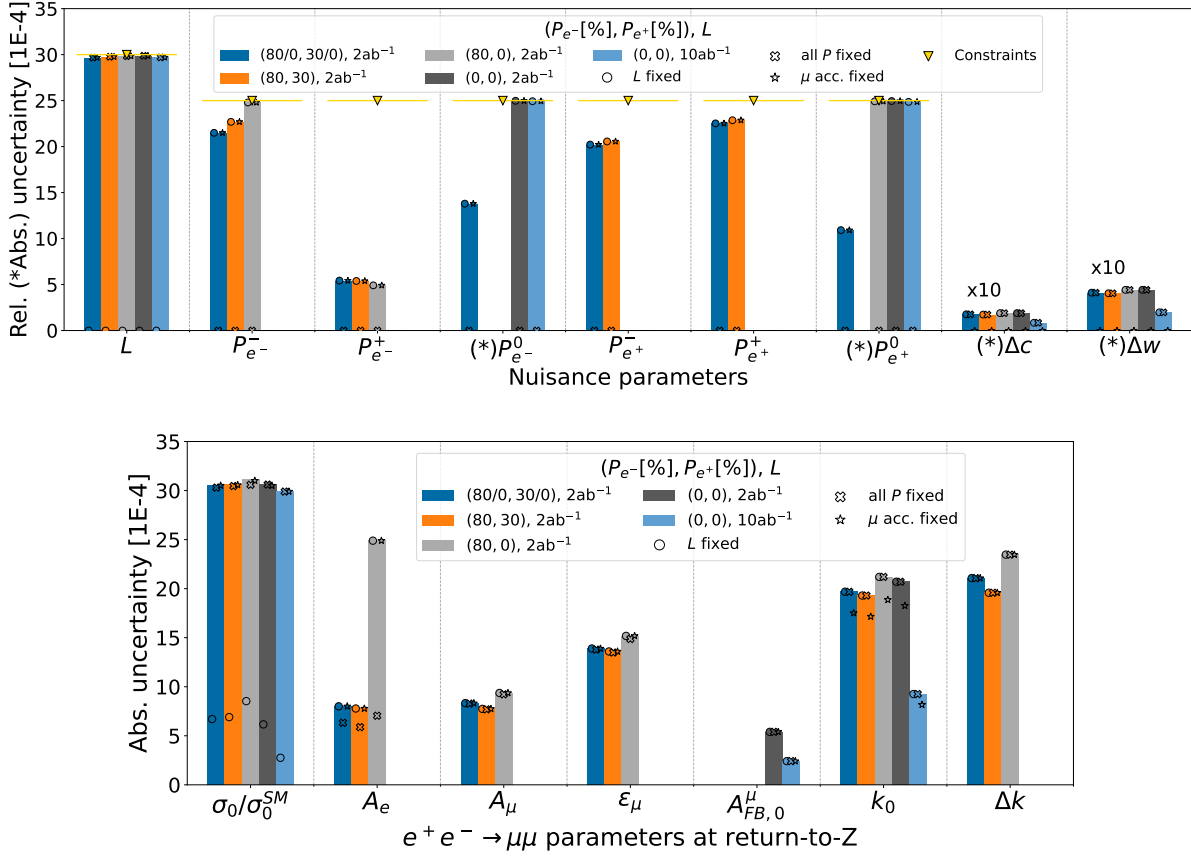


Figure 5.4: Precision to which (a) nuisance parameters, including the beam polarizations, and (b) 2-fermion physics parameters are determined from the combined $e^+e^- \rightarrow \mu^+\mu^-$ and $e^+e^- \rightarrow \mu^\pm\nu_\mu jj$ fit under different assumptions on the integrated luminosity and the beam polarizations. The yellow triangles with horizontal lines indicate the level of external constraints from the luminosity measurement and the polarimeters.

Chapter 6

ILC Detectors

6.1 Detector requirements for the physics program

The ILC accelerator design allows for one interaction region, equipped for two experiments. The two experiments are swapped into the Interaction Point within the so-called “push-pull” scheme. The experiments have been designed to allow fast move-in and move-out from the interaction region, on a timescale of a few hours to a day. In 2008 a call for letters of intent was issued to the community. Following a detailed review by an international detector advisory group, two experiments were selected in 2009 and invited to prepare more detailed proposals. These are the SiD detector and the ILD detector described in this section. Both prepared detailed and costed proposals which were scrutinised by the international advisory group and included in the 2013 ILC Technical Design Report [5]. These specific detector designs have been critical input to the design of the ILC itself. A future process is expected in which detector designs will be reconsidered, with optimisations of these two designs and alternative designs which are proposed. In this chapter the two TDR detector proposals are described.

The ILC detectors are designed to make precision measurements on the Higgs boson, W - and Z -boson, the top quark and other particles. The detector performance requirements are more ambitious than in the LHC experiments, as the experimental conditions are naturally very much more benign and because the detector collaborations have developed technologies specifically to take advantage of these more forgiving conditions. In particular, an e^+e^- collider provides much lower collision rates and events of much lower complexity than a hadron collider, and detectors can be adapted to take advantage of this. The radiation levels at the ILC are equivalent to approximately $10^{11}n/cm^2/year$ of NIEL (Non Ionising Energy Loss) dose, very modest compared with the LHC, where NIEL doses of up to $10^{16}n/cm^2$ are accumulated over the lifetime of the innermost tracking elements. One exception is the special forward calorimeter system very close to the beamline, where radiation exposure will be an issue.

The stringent requirement on the momentum resolution for charged particle tracks is driven by the need to precisely reconstruct the Z -boson mass in the Higgs recoil analysis. This requirement translates into an asymptotic momentum resolution for high-momentum tracks that is nearly an

order of magnitude better than achieved in the LHC experiments. It moreover requires that the detector material be kept to a minimum, to maintain excellent momentum resolution also for lower-momentum tracks.

The identification of jets that originate from the fragmentation of bottom and charm quarks, known as flavour tagging, plays an important role in the scientific program of the ILC. An excellent separation of bottom and charm jets from each other and from gluon jets is crucial for the measurement of the Higgs couplings. This requires a vertex detector with a much improved performance in comparison to the pixel detectors installed at the previous generation of electron-positron colliders and the LHC. The relatively low radiation levels are particularly relevant for the design of the innermost vertex detector elements that can be located very close to the beam.

At the same time, although they are studying electroweak particle production, it is essential that the ILC detectors have excellent performance for jets. At an e^+e^- collider, W and Z bosons are readily observed in their hadronic decay modes, and the study of these modes plays a major role in most analyses. To meet the requirements of precision measurements, the ILC detectors are optimized from the beginning to enable jet reconstruction and measurement using the particle-flow algorithm (PFA). This drives the goal of 3% jet mass resolution at energies above 100 GeV, a resolution about twice as good as has been achieved in the LHC experiments.

Finally, while the LHC detectors depend crucially on multi-level triggers that filter out only a small fraction of events for analysis, the rate of interactions at the ILC is sufficiently low to allow running without a trigger. The ILC accelerator design is based on trains of electron and positron bunches, with a repetition rate of 5 Hz, and with 1312 bunches (and bunch collisions) per train. The 199 ms interval between bunch trains provides ample time for a full readout of data from the previous train. While there are background processes arising from beam-beam interactions, the detector occupancies arising from these have been shown to be manageable.

The combination of extremely precise tracking, excellent jet mass resolution, and triggerless running gives the ILC, at 250 GeV and at higher energies, a superb potential for discovery.

Quantitatively the requirements on the detectors may be summarised by the following points:

- **Impact parameter resolution:** An impact parameter resolution of $5 \mu\text{m} \oplus \frac{10 \mu\text{m GeV}/c}{p \sin^{3/2} \theta}$ has been defined as a goal, where θ is the angle between the particle and the beamline.
- **Momentum resolution:** An inverse momentum resolution of $\Delta(1/p) = 2 \times 10^{-5} (\text{GeV}/c)^{-1}$ asymptotically at high momenta should be reached. Maintaining excellent tracking efficiency and very good momentum resolution at lower momenta will be achieved by an aggressive design to minimise the detector's material budget.
- **Jet energy resolution:** Using the paradigm of particle flow, a jet energy resolution $\Delta E/E = 3 - 4\%$ for light flavour jets should be reached. The resolution is defined in reference to light-quark jets, as the R.M.S. of the inner 90% of the energy distribution.
- **Readout:** The detector readout will not use any trigger, ensuring full efficiency for all possible event topologies. The readout should provide precision signal measurements with high channel granularity and dynamic range.

- **Powering** To allow a continuous readout, while also minimizing the amount of inactive material in the detector, the power of major systems will be cycled between bunch trains.

To meet these goals an ambitious R&D program has been pursued for more than a decade to develop and demonstrate the needed technologies. The results of this program are described in some detail in Ref. [214]. The two experiments proposed for the ILC, SiD and ILD, utilise and rely on the results from these R&D efforts.

Since the goals of SiD and ILD in terms of material budget, tracking performance, heavy-flavor tagging, and jet energy resolution are very demanding, it is important to provide information about the level of detailed input that enters our performance estimates. These are best discussed together with the event reconstruction and analysis framework that we will present in Chapter 7. In that section, we will present estimates of detector performance as illustrations at the successive stages of event analysis.

6.2 The ILD Detector

The International Large Detector, ILD, is a proposal for a multi-purpose detector at the ILC. The design of ILD is the result of more than a decade of work by an international group of scientists and engineers. Throughout this time ILD has profited from and at the same time driven extensive technological developments which make the advanced ILD design possible.

The particle flow concept [215] plays a central role in the ILD design, described in a number of documents. The basic concept and its validation were extensively discussed in the ILD Detector Baseline Document (DBD) in 2013 [5]. ILD has recently, in 2020 published an update to the DBD, the Interim Design Report, IDR [216]. A three-dimensional image of the detector is shown in Figure 6.1, together with an event display of a simulated top–anti-top event within it. Detailed full-simulation studies [5, 216] show that the ILD detector concept can reconstruct complex events with unprecedented precision, meeting all the requirements listed in section 6.1 above.

6.2.1 Concept of the ILD Detector

The science which will be done at the ILC has been summarised earlier in this document. It is strongly dominated by the quest for ultimate precision in measurements of the properties of key particles like the Higgs boson, the weak gauge bosons, and, once the center-of-mass energy is beyond its production threshold, the top quark (see for example [217] or [218] for recent summaries).

The anticipated precision physics program drives the requirements for the detector. The reasoning resulted in the conceptual design of a particle flow detector have been discussed above. ILD thus has the rather standard layout of a tracker and a calorimeter all inside a magnetic field, instrumentation down to rather low solid angles, and a powerful muon system surrounding the detector outside of the coil.

ILD is different from in the specific choice which has been made for the central tracker. Here ILD

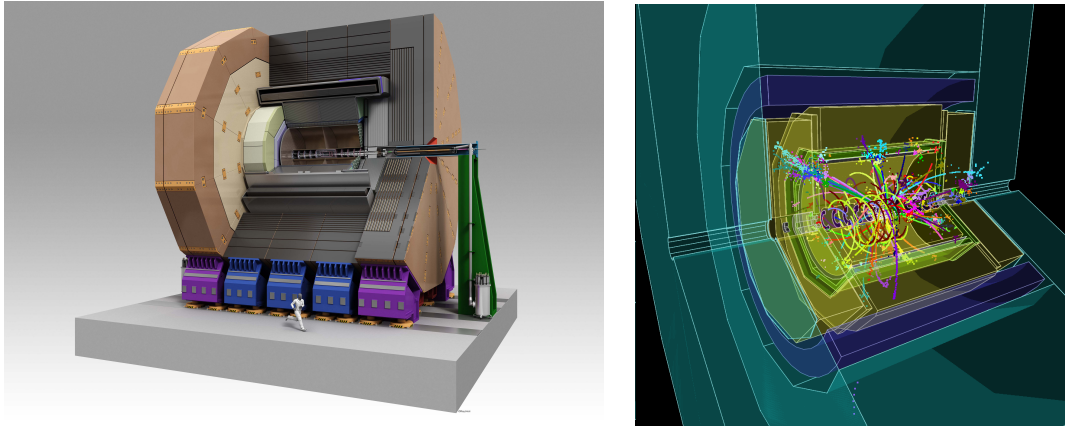


Figure 6.1: Left: Three-dimensional rendering of the ILD detector. Right: Event display of a simulated hadronic decay of a $t\bar{t}$ event in ILD. The colors of the tracks show the results of the reconstruction, each color corresponding to a reconstructed particle.

chose a large volume hybrid tracking system, with a silicon tracking system with excellent position resolution, combined with a large gaseous tracker which promises excellent efficiency combined with low material, together with a highly granular calorimeter in both the electromagnetic and hadronic sections. To ease linking between the tracker and the calorimeter, the calorimeter is placed within the solenoid magnet which provides a 3.5 T field. This choice is driven by the need to provide extremely high efficiency tracking over a large momentum range. The low material budget in a gaseous tracker combined with a large number of three-dimensional space points give an excellent performance for a wide range of topologies and energies.

A number of highly relevant physics processes require the precise reconstruction of exclusive final states containing heavy flavour quarks. This translates into the need for very precise reconstruction of the decay vertices of decaying particles, and thus implies a high resolution vertexing system close to the interaction region.

The ultimate performance of the detector system depends critically on the amount of material in the inner part of the ILD detector. The total material budget in front of the calorimeter should be below 10% of a radiation length, for the barrel part of the detector acceptance. As a consequence, this requires that the coil be located outside of the calorimeter system. The main parameters of the ILD detector concept are summarised in Table 6.1.

The whole detector should be operated without a hardware trigger to maximise the sensitivity to new physics signals. This in turn places stringent requirements on the readout electronics, in terms of both speed and power consumption. The integration of ILD is faced with the additional complexity to allow for a rapid movement of the detector in and out of the interaction region, the so-called push-pull scheme [219].

The ambitious requirements on the performance of the ILC detectors has sparked a broad R&D program, as described above. ILD has traditionally maintained very close and collaborative

Barrel	Technology	r_{in}/mm	r_{out}/mm	z_{max}/mm	
VTX	Silicon pixel	16	60	125	
SIT	Silicon pixel	153	303	644	
TPC	Gas	329	1770	2350	
SET	Silicon strip	1773	1776	2300	
ECAL	Silicon pads	1805	2028	2350	
HCAL	scintillator or RPC	2058	3345	2350	
Coil	4 Tesla Solenoid	3425	4175	2350	
Muon	Scintillator	4450	7755	4047	
Endcap	Technology	z_{min}/mm	z_{max}/mm	r_{in}/mm	r_{out}/mm
FTD 1	Silicon pixel	220	37	-	153
FTD 1	Silicon strip	645	2212	-	200
ECAL	Silicon pads	2411	2635	250	2096
HCAL	scintillator or RPC	2650	3937	350	3226
Muon	Scintillator	4072	6712	350	7716
BeamCal	GaAs pads	3115	3315	18	140
LumiCal	Silicon pads	2412	2541	84	194
LHCAL	Silicon pads	2680	3160	130	315

Table 6.1: Main parameters of the ILD detector for the barrel and the endcap part.

relations with these R&D collaborations.

The ILD concept from its inception has been open to new technologies. No final decision on subdetector technologies has been taken, and in many cases several options are currently under consideration. ILD is actively inviting new groups to join the effort and propose new ideas or improvements to the current concept [8].

In the following paragraphs, the different components of the ILD concept are introduced and discussed.

6.2.2 ILD vertexing system

The system closest to the interaction region is a pixel detector designed to reconstruct decay vertices of short lived particles with great precision. ILD has chosen a system consisting of three double layers of back-thinned pixel detectors. The innermost layer is only half as long as the others to reduce the exposure to background hits. Each layer will provide a spatial resolution around $3 \mu\text{m}$ at a pitch of about $17 \mu\text{m}$, and a timing resolution per layer of around $2\text{--}4 \mu\text{s}$, possibly lower. Current technological developments will most likely make it possible to resolve single bunch crossing. R&D is ongoing to explore the option of a significantly better timing resolution. Since the layers are specifically designed with a very low material budget, of close to 0.15% of a radiation length per layer, the vertex detector also serves as an efficient tracker for low momentum tracks, which due to the magnetic field do not reach the inner tracking system.

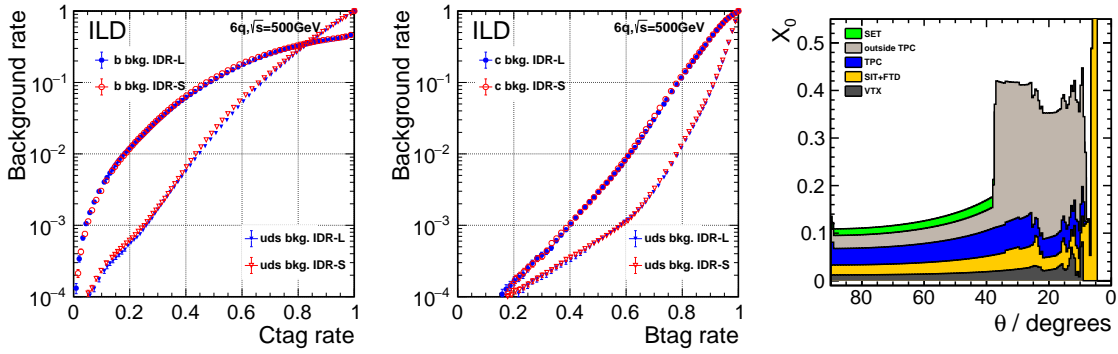


Figure 6.2: Flavour tag performance for the large and small ILD detector models. Background rate as a function of the c-tagging (left) and b-tagging (middle) efficiency for heavy quark and light flavour quark jets. Right: Material budget in ILD up to the calorimeter, in fraction of a radiation length. The different contributions are summed up to represent the cumulative radiation length at a given polar angle. (Figures from [216])

ILD is exploring several technological options for the vertex detector, and has not yet decided on a baseline. Some of the considered technologies are listed below.

Over the last 10 years the CMOS pixel technology has matured close to a point where all the requirements (material budget, readout speed, granularity) needed for an ILC detector can be met. The technology has seen a first large scale use in the STAR vertex detector [220], and more recently in the upgrade of the ALICE Inner Tracking System (ITS-2) [221].

Other technologies under consideration for ILD are DEPFET, which is also currently being deployed in the Belle II vertex detector [222], fine pitch CCDs [223], and also less far developed technologies such as SOI (Silicon-on-insulator) and Chronopix [224].

Very light weight support structures have been developed, which bring the goal of 0.15% of a radiation length per layer within reach. Structures that reach 0.21% X_0 in most of the fiducial volume are now used in the Belle II vertex detector [225].

In Figure 6.2 the purity of the flavour identification in ILD is shown as a function of its efficiency. The performance for b-jet identification is excellent, and charm-jet identification is also good, providing a purity of about 70% at an efficiency of 60%. The system also allows the accurate determination of the charge of displaced vertices, and contributes strongly to the low-momentum tracking capabilities of the overall system, down to a few 10's of MeV. An important aspect of the system leading to superb flavour tagging is the small amount of material in the tracker. This is shown in Figure 6.2 (right).

6.2.3 ILD tracking system

ILD has decided to approach the problem of charged particle tracking with a hybrid solution, which combines a high resolution time projection chamber (TPC) with a few layers of strategically placed

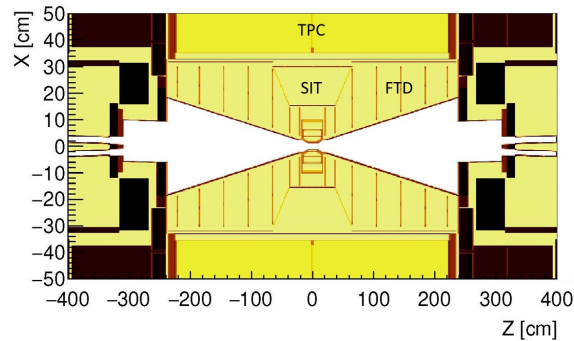


Figure 6.3: Layout of the inner Silicon (SIT) and forward Silicon (FTD) trackers surrounding the vertex detector.

Silicon strip or pixel detectors before and after the TPC. The technologies of the different tracking layers have not been decided yet. The baseline design calls for strips for the three intermediate tracking layers in front of the TPC and the external silicon tracker between the TPC and the ECAL. Recent advances in Silicon pixel technologies make it likely that the Silicon tracker part will be realised as a full pixel tracker. The layout of the inner tracking section is shown in Figure 6.3.

The time-projection chamber will fill a large volume about 4.6 m in length, spanning radii from 33 to 180 cm. In this volume the TPC provides up to 220 three dimensional points for continuous tracking with a single-hit resolution of better than $100 \mu\text{m}$ in $r\phi$, and about 1 mm in z . This high number of points allows a reconstruction of the charged particle component of the event with high accuracy, including the reconstruction of secondaries, long lived particles, kinks, etc.. For momenta above 100 MeV, and within the acceptance of the TPC, greater than 99.9% tracking efficiency has been found in events simulated realistically with full backgrounds. At the same time the complete TPC system will introduce only about 10% of a radiation length into the detector [226].

Inside and outside of the TPC volume a few layers of Silicon detectors provide high resolution points, at a point resolution of $10 \mu\text{m}$. In the forward direction, extending the coverage down to the beam-pipe, a system of two pixel disks (point resolution $5 \mu\text{m}$) and five strip disks (resolution $10 \mu\text{m}$, provide tracking coverage down to the beam-pipe. Combined with the TPC track, this will result in an asymptotic momentum resolution of $\delta p_t/p_t^2 = 2 \times 10^{-5} (\text{GeV}/c)^{-1}$ for the complete system. Since the material in the system is very low, a significantly better resolution at low momenta can be achieved than is possible with a current Silicon-only tracker. The achievable resolution is illustrated in Figure 6.4, where the $1/p_t$ -resolution is shown as a function of the momentum of the charged particle.

The time projection chamber enables the identification of the particle type of the crossing particle through the measurement of the specific energy loss, dE/dx , for tracks at intermediate momenta [227]. The achievable performance is shown in Figure 6.4 (right). ILD wants to achieve a goal of 5% relative dE/dx resolution in the TPC. Time of flight measurements can provide additional information, which is particularly effective in the low-momentum regime which is problematic for dE/dx . Figure 6.4 (right) shows in addition the effect of including time information (resolution 100 ps) from the first ECAL layers.

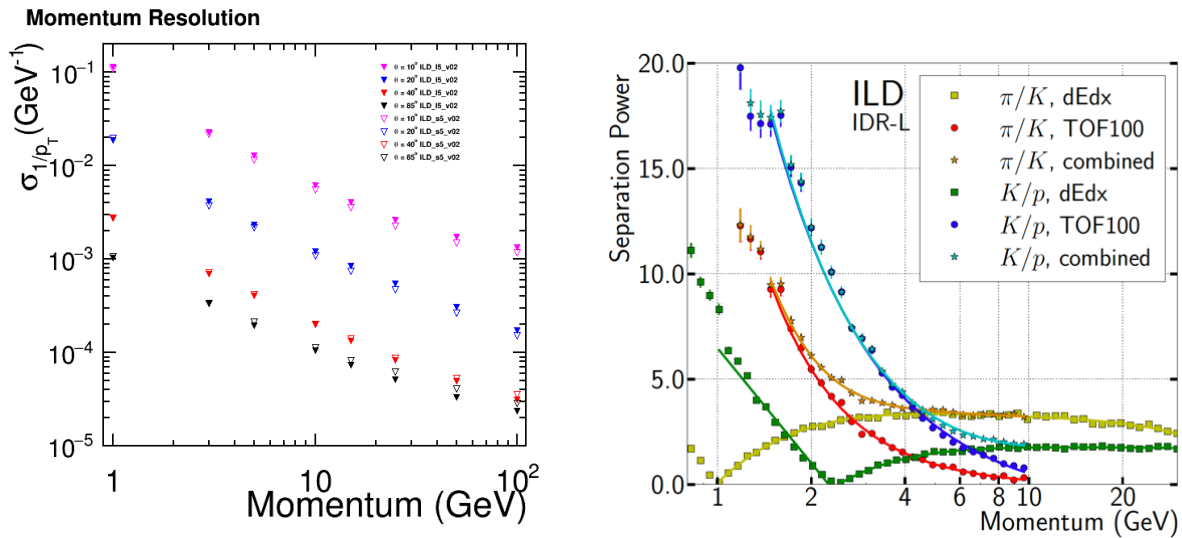


Figure 6.4: Left: Simulated resolution in $1/p_t$ as a function of the momentum for single muons. The different curves correspond to different polar angles. Right: Simulated separation power between pions and kaons and between kaons and protons, from dE/dx and from timing, assuming a 100 ps timing resolution of the first ECAL layers (Figures from [216]).

The design and performance of the TPC has been the subject of intense R&D over the last 15 years [228, 224]. A TPC based on the readout with micro-pattern gas detectors has been developed, and tested in several technological prototypes. The fundamental performance has been demonstrated, and solutions to construct a TPC with the required low mass have been developed. Most recently the performance of the specific energy loss, dE/dx , has been validated in test beam data. Based on these results, the TPC technology is sufficiently mature for use in the ILD detector, and can deliver the required performance (see e.g. [229, 230]).

6.2.4 ILD calorimeter- and muon system

A very powerful calorimeter system is essential to the performance of a detector designed for particle flow reconstruction. Particle flow stresses the ability to separate the individual particles in a jet, both charged and neutral. This puts the imaging capabilities of the system at a premium, and pushes the calorimeter development in the direction of a system with very high granularity in all parts of the system, both transverse to and along the shower development direction. A highly granular sampling calorimeter is the chosen solution to this challenge [231]. The conceptual and technological development of the particle flow calorimeter have been largely done by the CALICE collaboration (for a review of recent CALICE results see e.g. [232, 233]).

ILD has chosen a sampling calorimeter equipped with silicon diodes as one option for the electromagnetic calorimeter. Diodes with pads of about (5×5) mm² are used to sample a shower up to 30 times in the electromagnetic section. A self-supporting carbon-fiber-reinforced-polymer (CFRP)

incorporating tungsten plates supports the detector elements while minimizing non-instrumented spaces. In 2018 beam tests of detection elements in stacks and chained together into long cassettes made important steps towards the demonstration of the large scale feasibility of this technology. Extended tests in 2021 and 2022, including a compact DAQ compatible with the ILD design, are expected to assess the performance with high energy particles. A very similar system has been adopted by the CMS experiment for the upgrade of the endcap calorimeter, and will deliver invaluable information on the scalability and engineering details of such a system. The implementation of precise timing probably mostly in the first calorimeter layers, and the expected performances for single particles are currently under study. Adding timing capabilities of around 100 ps resolution or better to the first layers of the calorimeter would contribute to the capabilities of the ILD detector to identify particle types, in particular at low energies (see Figure 6.4(right)).

As an alternative to the silicon based system, sensitive layers made from thin scintillator strips are also investigated. Orienting the strips perpendicular to each other has the potential to realize an effective cell size of $5 \times 5\text{mm}^2$, with the number of read-out channels reduced by an order of magnitude compared to the all silicon case. A fully integrated technological prototype with 32 layers has been constructed by a joined effort of the R&D groups for the ILD Sc-ECAL and the CEPC-ECAL. It is currently under commissioning and will be tested in particle beam soon.

For the hadronic part of the calorimeter of the ILD detector, two technologies are studied, based on either silicon photo multiplier (SiPM) on scintillator tile technology [234] or resistive plate chambers [235]. The SiPM-on-tile option has a moderate granularity, with $3 \times 3\text{ cm}^2$ tiles, and provides an analogue readout of the signal in each tile (AHCAL). The RPC technology has a better granularity, of $1 \times 1\text{ cm}^2$, but provides only 2-bit amplitude information (SDHCAL). For both technologies, significant prototypes have been built and operated. Both follow the engineering design anticipated for the final detector, and demonstrate thus not only the performance, but also the scalability of the technology to a large detector. As for the ECAL the SiPM-on-tile technology has been selected as baseline for part of the upgrade of the CMS hadronic end-cap calorimeter, and will thus see a major application in the near future.

A rendering of ILD's barrel calorimeter is shown in Figure 6.5 (left).

The iron return yoke of the detector, located outside of the coil, is instrumented to act as a tail catcher and as a muon identification system. Both RPC chambers and scintillator strips read out with SiPMs have been investigated as possible technologies for the system. Up to 14 active layers, located mostly in the inner half of the iron yoke (see Figure 6.5 for more details) will be instrumented. To minimize the number of readout channels a new readout scheme [236] [237] has been developed within the RPC readout option. In this scheme, pads and pixels are interconnected in a special way which allows a precise position measurement based on at least 3 strips under different direction, achieving a very good granularity with limited number of electronic channels.

Three rather specific calorimeter systems are foreseen for the very forward region of the ILD detector [238]. LumiCal is a high precision fine sampling silicon tungsten calorimeter primarily designed to measure electrons from Bhabha scattering, and to precisely determine the integrated luminosity as discussed in Sec. 5.4.1. The LHCAL (Luminosity Hadronic CALorimeter) just outside the LumiCal extends the reach of the endcap calorimeter system down to smaller angles relative to the beam, and closes the gap between the inner edge of the ECAL endcap and the LumiCal.

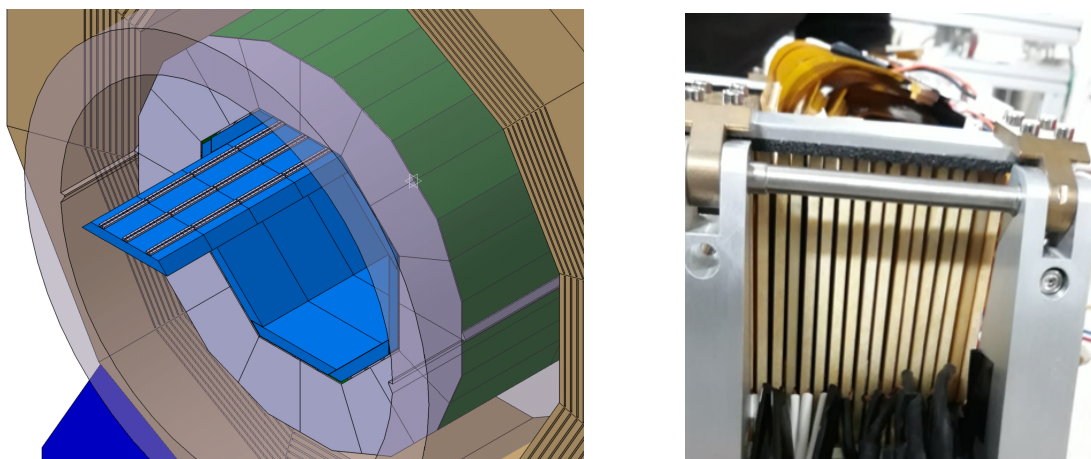


Figure 6.5: Left: Three-dimensional rendering of the barrel calorimeter system, with one ECAL stave partially extracted. Right: Prototype module of the lumical calorimeter.

Below the LumiCal acceptance, where background from beamstrahlung rises sharply, BeamCal, placed further downstream from the interaction point, provides added coverage and is used to provide fast feedback on the beam position at the interaction region. As the systems move close to the beam-pipe, the requirements on radiation hardness and on speed become more and more challenging. Indeed this very forward region in ILD is the only region where radiation hardness of the systems is a key requirement. A picture of a prototype of the Lumical calorimeter is shown in Figure 6.5(right).

6.2.5 ILD detector integration and costing

From the beginning, one of the major goals of the ILD concept group was to move the detector concept from a collection of technological ideas to a real detector that can actually be built, commissioned, and operated within given engineering and site-dependent constraints.

The main mechanical structure of the ILD detector is the iron yoke that consists of three barrel rings and two endcaps. The yoke provides the required shielding for radiation and magnetic fields and supports the cryostat for the detector solenoid and the barrel detectors, calorimeters and tracking system.

A common concept for the detector services such as cables, cooling, gases and cryogenics has been developed. The requirements are in many cases based on engineering prototypes of the ILD sub-systems.

The main detector solenoid is based on CMS experience and can deliver magnetic fields up to 4 T. A correction system for the compensation of the crossing angle of the ILC beam, the Detector Integrated Dipole, has been designed and can be integrated into the main magnet cryostat.

The cost of the ILD detector has been estimated at the time of the ILD interim design report,

IDR [216]. The total detector cost is about 379 Million EUR in 2018 costs. The cost of the detector is dominated by the cost of the calorimeter system and the yoke, which together account for about 60% of the total cost. A slightly smaller version of ILD, where the outer radius of ILD has been reduced by about 10%, but the length of ILD remains unchanged, results in a reduction of the cost by about 50 Million EUR.

6.2.6 Future developments of the ILD detector

The ILD detector group is actively investigating where new technologies might deliver significantly improved performance, expand the capabilities of the detector, or deliver equal performance at lower cost.

The fundamental design criteria of ILD - particle flow as a basis for a complete event reconstruction, excellent pattern recognition capabilities with high efficiency and coverage of the largest possible solid angle - are not at question and remain the basis of any design decisions. The studies on optimizing ILD summarised in the ILD IDR [216] have pointed out a number of areas of high potential where next-generation technologies might have a large impact.

Timing in a number of different sub-systems is one key development direction. Timing at the level of a few 10 ns is already part of the concept. Pushing this to below 100 ps will contribute significant additional capabilities in particle identification and in background reduction. Technologically this is a significant challenge. This option is explored in the tracking system, and in the calorimeter system.

Timing capabilities in the silicon detectors might go hand in hand with increased integration of functionality into the sensor. Moving to silicon systems with smaller feature size might allow the implementation of complex clustering or even tracking algorithms on individual pixels, which could change significantly the way these detectors are operated.

The current layout of the inner tracking system in ILD was optimized for acceptance, robustness towards background and low material budget. With new pixel technologies an all Pixel forward tracker with an optimized layout is an attractive option, which would also ease the transition from the current vertex detector to the forward tracker.

The further reduction of the material budget in the tracker remains a central goal of ILD. Experience from ongoing detector construction projects as the LHC upgrade detectors will provide valuable input, however, new approaches to support structures etc will be needed to really improve the situation further.

The current choice of ILD to implement a gaseous time projection chamber as central tracker remains a very attractive solution, where clear advantages have been demonstrated. The rapid development of silicon technologies on the other hand might open the way to find non-gaseous solutions which offer similar benefits. The combination of a gaseous detector with a highly granular silicon readout over large areas could point into a direction which will combine the best of both worlds.

The calorimeter continues to be an area of very active research, and many improvements to the

current technologies are expected. The application of these technologies to the LHC detectors will provide very important input.

A few rather concrete examples of R&D which could shape the development of ILD is summarised in the following section.

New technologies in ILD

The CMOS detector technology is seeing rapid developments. Based on ever smaller feature size very small pixels might be realised, anticipated to provide a spatial resolution of $<3\mu\text{m}$. They also open the perspective of achieving large multi-reticular sensors, which may be exploited to suppress considerably the material budget of the detector layers, which may become nearly unsupported. The evolution of the CMOS technology also prepares for breakthroughs in terms of time resolution, with projections going well below 1ns.

Another relevant R&D area is the possibility of including precise timing information of the individual signals in the calorimeter readout, turning the calorimeters into a 5D device. This can improve the shower reconstruction to identify the type of particles and also to reduce the noise. Like silicon and scintillator, RPC and, more precisely MRPC, are excellent fast timing detectors which can be exploited by equipping their readout electronics with fast timing capability. This R&D is starting now, studies using silicon systems with integrated amplification and explorative studies of detectors based on 65 nm feature size are being setup.

The general move to extremely large granularity comes at the prize of vast increase of the number of channels and the data volume to be handled and the power consumption of the system. Innovative ways to reduce the number of channels in areas of relatively low occupancies without sacrificing the individual precision will be an important challenge.

6.2.7 Science with ILD

ILD has been designed to operate with electron-positron collisions between 90 GeV and 1 TeV. The science goals of the ILC have been described in detail in [218], and results of numerous studies are reported in the following chapters of this document. It should be pointed out that the analyses which have been performed within the ILD concept group are based on fully simulated events, using a realistic detector model and advanced reconstruction software, and in many cases include estimates of key systematic effects. This is particularly important when estimating the reach the ILC and ILD will have for specific measurements. Determining, for example, the branching ratios of the Higgs at the percent level depends critically on the detector performance, and thus on the quality of the event simulation and reconstruction.

In many cases the performance assumed in the detector simulation has been cross checked with prototype test results. The key performance numbers for the vertexing, tracking and calorimeter systems are all based on results from test beam experiments. The particle flow performance, a key aspect of the ILD physics reach, could not be fully verified in the absence of a large scale detector prototype, but key aspects have been shown in experiments. This includes the single

particle resolution for neutral and charged particles, the particle separation in jets, the linking power between tracking and calorimetry, and detailed shower reconstruction important for particle flow.

While the physics case studies are based on the version of the ILD detector presented in the detector volume of the ILC DBD [239], ILD initiated a systematic benchmarking effort to study the performance of the ILD concept, and to determine in particular the correlations between science objectives and detector performance. The list of benchmark processes which have been studied is given in Table 6.2. Even if the ILC will start operation at a center-of-mass energy of 250 GeV, the ILD detector is being designed to meet the more challenging requirements of higher center-of-mass energies, since major parts of the detector, e.g. the coil, the yoke and the main calorimeters will not be replaced when upgrading the accelerator. Therefore, most of the detector benchmark analyses were performed at a center-of-mass energy of 500 GeV, and one benchmark even at 1 TeV. The assumed integrated luminosities and beam polarization settings followed the canonical running scenario [192]. In addition to the well-established performance aspects of the ILD detector, the potential of new features not yet incorporated in the existing detector prototypes, e.g. time-of-flight information, have also been evaluated.

The results of these studies were published in the ILD Interim Design Report [216]. They form the basis for the definition of a new ILD baseline detector model, which has been used for a new physics-oriented Monte-Carlo production for 250 GeV. Sample production with the most recent beam parameters of the accelerator [29] and significantly improved reconstruction algorithms is expected to lead to further improvements of the expected results of the precision physics program of the ILC [218].

Further ILD performance and physics potential studies are ongoing. Special attention is paid to understanding of systematic effects. Significant reduction of systematic uncertainties is possible in combined analysis of different channels, in particular when combining data taken with different beam polarization settings.

6.2.8 Integration of ILD into the experimental environment

ILD is designed to be able to work in a push-pull arrangement with another detector at a common ILC interaction region. In this scheme ILD sits on a movable platform in the underground experimental hall. This platform allows for a roll-in of ILD from the parking position into the beam and vice versa within a few hours. The detector can be fully opened and maintained in the parking position.

The current mechanical design of ILD assumes an initial assembly of the detector on the surface, similar to the construction of CMS at the LHC. A vertical shaft from the surface into the underground experimental cavern allows ILD to be lowered in five large segments, corresponding to the five yoke rings.

ILD is self-shielding with respect to radiation and magnetic fields to enable the operation and maintenance of equipment surrounding the detector, e.g. cryogenics. Of paramount importance is the possibility to operate and maintain the second ILC push-pull detector in the underground

Measurement	Main physics question	main issue addressed
Higgs mass in $H \rightarrow b\bar{b}$	Precision Higgs mass determination	Flavour tag, jet energy resolution, lepton momentum resolution
Branching ratio $H \rightarrow \mu^+\mu^-$	Rare decay, Higgs Yukawa coupling to muons	High-momentum p_t resolution, μ identification
Limit on $H \rightarrow$ invisible	Hidden sector / Higgs portal	Jet energy resolution, Z or recoil mass resolution, hermeticity
Coupling between Z and left-handed τ	Contact interactions, new physics related to 3rd generation	Highly boosted topologies, τ reconstruction, π^0 reconstruction
WW production, W mass	Anomalous triple gauge couplings, W mass	Jet energy resolution, leptons in forward direction
Cross section of $e^+e^- \rightarrow \nu\nu qq\bar{q}\bar{q}$	Vector Bosons Scattering, test validity of SM at high energies	W/Z separation, jet energy resolution, hermeticity
Left-Right asymmetry in $e^+e^- \rightarrow \gamma Z$	Full six-dimensional EFT interpretation of Higgs measurements	Jet energy scale calibration, lepton and photon reconstruction
Hadronic branching ratios for $H \rightarrow b\bar{b}$ and $c\bar{c}$	New physics modifying the Higgs couplings	Flavour tag, jet energy resolution
A_{FB}, A_{LR} from $e^+e^- \rightarrow b\bar{b}$ and $t\bar{t} \rightarrow b\bar{b}qq\bar{q}\bar{q}/b\bar{b}qql\nu$	Form factors, electroweak coupling	Flavour tag, PID, (multi-)jet final states with jet and vertex charge
Discovery range for low ΔM Higgsinos	Testing SUSY in an area inaccessible for the LHC	Tracks with very low p_t , ISR photon identification, finding multiple vertices
Discovery range for WIMPs in mono-photon channel	Invisible particles, Dark sector	Photon detection at all angles, tagging power in the very forward calorimeters
Discovery range for extra Higgs bosons in $e^+e^- \rightarrow Zh$	Additional scalars with reduced couplings to the Z	Isolated muon finding, ISR photon identification.

Table 6.2: table of benchmark reactions which are used by ILD to optimize the detector performance. The analyses are mostly conducted at 500 GeV center-of-mass energy, to optimally study the detector sensitivity. The channel, the physics motivation, and the main detector performance parameters are given.

cavern during ILC operation.

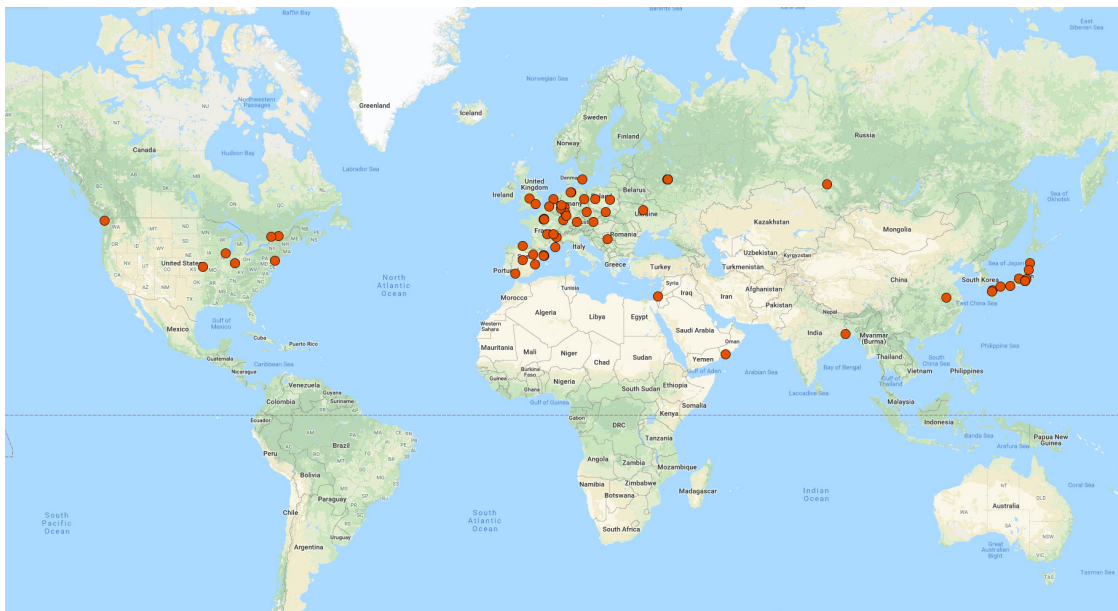


Figure 6.6: Map with the location of the ILD member institutes indicated.

6.2.9 The ILD Concept Group

The ILD collaboration initially started out as a fairly loosely organised group of scientists interested to explore the design of a detector for a linear collider like the ILC. With the delivery of the DBD in 2013, the group re-organised itself more along the lines of a traditional collaboration. The group imposed upon itself a set of by-laws which govern the functions of the group, and define rules for the membership of ILD.

In total 65 groups from 30 countries signed the letter of participation in 2015. At present (2021), 68 institutions are members, and a number of individuals have joined as guest members of ILD. A map indicating the location of the ILD member institutes is shown in Figure 6.6.

6.2.10 Conclusion and outlook

The ILD detector concept is a well developed integrated detector optimised for use at the electron-positron collider ILC. It is based on advanced detector technology, and driven by the science requirements at the ILC. Most of its major components have been fully demonstrated through prototyping and test beam experiments. The physics performance of ILD has been validated using detailed simulation systems. A community interested in building and operating ILD has formed over the last few years. It is already sizeable, encompassing 68 institutes from around the world. The community is ready to move forward once the ILC project receives approval.

6.3 The SiD Detector

6.3.1 Detector description and capabilities

The SiD detector concept is a general-purpose experiment designed to perform precision measurements at the ILC. It satisfies the challenging detector requirements resulting from the full range of ILC physics processes. SiD is based on the paradigm of particle flow, an algorithm by which the reconstruction of both charged and neutral particles is accomplished by an optimised combination of tracking and calorimetry. The net result is a significantly more precise jet energy measurement than that achieved via conventional methods and which results in a di-jet mass resolution good enough to distinguish between W s and Z s. The SiD detector (Fig. 6.7) is a compact detector based on a powerful silicon pixel vertex detector, silicon tracking, silicon-tungsten electromagnetic calorimetry, and highly segmented hadronic calorimetry. SiD also incorporates a high-field solenoid, iron flux return, and a muon identification system. The use of silicon sensors in the vertex, tracking, and calorimetry enables a unique integrated tracking system ideally suited to particle flow.

The choice of silicon detectors for tracking and vertexing ensures that SiD is robust with respect to beam backgrounds or beam loss, provides superior charged particle momentum resolution, and eliminates out-of-time tracks and backgrounds. The main tracking detector and calorimeters are “live” only during a single bunch crossing, so beam-related backgrounds and low-pT backgrounds from $\gamma\gamma$ processes will be reduced to the minimum possible levels. The SiD calorimetry is optimised for excellent jet energy measurement using the particle flow technique. The complete tracking and calorimeter systems are contained within a superconducting solenoid, which has a 5 T field strength, enabling the overall compact design. The coil is located within a layered iron structure that returns the magnetic flux and is instrumented to allow the identification of muons. All aspects of SiD are the result of intensive and leading-edge research aimed at achieving performance at unprecedented levels. At the same time, the design represents a balance between cost and physics performance. Nevertheless, given advances in technologies it is now appropriate to consider updates to the SiD design as discussed below. First, we describe the baseline SiD design for which the key parameters are listed in Table 6.3. The design is expected to meet all the requirements listed in section 6.1 above.

6.3.2 Silicon-based tracking

The tracking system (Fig. 6.8) is a key element of the SiD detector concept. The particle flow algorithm requires excellent tracking with superb efficiency and two-particle separation. The requirements for precision measurements, in particular in the Higgs sector, place high demands on the momentum resolution at the level of $\delta(1/p_T) \sim 2 - 5 \times 10^{-5}/\text{GeV}/c$.

Highly efficient charged particle tracking is achieved using the pixel detector and main tracker to recognise and measure prompt tracks, in conjunction with the ECAL, which can identify short track stubs in its first few layers to catch tracks arising from secondary decays of long-lived particles. With the choice of a 5 T solenoidal magnetic field, in part chosen to control the e^+e^- -pair background, the design allows for a compact tracker design.

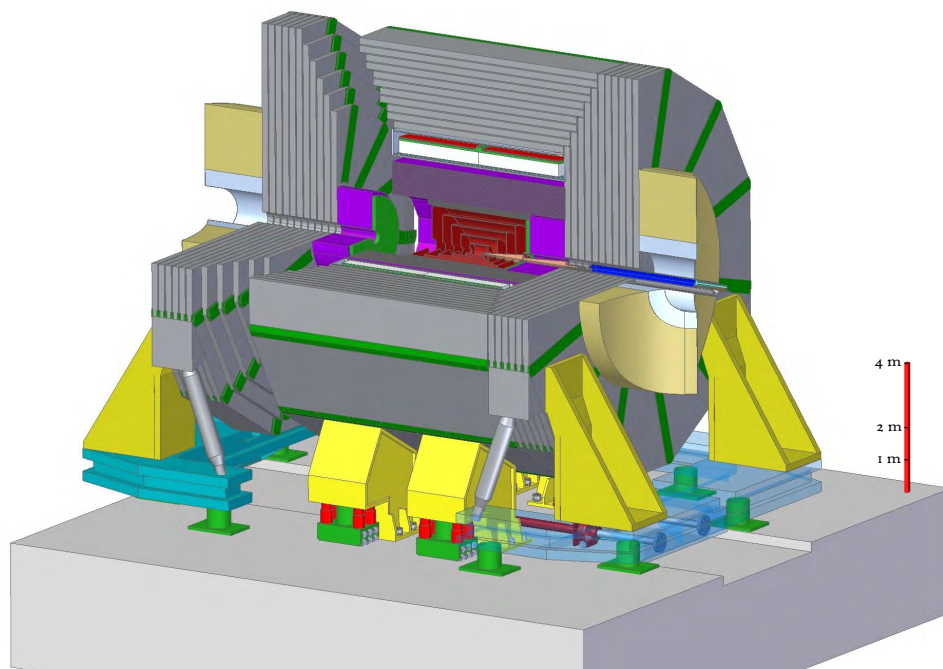


Figure 6.7: The SiD detector concept.

6.3.3 Vertex detector

To unravel the underlying physics mechanisms of new observed processes, the identification of heavy flavours will play a critical role. One of the main tools for heavy flavour identification is the vertex detector. The physics goals dictate an unprecedented spatial three-dimensional point resolution and a very low material budget to minimise multiple Coulomb scattering. The running conditions at the ILC impose the readout speed and radiation tolerance. These requirements are normally in tension. High granularity and fast readout compete with each other and tend to increase the power dissipation. Increased power dissipation in turn leads to an increased material budget. The challenges on the vertex detector are considerable and significant R&D is being carried out on both the development of the sensors and the mechanical support. The SiD vertex detector uses a barrel and disk layout. The barrel section consists of five silicon pixel layers with a pixel size of $20 \times 20 \mu\text{m}^2$. The forward and backward regions each have four silicon pixel disks. In addition, there are three silicon pixel disks at a larger distance from the interaction point to provide uniform coverage for the transition region between the vertex detector and the outer tracker. This configuration provides for very good hermeticity with uniform coverage and guarantees excellent charged-track pattern recognition capability and impact parameter resolution over the full solid angle. This enhances the capability of the integrated tracking system and, in conjunction with the high magnetic field, makes for a very compact system, thereby minimising the size and costs of the calorimetry.

To provide for a very robust track-finding performance the baseline choice for the vertex detector

SiDBarrel	Technology	In rad	Out rad	z extent
Vtx detector	Silicon pixels	1.4	6.0	\pm 6.25
Tracker	Silicon strips	21.7	122.1	\pm 152.2
ECAL	Silicon pixels-W	126.5	140.9	\pm 176.5
HCAL	Scint-steel	141.7	249.3	\pm 301.8
Solenoid	5 Tesla SC	259.1	339.2	\pm 298.3
Flux return	Scint-steel	340.2	604.2	\pm 303.3
SiDEndcap	Technology	In z	Out z	Out rad
Vtx detector	Silicon pixels	7.3	83.4	16.6
Tracker	Silicon strips	77.0	164.3	125.5
ECAL	Silicon pixel-W	165.7	180.0	125.0
HCAL	Scint-steel	180.5	302.8	140.2
Flux return	Scint/steel	303.3	567.3	604.2
LumiCal	Silicon-W	155.7	170.0	20.0
BeamCal	Semicond-W	277.5	300.7	13.5

Table 6.3: Key parameters of the baseline SiD design. (All dimension are given in cm).

has a sensor technology that provides time-stamping of each hit with sufficient precision to assign it to a particular bunch crossing. This significantly suppresses backgrounds.

Several vertex detector sensor technologies are being developed. One of these is a monolithic CMOS pixel detector with time-stamping capability (Chronopixel [240]), being developed in collaboration with SRI International. The pixel size is about $10 \times 10 \mu\text{m}^2$ with a design goal of 99% charged-particle efficiency. The time-stamping feature of the design means each hit is accompanied by a time tag with sufficient precision to assign it to a particular bunch crossing of the ILC – hence the name Chronopixel. This reduces the occupancy to negligible levels, even in the innermost vertex detector layer, yielding a robust vertex detector which operates at background levels significantly in excess of those currently foreseen for the ILC. Chronopixel differs from the similar detectors developed by other groups by its capability to record time stamps for two hits in each pixel while using standard CMOS processing for manufacturing. Following a series of prototypes, the Chronopixel has been proven to be a feasible concept for the ILC. The three prototype versions were fabricated in 2008, in 2012, and in 2014. The main goal of the third prototype was to test possible solutions for a high capacitance problem discovered in prototype 2. The problem was traced to the TSMC 90 nm technology design rules, which led to an unacceptably large value of the sensor diode capacitance. Six different layouts for the prototype 3 sensor diode were tested, and the tests demonstrated that the high capacitance problem was solved.

With prototype 3 proving that a Chronopixel sensor can be successful with all known problems solved, optimal sensor design would be the focus of future tests. The charge collection efficiency for different sensor diode options needs to be measured to determine the option with the best signal-to-noise ratio. Also, sensor efficiency for charged particles with sufficient energy to penetrate the sensor thickness and ceramic package, along with a trigger telescope measurement, needs to be determined. Beyond these fundamental measurements, a prototype of a few cm^2 with a final

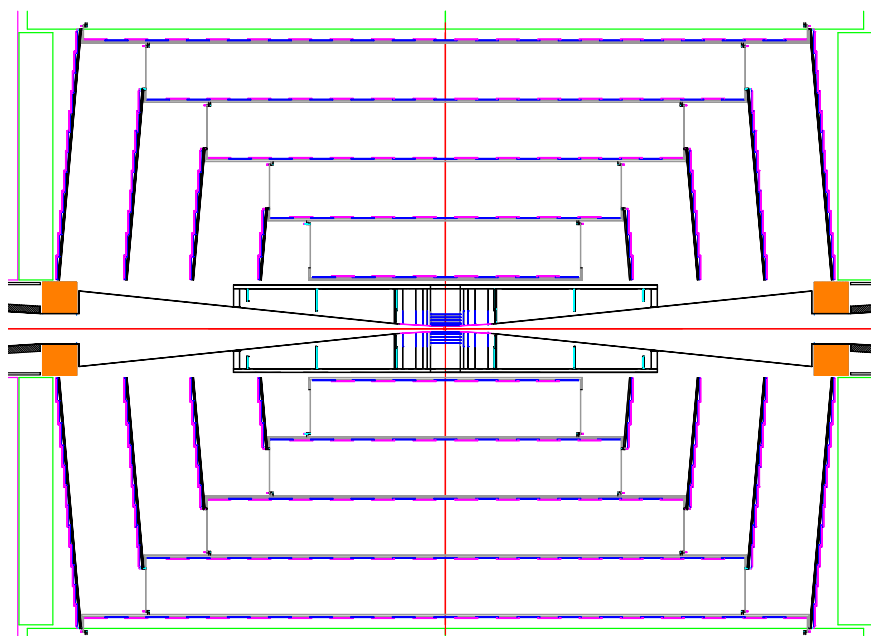


Figure 6.8: r-z view of vertex detector and outer tracker.

readout scheme would test the longer trace readout resistance, capacitance, and crosstalk.

A more challenging approach is the 3D vertical integrated silicon technology, for which a full demonstration is also close.

Minimizing the support material is critical to the development of a high-performance vertex detector. An array of low-mass materials such as reticulated foams and silicon-carbide materials are under consideration. An alternative approach that is being pursued very actively is the embedding of thinned, active sensors in ultra low-mass media. This line of R&D explores thinning active silicon devices to such a thickness that the silicon becomes flexible. The devices can then be embedded in, for example, Kapton structures, providing extreme versatility in designing and constructing a vertex detector.

Power delivery must be accomplished without exceeding the material budget and overheating the detector. The vertex detector design relies on power pulsing during bunch trains to minimise heating and uses forced air for cooling.

6.3.4 Main tracker

The main tracker technology of choice is silicon strip sensors arrayed in five nested cylinders in the central region and four disks following a conical surface with an angle of 5 degrees with respect to the normal to the beamline in each of the end regions. The geometry of the endcaps minimises the material budget to enhance forward tracking. The detectors are single-sided silicon sensors,

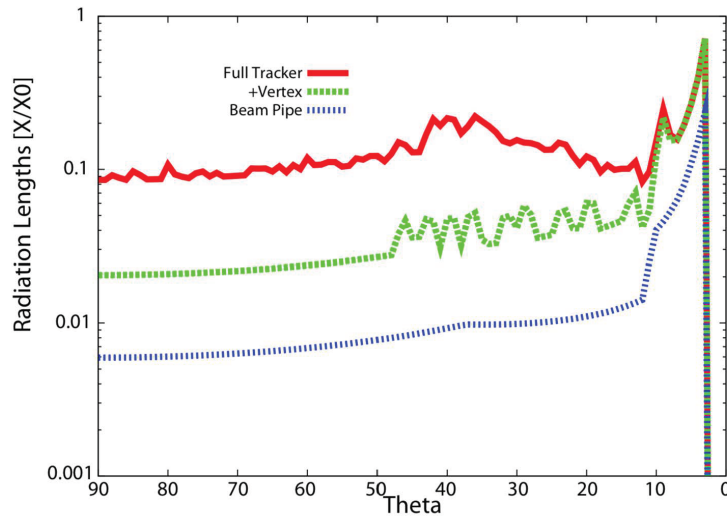


Figure 6.9: Material in the SiD detector, in terms of fractions of a radiation length, as a function of the polar angle.

approximately $10 \times 10 \text{ cm}^2$ with a readout pitch of $50 \mu\text{m}$. The endcaps utilise two sensors bonded back-to-back for small angle stereo measurements. With an outer cylinder radius of 1.25 m and a 5 T field, the charged track momentum resolution will be better than $\delta(1/p_T) = 5 \times 10^{-5}/(\text{GeV}/c)$ for high momentum tracks with coverage down to polar angles of 10 degrees. A plot of the material budget as a function of polar angle is shown in Fig. 6.9.

The all-silicon tracking approach has been extensively tested using full Monte-Carlo simulations including full beam backgrounds. Besides having an excellent momentum resolution it provides robust pattern recognition even in the presence of backgrounds and has a real safety margin, if the machine backgrounds will be worse than expected.

6.3.5 Main calorimeters

The SiD baseline design incorporates the elements needed to successfully implement the PFA approach. This imposes a number of basic requirements on the calorimetry. The central calorimeter system must be contained within the solenoid in order to reliably associate tracks to energy deposits. The electromagnetic and hadronic sections must have imaging capabilities that allow both efficient track-following and correct assignment of energy clusters to tracks. These requirements imply that the calorimeters must be finely segmented both longitudinally and transversely. In order to ensure that no significant amount of energy can escape detection, the calorimetry must extend down to small angles with respect to the beampipe and must be sufficiently deep to prevent significant energy leakage. Since the average penetration depth of a hadronic shower grows with its energy, the calorimeter system must be designed for the highest-energy collisions envisaged.

In order to ease detector construction the calorimeter mechanical design consists of a series

of modules of manageable size and weight. The boundaries between modules are kept as small as possible to prevent significant non-instrumented regions. The detectors are designed to have excellent long-term stability and reliability, since access during the data-taking period will be extremely limited, if not impossible.

The combined ECAL and HCAL systems consist of a central barrel part and two endcaps, nested inside the barrel. The entire barrel system is contained within the volume of the cylindrical superconducting solenoid.

SiD's reliance on particle flow calorimetry to obtain a jet energy resolution of $\sim 3\%$ demands a highly segmented (longitudinally and laterally) electromagnetic calorimeter. It also calls for a minimized lateral electromagnetic shower size, by minimizing the Moliere radius to efficiently separate photons, electrons and charged hadrons.

The SiD ECal design employs thirty longitudinal layers, the first twenty each with 2.50 mm tungsten alloy thickness and 1.25 mm readout gaps, and the last ten with 5.00 mm tungsten alloy. The total depth is 26 radiation lengths, providing good containment of electromagnetic showers.

Simulations have shown the energy resolution for electrons or photons to be well described by $0.17 / \sqrt{E} \oplus 0.009$, degrading a bit at higher energies due to changes in sampling fraction and a small leakage.

The baseline design employs tiled, large, commercially produced silicon sensors (currently assuming 15 cm wafers). The sensors are segmented into pixels that are individually read out over the full range of charge depositions. The complete electronics for the pixels is contained in a single chip, the KPiX ASIC [241], which is bump bonded to the wafer. The low beam-crossing duty cycle (10^{-3}) allows reducing the heat load using power pulsing, thus allowing passive thermal management within the ECal modules.

Bench tests of the KPiX bonded sensor with a cosmic ray telescope trigger yielded a Landau distribution with a peak of the signal at about 4 fC is consistent with our expectation for minimum-ionizing particles (MIP) passing through the fully-depleted 320 μm thick sensors. Crosstalk between channels has been managed and the noise distribution shows an RMS of 0.2 fC, well below the 4 fC MIP signal, and exceeding the ECal requirement.

The overall mechanical structure of the ECal barrel has been designed for minimal uninstrumented gaps. Input power and signals are delivered with Kapton flex cables. The KPiX chip has an average power less than 20 mW, resulting in a total heat load that is managed with a cold plate and water pipes routed into the calorimeter.

A first SiD ECal prototype stack of nine (of thirty) layers has been constructed and was exposed to a 12.1 GeV electron beam at the SLAC End Station Test Beam Facility. This data collection demonstrated good measurements of multiple particle overlap and reconstruction of overlapping showers [242]. Comparison of the deposited energy distribution in each of the nine layers also agrees well with simulations. An algorithm developed to count the number of incident electrons in each event was used to assess the ability of the calorimeter to separate two showers as a function of the separation of the showers, achieving 100% for separations of >10 mm.

The hadronic calorimeter has a depth of 4.5 nuclear interaction lengths, consisting of alternating steel plates and active layers. The baseline choice for the active layers is scintillator tiles read out via silicon photomultipliers. For this approach SiD is closely following the analog hadron calorimeter developments within the CALICE collaboration. In this context, the simulated HCAL energy resolution has been shown to reproduce well the results from the CALICE AHCAL prototype module exposed to pion beams.

6.3.6 Forward calorimeters

Two special calorimeters are foreseen in the very forward region: LumiCal for a precise luminosity measurement as discussed in Sec. 5.4.1, and BeamCal for the fast estimation of the collision parameters and tagging of forward-scattered beam particles. LumiCal and BeamCal are both compact cylindrical electromagnetic calorimeters centered on the outgoing beam, making use of semiconductor-tungsten technology. BeamCal is placed just in front of the final focus quadrupole and LumiCal is aligned with the electromagnetic calorimeter endcap.

LumiCal makes use of conventional silicon diode sensor readout. It is a precision device with challenging requirements on the mechanics and position control, and must achieve a small Moliere radius to reach its precision targets. Substantial work has been done to thin the silicon sensor readout planes within the silicon-tungsten assembly. Dedicated electronics with an appropriately large dynamic range is under development.

BeamCal is exposed to a large flux of low-energy electron-positron pairs originating from beamstrahlung. These depositions, useful for a bunch-by-bunch luminosity estimate and the determination of beam parameters, require radiation hard sensors. The BeamCal has to cope with 100% occupancies, requiring dedicated front-end electronics. A challenge for BeamCal is to identify sensors that will tolerate over one MGy of ionizing radiation per year. Sensor technologies under consideration include polycrystalline chemical vapor deposition (CVD) diamond (too expensive to be used for the full coverage), GaAs, SiC, Sapphire, and conventional silicon diode sensors. The radiation tolerance of all of these sensor technologies has been studied in a high-intensity electron beam.

For SiD, the main activities are the study of these radiation-hard sensors, development of the first version of the so-called Beam readout chip, and the simulation of BeamCal tagging for physics studies. SiD coordinates these activities through its participation in the FCAL R&D Collaboration.

6.3.7 Magnet coil

The SiD superconducting solenoid is based on the CMS solenoid design philosophy and construction techniques, using a slightly modified CMS conductor as its baseline design. Superconducting strand count in the coextruded Rutherford cable was increased from 32 to 40 to accommodate the higher 5 T central field.

Many iron flux return configurations have been simulated in two dimensions so as to reduce the fringe field. An Opera 3D calculation with the Detector Integrated Dipole (DID) coil has been

completed. Calculations of magnetic field with a 3D ANSYS program are in progress. These will have the capability to calculate forces and stress on the DID as well as run transient cases to check the viability of using the DID as a quench propagator for the solenoid. Field and force calculations with an iron endcap HCAL were studied. The field homogeneity improvement was found to be insufficient to pursue this option.

Conceptual DID construction and assembly methods have been studied. The solenoid electrical power system, including a water-cooled dump resistor and grounding, was established. Significant work has been expended on examining different conductor stabiliser options and conductor fabrication methods. This work is pursued as a cost- and time-saving effort for solenoid construction.

6.3.8 Muon system

The flux-return yoke is instrumented with position sensitive detectors to serve as both a muon filter and a tail catcher. The total area to be instrumented is very significant – several thousand square meters. Technologies that lend themselves to low-cost large-area detectors are therefore under investigation. Particles arriving at the muon system have seen large amounts of material in the calorimeters and encounter significant multiple scattering inside the iron. Spatial resolution of a few centimetres is therefore sufficient. Occupancies are low, so strip detectors are possible. The SiD baseline design uses scintillator technology, with RPCs as an alternative. The scintillator technology uses extruded scintillator readout with wavelength shifting fibre and SiPMs, and has been successfully demonstrated. Simulation studies have shown that nine or more layers of sensitive detectors yield adequate energy measurements and good muon detection efficiency and purity. The flux-return yoke itself has been optimised with respect to the uniformity of the central solenoidal field, the external fringe field, and ease of the iron assembly. This was achieved by separating the barrel and end sections of the yoke along a 30 degree line.

6.3.9 The machine-detector interface

A time-efficient implementation of the push-pull model of operation sets specific requirements and challenges for many detector and machine systems, in particular the interaction region (IR) magnets, the cryogenics, the alignment system, the beamline shielding, the detector design and the overall integration. The minimal functional requirements and interface specifications for the push-pull IR have been successfully developed and published [243, 244]. All further IR design work on both the detectors and machine sides are constrained by these specifications.

6.3.10 R&D issues for the SiD design

Monolithic Active Pixel Sensors

MAPS technology is being actively studied for the SiD tracking and electromagnetic calorimeter systems, with initial prototyping underway. For larger-scale objects like a full tracker or an ECAL

sensor, larger structures than the usual full-reticle size (roughly $2.5 \times 2.5\text{cm}^2$) units are required. Reticles would be stitched together with balcony circuitry on one or two (opposing) edges.

In terms of general MAPS R&D required for SiD, mastering of the stitching technology is required, as for such large areas - $O(\sim 100\text{m}^2)$ for the tracker and $O(\sim 1000\text{m}^2)$ for the ECAL - yield becomes an issue. The distribution of power and data over such a large area sensor will be a challenge as well and dedicated R&D is needed.

Given the timescales involved for the construction of an ILC detector like SiD, with the mainstay of construction happening at the end of decade, investment into new processes are needed, as the presently available processes will most likely not be available anymore. The most probable technology for a next-generation MAPS process are the $\sim 65\text{nm}$ CMOS processes that are just becoming available to the community. As CMOS processes use larger wafers (ten or twelve inch wafers) as well as taking advantage of a fully industrial process, the move to MAPS also has clear advantages in terms of a cost reduction for both the tracker and the ECAL.

Simulation studies of electromagnetic showers have demonstrated that the ILC TDR level resolutions, and even better, can be achieved with a digital hit/no-hit threshold MAPS ECAL. [245] The pixel structure of $25\ \mu\text{m} \times 100\ \mu\text{m}$ is chosen to optimize tracking and ECAL applications.

Hadron Calorimeter

Extensions to and optimization of the hadron calorimeter design will also address the following:

- inclusion of timing layers to assist the particle flow algorithm in separating the delayed shower components from slow neutrons from the prompt components.
- potential cost saving by making some of the outer layers thicker if there is no significant degradation in energy resolution.
- optimization of the boundary region between the ECAL and the HCAL and optimization of the first layers of the HCAL to best assist with the measurement of electromagnetic shower leakage into the HCAL.
- reconsideration of the effects of projective cracks between modules. There is some indication from earlier studies that projective cracks have no negative effect on energy resolution, but this needs further verification.
- exploration of alternative layouts for HCAL sectors in the end-caps.
- optimization of the boundary between the HCAL barrel and end-caps.

Muon system

- Optimization of number of instrumented layers, barrel and end-caps.
- Optimization of strip lengths, mainly for barrel system.

- Design for muon endcaps - twelve-fold geometry.
- Occupancies at inner radius of muon end-caps versus strip widths.
- Role of muon system as tail-catcher for HCAL. Consideration and implications of CALICE ECAL + HCAL + Tail-catcher test beam results.
- Potential for use of muon system in search for long-lived particles; timing and pointing capabilities.

Forward Calorimeters

Tasks remaining for the forward calorimeters, with participation in the FCAL R&D Collaboration, include:

- LumiCal: complete development of large dynamic range readout electronics.
- LumiCal: develop and demonstrate the ability to position and maintain the position of the calorimeter, particularly at the inner radius, in view of the steep dependence of the rate of Bhabha events on polar angle.
- BeamCal: continue the search for and testing of suitable sensor technology(s) capable of sustained performance in the very high radiation environment.
- BeamCal: continue the study of recognizing single electron shower patterns for tagging for physics studies in the face of high radiation background.

6.4 New Technologies for ILC Detectors

6.4.1 Introduction

The global particle-physics community continues to develop new ideas for improved sensors and detector systems. In this section, several promising new developments are briefly discussed. Some of these are new technologies that can be integrated in the existing detector concepts, others represent alternatives to the baseline choices made by ILD and SiD.

Since funding for detector R&D is scarce, it is important that the global program covers the essential R&D for the ILC. In Europe, CERN [246] and the ECFA detector R&D panel [247] have published road maps for the effort in instrumentation. A large EU Horizon 2020 project, AIDA Innova [248], unites the effort of seven European national laboratories, 30 universities and institutes and eight industrial partners. In the US, important directions for detector R&D are outlined in the report of the Office of Science Workshop on Basic Research Needs for HEP Detector Research and Development [249]. The "instrumentation frontier group" in the Snowmass process will draft a road map for detector R&D in the US.

Especially important is the synergy with detector construction projects on the intermediate time scale. These projects can validate promising new ideas, with sufficient resources for complete engineering designs and extensive prototyping. The construction phase provides valuable lessons about their practicality in large-scale production. We envisage that projects such as the upgrades of the LHC experiments, and the construction of specialized experiments such as Mu3e and experiments at FAIR and the EIC can act as “stepping stones” in the development of the optimal solutions for the ILC experiments. Smaller experiments, such as for example the LUXE experiment proposed at DESY, might provide an interesting platform to test specific technologies [250].

6.4.2 Low-mass support structures for Silicon trackers

The very strict performance requirements of the silicon tracking systems and vertex detectors has pushed the field to develop active and monolithic silicon sensors that can be thinned to 50 μm or less. To build a superb transparent tracking system this innovation in silicon sensors must be accompanied by important advances in the support structures and cooling systems that make a very important contribution to the material of today’s state-of-the-art detector systems. Integrated support and cooling solutions are required to meet the very challenging material budget of the ILC experiments.

An important step towards the integration of support structures was made by the DEPFET collaboration [251], with the development of the all-silicon ladder concept [252]. In this ladder design, all on-detector electronics and power and signal lines are integrated on the silicon sensor itself. A robust and stiff mechanical structure is obtained by selective etching of the handle wafer, such that an integrated “support frame” surrounds the thin sensor. The all-silicon ladder concept was proven in the Belle 2 vertex detector [253]. Similar self-supporting all-silicon structures can be produced for CMOS active pixel sensors by stitching multiple reticles. The development of the CMOS multi-chip ladder is part of the R&D for the upgrade of vertex detector envisaged in 2027 or 2028.

The PLUME collaboration has developed a double-sided CMOS ladder concept. The ladder design follows a classical approach: six sensors are connected to a low-mass flex-cable to form a module, then two modules are glued on both sides of a mechanical support to form the double-sided ladder. Most of the stiffness of this sandwich-type layer stems from the two modules rather than from the support, which serves essentially as a spacer and is made of a low-density open Silicon Carbide foam [254].

A more aggressive approach is followed by the Mu3e experiment [255] that envisages a Kapton support structure for their thinned CMOS sensors. The ALICE upgrade of the Inner Tracking System [221] envisage CMOS sensors thinned to approximately 50 μm . Innovative solutions to the support structures are being pursued, including a study of large, stitched sensors that are thinned and bent to form cylindrical structures around the beam pipe. The experience gained in these construction projects can have important implications in the ILC vertex detector and tracker design.

6.4.3 Integrated micro-channel cooling

The cooling of these ultra-low-mass detector systems represents an important challenge. Cooling by a loosely guided gas flow has been demonstrated by the heavy flavour tagger in the STAR experiment [256]. Gas-based cooling is also used to complement a traditional bi-phase cooling system in the Belle 2 pixel detector. The heat generated by the pixel sensors is effectively removed by a gas flow at several meters per second. Tests of the mechanical stability of prototypes in gas flows have been performed at CERN by ALICE and CLIC and at DESY by Belle 2. A facility is available for users at the University of Oxford under AIDA innova funding. The magnitude of vibrations induced by the gas flow in realistic prototypes can be kept at the level of a few μm .

Micro-channel cooling promises to bring down the material involved in traditional liquid or bi-phase cooling systems. The use of active silicon cooling plates has been pioneered by the NA62 experiment [257] that has operated the GigaTracker successfully for several years. Micro-channel cooling with evaporative CO_2 at pressures up to 60 bar is part of the Vertex Locator upgrade of the LHCb experiment. The production of VELO modules based on hybrid pixel detectors glued onto silicon micro-channel cooling plates produced at CEA-LETI was successfully completed in 2021 [258]. Installation in the LHCb experiment was still ongoing at the time of writing. Integration of micro-channels directly in the active sensor wafer [259, 260] offers the best possible cooling contact, with a thermal Figure-of-merit close to 1 K/W.

Micro-channel cooling is being considered for FCC-ee [261], where a vertex detector with fast read-out could be positioned close to the beam. In combination with a relatively high-temperature cooling system based on super-critical CO_2 , it might offer a relatively low-mass solution, that brings better control of the temperature than can be achieved with a forced gas flow. The engineering and implications on the material budget need to be studied further.

6.4.4 Dual read-out calorimetry

The 20-year-long *R&D* program on Dual-Readout Calorimetry (DR, DRC) of the DREAM/RD52 collaboration [262, 263, 264, 265, 266, 267, 268, 269] has shown that the effects of the fluctuations in the EM fraction of hadronic showers can be canceled by the independent readout of scintillation (S) and Čerenkov (C) light. The DR fibre-sampling approach achieves a high sampling frequency leading to a competitive EM energy resolution $\sim 10\%/\sqrt{E}$. Application of the DR procedure gives a stochastic term of the hadronic resolution close to or even below $30\%/\sqrt{E}$ with a small constant term. Test beam results also show excellent particle-ID performance.

The advancements in solid-state light sensors such as SiPMs have opened the way for highly granular fibre-sampling detectors with the capability to resolve the shower angular position at the mrad level or even better. In the present design 1-mm diameter fibres are placed at a distance of 1.5-2 mm (center to center) in a metal absorber. Brass, copper, iron and lead are currently under study. The lateral segmentation could then reach the mm level, largely enhancing the resolving power for close-by showers with a significant impact on π^0 and τ reconstruction quality. In addition the high Photon Detection Efficiency of SiPMs provide high light yields, thus reducing the effect of photon statistics. Readout ASICs providing time information with ~ 100 ps resolution may allow

the reconstruction of the shower position with ~ 5 cm of longitudinal resolution.

The large number and density of channels call for an innovative readout architecture for efficient information extraction. Both charge-integrating and waveform-sampling ASICs are available on the market and candidates for tests have been identified: the Weeroc Citiroc 1A charge integrator and the Nalu Scientific system-on-chip digitisers. A first implementation of a scalable readout system has been tested with a calorimeter prototype on particle beams. Looking further ahead, digital SiPMs (dSiPMs) could provide significant simplification of the readout architecture, but the technology is still in an early *R&D* phase.

The performance of a 4π DR calorimeter for an FCC-ee experiment has been studied with full GEANT4 simulation with good results on key physics processes. This is now the baseline choice for the IDEA [270] detector concept. Significant performance improvements have also been shown using deep-learning algorithms. Studies of the potential addition of a dual-readout crystal calorimeter in front find superb EM resolution, while maintaining the hadronic performance and even improving it by applying simple particle flow algorithms [271]. A more detailed description is found in Ref. [272].

6.4.5 Crystal electromagnetic calorimetry

As noted above, the CALICE and RD52/DREAM collaborations have demonstrated that both designs can achieve a jet energy resolution of 3-4% for jets expected from $W/Z \rightarrow qq$ decays [231, 273]. However, the EM energy resolution is expected to be $\sim 15\%/\sqrt{E}$ for Particle Flow and $\sim 10\%/\sqrt{E}$ for DREAM, largely because of the small sampling fractions. These resolutions are significantly worse than those of crystal ECALs [274, 275]. Thus, it is interesting to study the combination of the DREAM fiber HCAL with a crystal ECAL. This can potentially maintain or even improve the jet energy resolution while attaining the EM resolution of $< 3\%/\sqrt{E}$ [276]. A consortium of US teams is leading this R&D.

6.4.6 Liquid Argon calorimetry

Noble-liquid calorimeters have been successfully used in many high-energy collider experiments, such as ATLAS, D0 or H1. They feature high energy resolution, excellent linearity, uniformity, stability, and radiation hardness. These properties make a noble-liquid calorimeter an appealing candidate for an experiment at the next-generation Higgs factories, especially in the case of a program of high precision physics at the Z pole where an excellent control of the systematic uncertainties is required to match statistical precisions as low as 10^{-5} .

A design of a highly granular sampling noble liquid calorimeter was first proposed in the context of a FCC-hh experiment [277], and is now being revisited and optimised for a Higgs factory machine. In the central region, it consists of a cylindrical stack of 1536 lead absorbers (2mm thick), readout electrodes (1.2mm thick) and liquid argon active gaps, arranged radially but azimuthally inclined by $\sim 50^\circ$ with respect to the radial direction. This design allows for reading out the signals without creating any gaps in the acceptance, high sampling frequency, uniformity in ϕ , and can be build

with very good mechanical precision to minimise the constant term of the energy resolution. The use of liquid krypton as active material and of tungsten absorbers is being studied as it could result in a more compact design with better shower separation.

The use of readout electrodes allows to optimise the granularity of each of the 11 longitudinal compartments for the needs of particle-flow reconstruction and particle-ID. A total number of a few million cells can be achieved by using seven-layer PCBs, where the outermost layers provide the high voltage field in the noble-liquid gap, and next layers are signal pads, connected to the central layer where traces bring the signals to the outer edges of the electrodes. The trade-offs between granularity, noise and cross-talk in the design of the PCBs are being studied.

The expected noise levels assuming readout electronics outside the cryostat should allow the tracking of single particles and yield a total noise of about 50 MeV for an electromagnetic cluster. The alternative of using cold readout electronics placed inside the cryostat is also studied as it would achieve a much lower noise, and could simplify the design of the feedthroughs. R&D on high-density feedthroughs is indeed ongoing to allow the analogue readout of millions of channels without any performance degradation. A reduction of the amount of dead material in front of the calorimeter can be achieved thanks to the progress on 'transparent' cryostats using carbon or sandwiches of materials.

Better estimates of the expected performance (using the calorimeter alone and with particle-flow reconstruction), and answers on the feasibility of the designs of the PCBs, the readout electronics and the feedthroughs, will be available in the next months and years.

6.4.7 Digital pixel calorimetry

Initial proof-of-concept demonstrations of the use of digital electromagnetic calorimetry (DECAL) were made in the framework of ILC detector development [278, 279, 280]. The first proof-of-principle of a DECAL was made in the context of the ALICE experiment forward calorimeter proposal (FoCal) [281], with the design and fabrication of a multiple-layer prototype and corresponding measurements, proving the viability of the concept [282].

The fundamental principle underlying a DECAL is to measure energy by counting the number of charged shower particles using very high transverse granularity sampling layers. To avoid saturation effects and ensure competitive resolution and linearity, binary-readout CMOS pixels are used; these must be sufficiently small that the double-hit probability is negligible even in the core of high-energy electromagnetic showers. The small pixel size also has clear benefits in dense particle environments for pattern recognition algorithms such as particle flow, e.g. [283].

Digital calorimeters use a sandwich structure of silicon and tungsten layers, with Monolithic Active Pixel Sensors (MAPS) being a natural choice in terms of granularity and cost. The proof-of-principle prototype [282], also called EPICAL-1, required a total sensor area of almost 400 cm², and therefore the PHASE2/MIMOSA23 chip from IPHC [284] with a pixel size of 30 × 30 μm² was used for this R&D.

Current R&D is performed using a second generation DECAL prototype, the EPICAL-2, which

has an active area of approx. $3 \times 3 \text{ cm}^2$ per sensitive layer. These comprise state-of-the-art ALPIDE sensors, developed for the ALICE ITS and MFT [285], which have a similar pixel size to the MIMOSA. Measurements with this prototype have been performed with cosmic muons in the lab, and with test beams at both DESY in 2020 and the CERN SPS in 2021. This prototype has performed extremely well, surpassing the performance of EPICAL-1. The substantial experience with two prototypes using sensors from different developers and foundries has reliably demonstrated that the technology is a very good candidate for future calorimeters.

Full analysis of data from EPICAL-1 and preliminary results from EPICAL-2 show:

1. CMOS MAPS sensors work reliably in the high particle density environment of high-energy electromagnetic showers;
2. there are no substantial saturation effects due to shower particle overlap in the pixels up to energies of at least a few hundred GeV;
3. the energy resolution from test beam results at DESY is very similar to that from state-of-the-art in analogue silicon-tungsten calorimeters;
4. the single-shower position resolution is of the order of the pixel size or better.

The data obtained with EPICAL-2 will improve the understanding of the detection process and allow the development of improved reconstruction algorithms, including the correction of possible residual saturation effects.

While the work discussed above concentrates on a small scale prototype to further develop the new technology, parallel R&D activities are ongoing to solve the challenges related to scaling this up to a reasonable size. A very similar detector concept using the same technology is the basis for a development of a proton CT scanner for medical applications [286]—this addresses the development of large area pixel sensor layers for use in a calorimeter, including full connectivity and services.

6.4.8 Low gain avalanche detectors

Low-Gain Avalanche Diode (LGAD) sensors [287] are a promising technology that, due to their intrinsic signal amplification, could significantly reduce the sensor substrate thickness and hence the material budget of the Silicon tracking systems of the ILC experiments. The large signal-to-noise ratio and short rise time of the LGAD signal make them also suitable for the precise time stamping of charged particles [288, 289]. A tracker system based on these technologies could provide high-precision tracking and a timing resolution of the order of tens of picoseconds that would significantly enhance particle-identification capabilities, in particular for low-momentum charged-particle tracks.

LGADs are the current reference technology for timing detectors for charged particles in preparation for the high-luminosity upgrades of the LHC experiments. Large-area timing detectors based on this technology are envisaged for the CMS [290] and ATLAS [291] HL-LHC upgrades.

The adaptation of LGAD technology to the requirements of a high-precision tracking system for the ILC detectors involves two main challenges with respect to the current state of the art: high

fill factor and large area detector fabrication. Dedicated R & D activities are being carried out to address these challenges on the basis of specialized developments of the LGAD concept: inverted LGAD (iLGAD [287, 292]), trench-isolated LGAD (TI-LGAD [293]), and AC-coupled LGADs (AC-LGAD or RSD [294]).

6.4.9 New sensor technologies for highly compact electromagnetic calorimeters

The luminosity is a key parameter of any collider. For electron-positron colliders Bhabha scattering at small angles is the gauge process to approach a precision of 10⁻³ or better. To count Bhabha events compact electromagnetic calorimeters are the preferred technology. A small Moliere radius is of advantage, in particular in the presence of background. In addition, it keeps the size of the calorimeters small, and allows to define precisely the fiducial volume, important for the precision of the measurement. Tungsten is an absorber material with a very small Moliere radius. To instrument the calorimeter with sensors, gaps between tungsten plates have to be foreseen. In order to keep the Moliere radius near that of tungsten, these gaps must be very small, requiring thin assembled sensor planes. For this purpose GaAs sensors with aluminum traces integrated on the sensors are developed. These traces connect the sensor pads with bonding pads on the edge of the sensor. A flexible Kapton PCB with copper traces is bonded to the sensor and feeds the signals to the FE ASICs.

GaAs sensors are made of single crystals. High resistivity of 10⁹Ωm is reached by compensation with chromium. The pads are 4.7 × 4.7 mm², with 0.3 mm gap between pads. Pads consist of a 0.05μm vanadium layer, covered with a 1μm aluminum, made with electron beam evaporation and magnetron sputtering. The back-plane is made of nickel and aluminum of 0.02 and 1μm thickness, respectively. The sensors are 550μm thick with overall sizes of 51.9 × 75.6 mm². The active area is 74.7 × 49.7 mm² leading to 15 × 10 pads without guard rings. The signals from the pads are routed to bond pads on the top edge of the sensor by aluminum traces implemented on the sensor itself, thus avoiding the presence of a flexible PCB fanout. The traces are made of 1μm thick aluminum film deposited on the silicon dioxide passivation layer by means of magnetron sputtering. A prototype sensor is shown in Fig. 6.10 (left).

Details on the sensor structure can be seen in the cross-profile shown in Fig. 6.10 (right). More details on the aluminum traces are illustrated in Fig. 6.11(left).

Using several prototype sensors, the leakage current of all pads was measured as a function of the bias voltage. A typical example is shown in Fig. 6.11(right). At a bias voltage of 100 V the leakage current amounts to about 50 nA.

The implementation of the aluminum traces is a new technology. The response to relativistic electrons was measured in a test-beam of 5 GeV at DESY. A clear signal was observed, as can be seen in Fig. 6.12

The first results from test-beam measurements are very promising. detailed studies on homogeneity of the response, and cross talk are still ongoing. Currently these sensors are the baseline option for the electromagnetic calorimeter of the LUXE experiment.

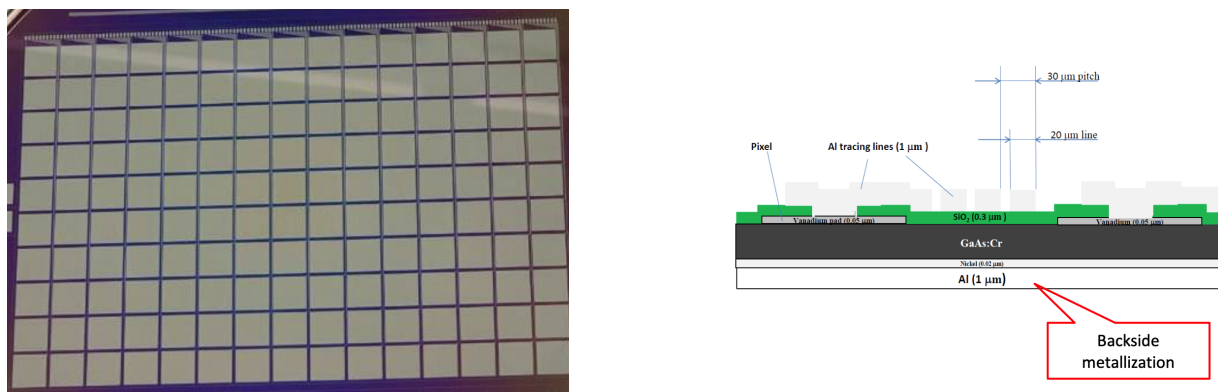


Figure 6.10: Left: Picture of a GaAs sensor. The bond pads are visible on top of the sensor, Right: Cross-profile of a GaAs sensor. The aluminum traces are positioned between the pads, on the top of the passivation layer.

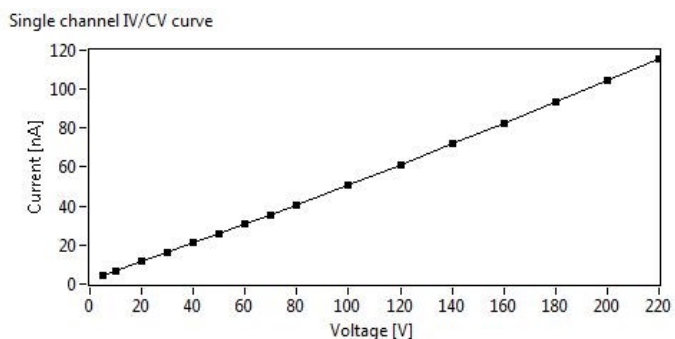
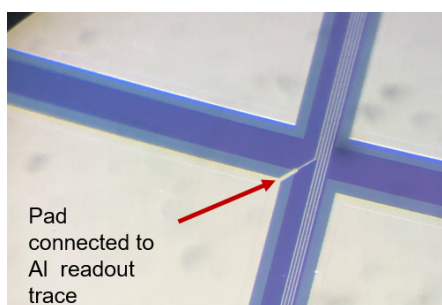


Figure 6.11: Left: Picture of the surface of a GaAs sensor. The aluminum traces are positioned between the pads, on the top of the passivation layer, Right: The leakage current of a pad as a function of the bias voltage, measured at 20°C.

6.4.10 Single crystal sapphire sensors for charged particle detection

For the operation in a harsh radiation environment, typical for near-beam detectors at LHC or free electron lasers like FLASH and XFEL, extremely radiation hard sensors are needed. In the past often CVD grown diamond sensors are used in such environment. Regardless of the excellent radiation hardness and low leakage current at room temperature, the application of diamond sensors is limited due to high cost, relatively small size and low manufacturing rate. As an alternative we suggest using sapphire sensors. Optical grade single crystal sapphire is industrially grown in practically unlimited amounts and the wafers are of large size and low cost. Sapphire sensors have been used so far in cases where the signal is generated by simultaneous hits of many particles, i.e., in the beam halo measurement at FLASH, XFEL and the CMS experiment at the LHC. It was found that the time characteristics of signals from sapphire sensors are similar to the ones

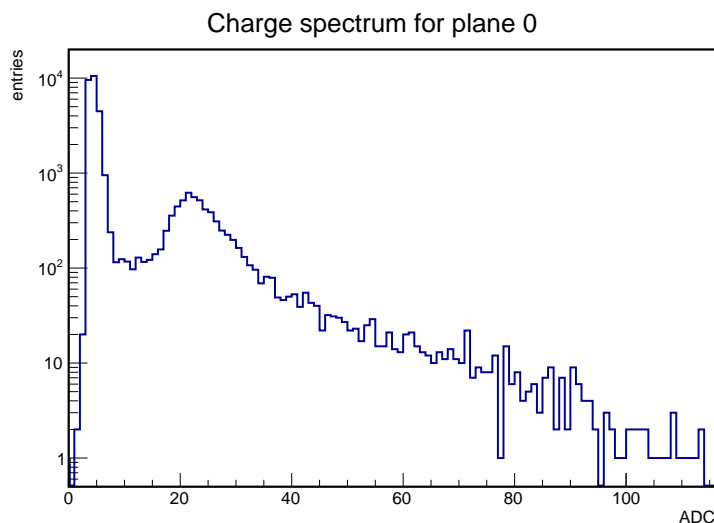


Figure 6.12: Distribution of signals measured with the GaAs pad sensors in an electron beam of 5 GeV.

from CVD diamond sensors. The radiation hardness of sapphire sensors was studied in a low energy electron beam up to an absorbed dose of 12 MGy.

A key parameter of the measurements is the Charge collection efficiency, CCE, defined as the ratio of the measured to the expected signal charge¹. The expected signal is determined from the energy loss on 5 GeV electrons in sapphire, and the energy needed to create an electron-hole pair. The detector is composed of metallized sapphire plates of $10 \times 10 \text{ mm}^2$ area and $525 \mu\text{m}$ thickness. The total thickness of this detector amounts to 14% of a radiation length. Since the response is depending on the direction with respect to the plane axis of the particles crossing it, interesting fields of applications are beam-halo rate or low angle scattering measurements. Basic characteristics, like the dependence of the CCE on the applied voltage and position resolved sensor response. More details can be found in Ref. [295].

Sapphire is a crystal of aluminum oxide, Al_2O_3 . Wafers were obtained from the CRYSTAL company. Single crystal ingots were produced using the Czochralski method and cut into wafers of $525 \mu\text{m}$ thickness. Contamination of other elements are on the level of a few ppm. The wafer was cut into quadratic sensors. Each sensor has dimensions 10.525 mm^2 , metallized on both sides with consecutive layers of Al, Pt and Au of 50 nm, 50 nm and 200 nm thickness, respectively.

To enhance the signal size, the orientation of the sapphire plates in the test beam measurements was chosen to be parallel to the beam direction. In addition, this orientation leads to a direction sensitivity. Only particles crossing fully the sensor parallel to the surface create the maximum signal. A stack of eight plates were assembled together, as shown in Fig. 6.13 (left). The leakage current of the sensors was measured as a function of the bias voltage. It amounts to less than 10 pA

¹The CCE corresponds to the effective drift path of charge carriers released by an ionising particle in the electric field in the sensor volume.

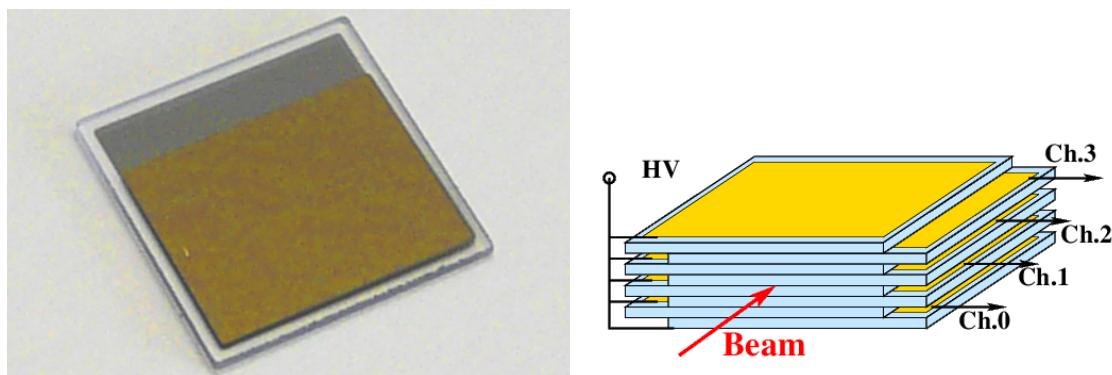


Figure 6.13: Left: Picture of a metallised sapphire sensor, Right: Schematic view of the sapphire sensor stack, consisting of 8 sensors. The direction of the beam electrons is indicated by the arrow and represents the z -coordinate. The y coordinate is perpendicular to the sensor plane.

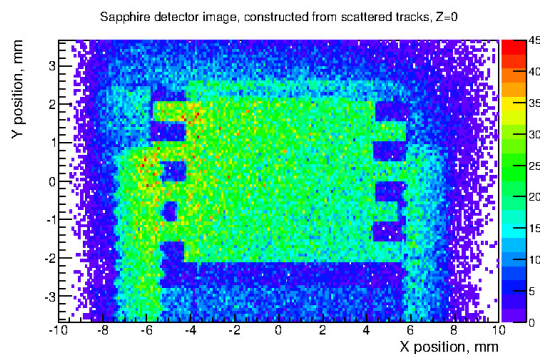


Figure 6.14: Image of the stack using electron tomography

at 1000 V.

In a first measurement sensors were exposed to a high-intensity electron beam at the linear accelerator DALINAC at TU Darmstadt. The beam energy was 8.5 MeV. The response of the sensors was measured as the signal current. The relative drop of the signal current, interpreted as the relative drop of the charge collection efficiency, CCE, is about 30% of the initial CCE after a dose of 12 MGy.

The stack, as shown in Fig. 6.13 (left), was studied in a 5 GeV electron beam at DESY. The trajectory of each beam electron was precisely measured in a pixel telescope before and after the stack. The impact point on the stack was predicted with a precision of better than $10\mu\text{m}$, and the scattering angle with a precision better than $50\mu\text{rad}$. Several millions of triggers were recorded at several bias voltages. Firstly, an electron tomographic picture of the stack was taken, as shown in Fig. 6.14. In this Figure the density of impact points is shown only for beam electrons deflected by

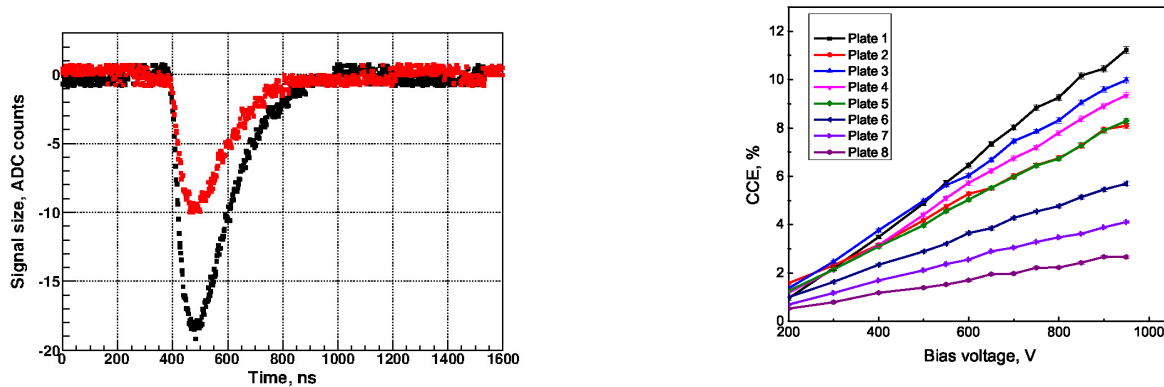


Figure 6.15: Left: Digitised analog signals for bias voltages of 550 (red) and 950 V (black) as a function of the time, Right: The CCD measured for all sensor plates as a function of the bias voltage.

an angle larger than 0.5 mrad. The position of the 5 sensor plates is clearly visible.

The signals from the sapphire sensors are amplified and digitised. An example of signals averaged over several triggers is shown in Fig. 6.15 (left) for bias voltages of 550 V and 950 V.

In almost cases a linear rise of the CCE is observed, reaching at 950 V e.g. for plane 1 a value of 10.5%. The measured CCE varies from sample-to-sample reflecting variation of the substrate quality. As can be seen, 5 out of the 8 sensor plates have a relatively high and similar CCE of about 7-10%, while three other plates have lower and different CCE values. The CCE was also measured as a function of the local y coordinate and described by a linear model of electron and hole drift taking into account recombination, trapping and space charges leading to a polarization field. As a result, the drift length of electrons is more than 10 times larger than the one of holes at the same field strength. About 50% of the produced electron-hole pairs recombine immediately.

6.4.11 Other novel sensor technologies

The Snowmass contributed paper [296] describes additional novel sensor technologies that might have important advantages for future e^+e^- experiments. Drivers of the technologies include radiation hardness, excellent position, vertex, and timing resolution, simplified integration, and optimized power, cost, and material. We describe these briefly in this section. These technologies are at different R & D stages, from early research to final operating scale; please see the individual references for more details.

Silicon sensors with 3D technology: Silicon sensors with 3D technology [297] have electrodes oriented perpendicular to their wafer surfaces. Due to the short drift lengths, these are very promising for compensation of lost signal in high radiation environments and for separation of pileup

events by precision timing. New 3D geometries involving p-type trench electrodes spanning the entire length of the detector, separated by lines of segmented n-type electrodes for readout, promise improved uniformity, timing resolution, and radiation resistance relative to established devices operating effectively at the LHC. Present research aims for operation with adequate signal-to-noise ratio at fluences approaching $10^{18}n_{\text{eq}}/\text{cm}^2$ with timing resolution on the order of 10 ps.

3D diamond detectors: The 3D technology is also being realized in diamond substrates [298], where column-like electrodes are placed inside the detector material by use of a 130 fs laser with wavelength 800 nm. When focussed to a 2 micron spot, the laser has energy density sufficient to convert diamond into an electrically resistive mixture of different carbon phases. The drift distance an electron-hole pair must travel to reach an electrode can be reduced below the mean free path without reducing the number of pairs created. Initial tests have shown that after $3.5 \times 10^{15} \text{ n/cm}^2$, a 3D diamond sensor with $50 \mu\text{m} \times 50 \mu\text{m}$ cells collects more charge than would be collected by a planar device and shows less damage due to the shorter drift distance.

Beyond CMOS: submicron pixels for vertexing: A pixel architecture named DoT-PiX [299] has been proposed on the principle of a single n-channel MOS transistor, in which a buried quantum well gate performs two functions—as a hole-collecting electrode and as a channel current modulation gate. The quantum well gate is made with a germanium layer deposited on a silicon substrate. The active layers are of the order of 5 microns below the surface, permitting detection of minimum ionizing particles. This technology is intended to achieve extremely small pitch size to enable trigger-free operation without multiple hits in a future linear collider, as well as simplified reconstruction of tracks with low transverse momentum near the interaction point. The necessary simulations have been made to assess the functionality of the proposed device. The next step is to find out what is the best process to obtain the functionality and to reach some required specifications.

Thin film detectors: Thin film detectors [300] have the potential to be fully integrated, while achieving large area coverage and low power consumption with low dead material and low cost. Thin film transistor technology uses crystalline growth techniques to layer materials, such that monolithic detectors may be fabricated by combining layers of thin film detection material with layers of amplification electronics using vertical integration.

Scintillating quantum dots in GaAs for charged particle detection: Lastly, a technology is under development in which a novel ultra-fast scintillating material employs a semiconductor stopping medium with embedded quantum dots [301]. The candidate material, demonstrating very high light yield and fast emission, is a GaAs matrix with InAs quantum dots. The first prototype detectors have been produced, and pending research goals include demonstration of detection performance with minimum ionizing particles, corresponding to signals of about 4000 electron-hole pairs in a detector of 20 micron thickness. A compatible electronics solution must also be developed. While the radiation tolerance of the device is not yet known, generally quantum dot media are among the most radiation hard semiconductor materials.

These sensor technologies and others still to be developed offer the promise of still higher performance in the ILC detectors. We encourage further development, with new collaborators, in all of these directions.

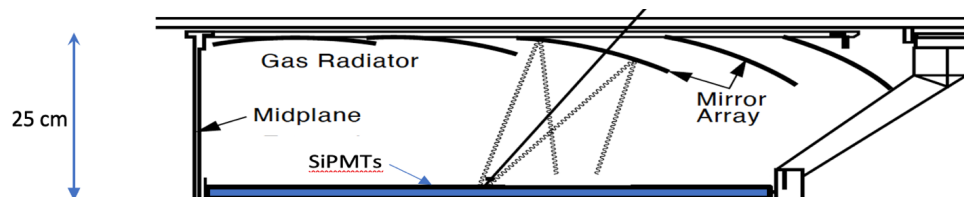


Figure 6.16: Proposed gaseous RICH detector addition to SiD/ILD [302].

6.4.12 Gaseous RICH detector for particle ID at ILC

Particle ID can be important for some ILC analysis, in particular, the measurement of $\Gamma(H \rightarrow s\bar{s})$ described in Sec. 8.1.2. Here we describe a possible RICH detector for π/K separation up to 25 GeV/c [302]. It is well known that a gaseous RICH detector is the only way to reach π/K separation up to 30-40 GeV/c. The detector concept is shown in Fig. 6.16. An initial choice for the RICH detector thickness is 25 cm active length to minimize magnetic field smearing effects. The RICH detector uses spherical mirrors and SiPMT photon detectors. The design in the figure resembles the SLD CRID gaseous RICH detector; however, introducing SiPMT-based design improves the performance substantially. Although we have selected a specific type of SiPMT to make our estimates, we believe that the photon detector technology will improve over the next 15 years, both in terms of noise performance, timing capability, pixel size and detection efficiency. The overall aim is to make this RICH detector with as low mass as possible in order not to degrade the calorimeter performance. This requires for mirrors made of beryllium and a structure made of low mass carbon-composite material. Another important aspect is to make the RICH detector depth as thin as possible to reduce the cost of the calorimeter.

Chapter 7

ILC Detector Simulation

7.1 ILC Fast Simulation Frameworks

As a first step to get started with ILC physics one can use fast simulation tools that can be used to quickly generate substantial samples of simulated and reconstructed events. Situations where this is desirable include detector optimisation and new physics searches. In these cases, similar processes need to be simulated and reconstructed at a, potentially very large, number of different conditions. In the first case, one needs to modify various aspects of the detector in steps, in the latter, one needs to explore the entire allowed parameter space of a theory for new physics. In addition to these cases, fast simulation is also an asset for simulating high cross section SM processes, such as $\gamma\gamma$ processes, where the investment in processor power and intermediate storage might be prohibitively large to attain the goal that simulation statistics should be a negligible source of systematic uncertainty. The ILC community uses two tools for fast simulation that are described in the following:

7.1.1 DELPHES for ILC

DELPHES [303] is a fast, parameterized simulation framework for generic collider detectors, developed originally for phenomenological studies at hadron colliders like the LHC. In its recent incarnation the DELPHES framework has been modularized and an attempt has been made to roughly emulate a particle-flow reconstruction philosophy [304] a feature that is crucial for its applicability to the ILC. DELPHES also integrates the FastJet [305] package allowing to directly run the most common jet clustering algorithms in use for the ILC. A specific collider detector is mimicked in DELPHES via the specification of efficiencies and resolutions for the long lived final state particles, based on their charge, momentum, polar angle¹ and type (charged/neutral hadron, photon, electron or muon). A dedicated DELPHES card: *delphes_card_ILCgen.tcl* with parameterizations for a generic ILC detector has been created [306, 307] and is shipped with the DELPHES source code [308]. The parameterization of the detector and reconstruction performance is based on the latest results of the ILD-IDR [309], where due to the nature of the rather coarse simulation accuracy of the

¹DELPHES uses pseudo-rapidity η instead of polar angle

DELPHES approach any potential differences to the SiD detector performance can be neglected for studies carried out with DELPHES. Fig. 7.1a shows a comparison of the transverse momentum resolution for charged particles at different angles as simulated with DELPHES compared to a full simulation and reconstruction for the ILC detector as well as the jet energy resolution for di-jet events of different quark flavors (Fig. 7.1b). DELPHES can read many standard generator formats

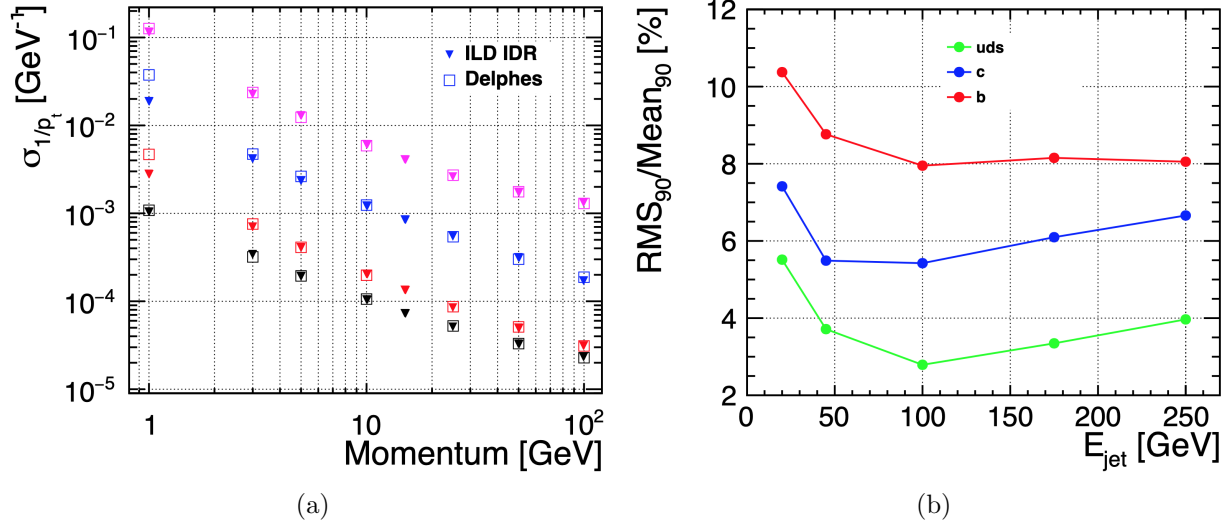


Figure 7.1: (a): transverse momentum resolution for different polar angles for the ILC full simulation and for the ILCgen DELPHES parameterization. (b): jet energy resolution for the ILCgen simulation

such as *stdhep* and produces ROOT [310] output files by default. With the *delphes2lcio* [311] tool standard LCIO miniDST can be created (see section 7.3.3).

7.1.2 SGV

The SGV program[312] used at ILC has a more sophisticated way of simulating the response to charged particles than the Delphes program described above. The time to simulate and reconstruct an event is similar to the time it takes to generate it ($\sim 1 - 10$ ms). The response of the detector is as far as possible calculated from the detector design (so there is no need to parameterize pre-existing full simulation results). SGV has been shown to compare well both with full simulation and with real data [313].

The program uses a simplified “*cylinders-and-discs*” description of the detector, which is used to calculate the Kalman-filtered track-helix covariance matrix of each generated charged particle. By Cholesky [314] decomposition of the covariance matrix, the track-parameters are simulated in a way such that all correlations are respected. The calorimetric response is calculated from the expected single-particle performance of the different components of the calorimetric system, for each particle impinging on it. Optionally, the effects of shower-confusion can be included. To reduce the needed storage for a Giga-event size sample, event filtering can be applied at different

steps of the processing, directly after generation, after the detector response is known, or after higher-level event analysis is done. Events passing all filters are output in LCIO DST-format, and can seamlessly be further analyzed within the Marlin framework.

7.2 ILCSoft framework

Accurate and detailed modeling of the physics interactions as well as the detector response are crucial for making realistic predictions about the expected physics and detector performance. The ILC software for detector simulation, reconstruction and analysis is entirely based on the common linear collider software ecosystem called *iLCSoft* [315]. The main core software tools in iLCSoft are the common event data model and persistency tool LCIO [316], the C++ application framework Marlin [317] and the generic detector description toolkit DD4hep [318, 319]. DD4hep provides a single source of information for describing the detector geometry, its materials and the readout properties of individual sub detectors. Various components of DD4hep provide different functionalities. Here we use DDG4, the interface to full simulations with Geant4 [320] and DDRec the specialized view into the geometry needed for reconstruction. In the following we briefly describe the main features of the full simulation and reconstruction tools in use for ILC and SiD, more details can be found in the corresponding chapters of [309] and [6].

7.2.1 Simulation models

Both ILC detector concept groups have developed detailed and realistic simulation models with realistic geometrical dimensions, material budgets, imperfections and cables and services. Wherever possible, realistic simulations and parameterizations for the individual sub detectors have been implemented based on available test beam results for the proposed technology. Great care has been taken to include realistic material estimates, established by the detector R&D groups, in particular in the tracking region where the material budget has a direct impact on the detector performance. Examples of the inner tracking regions as implemented in the realistic simulation models for SiD and ILD are shown in Fig 7.2.

7.2.2 Event reconstruction

The reconstruction of simulated events in the ILC detectors is done with a number of dedicated algorithms implemented in Marlin. For the digitization of tracking detectors and calorimeters dedicated modules exist that provide a parameterization of the expected resolutions as established by the R&D collaborations taking into account effects like cross talk, electronic noise and signal collecting efficiencies. The reconstruction of charged particle tracks is performed with a variety of pattern recognition algorithms implemented in the MarlinTrk [321] package. This is followed by sophisticated clustering and particle flow algorithms from PandoraSDK [322] that delivers a complete collection of reconstructed particles or so called *particle flow objects*. Additional high level reconstruction algorithms, like jet clustering with FastJet [305], vertexing and flavor tagging with

LCFIPlus [323], particle identification using dE/dx -information and time-of-flight measurements complete the event reconstruction for final physics analyses.

7.3 ILC SM Background Samples

7.3.1 Event generation

ILC physics sample generation is typically done with the Whizard [324] event generator providing crucial features like correct treatment of ISR and FSR via creation of photons as individual final state particles. Whizard uses tree-level matrix elements and loop corrections to generate events with the final state partons and leptons based on a realistic beam energy spectrum, the so called *hard sub-process*. The hadronization into the visible final state is performed with Pythia [325] tuned to describe the LEP data. The correct beam energy input spectrum for a given collision energy and set of accelerator parameters is created with Guinea-Pig [326], a dedicated simulation program for computing beam-beam interactions at linear colliders.

7.3.2 Beam induced background

The strong beam-beam interactions lead to two distinct sources of backgrounds:

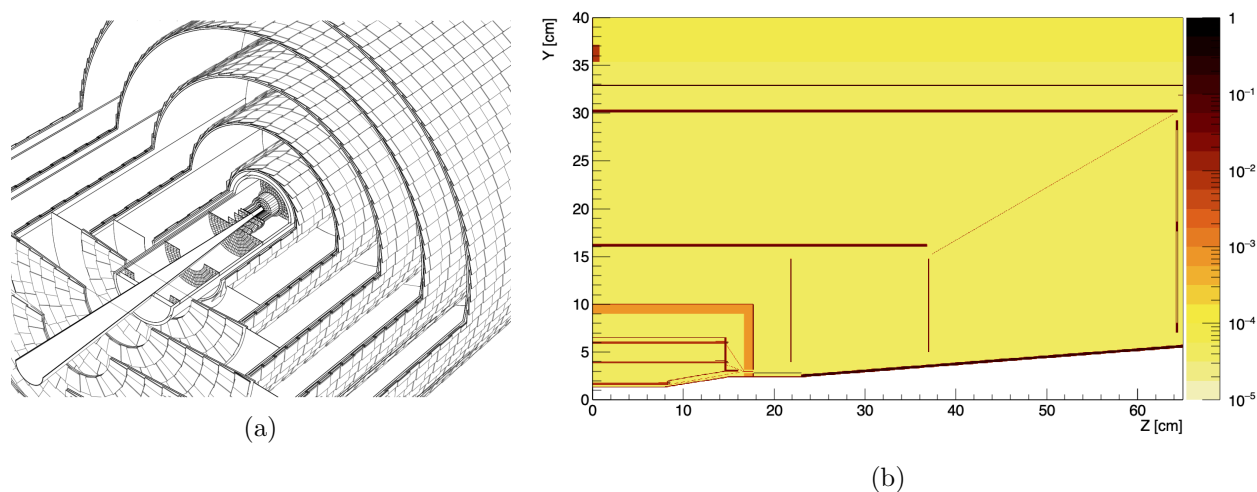


Figure 7.2: (a): cut-away view of the tracking system as implemented in the *SIDLOI3* simulation model (from [5]). (b): Material scan in inner tracking region of the ILD simulation model showing detector components of the VTX, SIT and FTD as well as dead material from the beam pipe, support structures, cables and services. Plotted is the local material budget per bin in units of X_0 with an arbitrary scaling factor applied.)

- the creation of incoherent e^+e^- -pairs that are the source of the dominating background at the ILC. These electrons and positrons are predominantly created in a forward cone as shown in Fig 7.3 for the ILD detector. It is this cone that restricts the minimal allowed radius of the innermost layer of the vertex detector of any linear collider detector as can be seen in Fig. 7.3.
- creation of $\gamma\gamma \rightarrow hadrons$ events, due to the interaction of beamstrahlung photons. This type of events is generated for $\gamma\gamma$ cms-energies from 300 MeV to 2 GeV with a dedicated generator based on [327], whereas for higher energies Pythia is used.

For realistic physics analyses and detector studies for the ILC it is important to take these backgrounds into account. This is typically done through event overlay techniques in the iLCSoft based full simulation and reconstruction chains of ILD and SiD.

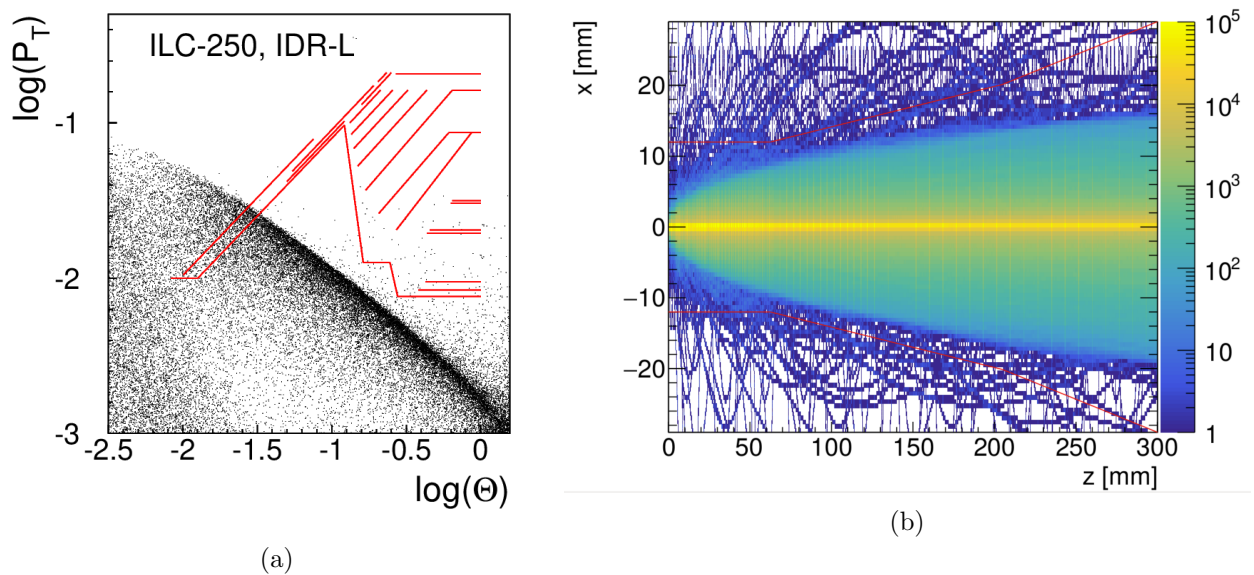


Figure 7.3: (a): Cones of incoherent e^+e^- -pairs in the ILD detector for $E_{cms} = 250$ GeV as created with GuineaPig. Shown is $\log p_t$ of the particles (radius of the helical trajectory) as a function of $\log \theta$. Also shown are the inner detector elements of the ILD detector (horizontal lines represent barrel elements and diagonal lines represent end-cap elements). (b): Cone of background from incoherent e^+e^- -pairs, generated with Guinea-Pig and simulated in the 5 T B-field of the SiD detector (from [328]).

7.3.3 Event Samples and data formats

Large sets of SM samples for the ILC have been generated for $E_{cms} = 250, 350, 500, 1000$ GeV are available at [329]. Data sets with miniDSTs created with DELPHES and SGV of these generated samples are also available at this web site. Access to more realistic fully simulated and reconstructed

event samples from ILD or SiD is possible via a lightweight guest membership. The web-site [329] provides additional information on ILC simulation resources and tools.

All ILC fast and full simulation and reconstruction tools can provide the common data format LCIO as output. The LCIO event data model (see Fig. 7.4a) is the de facto standard for ILC physics and detector studies. Recently a particularly lightweight set of output collections for ILC event data has been defined, the *miniDST*-format. By starting out with developing an analysis with DELPHES or SGV based on *miniDST*'s one can later easily move to a more realistic analysis based on full simulation using the same format with only minor modifications as shown in Fig. 7.4b.

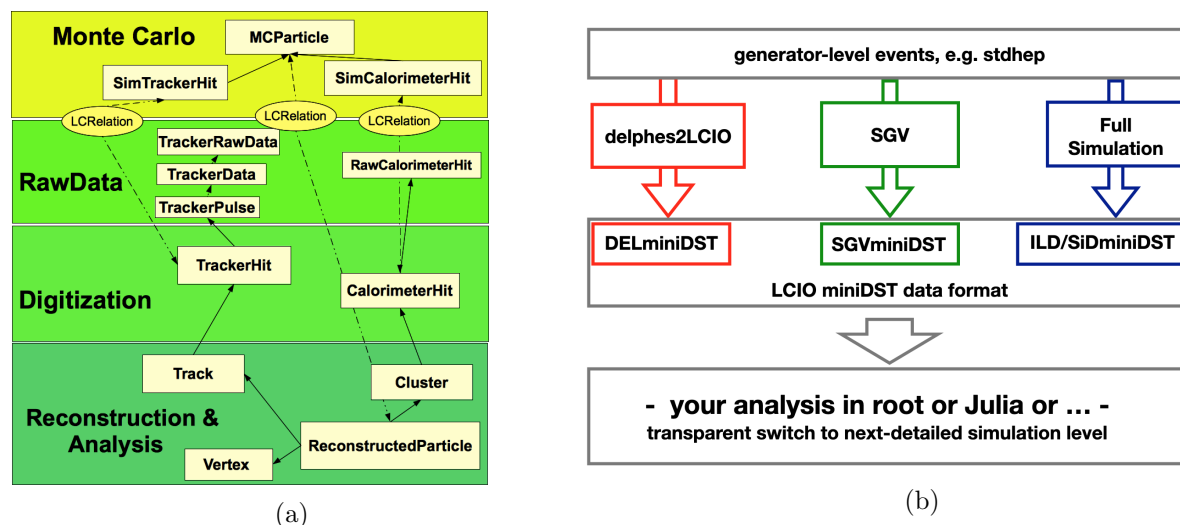


Figure 7.4: (a): Schematic view of the hierarchical event data model of LCIO. (b): Using the miniDST format a common analysis code can be developed that works with all simulation and reconstruction tools presented above.

Chapter 8

ILC Physics Measurements at 250 GeV

The first stage of the ILC will be at a CM energy of 250 GeV. In this chapter, we will describe aspects of the ILC experimental program that are specific to 250 GeV, in particular, the study of the Higgs boson in the process $e^+e^- \rightarrow ZH$. We will also discuss precision SM tests that are available this energy—in particular, the measurement of the triple gauge couplings through $e^+e^- \rightarrow W^+W^-$ and tests of QCD in $e^+e^- \rightarrow$ jets. Aspects of the ILC program that benefit from higher energy—in particular, searches for new particles in pair-production and fermion-fermion scattering—will be discussed over the whole ILC program in Chapter 10.

8.1 Higgs – conventional decays

The precise measurement of “conventional” Higgs decay branching ratios is key to probing virtual effects of new physics in the Higgs sector. The value of the Higgs boson mass is now known from the LHC to part per mil precision, and this precision will be improved at the ILC. By combining this value with other precisely known SM inputs, it will be possible to predict the absolute strengths of Higgs boson couplings to the 0.1% level. Many models of new physics lead to variations in the Higgs couplings, typically leading to few-% variations of Standard Model Higgs couplings for new physics at the TeV scale. Thus, the measurement of these couplings to the %-level precision or better is one of the major goals of the Higgs program at high energy electron–positron colliders such as the ILC.

Higgs production in electron–positron collisions at 250 GeV is dominated by the associated production of Higgs and Z bosons (“Higgs-strahlung”), as shown in Fig. 8.1 [330]. Because electron–positron collisions provide an initial state with well-defined four-momentum, this process allows the identification of Higgs bosons by considering the mass recoiling against an identified Z boson, without any reference to the decay products of the Higgs. A typical reconstructed recoil mass distribution is shown in Fig. 8.1.

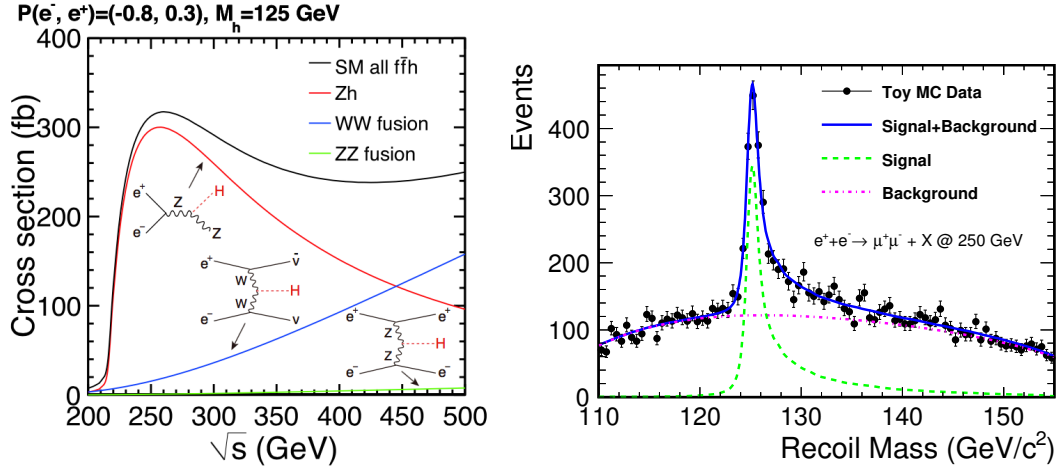


Figure 8.1: Left: Cross sections for the three major Higgs production processes as a function of center of mass energy [2]. The Zh “Higgs-strahlung” process dominates at 250 GeV. Right: Recoil mass spectrum against $Z \rightarrow \mu^+\mu^-$ for signal $e^+e^- \rightarrow Zh$ and SM background at 250 GeV [331].

Higgs-strahlung events at ILC250 in which the Z decays to hadrons or charged leptons will provide the experimenter a sample of about half a million Higgs bosons that is almost completely unbiased with respect to the Higgs decay mode. Such a sample is very useful for making precise and unbiased measurements of the Higgs boson’s properties, for example the partial cross-sections to different Higgs decay modes $\sigma_{ZH} \times BR(H \rightarrow X)$. At the same time, this sample can provide a precise value of Higgs boson mass from the position of the recoil mass peak. An order of magnitude improvement in precision over the current measurement is needed because the Higgs branching ratios to WW^* and ZZ^* depend strongly on the Higgs boson mass, and the recoil technique can meet this goal.

Because the identification of the Higgs boson does not depend on the decay mode, it is also possible at an e^+e^- collider to measure the total Higgs-strahlung production cross-section in the different ILC beam polarization setups. Combining these results with other ILC measurements, it is possible to extract absolutely normalized values for the couplings of the Higgs boson to its various final states, and for the Higgs boson width. We will present the precision on these quantities expected from a global fit to ILC data in Chapter 12.

ILC also presents an opportunity to probe the Higgs boson’s CP properties, a key to understanding the potential for baryogenesis at the electroweak scale, in its interaction both with τ leptons and with massive vector bosons.

Projections for the experimental precisions attainable at the ILC are based on full simulation studies which take into account experimental conditions such as beam energy spread and beam background processes, as well as detailed simulation of the experimental apparatus and realistic data analysis techniques.

8.1.1 Zh cross-section and Higgs mass

The recoil mass distribution shown in Fig. 8.1 can be used to extract the total Zh production cross-section and the Higgs boson mass, by consideration respectively of the area and position of the signal peak [331]. The cross-section will be measured in all ILC beam polarization combinations, switching between dominantly left- and right-handed electrons and positrons. The cross-section σ_{Zh} in the two major polarization combinations will be measured to a precision of 1%. The asymmetry between these measurements in different polarizations offers an important additional input to the global understanding of Higgs couplings. At ILC-250, the precision on the Higgs mass is expected to reach 14 MeV using the recoil mass method [331].

The Higgs mass can also be directly reconstructed from its decay products, providing complementary measurements. A demonstration in the case of the dominant Higgs decay to $b\bar{b}$ can be found in [332], while rare Higgs decays to final states which can be very precisely measured, such as two or four muons and/or electrons, can also provide very competitive precision despite the limited numbers of events [333].

8.1.2 Hadronic decays

The majority of Higgs bosons will decay into hadronic final states; within the SM we expect dominant contributions from b-quarks, c-quarks, and gluons. The experimental separation of these hadronic contributions relies on jet flavor tagging. The keys to distinguishing jet flavor are the identification of displaced vertices produced in the decay of meta-stable particles, of leptons within hadronic jets originating from massive hadron decays, and particle identification, in particular the ability to identify kaons.

The reconstruction of displaced vertices is aided by the tiny ILC interaction region and the vertex detector, with its few-micron hit position resolution and first layer placed only ~ 15 mm from the IP. Figure 8.2 shows the excellent b- and c-tagging performance achieved by the LCFIplus algorithm in full simulation studies of the ILDCONCEPT at ILC.

Applying the LCFIplus algorithm to hadronically decaying Higgs bosons produced at ILC250, assuming the nominal $2 ab^{-1}$ total integrated luminosity, the partial cross-section $\sigma_{Zh} \times BR(H \rightarrow b\bar{b})$ can be measured to 0.7%, and $\sigma_{Zh} \times BR(H \rightarrow cc, gg)$ to around 4% precision [334] in each of the major polarization combinations. The expected signal and major backgrounds, from a full simulation study of $H \rightarrow b\bar{b}$, are shown in Fig. 8.3. For cc , especially, the direct nature of the measurement as well as the high level of precision contrasts markedly with the situation at the LHC.

The identification of $H \rightarrow s\bar{s}$ decays presents a significant experimental challenge due both to its subtle signature and its small expected branching ratio. Huge multi-jet backgrounds make it nearly impossible to probe the strange Yukawa coupling via direct $H \rightarrow s\bar{s}$ searches at the LHC. At the ILC, studies in progress indicate that the observation of this process, though challenging, might be possible. Potentially useful experimental techniques and detector capabilities include the reconstruction of decaying V^0 mesons as well as K/π particle discrimination through measurements

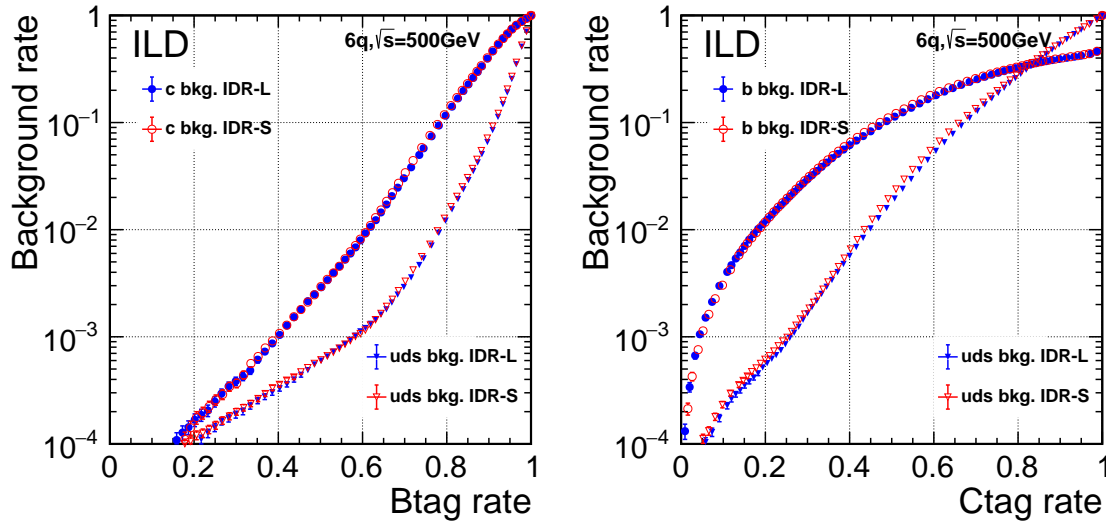


Figure 8.2: B-tag (left) and c-tag (right) performance in full-simulation studies of two variants of the ILD concept, IDR-L and IDR-S (figure from [216]).

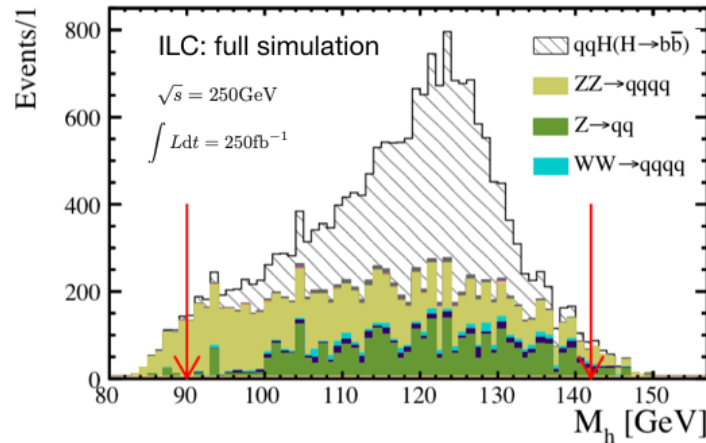


Figure 8.3: Comparison of signal and backgrounds from ILC full simulation for the measurement of the $\sigma \times BR$ for $H \rightarrow b\bar{b}$, for 250 fb^{-1} of ILC data at 250 GeV, from [335].

of the energy loss dE/dx of charged particles, and the use of time-of-flight or modern and compact Cherenkov detectors (see Sec. 6.4.12). A limit on the $s\bar{s}$ branching ratio at a factor of about 5 above the SM value would already be a significant constraint on flavor models (see Sec. 14.4), and the studies in [336] confirm that this is achievable. Better understanding and thus rejection of the backgrounds from Z bosons and other Higgs decays could further improve this measurement.

8.1.3 Leptonic decays

The measurements of Higgs decays to τ leptons and muons are feasible at ILC if these branching fractions are roughly at the levels predicted in the SM. The decay branching ratio to τ leptons is relatively large in the SM. In addition, Higgs decays to $\tau^+\tau^-$ are straightforward to recognize in the ILC experimental environment, allowing identification of these decays with high precision. This should lead to a precision at ILC-250 of better than 2% in the measurement of the partial cross-section $\sigma_{Zh} \times BR(H \rightarrow \tau\tau)$ [337] in each major polarization combination.

The small branching ratio to muons limits the statistics available at ILC. The predicted precision on $\sigma_{Zh} \times BR(H \rightarrow \mu\mu)$ at ILC-250 is 38% in each polarization set [338]. It should be noted that an LHC measurement of the ratio of branching ratios $BR(H \rightarrow \mu\mu)/BR(H \rightarrow ZZ^*)$ can be combined with ILC data to produce an absolutely normalized value of the Higgs boson coupling to muons.

Direct observation of the Higgs coupling to electrons is essentially impossible at ILC if the branching fraction is that predicted by the SM. The final state can in principle be well reconstructed, so if this channel is very significantly enhanced with respect to the SM, for example to a level similar to the branching ratio to muons, it can be observed at ILC.

8.1.4 Electroweak boson decays

The measurements of the Higgs branching ratios to WW^* and ZZ^* play an important role in the global probing of the Higgs sector, since these same couplings are involved in Higgs production via WW -fusion and Higgs-strahlung, respectively. These therefore allow direct extraction of the total Higgs decay width $\Gamma_h = \Gamma_{WW[ZZ]}/BR_{WW[ZZ]}$.

The large number of different final states make for a complex analysis. A recent study of Higgs decay to ZZ^* estimated that $\sigma_{Zh} \times BR(H \rightarrow ZZ)$ can be measured to a precision of 8% in each of the major polarization stages of ILC-250 by making use of a variety of Z and h decays modes [339]. A precision of 2.4% is expected on the corresponding measurements of $\sigma_{Zh} \times BR(H \rightarrow WW)$.

Rare loop-induced Higgs decays to $\gamma\gamma$ and γZ can also be sought at ILC-250, although the small SM branching ratios will severely restrict the statistical precision of these measurements. In the case of $\gamma\gamma$, a precision of 18% on the partial cross-section is expected at ILC-250 in each of the two major polarization samples. As for muons, though, an LHC measurement of a ratio of branching ratios can be combined with ILC data to obtain a normalized coupling value.

The $h\gamma Z$ coupling can also be probed via the $e^+e^- \rightarrow \gamma h$ process, whose cross-section is also maximal around 250 GeV. The cross-sections in the SM are rather small, for example 0.20 fb for the beam polarization $P(e^-, e^+) = (-0.8, +0.3)$. Upper limits at 95% on the production cross-sections in the different polarization scenarios can be set at 1.8 fb for the same beam polarization [340]. The polarization-dependence of this limit and the implications for limits on SMEFT parameters are discussed in [341].

8.1.5 CP properties

CP properties of the Higgs boson can be probed in its decays to τ leptons [342], or in its coupling to the EW bosons W and Z [343].

In the τ decay channel, the τ decay products act as polarimeters, providing an estimate of the spin orientation. The correlation between the two τ s' polarimeter components perpendicular to the τ momentum direction is sensitive to their CP state. The clean experimental environment at ILC and the high precision detectors being developed are conducive to accurate reconstruction of τ lepton decays, allowing good reconstruction of τ polarimeter information. Mixing between odd and even CP components of the τ pair can be probed with a precision of 75 mrad at ILC-250 [342, 344].

The couplings of the Higgs to WW and ZZ , both in decay and production, also provide sensitive probes of CP violation effects. Anomalous CP-violating couplings can affect angular correlations between vector boson decay planes. Limits of around 7% on CP violating terms in the HVV coupling can be achieved at ILC-250, and further improved at higher ILC energies [343, 335].

8.2 Higgs – exotic decays

Higgs exotic decays provide unique opportunities to probe a broad class of new physics models [345]. Studying the Higgs exotic decay precision would help reveal new physics, especially hidden sector dynamics through this generic Higgs portal. The physics we can learn from the Higgs exotic decay program is also complementary to the Higgs coupling precision measurements.

The fact that the Higgs boson is produced at 250 GeV mainly in association with a Z boson implies that events with a single isolated Z boson provide a tag for Higgs decay to completely invisible final states. There is a SM decay $H \rightarrow 4\nu$, but this has a predicted branching fraction of 0.1%, giving a significant window for the discovery of invisible decays due to new physics. At the ILC, it is expected that, if this mode is not observed, it will be possible to place a 95% confidence upper limit on this branching ratio of 0.16% [346, 347].

In addition to the completely invisible decay, the Higgs boson has many possible modes of exotic decay that are forbidden in the SM, including partially invisible decays and flavor-changing decays. Many of these decay modes, especially hadronic decays, are very challenging to observe at hadron colliders. An initial survey of these possibilities has been carried out in [348], and this study has shown promising sensitivities at lepton colliders across the range of these modes. The study focuses on two-body Higgs decays into BSM particles, dubbed as X_i , $h \rightarrow X_1 X_2$, which are allowed to decay further, to up to four-body final states. The cascade decay modes are classified into four cases, schematically shown in Fig. 8.4. Decays with these topologies are motivated by a large class of BSM physics, such as singlet extensions, two-Higgs-doublet-models, SUSY models, Higgs portals, gauge extensions of the SM [345, 348, 349, 350].

For ILC running at the center of mass energy 250 GeV, the essential Higgs production mechanism is Z -Higgs associated production $e^+e^- \rightarrow Zh$. The Z boson with visible decays enables Higgs tagging using the “recoil mass” technique. A cut around the peak of the recoil mass spectrum

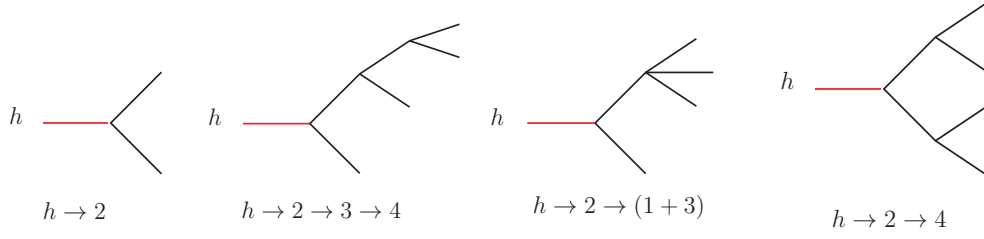


Figure 8.4: Representative topologies of the Higgs exotic decays.

would remove the majority of the SM background. To demonstrate a typical Higgs exotic search at ILC, we discuss here the analysis of benchmark processes $H \rightarrow jj + \cancel{E}_T$. In the last part of this section, we present the summary for Higgs exotic decay physics potential at ILC for an integrated luminosity of 2 ab^{-1} and provide an outlook for future studies and improvements.

For event simulation, we generate both the signal and the background events for a 250 GeV electron-positron collider with `MadGraph5` at parton level [351]. Our parameter choices for the detector effects and our pre-selection cuts are chosen to be universal for the analyses for all Higgs exotic decay modes. All of the visible particles in the final state are required to have $|\cos \theta| < 0.98$. The final state particles are required to be well-separated with

$$y_{ij} \equiv 2 \min(E_i^2, E_j^2) (1 - \cos \theta_{ij}) / E_{vis}^2 \geq 0.001. \quad (8.1)$$

We only study the cases where the Z boson decays into $\ell^+ \ell^-$ where $\ell^\pm = e^\pm, \mu^\pm$. The signal events are required to contain at least one pair of opposite-sign, same-flavor charged leptons with an opening angle greater than 80° and satisfying $E_\ell > 5 \text{ GeV}$ and $|m_{\ell\ell} - m_Z| < 10 \text{ GeV}$, where $m_{\ell\ell}$ is the invariant mass of the di-lepton system. The recoil mass is defined as $m_{\text{recoil}}^2 \equiv s - 2\sqrt{s}E_{\ell\ell} + m_{\ell\ell}^2$ where $E_{\ell\ell} = E_{\ell^+} + E_{\ell^-}$. The recoil mass is required to satisfy $|m_{\text{recoil}} - m_h| < 5 \text{ GeV}$. To suppress the ISR contribution to the backgrounds¹, for Higgs exotic decay modes without missing energy, we require the events to have the total visible energy $E_{vis} > 225 \text{ GeV}$. We mimic the detector resolution effect by adding Gaussian smearing effects on the four-momentum of the particles, as detailed in Ref. [348].

For the $H \rightarrow jj + \cancel{E}_T$ analysis, we assume that the SM-like Higgs boson decays into $X_2 X_1$ with X_1 invisible and X_2 having the decay $X_2 \rightarrow X_1 jj$ through an off-shell intermediate state. Beyond the pre-selection cut and the recoil mass cut, we require that there are two additional jets that satisfy $E_j > 10 \text{ GeV}$ and $|\cos \theta_j| < 0.98$. The dominant background after the recoil mass cut will be the Higgsstrahlung process with $h \rightarrow ZZ^* \rightarrow q\bar{q}\nu\bar{\nu}$.

We use the likelihood function of the $m_{jj} - \cancel{E}_T$ distribution to derive the exclusive limit. The results are shown in Fig. 8.5 in the plane of X_1 , mass m_1 , and the mass splitting between X_2 and X_1 , $m_2 - m_1$ for $h \rightarrow jj + \cancel{E}_T$. The exclusion limits on the branching fraction in the bulk region of the parameter space reach $3 \times 10^{-4} \sim 8 \times 10^{-4}$ for $h \rightarrow jj + \cancel{E}_T$. We can see that when the mass splitting $m_2 - m_1$ is around 80 GeV, the future lepton colliders have the strongest sensitivities on

¹Corrections from beamstrahlung effect [352] and ISR effect [353] need to be carefully taken into account for certain processes relying on a precise reconstruction of the recoil mass.

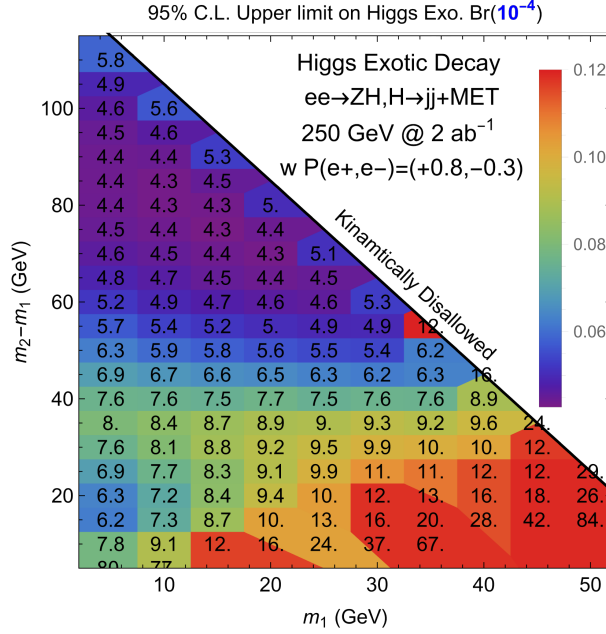


Figure 8.5: The 95% C.L. upper limit on the Higgs exotic decay branching fractions into $jj + \cancel{E}_T$ arising from a decay $H \rightarrow X_2 X_1$, as described in the text, with X_1 a stable particle of mass m_1 and X_2 higher in mass by $m_2 - m_1$.

these Higgs exotic channels, reaching around 4.3×10^{-4} for $h \rightarrow jj + \cancel{E}_T$. When X_1 is light and $m_2 - m_1$ is large, the energy is shared by the two jets and the X_1 . Consequently, when the mass splitting $m_2 - m_1$ is around 80 GeV, the dijet invariant mass will be around 40–60 GeV, falling in the “valley” of low SM background. For heavier X_1 , the MET will be lower due to less momentum available for the LSP.

To further demonstrate the search of Higgs exotic decay, a more realistic analysis based on full detector simulation has been carried out at the ILC [354], focusing on one of the representative channel where Higgs decays into a pair of light new scalars (ϕ) both of which decay into a pair of b -quark. A set of masses for the scalars from 15 GeV to 60 GeV are studied as benchmarks. Higgs-strahlung process $Z \rightarrow e^+ e^- / \mu^+ \mu^-$ is employed as the Higgs production channel. The signal final state consists of two isolated leptons and four b -jets. This is a very clean channel thanks to the excellent b -tagging performance and very narrow leptonic recoil mass spectrum. It turns out that the dominant background after all the selection cuts are from SM Higgs decay. The distributions of the reconstructed average of two scalar masses are shown in Fig. 8.6 for the remained signal and background events assuming a branching ration of 1% for $H \rightarrow 4b$ and the scalar mass of 30 GeV, where the signal resonance peak from exotic decay can be clearly seen. By combining two leptonic channels, the 95% confidence level upper limit of $BR(H \rightarrow 4b)$ is expected to be around 0.1% for all the four benchmark scalar masses (15/30/45/60 GeV) with an integrated luminosity of 900 fb^{-1} for each left-handed and right-handed polarization at the ILC250.

A large number of similar analyses are described in [348]. We summarize the results in Fig. 8.7,

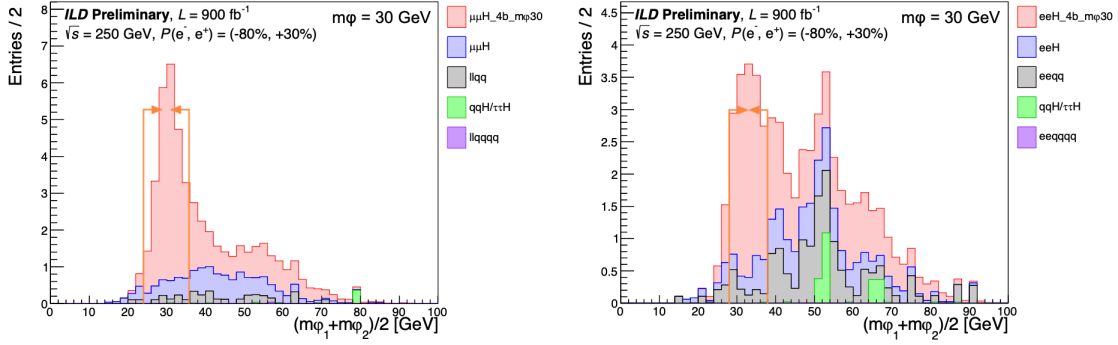


Figure 8.6: Stacked distribution of reconstructed average scalar mass for the signal $e^+e^- \rightarrow l^+l^-H$, $H \rightarrow \phi\phi \rightarrow (b\bar{b})(b\bar{b})$ and background events based on full detector simulation, at $\sqrt{s} = 250$ GeV with an integrated luminosity of 900 fb^{-1} . Left figure is for $P(e^-, e^+) = (-0.8, +0.3)$ and right is for $P(e^-, e^+) = (+0.8, -0.3)$.

giving the expected limits for the ILC with 2 ab^{-1} integrated luminosity. We also include the projected LHC sensitivities in gray bars. We use the up-to-date projected sensitivities for the LHC constraints, but many do not exist or are very conservative. More recent studies, e.g., Ref. [355] on $h \rightarrow 4\tau$, and Ref.C [354] on $h \rightarrow 4b$, show consistent projection on sensitivities as well.

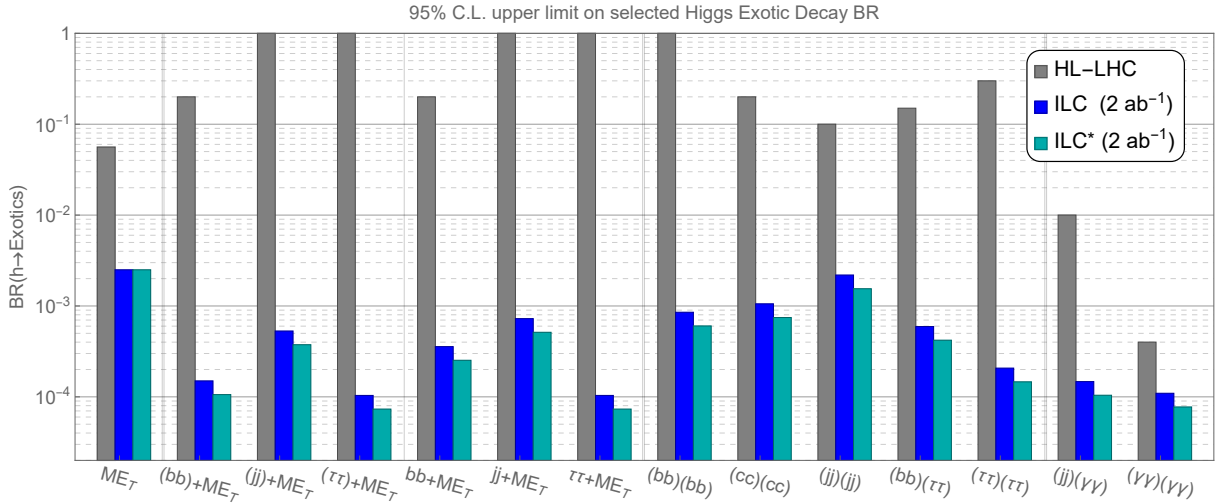


Figure 8.7: The 95% C.L. upper limit on selected Higgs exotic decay branching fractions at HL-LHC and ILC, based on Ref [348]. The ILC curves are derived using results from Ref [348] with leptonic decaying Z boson in the $e^-e^+ \rightarrow ZH$ process. The ILC* scenario further utilizes the hadronically decaying Z boson and includes an estimated (indicative) improvement of 40%. Each set of three bars describes a different topology of exotic Higgs decay. For a recent review on current LHC constraints, see Ref. [350].

The LHC will provide strong constraints on many many channels that can be characterized

with muons, electrons, and photons. In the summary Fig. 8.7, the exotic Higgs decay channels are some of those that are difficult to constrain at the LHC. For these channels, which rely on signals from jets, heavy quarks, and τ s, the improvements over the LHC expectations vary from one to four orders of magnitude. This great advantage benefits from the low QCD background and Higgs tagging from the recoil mass technique at future lepton colliders. For the Higgs exotic decays without missing energy, the improvement varies between two to three orders of magnitude, except for the one order of magnitude improvement for the $(\gamma\gamma)(\gamma\gamma)$ channel. Here the possibility at the LHC of reconstruction of the Higgs mass from the final state particles provides additional signal-background discrimination power. Channels with electrons, muons, and photons, which are relatively clean objects at the LHC, can take advantage of the higher statistics available from the HL-LHC.

Many new and interesting channels deserve further study. Higgs exotic decays of $H \rightarrow XX \rightarrow 4f$ where the intermediate resonant particle X mass is below 10 GeV is one of these channels. This scenario is particularly motivated by the recent discussion of the connection between Higgs exotic decay and strongly first order electroweak phase transitions [356, 357]. In this region, the particle X can be long-lived, so the study should be extended into long-lived particle regime [358].

Another example is the Higgs decay into a dark shower, that is, a shower of dark-sector particles.² These can either decay promptly or be long-lived, and their decay back to visible SM particles can be either hadronic or leptonic. The process is motivated by generic considerations of hidden sector strong dynamics. It also appears in the discussion of neutral naturalness [360]. Current studies have been focusing on the Higgs decays into a pair of twin glueballs [361, 362, 358, 363], but this is only a subclass of the generic Higgs decays into these final states. This dark shower channel is also motivated by the class of models with large number of light scalars [364], e.g., NNaturalness [365], EW scale as a trigger [366], and delayed or non-restored electroweak symmetry [367, 368, 369, 370]. The phenomenological study of this general class of models is complex, and this is especially true at the LHC due to the challenges of triggers and backgrounds. The triggerless operation of the ILC detectors, where any novel Higgs decay can be recorded and identified, provides a strong advantage.

8.3 Triple gauge couplings

A second major goal of the 250 GeV ILC program is to carry out precision measurements on the W boson. Improvements in quantities relevant to precision electroweak observables—the W mass, width, and decay branching ratios—will be discussed in Chapter 9. Here we discuss the improvement in the direct measurement of the W boson interactions.

The electroweak interactions of a pair of W bosons of lowest dimensionality are described by

²These can be bosons or be fermions, for example, composite neutrinos [359].

the Lagrangian

$$\begin{aligned} \Delta L = & ig_V \left\{ V^\mu (W_{\mu\nu}^- W^{+\nu} - W_{\mu\nu}^+ W^{-\nu}) + \kappa_V (W_\mu^+ W_\nu^- V^{\mu\nu}) \right. \\ & \left. + \frac{\lambda_V}{m_W^2} W_\mu^{-\nu} W_\nu^{+\rho} V^{\mu\rho} \right\}, \end{aligned} \quad (8.2)$$

where $V = \gamma, Z$, and $W_{\mu\nu}^\pm$ and $V_{\mu\nu}$ are the gauge boson field strengths. Always, $g_\gamma = e$, reflecting the electric charge of the W boson. In the SM, $g_Z = -\frac{c_w}{s_w}$, $\kappa_\gamma = \kappa_Z = 1$, and $\lambda_\gamma = \lambda_Z = 0$, with s_w, c_w the sine and cosine of θ_w . In the most general setting, the 5 free coefficients are all independent of one another. However, there are two $SU(2) \times U(1)$ relations,

$$(\kappa_Z - 1) = -\frac{s_w^2}{c_w^2} (\kappa_\gamma - 1) \quad \lambda_\gamma = \lambda_Z. \quad (8.3)$$

This leaves three free parameters to be determined.

New interactions at the TeV scale, especially mixing of the W bosons with new elementary or composite vector bosons, can generate small corrections to these couplings, suppressed by a factor m_W^2/M^2 , where M is the heavy mass scale. Electroweak loop diagrams give computable corrections to the triple gauge coupling (TGC) parameters at the 10^{-3} level. Searches for these effects require high precision in the reconstruction of the full reaction producing the W bosons.

The TGC parameters also play an important role in the Higgs boson program. As we will discuss in Chapter 12, our determination of the Higgs boson width and the normalization of Higgs couplings is based on a fit using SM Effective Field Theory. This fit relies not only on measurements of Higgs processes but also on other ILC electroweak measurements. The TGC parameters play an important role. For this reason also, it is essential to have precise determinations of the TGC parameters at 250 GeV.

In this section, we will discuss the measurements of the TGC parameters at the ILC at 250 GeV, based on W^+W^- production and on single W production. The impact of higher center-of-mass energy measurements will be described in Section 10.3.

At LEP, the three couplings g^Z , κ_γ and λ_γ have been constrained at the level of a few 10^{-2} . Limits have been derived in fits of individual parameters, fixing the other two to their SM values [371], as well as in two- and three-parameter fits, which allowed two or all three couplings to vary simultaneously [372, 373, 374, 375]. The same three parameters are currently being studied at the LHC, for example, in [376], reaching precisions between 6 and 8×10^{-3} in single-parameter fits and between 7 and 12×10^{-3} in two-parameter fits. In these analyses, g_Z and κ_γ show a strong, almost 100% correlation. For the HL-LHC, generator-level projections of three-parameter fits have been performed based on NLO cross-sections and assumptions on efficiencies derived from the corresponding 8 TeV ATLAS and CMS analyses [377]. This study projects precisions between 2 and 5×10^{-3} , with the same strong correlation between g_1^Z and κ_γ . It also evaluated the effect of non-SM Z-fermion couplings (in particular the $q\bar{q}Z$ couplings) by letting them float in the fit within 2σ bounds from fits to LEP data. This has a huge impact on the ability to extract g^Z and κ_γ : their constraints weaken to the level of $1\text{--}2 \times 10^{-2}$. This highlights an important area of ILC-LHC

interplay: the couplings of the Z boson to fermions will be measured to unprecedented precision both at the Z pole and – more relevant here – at higher energies, as discussed in sections 9.2, 9.3 and 10.4 of this report.

Most studies of the capability of future e^+e^- linear colliders to constrain triple gauge vertices have been performed at a center-of-mass energy of 500 GeV. These range from studies based on full, Geant4-based simulations of the ILD detector concept focusing on the $WW \rightarrow \mu\nu qq$ and $WW \rightarrow e\nu qq$ channels and the determination of the three LEP couplings [207] to theory-level studies showing that with polarized beams, all 28 real parameters of the most general possible Lagrangian for triple gauge interactions can be determined [378, 379, 380]. The results of the full simulation studies, which included only a subset of channels and observables, as will be discussed in section 10.3, have been extrapolated to $\sqrt{s} = 250$ GeV in Sec. 2.3.3.2 of [208], with rather conservative assumptions on the change in the impact of detector effects with center-of-mass energy. This extrapolation yields precisions between 8 and 10×10^{-4} . Notably it also shows that the correlation between g_1^Z and κ_Z in e^+e^- collisions depends on the center-of-mass energy and the beam polarizations, and can even change sign. Thus, runs with different energies and polarizations can eliminate any blind direction.

Finally, the expected impact of including all channels and using an unbinned log-likelihood fit to all observables (instead of binned fit to a reduced set of observables) improves the projections for ILC250 to the level of $4 - 6 \times 10^{-4}$ — nearly a full order of magnitude better than the previously discussed HL-LHC expectations, even when fixing Z -fermion couplings for the HL-LHC. A comparison with the higher energy stages of the ILC is shown in Fig 10.9.

At the ILC, triple gauge vertices can also be studied in single- W production, $e^+e^- \rightarrow e^\pm W^\mp \nu_e(\bar{\nu}_e)$. This adds another independent data set to the determinations. It also brings up another issue. At the ILC, the single and pair production of W bosons are used not only to measure the TGCs but also to serve as standard candles to gauge the luminosity-weighted and long-term averaged beam polarization values. This raises the question of whether effects of anomalous couplings and beam polarization can be reliably disentangled, and whether beam polarizations introduce an additional uncertainty. Furthermore, there is the question of possible impact from the other involved vertices, namely the $e - \nu - W$ vertex in all t -channel contributions and the $e - e - Z$ vertex in s -channel WW and t -channel single- W production. In order to address these questions, a fit to a variety of binned generator-level $e^+e^- \rightarrow f\bar{f}$, $e^+e^- \rightarrow W^+W^-$ and single- W distributions has been pioneered in [208] and further developed in [381, 210, 382]. The results of a fit to differential distributions from $e^+e^- \rightarrow \mu^+\mu^-$ and $e^+e^- \rightarrow \mu\nu qq$ at 250 GeV, which treats not only the three triple gauge couplings, but also (unpolarized) total cross-sections, left-right asymmetries, the angular acceptance and the beam polarizations as free parameters, is displayed in Fig 8.8 for various assumptions on the integrated luminosity and beam polarizations. For the ILC-like configuration (orange bars), the triple gauge couplings are determined at the level of 10 to 15×10^{-4} in this much more general fit from the muon final state only. With the final state with electrons also included, this would correspond to precisions of 7 to 11×10^{-4} . Within the uncertainty of the extrapolation and the different number of observables and free parameters, this compares very well with the 8 to 10×10^{-4} from the extrapolation of the full simulation analysis and shows that the ILC measurements will be extremely robust against consideration of additional free parameters.

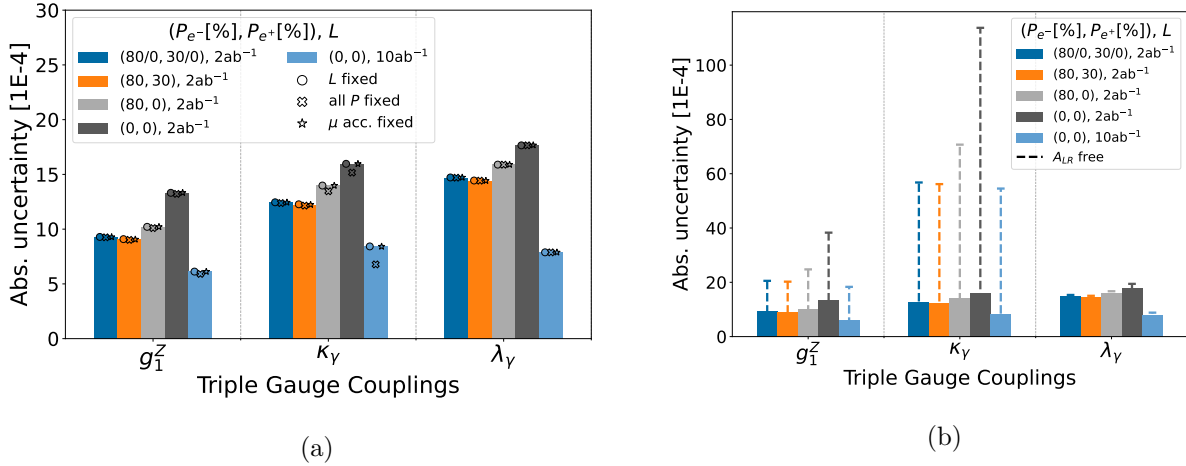


Figure 8.8: (a) Expected precisions at $\sqrt{s} = 250$ GeV of charged TGCs for different assumptions on the beam polarizations and the integrated luminosity. Note that these appear more pessimistic than in Fig. 10.9 since here only the $\mu\nu q\bar{q}$ channel is used in a binned three-angle analysis (b) Effect of floating the left-right asymmetry of the the Zee coupling in the fit. This underlines, first, the importance of independently measuring this this quantity — not only on the Z pole, but at 250 GeV — and, second, the increased robustness of the fit due to beam polarization, which reduces the dependence on the left-right asymmetry considerably. Both from [210, 382].

We emphasize that the use of beam polarization plays an important role. Since the effect of anomalous TGCs on the differential cross-sections differs between $e_L^- e_R^+$ and $e_R^- e_L^+$, the ability to take data in different polarization configurations adds qualitatively new information. This leads to improvements of 40%, 30% and 20%, respectively, for g_Z , κ_γ and λ_γ , compared to the case of unpolarized beams. Thus, the additional information provided by the polarized beams is equivalent to a factor 1.5 to 2 more luminosity. Figure 8.8 also shows another important aspect, concerning the robustness against finite knowledge of other SM parameters. When the left-right asymmetry in the Zee coupling is set free in the fit, the uncertainties on g_Z and κ_γ for the unpolarized case are a factor of two larger than in the polarized case. This shows that the additional information from the polarization reduces the dependency on residual parametric and theoretical uncertainties that enter the analysis of WW production.

8.4 Precision QCD

The theory of Quantum Chromodynamics is one of the central elements of the Standard Model, and plays a dominant role in understanding a wide range of collider experiments. Due to their QCD neutral initial state, e^+e^- colliders are the simplest setting in which to study the dynamics of energy flow in QCD, enabling precision measurements well beyond what is possible in hadron colliders. While e^+e^- colliders such as the ILC allow the precision measurement of QCD parameters, such

as α_s , their legacy is much larger due to the notions of factorization and universality, which allow detailed measurements of QCD final states to be applied in the search for new physics in hadronic colliders.

To emphasize the immense impact that the ILC would have on studies of QCD, it is worth recalling the impact that LEP has had, as well as emphasizing some of its shortcomings that the ILC would be able to fill. While a wide variety of event shapes were measured at LEP, since LEP ran at the Z -pole, these were primarily dijet event shapes measured on quark jets. These data have had a profound impact on the study of jets at the LHC in the fact that quark jets are extremely well modelled in parton shower Monte Carlo programs, since their non-perturbative effects can be tuned against this rich dataset. On the other hand, gluon jets, which were not produced that often at LEP, but are copiously produced at the LHC, are poorly modeled. The precision measurement of event shapes have also enabled precision extractions of the strong coupling constant, α_s [383, 384].

In the time since LEP there has been massive theoretical progress, driven by a renewed interest in studying the dynamics of jets in jet substructure at the LHC. The high energies and remarkable angular resolution of the LHC have enabled the detailed structure of energy within jets to be measured, requiring new calculational techniques to be developed. This was originally driven by the fact that the energy pattern within jets can be used to distinguish jets initiated by a light quark or gluon from jets initiated by an electroweak scale boson. The techniques developed with this initial motivation in mind have enabled a variety of new ways of understanding the dynamics of QCD with increasing sophistication. This includes both qualitative advances in the design of observables for probing specific features of QCD, as well as advances in theoretical techniques for event shape calculations. For a review, see [385, 386] It is therefore worth asking what one could do with a fresh slate if one had a new e^+e^- machine for understanding QCD. This section provides a brief overview of some such possibilities, as well as more detailed references for the interested reader, emphasizing that the higher energies and better resolution calorimeters of the ILC would be transformative for QCD.

Energy Flow Observables in QCD

Measurements of the flow of radiation in collider events provide one of the most interesting tests of our understanding of QCD. High energy collisions are particularly interesting, since they provide a probe of the dynamics of QCD from asymptotically free quarks and gluons, through the confining phase transition to free hadrons at asymptotic infinity. Energy flow in colliders can be studied either using event shapes, which can be thought of as resolution variables about an underlying S -matrix element of quarks and gluons, or using correlation functions, which measure statistical properties of the radiation. Both approaches have seen significant progress driven by jet substructure at the LHC, giving rise to many interesting new observables that could be measured at the ILC, providing a significantly extended understanding of energy flow in quantum field theory.

New Event Shape Observables

Event shape observables, which constrain radiation about a particular S -matrix element are particularly useful at the LHC for identifying boosted electroweak scale bosons decaying into jets. There has therefore been significant progress in their understanding, and many new observables have been proposed. In particular, one of the most important outputs of the jet substructure program is the ability to design event shape observables with specific properties. Such observables were simply not available in the LEP era, and would therefore be extremely interesting to measure at the ILC.

While there are endless examples of such observables, here we content ourself with describing one particular class of observables, namely “groomed” observables [387, 388]. One of the insights of the jet substructure program has been the introduction of grooming algorithms that systematically remove low energy soft radiation. Such low energy soft radiation generically contributes the leading hadronization corrections, and therefore grooming can significantly reduce non-perturbative effects. For a generic infrared and collinear safe observable, one can then measure its “groomed” counterpart, which will also be IRC safe. Although these observables are theoretically cumbersome, due to the fact that they reduce non-perturbative corrections they can be practically useful, for example for measurements of α_s .

These “groomed” observables have received significant theoretical attention due to their use in jet substructure. However, since they were introduced post-LEP, they have not been measured in an e^+e^- environment. An example of a theoretical prediction for a groomed observable is shown in Fig. 8.9, taken from [389]. Measurements of these observables are useful for fundamental studies of QCD, and also would provide insights into their behavior at the LHC, but in a simpler context.

Characterizing QCD with Correlation Functions

Since the LEP era there has been a significant improvement in our understanding of energy flow in collider experiments, driven quite interestingly, by purely formal developments. While the observables in the previous section were so called “jet shape” observables, if the goal is to understand the structure of the underlying theory, one may be curious why one does not proceed in the standard manner taken for other physical systems, namely measuring correlation functions. Unlike for condensed matter systems where one typically characterizes systems by correlation functions of local operators, building up from low point correlators, in collider experiments one cannot measure correlation functions of local operators. However, instead, one can measure certain non-local light-ray operators called energy flow operators, defined as integrals of the stress tensor along null infinity in a direction characterized by a unit vector \vec{n} [390]

$$\mathcal{E}(\vec{n}) = \lim_{r \rightarrow \infty} \int_0^{\infty} dt r^2 n^i T_{0i}(t, r\vec{n}). \quad (8.4)$$

One can then characterize the system by measuring correlation functions of $\langle \mathcal{E}(\vec{n}_1) \mathcal{E}(\vec{n}_2) \cdots \mathcal{E}(\vec{n}_k) \rangle$ of these operators. These objects are particularly simple theoretically, since they exhibit symmetry properties similar to standard correlation functions of local operators, and are also governed by

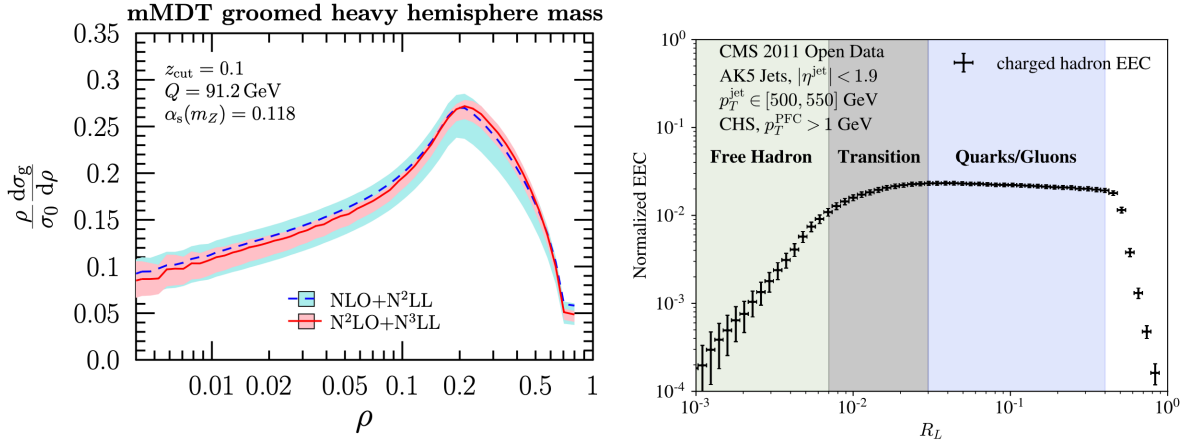


Figure 8.9: (a) The groomed mass observable in e^+e^- [389]. (b) A precision measurement of the two-point correlator in the collinear limit at the LHC [397]. Both of these new observables provide interesting probes of α_s

an operator product expansion. This enables one to discuss jet phenomenon in the language of correlation functions, and there has been a significant program to make this a phenomenological reality [391, 392, 393, 394, 395, 396]. Furthermore, they exhibit simple structures in perturbation theory. One can show that jet shape observables are infinite sums over these correlation functions, and hence they lose many of these desirable theoretical properties.

Although the two-point correlator was measured at LEP, it was not studied in detail in the OPE limit to look for scaling behavior, and higher point correlators, which probe more interesting features of the theory, such as spin correlations, were never measured. A measurement of the two-point correlator using Open Data from the CMS experiment is shown in Fig. 8.9, illustrating beautiful scaling behavior of weakly coupled quarks and gluons, and a transition to the scaling of free hadrons [397]. Measurements of this quality in the ILC environment would provide remarkable insights into the dynamics of QCD jets, and the hadronization transition.

The ILC would provide a beautiful environment where one can rethink how jets are studied and measure in detail the structure of multi-point correlators in QCD. These are of significant interest for understanding QCD, but also provide insight into the behavior of perturbative nearly conformal theories more general, and have been the focus of much recent interest of the theoretical community (see e.g. [398]). Precision measurements of these correlators would build a bridge between the QCD phenomenology and formal theory communities which would result in significant progress.

Precision Extractions of α_s with Old and New Observables

One of the key parameters of interest in QCD is the value of the strong coupling constant, α_s . Since this is an arbitrary parameter of the theory, it can only be obtained by comparison precision theoretical predictions with experimental measurements. While there are many different possible

observables that can be used to constrain the value of α_s , measurements of the distribution of energy in e^+e^- have proven to be competitive. However, there is currently an unresolved tension between extractions of α_s from event shape extractions at LEP as compared with lattice based extractions. Resolving this tension is important to illustrate a consistent understanding of QCD at the percent level.

The most precise extractions of α_s from event shapes are based on thrust and the C -parameter [383, 384], which are closely related double logarithmic observables. To understand any possible issues in these extractions, it is crucial to have measurements based on other observables. Two observables that can be computed to high accuracy that exhibit significant differences from thrust/ C -parameter are the groomed thrust event shape, and the energy-energy correlators.

One of the complexities in extractions of α_s from event shapes is that one has to incorporate non-perturbative power corrections. These power corrections cannot be computed from first principles, and therefore must be simultaneously fit for along with the value of α_s . One approach to reducing this potential uncertainty is to use grooming algorithms, inspired by the study of jet substructure at the LHC, to reduce non-perturbative corrections from low energy soft radiation. This makes the groomed thrust a potentially appealing observable for extractions of α_s . Much like the thrust observable, its resummation is governed by the cusp and collinear anomalous dimensions, but grooming reduces it to a single logarithmic observable, and reduces the non-perturbative corrections. Due to this differing theoretical structure, an extraction of α_s from the groomed thrust would provide a relatively independent measurement of the value of α_s . The groomed thrust can be computed to high perturbative accuracy, using a factorization formula. This is shown in Fig. 8.9. Furthermore, non-perturbative corrections to the groomed thrust distribution have been studied in [399].

While the groomed thrust provides many complementary features to the standard thrust based extraction of α_s , it is ultimately based on the same event shape paradigm, and therefore similar assumptions enter in the treatment of non-perturbative effects. Another interesting complementary measurement would be to perform a measurement of the two-point energy correlator in the collinear limit [400]. The collinear limit is described by completely different physics (fixed spin DGLAP) than the Sudakov region, and furthermore, since the energy correlators are not event shape observables, they have a different structure for their non-perturbative effects. However, despite being an old observable that was measured at LEP, extractions of α_s from the collinear limit were never performed at LEP. We believe that this is partially due to the angular resolution of the calorimeters. Comparing the measurement of the two-point correlator at LEP vs. using the modern calorimetry of the LHC shows a completely different understanding of the collinear limit. Achieving a similarly precise measurement in the clean e^+e^- environment of the ILC would be extremely valuable for precision measurements of α_s , and would hopefully resolve the longstanding tensions in its extracted values.

In addition to the precision determination of α_s , the ILC will also add to our knowledge of another basic QCD parameter, the bottom quark mass. Methods for improved measurements of m_b and, in particular, the evolution of this parameter under QCD running, are described in [401].

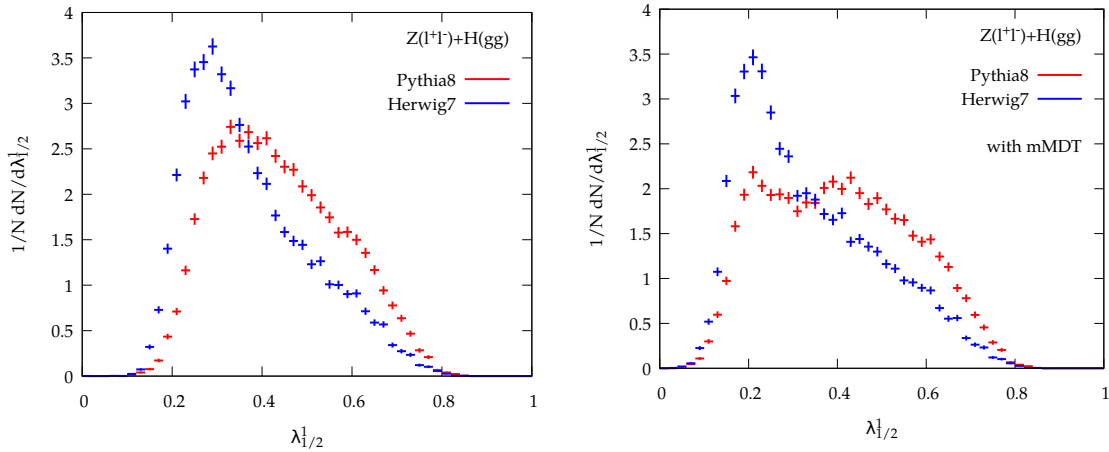


Figure 8.10: Generalized angularities (a), and groomed angularities (b) measured on gluon jets with different event generators. Large discrepancies are observed due to a lack of tuning data. Figures courtesy of Gregory Soye.

Gluons from the Higgs

As compared with LEP, a particular advantage of the ILC for the study of QCD is the availability of pure samples of gluon jets through the process $e^+e^- \rightarrow HZ$, with Z decay to leptons and Higgs boson decay to gg [402]. This would be a unique feature of the ILC. At the LHC, one of the primary issues in understanding precision jet substructure is the difficulty in disentangling quark and gluon jets. As such the study of properties of gluon jets in QCD is extremely poor; this is reflected in large discrepancies in different parton shower simulations shown in Fig. 8.10. This lack of understanding of gluon jets, and in particular their non-perturbative properties, is a major issue and a leading uncertainty in many new physics searches at the LHC. One of the promises of jet substructure is that it offers the potential of discriminating quark vs. gluon jets to identify new physics signals. However, this requires a detailed understanding of both quark and gluon jets. Currently, quark vs. gluon tagging has not fulfilled its promise due to large uncertainties in the modelling of gluon jets. Having pure samples of gluon jets in QCD would significantly change this situation and have a major impact on the LHC physics program.

Although the understanding of gluon jets is quite poor, there in fact exist a wide range of precision perturbative calculations of event shapes on $H \rightarrow gg$, which have never been compared to data. Two examples, the thrust event shape and the energy-energy correlator, are shown in Fig. 8.11. These predictions have never been compared with data. Since the perturbative features of gluon jets are well understood, and already available to high accuracies, comparison with data would enable detailed studies of the non-perturbative structure of gluon jets.

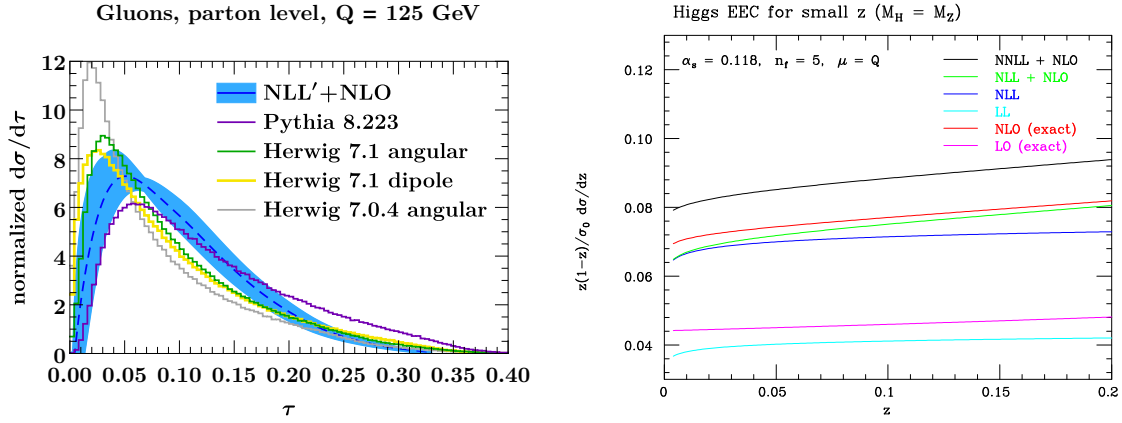


Figure 8.11: Precision perturbative calculations in $H \rightarrow gg$. In (a) we show a double logarithmic Sudakov event shape observable [403], and in (b) and single logarithmic collinear observable [400].

QCD for the Higgs

Although the primary focus of this section is on the use of ILC for learning about QCD, due to its close relation to the other topics in this section, it is also interesting to briefly mention how newly developed jet substructure tools, in particular quark vs. gluon tagging just discussed, can be used to provide new handles on the Higgs boson at the ILC. One of the interesting questions about the Higgs boson that is difficult to study directly at the LHC are its couplings to light (u,d,s) quarks. While these couplings can be probed at the LHC by precise measurements of the p_T spectrum of the Higgs, potentially enabling measurements at the level of $y_s \leq 0.5y_b$, this requires a precise understanding of the gluon/quark luminosities.

At the ILC, precision measurements of event shapes on Higgs decays can provide much more precise handles on the light quark Yukawa couplings due to the differing radiation patterns of quark and gluons. In particular, [404] was able to achieve $y_{u,d,s} \leq 0.091 y_b$ and 95% confidence. This was using a fairly conservative approach of a single event shape, thrust. This is shown in Fig. 8.12. Almost certainly with more sophisticated event shapes, this bound could be significantly improved, and would provide an interesting example of the interplay between precision QCD measurements and the Higgs program at the ILC.

New Non-Perturbative Inputs

Another important part of the legacy of LEP is the measurement of universal non-perturbative functions of QCD. Although there are currently no methods for first principles calculations of non-perturbative Lorentzian observables in QCD, much of the predictivity of QCD comes from factorization theorems which express cross sections in terms of universal non-perturbative functions. Famous examples measured at LEP include fragmentation functions. These can then be used in other colliders, such as at the LHC, and have had a large impact on the collider physics program.

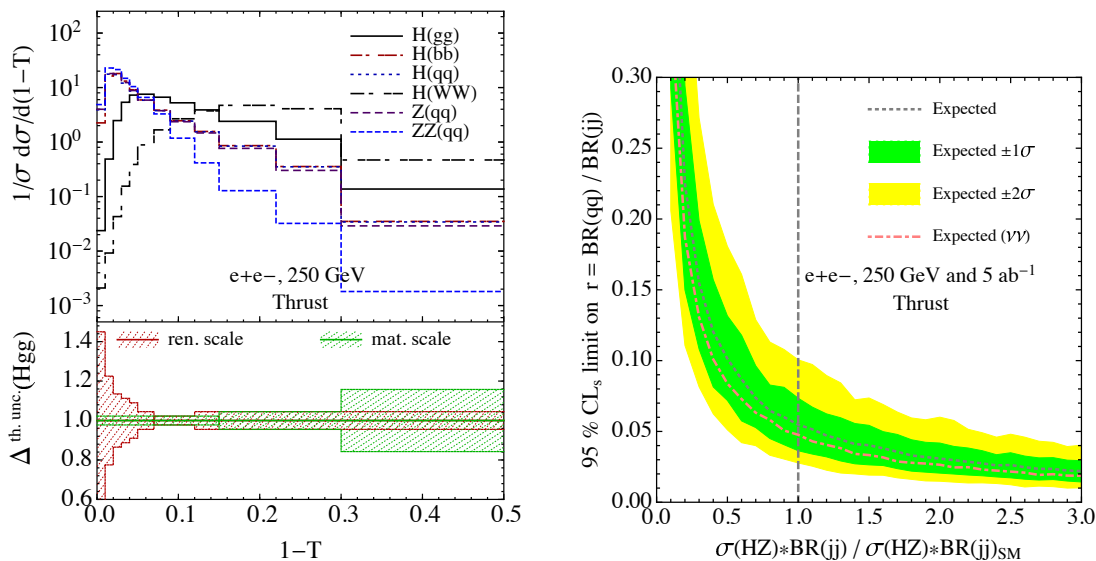


Figure 8.12: Precision measurements of event shapes on Higgs decays used to bound the light quark Yukawas [404].

While it is clear that measurements at the ILC would improve our understanding of fragmentation functions, since these functions have been discussed extensively in the literature, here we focus on universal non-perturbative inputs that were not defined at the time of LEP, which could be measured precisely at ILC, and would have a significant impact on the LHC physics program.

Measurements at the LHC rely strongly on the use of tracking information. This is both due to the fact that tracking is less sensitive to pile-up, which will become increasingly important in the high-luminosity era, and because of the remarkable angular precision of the tracker, which is particularly important for many jet substructure measurements. However, only observables that are completely inclusive over the spectrum of final states can be computed purely from perturbation theory, and therefore the calculation of track based observables (which distinguish final state particles based on their charge) requires some non-perturbative input. Still, the situation is not hopeless, since this non-perturbative information is universal. It can be parametrized by so-called “track functions” [405, 406], which describe the fraction of energy carried by charged particles from a fragmenting quark or gluon. These can be viewed as generalizations of fragmentation functions, since they encode correlations among the final state hadrons due to the fact that a single fragmenting quark or gluon can decay into multiple charged hadrons. The track functions must be measured experimentally using well-defined quark and gluon jet sources.

Recently it has been shown how to compute jet substructure observables at high precision incorporating track functions [407, 408], which gives promise for precision jet substructure measurements at the LHC. However, despite this new found theoretical understanding, track functions have never been experimentally measured. Furthermore, such measurements in archived LEP data are difficult

due to the lack of gluon jets.

The ILC would provide very clean sources of quark and gluon jets on which one could precisely measure the quark and gluon track functions. This would be synergistic with the high luminosity LHC physics program, and would be a particularly valuable contribution with many applications.

QCD in $\gamma\gamma$ Interactions

Beyond e^+e^- annihilation, there are additional reactions at an e^+e^- collider that are fascinating from the point of view of QCD. These include, especially, the regimes where a fixed-order perturbative approach needs to be supplemented by one or more all-order resummations. In the high-energy or *Regge* limit, large center-of-mass energy logarithms enter the perturbative series with a power that increases with the order, thus compensating the smallness of the strong coupling. Therefore, the convergence of the perturbative series is spoiled and an all-order resummation of these large logarithms must be carried out. The most powerful tool to perform this resummation is the Balitsky–Fadin–Kuraev–Lipatov (BFKL) approach [409, 410, 411, 412] (see Ref. [413] for recent applications), where amplitudes for high-energy reactions are elegantly factorized via a convolution between two impact factors, describing the production of an identified final-state object from the corresponding initial-state particle, and a process-independent Green’s function. This factorization has been proven up to the next-to leading logarithmic accuracy (NLA).

The best opportunities to test this resummation come in the scattering of small transverse-size objects, in particular, objects with no hadronic activity in the initial state. A particularly interesting setting is the case of the total hadronic cross section hadronic two virtual photons. In this $\gamma^*\gamma^*$ reaction, the BFKL theory predicts a growth of the total cross section with energy [414, 415, 416, 417, 418, 419]. Unfortunately, the only data available to test this prediction is that from LEP 2. A sample of events with higher collision energy and better detector performance for forward reactions would be very advantageous. Another reaction that probes this physics is $(\gamma^*\gamma^* \rightarrow VV$ reaction, with two vector mesons (V) detected in the final state. NLA predictions for the diffractive electroproduction of ρ mesons were provided in Refs. [420, 421, 422], and comparisons with LEP 2 data for the double diffractive J/Ψ photoproduction were done in Ref. [423]. The impact factor for the production of forward heavy-quark pair was recently calculated [424, 425], and first predictions of cross sections and azimuthal-angle correlations for the double heavy-quark pair photoproduction were presented for LEP2 energies as well as for the energies of future linear e^+e^- colliders [424, 426]. The BFKL resummation is an important aspect of QCD that is very difficult to test in hadronic collisions, but these reactions give the opportunity for tests in which the dependence on the photon virtuality gives additional powerful information.

Chapter 9

ILC Precision Electroweak Measurements

9.1 Introduction

The ILC, which will provide a thousand-fold increase in the accumulated data-sets compared to prior e^+e^- experiments, polarized beams, and the potential to take data at a wide range of center-of-mass energies, will offer the opportunity to advance knowledge of the precision electroweak (PEW) sector. The measurement precision will far exceed the precision achieved in the legacy measurements from LEP/SLC near the Z pole [427] and from LEP at higher center-of-mass-energies up to 208 GeV [371]. The underlying assets are much higher statistics, precise modern detectors with much improved reconstruction of particle and jet momenta, polarized beams, and improved theoretical modeling.

Adequate control of systematic uncertainties is mandatory. This includes detector calibration and alignment, control of reconstruction efficiencies and geometrical acceptance, determination of the center-of-mass energy, differential luminosity, integrated luminosity, and the polarization of the beams. These need to be maintained over years of accelerator operation and are a critical prerequisite for extracting the maximum physics out of dedicated physics runs at special center-of-mass energies such as the WW threshold and especially at the Z pole. Such running is already feasible with the initial 250 GeV ILC accelerator described in Chapter 4 as discussed in [119].

ILC operation must be crafted so as to exploit opportunities for special runs to address individual electroweak quantities such as the W and Z masses, while maintaining sufficient luminosity and time to deliver on the Higgs, top, and Higgs self-coupling programs. The various ILC data-taking configurations will impact the knowledge gained for each PEW observable in different ways. Having several measurement methods for the same observable with complementary systematic uncertainties should lead to improved knowledge.

Examples of the configurations under consideration are:

- Running synergistic with the core physics program. A good example is a LEP2-style measurement of the W mass that is well suited to exploiting data collected at the center-of-mass energy of 250 GeV.
- Complementary methods enabled by high energy running, such as measurement of Z properties using radiative return events.
- A dedicated physics run using a polarized scan near the Z pole accumulating a data sample of 100 fb^{-1} and up to 4 B Z s.
- Short few day pilot runs near the Z pole, each accumulating at least 10M hadronic Z s, for detector calibration and alignment, and for physics. Each such sample would be roughly comparable to the whole LEP-1 program and would permit calibration of the tracker momentum-scale to a statistical uncertainty of 2.5 ppm.
- A dedicated physics run with a polarized scan near the WW threshold.

After describing some of the measurement techniques and prospects, we will revisit these issues more quantitatively. For now let us summarize our current thinking:

1. An accelerator built for running above ZH threshold should be exploited as much as possible using data that can be collected along with Higgs production. So a clear case needs to be made for the added benefit of dedicated extensive runs at lower energies.
2. The opportunities to make large improvements in the Z observables with a dedicated scan are obvious and warrant dedicated exploitation once the accelerator has been upgraded in luminosity by bunch doubling. In order to evaluate better the eventual reach and required running time, the Z pilot runs should be used early in the ILC program to gain valuable experience. They will also serve as a rich physics sample, a valuable resource for calibration and alignment for the higher energy running, and a high statistics benchmark for the tuning of hadronization models.
3. The W mass can already be measured rather well with the standard ILC program, likely obviating the need for substantial time investment in a dedicated run near threshold. Nevertheless, the potential for such a dedicated run with as high as possible beam polarizations should be retained given the perceived uniqueness of the threshold-based observables.

Our expectations for the precisions with which the ILC will measure electroweak observables are summarized in Table 9.1.

9.2 Radiative Return to the Z

The ILC running at 250 GeV will already produce a data set that will allow substantial improvements of our knowledge of precision electroweak observables. One of the high-cross-section reactions at 250 GeV is the radiative return to the Z , $e^+e^- \rightarrow Z\gamma$. In this reaction, the Z is produced in

Quantity	Value	current $\delta[10^{-4}]$	Z pole		ILC250	
			$\delta_{stat}[10^{-4}]$	$\delta_{sys}[10^{-4}]$	$\delta_{stat}[10^{-4}]$	$\delta_{sys}[10^{-4}]$
boson properties						
m_W	80.379	1.5	-	-	-	0.3
m_Z	91.1876	0.23	-	0.022	0.08	-
Γ_Z	2.4952	9.4	0.5	-	6	-
$\Gamma_Z(had)$	1.7444	11.5	-	4.	-	-
Z-e couplings						
$1/R_e$	0.0482	24.	2.	5	5.5	10
A_e	0.1513	139.	1.5	1.2	12.	9.
g_L^e	-0.632	16.	1.0	3.2	2.8	7.6
g_R^e	0.551	18.	1.0	3.2	2.9	7.6
Z- ℓ couplings						
$1/R_\mu$	0.0482	16.	2.	2.	5.5	10
$1/R_\tau$	0.0482	22.	2.	2.	5.7	10
A_μ	0.1515	991.	2.	5	54.	3.
A_τ	0.1515	271.	2.	5.	57.	3
g_L^μ	-0.632	66.	1.0	2.3	4.5	7.6
g_R^μ	0.551	89.	1.0	2.3	5.5	7.6
g_L^τ	-0.632	22.	1.0	2.8	4.7	7.6
g_R^τ	0.551	27.	1.0	3.2	5.8	7.6
Z-b couplings						
R_b	0.2163	31.	0.4	7.	3.5	10
A_b	0.935	214.	1.	5.	5.7	3
g_L^b	-0.999	54.	0.32	4.2	2.2	7.6
g_R^b	0.184	1540	7.2	36.	41.	23.
Z-c couplings						
R_c	0.1721	174.	2.	30	5.8	50
A_c	0.668	404.	3.	5	21.	3
g_L^c	0.816	119.	1.2	15.	5.1	26.
g_R^c	-0.367	416.	3.1	17.	21.	26.

Table 9.1: Projected precision of precision electroweak quantities expected from the ILC. Precisions are given as *relative* errors ($\delta A = \Delta A/A$) in units of 10^{-4} . The column labelled “Z pole” refers to the dedicated Z pole run described in Sec. 4.1.4; the column labelled “ILC250” refers to values that can be obtained from radiative return events at 250 GeV. REMARK: The table is taken from Ref. [428] but also reflects some updates and corrections.

the forward direction but still accessible to the ILC detectors. We will explain in a moment that the photon, which is produced in the opposite forward direction, does not need to be observed to provide a very clean event sample. The ILC program, with 2 ab^{-1} of data, will produce roughly 77 million hadronic Z s and 12 million leptonic Z s, a substantial increase over the event sample of LEP. Further, these events are produced with polarized beams, so that, for polarization observables, the event sample to compare with is that of SLC. The full power of the ILC detectors can be used for flavor identification.

We tag the signal events for the radiative return analysis based on the polar angles of the two fermions from $Z \rightarrow f\bar{f}$. To describe the method simply, we will use the approximations that the fermions are massless and the photon is collinear to the beam directions. This is already quite close to realistic, and the approximations can be relaxed with small corrections. Then let E_i and θ_i , $i = 1, 2$, denote the energy and polar angle, respectively, of each final lepton or jet. Transverse momentum conservation implies that $E_1 \sin \theta_1 = E_2 \sin \theta_2$. The fermion pair is boosted only in the beam direction. The boost factor can be determined as

$$|\beta| = \frac{|E_1 \cos \theta_1 + E_2 \cos \theta_2|}{E_1 + E_2} = \frac{|\sin(\theta_1 + \theta_2)|}{\sin \theta_1 + \sin \theta_2}. \quad (9.1)$$

It is interesting that the E_i cancel out, so β only depends on θ_1 and θ_2 . The invariant mass of the fermion pair, m_{12} , can then be reconstructed as

$$m_{12}^2 = \frac{1 - |\beta|}{1 + |\beta|} \cdot s, \quad (9.2)$$

where \sqrt{s} is the center-of-mass energy. For the signal events we expect that m_{12} peaks at m_Z and, for $\sqrt{s} = 250 \text{ GeV}$, $|\beta|$ peaks at 0.76. The angles θ_1 and θ_2 can be measured very precisely at the ILC detectors, so that the signal events can be tagged without the need to observe the ISR photon.

This method was actually used at LEP2 [429], though mainly for calibrating the beam energy due to the limited statistics. But at ILC250, we will expect 90 million of such radiative events, a factor of 5 (100) more than the total number of Z produced at LEP (SLC).

A fast simulation study has been performed for the A_e measurement using the $e^+e^- \rightarrow \gamma Z$, $Z \rightarrow q\bar{q}$ channels and the full SM background [430]. This has now been followed by a full-simulation analysis [431, 432]. After all of the selection cuts, the signal efficiency is 53% and the remaining background events, due to systems with approximately the Z mass from other processes, are almost negligible, as shown in Fig. 9.1. For the results shown, realistic effects from finite fermion mass and beam crossing angles have already been taken into account. From the measured cross sections for the left- and right-handed beam polarizations, the statistical error on A_e for 2 ab^{-1} data in the ILC250 scenario is estimated to be 0.00018, including also an estimate of the contribution of leptonic Z decays. This is a relative error of $\delta A_e = 11.9 \times 10^{-4}$. This is a factor of 9 improvement over the current uncertainty on A_e . By taking into account all realistic SM $2f$ and $4f$ background events, the signal over background ratio can be controlled to better than 20/1. After all selection cuts the distribution of the reconstructed invariant mass of two jets for remained signal and background events are shown in Fig. 9.2 for $P(e^-, e^+) = (-0.8, +0.3)$ (left) and $P(e^-, e^+) = (+0.8, -0.3)$ (right), and linear scale (top) and logarithmic scale (bottom). Most of the systematic errors in the cross section measurement for each beam polarization, such as those from uncertainties on

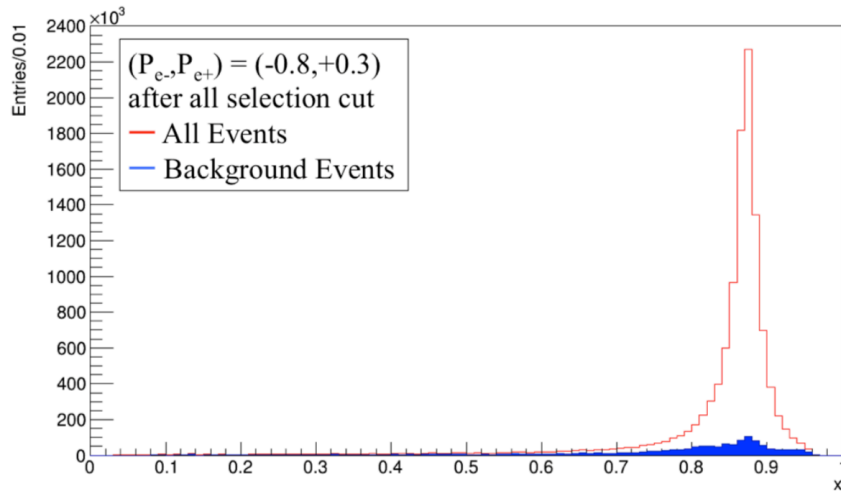


Figure 9.1: Reconstructed distribution of $x \equiv \frac{2|\beta|}{1+|\beta|}$ for the signal $e^+e^- \rightarrow \gamma Z$, $Z \rightarrow q\bar{q}$ and background events, at $\sqrt{s} = 250$ GeV with an integrated luminosity of 250 fb^{-1} .

event selection efficiency and integrated luminosity, are correlated. Thus they will essentially be cancelled out in the measurement of the cross section asymmetry for A_e . It is pointed out in [431] that in order to match the expected statistical error of A_e , the uncorrelated relative uncertainty on efficiency and luminosity should be controlled to 0.016%. The systematic uncertainty due to finite knowledge of the beam polarizations has been discussed in Sec. 5.4.3, we have explained that all four polarizations values as well as further nuisance parameters can be determined simultaneously with A_e from the collision data themselves. From the comparison of the A_e precision obtained when all polarisation values are free parameters to a fit where they are fixed to their true values [210], the residual impact of the polarization uncertainty on A_e has been estimated to be 1.2×10^{-4} . Note that, as also discussed in Sec 5.4.3, this uncertainty reduces with increasing statistics, down to an even smaller residual from uncorrectable point-to-point uncertainties.

In principle, the value of A_e also depends on the CM energy in the $e^+e^- \rightarrow Z\gamma$ reaction. The polarization asymmetry actually measured in this reaction has the form [433]

$$A_{obs} = A_e + \Delta A, \quad (9.3)$$

where ΔA is a correction due to interference between the contributions to the $e^+e^- \rightarrow f\bar{f}\gamma$ from the resonant diagram with an intermediate Z and the nonresonant diagram with an intermediate γ . At the Z pole, the interference term has significant energy-dependence, requiring excellent knowledge of the CM energy. This will be an issue in Sec. 9.3. However, for the radiative return process at 250 GeV, the dependence $\Delta A_e/\Delta E_{CM}$ is negligible, 3 orders of magnitude smaller, because the signal events are populated over the full Z mass peak which is far away from the nominal center-of-mass energy.

For A_f measurements other than A_e , we need to measure the left-right forward-backward asymmetry A_{LRFB} . A dedicated simulation study for A_f ($f = b/c/\mu/\tau$) has not yet been performed.

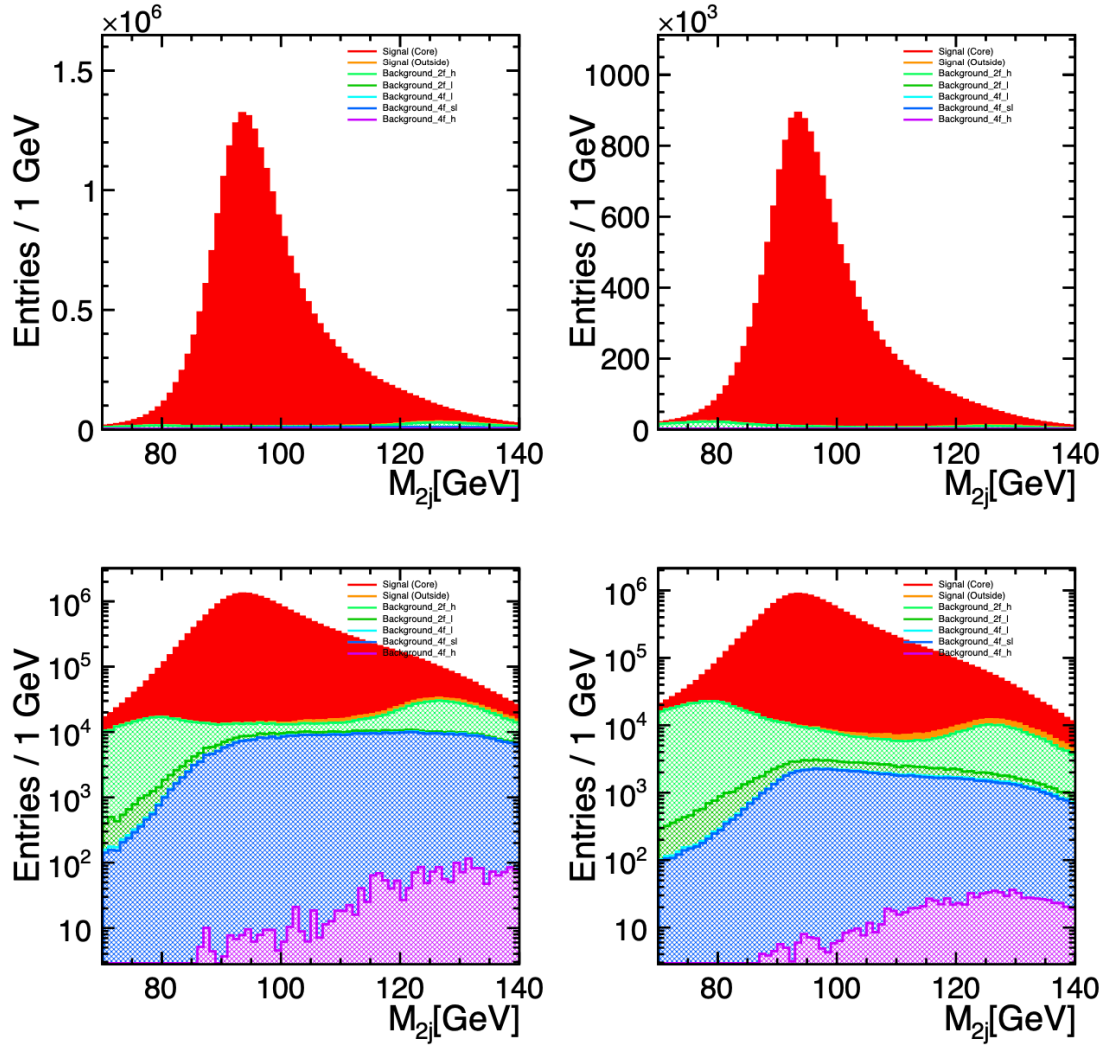


Figure 9.2: Reconstructed distribution of 2-jet invariant mass for the signal $e^+e^- \rightarrow \gamma Z$, $Z \rightarrow q\bar{q}$ and background events based on full detector simulation, at $\sqrt{s} = 250$ GeV with an integrated luminosity of 900 fb^{-1} . Top two figures are in linear scale and bottom two are in logarithmic scale. The left two are for $P(e^-, e^+) = (-0.8, +0.3)$ and the right two are for $P(e^-, e^+) = (+0.8, -0.3)$.

Nevertheless we can estimate the signal efficiency in two steps based on existing simulation analyses. The first step is to tag the signal events as from radiative return, just as in the A_e measurement. The second step is to identify the flavor and charge of the fermion. For example, the efficiency for the A_b measurement can be estimated to be $73\% \times 40\%$ in which the 73%, for tagging the hadronic radiative return event, is from fast simulation analysis described above [430], and the 40%, for b -tagging and b charge identification, is from a full simulation analysis described in [434]. The statistical error of A_b is then estimated to be $\Delta A_b = 0.00053$, a relative uncertainty of $\delta A_b = 5.7 \times 10^{-4}$. Similarly, the efficiencies for A_c , A_τ and A_μ can be derived from full simulation results in [435, 436, 437]. These are estimated to be $73\% \times 10\%$, 80%, and 88%, respectively. Their statistical errors are summarized in Table 9.1. The impact of the polarization uncertainties on the final-state asymmetries is negligible, as can be seen for the example of A_μ in Fig. 5.4 by comparing the full bars (free polarization parameters) to the open crosses (fixed polarizations).

The measurements of

$$R_q \equiv \Gamma(Z \rightarrow q\bar{q})/\Gamma(Z \rightarrow \text{hadrons}) \quad \text{and} \quad 1/R_\ell \equiv \Gamma(Z \rightarrow \ell^+\ell^-)/\Gamma(Z \rightarrow \text{hadrons}), \quad (9.4)$$

for $q = b/c$ and $\ell = e/\mu/\tau$, are simpler to describe, since we only need to measure the total rate for each flavor without the need to identify the charge. The signal efficiencies can be estimated based on the same analyses cited above [430, 434, 435, 436, 437]. The expected statistical errors are summarized in Table 9.1. The dominant systematic errors would come from the uncertainties in the flavor-tagging efficiencies, estimated in [438] to be 0.1% for $f = e/\mu/\tau/b$ and 0.5% for $f = c$.

Noting that R_e is expected to be improved by a factor of 2 over the current uncertainty [439], it is interesting to convert this to a value of the quantity $\Gamma_e \equiv \Gamma(Z \rightarrow e^+e^-)$, which is a useful input to the SMEFT global fit for Higgs boson couplings that will be discussed in Sec. 12.3. Γ_e can be derived from the measurements of the cross section of Z to hadrons σ_{had} , the Z total width Γ_Z , and R_e , with the uncertainty estimated as

$$\delta\Gamma_e = \frac{1}{2}\delta\sigma_{\text{had}} \oplus \frac{1}{2}\delta\Gamma_Z \oplus \frac{1}{2}\delta R_e, \quad (9.5)$$

where δ denotes a relative uncertainty: $\delta A = \Delta A/A$. With the current uncertainties for σ_{had} and Γ_Z from [439], and expected uncertainty for R_e at ILC250, we expect the precision for Γ_e to decrease to $\delta\Gamma_e = 0.86 \times 10^{-3}$. This improves over the current relative uncertainty on $\Gamma(Z \rightarrow \ell^+\ell^-)$ of 1.02×10^{-3} and also allows us to relax the assumption of lepton universality in this input to the SMEFT fit.

9.3 Di-fermion production

Electroweak di-fermion production is the process $e^+e^- \rightarrow f\bar{f}$, with $f \neq e$. At general CM energies, this process is dominated by s -channel photon and Z exchange. Thus, the cross section depends on the couplings $Q_{e,f}^\gamma$ of the initial and final state particles to the photons and the couplings Q_{fL}^Z , Q_{fR}^Z , of fermions with left-handed and right-handed helicity to the Z boson. There may also be contributions from a potential Z' boson of new physics. In this section, we will discuss the general case and then specialize to the study of fermion couplings at the Z pole.

9.3.1 Di-fermion production at general CM energies

At a general E_{CM} , the tree-level production amplitude for $e^+e^- \rightarrow f\bar{f}$ is given by $\mathcal{M} = e^2 \mathcal{Q}_{eifj}/s$, where

$$\mathcal{Q}_{eifj} = Q_e^\gamma Q_f^\gamma + \frac{Q_{e_i}^Z Q_{f_j}^Z}{\sin^2 \theta_W \cos^2 \theta_W} \frac{s}{s - M_Z^2 + i\Gamma_Z M_Z} + \sum \frac{Q_{e_i}^{Z'} Q_{f_j}^{Z'}}{\sin^2 \theta_W \cos^2 \theta_W} \frac{s}{s - M_{Z'}^2 + i\Gamma_{Z'} M_{Z'}} \quad (9.6)$$

with $i, j = L, R$, $Q_{e,f}^\gamma$ the electromagnetic charges, Q_{e,f_i}^Z the helicity-dependent charges for the Z boson couplings, and θ_W the weak mixing angle at Born level. The first two terms come from s -channel photon and Z diagrams. This second term may be affected by $Z - Z'$ mixing as for example suggested in [440]. The third term takes into account couplings to new vector bosons Z' , as for example heavy Kaluza-Klein recurrences included in Randall-Sundrum models with warped extra dimensions. The relative importance of the contributions is determined by the Breit-Wigner functions. We will discuss the ILC sensitivity to Z' resonances in Sec. 10.4.

The differential cross section of the process $e^+e^- \rightarrow f\bar{f}$ for relativistic polarized electron, with polarization \mathcal{P}_{e^-} and positron beams, with polarization \mathcal{P}_{e^+} , can be expressed as [427, 441, 442].

$$\frac{d\sigma}{d\cos\theta} = \frac{3}{4}(1 + |\mathcal{P}_{e^-}| |\mathcal{P}_{e^+}|)(1 - \mathcal{P}_{\text{eff}} A_{LR}) \left(\frac{1}{2} \sigma_{0,HC}(1 + \cos^2\theta) + (\sigma_{0,HV}/\gamma_f) \sin^2\theta \right) + [\sigma_0(1 + |\mathcal{P}_{e^-}| |\mathcal{P}_{e^+}|)((A_{FB})_0 - \mathcal{P}_{\text{eff}} A_{LRFB})] \cos\theta \quad (9.7)$$

where θ is the polar angle of the final state fermion, $\mathcal{P}_{\text{eff}} = (\mathcal{P}_{e^-} - \mathcal{P}_{e^+})/(1 + |\mathcal{P}_{e^-}| |\mathcal{P}_{e^+}|)$ is the effective polarization, as in (5.10), and γ_f is the boost of the final state fermions.

The differential cross section contains four linearly independent quantities:

- The total unpolarized cross section σ_0 split into a helicity-conserving, $\sigma_{0,HC}$, and a helicity-violating part $\sigma_{0,HV}$. In the Standard Model the helicity violating part vanishes at relativistic energies of the final state fermion. In practice the actual cross-section for a given fermion is often normalised to the total hadronic cross section σ_{had} yielding $R_q = \sigma_q/\sigma_{had}$ and $1/R_\ell = \sigma_\ell/\sigma_{had}$ in case of final state quarks and leptons, respectively;
- The unpolarized forward backward asymmetry $(A_{FB})_0$; For given beam polarization ‘-+’ it is defined as

$$(A_{FB})_0 = \frac{(\sigma_F - \sigma_B)_{-+} + (\sigma_F - \sigma_B)_{+-}}{2\sigma_0(1 + |\mathcal{P}_{e^-}| |\mathcal{P}_{e^+}|)} \quad (9.8)$$

with $\sigma_{F,B}$ being the cross sections in the forward and backward hemispheres with respect to the electron beam direction.

- The left-right asymmetry A_{LR} defined as

$$A_{LR} = \frac{1}{|\mathcal{P}_{\text{eff}}|} \frac{\sigma_{-+} - \sigma_{+-}}{2\sigma_0(1 + |\mathcal{P}_{e^-}| |\mathcal{P}_{e^+}|)} = \frac{1}{|\mathcal{P}_{\text{eff}}|} \cdot A_{LR}^{\text{obs.}} \quad (9.9)$$

The superscript ‘obs’ indicates the measured quantity.

- The left-right-forward-backward asymmetry A_{LRFB} defined as

$$A_{LRFB} = \frac{1}{|\mathcal{P}_{\text{eff}}|} \frac{(\sigma_F - \sigma_B)_{-+} - (\sigma_F - \sigma_B)_{+-}}{2\sigma_0(1 + |\mathcal{P}_{e-}| |\mathcal{P}_{e+}|)} = \frac{1}{|\mathcal{P}_{\text{eff}}|} \cdot A_{LRFB}^{\text{obs.}} \quad (9.10)$$

These quantities depend on the combinations Q_{eif_j} defined in (9.6). These or similar quantities derived from (9.7) can be used to determine independently four different individual couplings or four combinations. In all observables, the couplings to the Z enter linearly through the γ/Z interference for CM energies away from the Z pole. This allows us to determine the actual sign of the couplings. The two asymmetries A_{LR} and A_{LRFB} are only available with polarized beams. In the Standard Model these are of the form $(Q_{eL}^Z - Q_{eR}^Z) \times A(Q_e^\gamma, Q_f^\gamma, Q_{eL,R}^Z, Q_{fL,R}^Z)$ in case of A_{LR} and $\beta_f(Q_{fL}^Z - Q_{fR}^Z) \times A'(Q_e^\gamma, Q_f^\gamma, Q_{fL,R}^Z, Q_{eL,R}^Z)$, with $\beta_f = \sqrt{(\gamma_f^2 - 1)/\gamma_f^2}$, in case of A_{LRFB} . In addition $(A_{FB})_0$ is of the form $\beta_f(Q_{fL}^Z - Q_{fR}^Z)(Q_{eL}^Z - Q_{eR}^Z) \hat{A}(Q_e^\gamma, Q_f^\gamma, Q_{fL,R}^Z, Q_{eL,R}^Z)$. All asymmetries thus vanish close to the production threshold of the fermions yielding reduced sensitivity to the weak part of the interaction.

On the Z pole, these expressions simplify considerably. A_{LR} depends only on the couplings of the electrons while A_{LRFB} depends only of the final state fermion couplings to the Z . More precisely,

$$(A_{FB})_0 = \frac{3}{4} \mathcal{A}_e \mathcal{A}_f, \quad A_{LR} = \mathcal{A}_e, \quad A_{LRFB} = \frac{3}{4} \mathcal{A}_f \quad (9.11)$$

with the fermion asymmetries $\mathcal{A}_{e,f}$ given as

$$\mathcal{A}_{e,f} = \frac{\left(Q_{(e,f)L}^Z\right)^2 - \left(Q_{(e,f)R}^Z\right)^2}{\left(Q_{(e,f)L}^Z\right)^2 + \left(Q_{(e,f)R}^Z\right)^2} \approx 8(1/4 - |Q_f| \sin^2 \theta_{\text{eff}}^{(e,f)}). \quad (9.12)$$

Here, $\theta_{\text{eff}}^{(e,f)}$ is the effective weak mixing angle. This is close to the underlying parameter θ_W but differs by radiative corrections that are in general different for each fermion species. Usually, all leptons are assigned a single value θ_{eff}^ℓ . Inspecting (9.11) and (9.8) through (9.9) and remembering that $\mathcal{A}_e \approx 0.15$ in the Standard Model, we see that stronger beam polarization compensates smaller luminosity. That is why SLD delivered as precise or even more precise results on asymmetries than LEP 1 despite having about 30 times fewer produced Z s.

The fractional production for each fermion flavor is given by

$$R_q, 1/R_\ell \propto \left(Q_{fL}^Z\right)^2 + \left(Q_{fR}^Z\right)^2 \quad (9.13)$$

On the Z pole, the clean separation between initial and final state couplings allows for the determination of the initial and final state couplings without the assumption of flavor universality.

The argumentation above relies heavily on the availability of initial state beam polarization. In principle the electroweak couplings can also be extracted by analysing the final state polarization. This is readily possible for τ leptons (and t quarks at higher energies), for which the polarization can be derived from the decay particles. At the ILC, the analysis of the final state polarization could be useful as an independent cross-check.

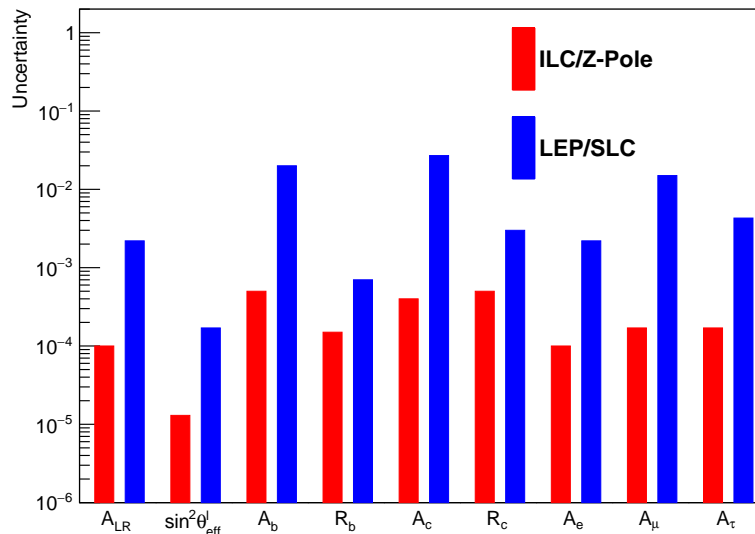


Figure 9.3: Summary of the precision achievable for ILC Z-Pole running compared with LEP/SLC results [427] for observables and derived quantities that are described in the text.

9.3.2 Di-fermion production at the Z pole

We now concentrate on the results expected from the program of dedicated running at the Z pole. Figure 9.3 shows the precision that can be expected for key quantities from ILC running at the Z -pole.

An important benchmark quantity is the measurement of A_{LR} that can be used to determine $\sin^2 \theta_{\text{eff}}^l$, as in (9.12). The precisions are related through $\Delta \sin^2 \theta_{\text{eff}}^l \approx \Delta A_{LR}/8$. Projected uncertainties on A_{LR} are shown in Table 9.2 for two scenarios of assigned integrated luminosity and for two scenarios of available beam polarizations.

The A_{LR} uncertainty is dominated by how well one can determine the effective beam polarization using the cross-sections measured from each of the four helicity configurations available with polarized electron and positron beams. The basic method, described in [443], relies on the availability of positron polarization, and benefits from higher positron polarizations. Systematic uncertainties are expected to be controlled sufficiently for the data-sets envisaged at ILC. In the most conservative scenario (100 fb^{-1} and standard beam polarizations), the combined statistical and systematic uncertainty on A_{LR} is 3.2×10^{-5} corresponding approximately to an uncertainty of 4.0×10^{-6} on $\sin^2 \theta_{\text{eff}}^l$. The former precision is about a factor of 50 better than SLD and the latter is about a factor of 30 better than that from LEP1/SLD and a factor six better than the current best Standard Model prediction for $\sin^2 \theta_{\text{eff}}^l$. [439].

Figure 9.3 illustrates also that the expected precision on the asymmetries are similar for the three leptons in contrast to LEP/SLD where they differed by up to a factor of seven. The results for \mathcal{A}_μ

L (fb ⁻¹)	N_Z^{had}	$ P(e^-) $ (%)	$ P(e^+) $ (%)	ΔA_{LR} (stat.)	ΔA_{LR} (syst.)
100	3.3×10^9	80	30	2.3×10^{-5}	1.9×10^{-5}
100	4.2×10^9	80	60	2.0×10^{-5}	1.7×10^{-5}
250	8.4×10^9	80	30	1.4×10^{-5}	1.3×10^{-5}
250	1.1×10^{10}	80	60	1.3×10^{-5}	1.3×10^{-5}

Table 9.2: Estimated uncertainties on A_{LR} for four different scenarios of Z-pole running with data-taking fractions at $\sqrt{s} = 91.2$ GeV in each of the four helicity configurations $(-+)$, $(+-)$, $(--)$, $(++)$ chosen to minimize the statistical uncertainty on the asymmetry. The quoted statistical uncertainty includes Bhabha statistics for relative luminosity. The systematic uncertainty includes 5 ppm uncertainty on the absolute center-of-mass energy and a 1% understanding of beamstrahlung effects.

and, especially, \mathcal{A}_τ are supported by full simulation studies at higher energies [436, 437]. The study in Ref. [436] shows that the τ polarization can be measured with a statistical precision of 0.5%–1% even at 500 GeV. At this energy the τ decay products are extremely collimated. The reconstruction will therefore be easier at smaller centre-of-mass energies. This uncertainty translates into precision on the couplings at the Z pole given in Table 9.1. Figure 9.3 and Table 9.1 also include results on the heavy quarks c, b that will be discussed next.

In recent years the community has carried out detailed studies of the processes $e^+e^- \rightarrow b\bar{b}$ and $e^+e^- \rightarrow c\bar{c}$ at $\sqrt{s} = 250$ GeV. The expected polar angle distribution for $e^+e^- \rightarrow b\bar{b}$ with the two ILC polarization settings is shown in Fig. 9.4 [444]. It illustrates very clearly that the two combinations of beam polarization yield different sensitivities for the underlying electroweak couplings.

The result makes use of the correct determination of the charge of the final state quark and is therefore an important benchmark for detector optimisation in terms of measuring secondary vertices and particle ID. A careful analysis of systematic uncertainties has been carried out that includes the uncertainties on the hadronic 2-jet cross section from the normalisation in R_q , the beam polarization, and the influence of initial state radiation. The last of these requires the detection of the ISR photon among the two jet final state, which calls for the availability of highly granular calorimeters that allow for efficient particle separation. Overall, the statistical and systematic uncertainties on the observables A_{FB} and R_q are of the order of 1–3 parts per mil and is dominated by uncertainties on selection efficiencies due to ISR. On the Z pole, these uncertainties can be neglected. The impact of the polarization uncertainty on the forward-backward (or final-state) asymmetries is negligible, as can be seen for the example of A_μ in Fig. 5.4 by comparing the full bars (free polarization parameters) to the open crosses (fixed polarizations).

9.4 *W and Z boson masses*

Improved measurement of the masses and widths of the W and Z bosons are primary goals for precision tests of the SM in the electroweak sector. The ILC program with polarized beams and all standard stages of the machine is well suited to measurements in the W sector, and especially

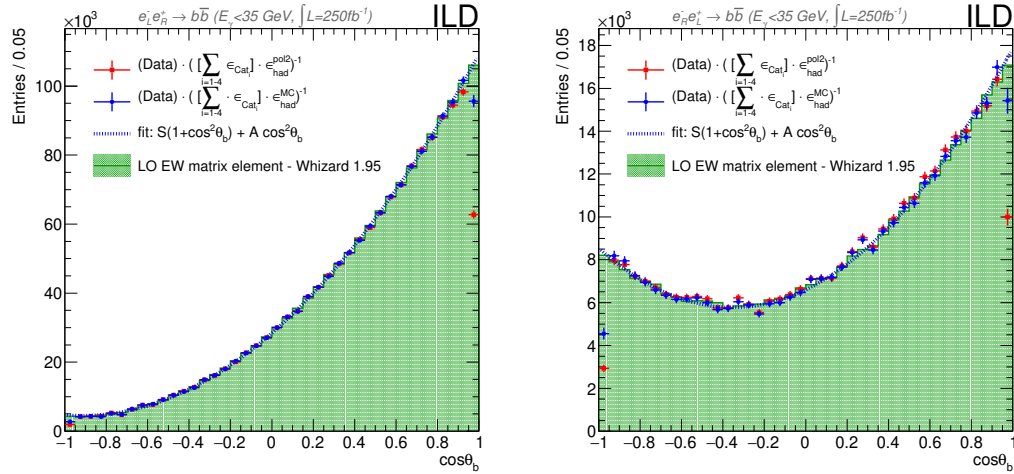


Figure 9.4: Distributions of $\cos\theta_b$ obtained for $e_L^- e_R^+$ (left) and $e_R^- e_L^+$ (right). The generator distribution is the green histogram and the red and blue dots show the reconstructed distributions after correction charge for charge migration and two different methods for the correction for efficiency and acceptance.

at $\sqrt{s} = 250$ GeV where data can be collected synergistically with Higgs boson related studies. Ultimate precision on Z observables benefits from dedicated running at the Z .

9.4.1 Measurement of m_W

The W mass is a prime target for the ILC. Improvements of the measurement are understood to be very tractable based on extrapolations of measurements from LEP2 both well above the W -pair threshold, and at the W -pair threshold. Prior prospects for such measurements are summarized in Tables 1-9 and 1-10 in [445] and discussed in [428].

Measurements of m_W from LEP2, the Tevatron, ATLAS, and LHCb have led to today's PDG precision of 12 MeV, with the best single experiment measurements being those from D0, with a precision of 23 MeV [446], and from ATLAS, with a precision of 19 MeV [447]. Recently, a new measurement from CDF has given a value with a precision of 9 MeV [448]. However, it is in significant tension with the earlier results. All of these measurements are dominated by systematic uncertainties. Further improvements from long-existing hadron collider data sets at the Tevatron and LHC are possible; it was suggested in [445] that the LHC could eventually improve the uncertainty on the W mass to 5 MeV. But, given the predominant systematic uncertainties, and limited progress over many years, this aspirational goal remains very challenging.

It is then interesting to study the challenges to a high-precision measurement of m_W at lepton colliders. Data sets at LEP2 totalled 0.7 fb^{-1} per experiment, leading to statistically limited measurements. The ILC is expected to produce much larger data sets of 2 ab^{-1} at $\sqrt{s} = 250$ GeV

and 4 ab^{-1} at $\sqrt{s} = 500 \text{ GeV}$ both with polarized beams. These samples should lead to over 140 M produced W bosons.

There are a number of promising approaches to measure the W mass at an e^+e^- collider such as ILC. The statistical power of the anticipated data sets is illustrated in Table 9.3. Shown are the statistical uncertainties on m_W and Γ_W from fitting the measured W boson invariant mass distribution based on 100M reconstructed W bosons for a range of assumed experimental mass resolutions. We see that, for a typical mass resolution of 2.5 GeV, the statistical uncertainty on m_W would be 0.35 MeV from such a sample. Additionally, by fitting the mass, width, and Gaussian experimental mass resolution, the total width could similarly be determined from the lineshape with a statistical uncertainty of 1.0 MeV. With non-negligible systematic uncertainties associated with measurement of the center-of-mass energy scale, the luminosity spectrum, the lepton and jet energy scales, overlay, hadronization, the integrated luminosity, radiative corrections, and backgrounds, it will be challenging at any e^+e^- collider to reach the 1 MeV overall uncertainty scale on m_W .

σ_M (GeV)	Δm_W (MeV)	$\Delta \Gamma_W^a$ (MeV)	$\Delta \Gamma_W^b$ (MeV)
1.0	0.21	0.41	0.63
2.5	0.35	0.63	1.0
4.0	0.50	0.89	1.6

Table 9.3: Statistical uncertainties for m_W and Γ_W for 100M W bosons. These are estimated from a simple parametric fit of the Breit-Wigner lineshape convolved with a range of constant Gaussian experimental mass resolutions, σ_M , ranging from 1 to 4 GeV. The m_W uncertainty is evaluated with a one parameter fit with the mass resolution and width fixed. The corresponding uncertainties on the W width are evaluated either with the mass resolution fixed and known perfectly from a two parameter fit (Γ_W^a), or more realistically, from a three parameter fit (Γ_W^b) that also fits for the mass resolution.

Given this expectation that measurements will be systematics limited, it is appropriate to also consider W mass measurement methods that have promising systematic behavior in this high statistics regime. The various methods for m_W measurement are as follows:

1. **Constrained reconstruction.** Kinematically-constrained reconstruction of W^+W^- using constraints from *four-momentum conservation* and optionally mass-equality, as was done at LEP2.
2. **Hadronic mass.** Direct measurement of the *hadronic mass*. This can be applied particularly to single- W events decaying hadronically or to the hadronic system in semi-leptonic W^+W^- events. This method does not rely directly on knowledge of the beam energy or its distribution. A full simulation study [449] indicates a statistical sensitivity of 2.4 MeV on m_W using the hadronic mass in semi-leptonic W^+W^- events at $\sqrt{s}=500 \text{ GeV}$ using the favorably polarized data-set.
3. **Lepton endpoints.** The two-body decay of each W leads to endpoints in the lepton energy

spectrum at

$$E_\ell = E_b(1 \pm \beta)/2, \quad (9.14)$$

where β is the W velocity. These can be used to infer m_W . The endpoints correspond to leptons parallel and anti-parallel to the W flight direction. This technique can be used for both semi-leptonic and fully-leptonic WW events with at least one prompt electron or muon.

4. **Di-lepton pseudo-mass.** In WW to dilepton events, with electrons or muons, one has six unknown quantities, namely, the three-momenta of each neutrino. Assuming four-momentum conservation and equality of the two W masses, one has five constraints. By assuming that both neutrinos are in the same plane as the charged leptons, the kinematics can be solved to yield two “pseudo-mass” solutions that are sensitive to the true W mass. This technique was discussed in Appendix B of [450] and used along with the lepton endpoints by the OPAL experiment at LEP2 [451].
5. **Polarized Threshold Scan.** Measurement of the W^+W^- cross-section near threshold with longitudinally polarized beams is discussed in [452] and references therein. The ability to “turn-on” and “turn-off” the signal with polarized beams, a capability unique to ILC, allows a precise in-situ measurement of the background.

Methods 1, 2, 3, 4 can all exploit the standard ILC program at 250 GeV and above. Method 5 needs dedicated running near $\sqrt{s} = 161$ GeV. Methods for measuring the W mass at e^+e^- colliders were explored extensively in the LEP2 era; see [453, 454] and references therein.

For ILC-sized data sets, the constrained reconstruction approach (method 1) will likely be restricted to semi-leptonic events so as to avoid the final-state interaction issues that beset the fully hadronic channel. With the large data-sets of WW events expected above threshold, the expectation is that this measurement will be systematics limited. With much improved detectors compared to LEP2 and with much better lepton and jet energy resolution, it is expected that uncertainties at the few MeV level can be targeted. Table 1-9 in [445] estimates an uncertainty of 2.8 MeV at $\sqrt{s} = 250$ GeV based on extrapolating LEP2 methods using only the semi-leptonic channels with electrons or muons.

Method 2 is based purely on the hadronic mass and was not used explicitly at LEP2. With the increased cross-section for singly-resonant events ($e^+e^- \rightarrow W e \nu$) at higher \sqrt{s} , the excellent resolution for particles in jets expected from particle-flow detectors, and the availability of control channels with hadronic decays of the Z , an opportunity exists to make a competitive measurement also using this method. However the demands on the effective jet energy scale calibration are very challenging. It was estimated (Table 1-10 in [445]) that a m_W uncertainty of 3.7 MeV could be reached. This is likely to be dominated by the hadronic energy scale systematic uncertainty.

The endpoints method 3 was only used for fully leptonic events at LEP2. It has the inherent advantage that the systematic uncertainties are dominated simply by the uncertainties on the lepton energy scale and the beam energy, given that one can express m_W in terms of the endpoints as follows:

$$m_W^2 = 4E_l(E_b - E_l). \quad (9.15)$$

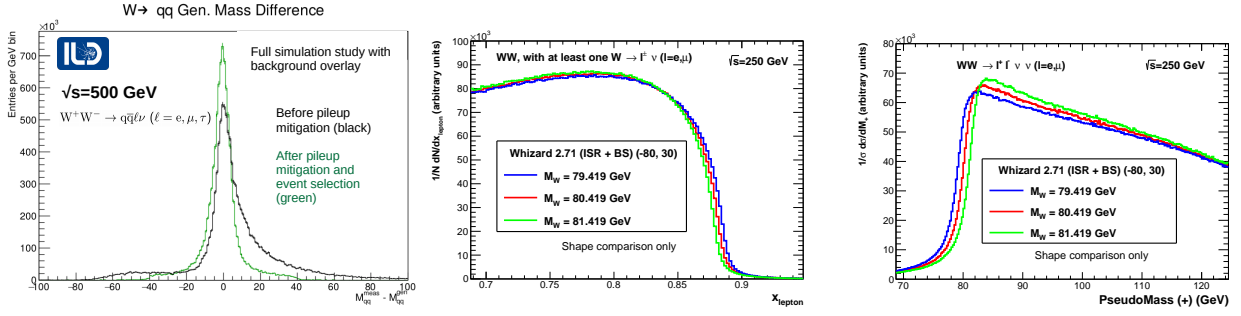


Figure 9.5: Illustrations of sensitivity to m_W . Hadronic mass resolution (left) in semi-leptonic events from full simulation study at $\sqrt{s} = 500$ GeV [449]. Endpoints and pseudomass methods at $\sqrt{s} = 250$ GeV (right).

This can also be used as a simple complementary method for semi-leptonic events, but of course it will be strongly correlated with the constrained reconstruction method.

The pseudo-mass method and the endpoints method were applied to the fully leptonic channel in [451]. Little correlation (+11%) was found between the two methods, indicating that the two methods can be independently effective and can be combined. An updated study including beamstrahlung effects based on [455] using these leptonic observables with just the 2 ab^{-1} of $\sqrt{s} = 250$ GeV data projects a statistical uncertainty on m_W of 4.4 MeV (including the semi-leptonic channel endpoints). Experimental systematic uncertainties are expected to be under good control.

Method 5 needs dedicated running near $\sqrt{s} = 161$ GeV. This is now feasible for the ILC machine. The expected integrated luminosity is about $125 \text{ fb}^{-1}/\text{year}$ if the run is done after the bunch doubling luminosity upgrade. The use of a threshold scan with polarized electron and positron beams to yield a precision measurement of m_W at ILC was studied in [452]. One of the potentially dominant systematic uncertainties, the background determination, is under very good experimental control because of the polarized beams. This is difficult to achieve with an unpolarized collider. Errors at the few MeV level can be envisaged. With 100 fb^{-1} , and polarization values of (90%, 60%), the estimated uncertainty is

$$\Delta m_W(\text{MeV}) = 2.4 (\text{stat}) \oplus 3.1 (\text{syst}) \oplus 0.8 (\sqrt{s}) \oplus \text{theory} , \quad (9.16)$$

with these values added in quadrature, amounting to an experimental uncertainty of 3.9 MeV. With standard ILC polarization values of 80% and 30% the estimated precision is 6.1 MeV. Eventual experimental precision approaching 2 MeV from this approach can be considered at ILC if one is able to dedicate 500 fb^{-1} to such a measurement, and the physics perspective of the day demands it. There are excellent prospects for very competitive ILC measurements of the W mass from the four other methods using data collected above the production threshold for Higgs bosons, and so it would seem premature to make exclusive running at W -pair threshold a requirement for the ILC run plan. Nevertheless, given the complementary nature of a threshold-based measurement it is prudent to retain accelerator compatibility with such a scenario.

Given that the leading experimental systematic uncertainties for the different methods are reasonably complementary, it is expected that, with the combination of these five different methods, ILC will be able to measure m_W to at least 2.5 MeV. This uncertainty can potentially already be reached with data-taking at $\sqrt{s} = 250$ GeV.

9.4.2 Measurement of m_Z and Γ_Z

Measurements sensitive to m_Z and Γ_Z are feasible with modest improvements over LEP at center-of-mass energies such as $\sqrt{s} = 250$ GeV using the reconstructed di-lepton invariant mass in radiative return events. A study using $e^+e^- \rightarrow \mu^+\mu^-$ at $\sqrt{s} = 250$ GeV indicates a statistical sensitivity to m_Z of 1.0 MeV and 2.2 MeV on Γ_Z [456]. Including similar sensitivity in the e^+e^- decay channel, leads to corresponding estimated uncertainties of 0.7 MeV and 1.5 MeV respectively from the two lepton channels combined.

Ultimate precision on both quantities would benefit from dedicated running at the Z pole. Significant improvement on m_Z requires excellent control of the absolute scale of the collision center-of-mass energy. There are prospects for statistical control of the center-of-mass energy scale at the 1 ppm level or below based on measuring dimuon events, and relying on exquisite knowledge of the tracker momentum scale. Presuming that one can reach a 2 ppm target uncertainty, a polarized lineshape scan with 100 fb^{-1} would allow measurement of m_Z to 0.2 MeV with the uncertainty dominated by this scale uncertainty. The measurement of Γ_Z depends on point-to-point systematic uncertainties on the center-of-mass energy scale; it is expected that these should be under good control leading to a Γ_Z uncertainty of 0.12 MeV driven mostly by statistics. Related studies are discussed in more detail in [457].

9.5 W boson branching fractions

With the large data sets envisaged at ILC, one can also target much improved measurements of the WW production cross section and the individual W decay branching fractions. This would use the ten different final state cross sections available from WW production: the six WW final states associated with fully leptonic final states with two charged leptons (dielectrons, dimuons, ditaus, electron-muon, electron-tau and muon-tau), the three semileptonic WW final states, one for each lepton flavor, and the fully hadronic WW final state. This follows the methodology used at LEP2 [458, 459, 460, 461].

The ten measured event yields can be fitted for an overall WW cross section, σ_{WW} , at each center-of-mass energy, and the three individual leptonic branching fractions, B_e , B_μ , and B_τ with the overall constraint that

$$B_{\text{had}} = 1 - B_e - B_\mu - B_\tau, \quad (9.17)$$

taking into account background contributions in each channel. With ten channels and four fit parameters, there is some redundancy in the fitting procedure. This means that the parameters can be determined well even if the more challenging channels, namely the fully hadronic, the semileptonic with a tau, and the di-tau channel would end up being systematically limited. At LEP2,

the signal process was modelled simply through the three dominant, doubly resonant Feynman diagrams (so called CC03 process), while other diagrams and their interferences resulting in the same four fermion final state, such as those for ZZ or $W\epsilon\nu$, were treated as background. These “4f-CC03” corrections were typically about 10% depending on final state. A complete calculation of $e^+e^- \rightarrow 4f$ final states would need to be used in the high statistics regime.

We have looked into the feasibility of this method for ILC250, building on LEP2 studies at $\sqrt{s} \approx 200$ GeV, by putting together a fit ansatz that assumes identical efficiencies and mis-classification probabilities for all ten WW channels [451]. For the purpose of making an estimate for this report, we concentrate on the impact of a single subsample of the data. The actual analysis at the ILC will be based on a global fit to the results from all polarization modes at all center-of-mass energies.

Of the total 2 ab^{-1} to be collected at ILC250, 0.9 ab^{-1} is to be collected with $e_L^- e_R^+$ enhanced collisions. These benefit from a WW cross section enhancement over unpolarized beams of a factor of 2.32 for -80% , $+30\%$ beam polarizations. The estimated background per selection channel depends on the polarization asymmetry of the different backgrounds and is estimated to be about $+29\%$ for the important two-fermion background from hadronic events. Taking this effect that leads to an increased background, and the decreased background estimated from $1/s$ scaling, we find that the unchanged OPAL background estimate is a good first estimate, and believe that this is a reasonably conservative estimate. We have based our estimates of statistical uncertainties on the size of this subsample. We assume that the other 55% of the data set with the less favorable beam polarization configurations is used to measure and test the background modeling and have neglected it for now in estimating statistical sensitivity.

We also include the 6% reduction in unpolarized cross section at $\sqrt{s} = 250$ GeV. Given that ILC detectors will have much improved forward hermeticity, jet and lepton energy resolutions, vertexing, and electron, muon, and tau identification, it is very reasonable to expect that the efficiency and background performance would be much better. One effect that is more difficult at higher \sqrt{s} is a more forward polar angle distribution of the W decay products. We find that 94.7% of leptons in semi-leptonic events have a polar angle satisfying, $|\cos\theta| < 0.975$, whereas at $\sqrt{s} = 200$ GeV, the corresponding fraction is 96.7%.

It is straightforward to estimate statistical uncertainties and we have done so for a number of scenarios. For systematic uncertainties, there are five that come to mind:

- absolute integrated luminosity: The precision is likely limited to about 0.1%; however, to a great extent, this value cancels out of the determination of branching ratios.
- lepton efficiencies: This can be measured with high precision using control samples of dileptons as was done for precise Z lineshape measurements preferably using a tag-and-probe method. The key element is efficiency within the geometrical acceptance. With control samples totalling 10^7 leptons, statistical uncertainties of 3×10^{-5} can be targeted assuming highly efficient lepton identification.
- hadronic system modeling: Uncertainties of order 0.03% seem feasible based on LEP1 hadronic Z studies targeted at estimating the hadronic efficiency/acceptance.

Event selections	B_e	B_μ	B_τ	R_μ	R_τ	R_{had}
All 10	4.2	4.2	5.1	6.1	7.5	3.0
9 (not fully-hadronic)	5.9	5.9	6.4	6.1	7.5	6.7
9 (not tau-semileptonic)	4.6	4.6	7.9	6.1	10.8	3.2
8 (not f-h and not τ -semileptonic)	8.3	8.3	7.9	6.1	12.8	7.6
7 (not f-h and not τ -sl and not di- τ)	9.1	9.1	10.6	6.1	16.7	7.6

Table 9.4: Statistical uncertainties, expressed as relative uncertainties in units of 10^{-4} for the leptonic branching fractions of the W boson (B_e , B_μ and B_τ) and the ratios of branching fractions $R_\mu = B_\mu/B_e$, $R_\tau = B_\tau/B_e$, and $R_{\text{had}} = B_{\text{had}}/(B_e+B_\mu+B_\tau)$. The lines of the table refer to different choices of the included event selections. The values assume ILC measurements at $\sqrt{s} = 250$ GeV using the 45% of the 2 ab^{-1} integrated luminosity with enhanced $e_L^- e_R^+$ collisions, with the same efficiencies and the same background cross sections as in the OPAL measurement [461]. The uncertainties given for R_μ , R_τ are from a separate fit using the (B_e , R_μ and R_τ) parametrization. Similarly the uncertainty for R_{had} is from a fit using a (B_e , B_μ and R_{had}) parametrization.

- fake τ candidates from hadronic events: One needs to be able to model the rate of isolated tracks from hadronic systems that can fake tau candidates. This should be easier to reduce than at LEP2 given the excellent vertexing performance envisaged.
- background estimation: This will be controlled with the less signal-favorable beam polarization configurations.

In Table 9.4 we show expected absolute statistical uncertainties for three different parameterizations, one based on the three leptonic branching fractions, (B_e , B_μ and B_τ), one based on B_e and the ratios B_μ/B_e and B_τ/B_e and one based on B_e , B_μ , $R_{\text{had}} = B_{\text{had}}/(B_e + B_\mu + B_\tau)$ that is appropriate for sensitivity to α_S . Five different configurations of included event selections are considered, indicating a reasonable degree of robustness. The fits also fit for the cross section but the absolute value is likely to be systematics limited. It can be seen that fractional statistical uncertainties on B_e below 0.1% and as low as 0.03% can be envisaged. The fits do not assume lepton universality. The data set considered consists of 29.7 million WW candidates. The efficiency systematics seem not to be limiting. The main systematic issue is likely to be the background estimation that should be facilitated with the various polarized data sets. The event selection purity will likely need to be tightened to reduce systematics from backgrounds, but the current statistical estimates should be a reasonable starting point. Furthermore the data-sets at $\sqrt{s} = 500$ GeV would double the useful statistics for such measurements.

Chapter 10

ILC Physics Measurements at 350, 500, and 1000 GeV

At the higher-energy stages of the ILC at 350 GeV, 500 GeV, and 1 TeV, new processes appear in e^+e^- annihilation, giving new opportunities for consequential discoveries. At 350 GeV and above, the ILC can study the top quark in pair-production, bringing the precision capabilities of e^+e^- colliders to bear on this heaviest SM particle. In Higgs physics, the new reaction of Higgs boson production by WW fusion opens up, providing a second large data set to explore the Higgs boson properties. Also, the processes of Higgs pair production, sensitive to the Higgs boson self-coupling, and the Higgs boson associate production with top quarks, become accessible. In this chapter, we will review the prospects for the study of these reactions. We will also revisit the study of triple gauge couplings (TGCs) and discuss in some detail the study of e^+e^- annihilation to quark and lepton pairs. Finally, we will review the prospects for the ILC to discover new particles hidden from searches at the LHC.

10.1 Top quark

Pair production of the top quark can be studied at the ILC in two distinct regimes, first, at the threshold, and, second, at energies where the top quarks have relativistic velocities. These programs complement one another in addressing the principal open issues for the top quark—determining its mass with ultimate precision, exploring its connection to the electroweak interactions, and exploring its role in models of flavor. A fourth crucial issue, the measurement of the top quark coupling to the Higgs sector will be discussed in Sec. [10.2.3](#).

10.1.1 Top quark mass

The top quark mass is one of the fundamental parameters of the Standard Model that must be determined experimentally. Direct measurements at hadron colliders based on Monte Carlo tem-

plate fits to the reconstructed top quark decay products reach a precision down to 600 MeV at the LHC [462, 463] and the Tevatron [464]. Combinations can further improve [465, 463]. Extractions of the top quark pole mass from measured cross sections using first-principle, fixed-order calculations have reached GeV precision [466].

Top quark mass measurements at the HL-LHC are expected to reach an experimental precision of a few hundred MeV [377], while work is ongoing to improve Monte Carlo generators [467, 468] and to provide a robust interpretation of the Monte Carlo mass parameter in a field-theoretical mass scheme [469, 470, 471]. A complete and recent review can be found in Ref. [472]. However, this review also discusses the limitations of interpreting on-shell top quark mass values in terms of more the fundamental short-distance top quark mass parameter. These come both from QCD uncertainties in the relation [473] and from possible non-perturbative contributions.

An electron-positron collider with sufficient energy to produce top quark pairs has excellent potential to measure the top quark mass with even better precision and to make a tighter connection to the underlying short-distance value. It was realized even before the discovery of the top quark that a scan of the center-of-mass energy of the collider through the top quark pair production threshold yields a very precise top quark mass measurement [474, 475, 476, 477], with a rigorous interpretation. Since then, the theory predictions for the threshold scan have reached NNNLO precision [478] and an NNLL resummation [479] has been performed. The threshold mass that is most naturally extracted from a comparison to the theory can be converted to the \overline{MS} scheme (or any other scheme) at four-loop accuracy [473], with an intrinsic uncertainty due to missing higher orders of $\mathcal{O}(10 \text{ MeV})$ and a parametric uncertainty of $\mathcal{O}(50 \text{ MeV})$ with the current α_s world average [465].

Phenomenological studies of the threshold scan in realistic conditions have been performed by several groups [480, 481, 482, 483]. Fits are performed on pseudo-experiments with an integrated luminosity of 100–200 fb^{-1} divided over up to 10 center-of-mass energies. Apart from the top quark mass, the threshold scan is sensitive to the strong coupling, the top quark Yukawa coupling and the top quark width. Typically, several parameters are floated simultaneously in the fits.¹ Importantly, recent studies take into account the theory uncertainty [484, 485], that is expected to be the dominant source of uncertainty for a top quark mass measurement in a threshold scan at an e^+e^- collider. The statistical uncertainty can be reduced to approximately 20 MeV, depending on the number of free parameters and the number and range of the energy points [486, 487]. The systematic uncertainty from missing higher orders in the prediction and the parametric uncertainty due to the strong coupling constant add up to approximately 50 MeV, with the current state-of-the-art calculations and world average for α_s . A simulated scan of the top quark threshold, from [480], is shown in Fig. 10.1.

While the threshold is generally considered to be the “golden” top quark mass determination, alternative methods have been studied by several groups. A direct mass measurement can be performed at any center-of-mass energy above the top quark pair production threshold. The comparison of this measurement to the threshold value will provide important information on the

¹These studies are valid within the SM, releasing only the relation between the width and the mass. The interplay between the top-quark mass extraction and electroweak coupling uncertainties (parameterized in an effective field theory) has not been studied yet.

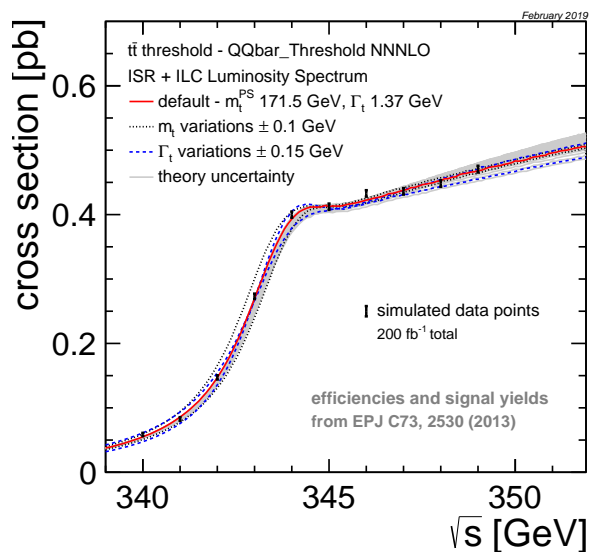


Figure 10.1: A simulated top quark threshold scan with a total integrated luminosity of 200 fb^{-1} . The bands around the central cross section curve show the dependence of the cross section on the top quark mass and width, illustrating the sensitivity of the scan. The error bars show the statistical uncertainties, taking into account signal efficiencies and backgrounds. From [480].

interpretation of the MC mass parameter. The CLIC-DP collaboration has estimated that a statistical uncertainty of 30 MeV (40 MeV) is expected in the $l+\text{jets}$ (all-hadronic) channel after collecting 500 fb^{-1} at $\sqrt{s} = 380 \text{ GeV}$ [480].

A measurement of the differential cross section of radiative $e^+e^- \rightarrow t\bar{t}\gamma$ events, where the top quark pair is produced in association with a hard photon from Initial State Radiation (ISR) can yield a top quark mass determination [488]. The measurement of the photon energy gives an event-by-event determination of the effective center-of-mass energy and allows to map out the $t\bar{t}$ threshold with data collected at any center-of-mass energy below $\sim 1 \text{ TeV}$. The expected precision is approximately 110 MeV for CLIC380 (1 ab^{-1} at $\sqrt{s} = 380 \text{ GeV}$ and approximately 150 MeV for ILC500 (4 ab^{-1} at $\sqrt{s} = 500 \text{ GeV}$), including theoretical and experimental systematic uncertainties. This approach is competitive with the HL-LHC expectation, and the method maintains flexibility in, and control over, the field-theoretical mass scheme. Moreover, a combination with the mass obtained from the threshold scan moreover enables a study of the scale dependence (“running”) of the top quark mass, testing the evolution predicted by renormalization group evolution.

Operation of the ILC at the top mass threshold and beyond can thus provide a top quark mass measurement with a precision well beyond what is achievable at hadron colliders and also clarify the various top quark mass definitions in terms of a well-understood field-theoretical framework.

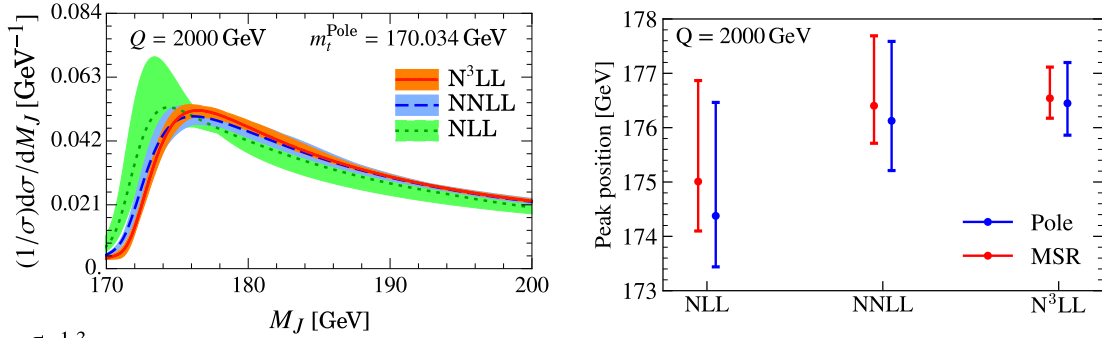


Figure 10.2: (a) The jet mass distribution on boosted top quark jets. (b) The peak position extracted using Pole mass or MSR mass schemes. [489]

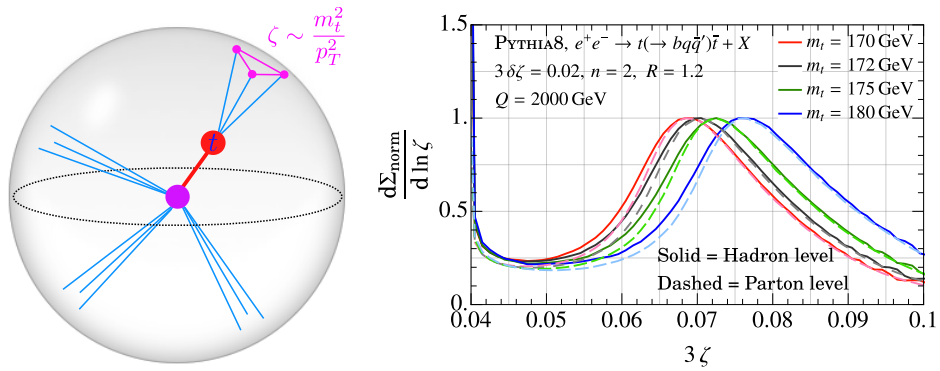


Figure 10.3: (a) The angular scale of the top quark as probed by a three point correlation function. (b) The angular distribution for different top masses. Hadronization has an extremely minor impact on the peak position, leading to a clean probe of the top quark mass with perturbative physics [396].

10.1.2 Boosted top quarks

Additional tools for the top quark mass measurement become available in the highest energy running of the ILC at 1 TeV. At these energies, we enter the “boosted top” regime in which the top quark decay products are boosted in to a single fat jet. This brings in interesting QCD issues and also gives two new, complementary methods for the top quark mass measurement. The first is a measurement using the two-jettiness observable, and the second is a measurement using the three-point energy correlator.

The most well established program to measure the top quark mass using event shapes in e^+e^- is to use the two-jettiness (thrust) observable [489]. In the limit of boosted top quarks, the two-jettiness observable effectively measures the sum of the masses of the two jets arising from the decay products of the boosted top quarks. It thus exhibits strong sensitivity to the value of the top quark mass. Since it is an inclusive event shape observable, one can derive a rigorous factorization theorem for the observed distribution using a combination of SCET and HQET, which factorizes the dynamics at different scales, allowing in particular for a rigorous field theoretic treatment of the top quark mass in a short distance scheme. This distribution has been computed at next-to-next-to-next-to leading logarithmic accuracy, and suggests that perturbative uncertainties at the order of 100 MeV can be achieved for the top quark mass. A plot of the distribution is shown in Fig. 10.2.

More recently, an alternative approach to measuring the top quark mass was put forward [396], particularly motivated by developing a clean understanding in the complex LHC environment. One of the issues with measurements based on the jet mass is that the mass is sensitive to soft contamination and non-perturbative effects. Instead of measuring the mass directly, one can flip the measurement of the mass into a measurement of the angular scale of the top decay products as measured by a three-point correlation function. Unlike the behavior in a conformal theory, these correlators will exhibit a sharp peaked structure at the angular scale $\zeta \sim m_t^2/Q^2$. The location of the peak therefore provides direct sensitivity to the top quark mass. However, unlike the jet mass, the location of the peak is unaffected by soft contamination and hadronization. This is seen in Fig. 10.3. Furthermore, this measurement is quite interesting from the point of view of precision QCD, since it probes the structure of multipoint energy correlations on top decays.

10.1.3 Top quark electroweak couplings

In many extensions of the Standard Model, the top quark plays a special role. Composite Higgs models, for instance, generally predict sizeable deviations for the top quark electro-weak couplings [490]. Precise measurements of these couplings can therefore constrain broad classes of composite Higgs scenarios [491, 492, 493].

Since the top quark could not be studied at the previous generation of electron-positron colliders, its interactions with the neutral gauge bosons of the Standard Model are relatively poorly constrained. Studies of top quark pair production at hadron colliders have characterized the strong interaction of the top quark in detail, and single top quark production and top quark decay are a sensitive probe of the charged-current interaction. The interactions with the photon and Z -boson

have only become accessible with the observation of rare associated production processes, such as $pp \rightarrow t\bar{t}X$ and $pp \rightarrow tXq$, with $X = \gamma, Z$. (The coupling of the top quark to the Higgs boson will be discussed in Sec. 10.2.3.) Recent comparisons of cross section measurements to SM predictions have reached a precision of 10-15%, with statistical, experimental and theoretical uncertainties contributing with roughly equal weight [494]. Top quark EW operators can also be constrained through loop-level effects of off-shell degrees-of-freedom in the top quark pair production rate [495], which could provide complementary bounds of competitive precision for some operator coefficients.

The potential of LHC run 3 and the HL-LHC stage to improve these measurements has been studied in Ref. [377] for $t\bar{t}V$ production and EW single top production. A complete set of estimates for the HL-LHC expectations can be found in Ref. [496], refining earlier results of [497]. These studies adopt the S2 scenario also used for the Higgs sector [498]. That is, they extrapolate LHC run 2 results by scaling the statistical and experimental systematic uncertainties with the inverse square root of the luminosity, while assuming that the uncertainties in the theoretical SM predictions and uncertainties due to Monte Carlo modelling are reduced by a factor 2 with respect to today's state of the art.

The ILC offers a unique opportunity to go beyond these studies in measuring the electro-weak couplings of the top quark [499, 500]. These measurements are among the prime targets of the ILC top physics programme. The pair-production process in e^+e^- collisions probes the $t\bar{t}Z$ and $t\bar{t}\gamma$ vertices directly. The contributions from the photon and Z -boson are disentangled by using the two polarization configurations. Figure 10.4 shows the comparison of the ILC expectations to current results from LHC and the prospects for HL-LHC; the comparison is expressed in terms of bounds on the coefficients of 2-fermion dimension-6 operators in the Effective Field Theory description of the top quark couplings. The measurements of top quark production rates at the ILC improve the measurement of the EW couplings and the corresponding bounds on the relevant EFT operator coefficients by two orders of magnitude with respect to the current LHC results, and by well over an order of magnitude with respect to HL-LHC expectations. Data above the top quark pair production threshold are clearly required to provide tight bounds on the operator coefficients that affect the top quark couplings.

Measurements at two center-of-mass energies above the $t\bar{t}$ threshold allow to disentangle contributions of the relevant two-fermion and four-fermion operators in the SMEFT [501]. The prospects for constraints on the $e^+e^-t\bar{t}$ four-fermion operators with the 1 TeV run envisaged at the ILC yield 68% CL bounds of order $C/\Lambda^2 \sim 10^{-3}TeV^{-2}$ [501] and form a powerful test for scenarios with composite (right-handed) top quarks [370] for compositeness scales well beyond the center-of-mass energy.

Dedicated CP-odd observables yield powerful constraints on CP violation in the top sector [502]. Other processes, such as single top quark production and vector-boson-fusion production at high energy provide complementary information [480].

There is a subtle interplay between the Higgs and top physics programmes, since the top quark couplings affect the loop diagrams for $gg \rightarrow H$ production at the LHC and $H \rightarrow \gamma\gamma$ and $H \rightarrow Z\gamma$ decays at the LHC and ILC [503]. Precision measurements of tree-level processes, such as $e^+e^- \rightarrow ZH$ production, gain a sensitivity to top EW couplings through loop corrections. Precise measurements of top quark couplings are required to fully constrain all of the degrees of freedom

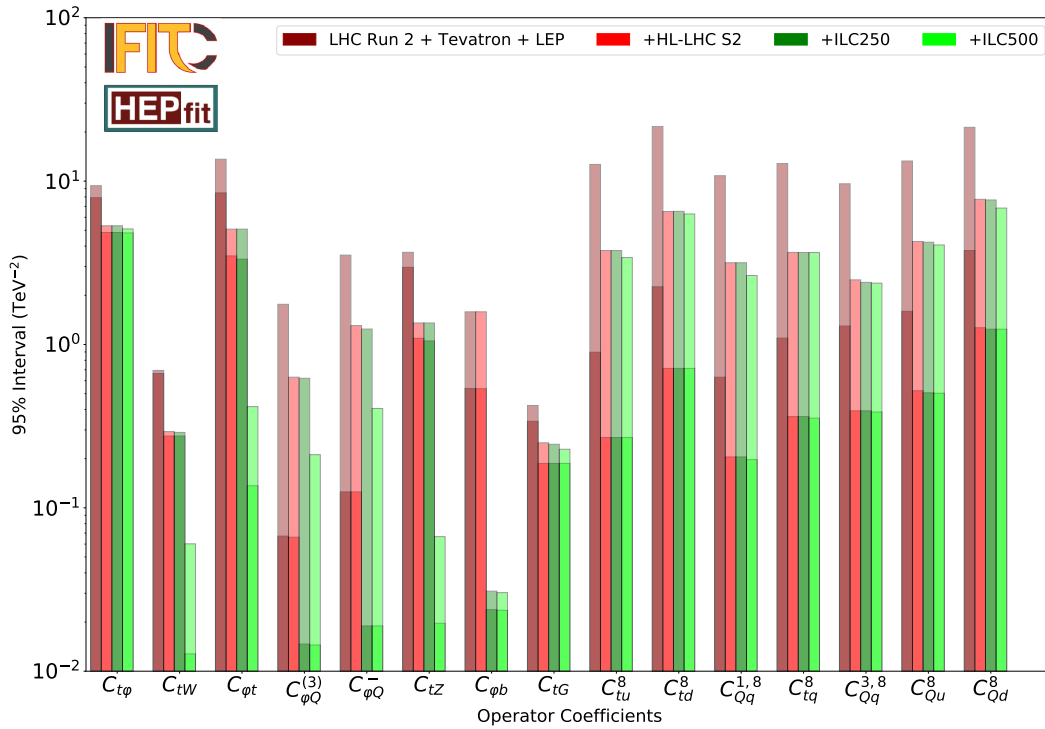


Figure 10.4: Comparison of current 95% CL bounds on the coefficients of the two-fermion SMEFT operators that affect the top and bottom quark EW couplings and the four-fermion operators $q\bar{q}t\bar{t}$. The LHC bounds correspond to the results of Ref. [494], the HL-LHC S2 projection follows Ref. [497] and the HL-LHC Higgs report [498], while the ILC prospects are based on Ref. [501]. Bars with dark shading show constraints on individual couplings considered separately, while bars with light shading show constraints from a global fit to the full set of operators.

of the Higgs EFT [504].

10.1.4 Searches for FCNC interactions of the top quark

Processes with flavour-changing neutral currents (FCNC) are forbidden at tree level in the SM and are strongly suppressed at higher orders by the Glashow-Iliopoulos-Maiani (GIM) mechanism. The branching fractions for top quark FCNC decays $t \rightarrow qX$, where $q = u, c$ and $X = \gamma, g, Z, H$, are of the order of 10^{-12} – 10^{-16} . Some extensions of the SM predict a strong enhancement of the FCNC top quark decay rates, increasing the branching fraction up to 10^{-4} .

The search for FCNC interactions of the top quark at the LHC has reached excellent sensitivity for the tqX vertex. The current 95% CL bounds based on searches for top decays and single top production with the partial run 2 data are equivalent to branching fractions of $10^{-3} - 10^{-5}$ and are expected to improve significantly with the HL-LHC data [377, 505, 506].

An e^+e^- collider has a very specific role in the search programme for FCNC couplings. The LEP bounds from searches for $e^+e^- \rightarrow t\bar{q}, \bar{t}q$ remain competitive for tqZ and $tq\gamma$ and in particular the $tqll$ operators [507]. The 250 GeV phase of a Higgs factory is expected to improve the LEP bounds by one to two orders of magnitude [508], yielding competitive results in comparison with the full HL-LHC prospects. The higher-energy stages of the ILC are particularly relevant for the bounds on four-fermion operators e^+e^-tq . The sensitivity to these operators increases very strongly with the higher-energy operation [509].

The current 95% CL bounds on the EFT operator coefficients are compared to the prospects of the HL-LHC (3 ab^{-1} at 14 TeV), and three energy stages of the ILC (2 ab^{-1} at 250 GeV, 4 ab^{-1} at 500 GeV and 8 ab^{-1} at 1 TeV) in Fig. 10.5. The current LHC bounds and HL-LHC projections from [] are indicated as dark red and purple arrows, respectively, where the upper arrow corresponds to up quarks and the lower one to charm quarks. The expected bounds for the several ILC energy stages, shown as solid bars, are extrapolated from the study of Ref. [510, 511]. More details of the procedure are given in Ref. [509]. The increase in sensitivity is particularly pronounced for the e^+e^-tq operators, that are found to scale roughly as $s^{-3/2}$.

10.2 Higgs

In this section, we discuss additional Higgs boson reactions that become accessible to the ILC at 500 GeV.

10.2.1 WW fusion

As well as providing additional Higgs-strahlung events, ILC collisions at 500 GeV will provide a large sample of Higgs bosons produced via the WW fusion process. While the resulting set of Higgs bosons cannot be identified using the unbiased recoil mass method applicable to Higgs-strahlung, they none the less provide an important sample to further probe the Higgs sector. The

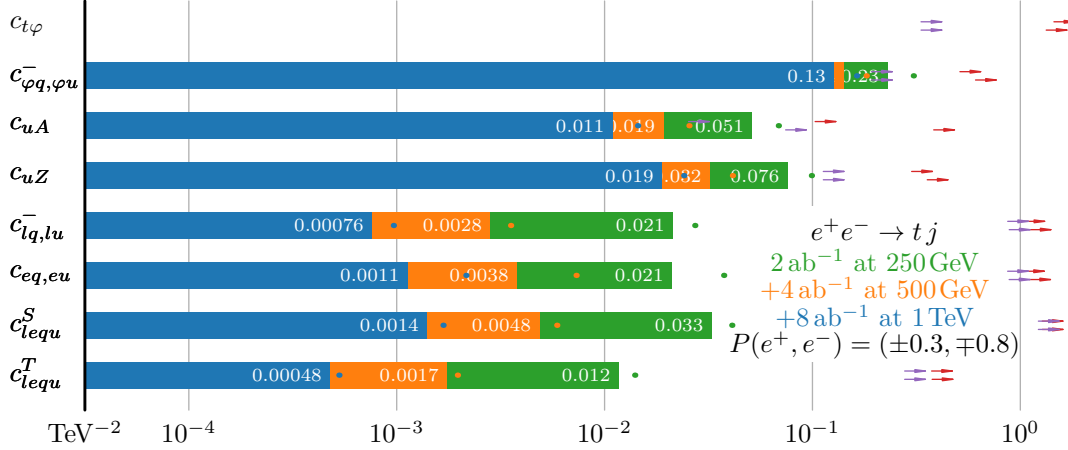


Figure 10.5: The projected 95% C.L. bounds on the EFT operator coefficients that give rise to the FCNC $e^+e^- \rightarrow tq$ production process. The bounds are given in units of TeV^{-2} for the LHC run 2 (dark red arrows), for the HL-LHC (purple arrows) and for the three nominal ILC stages: 250 GeV (green bars), 500 GeV (orange bars) and 1 TeV (blue bars). The round markers of the same color represent the expected bounds without beam polarization.

number of Higgs bosons produced at ILC-500 will be similar to the number at ILC-250, providing comparable statistical power as at ILC-250 for all the measurements at 250 GeV discussed in Sec. 8.1. The experimental techniques and background composition are different at the different energies, production methods and beam polarizations, providing a range of systematic checks by comparing measurements of related observables made under different conditions, before combining the measurements to achieve optimal sensitivity while also testing the internal consistency of the measurements when interpreted within the Standard Model.

The comparison of Higgs production in the Zh and WW -fusion processes, enabled respectively by the hZZ and hWW couplings, with the measured decay branching ratio to WW^* and ZZ^* will allow independent checks of the Higgs couplings to $V(= W/Z)$. The experimental sensitivity to anomalous HVV couplings, whose effects typically grow with energy, will be significantly enhanced at ILC-500.

The impact of ILC-500 data on the understanding of the Higgs sector is clearly demonstrated later in this report, for example in Fig. 12.1.

10.2.2 Higgs self-coupling

At center-of-mass energies of at least 500 GeV, the self-interaction of the Higgs boson, in particular the triple-Higgs coupling λ , can be probed directly by studying the production of Higgs boson pairs. There are two relevant di-Higgs production processes, double Higgs-strahlung, $e^+e^- \rightarrow ZHH$, and di-Higgs production in WW fusion, $e^+e^- \rightarrow \nu\bar{\nu}HH$. The cross sections for these reactions as a function of the center-of-mass energy are shown in Fig. 10.6. While the WW fusion becomes important at and above 1 TeV, the cross-section for double Higgs-strahlung reaches a maximum

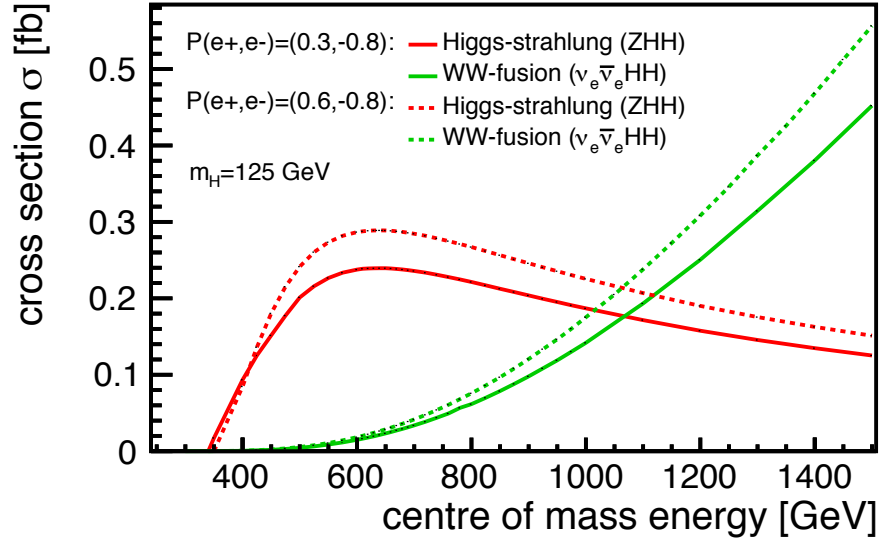


Figure 10.6: Cross-sections for double Higgs production in the SM via Higgs-strahlung and WW fusion as a function of the center-of-mass energy [512].

around 500 – 600 GeV. We will argue that it is important to provide running both near 500 GeV and at 1 TeV so that both of these reactions can be studied.

The prospects for measuring double Higgs production through these two reactions was studied at the time of the ILC TDR. The reactions were simulated using full, Geant4-based simulation of the ILD detector, using the state-of-the-art reconstruction tools at the time [5], both at $\sqrt{s} = 500$ GeV [512, 513] and 1 TeV [513]. These studies found that, if the self-coupling takes its SM value, then double Higgs-strahlung can be observed at $E_{CM} = 500$ GeV with a significance of 8σ , combining the $HH \rightarrow b\bar{b}b\bar{b}$ and $HH \rightarrow b\bar{b}WW^*$ channels. This would translate into a measurement precision on λ of 27%. The analysis assumed that all other couplings of the Higgs bosons take their SM values, but subsequently it was shown that the ILC single-Higgs measurements strongly control possible variations, enough to add only a negligible uncertainty [514]. We will discuss this point further in Sec. 12.5. When the ILC runs at $E_{CM} = 1$ TeV, it will be possible to add the measurement with the double Higgs production from WW fusion. This will improve the determination of (the SM value of) λ to a relative precision of 10%.

Over the past few years, there have been many improvements in the planned ILD detector that are relevant for these measurements. The b -tagging efficiency in ILD has been improved by 5% at the same level of purity [216]. This improvement and the inclusion of $HH \rightarrow \tau^+\tau^-b\bar{b}$ have been estimated to improve the ILC500 precision on λ from the 27% mentioned above to 21 – 22% [512]. Another limiting factor for the double Higgs-strahlung analysis is the invariant di-jet mass reconstruction, important for separating ZHH from ZZH and ZZZ backgrounds. New developments in correcting for missing energy from neutrinos in semi-leptonic heavy quark decays and kinematic fitting show striking improvements on the di-jet mass reconstruction [515]. Further improvements on the jet clustering and on the flavor tag are being expected from deep learning

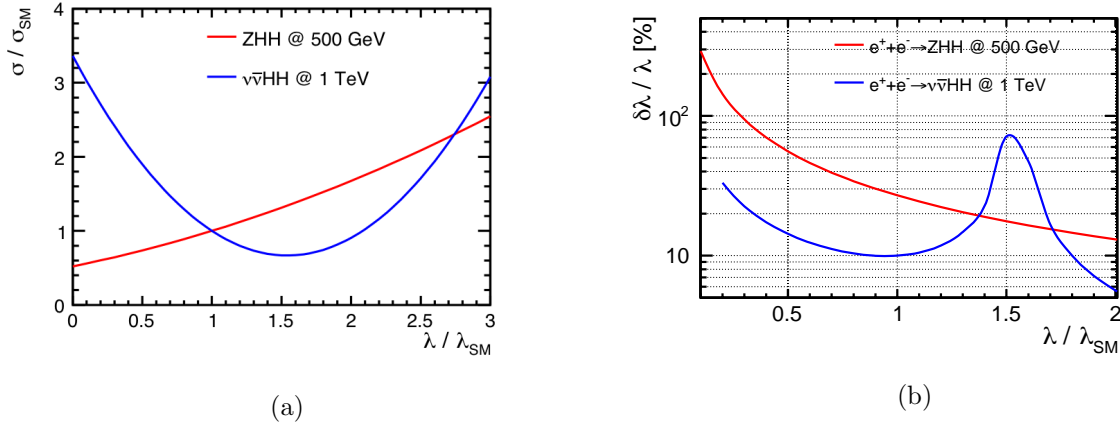


Figure 10.7: (a) Cross-sections for double Higgs production via Higgs-strahlung (at $\sqrt{s} = 500$ GeV) and WW fusion (at 1 TeV) as a function of the triple-Higgs coupling (normalised to its SM value) [512]. (b) Expected precision from each of the two ILC reactions as a function of the actual value of λ relative to the SM value.

approaches [516] as well as from a full exploitation of the charged hadron identification capabilities of ILD [517]. Propagation of all of these improvements of the high-level reconstruction to the full double Higgs-strahlung analysis carries the potential to bring the ILC500 sensitivity to better than 20%.

The availability at the ILC of two different HH production reactions becomes more important when one realizes that the real goal of this measurement is to demonstrate a Higgs self-coupling different from that of the SM. In models with extended Higgs sectors, the self-coupling can deviate significantly from its SM value, even if other Higgs couplings are rather SM-like. For instance in models with two Higgs doublets (2HDM) where all fermions couple only to one Higgs doublet (“Yukawa type I”) values of $-0.5 \lesssim \lambda/\lambda_{\text{SM}} \lesssim 1.5$ are possible even after taking into account theoretical and experimental constraints [518, 519] (where higher-order corrections can enhance these values [520]). In models with singlet scalars that mix with the Higgs boson, even larger enhancements are possible. Models of electroweak baryogenesis typically require large enhancements in λ , by a factor 1.5–2.5 [521]. We discuss this point further in Sec. 13.2. On the other hand, there are models in which λ decreases with respect to the SM value.

Ideally, we would like to be maximally sensitive to modifications in λ no matter what the sign turns out to be. It is thus remarkable that the two ILC reactions complement each other neatly in this respect. In both double-Higgs reactions, the Higgs self-coupling gives only one contribution to the full amplitude and thus appears in interference with other SM effects. For the WW fusion reaction, this interference is destructive, so a small increase in λ leads to a decrease in the cross section. For the double-Higgs-strahlung process, the interference is constructive, leading to an increase in the cross section as λ increases. This effect is shown in Fig. 10.7. An increased cross section leads to greater sensitivity to the value of λ . At the ILC, whether λ increases or decreases, one of the possible reactions will increase in cross section and reflect this improved

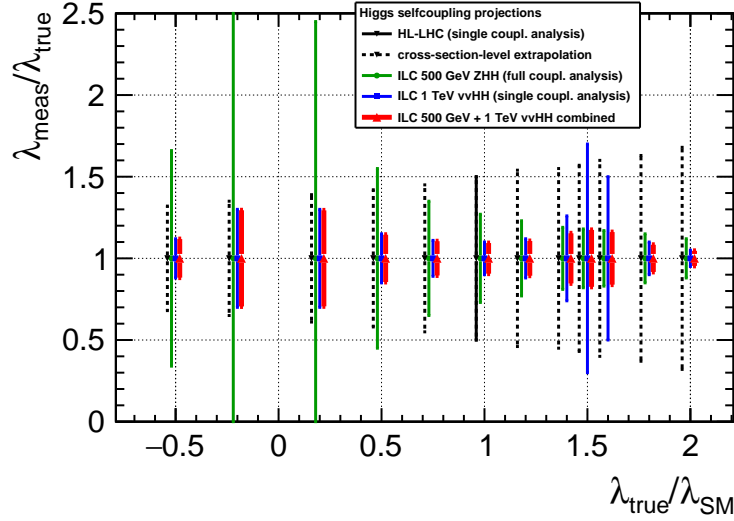


Figure 10.8: Expected uncertainties in the determination of the Higgs self coupling at the HL-LHC and the ILC as a function of λ/λ_{SM} . The HL-LHC value for the SM value of λ is that projected by the ATLAS collaboration in [522] that is then extrapolated to other values of the coupling. The ILC measurements at 500 GeV and 1 TeV are shown separately and, in red, in combination [512].

sensitivity. The situation is quite different at proton colliders such as the LHC. The dominant process of double Higgs production, $gg \rightarrow HH$, is a fusion process with destructive interference. The double-Higgs-strahlung process, which is higher order in the electroweak coupling, has a cross section smaller by many orders of magnitude. At the ILC, though, there are two reactions whose results can be combined to guarantee a measurement of the self-coupling at the level of at least 30% for any value of the self-coupling nature might have chosen. Figure 10.8 shows the effect of this synergy in comparison with an extrapolation of the uncertainty projections from the ATLAS collaboration [522] to non-SM values of λ .

10.2.3 Top quark Yukawa coupling

The top quark is the SM particle with the strongest coupling to the Higgs boson. The top quark Yukawa coupling has a value close to 1 in the SM. It is therefore important to understand this value and its relation to the top quark mass. The Higgs boson discovery channels at the LHC are sensitive to this coupling indirectly, through Higgs production and decay channels such as $gg \rightarrow H$ and $H \rightarrow \gamma\gamma$; in the SM, these proceed primarily through top quark loops. Under certain assumptions, the Higgs production and decay rates can yield a precise bound on the top quark Yukawa coupling. A more direct, and more robust, measurement is possible in the associated $pp \rightarrow t\bar{t}H$ production process, observed in 2018 [523, 524]. The projection for the HL-LHC envisages an uncertainty of approximately 3% on the signal multiplier κ_t dominated by theory uncertainties [498]. Several groups have studied the interplay between

At the ILC, indirect probes are also available: the $H \rightarrow \gamma\gamma$, $H \rightarrow gg$ and $H \rightarrow Z\gamma$ channels provide sensitivity to the top Yukawa coupling already in 250 GeV data. These measurements can determine the top Yukawa coupling with $\sim 1\%$ precision, under the assumption that no new particles enter in the loops. These measurements may therefore provide an early indication of new physics, but a deviation of the SM cannot be unambiguously pinpointed. In more general EFT fits, the constraint on the coefficient $C_t\phi$ of the operator that shifts the top Yukawa coupling obtained from these indirect probes is not robust, as its effect is degenerate with poorly bounded degrees of freedom [504].

The $t\bar{t}$ threshold scan offers an indirect determination that is more specific for the top quark Yukawa coupling. The production rate close to threshold is sensitive to Higgs-exchange effects and can yield a competitive precision of 4% on the top-quark Yukawa coupling [525]. However, the current uncertainty in state-of-the-art calculation would add a 20% theory uncertainty [485] and there is no clear perspective to reduce or circumvent this uncertainty.

The direct measurement in $e^+e^- \rightarrow t\bar{t}H$ production requires a center-of-mass energy of at least 500 GeV. The cross section rises sharply around that energy; raising the center-of-mass energy to 550 GeV enhances the production rate by a factor or approximately four and the measurement of the $t\bar{t}H$ coupling by a factor two. Several groups have performed detailed full-simulation studies at center-of-mass energies ranging from 500 GeV to 1.4 TeV [526, 527, 525]. With 4 ab^{-1} at 550 GeV, a precision of 2.8% is expected on the top Yukawa coupling, which could improve to 1% with 8 ab^{-1} at 1 TeV. Measurements at multiple center-of-mass energies and with different beam polarizations can further characterize the $t\bar{t}H$ coupling [528].

Another important target requiring center-of-mass energies between 600 GeV and 1 TeV are the CP properties of the $t\bar{t}H$ coupling. Achievable constraints have been studied at the cross-section level [529], showing a significant improvement due to polarized beams. A detailed detector-level study of the relevant observables remains an interesting task for future studies.

10.3 Triple gauge couplings

The ILC prospects for triple gauge coupling measurements at $\sqrt{s} = 250 \text{ GeV}$ have been introduced in Section 8.3. These have actually been extrapolated from previous studies at $\sqrt{s} = 500 \text{ GeV}$ and 1 TeV based on full simulation of the ILD detector concept [207, 530]. At higher energies, the relative effect on the differential cross section of the three TGC parameters g_Z , κ_γ , and λ_γ increases proportional to s/m_W^2 . There are a number of experimental effects that become more challenging at higher energies — more forward-boosted event topologies, higher pile-up from beamstrahlung pairs and photoproduction of low- p_t hadrons — the fundamental gain in sensitivity with s dominates by far. Figure 10.9 summarizes the current state of the expected precisions, as discussed in more detail in the following paragraphs.

The full simulation study at 500 GeV [207] was limited to a binned analysis of three (out of five) angles in the $WW \rightarrow \mu\nu qq$ and $WW \rightarrow e\nu qq$ channels. For an integrated luminosity of 500 fb^{-1} , this study found statistical uncertainties of $(6.1, 6.4, 7.2) \times 10^{-4}$ for g_1^Z , κ_γ and λ_γ , respectively. An unbinned likelihood or optimal observable analysis of all five angles, including also fully hadronic

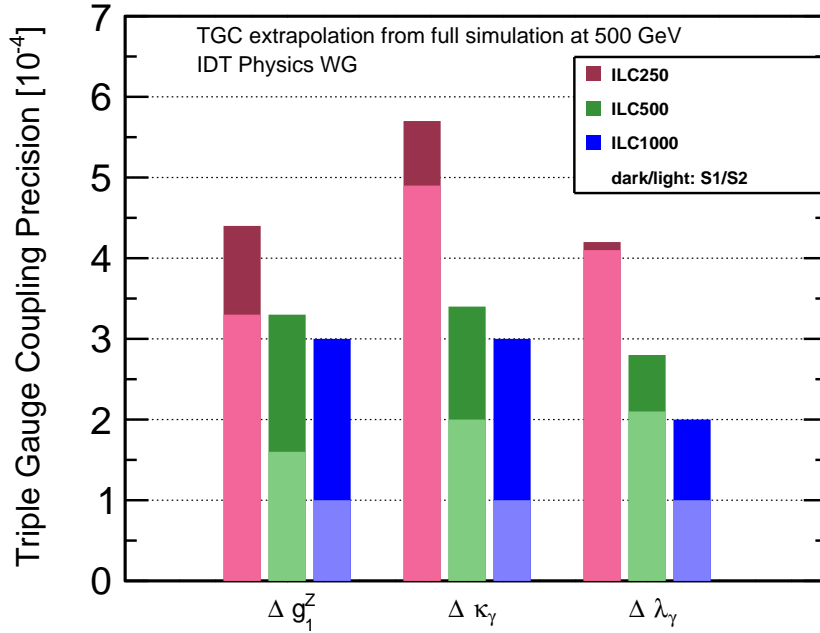


Figure 10.9: Expected precisions on the three triple gauge coupling parameters at the three energy stages of ILC. The results at 500 GeV and at 1 TeV are based on the ILD full simulation analyses of semi-leptonic W pair production, extrapolated to include improvements from the fully hadronic channel and single- W production as well as for upgrading from a binned analysis of three angles to an optimal observable technique [208]. The S1 scenario assumes the systematic uncertainties from [208], the S2 illustrates the hypothetical reduction by a further factor 2-3 to the level of 1×10^{-4} .

WW events as well as single- W events has been estimated [531] to improve these numbers by a factor of 2.4 for g_1^Z and by a factor of 1.9 for κ_γ and λ_γ . Assuming the full integrated luminosity of ILC500 instead of only 500 fb^{-1} gives another factor of 2 improvement to $(1.3, 1.7, 1.9) \times 10^{-4}$. At this level of precision, systematic uncertainties need to be considered. As shown in [210], the effects of a finite knowledge of the luminosity and the beam polarizations are negligible when including them as nuisance parameters in a global fit. The effect of different per mil-level uncertainties on the selection efficiency and percent-level uncertainties on the residual background has been evaluated in [207] by propagation through the whole analysis chain, thereby treating them as fully uncorrelated between data sets and observables, obviously a very pessimistic assumption. Based on considerations of correlated uncertainties and nuisance parameters in global fits, more recent studies expect that systematic uncertainties of $(3, 3, 2) \times 10^{-4}$ can be reached [208]. In total, the expected precisions on the three couplings thus reach $(3.3, 3.4, 2.8) \times 10^{-4}$ for ILC500.

The full simulation study at 1 TeV [530] found statistical precisions of $(1.9, 1.7, 2.7) \times 10^{-4}$ for a luminosity of 1 ab^{-1} with the same analysis technique as at 500 GeV (semileptonic W pairs, binned analysis using three angles). A simple scaling to the full luminosity of 8 ab^{-1} renders the

statistical uncertainty negligible with respect to the systematic uncertainties as given above. Thus, an adequate estimate of the 1 TeV prospects requires a thorough re-analysis of the systematic effects. It has already been shown that any global scaling as well as the variation of a simple angular cut-off can be determined from the data without any loss of precision on the TGCs [210]. But a complete treatment of the remaining backgrounds in a multivariate fit still remains to be done. In Fig. 10.9 we present the expected precisions on the TGC parameters assuming the currently understood level of systematic uncertainties and the result of possible improvements by a factor 2-3 to the level of 1×10^{-4} .

10.4 Quark and lepton pair-production

The pair productions of leptons and quarks at ILC are also an important probe for new physics via precise measurements of total and differential cross sections. We have reviewed the formulae governing these processes in Sec. 9.3.1.

10.4.1 Full simulation studies

Lepton pair production, $e^+e^- \rightarrow \ell^+\ell^-$ ($\ell = e, \mu, \tau$), gives distinguishable signatures with pure-leptonic final states. Most of the SM background can be efficiently removed by selection of visible energies (~ 250 GeV except for $\tau\tau$ final states) and angular selection (back-to-back topology). Since the high-energy phenomena like Z' and loop contribution of WIMPs are more sensitive to high q^2 , cutting low q^2 events do not significantly degrade the physics reach.

A full simulation study has been done for e^+e^- and $\mu^+\mu^-$ final states with $\sqrt{s} = 250$ GeV [437]. The event selections of track parameters for particle ID, visible energy and rejecting forward tracks give almost pure signal samples without significantly cut effective signals. The signal efficiency is more than 98% for μ pair final states and more than 97% for e pair final states at $|\cos\theta| < 0.95$ without significant dependence on the polar angle in the range. The remaining background is negligibly small. Full-simulation studies for c and b pair production have been reviewed earlier in Sec. 9.3.2.

Tau-pair production has been separately studied with $\sqrt{s} = 500$ GeV again with ILD detector simulation [436, 532]. It shows that the selection efficiency of tau-pair events with at least one tau decaying hadronically can be as high as 70% while remaining background is $< 10\%$ of the signal contribution. Thanks to the highly-granular calorimeters, the tau decay channel can be identified by separating charged tracks and photons in the narrow jet of tau decay products. Expected performance of tau polarization is around 1%, which adds another observable to explore BSM models. A study on further improvement on the polarization measurement using impact parameters of tau products is ongoing [532].

Model	250 GeV, 2 ab ⁻¹		500 GeV, 4 ab ⁻¹		1 TeV, 8 ab ⁻¹	
	excl.	disc.	excl.	disc.	excl.	disc.
SSM	7.7	4.9	13	8.3	22	14
ALR	9.4	5.9	16	10	25	18
χ	7.0	4.4	12	7.7	21	13
ψ	3.7	2.3	6.3	4.0	11	6.7
η	4.1	2.6	7.2	4.6	12	7.8

Table 10.1: Projected limits on Z' bosons in standard models, from the study of $e^+e^- \rightarrow ff$. The values presented, given in TeV, are the 95% exclusion limits and the 5σ discovery limits for the successive stages of the ILC program up to 1 TeV.

10.4.2 Z' limits

Given the ability of the ILC to measure these pair-production cross sections precisely, we can explore the possibility of searching for contributions from s -channel exchange of Z' bosons, additional neutral vector gauge bosons coupled to SM fermions. The coupling constants differ depending on the model. Some standard models used as benchmarks are the Sequential Standard Model (SSM), the Alternative Left-Right symmetric model (ALR), and models in which the Z' is a vector boson from the grand unification group E_6 . The SSM assumes the same coupling constants as SM Z . The ALR is based on an model in which the electroweak symmetry is extended to $SU(2)_L \times SU(2)_R \times U(1)$. The E_6 model is a string-motivated model which naturally introduces Z' as a linear combination of the two extra $U(1)$ gauge bosons Z_ψ and Z_χ : $Z' = Z_\chi \cos \beta + Z_\psi \sin \beta$. IT is common to choose three values of the β parameter: $\beta = 0$ (χ model), $\beta = \pi/2$ (ψ model) and $\beta = \pi - \arctan\sqrt{5/3}$ (η model).

For each of these models, we can use the ILC expectations for $e^+e^- \rightarrow f\bar{f}$ processes ($f = b, c, e, \mu, \tau$) to derive exclusion and discovery limits. Here we assume fixed efficiency for each final state: $c_b = 0.29, c_c = 0.07, c_e = 0.97, c_\mu = 0.98, c_\tau = 0.65$, based on full-simulation studies. The SM background is small enough compared with the signal events that it does not need to be considered. The expected signal events are estimated from tree-level differential cross section at the polar angle of $|\cos \theta| < 0.9$ with 19 points. Systematic uncertainty of 0.1 to 0.5% depending on the final states are included to calculate the mass limits. Table 10.1 shows the obtained exclusion and discovery limit after combining all five final states [533].

In a similar way, we have investigated the sensitivity to Z' bosons arising from specific models based on warped 5-dimension backgrounds, as in Randall-Sundrum theory [534]. The results for models presented in [440, 535, 536] are shown in Fig. 10.10. As is pointed out in [535], it is important to measure di-fermion production for all fermions and for different CM energies, since the effect of new Z' bosons can dependent strongly on flavor and beam polarization and will increase with increasing beam energy.

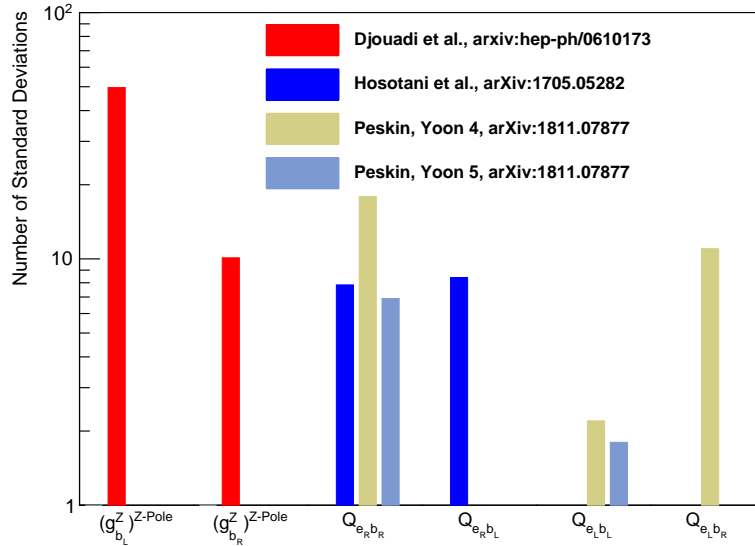


Figure 10.10: Visibility of deviations from the SM predictions in $g_{b_j}^Z$, $g_{b_j}^Z$ (to do: still missing in this plot) and the helicity amplitudes $Q_{e_i b_j}$, in standard deviations, from combined ILC250/Z-Pole running, expected from new physics models with Randall-Sundrum extra dimensions [440, 537, 536].

10.4.3 Indirect WIMP search

One can also use $e^+e^- \rightarrow ff$ final states to carry out a generic search for a WIMP dark matter particle χ . If χ has nontrivial electroweak quantum numbers, it will appear in a $Z \rightarrow \chi\chi \rightarrow Z$ loop diagram and give a correction to the Z coupling constants. The correction depends only on the quantum numbers, spin, and mass of χ and is independent of model details [538, 539]. We investigated three well-motivated types of WIMPs: wino ($SU(2)_L$ triplet and $U(1)_Y$ hypercharge of 0), Higgsino ($SU(2)_L$ doublet and $U(1)_Y$ hypercharge of $\pm 1/2$) and Minimal Dark Matter ($SU(2)_L$ pentet and $U(1)_Y$ hypercharge of 0).

Table 10.2 shows the exclusion limits from this study, based on $e^+e^- \rightarrow ee, \mu\mu$ final states at $\sqrt{s} = 250$ GeV. We use 20 angular bins of $\cos\theta = -0.95$ to 0.95 with systematic error assumed to be 0.1% on each bin. The limit on the χ mass from direct production is $< \sqrt{s}/2$, so indirect search gives a larger discovery potential for these WIMPs. With enough statistics, it is possible to separate the effects of WIMP models and Z' models using the angular distribution of the deviation of the cross section from the SM prediction.

10.5 New Particle Searches – TeV Scale

In this section, we will discuss the prospects at the ILC for the direct discovery of new particles. Our discussion will of course be given in the context in which the LHC experiments have carried out

Model	2σ exclsion
wino	240 GeV
Higgsino	180 GeV
Minimal Dark Matter	500 GeV

Table 10.2: Projected limits on WIMP indirect search with $e^+e^- \rightarrow ee, \mu\mu$ with $\sqrt{s} = 250$ GeV, 4 ab^{-1} integrated luminosity.

a large number of new particle searches, some reaching deeply into the mass region above 1 TeV. Still, we will explain, experiments at e^+e^- colliders can bring a complementary approach to new particle searches and open new and very interesting windows for discovery [540, 541].

In general, the new particle searches done at the LHC have focused on scenarios within each theory of new physics that give the *best* possible experimental prospects to observe new physics. This gives a chance to find such signs far out in a hitherto uncharted land. However, there is no guarantee that new physics would be discovered even if it is within the kinematic reach of the experiment. The actual parameters of the theory might be far from the ones giving the optimal signature sought in these analyses.

It is a rather different perspective to concentrate on the *worst* possible points in the theoretical parameter space. This clearly cannot reach as far out as in the previous case, but now a negative result would make it possible to claim that the new physics theory is ruled out at *all* possible parameter values below the kinematic reach of the experiment. It would also make discovery of the new physics *guaranteed* if it is indeed energetically reachable.

Lepton colliders have a lower reach in energy, but excel in fully exploiting all possible manifestations of new physics within reach. As the e^+e^- initial state implies electroweak production, the background rates will be quite low. This has consequences for the detector design and optimization: The detectors can feature close to 4π coverage, and they do not need to be radiation hard, so that the tracking system in front of calorimeters can have a thickness as low as a few percent of a radiation-length. In addition, the low rates means that the detectors needn't be triggered, so that *all* produced events will be available to analysis. Furthermore, at an e^+e^- machine, point-like objects are brought into collision, meaning that the initial state is fully known, and that the full beam energy is carried by the interacting objects. The beam-spot is sub-microscopic in size, allowing experimenters to find displaced vertices at much smaller distances, even in channels (like $\tilde{\tau}$ pair production), where there is no reconstructable primary vertex.

These features also are relevant in exploiting the LHC's blind-spots, in particular, any signal stemming from processes without QCD interactions or with only soft final states. Here, trigger-less operation of almost fully hermetic detectors is a great advantage. Often, in reactions of this type, only kinematic reconstruction of the full event can reveal BSM physics. These reactions can be studied powerfully at a lepton collider.

This section will mainly review studies of specific models of new physics. However, it is critical that a model-focused search program of future colliders be complemented by model-agnostic strategies. Machine learning tools are becoming increasingly powerful in searching for event classes

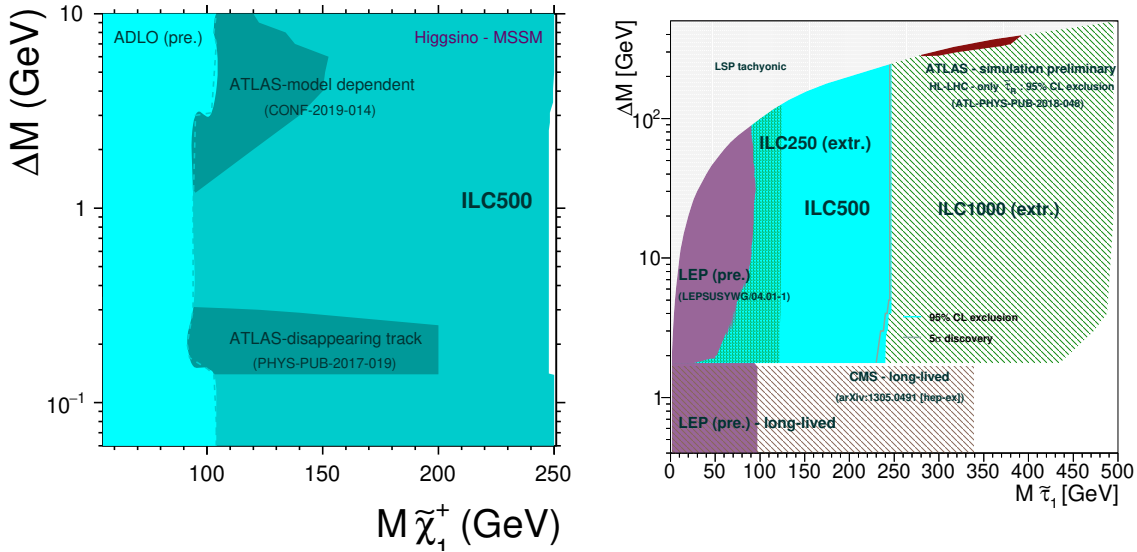


Figure 10.11: Exclusion and discovery reaches for a $\tilde{\chi}_1^\pm$ (left), or a $\tilde{\tau}_1$ (right). In both cases, the horizontal axis is the mass of the charged SUSY particle and the vertical axis is the mass splitting between this state and the (neutral) lightest SUSY particle.

that differ from those generated by the SM, efficiently exploring representations of the data in high-dimensional feature spaces. A variety of new methods have been proposed to carry out anomaly detection beyond the standard classification approach (see, for example [542]). The study [543] explores multiple ways to implement such searches at e^+e^- colliders, providing sensitivity to generic new hadronic resonances via training with imperfect or missing labels. With the triggerless operation of the ILC, we must be alert for surprises, so it will be important to adapt these methods to the e^+e^- environment.

Many studies of searches at ILC are done in full simulation using the full simulation tools presented in Chapter 7. This is essential for searches with difficult signals or large backgrounds, in particular, studies of SUSY and dark sector models with very small visible energy. Also for channels with small expected signals, full simulation is important, as it is expected that systematic errors would dominate over statistical ones in such cases.

However, this chapter also includes studies done by members of the broader community using fast simulation resources such as SGV or DELPHES, described in 7.1. In each case, we will make clear what level of tool was used in the analysis.

10.5.1 SUSY

We begin our review with supersymmetry (SUSY) [544, 545, 546, 547, 548, 549], for several reasons. Not only is SUSY the most complete theory of BSM, it can also serve as a template for BSM in

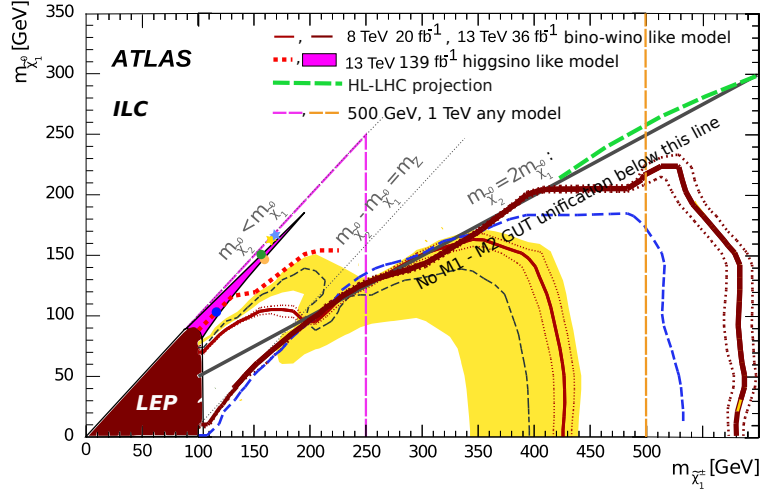


Figure 10.12: Observed or projected exclusion regions for a $\tilde{\chi}_1^\pm$ NLSP, for LEP II, LHC, HL-LHC. The vertical lines indicate the model-independent reach of ILC-500 and ILC-1000. The symbols very close to the line $M_{\tilde{\chi}_1^0} = M_{\tilde{\chi}_1^\pm}$ indicate the location of the Higgsino LSP models shown in Fig. 10.13.

general, since almost any new topology can be obtained in some flavor of SUSY, in particular if also possible violation of R-parity and/or CP-symmetry, or non-minimal models are considered. In addition, it is the paradigm that has been most studied with detailed detector simulation. In most cases, studies were done with full simulation with all SM backgrounds and all beam-induced backgrounds included. It is true that SUSY is under some stress by recent LHC results. However, ILC offers different angles to explore the properties of SUSY compared to LHC, with loop-hole free searches and complete coverage of compressed spectra. The missing corners of the SUSY model space have specific interest, and they can be covered by ILC.

General principles such as naturalness, the hierarchy problem, and the nature of dark matter (DM) still point to a light electroweak sector of SUSY. In addition, experimental anomalies such as the observed value of the magnetic moment of the muon [550] call for a light electroweak sector of SUSY [551, 552]. Except for the third generation squarks, the colored sector, where pp machines excel, does not provide any insight into any of these issues.

Particular attention, under the name “Natural SUSY” [553], has been given to the relation for the Higgsino parameters

$$m_Z^2 = 2 \frac{m_{H_u}^2 \tan^2 \beta - m_{H_d}^2}{1 - \tan^2 \beta} - 2 |\mu|^2. \quad (10.1)$$

This implies that that requiring low fine-tuning leads to the condition that the Higgsino mass-parameter μ must be $\mathcal{O}(m_Z)$, so that, whatever are the masses of the colored SUSY particles, the Higgsino sector must be close to the weak scale.

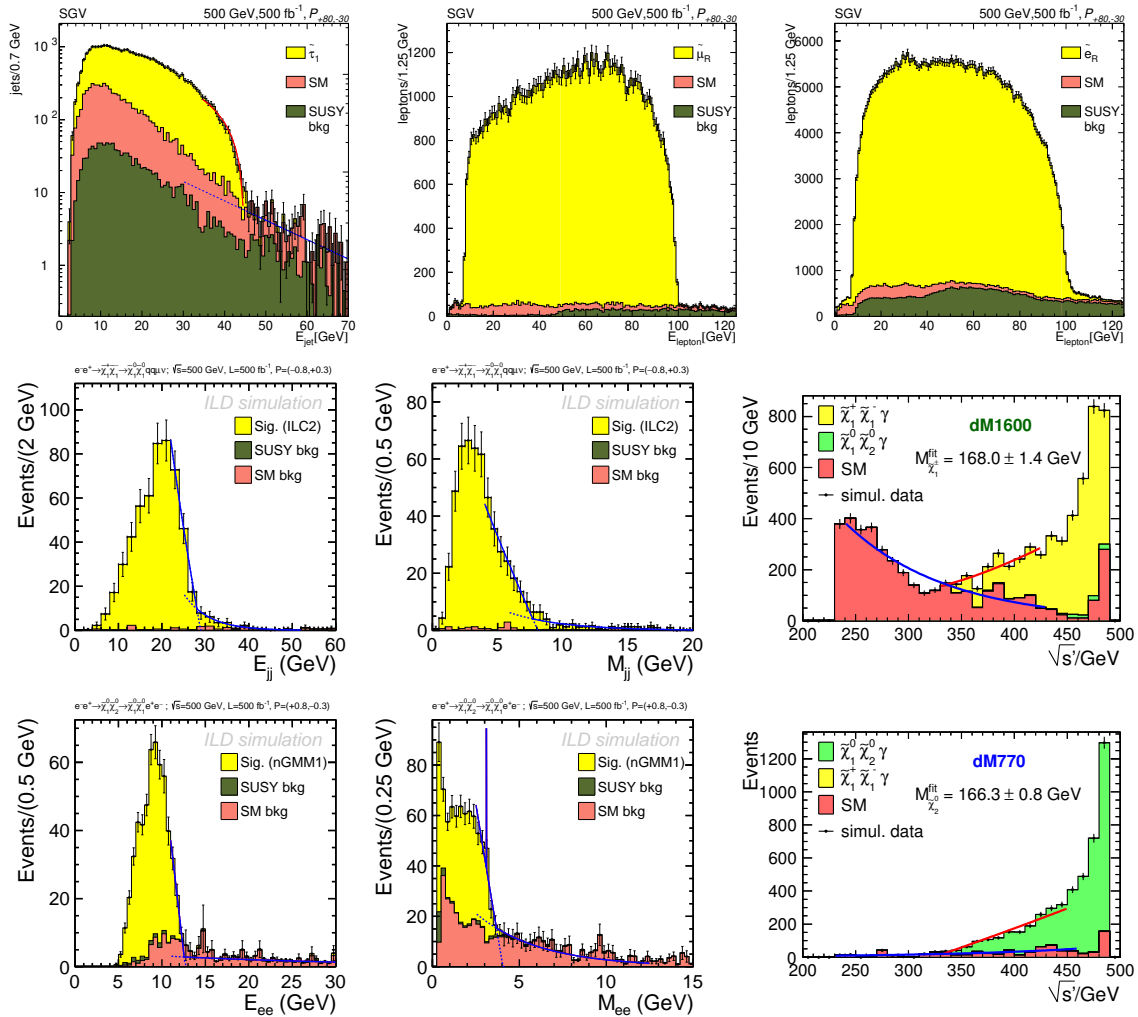


Figure 10.13: Top row: $\tilde{\tau}$, $\tilde{\mu}$ and \tilde{e} spectra. Middle and bottom rows: Observables for three different Higgsino-LSP models. The middle row shows the case of $\tilde{\chi}_1^\pm$ production, the bottom one that of $\tilde{\chi}_2^0$ production.

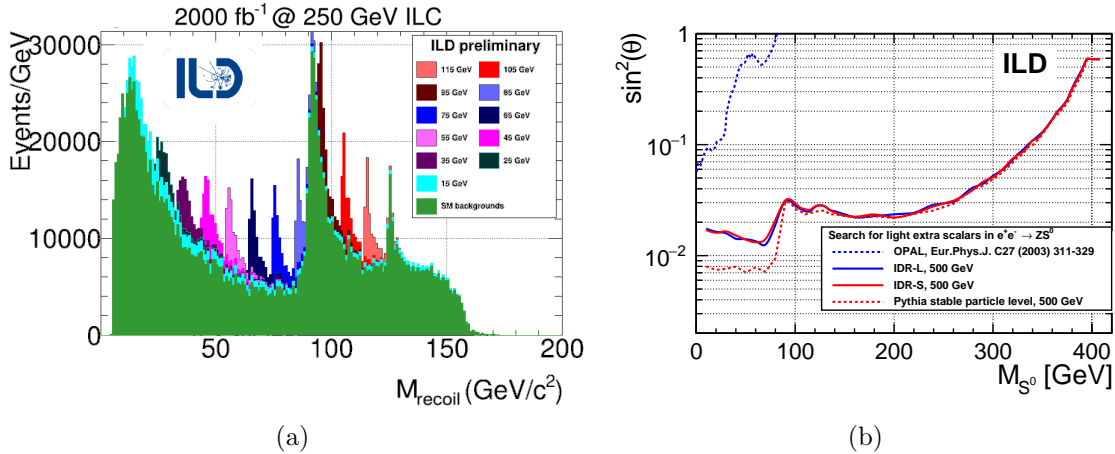


Figure 10.14: (a) Recoil mass distributions for several new scalars and the SM background. (b) Projected exclusion limit for new scalars, in terms of the coupling compared to the coupling an SM Higgs at the same mass would have.

There are also theoretical arguments for small mass gaps in the electroweak SUSY spectrum. If the lightest SUSY Particle (the LSP) is Higgsino or Wino, there must be other bosinos close in mass to the LSP, since the \tilde{H} and \tilde{W} fields have several components with parametrically small splittings in mass. Only a Bino-LSP can have a large mass difference, $\Delta(M)$, between the LSP and the next to lightest SUSY Particle (the NLSP). However, in the case of a Bino LSP, an overabundance of DM is expected [554], and to avoid such a situation, a balance between early universe LSP production and annihilation is needed. A method for enhancing the annihilation of SUSY particles that is ready at hand is $\tilde{\tau}$ co-annihilation, and for this process to operate, the masses of $\tilde{\tau}$ and $\tilde{\chi}_1^0$ should be within a few GeV of one another.

In the case of such compressed, low $\Delta(M)$, spectra, most sparticle-decays are via cascades, in which the last decay in the cascade—that to SM particles and the LSP—features small $\Delta(M)$. For such decays, current LHC limits have many qualifications, and only the limits from LEP 2 [555, 556, 557, 558, 313, 559, 560] are model-independent.

At ILC, one can perform a loophole-free search for SUSY because, in SUSY, the properties of the NLSP production and decay are completely predicted given the LSP and NLSP masses, due to the SUSY-principle that the couplings of particles and sparticles are related by symmetry. Note that this does not depend on the (model dependent) SUSY breaking mechanism. In R-parity conserving models, the final stages of a cascade decay are highly constrained. By definition, there is only one NLSP, and this particle must have a 100% BR to its (on- or off-shell) SM-partner and the (stable or unstable) LSP. Also, there is only a handful of possible candidates to be the NLSP. Hence by performing searches for every possible NLSP, we can obtain model independent exclusions and discovery reaches in the $M_{NLSP} - M_{LSP}$ plane, separately for each NLSP candidate, or globally. In models with R-parity violation, there are different decay patterns, but these can also be classified and, typically, lead to more stringent limits in a setting where the full event can be reconstructed.

Examples of this procedure are shown in Fig. 10.11 for the cases of a $\tilde{\chi}_1^\pm$ [561] or a $\tilde{\tau}_1$ [562, 563] NLSP. The $\tilde{\chi}_1^\pm$ is a conservative extrapolation from the LEP results, while the $\tilde{\tau}_1$ one is obtained with *full* detector simulation, in which the $\tilde{\tau}$ and LSP properties were chosen such that the limit is the weakest possible one, i.e. the experimentally “worst possible” case. In the figure, it can be seen that the discovery and exclusion reaches are almost the same, and the reach is quite close to the kinematic limit $2M_{NLSP} = E_{CM}$. It should also be noted that the HL-LHC projection from ATLAS is exclusion only, and is for specific assumptions on the $\tilde{\tau}$ properties, assumptions that are not the most pessimistic. In Fig. 10.12, the various current or projected limits are shown in a single plot [561, 564, 565, 566, 567, 568]. It should be noted that below the heavy black line, GUT unification of the Bino and Wino mass-parameters M_1 and M_2 is not possible: The difference between $M_{\tilde{\chi}_1^0}$ and $M_{\tilde{\chi}_1^\pm}$ cannot be larger than what the line indicates, if such a unification is realized.

In fact, at the ILC, SUSY discovery would happen at quite low levels of integrated luminosity. Either the process is not in reach and there is no sign of it, or it will be discovered straightforwardly. This means that studies of SUSY at ILC would almost directly enter into the realm of precision measurements. The plots in Fig. 10.13 show a number of examples of the kind of signals that would be expected, as seen in detector simulation studies. The top row shows slepton signals ($\tilde{\tau}$, $\tilde{\mu}$ and \tilde{e}) in a $\tilde{\tau}$ co-annihilation model [569]. The following rows show typical chargino and neutralino signals in different Higgsino LSP model. The left-hand two plots are models with moderate (a few to some tens of GeV) ΔM [570], while the right-hand plots are for a model with very low (sub-GeV) ΔM [571]. In all of the illustrated cases, it was found that the SUSY masses could be determined at the sub-percent level, the polarized production cross-sections to the level of a few percent. Many other properties could also be obtained from the same data, such as decay branching fractions, mixing angles, and sparticle spins.

10.5.2 New scalars

Many BSM models predict the existence of a new Higgs-like scalar (S), produced in $e^+e^- \rightarrow Z^* \rightarrow ZS$, with the decay pattern of S different from that of the Higgs boson. Such a state could have escaped detection at LEP if its production cross-section is much lower than that of a SM Higgs at the same mass. Hence, a search for such a state should be done at all accessible masses, and without any assumption on the decay modes. At an e^+e^- collider this can be done using the recoil-mass, *i.e.*, the mass of the system recoiling against the measured Z . In [574], a full detector simulation study was performed, and it was found that couplings down to a few percent of the SM-Higgs equivalent can be excluded; see Fig. 10.14.

In models with much smaller couplings of extended Higgs bosons to the Z boson, the ILC can search for the pair production of the new bosons. The primary reactions are $e^+e^- \rightarrow AH$, where H is a heavy neutral CP-even boson and A is a heavy neutral CP-odd boson, and $e^+e^- \rightarrow H^+H^-$. If the new Higgs bosons decay into final states that are completely visible in the ILC detectors, the discovery of these reactions is straightforward almost all of the way up to the production thresholds $E_{CM} = m_A + m_H$ or $E_{CM} = 2m_{H^+}$ [575]. However, there are more difficult cases, and these also have significant opportunity for discovery at the ILC. An example is the Inert Doublet Model (IDM) [576, 577, 578, 579]. This is a 2-Higgs doublet model with a Z_2 symmetry that prevents

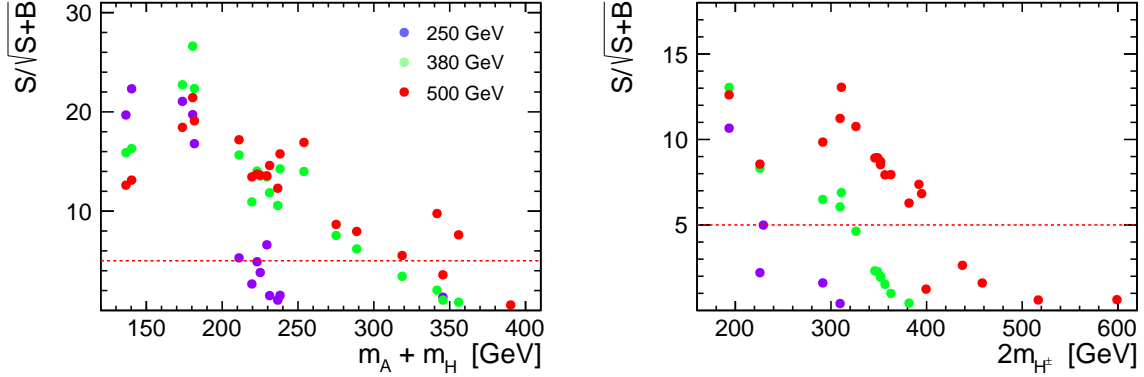


Figure 10.15: Significance of the deviations from the Standard Model predictions for the extended Higgs bosons of the Inert Doublet Model, as expected for 1 ab^{-1} of data collected at center-of-mass energy of 250 GeV, 380 GeV and 500 GeV, from [572, 573]. Left: for events with two muons in the final state ($\mu^+\mu^-$), as a function of the sum of neutral inert scalar masses; Right: for events with an electron and a muon in the final state ($e^+\mu^-$ or $e^-\mu^+$) as a function of twice the charged scalar mass.

the scalars of the second doublet from coupling directly to the SM fermions. This implies that the lightest particle in the second doublet will be stable and can be a candidate for the particle of dark matter. Models with IDM scalar masses of the order of 100 GeV are still consistent with constraints from direct detection experiments, relic density of dark matter, as well as with all collider and low-energy limits. In this model, the final neutral boson (it is assumed to be H) is invisible. The visible signals are leptons emitted in the decay of the A or H^\pm to the H through off-shell or on-shell W or Z exchange (depending on the scalar mass difference). The phenomenology of this model has been studied extensively in [572, 573, 580, 581, 582]. Working with the benchmark scenarios proposed in [583, 584], this study investigated the significance of signatures with two muons or an electron and a muon in the final state. The results are presented in Fig. 10.15. For the integrated luminosity of 1 ab^{-1} , the expected discovery reach of 500 GeV ILC extends up to the sum of neutral scalar masses of 330 GeV and up to charged scalar masses of 200 GeV. The ILC capabilities for models with light, weakly coupled scalar bosons are reviewed in [585, 586].

Another feature that can appear in models with extended scalar sectors that does not arise in SUSY is the possibility of scalars or fermions in higher representations of electroweak $SU(2)$, for example, $I = \frac{3}{2}$ or 2. In [587], the phenomenology of a model of this type motivated by the muon $g - 2$ anomaly is studied at e^+e^- colliders.

10.5.3 WIMP dark matter

The primary probe at the ILC for the direct production of *WIMP dark matter* are photons emitted as initial-state radiation in association with the pair production of invisible dark matter particles. Such a Mono-photon search is analogous to Mono- X searches at the LHC. The main backgrounds

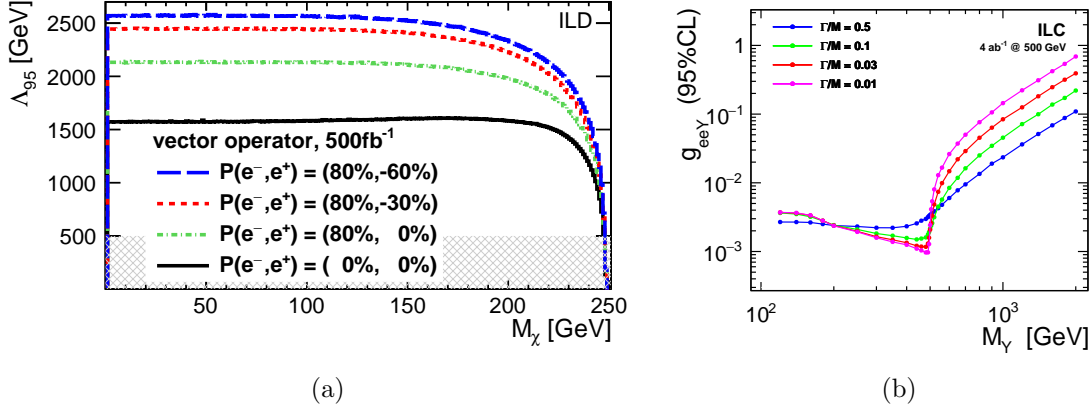


Figure 10.16: (a): Observational reach (2σ) of the ILC for a fermionic WIMP with a WIMP-fermion vector coupling in terms of the WIMP mass for four different beam-polarization configurations [588]. (b): Expected limits on the vector mediator coupling to electrons for the ILC running at 500 GeV and different fractional mediator widths, as a function of the mediator mass [589].

to this search are the radiative neutrino production and the radiative Bhabha scattering process, in which the outgoing electron and positron escape undetected in the beam pipe. The neutrino production is irreducible, but its dominant contribution, from t -channel W exchange, is present only from the $e_L^- e_R^+$ initial state. At LEP, searches for photon events with missing energy were performed [590, 591], and were later re-analyzed within the effective operator framework. [592].²

The prospects to detect WIMPs with such methods at the ILC and to determine their properties have been studied for a center-of-mass energy of 500 GeV in detailed detector simulation [593, 588]. Also at the ILC, the experimental sensitivity has been interpreted in the framework of effective operators. Figure 10.16(a) shows the exclusion reach found at 500 GeV in the effective operator approach [588]. The importance of beam polarization in achieving these results has already been discussed in Sec. 5.3. For the full 500 GeV-program of the ILC, scales of new physics (Λ) of up to 3 TeV can be probed, while the 1 TeV-energy-upgrade of the ILC would extend this even to 4.5 TeV or more, depending on the integrated luminosity. At 250 GeV, the full reach will be attained already at a modest integrated luminosity.

The EFT approach is only valid if the considered new physics mass scale (mediator mass) is much higher than the collision energy. This is the case when we assume the mediator coupling to SM particles is large. However, scenarios with light mediator exchange are still not excluded by the existing data for couplings of the order of 0.01 and below. Assuming that the total mediator width is dominated by the DM partial width, cross section limits extracted from the analysis of mono-photon event spectra, calculated for fixed mediator mass and width hardly depend on the DM particle type or coupling structure. Limits on the vector mediator coupling to electrons, expected from the combined analysis of the data taken with different beam polarizations at 500 GeV ILC, with systematic uncertainties taken into account, are presented in Fig. 10.16(b) [589, 594]. For proper

²Note that under LEP or ILC conditions the effective field theory approximation is accurate, while this assumption is questionable in similar analyses at hadron colliders.

modeling of mono-photon events, dedicated simulation method was proposed [595]. The study was based on the Delphes fast simulation framework with dedicated ILC detector model [306, 307], see section 7.1.

A broad parameter region of the light scalar mediator scenario is also not excluded, with its thermal relic abundance being consistent with the observed dark matter density. Since the mediator couples directly to the Higgs boson in a renormalizable way, another exciting signal is expected at the ILC, the exotic Higgs decay into a pair of the mediators. The ILC could efficiently search for the decay, especially when the mediator decays into a pair of bottom quarks, as mentioned in section 8.2 [354]. On the other hand, the leptophilic mediator is another interesting scenario. The mediator carries a lepton number and connects the dark matter with SM leptons, making the dark matter leptophilic. The scenario is also not excluded by the existing data, with its thermal relic being consistent with the observed dark matter density. The ILC will play a crucial role in searching for the scenario via the mediator pair production [596], and the mono-photon (a pair production of the dark matters associated with a photon) process [597] even at the 250 GeV running.

10.5.4 Heavy neutrinos

The ILC also has a role to play in testing models of neutrino mass. It is possible to give a mass to neutrinos by adding to the SM a set of right-handed neutrinos with conventional Yukawa couplings. However, this is usually considered inadequate to explain the very small sizes of neutrino masses. To solve this problem, new heavy particles are introduced such that, when these are integrated out, a dimension-5 term called the Weinberg operator is generated [598],

$$\Delta\mathcal{L} = -\alpha_{ij} \frac{(\epsilon_{ab} H_a^\dagger \bar{L}_{bi})(\epsilon_{a'b'} H_{a'}^\dagger L_{b'j}^c)}{M} + h.c. \quad (10.2)$$

When the Higgs field develops its vacuum expectation value, this leads to a Majorana-type mass matrix for the light neutrinos, with $m_{ij} = \alpha_{ij} v^2 / M$. In most discussions, it is assumed that this operator arises from integrating out heavy right-handed neutrinos. With neutrino Yukawa couplings of order 10^{-3} , the right-handed neutrinos would have masses of order 10^{10} GeV.

However, in fact, there are three distinct possibilities for the generation of the term (10.2) [599, 600]. The case just discussed is the Type I seesaw. In the Type II seesaw, the heavy particle integrated out is a isospin triplet scalar; in the Type III seesaw, the heavy particle is an isospin triplet Majorana fermion. Like the vector bosons of extended gauge symmetries discussed in Sec. 10.4, these particles may have their own symmetry constraints that put their masses at the TeV scale and dimensionless couplings to neutrinos proportional to small mixing angles [601, 602].

Current constraints on the Type II models are shown in Fig. 10.17, from [603]. These models contain a doubly-charged scalar boson H^{++} that, for sufficiently low masses, is directly pair-produced at colliders. At the LHC, it is straightforward to search for this particle in its decay to like-sign dileptons, but this might not be the dominant mode. The alternative decay mode, to the 3-body $W^+ f \bar{f}$, will benefit from the ability at an e^+e^- collider to completely reconstruct events in leptonic and multi-jet final states.

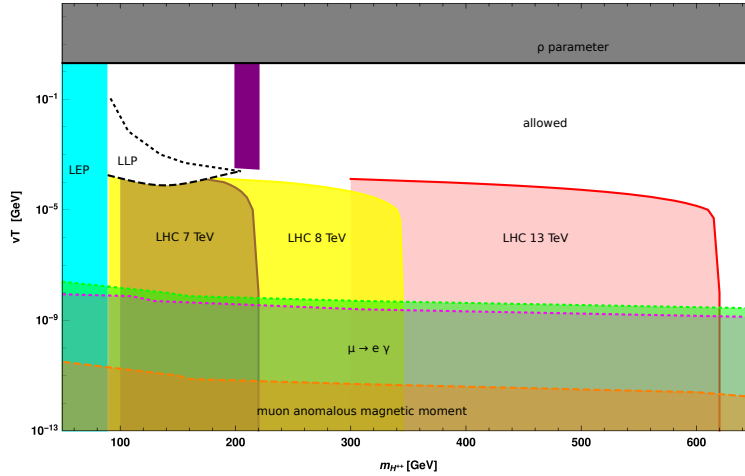


Figure 10.17: Parameter space of the type-II seesaw model in the plane of the mass of the doubly-charged scalar boson H^{++} and the vacuum expectation value v_T of the neutral component of the $I = 1$ scalar field, from [603]. The upper limit on v_T comes from the value of the ρ parameter. The strongest lower limits come from direct searches for H^{++} in its decay to like-sign dileptons. The region labeled LLP can be explored at the LHC in searches for displaced decays. In the remaining allowed region, the dominant decays of the H^{++} are 3-body decays to $W^+ f \bar{f}$.

In Type III models, the most stringent bounds come from searches for pair-production of the $I = 1$ fermions, for example, $q\bar{q} \rightarrow \Sigma^+ \Sigma^0$. The phenomenology of these particles has been studied at both pp and e^+e^- colliders [604, 606]. The Σ particles decay to W or Z plus a lepton through the heavy/light lepton mixing. At the LHC, one can search for a trilepton plus missing energy final states under the assumption that the e and μ decay channels are dominant or at least democratically produced. The lower limits on the Σ masses are at roughly 900 GeV [607, 608, 609]. At e^+e^- colliders, it is also possible to search for the single production of the Σ states together with a lepton using the W hadronic decay mode, by searching for the final state $e + J + \cancel{E}_T$, where J is a boosted jet with 2-jet substructure. This search has been studied in parametric fast simulation at the 1 TeV ILC in [604], leading to the expected limits on the heavy/light mixing angle shown in Fig. 10.18. Results for 3 TeV are also shown.

The possibility of searching for the heavy right-handed neutrino production at 500 GeV and 1 TeV ILC was also studied within the model assuming heavy neutrino mixing with all lepton flavors [612]. The study was based on the Delphes fast simulation framework, using dedicated ILC detector model [306, 307], see section 7.1. For the light-heavy neutrino pair production, with the subsequent decay of the heavy neutrino into two quarks and a charged lepton, direct reconstruction of the neutrino mass is possible, see Figure 10.19a for the channel involving muons in the final state. The limits on the heavy neutrino-lepton coupling (effectively the neutrino mixing angle) expected from the multivariate analysis of the collected data are presented in Figure 10.19b. Results from ILC running at 500 GeV and 1 TeV are compared with the corresponding limits for 3 TeV CLIC, current constraints from LHC and future limit estimates for hadron colliders. Within the kinematic reach, the limits expected for lepton colliders are orders of magnitude better than those coming

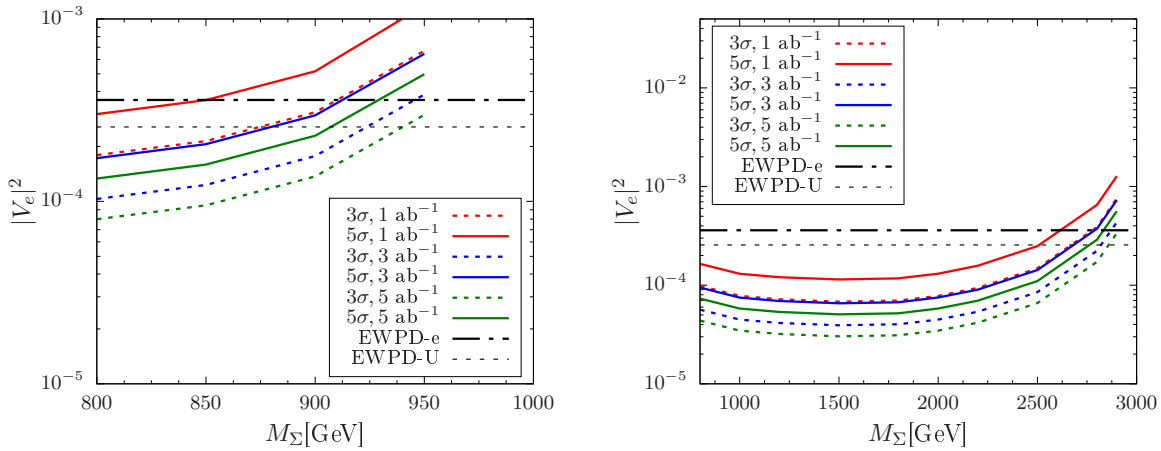


Figure 10.18: Sensitivity reach in the mixing angle for production of the heavy $I = 1$ lepton in Type III seesaw models, using the final state $e + \cancel{E}_T +$ boosted jet, from [604]. Left: ILC at 1 TeV with varying levels of integrated luminosity; Right: e^+e^- at 3 TeV with varying levels of integrated luminosity. The solid lines show upper bounds from precision electroweak observables, from [605].

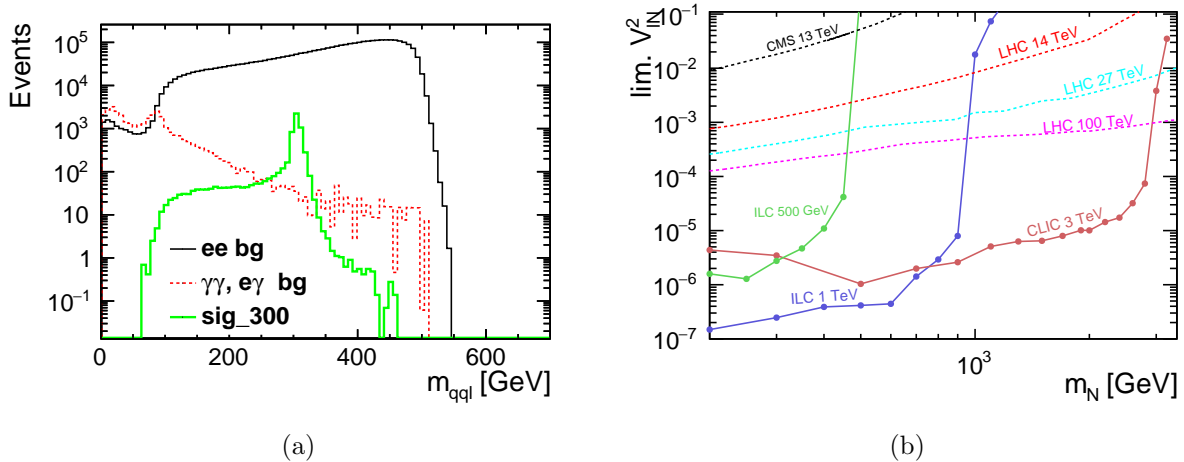


Figure 10.19: Left: $qq\bar{l}$ mass distribution for ILC500 for muons in the final state. Black solid line stands for the e^+e^- background, red dashed line for the γ -induced background and thick green line for a reference signal scenario (Dirac neutrino with a mass of 300 GeV). Right: limits on the coupling V_{lN}^2 for different colliders (solid lines: ILC500 – green, ILC1000 – violet, CLIC3000 – dark red). Dashed lines indicate limits from current and future hadron colliders based on [610, 611]. Figure taken from [612].

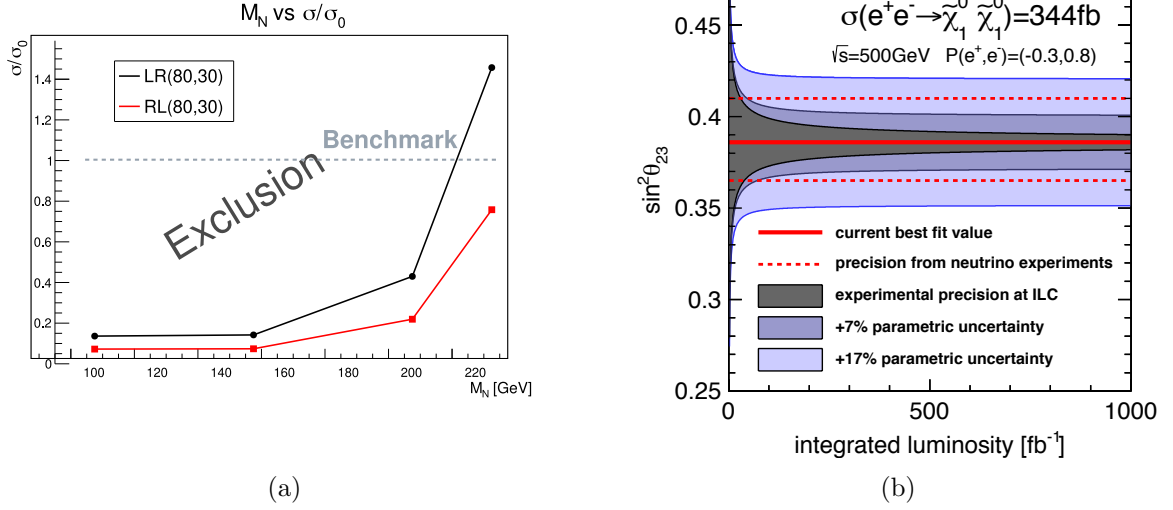


Figure 10.20: (a) Exclusion reach for Right-handed Heavy Neutrinos. (b) Comparison of the value of the neutrino atmospheric mixing angle $\sin^2 \theta_{23}$ to the value obtained from the ILC measurements of the neutralino decay branching ratios in the R-parity violating model described in the text, from [613].

from current and future hadron colliders. The results were obtained for the Dirac neutrinos but it was verified that the limits for the Majorana particles would be of the same order.

Another model that has been studied in *full* simulation is *heavy right-handed majorana neutrinos* [614, 615]. In this model, the striking signal is the observation of same flavor, same charge (SFSC) leptons. While SFSC as such are not rare in the SM, they will typically occur in association with neutrinos, leading to missing energy. In the studied model, due to the majorana nature of the heavy neutrino, they can decay completely visibly, with no missing energy. As missing energy is not observable at pp colliders (only missing *transverse* energy or momentum), such signals are difficult to detect at LHC. At ILC, on the other hand, the observation of missing energy is straight-forward, for reasons explained above. Figure 10.20(a) shows that the ILC running at $E_{CMS} = 500$ GeV can exclude pair-produced right-handed majorana neutrinos up to at least $M_N = 225$ GeV.

There is one more scenario for neutrino mass involving R-parity violating SUSY. One possible R-parity violating term is the bi-linear coupling in the superpotential

$$\Delta W = -\epsilon_{ab} \epsilon_i L_{ia} H_{ub} \quad (10.3)$$

Together with small induced sneutrino masses, this term leads to small neutrino masses of order $|\epsilon_i|^2$ [616]. It is interesting that the same mixing angles appear in the neutrino mass matrix and the decay amplitudes for the lightest neutralino decay (which is now allowed) to $W\ell$ [617]. With observation of neutralino pair production and decay, it is possible to test this theory by comparing the observed values of the mixing angles. This analysis was also studied in *full* simulation in [613].

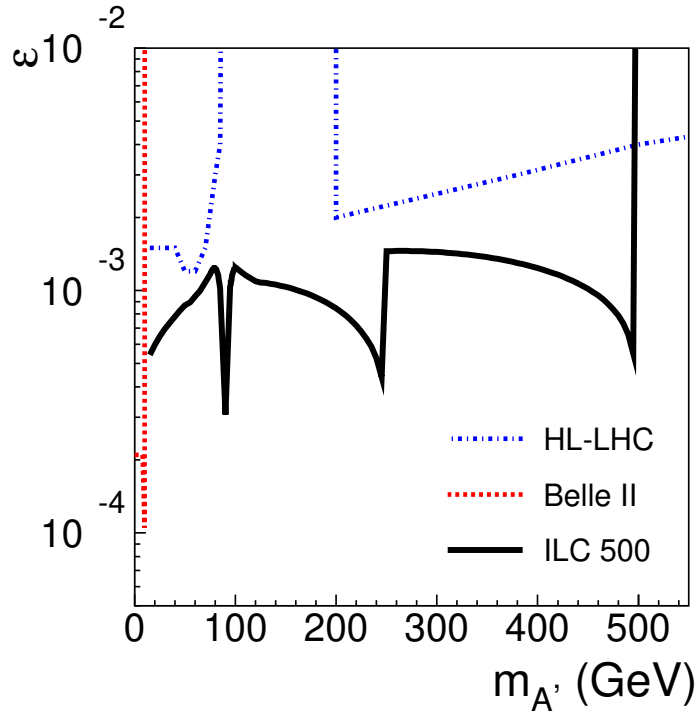


Figure 10.21: Projected reach of HL-LHC, Belle-II and the ILC for the dark Z gauge boson, in terms of its mass and the kinetic mixing parameter ϵ [618, 619].

The comparison of the measurement that could be obtained at the ILC at 500 GeV with the observed value of the neutrino atmospheric mixing angle is shown in Fig. 10.20(b).

10.6 New particle searches – Dark Sector

Many extensions of the Standard Model contain fields that do not carry any SM gauge charges. Such fields are said to belong to the “dark sector”, and may include sterile neutrinos, additional gauge bosons, and particles responsible for dark matter. A brief review of the commonly used set of benchmark models for dark sectors and their interactions with the SM is contained in Section 11.1. The common feature of dark-sector particle candidates is their feeble couplings to the SM, typically orders of magnitude smaller than the SM gauge interactions. High luminosity and the clean environment of the ILC offer unique opportunities to search for such particles. If signals of such particles are found, the precisely characterized initial state and beam polarization may be crucial to determine their nature.

The ILC will offer two complementary avenues to search for the dark sector particles. First, additional detectors mounted at the ILC beam dumps will provide unmatched sensitivity to dark

sector particles with masses below 10 GeV or so. This will be covered in detail in Section 11.3. Second, the general-purpose detectors at the main IP have sensitivity to signals of the dark sector particles with masses up to the full ILC center-of-mass energy. Here, we focus on this latter case. As an example, consider a “dark Z ”, the gauge boson of an additional $U(1)_D$ gauge group. The interactions of the dark Z with the SM are induced by kinetic mixing of the $U(1)_D$ with the hypercharge, inducing mixing with the photon and Z . It can also be produced through mass mixing if there exist additional Higgs field(s) charged under both $U(1)_D$ and the SM gauge groups. Unlike the Z' bosons that have been extensively considered in the literature, the dark Z does not have direct gauge couplings to SM fermions, greatly weakening experimental constraints. The dark Z can be produced at the ILC through $e^+e^- \rightarrow A' + \gamma$. The projected reach of HL-LHC, Belle-II, and the ILC (combining 250 GeV and 500 GeV runs) are shown in Fig. 10.21.³ There exists a parameter range where the ILC would be the first experiment to discover this new physics. If the discovery is made, either at the HL-LHC or the ILC, the ILC will have a unique capability to precisely measure the dark Z couplings and determine their chiral structure. The dark Z will appear as a (very narrow) resonance in e^+e^- annihilation, so short dedicated ILC run with $\sqrt{s} \approx m_{A'}$ could provide this information, just as LEP and SLD measured the SM Z properties. This is illustrated in Fig. 10.22, which also demonstrates how this measurement can be used to discriminate among possible dark Z models (*e.g.* parity-violating vs. parity-conserving, and kinetic vs. mass-mixing.) Dark Z bosons could also be observed through their coupling to the Higgs portal, leading to $H \rightarrow Z_D Z_D$. A study of Higgs decay to a dark Z pair followed by dijet and dilepton decays is presented in [620].

If the dark sector contains a scalar field S , couplings $S|H|^2$ or $S^2|H|^2$ are possible. If $m_S < m_h/2$, these couplings would induce exotic Higgs decays. The specific signatures depend on the details of the dark sector model, but we have seen in Sec. 8.2 that the ILC can identify very many exotic Higgs decay modes. In models where S is stable or decays purely within the dark sector, such decays will appear as $h \rightarrow$ invisible. The ILC offers an exquisite sensitivity in this channel, extending the HL-LHC reach on the branching ratio by a factor of 20. On the other hand, in models where dark sector states can decay back to the SM, visible signatures may appear. A well-motivated example is the decay $S \rightarrow b\bar{b}$. This is the dominant decay if $m_S > 2m_b$ and the flavor texture of its couplings is aligned with the SM Yukawas. This results in a $4b$ final state, which is notoriously difficult to discern at the LHC but will be accessible at the ILC. Another possibility is that $m_S > m_h/2$, so that no new Higgs decays are induced. This case is very challenging at hadron colliders, especially if the S field carries quantum numbers that forbid its mixing with the Higgs (as happens, for example, in models where S is the dark matter particle). The ILC will offer a unique window on this scenario through a very precise measurement of the $e^+e^- \rightarrow hZ$ cross section, sensitive to one-loop corrections induced by S loops [622].

Another well-motivated experimental target is a pseudo-Goldstone boson of a spontaneously broken global symmetry in the dark sector, with coupling structure motivated by the familiar QCD axion. Such “axion-like particle”, or ALP, can be produced at the ILC in association with photons, Z , or Higgs, and detected through its decays to photons or e^+e^- pairs. ILC searches will be

³This analysis assumes that the dark Z decays back into SM particles. An alternative scenario is that the dark Z decays invisibly to other dark sector states. In this case, the γ +missing energy signature discussed in Sec. 10.5.3 can be used to search for the dark Z at the ILC.

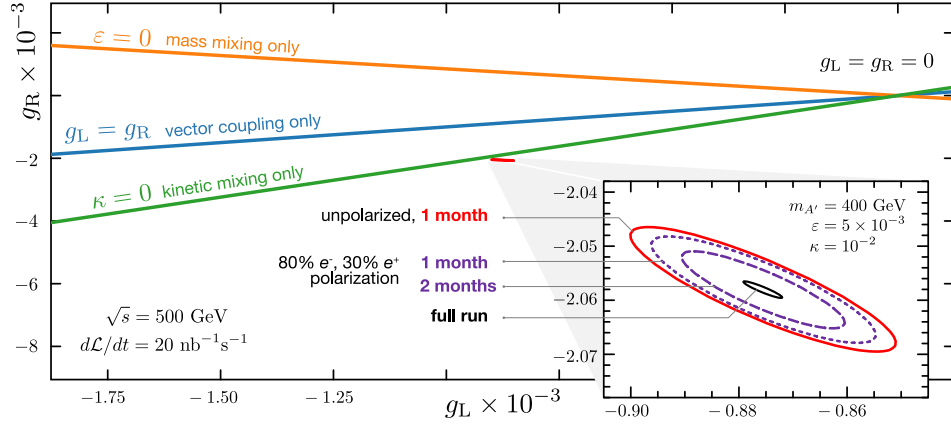


Figure 10.22: Left- and right-handed couplings of dark Z to leptons, measured by a short dedicated ILC run on the dark Z resonance (assumed to be at 400 GeV in this illustrative example). The benchmark model generates parity-violating dark Z couplings to matter through a combination of mass and kinetic mixing. Orange, blue and green lines correspond to alternative models that can be ruled out by this measurement. From Ref. [621].

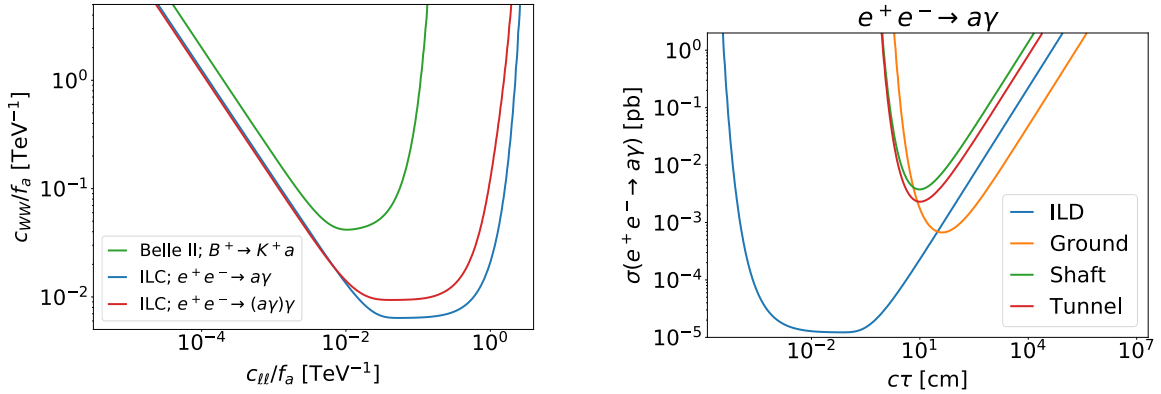


Figure 10.23: Left panel: Sensitivity projections for long-lived ALPs with $m_a = 300$ MeV at the ILC and at Belle II, as a function of the couplings c_{WW}/f_a and c_{ll}/f_a . Right panel: Sensitivity projections for long-lived ALPs with $m_a = 300$ MeV at the ILC main detector (ILD), and three dedicated far-detector options (Ground, Shaft, and Tunnel). From Ref. [625].

sensitive to ALPs in the 1–500 GeV mass range, with couplings 1–2 orders of magnitude below the current limits [623, 624].

Dark-sector models often contain long-lived particles (LLPs), which have macroscopic decay lengths due to their small couplings. The ILC offers excellent capabilities to search for the LLPs,

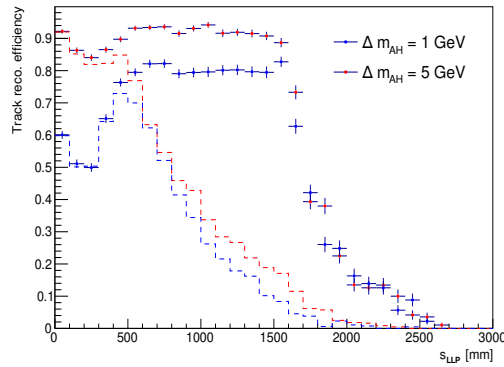


Figure 10.24: Efficiency of track reconstruction as a function of the long-lived particle decay length s_{LLP} , for example scenarios with decays of heavy neutral scalar A to lighter heavy scalar H and a pair of muons, for two heavy scalar mass differences of 1 GeV and 5 GeV.

thanks to clean environment and hermetic angular coverage of the detector. A recent study [625] found that for LLPs produced with a typical cross section of a few picobarns, the ILD detector could probe lifetimes up to 300 ns, or proper decay lengths up to 100 m. This capability will open up new opportunities to search for dark-sector models. For example, for long-lived ALPs with masses below 1 GeV, the sensitivity of this search will significantly exceed the reach of the search for displaced vertices in meson decays at Belle II; see Fig. 10.23. Moreover, Ref. [625] compared the reach of the displaced-vertex search at the main general-purpose ILC detector to that of a potential dedicated “far” detector, which could be placed in the planned underground cavities or on the ground specifically to search for LLP decays. It was found that a realistically sized far detector can provide at best a moderate improvement over the already impressive sensitivity of the main detector. These conclusions apply quite generally to searches for long-lived particles at the ILC.

A high precision pixel vertex detector is crucial for reconstruction of LLP decays, both for SM states (heavy flavour tagging) and possible BSM candidates, for the expected decay lengths in the range of micrometers to millimeters. For larger decay lengths, of the order of centimeters and meters, reconstruction of LLP decays has to be based on central tracking. Time Projection Chamber (TPC) of the ILD has strong advantages for this purpose, since it has almost uniform response to charged particles, independent on the particle production point and direction. This was confirmed with dedicated full simulation study, preliminary results of which are shown in Fig. 10.24. The efficiency of track reconstruction is shown for two example scenarios with decays of heavy neutral scalar A (LLP) to lighter heavy scalar H (DM candidate) and a pair of muons. High and uniform reconstruction efficiency is expected for LLP decays inside the TPC volume even for very low mass difference between the two exotic states (i.e. very soft visible final state). For global track reconstruction cut on the track impact parameter has to be released, otherwise the efficiency is degraded significantly (dashed lines in Fig. 10.24). A similar study of long-lived particle capabilities for the silicon tracker of the SiD detector is presented in [626].

Chapter 11

ILC Fixed-Target Program

In addition to its central collider, the ILC accelerator can host a number of additional detectors, including detectors for fixed-target experiments and beam dump experiments. These can provide the setting for a multi-faceted program. The main purpose of these experiments will be to search for dark sector particles interacting only feebly with the Standard Model. The intense and high-energy electron and positron beams that the ILC makes available also have uses in nuclear and hadron physics and in studies of strong-field QED. They can also provide resources for developing advanced electron and positron accelerators.

In this chapter, we will present the variety of fixed-target and remote experiments that could be mounted at the ILC site and estimate their potential both for dark sector searches and for other physics questions.

11.1 The physics of light Dark Sectors

Many extensions of the Standard Model contain fields that do not carry SM gauge charges. Such fields are said to belong to the “dark sector”. From the observational point of view, such singlet fields are motivated by the existence of dark matter, as well as by the baryon-antibaryon asymmetry. From a more theoretical side, they appear frequently in models of gauge unification, string theory compactifications, *etc.* Dark sectors can also address some of the current SM anomalies such as the anomaly in $(g - 2)_\mu$. Dark sector particles with masses at or below the GeV scale are particularly motivated since they can naturally lead to thermal dark matter scenarios. Dark sector fields may still have non-gauge couplings to the SM, allowing them to be produced and detected in collider experiments. Particularly, as we describe below, dark sector particles can communicate with SM particles through the so-called “portal interactions”.

The field content of the dark sector and the structure of its interactions with the SM are not strongly constrained by theoretical considerations or by data, and a large variety of viable models are possible. Focusing on *renormalizable* couplings between dark sector and SM fields provides a useful set of benchmark models to explore this physics scenario.

- **Dark Photon Portal:** If the dark sector contains an abelian gauge group, $U(1)_D$, its gauge field can couple to the SM via the “kinetic mixing” term $\mathcal{L} = \epsilon F_D^{\mu\nu} F_Y{}_{\mu\nu}$, where F_Y and F_D are the $U(1)_D$ and the SM hypercharge field-strength tensors, respectively. The kinetic mixing induces a coupling of A' , the gauge boson associated to $U(1)_D$, to the SM. If $m_{A'} \ll M_Z$, A' simply couples to the electromagnetic current, while a heavier A' acquires Z -like couplings (the latter scenario is often described as a “dark Z ”).

A light dark photon ($m_{A'} < 10$ GeV) can be produced at the ILC beam dump through electron - positron pair-annihilation, and bremsstrahlung productions. Once produced, the dark photon can be long lived, propagate through the dump and then decay to SM particles like e^+e^- in the decay volume. The dark photon can also decay invisibly (e.g. to DM). As we will discuss in Sec. 11.3, in both cases, detectors placed behind the dump will offer new sensitivity to the dark photon parameter space.

- **Higgs Portal:** If the dark sector contains a dark scalar field S , the couplings $S|H|^2$ or $S^2|H|^2$ are possible, where H is the SM Higgs doublet. If $m_S < m_h/2$, the $S^2|H|^2$ coupling induces exotic Higgs decays of the type $H \rightarrow SS$. (the ILC sensitivity to exotic Higgs decays is discussed in Sec. 8.2.) Furthermore, relatively light scalars, S , could be produced in the dump through electron - positron pair-annihilation, the Primakoff process, and bremsstrahlung, thanks to the S mixing with the SM Higgs possibly induced by the $S|H|^2$ and $S^2|H|^2$ operators. Because of this mixing, the dark scalar can decay back to SM particles.
- **Neutrino Portal:** A right-handed neutrino, N , is a SM singlet, and as such may be considered to belong to the dark sector, coupled to the SM through the neutrino portal interaction, HLN , where L is the SM lepton doublet. This operator induces the mixing of the sterile neutrino with the SM active neutrinos, leading to the production of sterile neutrinos in the dump and to its subsequent decay into SM particles.

It is customary to add another benchmark to this list, which involves dimension-5 couplings but is very well theoretically motivated: the “axion portal”. Finally, new dark gauge bosons arising from gauging anomaly-free approximate symmetries of the SM are also well studied in the literature:

- **Axion Portal:** A pseudo-scalar singlet, a , can couple to the SM via $aF\tilde{F}$, where F is the EM (or other gauge) field strength tensor. This coupling is allowed if a is a Nambu-Goldstone boson, such as the axion. While the original motivation comes from the “QCD axion” solution to the strong CP problem, phenomenological studies also consider a more general possibility of “Axion-Like Particle” (ALP), whose masses and couplings are not constrained by the QCD axion model. If sufficiently light, ALPs can be produced in the ILC dump through Primakoff production and then decay to photons thanks to the $aF\tilde{F}$ coupling.
- $U(1)_{e-\mu}$, $U(1)_{e-\tau}$, $U(1)_{\mu-\tau}$: The corresponding gauge bosons, Z' , couple to some of the leptons of the SM. Because of these couplings, they will be produced in the dump from electron (or positron) scattering with the dump nuclei. Z' will decay back to either the charged leptons or the neutrinos of the SM, giving rise to either a visible or invisible signature to be searched for in a detector placed after the dump.

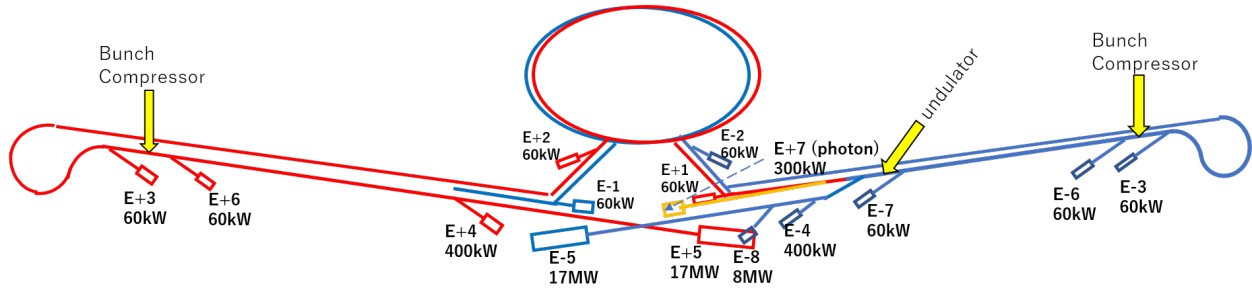


Figure 11.1: Distribution of beam dumps over the ILC facility. The electron, positron and photon beamlines are colored blue, red and yellow, respectively.

11.2 ILC Facilities for fixed-target experiments

The ILC can provide very high energy, high intensity, low emittance electron and positron beams. The unique beams can also be used for purposes other than the collider experiments. The single-pass nature of ILC allows us to use the beams even destructively so long as the influence to the collider experiments is not significant.

The most appropriate locations of using the beams are the beam dumps. There, very high intensity electron and positron beams interact with thick targets, hopefully producing large numbers of highly penetrating particles. There are 15 beam dumps distributed over the entire facility. Their locations are schematically shown in Figure 11.1. In this section, we will briefly describe only those which may be useful for some of the fixed target experiments.

Main dumps (E-5, E+5)

The main dumps (E-5 and E+5) are located about 300 m downstream of the interaction point (IP). Each of them accepts the full power beam (125 GeV, 2.5 MW) of the ILC250 beam. The main body of the dump is a water tank of cylindrical shape, 1.8 m diameter, ~10 m length, filled with high-pressure (~10 atm for ILC500) water. This is followed by a shield several tens of meter long, designed to absorb muons created in the dump. This muon shield can be split into many pieces so that appropriate locations can be chosen to insert the detectors for fixed target experiments. The accelerator carrying the opposite beam to the IP is running nearby. The beam-center spacing is 0.014 (crossing angle) \times 300-400 m = 4-6 m. This will limit the size of the region available for a fixed target experiment.

There have already been several proposals to make use of the secondary particles from these dumps. Experiments parasitic to the collider experiment are normally expected so that the beams come to the dumps after beam-beam interaction at the IP. It may also be possible to plan a dedicated machine time in principle but it is better to use the tune-up dumps (E-4, E+4) unless the full power beam is necessary. Also it is almost impossible to make use of the beam between IP and the dump, by either placing a target or by extracting the beam, because of the safety issue.

Tune-up dumps (E-4, E+4)

Another location to make use of the full energy beam (but at lower power) is the tune-up dumps E−4 and E+4. These dumps are used for the commissioning of the main linacs. Here, the electron or positron beam can be extracted from the main beam line so that it does not go to the experimental hall. Up to 400 kW (including a 20% margin) can be accepted. These dumps will also be used in case of an emergency. When a highly off-energy or other erroneous beam is detected, fast kickers are excited to eject the beam to these tune-up dumps. The field rise time is shorter than the bunch spacing (554 ns) and the duration is more than 100 μ s, corresponding to more than 200 bunches.

These dumps can be used in two different modes, dedicated and parasitic. In the latter mode a part of the beam (some small number of bunches or pulses) is extracted during normal collider operation using fast kickers. However, for either mode of operation, it must be recognized the devices of the dumps (dump body, kickers, etc.) are not necessarily designed for routine operation at 5 Hz. Deliberate planning between the experimental and accelerator teams is mandatory.

One possible proposal to make use of E \pm 4 is the QED experiment (Sec. 11.4). In this case, the beam interacts with a high-power laser whose repetition rate is limited, so it suffices to extract the last bunch in a 1312 bunch train during the regular collider operation. The required kicker is simple (500 ns rise time, no flat-top necessary, no constraint of fall time, 5 Hz) and can be installed in the main beamline. The emergency kicker need not be used for this purpose. A major challenge for this proposal is how to transport the laser beam deep underground if the laser is housed on the surface.

Photon dump (E+7)

The baseline design of ILC adopts a positron source using helical undulators. The 125 GeV electron beam emits photons which produce the positron beam. The energy of the photons is several MeV and the number of photons is $\sim 10^{17}$ per second. After producing positrons, these photons are dumped at ~ 2 km downstream. The total photon power is about 60 kW. (The design limit of the dump is 300 kW because of future upgrade.) This can be a unique source of gamma rays although the parameters are driven by the requirement of the collider operation.

Beams with low bunch charge

Colliders prefer high bunch charge because the luminosity is proportional to bunch charge square. However, some fixed target experiments may prefer a lower bunch charge with a shorter bunch spacing. CW operation is impossible because the klystrons allow only pulsed operation (duty factor $\sim 1\%$). What may be done at most is to fill all buckets of 1.3 GHz with weak bunches (population up to $\sim 2 \times 10^7$) with the pulse length ~ 0.7 ms by introducing a different electron gun. The damping ring is not compatible with this beam format, hence a beamline, a few hundred meter long, is needed to bypass the damping ring. There are several other issues expected (e.g., emergency issue) so that serious discussion with accelerator team is needed. A positron beam of such a format seems to be very difficult to produce due to the large emittance of the positron source.

It is easy to reduce the bunch charge with the bunch spacing fixed. This is possible only in dedicated modes. The only issue is whether the beam is visible by the monitors for orbit control.

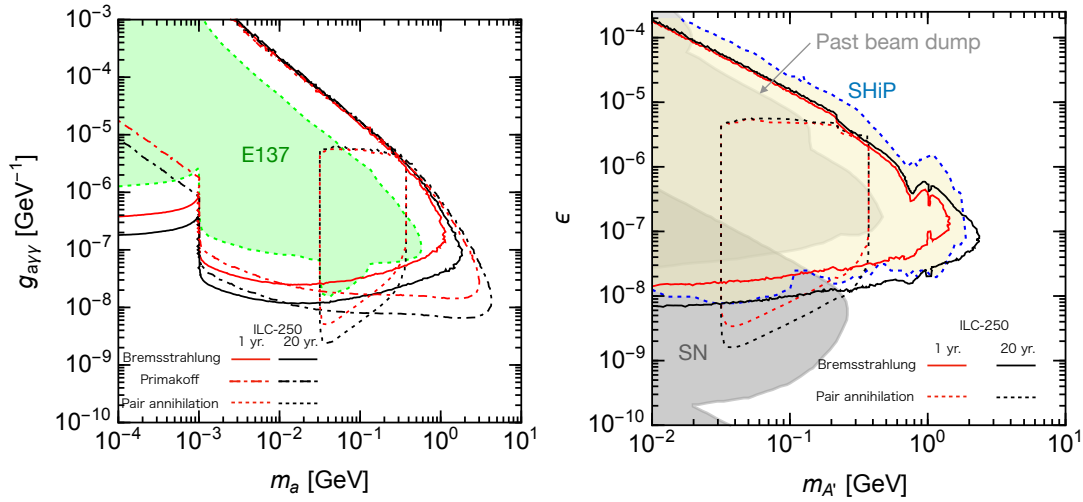


Figure 11.2: The reach of a beam-dump experiment at the ILC-250 for axion-like particles (left) and dark photons (right). Taken from Ref. [629]. See also [630] for another study of the reach on axion-like particles.

It may be possible to add a ‘pilot bunch’ with normal charge for orbit control. Another possibility, depending on the nature of the experiment, is to scrape the halo particles by a movable target during the normal collider experiment. This is appropriate in the tune-up dump line. The safety issue must be carefully considered.

11.3 Dark Sector particle searches

Dark sector particles could be produced from the interactions of either the e^- or the e^+ beam with the corresponding beam dump. Since such particles are very weakly coupled to ordinary matter, they could propagate through the beam dump and the muon shield without interacting, and decay back to the SM after that. Such events could be probed by detectors located 50–100 m away from the beam dump and behind the muon shield, searching for visible decay products (e.g. signatures involving two or more leptons, or two or more photons) [627]. Alternatively, the dark sector particles could decay to other dark sector states, such as the stable DM particles. A detector could be mounted behind the muon shield to search for elastic scattering of DM particles on atomic electrons, similarly to what has been proposed for the BDX experiment at Jefferson Lab [628].

In this section, we discuss the discovery prospects of (both visible and invisible) dark particles at the ILC beam dump experiment. The ILC environment offers unique advantages for this type of physics: highest-energy lepton beams available at any existing or planned machine; very high integrated luminosity (about 4×10^{21} particles on target per year for the main beam dumps at ILC-250) and the availability of both electron and positron beams. These features will enable the ILC experiments to expand the reach of searches for dark particles to higher masses and smaller couplings.

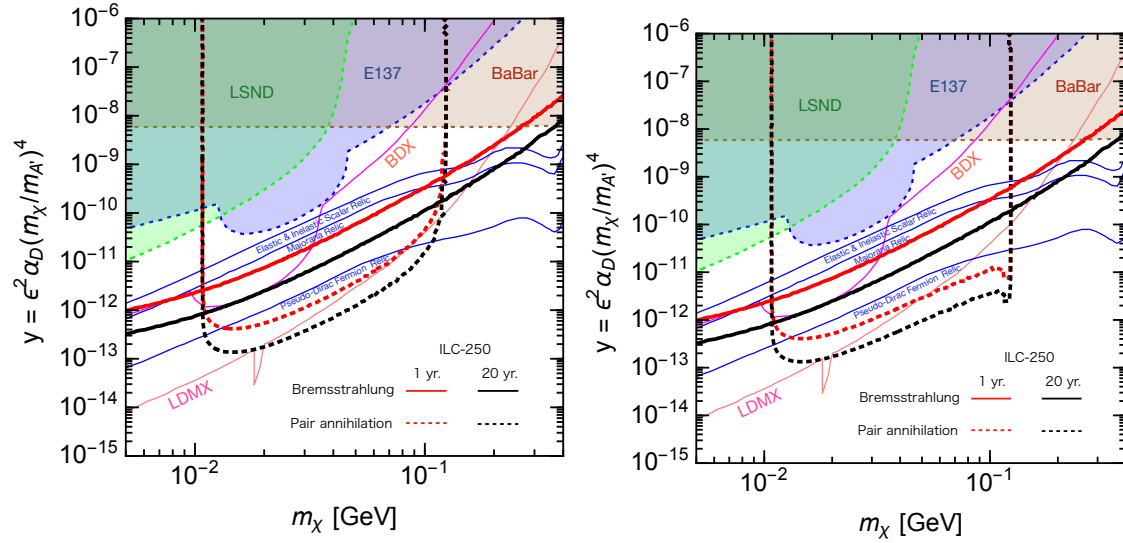


Figure 11.3: Reach of the ILC search for dark photon decaying invisibly to a pair of stable dark matter particles. For comparison, the current constraints (shaded) and reach of proposed BDX and LDMX experiments are also shown. Blue lines indicate the parameters where the DM thermal relic density matches the observed value.

As an example, the expected ILC reach for visibly-decaying ALPs and dark photons is shown in Fig. 11.2. In both cases, the ILC will greatly expand the reach of the currently available experiments, probing higher dark particle masses and smaller couplings. Similar improvements were demonstrated for leptophilic gauge bosons, such as $U(1)_{\mu-\tau}$ [631], or for dark scalars [630]. If a dark-sector particle is discovered, the ILC can probe its nature and discriminate among theoretical models. Uniquely among the proposed experiments, the ILC can measure and compare the production rates at electron and positron beam dumps, as well as study the dependence on the rates on beam polarization.

It is worth noting that the main ILC detector also has an impressive sensitivity to visibly decaying LLPs produced in hard processes at the collider IP; see section 10.6, in particular Fig. 10.23. Dedicated “far” detectors to search for LLPs produced at the main IP have also been explored, but were shown to not provide significant improvements in sensitivity for realistic parameters [625].

The reach of a search for a dark photon decaying invisibly to a pair of dark matter particles is shown in Fig. 11.3. This search relies on detection of elastic scattering of DM particles on an atomic electron in the detector placed 100 m downstream of the beam dump behind a muon shield, and is conceptually similar to the proposed BDX experiment [628]. The ILC experiment will probe the parameter space of this model far beyond the current constraints. In particular, a broad range of parameters where the model can reproduce the observed DM relic density through thermal freeze-out can be probed (see the blue lines in the figure). Note that the experiment at the positron dump (right panel of Fig. 11.3) has a somewhat higher reach than the electron-dump counterpart, due mainly to the additional dark photon production channel $e^+e^- \rightarrow A'$ (with e^- being an atomic electron inside the dump). Once again, if a signal is discovered, the availability of e^- and e^+ beams

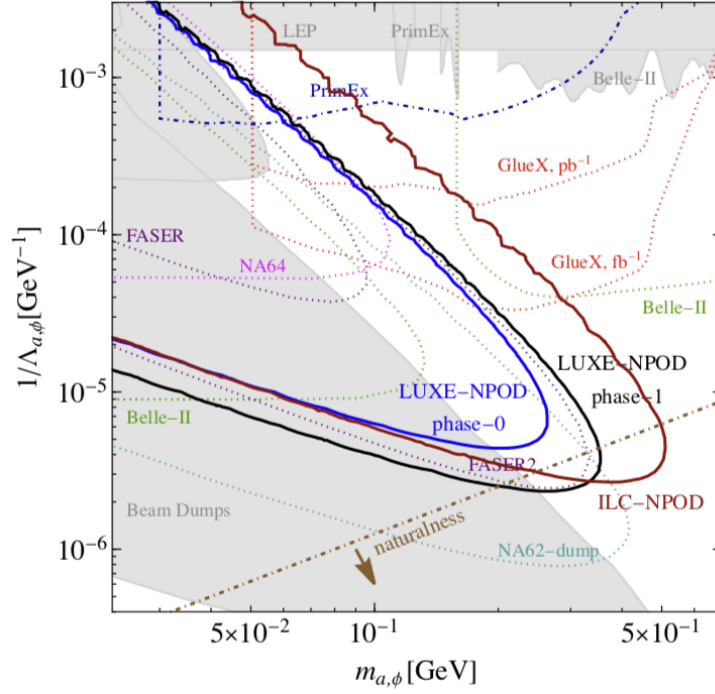


Figure 11.4: Sensitivity of the ILC version of the LUXE-NPOD experiment [634] searching for scalar and axion-like particles that couples to photons. The sensitivity is expressed in terms of parameters Λ_a and Λ_ϕ defined in eq. (11.1).

with closely matched parameters, as well as beam polarization, will give the ILC the unique ability to discriminate among possible theoretical interpretations.

The ILC beam dumps also offer an excellent setting to search for heavy neutral leptons. By following the production of neutral leptons from the primary ILC interaction point and from lepton decays and inelastic scattering in the beam dump, the studies [632, 633] show that the ILC beam dump experiments can be sensitive to mixing angles as small as $|U_\mu| \sim 10^{-10}$ and $|U_\mu| \sim 10^{-8}$.

In addition to using the main beam dumps, the ILC offers other interesting opportunities for novel dark sector particle searches. For example, a high-powered laser can be mounted at one of the tune-up beam dumps. This setup will enable the exploration of strong-field QED, as discussed below. Interactions of the electron beam with the laser field will also produce a high-luminosity photon beam, which can in turn interact with a target to produce dark sector particles such as ALPs. An effective Lagrangian describing the coupling of an ALP a or a scalar ϕ to the photon field can be written

$$\mathcal{L} = \frac{a}{4\Lambda_a} F_{\mu\nu} \tilde{F}^{\mu\nu} + \frac{\phi}{4\Lambda_\phi} F_{\mu\nu} F^{\mu\nu} . \quad (11.1)$$

and the sensitivity of such experiments can be described as limits on the parameters Λ_a , Λ_ϕ .

This experimental concept was developed for the LUXE-NPOD experiment proposed at DESY [634].

The high energy and intensity of the ILC beams will greatly expand its sensitivity. The limits expected from the ILC fixed target program are shown in Fig. 11.4. Another interesting possibility is to use the photon beam produced by the positron source to search for ALPs based on the “light-shining-through-the-wall” concept. This and other schemes are currently being investigated.

11.4 Experiments on strong-field QED

The electron beam of 120 GeV available for fixed-target experiments will also provide another experimental program, one on QED in very strong fields. At the *Schwinger critical field* of

$$eE = m_e^2 \text{ or } E = 10^{18} \text{ V/m} \quad (11.2)$$

the QED vacuum becomes unstable with respect to spontaneous e^+e^- pair creation. This suggests a new regime of QED that has not yet been studied in the laboratory. The subject of QED in strong background fields has recently been reviewed in Ref. [635].

A figure of merit is defined by

$$\chi = eE_e/m_e^2 \quad (11.3)$$

where E_e is the external electric field measured in the electron rest frame. Currently, the highest χ achieved in the laboratory is $\chi \sim 0.3$ at the SLAC experiment on nonlinear QED E-144 [636, 637, 638]. This experiment observed the nonlinear Compton and Breit-Wheeler processes

$$e^- + n\gamma_l \rightarrow e^- \gamma \quad \text{and} \quad e^- + n\gamma_l \rightarrow e^- e^+ e^-, \quad (11.4)$$

where γ_l denotes a laser photon, up to $n = 4$. This experiment observed successively smaller rates for increasing n . However, as the laser field strength increases, it becomes necessary to resum contributions from all higher n using dedicated nonperturbative analysis. The rates of these nonlinear QED phenomena become comparable to the single-photon rates at $\chi \sim 1$.

Such large fields are not only of conceptual interest. The corresponding magnetic fields of

$$B = 10^{14} \text{ gauss} \quad (11.5)$$

are observed in magnetars, pulsars with large magnetic fields that are responsible for Fast Radio Bursts and other extreme astrophysical phenomena, and such large fields are also likely to be present in active galactic nuclei. These systems also host electron-positron plasmas that may have unique and surprising properties. Such high fields also occur in the bunch-bunch collisions at TeV e^+e^- colliders. In both cases, we need laboratory experiments to develop and calibrate the plasma evolution codes that are needed to model these systems.

To achieve fields above the Schwinger critical field in the laboratory, the best method is to interact a relativistic electron beam with an intense laser beam. In a head-on collision with an electron of energy $\gamma_e m_e$, the intensity of the laser field is increased by γ_e^2 when viewed in the frame of the electrons, boosting the laser fields to very high intensity. A 2 GeV electron beam on a focused pulse from a 10 PW laser can achieve $\chi \sim 1$ in the frame of the electrons, and we can

imagine going higher both in the laser intensity and the in the electron beam energy. The E-144 experiment collided a 50 GeV electron beam with pulses from a 1 TW laser. Today, there are two new initiatives. The experiment E-320, at SLAC's FACET-II facility, now commissioning, will interact a 13 GeV electron beam with a 20 TW laser [639, 640]. The LUXE experiment, planned at DESY, will interact a 16.5 GeV electron beam with a 40 TW laser [641, 250]. Both experiments should reach χ values above 1, with possible upgrades to reach $\chi \sim 5 - 10$.

In the mid-2030's, we should have available 100 PW lasers at wavelengths of 1μ . Such high-power lasers are mainly limited in repetition rate, so one might imagine 100 PW pulses at 1 Hz or 10 PW pulses at 10 Hz. We estimate the pulse sizes at 2μ in diameter, with a pulse length of 40 fsec or 120μ . For electron energies of 120 GeV, $\gamma_e = 2.4 \times 10^5$, and ILC beam sizes, these conditions lead to

$$\chi \sim 250 \tag{11.6}$$

deep in the regime beyond the critical field. In this strong field, the radiation length is about 0.3μ .

We envision three stages of strong QED experiments. First, in normal incidence, high energy single electrons would pass through the laser bunch with an optical depth of a few radiation lengths. With a tracker and calorimeter the interaction point to measure the final e^+ , e^- and γ momenta and energies, this experiment would study the primary radiation processes at $\chi \sim 100 - 200$. Second, in head-on collisions, single electrons would initiate QED showers leading to the coherent production of an e^+e^- plasma. The features of this plasma have been simulated in [642]. It will be fascinating to observe the dynamics and modes of excitation of this plasma. Third, an electron beam with bunches of 10^7 particles or more would be collided head-on with the laser bunches. This would produce a dense, incoherent e^+e^- plasma of astrophysical interest. This three-stage program would enter and fully characterize this new regime of QED.

The requirements of the first stage of the program, for single- or few-electron collision and particle tracking and calorimetry, are very similar to the requirements for the LDMX-type dark matter experiment described in the previous subsection. Thus, these experiments could be located in the same experimental hall, swapping targets but keeping much of the infrastructure in place.

Chapter 12

Precision Tests of the Standard Model

12.1 Precision Standard Model theory for ILC

To achieve the goals described in sections 8 and 9, precise predictions for the Standard Model (SM) expectations of the relevant observables are needed. A detailed discussion of the required theory work for studies at $\sqrt{s} \approx 91$ GeV, 160 GeV and 250 GeV can be found in Ref. [643] and references therein. The necessary improvement can be split into three categories:

- Fixed-order calculations: For the Z -pole program, electroweak N³LO corrections as well as leading N⁴LO corrections for the effective Z -fermion vertices are needed. Here “leading” refers to corrections enhanced by powers of the top Yukawa coupling and/or QCD strong coupling. For the 250-GeV program and physics at the WW threshold, NNLO electroweak corrections for $2 \rightarrow 2$ scattering processes are mandatory. In addition, calculations of Higgs decay amplitudes must be completed to NNLO order, in particular, for the Higgs decay $H \rightarrow 4f$. Higher-order QCD corrections to $H \rightarrow gg$ and $H \rightarrow b\bar{b}$ are also needed.

The estimated impact of these corrections on a few key quantities is illustrated in Tab. 12.1. The values in this table should be taken with a grain of salt, since any theory error evaluations of currently unavailable calculations are somewhat speculative.

- To study effects of detector acceptance and background subtraction, Monte-Carlo tools need to be created with the precision of the expected measurements. This requires an accurate treatment of multi-photon initial state radiation and awareness of beam polarization. Furthermore, the Monte-Carlo programs must be matched to the fixed-order calculations discussed in the previous bullet point. Beyond the leading order QCD and electroweak corrections must be merged in an appropriate way. For a more detailed discussion of QED effects, see Ref. [644].
- Theoretical predictions for the precision observables within the SM also require a range of SM parameters as inputs, most notably the top and bottom quark mass, $m_{t,b}$, the strong coupling α_s , and the running electromagnetic coupling at the weak scale, $\alpha(M_Z)$. m_t can be measured

	Current theory error	Projected theory error
M_W [MeV]	4	1
$\sin^2 \theta_{\text{eff}}^\ell$ [10^{-5}]	4.5	1.5
Γ_Z [MeV]	0.4	0.15
R_ℓ [10^{-3}]	6	1.5
$\sigma(HZ)$	1%	0.3%
$\Gamma[H \rightarrow b\bar{b}]$	$< 0.4\%$	0.2%
$\Gamma[H \rightarrow gg]$	3%	1%
$\Gamma[H \rightarrow WW^*]$	0.5%	$< 0.3\%$

Table 12.1: Current and projected theory uncertainties from missing higher orders for the SM prediction of various key precision observables at the ILC (from Ref. [643]). The projected future scenario assumes the availability of N³LO corrections and leading N⁴LO corrections for Z-pole observables, and NNLO electroweak corrections and higher-order QCD corrections for Higgs observables.

with high precision at the ILC, but its extraction from the data requires resummed higher-order QCD corrections computed in an effective field theory framework (see section 10.1.1 for more details). More precise determinations of m_b , α_s and $\alpha(M_Z)$ may be possible with improved lattice QCD calculations [645].

The strong coupling α_s can also be extracted from measurements at ILC itself. One option is the analysis of jet rates and event shapes in $e^+e^- \rightarrow jets$ (see e.g. Refs. [646, 647] and references therein). These methods are subject to sizeable non-perturbative QCD effects that are not fully understood at this point, but further theory developments could make this an attractive option for a high-precision determination of α_s . Another possibility is the determination of α_s from the branching ratio $\Gamma[Z \rightarrow \text{had.}]/\Gamma[Z \rightarrow \ell\ell]$, which is practically free of non-perturbative QCD effects. However, new physics effects can also modify the Z-fermion couplings, so that this extraction method becomes model dependent. Both of these methods could complement a future lattice-QCD determination of α_s with improved precision.

Instead of running on the Z pole, ILC can also produce high-precision measurements of Z boson properties by using the radiative return method at $\sqrt{s} = 250$ GeV, as described in section 9.2. A detailed study of the theoretical needs for this program is still lacking. It will require the evaluation of multiple emissions of collinear initial state photons, see e.g. Ref. [648], as well as full SM corrections to the process $e^+e^- \rightarrow \gamma Z$.

12.2 Standard Model Effective Field Theory

To demonstrate that the SM is violated, it is only necessary to compare a precise theoretical calculation of an appropriate process to an experimental measurement. Usually, though, we want more than this. If a deviation from the SM is found, we would like to pinpoint its origin and express

the deviation in such a way that it can be compared to theoretical models that extend the SM. One way to do this is to follow the route that we took in our discussion of WW pair production in Sec. 8.3, introducing new parameters into the expressions for the production amplitudes and then fitting these parameters to experiment. For the Higgs boson couplings, there is a similar approach, called the κ parameterization [649]. These approaches are frankly phenomenological. In the two case just discussed, the parametrizations are not accurate beyond the leading order and so are inappropriate for precision studies. In addition, these approaches are applied separately for each process under study and thus cannot take into account the synergies that result from combining data from different reactions into a common fit. To address these problems, we need a method that is better grounded in theory.

A powerful solution to these problems is given by Effective Field Theory. In this approach, we view the Standard Model as a part of a larger, more general, theory, that might contain many additional particles. This theory would be described by an underlying Lagrangian \mathcal{L}_0 . The simplest way to proceed from this general starting point is to assume that all particles beyond those of the Standard Model itself are much heavier than the W and Z ; we will use M to represent their mass scale. It is then possible to integrate out all of the fields associated with the new heavy particles. This produces an effective Lagrangian in which the corrections due to the heavy particles are represented by operators that depend on the light fields. We can represent the result of this calculation as a sum over operators of successively higher dimensions,

$$\mathcal{L}_{eff} = \mathcal{L}_4 + \sum_i \frac{b_i}{M} \mathcal{O}_i + \sum_j \frac{c_j}{M^2} \mathcal{O}_j + \dots \quad (12.1)$$

In this expression, \mathcal{L}_4 contains all possible operators of dimension 4 and lower, the \mathcal{O}_i are operators of dimension 5, the \mathcal{O}_j are operators of dimension 6, and so on. The allowed operators are restricted by symmetry, since \mathcal{L}_{eff} must have the symmetries of \mathcal{L}_0 after whatever symmetry breaking is generated at the scale M . The factors of M in (12.1) reflect the dimensions of the operators and the requirement that \mathcal{L}_{eff} has the units of (mass)⁴.

There is a very attractive assumption that restricts this framework. We can take the effective Lagrangian \mathcal{L}_{eff} to have the gauge symmetry $SU(3) \times SU(2) \times U(1)$ and the field or particle content of the SM. A stronger assumption is that the Higgs field is present in \mathcal{L}_{eff} as an $SU(2)$ doublet field $\Phi(x)$ as in the SM. Then the SM gauge symmetries are realized linearly on the fields in \mathcal{L}_{eff} . Physically, this assumption treats the Higgs boson as light field at the scale m_W while it treats all BSM effects as resulting from heavy fields at the scale M . In the effective Lagrangian, the Higgs field is the sole source of $SU(2) \times U(1)$ symmetry breaking. Operators in \mathcal{L}_0 that obtain expectation values after electroweak symmetry breaking are represented in the effective theory as terms of the form

$$\mathcal{O}_j \rightarrow A \Phi^\dagger \Phi \quad (12.2)$$

where A is the result of a loop calculation involving the heavy fields, either a c-number or a more general invariant function of the field Φ . This framework is called Standard Model Effective Field Theory (SMEFT).

These assumptions lead to some simplifications. It is well-known that the SM is the most general renormalizable quantum field theory with the known particle content and the gauge symmetry

$SU(3) \times SU(2) \times U(1)$. Thus, \mathcal{L}_4 in (12.1) is exactly the SM Lagrangian. The only possible operators of dimension 5 are neutrino mass terms (10.2), and, similarly, operators with odd dimension parametrize fermion-number-violating interactions. Thus, for the description of collider physics, we can restrict ourselves to operators of even dimension. We then rewrite (12.1) as

$$\mathcal{L}_{eff} = \mathcal{L}_{SM} + \sum_j \frac{c_j}{v^2} \mathcal{O}_j + \sum_k \frac{d_k}{v^4} \mathcal{O}_k + \dots \quad (12.3)$$

To quote definite values for the coefficients c_j , d_k , *etc.*, we will use the electroweak symmetry breaking scale $v = 246$ GeV as the dimensionful quantity. Then, if M is at the TeV scale, the coefficients in (12.3) would naturally be of the order of magnitude: $c_j \sim 10^{-2}$, $d_k \sim 10^{-4}$, *...*, perhaps with additional suppression by small coupling constants. In this naive method of estimation, the Higgs boson couplings, TGCs, and 4-fermion couplings would be expected to receive corrections at the percent level from the c_j coefficients of dimension-6 operators while the effect of the d_k coefficients would be ignorable. Of course, the actual values of the SMEFT coefficients would be determined in each particular theoretical model, which might provide large or small order-1 factors. But we will take as a working assumption that dimension-6 coefficients give the only relevant corrections at the levels of precision that will be achieved by Higgs factories. This framework has model-dependence, but that dependence is weak. In particular, it does not prejudice us toward any specific type of model but rather incorporates on an even footing models from weakly coupled scalar extensions, to supersymmetry, and to composite Higgs and extra dimensional models of new physics.

There might be several reasons to question these assumptions. First, as we have emphasized in Sec. 10.5, there might be new particles that exist in the mass region of a few hundred GeV but have not been discovered in LHC searches. Such particles might give large corrections to \mathcal{L}_{eff} that are not well described by dimension 6 operators alone. The discovery of large corrections will of course be welcome; as for the interpretation, it should be noted that the effects of the top quark and the Higgs boson on precision electroweak observables are well-described by the S and T parameters, which are linear combinations of the dimension 6 coefficients, even though these particles do not have masses much greater than the Z mass. Second, there might be very light new particles, such as those described in Secs. 10.6 and 11.1. We will assume that these particles can give additional contributions to the Higgs boson width but do not affect the precision electroweak observables. This is plausible because of their very feeble couplings.

A more general issue is our assumption that the Higgs boson is the sole source of $SU(2) \times U(1)$ symmetry breaking. It is possible that there is an additional $SU(2) \times U(1)$ -breaking expectation value in what we have deemed the heavy sector. This might be reflected in a special treatment of the mass generation for the top quark with respect to that for the vector bosons. Another possibility is that a new scalar obtains a large fraction of its mass from the Higgs boson. In these cases, the appropriate effective Lagrangian would be one with only the subgroup $SU(3) \times U(1)$ realized linearly and the broken generators of $SU(2) \times U(1)$ realized nonlinearly. This is called the Higgs Effective Field Theory (HEFT) or the Electroweak Chiral Lagrangian (EWChL) [650, 651]. The HEFT allows considerably more parameter freedom than the SMEFT. In particular, while in the SMEFT the deviations from the SM values of the Higgs boson couplings are naturally of the order of several percent, in the HEFT these deviations are unconstrained by dimensional analysis and can be of

order 1. The LHC experiments have measured the Higgs boson couplings to be in good agreement with their SM values at the 10–20% level. This situation is expected in the SMEFT—and points to smaller corrections that can be measured at the next level of precision—but it requires special explanation in the HEFT. For that reason, we consider the SMEFT to be preferred experimentally, and we will work in that context. It is possible but rather difficult to distinguish the HEFT and SMEFT frameworks experimentally. This requires measurement of several cross sections for multiple Higgs production. Please see [652, 653, 654] for a detailed discussion.

In this report, we will use the SMEFT as a practical tool for combining measurements from a number of different ILC reactions in a coherent framework. The next section will explain how we do this. Other approaches to the global fitting of SMEFT parameters to data from e^+e^- Higgs factories are described in [655, 656, 657]. Despite the differences in philosophy among these papers, the actual results are in good agreement, giving confidence in the validity of this approach.

12.3 A practical SMEFT analysis for ILC

The ILC requires a model framework to make specific statements about the Higgs boson couplings and electroweak observables. An important property of the Higgs boson is its total width Γ_H . The total width of the Higgs boson must be known to interpret the data. The most commonly measured observable is the rate of a Higgs boson process, which is given by

$$\sigma \cdot BR(e^+e^- \rightarrow A\bar{A}) = \sigma(e^+e^- \rightarrow H + X) \cdot \frac{\Gamma(H \rightarrow A\bar{A})}{\Gamma_H} \quad (12.4)$$

Theoretical predictions, both in the SM and in new physics models, are given for the absolutely normalized partial widths $\Gamma(H \rightarrow A\bar{A})$. To extract these, we need to know Γ_H . On the other hand, Γ_H has the SM value of 4.3 MeV for a 125 GeV Higgs boson mass. This value is so small that it cannot be extracted with high precision directly from experiment, either at e^+e^- or at hadron colliders. To determine Γ_H , we need a model.

The model used to extract Γ_H should on the one hand be general and model-independent, while on the other hand it should have few enough parameters that these can all be determined from data without degeneracies. Such a model must be a compromise, but hopefully we can use theory insight to choose a model that satisfies both requirements as well as possible.

It is quite remarkable that the ILC provides a sufficiently large number of measurements of sufficient specificity that we can use SMEFT as a model to reconstruct the Higgs width. General SMEFT has of course an infinite number of parameters, and even truncating SMEFT to consider only dimension-6 baryon- and lepton-number conserving operators leads to 76 new coefficients for 1 generation and 2499 for three generations. However, the set of coefficients involved in ILC reactions at the tree level is much smaller. We will argue in a moment that 18 operators suffice. Choosing these as parameters of the model, we add 4 relevant SM parameters and 2 parameters representing the Higgs boson decay rates to invisible and unclassified exotic decay modes. Removing, for the moment, the Higgs self-coupling and a particular 4-fermion operator constrained by measurements in that sector, we arrive at a practical SMEFT fitting scheme with 22 parameters [514, 658]. These

parameters can be fit to measurements of Higgs decays. But also, since the SMEFT Lagrangian is intended to be a complete low-energy representation of particle physics, we can add data from precision electroweak measurements, $e^+e^- \rightarrow W^+W^-$, fermion pair production, and other reactions that can be studied at the ILC. With care, we can also make use of particular quantities measured at the LHC. This gives a robust framework to use in translating the ILC data to absolutely normalized values of the Higgs boson partial widths and the value of the total Higgs width Γ_H .

The model prescriptions for this “model-independent” framework are:

1. We truncate the SMEFT to renormalizable and dimension-6 operators only. The fit is done strictly at the linear level in SMEFT operator coefficients.
2. We calculate the new physics contributions to ILC processes at the tree level only, and drop all operators that do not contribute in the tree-level expressions. It is consistent to drop all 4-fermion operators except for the operator that corrects G_F and to drop all operators that contain quark and gluon fields except for the operators that correct the W and Z total widths. In this framework, corrections to the Higgs boson self-coupling do not contribute to the set of observables that we consider. We will discuss fits including the Higgs self-coupling in Sec. 12.5.
3. Given the strong constraints that will result from measurements of $e^+e^- \rightarrow \mu^+\mu^-$, we drop the 4-fermion contribution to G_F .
4. We assume lepton universality. That is, we assign the same coefficients to corresponding operators with e , μ , and τ .
5. Results from the LHC and expected results from the HL-LHC can be added only if these do not expand the set of SMEFT operators included in the fit. We expect that the ratios of Higgs boson branching ratios to $\gamma\gamma$, ZZ^* , $Z\gamma$, and $\mu^+\mu^-$, all measured in central Higgs boson production, meet this criterion, and we will include only these inputs.
6. We drop all CP-violating operators and all operators giving flavor-nonconserving Higgs boson decays. This is justified because these operators with coefficients c_i contribute to the CP-conserving, flavor-conserving Higgs observables only in order c_i^2 , while we keep new physics contributions in linear order only. Of course, it is extremely important to search for these couplings, as we have emphasized in Sec. 8.1, but these searches are outside the fit presented here.
7. We include invisible and unclassified exotic decays of the Higgs boson with two parameters, the Higgs branching ratios to these modes. We assume that the light states into which the Higgs boson could decay have no effect on precision electroweak observables. Note that Higgs decays to invisible final states are directly measurable from $e^+e^- \rightarrow HZ$ by observing the Z recoil against nothing. Also, very general classes of modes of Higgs decay to exotic final states are directly observable, as explained in Sec. 8.2. Thus, leaving this branching ratio as a free parameter is a very conservative assumption.

It can be shown that the assumptions 3 and 4 can be dropped from the analysis with almost no effect on the projections for Higgs couplings by including additional ILC measurements in the fit.

To analyze this point, we must carry out a more complicated fit with many additional parameters. Such a fit would also include the separate precision electroweak results for e , μ , and τ and estimates of the precision with which 4-fermion processes will be measured at the ILC. This fit is described in the presentation [659]; it gives essentially the same results as those shown below. It is noteworthy that our fits are so overconstrained that G_F is not needed as an input.

These assumptions do include the assumption of a clear separation in mass scale between the particles of the SM—including the Higgs boson—and particles mediating new interactions. However, there is no assumption that the new physics model be of a specific type, for example, weak or strong coupling, leptophilic or leptophobic, *etc.* The use of SMEFT has a clear advantage over other modelling schemes for the Higgs width in that it allows us to use constraints from the well-established gauge symmetry $SU(2) \times U(1)$ to reduce the number of parameters.

We then take the set of SMEFT operator coefficients used in the practical fit as a subset of the full set of dimension 6 operators in the Warsaw basis [660]. Our effective Lagrangian is

$$\mathcal{L} = \mathcal{L}_{SM} + \mathcal{L}_H + \mathcal{L}_{W,B} + \mathcal{L}_{\Phi\ell} + \mathcal{L}_{\Phi q} + \mathcal{L}_{\Phi f} + \mathcal{L}_g . \quad (12.5)$$

Here \mathcal{L}_{SM} is the Standard Model Lagrangian, Φ is the scalar Higgs doublet field. For definitiveness, we take the defining mass scale of the dimension 6 operator coefficients to be $v = 246$ GeV. Then the dimension 6 terms are given by, for the terms depending only on the Higgs and vector boson fields,

$$\begin{aligned} \mathcal{L}_H &= \frac{c_H}{2v^2} (\partial_\mu \Phi^\dagger \Phi)^2 + \frac{c_T}{2v^2} (\Phi^\dagger \overleftrightarrow{D}^\mu \Phi) (\Phi^\dagger \overleftrightarrow{D}_\mu \Phi) - \frac{\lambda c_6}{v^2} (\Phi^\dagger \Phi)^3 \\ \mathcal{L}_{W,B} &= \frac{g^2 c_{WW}}{v^2} (\Phi^\dagger \Phi) W_{\mu\nu}^a W^{a\mu\nu} + \frac{2gg' c_{WB}}{v^2} (\Phi^\dagger t^a \Phi) W_{\mu\nu}^a B^{\mu\nu} \\ &\quad + \frac{g'^2 c_{BB}}{v^2} (\Phi^\dagger \Phi) B_{\mu\nu} B^{\mu\nu} + \frac{c_{3W}}{6v^2} \epsilon_{abc} W_\mu^{a\nu} W_\nu^{b\rho} W_\rho^{c\mu} . \end{aligned} \quad (12.6)$$

The terms depending on the Higgs fields and the electron fields are

$$\begin{aligned} \mathcal{L}_{\Phi\ell} &= \frac{c_{\Phi L}}{v^2} (\Phi^\dagger i \overleftrightarrow{D}_\mu \Phi) (\bar{L}^\dagger \gamma^\mu L) + \frac{4c'_{\Phi L}}{v^2} (\Phi^\dagger t^a i \overleftrightarrow{D}_\mu \Phi) (\bar{L}^\dagger t^a \gamma^\mu L) \\ &\quad + \frac{c_{\Phi E}}{v^2} (\Phi^\dagger i \overleftrightarrow{D}_\mu \Phi) (\bar{e}^\dagger \gamma^\mu) , \end{aligned} \quad (12.7)$$

where L and e are the left- and right-handed fields of the first lepton generation and $t^a = \sigma^a/2$ is the weak isospin generator. The operators depending on the Higgs fields and other quark and lepton fields are defined similarly. In these formulae,

$$\begin{aligned} \Phi^\dagger \overleftrightarrow{D}_\mu \Phi &= (\Phi^\dagger D_\mu \Phi - (D_\mu \Phi)^\dagger \Phi) \\ \Phi^\dagger \overleftrightarrow{D}_\mu^a \Phi &= (\Phi^\dagger t^a D_\mu \Phi - (D_\mu \Phi)^\dagger t^a \Phi) \end{aligned} \quad (12.8)$$

The dimension-6 operator that shift the Higgs- τ Yukawa coupling is

$$\mathcal{L}_{\Phi\tau} = \frac{y_\tau c_\tau}{v^2} (\Phi^\dagger \Phi) (\bar{L}_\tau \cdot \Phi e_\tau) , \quad (12.9)$$

and the other operators that contribute to scalar couplings are constructed in a similar way. There are dimension-6 operators that couple to the Higgs boson through a magnetic moment interaction, but these do not contribute to Higgs couplings at the tree level. The operator

$$\mathcal{L}_g = \frac{g_s^2 c_{gg}}{v^2} (\Phi^\dagger \Phi) G_{\mu\nu}^a G^{a\mu\nu} \quad (12.10)$$

shifts the Higgs boson partial width to gluons. This partial width also receives corrections from loop diagrams involving the top quark and SMEFT operators associated with the top quark. But we are concerned here with only one amplitude, the Hgg coupling on the Higgs boson mass shell, so we will represent all of these effects by the single parameter c_{gg} .

Our practical SMEFT fit then contains 4 SM parameters, 6 parameters from (12.6) (excluding c_6), 3 parameters from (12.7), 2 additional combinations of coefficients that shift the W and Z widths, 5 parameters of the form (12.9) for the Higgs couplings to b , t , c , μ , and g , plus the two parameters for invisible and exotic Higgs decays mentioned in point 6 of our assumptions, for a total of 22 parameters.

12.4 Expectations for the practical SMEFT fit

We are now ready to present the expected uncertainties on individual Higgs boson couplings that arise from the SMEFT fit described in the previous section. The results here represent a minor update of the similar fit presented in [428]. Similar fits with slightly different assumptions but very similar results have been carried out in [656].

As we have described in [428], the inputs to the fit are the defining SM observables α , m_Z , G_F , and m_h , and the additional electroweak observables m_W , A_ℓ , $\Gamma(Z \rightarrow \ell^+\ell^-)$, Γ_Z , and Γ_W . For Γ_W , we expected that this can be improved to a determination at the level of 10^{-3} from the electroweak and the value of $BR(W \rightarrow \ell\nu)$ measured in $e^+e^- \rightarrow W^+W^-$. Our new, still preliminary, studies show that this is conservative. We also include the measurements of the cross section for $e^+e^- \rightarrow HZ$ and the various $\sigma \times BR$ values for Higgs decays in this mode, including the invisible mode, corresponding values of $\sigma \times BR$ in the WW fusion reaction, and the measurements of the TGC parameters. Our methods for obtaining estimates of uncertainties in these quantities were explained in Chapters 8 and 10. In all cases, the integrated luminosities used are those in run plan shown in Fig. 5.2. Finally, to close the fit, we need some measurements from the LHC, in particular, the ratios of branching ratios of the Higgs boson to ZZ , $\gamma\gamma$, γZ , and $\mu^+\mu^-$. With these inputs, the 22-parameter fit has no unconstrained direction.

The results from the fit are shown in Fig. 12.1 and in Tables 12.2 and 12.3. In the figure and in Table 12.2, we show the expectations from the 22-parameter fit, and, for comparison with SMEFT fits in [656], and elsewhere, expectations from a 20-parameter fit that assumes that the Higgs boson has no exotic decays. We also include the improved estimates for and the Higgs self-coupling and the top quark Yukawa coupling that were presented in Secs. 10.2.2 and 10.2.3.

It is interesting to ask what level of precision in the precision electroweak observables is needed to achieve the values quoted in this table. Actually, the projected uncertainties in Table 12.2 are

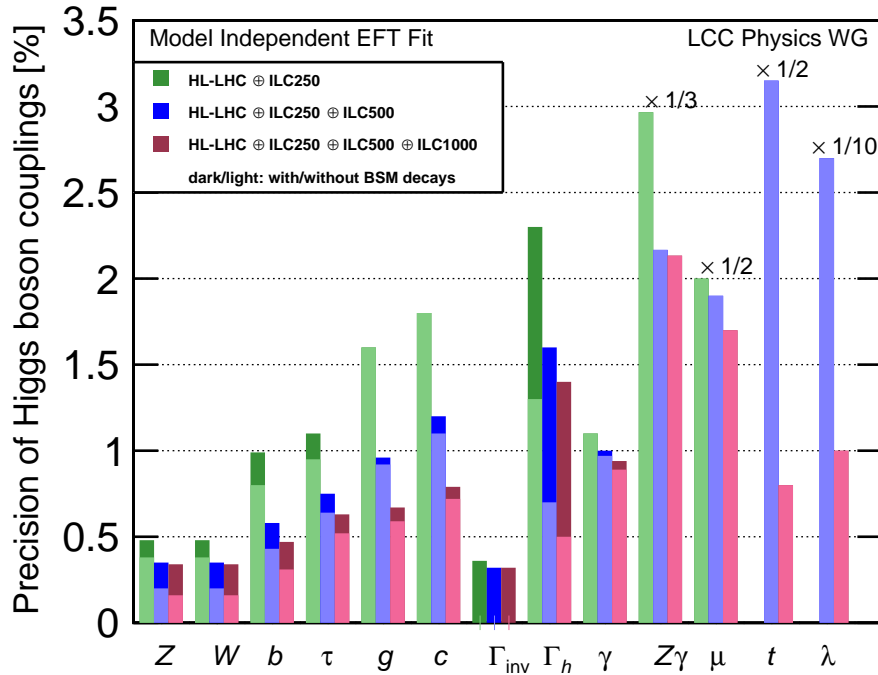


Figure 12.1: Projected Higgs boson coupling uncertainties for ILC250, ILC500, and ILC1000, also incorporating results expected from the HL-LHC, based on the SMEFT analysis described in the text. The darker bars show the results allowing invisible and exotic Higgs decay channels; the lighter bars assume that these BSM decays are not present. The column λ refers to the HHH coupling. In the last four columns, all bars are rescaled by the indicated factor. From [428].

obtained using only the level of precision that is achievable from running at 250 GeV and analyzing the radiative return reactions to improve the uncertainty in A_ℓ . It is difficult to see improvements beyond this point as long as the possibility of uncharacterized exotic decays is included in the fit. So, in Table 12.3, we assume that there are no exotic decays and carry out the 20-parameter fit using the levels of precision expected from radiative return, from the dedicated Z pole program discussed in Sec. 9.3, and from the levels of precision expected from the TeraZ program at the FCC-ee [661].

12.5 Expectations for the Higgs self-coupling

Up to this point, we have not included in our fits the coefficient c_6 that modifies the Higgs self-coupling,

$$c_6 = \lambda_{eff}/\lambda . \quad (12.11)$$

coupling	ILC250		ILC500		ILC1000	
	full	no BSM	full	no BSM	full	no BSM
hZZ	0.49	0.38	0.35	0.20	0.34	0.16
hWW	0.48	0.38	0.35	0.20	0.34	0.16
hbb	0.99	0.80	0.58	0.43	0.47	0.31
$h\tau\tau$	1.1	0.95	0.75	0.63	0.63	0.52
hgg	1.6	1.6	0.96	0.91	0.67	0.59
hcc	1.8	1.7	1.2	1.1	0.79	0.72
$h\gamma\gamma$	1.1	1.0	1.0	0.96	0.94	0.89
$h\gamma Z$	8.9	8.9	6.5	6.5	6.4	6.4
$h\mu\mu$	4.0	4.0	3.8	3.7	3.4	3.4
htt	—	—	6.3	6.3	1.0	1.0
hhh	—	—	20	20	10	10
Γ_{tot}	2.3	1.3	1.6	0.70	1.4	0.50
Γ_{inv}	0.36	—	0.32	—	0.32	—

Table 12.2: Projected uncertainties in the Higgs boson couplings for the ILC250, ILC500, and ILC1000, with precision LHC input. All values are *relative* errors, given in percent (%). The columns labelled “full” refer to a 22-parameter fit including the possibility of invisible and exotic Higgs boson decays. The columns labelled “no BSM” refer to a 20-parameter fit including only decays modes present in the SM.

coupling	ILC250			ILC500		
	RadRtrn	GigaZ	TeraZ	RadRtrn	GigaZ	TeraZ
hZZ	0.38	0.35	0.30	0.20	0.20	0.19
hWW	0.38	0.35	0.31	0.20	0.20	0.19
hbb	0.80	0.78	0.77	0.43	0.43	0.43
$h\tau\tau$	0.95	0.94	0.92	0.63	0.63	0.63
hgg	1.6	1.6	1.6	0.91	0.91	0.91
hcc	1.7	1.7	1.7	1.1	1.1	1.1
$h\gamma\gamma$	1.0	1.0	1.0	0.96	0.96	0.96
$h\gamma Z$	8.9	8.5	7.9	6.5	6.4	5.8
$h\mu\mu$	4.0	3.9	3.9	3.7	3.7	3.7
Γ_{tot}	1.29	1.26	1.21	0.70	0.70	0.69

Table 12.3: Projected uncertainties in the Higgs boson couplings for the ILC250 and ILC500, with precision LHC input, showing the dependence on precision electroweak measurements. All values are *relative* errors, given in percent (%). The fit assumes that there are no exotic Higgs boson decays. The columns labelled RadRtrn use the uncertainties expected from the radiative return events at 250 GeV. The columns labelled GigaZ use the uncertainties expected from the ILC dedicated Z pole program discussed in Sec. 9.3. The columns labelled TeraZ use the uncertainties expected from the TeraZ program at the FCC-ee [661].

coupling	ILC500		ILC500 w. c_6	
	full	no BSM	full	no BSM
hZZ	0.35	0.20	0.37	0.21
hWW	0.35	0.20	0.37	0.21
hbb	0.58	0.43	0.60	0.43
$h\tau\tau$	0.75	0.63	0.78	0.64
hgg	0.96	0.91	0.97	0.92
hcc	1.2	1.1	1.2	1.1
$h\gamma\gamma$	1.0	0.96	1.0	0.97
$h\gamma Z$	6.5	6.5	7.0	6.4
$h\mu\mu$	3.8	3.7	3.8	3.7
c_6	—	—	53.	52.
Γ_{tot}	1.6	0.70	1.6	0.70
Γ_{inv}	0.36	—	0.32	—

Table 12.4: Projected uncertainties in the Higgs boson couplings for the ILC500, including loop effects proportional to the Higgs self-coupling. All values are *relative* errors, given in percent (%). The rest of the notation is as in Table 12.2.

Still, the measurement of the Higgs self-coupling is an important goal for future colliders. We have discussed already in Sec. 10.2.2 how the ILC can determine the Higgs self-coupling through two separate processes for double Higgs production. Here we will fill in some details of the interpretation of these processes in SMEFT.

The reaction of double Higgs-strahlung, $e^+e^- \rightarrow ZHH$, contains both diagrams with double Higgs emission from the Z as well as a diagram containing the Higgs self-coupling. There are also several new vertices from the dimension-6 SMEFT Lagrangian that contribute to this process. Thus, it is not correct to treat the effect of the self-coupling in isolation. One must consider all possible effects on the cross section from dimension-6 SMEFT contributions, and it might not be that the variation of the self-coupling is the dominant one. This question was addressed in [514]. The intermediate result did not look promising. For unpolarized beams at ILC500, the dependence of the cross section on SMEFT parameters includes

$$\sigma/\sigma_{SM} = 1 + 0.56c_6 - 4.15c_H + 15.1c_{WW} + 62.1(c_{\Phi L} + c'_{\Phi L}) - 53.5c_{\Phi E} + \dots, \quad (12.12)$$

In addition to c_6 , many other dimension-6 coefficients affect this process, and some enter with very large numerical factors. However, all of the other dimension-6 parameters in (12.12) are strongly constrained by the SMEFT analysis of single-Higgs production, sufficiently so that the effect of those terms is completely negligible with respect to the statistical error on the value of the cross section.

It is also possible to extract information on the Higgs self-coupling from the values of single-Higgs cross sections. The Higgs self-coupling enters the cross section for $e^+e^- \rightarrow HZ$ and the partial widths for $H \rightarrow ZZ^*$ and $H \rightarrow WW^*$ through a vertex correction shown in Fig. 12.2. In [662], it was pointed out that the vertex loop correction has a sharp dependence on the momentum of the

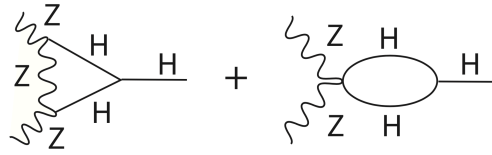


Figure 12.2: Vertex correction giving a dependence of the HZZ and HWW vertices on the Higgs self-coupling.

off-shell vector boson near the threshold for $V^* \rightarrow HV$ and, thus, the effect might be measurable at e^+e^- colliders. At ILC250, the size of the enhancement to the $e^+e^- \rightarrow HZ$ cross section is about 1.5%. Again, the effect can easily be obscured by variation of other SMEFT parameters. The formula comparable to (12.12) for this cross section at 250 GeV is

$$\sigma/\sigma_{SM} = 1 + 0.015c_6 - c_H + 4.7c_{WW} + 13.9(c_{\Phi L} + c'_{\Phi L}) - 12.1c_{\Phi E} + \dots, \quad (12.13)$$

In particular, the effect at any single energy is highly degenerate with an enhancement of the HZZ coupling, for example, through a change in c_H . It is possible to gain some sensitivity by comparing the $e^+e^- \rightarrow HZ$ cross sections at two different energies, for example, 250 and 500 GeV. Table 12.4 shows the effect of a SMEFT fit that adds the 1-loop contributions to the Higgs vertices to the calculation of tree diagrams. This analysis gives an uncertainty of 53% on c_6 , which can slightly improve the uncertainty from the more direct measurement of double Higgs production. More relevant, though, is the fact that the determination of the other SMEFT parameters contributing to the Higgs boson couplings is very robust with respect to the addition of this parameter.

Chapter 13

Big Physics Questions Addressed by ILC

The discovery of the 125 GeV Higgs boson poses even more questions that it answers. Within the SM, the Higgs boson explains the the origin of all particle masses through the Higgs mechanism. The 125 GeV boson seems to fulfill this role, but still there remain many questions both about this boson and about the SM itself. Is this boson solely responsible for the breaking of electroweak symmetry and the generation of mass? Is it a singleton, or is it merely the first of several Higgs bosons? What sets the mass parameter for this boson? Can we explain electroweak symmetry breaking in physical terms, with a theory in which that mass is computable? If the SM is correct up to very high scales and the its parameters are equal to the current central values, the vacuum we see is unstable. Is this the true situation, and, either way, what is the true behavior of the vacuum of the universe far in the future? In addition, the discovery of the Higgs boson sharpens questions that have been asked since the SM was first formulated. What is the origin of flavor and the fermion generations? Why is there more matter than antimatter? What is the nature of dark matter? What other types of new matter exist in nature?

Through its comprehensive set of precision measurements of the couplings of the 125 GeV Higgs boson, and through its larger program of measurements of electroweak reactions at the weak-interaction scale, the ILC has the power to give insight into all of these questions. In this chapter, we will outline these questions in more detail and describe their relation to ILC measurements. In the next chapter, we will illustrate the insights from the ILC in a complementary way, through quantitative comparison of the ILC projected measurements with the predictions of models of physics beyond the SM.

13.1 Can the Standard Model be exact to very high energies?

At TeV energies, the Higgs field quartic coupling increases with energy due to renormalization-group running. However, it is a prediction of the SM that this coupling turns over and begins to

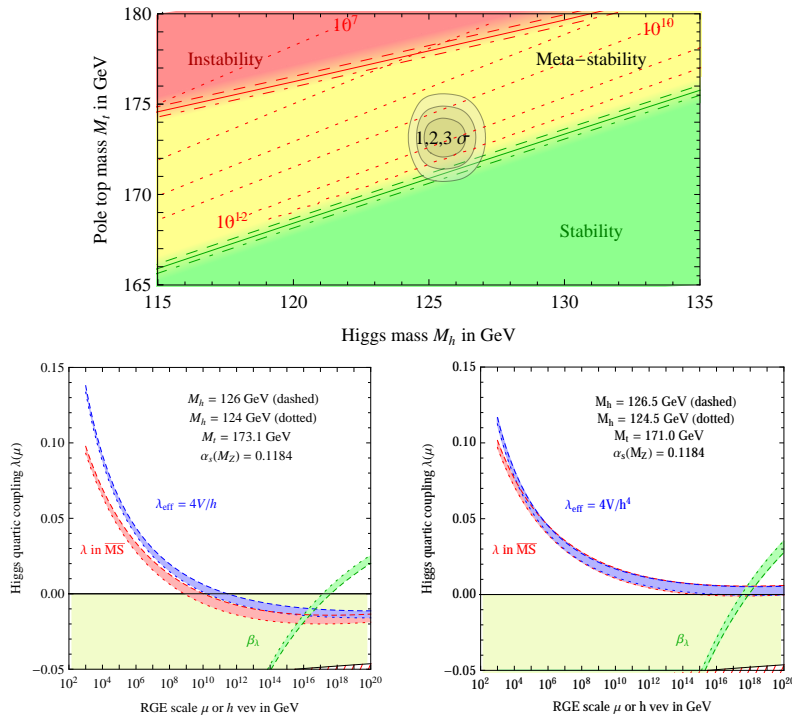


Figure 13.1: top: Regions of stability, metastability, and instability of the SM vacuum, shown as a function of m_H and m_t , showing the current best values in the region of metastability. bottom: Renormalization-group evolution of the Higgs quartic coupling to large Q assuming $m_t = 173.1$ GeV (left) and $m_t = 171.0$ GeV (right). From [663].

decrease at very high energies. For the current central values of SM parameters, the Higgs quartic coupling becomes negative at about 10^{11} GeV, leading to a vacuum instability, assuming that the SM is still exact at those energies. Within the SM, the outcome depends sensitively on the values of the Higgs boson mass and the top quark mass. We do not know today what the SM predicts for our universe.

Precision measurements of these two quantities to the accuracy projected for the ILC will resolve this. The nature of the SM vacuum state as a function of the top quarks and Higgs boson masses has been studied in [663] and more recently in [664, 665]. The current situation is shown in Fig. 13.1. As we can see from the bottom graphs in this figure, a change of 2 GeV in the central value of the top quark mass brings us from eventual instability to stability. Since the calculation uses the short-distance value of the top quark mass, the uncertainty must include the error in converting the top quark mass as measured in experiment (*e.g.*, the pole mass) to a short-distance value (*e.g.*, the \overline{MS} mass). Thus, this calculation, within the SM, requires very precisely understood inputs at the energy of the electroweak scale. We have seen above that the ILC will determine the Higgs boson mass to a precision of 15 MeV and the short-distance top quark mass to a precision of 40 MeV, well within the requirements for a definitive statement.

If the future experiment proves the SM vacuum metastable, two possibilities arise. On the one hand, the SM could be exactly correct up to the scale of the instability. In that case, we will need to understand how the universe before the electroweak phase transition settled down to the metastable vacuum of today. Alternatively, new physics may arise below the energy scale of 10^{10} GeV, where the value of the four-point interaction of the Higgs boson becomes negative, and this could change the physics of the Higgs potential in such a way as to make the vacuum state stable. Such new physics may exist above the scale of 1 TeV or so, which is directly or indirectly explored in current particle experiments, but it may also occur at lower scales, since the nature of the Higgs boson remains largely unexplored.

Another intriguing possibility is that the Higgs boson and top quark masses are such that the balance point toward instability is moved just to Planck scale, as indicated in the right-hand graph in Fig. 13.1. In this case, it is possible to arrange that the Higgs field is the inflaton which is responsible for generating cosmic structure [666, 667].

We do not know whether the Standard Model is correct up to high energy scales. If we relax this assumption, there are relatively straightforward extensions of the Standard Model that can make the vacuum stable. For example, in a model where singlet scalar fields interact with the Higgs boson, the vacuum can be stable for some parameter regions of the model. It is even possible that such extension of the SM can accommodate dark matter by requiring Z_2 symmetry. The Higgs boson couplings can be different from the standard model ones, and such deviations may be detected by the precision measurement of the Higgs bosons. These models can contain additional first-order phase transitions. In this case, significant gravitational waves may be produced by a phase transition in the early universe and observed as a background in low-frequency gravitational wave observations.

It is also possible that the Higgs sector is stabilized by high symmetry. Such a symmetry would require many new particles to completely change the Higgs boson interaction and its high-energy behavior. An example of such a scenario is the appearance of supersymmetry at high energies. In a supersymmetric model, all bosons have partner fermions and vice versa due to the symmetry of the theory. The model also relates Higgs four-point couplings to the fourth power of gauge couplings so that the scalar potential is bounded from below. The supersymmetric models have at least two Higgs doublets, namely, five Higgs bosons. In addition, the down-type quarks and leptons can have large Yukawa coupling. The Higgs boson decay can receive significant corrections detectable by the Higgs factories if the masses of the additional Higgs bosons are around 1 TeV. In addition to that, the predicted partners can be directly searched for at a linear collider or through the measurement of oblique corrections.

The other new physics possibility between the Planck scale to the weak scale is the change of space-time. In the warped extra-dimensional model, the Higgs boson can be the field in the IR brane. Yukawa coupling to the fermions is determined by the overlap of the fermion wave function in 5 dim to the Higgs boson on the brane. The effective field theory involving Higgs boson higher-order terms can express the physics picture, and the precision study of Higgs interaction can provide crucial information.

It is quite generally true that the high-precision measurement of Higgs boson and top quark masses can give profound insight into all of these possibilities. The measurement must be carried

out with a high degree of confidence and control of experimental and theoretical systematic errors. That is possible uniquely at an e^+e^- collider such as the ILC.

13.2 Why is there more matter than antimatter?

The origin of matter is no less compelling a mystery than the origin of mass. Assuming inflationary cosmology, the universe began in a state with equal amounts of matter and antimatter. From this starting point, the abundance of matter over anti-matter can be explained starting from symmetric initial conditions if some epoch in the early universe satisfies the Sakharov conditions— B violation, C and CP violation, and loss of thermal equilibrium. These ingredients seem suggestively present in the quark sector of the SM itself, but, quantitatively, the asymmetry generated is too small by 10 orders of magnitude. The problem is that the quarks that are sensitive to the CP-violating CKM angles are very light compared to the Higgs vacuum expectation value. So it is possible to generate the observed baryon asymmetry in simple extensions of the Standard Model in which there are new particles and new sources of CP violation at or above the weak interaction scale. These models must also include a mechanism for taking the universe out of thermal equilibrium, such as a first-order phase transition or late-decaying particles. Models in which the out-of-equilibrium events take place at or below the TeV scale can be directly tested at the ILC. A prominent class of models is that in which the electroweak transition itself becomes first-order due to the coupling of the Higgs boson to other new particles. Another interesting class of model involves dark sector particles or heavy neutrinos that would be revealed at the ILC.

In the SM, the electroweak phase transition (EWPT) is predicted to be a second-order, or nearly so. A first-order phase transition, necessary for electroweak baryogenesis, requires a substantial modification of the SM Higgs potential at finite temperature. Generically, this is only possible if new particles with substantial couplings to the Higgs boson, and with masses below the TeV scale, are present. Such particles can be searched for directly at the LHC, and some possibilities (for example, top quark partners in supersymmetric models) are already strongly constrained. However, other options, such as new gauge-singlet scalar fields coupled to the Higgs, remain wide open. Precision Higgs measurements at the ILC will be sensitive to such scenarios. In particular, the $e^+e^- \rightarrow Zh$ cross section will be measured at the level sensitive to generic one-loop corrections to the Higgs propagator. This measurement will probe a wide range of first-order EWPT models, including those with a gauge-singlet scalar. Likewise, models with a first-order EWPT typically predict significant deviations in the Higgs cubic coupling, which can be discovered at the 500 GeV or 1 TeV ILC upgrade.

An illustrative scan of the parameter space of a model with a single real scalar mixing with the SM Higgs boson is shown in Fig. 13.2 [668]. The blue points represented models with a strongly first-order electroweak phase transition. In this class of models, the Higgs self-coupling is enhanced almost by a factor of 2, and the Higgs couplings to ZZ is has a relatively large correction (about 5%) compared to the SM prediction. With the precisions explained in previous sections, uncertainties of 23% on the Higgs self-coupling and 0.4% on the HZZ coupling after the 500 GeV stage, the ILC will be able to discover these effects with high confidence.

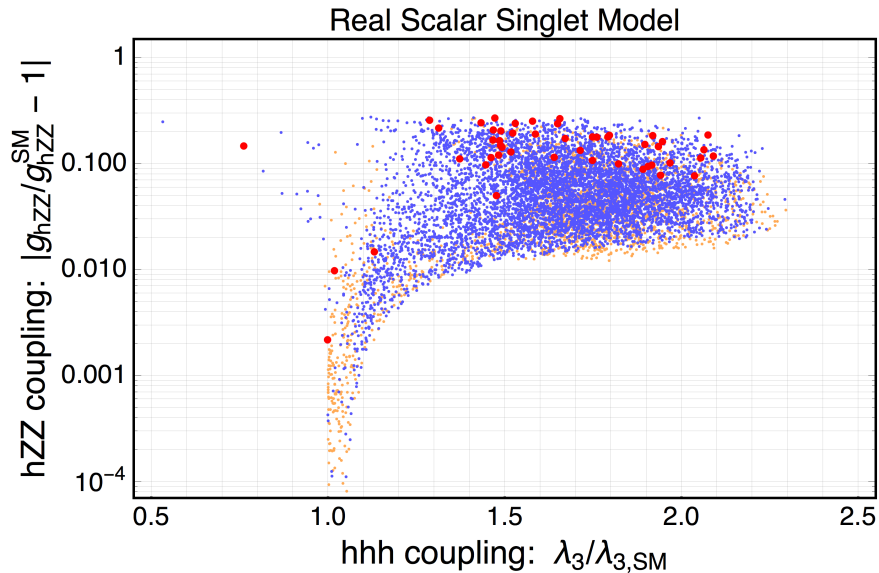


Figure 13.2: Scan of the parameter space for a model of baryogenesis at the electroweak scale with one new electroweak singlet Higgs field mixing with the SM Higgs doublet, from [668]. Blue points represent models with a strong first-order electroweak phase transition, required for successful baryogenesis.

The exploration of models of electroweak baryogenesis will also include tests for CP violation in Higgs boson and top quark decays. There is an alternative class of baryogenesis models, called “leptogenesis”, in which the CP violation and the out-of-equilibrium dynamics occurs in the neutrino sector. This can also be tested at the ILC if the relevant heavy neutrinos are at the weak scale. We will discuss both these issues in the following chapter.

13.3 What is the dark matter of the universe?

Perhaps the most compelling evidence for physics beyond the Standard Model comes from the sky, with a host of concordant observations indicating that baryons comprise only a fraction of the matter in the universe. Although viable dark matter candidates span many decades in mass, the near-coincidence of dark matter and baryon abundances suggests a non-gravitational mechanism to connect the two. This singles out dark matter candidates at or below the weak scale that interact with the Standard Model through one of several possible portals. We have discussed in Chapters 8, 10, and 11 that these models often have special difficulties for the discovery of new particles at hadron colliders, difficulties that can be overcome at the ILC.

Famously, a particle with a mass in the GeV-TeV range, coupled to the SM via weak-scale interactions, naturally has the right relic density to explain the observed DM. Such Weakly-Interacting Massive Particles (WIMPs) can be pair-produced at colliders. Once produced, WIMPs escape the detector, leading to a missing energy signature. The reach of the ILC to WIMPs in the

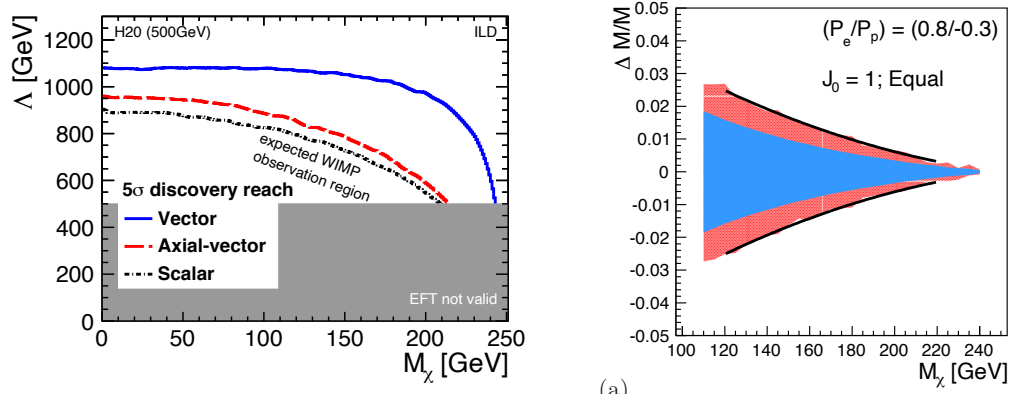


Figure 13.3: Left: ILC reach for dark matter particle coupled to electrons through an effective dim-6 operator of various spin structures. Right: Fractional accuracy of WIMP mass determination at the ILC using the fit to a photon spectrum in the γ +inv. final state.

model-independent γ +MET channel is shown in Fig. 13.3. As we have shown in Fig. 5.3 and the associated discussion, the ILC beam polarization can be used to analyze and control backgrounds, adding power to this search. The ILC is sensitive to the lepton (specifically, electron) coupling of the WIMP, making the ILC search complementary to those at hadron colliders and nuclear-recoil direct detection searches which are primarily sensitive to the WIMP coupling to quarks and gluons.

The WIMP can also be produced in decays of other, heavier BSM particles. A well-studied example of this production mechanism occurs in supersymmetric models, where the lightest supersymmetric particle (LSP) can play the role of WIMP dark matter. In many models, the LSP is nearly degenerate in mass with other electroweak-ino states, while strongly-interacting superpartners are much heavier. Such models pose difficulties for searches at hadron colliders due to small cross sections and soft visible energy deposits. The democratic production and clean environment in the ILC collisions allow for efficient searches for this physics. We have discussed the experimental aspects of this search in Sec. 10.5.

While WIMP paradigm is attractive, there are many alternative scenarios for microscopic origin of dark matter. The ILC will be able to shed light on many of these alternatives. For example, the DM may reside in a “dark sector”, a set of fields with no SM gauge interactions (but potentially rich structure of interactions among themselves). Such dark sectors are connected to the SM via a “portal” interaction. A simple and natural portal to DM can be provided by a dark photon, a new $U(1)$ gauge boson which couples both to the SM (via kinetic mixing with the SM $U(1)$ gauge group) and to the dark sector. The ILC will be able to search for the dark photon in two ways. First, it can be produced at the main interaction point, and detected either through its decays back to the SM or the missing-mass peak in the spectrum of the associated SM photon. Second, an additional detector placed 10-50 m downstream of the ILC beam dump can exploit the high current end energy of the ILC beams to extend the sensitivity to sub-GeV dark photons. We have discussed the experimental aspects of this search in Sec. 11.3.

Another natural candidate for a portal to the dark sector is the Higgs boson. Higgs decays into dark-sector states can provide a window into the dark sector. Such decays may result in an invisible Higgs decay signature, which can be accessed at the ILC with sensitivity a factor of 20 better than that expected at HL-LHC. Alternatively, some of the produced dark-sector states can decay back to SM particles, lead to exotic multi-particle final states in Higgs decays. For example, in models of asymmetric dark matter consisting of bound states of a confining gauge group (similar to QCD) in the dark sector, Higgs decays may produce events known as “dark showers”, characterized by multiple displaced vertices. Thanks to the large sample of Higgs bosons that will be collected and clean environment with low track multiplicity, the ILC offers unparalleled opportunities to search for such phenomena. We have reviewed searches for such exotic Higgs decays in Sec. 8.2.

If a signature of the dark matter particle (or an associated mediator particle) is discovered, either at the ILC or in another experiment, the ILC can play a crucial role in determining the properties of this particle such as its mass and spin, as well as strength and structure of its couplings to the SM. For example, the WIMP mass can be determined with a 1-2% accuracy by fitting the photon spectrum from the model-independent γ +invisible signature; see Fig. 13.3. Such measurements are challenging at hadron colliders. Further, the polarized beams at the ILC may help to disentangle the chiral structure of the couplings. In some models, the ILC may even provide enough information to calculate the relic abundance of the discovered stable particle(s), and to test whether it is indeed responsible for the observed dark matter.

We will bring together all of the ILC approaches to the search for dark sector particles and summarize their sensitivity in the next chapter.

13.4 What is the energy scale of new physics?

The Higgs boson is an exquisitely sensitive barometer for new physics, with any deviation in its properties from the Standard Model prediction providing a smoking gun indication of new physics. If new physics enters at or above the weak scale, these deviations can be systematically captured in effective field theory extensions of the Standard Model that encode the energy scale of new physics. In this section we interpret the SMEFT projections of section 12 in terms of motivated scenarios for new physics, translating ILC precision into qualitative lessons about the nature of the Higgs boson, its potential, and its coupling to other Standard Model particles.

In the next chapter, we will describe the relation between the levels of precision that will be reached in the ILC experiments and the predictions of specific models of new physics. We will demonstrate that the ILC is robustly sensitive to the predictions of these models, and that the pattern of deviations of the Higgs couplings from the SM predictions gives insight into the nature of new physics responsible for those deviation. Here, we will discuss a higher-level issue: What does the high-precision study of the Higgs boson tell us in general about the scale of new physics? Can we use this information to make fundamental tests of the SMEFT framework and of the quantum field theory description of the Higgs boson more generally?

The scale of new physics: The observation of any deviation from Standard Model predictions would be an unambiguous indicator of new physics. As we have discussed in the previous chapter, this can then be interpreted within the SMEFT framework, in terms of nonzero Wilson coefficients c_i/Λ^2 for a set of irrelevant operators. If such deviations can be well-described by dimension-6 operators in SMEFT, their size would allow us to infer the ratio of the couplings and masses of new physics. At the ILC, the anticipated sensitivity to Wilson coefficients of dimension-6 operators ranges from the few percent to per-mil level, depending on both the nature and number of operators in question. If new particles interact with the Standard Model at tree level with generic $\mathcal{O}(1)$ couplings, this could provide indirect evidence for particles as heavy as tens of TeV. If new particles instead interact only at loop level, the ILC remains sensitive to new particles between the weak scale and the TeV scale. Such particles need not carry Standard Model quantum numbers, in which case they would have remained undetected at the LHC.

Constraints on Wilson coefficients coming from null results at the ILC would provide strong evidence for a mass gap between the weak scale and the TeV scale, though the strength of the inferred bounds varies from model to model. It should be noted that constraints on dimension-6 operators do not generally provide an unambiguous exclusion of new physics, since contributions from different UV degrees of freedom to a given Wilson coefficient may partially or wholly cancel. As we will discuss shortly, constraints on dimension-8 operators can provide an unambiguous exclusion of new physics up to the corresponding scale due to positivity bounds that forbid cancellations among different UV contributions.

The “size” of the Higgs: A key higher-dimension SMEFT operator of broad significance is

$$\mathcal{O}_H = \frac{1}{2\Lambda^2} (\partial_\mu |H|^2)^2, \quad (13.1)$$

the leading nontrivial form factor for the Higgs field. The scale Λ associated with \mathcal{O}_H encodes the effective “size” of the Higgs boson, which may arise due to quantum corrections from new particles or compositeness of the Higgs itself. The leading effect of \mathcal{O}_H on Higgs properties is to generate a universal shift in Higgs couplings relative to their Standard Model values. This shift necessarily drops out of ratios of branching ratios typically measured at hadron colliders. We can sensitive to this parameter only if we can measure the Higgs partial width in absolute terms. Thus, the direct measurement of the Zh cross section at the ILC using the recoil Z boson as a tag allows the first unambiguous probe of \mathcal{O}_H .

Among other things, bounds on (or measurement of) \mathcal{O}_H quantify the extent to which the observed Higgs boson is an elementary or composite scalar. A sharp target is provided by the ratio of the Higgs’ size to its Compton wavelength. This ratio is of order unity for fully composite scalars, while smaller values correspond to increasingly elementary scalars. To date the neutral pion is the most elementary-seeming (pseudo)scalar yet observed in nature, with a ratio of size to Compton wavelength on the order of $\sim 1/6$. LHC measurements of Higgs properties do not yet probe pion-like levels of compositeness, and retain some degree of model-dependence. At the ILC, observation of \mathcal{O}_H would provide compelling evidence for the compositeness of the Higgs, while sufficiently stringent bounds would ultimately indicate that the Higgs is the most elementary scalar observed to date.

The Higgs self-coupling: A second key operator at dimension 6 is $\mathcal{O}_6 = |H|^6/\Lambda^2$, which gives the leading correction to the Higgs self-coupling in the SMEFT framework. The anticipated precision of the ILC's constraint on \mathcal{O}_6 is sufficient to unambiguously establish the non-zero self-interaction of the Higgs boson. This would, in turn, be the first observation of a self-interacting particle whose interaction preserves all of its internal quantum numbers. Conversely, if the ILC measures a nonzero value of the SMEFT coefficient of \mathcal{O}_6 , this would immediately indicate new physics below the TeV scale.

Positivity tests of analyticity and unitarity: In local, unitary quantum field theories, the basic assumption of relativistic causality implies that amplitudes are analytic functions of their kinematic variables. This analyticity in turn implies positivity bounds in the space of SMEFT couplings [669]. On one hand, these may be viewed as theoretical constraints that sharpen the interpretation of experimental results by narrowing the space of allowed couplings and precluding cancellations between different UV contributions. On the other hand, they may be viewed as an opportunity for direct experimental tests of the axiomatic principles of quantum field theory such as analyticity, unitarity, and locality [670]. Experimental probes of positivity bounds are challenging because the vast majority apply to operators at dimension eight and higher on account of the energy growth required to impose UV-insensitive bounds. The effects of dimension-8 operators are typically subleading to those of dimension-6 operators, which are generally not subject to generic positivity bounds.

Nonetheless, there are a number of observables for which dimension-8 operators provide the leading contributions, enabling tests of positivity bounds at colliders. At the LHC, diboson production allows for sharp tests of positivity bounds on anomalous quartic gauge couplings [671, 672]. But the ILC is particularly well-positioned to test positivity bounds on account of its clean environment and the ability to make measurements at multiple well-defined center-of-mass energies, which can be used to disentangle contributions from operators with different scaling dimensions.

Particularly interesting tests can be carried out in a process that is very straightforward to measure at the ILC, $e^+e^- \rightarrow \gamma\gamma$. In SMEFT, this process receives no corrections at dimension 6; the first higher-dimension corrections are of dimension 8. It is shown in [673], the dimension 8 corrections necessarily increase the differential cross section; a correction that would contribute negatively is forbidden by positivity. Because a dimension 8 operator is involved, the test is sensitive to new mass scales M only in the few-TeV range, though the question might also be pursued at higher-energy e^+e^- colliders.

Further channels in which it is possible to test positivity include $e^+e^- \rightarrow e^+e^-$ scattering [674], $e^+e^- \rightarrow Z\gamma$, $e^+e^- \rightarrow ZZ$ are presented in [671]. The last of these reactions gets no dimension 6 corrections; in the other cases, ILC sensitivity to dimension-8 operators is sufficient to give unambiguous tests of positivity bounds, even in the presence of dimension-6 operators. In other processes of e^+e^- annihilation to vector bosons, the assumption that deviations from the SM arise from dimension-6 operators leads to specific predictions, such as relations between the γWW and ZWW trilinear couplings and the absence of corrections to $e^+e^- \rightarrow ZZ$, that can be tested with detailed measurements of the differential cross sections. Deviations from these predictions must be attributed to dimension-8 contributions. Through these analyses, the ILC can probe bedrock

principles of quantum field theory, and, in the event of null results, can unambiguously exclude new physics in the relevant channels.

The linear realization of electroweak symmetry: Although the $SU(2)_L \times U(1)_Y$ -symmetric Standard Model EFT (SMEFT) is currently the preferred effective field theory extension of the Standard Model, it is not the only possibility. As we have already described, it is an assumption in SMEFT that any additional sources of electroweak symmetry breaking beyond the observed Higgs boson are associated with large mass scales that can be cleanly integrated out. If there are additional sources of electroweak symmetry breaking below 1 TeV or if there are heavy particles that still acquire most of their mass from the Higgs field, this would require using a different, more inclusive effective field theory. In Sec. 12.2, we described an alternative HEFT in which the Higgs field belongs to a nonlinear realization of weak-interaction $SU(2)$. At present, it is possible for either SMEFT or HEFT to describe deviations from the Standard Model, leaving unresolved whether electroweak symmetry is linearly or non-linearly realized by the known fundamental particles. This question is unlikely to be answered decisively at the LHC, leaving a compelling open question for the ILC.

If precision measurements of Higgs couplings at the ILC are not well-fit by SMEFT operators at dimension 6, HEFT may provide the more appropriate description. This would suggest that electroweak symmetry is not linearly realized by the particles of the Standard Model and signal the presence of non-decoupling new physics between the weak scale and a few TeV. On the other hand, consistency of ILC precision measurements with Standard Model predictions—and, in particular, verification of the Higgs coupling constant relations predicted by SMEFT—would significantly narrow the types of UV physics associated with HEFT. Future energy upgrades of the ILC could decisively determine whether electroweak symmetry is linearly realized by the known fundamental particles by probing scattering processes at the \sim few TeV scale.

13.5 Why is electroweak symmetry broken?

Behind all of these questions, there is another very important one. All of the questions that we have discussed in this section eventually point back to mysteries about the Higgs boson.

The structure of the SM is such that the interactions of gauge bosons and fermions are specified completely by their quantum numbers and the values of the $SU(3) \times SU(2) \times U(1)$ gauge couplings. These couplings are dimensionless. For energies above a few GeV, all three of these couplings are weak. This part of the SM is easy to understand and has been tested in great detail through precision electroweak measurements and measurements of quark and gluon reactions at the LHC.

Any property of the SM that goes beyond this—including the basic mass scale of the model, the mass spectrum of quarks and leptons, and the origin of CP violation—necessarily involves the Higgs boson. The explanation that the SM gives for these aspects comes in the form of renormalizable parameters, the Higgs field mass and quartic terms and the Higgs-fermion Yukawa couplings. These are adjustable inputs to the quantum field theory. These input parameters are subject to some general phenomenological constraints, but attempt to compute these parameters

from first principles have always led to paradoxes (such as the Gauge Hierarchy Problem). This is why the SM is often described as an effective theory that represents a more fundamental theory at higher energies. We are now at the point where we need to know how that more fundamental theory is constructed.

A basic physics question that we can ask about that more fundamental theory is, why is the $SU(2) \times U(1)$ symmetry of SM spontaneously broken? Like the values of the fermion masses, spontaneous symmetry breaking is an input to the SM. It comes in the assignment of a negative value to the Higgs field mass parameter μ^2 . This value cannot be determined from first principles. The connection between the physical and the “bare” value of μ^2 is not well-defined and these quantities can easily have different signs. This is a symptom of the fact that the SM is only a phenomenological theory. It cannot answer the why questions, not this one, not any of the others that we have listed above.

This situation stands in sharp contrast to our knowledge about spontaneous symmetry breaking acquired from the study of superconductivity, magnetism, and other condensed matter phenomena, pairing in nuclear physics, and even chiral symmetry breaking in low-energy QCD. In each case, there is a fascinating story that explains the why of the broken symmetry state. Some theorists are dismissive of similar explanations in “fundamental” physics. We disagree. It is true that any explanation of EWSB requires new physics beyond the SM. But, to us, this means that there is an opportunity to discover new fundamental forces now unknown. We ought to be grasping for it.

Models that explain the phenomenon of electroweak symmetry breaking (EWSB), require structure beyond the SM, but this can come in one of many forms. The theoretical literature contains a large number of different types of models that address this question. It is useful to divide these models roughly into categories. New theoretical ideas can give rise to new categories, but always with the imperative to explain the mass parameter of EWSB, the Higgs field vacuum expectation value $v = 246$ GeV. In the following, we will refer to physics at the “TeV scale”, with new particles of mass from 100 GeV to a few TeV, the “10 TeV scale”, with new particles in the range 5–50 TeV, and a “very high scale”, with new particles above 10^9 GeV and possibly up to the Planck scale.

Here is a sampling of models found in the literature:

- **Models with a fundamental scalar field at the TeV scale:** Here the Higgs field is a fundamental field. To avoid the conceptual problems of the SM and to allow the Higgs potential to be computable, this the Higgs field must be supplemented by additional fields providing add structure. An example is the Minimal Supersymmetric Standard Model. Here, the Higgs potential can be computed in terms of the masses and couplings of supersymmetric particles, which in principle can be measured independently by experiments. The negative value of μ^2 can be generated by a loop diagram involving \tilde{t}_L , \tilde{t}_R , and the Higgs field Φ_u , and this mechanism is testable after observation of these particles.
- **Models with a scalar field composite at the TeV scale:** Here EWSB is due to new strong interactions at the TeV scale, as in the original Technicolor models. These models do not include a light Higgs boson doublet, but they may include a Higgs “imposter”, for example, a light scalar dilaton. These models are allowed by the current LHC data only with considerable tuning [675].

- **Models with a scalar field composite at the 10 TeV scale:** Here EWSB is due to new strong interactions at a higher scale, with the Higgs field mass term protected by symmetry. For example, the Higgs doublet field can appear as a set of Goldstone bosons of the strong interaction theory. Little Higgs models are examples of models of this type. In these models, additional new TeV-scale particles such as vectorlike top quark partners are needed to build computable models of EWSB. These partners can be evade LHC constraints by being heavier than the limits or by being color-singlet, a class of models called “neutral naturalness”.
- **Models with extra dimensions:** In such models, the Higgs doublet field can arise as the 5th component of a 5- or higher-dimensional gauge field. Randall-Sundrum models fall into this class. The higher-dimensional field excitations (“Kaluza-Klein excitations”) play an essential role in the computation of the Higgs potential and EWSB.
- **Models with fundamental scalar fields from very high scales:** Here the Higgs doublet is a fundamental scalar field arising at very high energy scales. For example, in the Relaxion model, the Higgs potential evolves on cosmological time scales along with the early expansion of the universe. Another example is Nnaturalness, in which the fundamental theory at the Planck scale contains a large number N of copies of the Higgs doublet with random μ^2 values, of which one has a mass at the TeV scale [365]. In these models, the presence of the fundamental scalar field is given and the mechanism only serves to solve the Gauge Hierarchy Problem. Often, extreme parameter values are needed. For example, in Nnaturalness, one requires $N \sim 10^{60}$.

The type of model dictates whether the model has the power to solve other questions about the SM such as the values of the fermion masses. In supersymmetry, these values are set by the values of Yukawa couplings at the scale of Grand Unification. In models in which the Higgs field is a Goldstone boson or an extra-dimensional vector field component, there is a possibility that the fermion Yukawa couplings can be generated dynamically at the TeV or 10 TeV mass scale.

Though some of these models, especially those of the last class, can be very difficult to test with colliders, all of the classes contain models with new particles at the TeV scale, plausibly within the reach or just beyond the reach of the LHC. These particles can also give tree-level or radiative corrections to the properties of the Higgs boson at the 5% level that can be discovered in a program of precision Higgs measurements. The very different physics origins of EWSB in these classes of models implies that the predictions for new particles and anomalous Higgs coupling are very different from one class of models to another. This gives the possibility that both direct and indirect effects of new particles can distinguish the classes and set us on the road to understanding correctly the origin of EWSB

In the next chapter, we will see how the various issues described in this chapter can be addressed by measurements that the ILC will make possible.

Chapter 14

ILC and Models of Physics Beyond the Standard Model

In the previous chapter, we discussed the major questions of particle physics and explained in general terms the ability of the ILC to address those questions. In this chapter, we will continue that discussion by reviewing the ILC capabilities in terms of specific models of new physics. This will make more concrete the relationship between the big questions and the ILC capabilities for measurements and new particle searches that we have presented in Chapters 8–12.

It is not clear to us that the case for the ILC needs to be tied to specific model-dependent goals. As we have explained in Sec. 12.2, under the general assumptions of SMEFT, the relative deviations of the Higgs boson couplings from their SM expectations are expected to be less than 10%. These levels are not yet probed by LHC results and are expected to be out of the reach of the HL-LHC for 5σ discovery. The same is true of the top quark couplings to the SM gauge sectors. On the other hand, new physics models predict deviations accessible to the ILC, and different models predict different patterns. Thus, the ILC will provide a window into physics beyond the SM that is rich in character and, today, totally unexplored. Nevertheless, considerations of specific models can be useful in illustrating the variety of insights that the ILC could produce.

14.1 ILC and dark matter

The ILC can give insight into the particle identity of dark matter by discovering the dark matter particle or associated particles of a dark sector. The search for the dark matter particle is a broad program that is being carried out using many different strategies, including searches at accelerators both at GeV and TeV energies. The ILC will add a number of new capabilities that extend or complement these programs.

The possible candidates for the dark matter particle span an enormous range, from axions whose Compton wavelength is the size of a galaxy to black holes of almost a solar mass. But a particularly attractive class of candidates lies in the center of this range. This is the “thermal WIMP”, a stable,

weakly-interacting neutral particle that interacts strongly enough with SM particles to come to thermal equilibrium in the early universe. The number density of such particles is set by their freeze-out density, the density at which, when the universe becomes sufficiently cold, they cannot find partners with which to annihilate and thus reach a constant density co-moving with the expansion of the universe. The simplest models of thermal freeze-out predict that an annihilation cross section of roughly 1 pb leads to a WIMP density comparable to the measured dark matter density in the universe. This value can be met in several ways: (1) by a particle with mass of order 100 GeV and couplings of electroweak strength, (2) by particles with weaker couplings and comparably smaller masses, and (3) by particles with stronger couplings and comparably larger masses.

Models of supersymmetry and other models of electroweak symmetry breaking often contain stable neutral particles of the first type. However, these models are now strongly challenged by the limits on supersymmetric particles from the LHC and the limits on the WIMP cross section on matter from direct detection experiments. Specific cases remain in play, as we will discuss below. Models of the second type can be achieved through the idea of a dark sector, a new sector of particles with zero quantum numbers under that SM gauge symmetries that are connected very weakly to SM particles through specific operators called “portals”. We have reviewed the structure of such models in Sec. 11.1. Models of the third type require higher-energy accelerators. They turn out to be especially difficult to study with hadron colliders and thus provide a motivation for higher energy lepton colliders. We will discuss this point further in Secs. 15.1 and 15.2.

We have explained in Secs. 10.5.3 and 10.6 that the search for events of the type $e^+e^- \rightarrow \gamma +$ missing energy at the ILC can be a powerful probe both for WIMPs in the 100 GeV mass region and for dark sector particles. For WIMPs of the first type, the production cross sections are of electroweak strength and thus are large enough to provide a substantial event sample. The WIMPs would not be observed in collider detectors, but their presence can be inferred by the observation of initial state radiation. We have emphasized in Sec. 10.5.3 that linear e^+e^- colliders have many advantages for this search. Initial-state photon radiation does not depend on non-perturbative quantities such as parton distribution functions but rather is given by QED theory at part-per-mil precision. The ILC detectors operate without a trigger and are capable of recognizing very small energy distributions at angles close to the beam director. The use of electron and positron beam polarization allows backgrounds to be directly measured. All of these features allow sensitivity to WIMPs at masses close to 1/2 of the CM energy. For dark sector models, the sensitivity of the ILC is limited by the strength of the mixing through the gauge portal. Still, the ILC can be sensitive to mixing parameters as small as $|\epsilon|^2 \sim 10^{-5}$ for mass regions that extend beyond those of other colliders.

In supersymmetric models, and in other models of electroweak symmetry breaking that predict dark matter candidates, there is another important production mechanism for the dark matter particle. A collider can produce a heavier state that decays to the dark matter matter particle, depositing in the process observable energy. ILC examples in supersymmetry are the reactions $e^+e^- \rightarrow \tilde{\chi}_1^+ \tilde{\chi}_1^0$ or $e^+e^- \rightarrow \tilde{\tau}^+ \tilde{\tau}^-$ with subsequent decays of the SUSY particles $\tilde{\chi}_1^0$ plus SM particles. This process can be difficult to observe at hadron colliders if the mass gap between the the heavier SUSY particle and the $\tilde{\chi}_1^0$ is small, leading to a small energy deposition. In practice, mass gaps less than 10 GeV lead to difficult for LHC experiments in triggering and signal recognition [565]. The LHC experiments can recover sensitivity for very small mass gaps that lead to observable

lifetimes. However, there are physics reasons for models to fall into this gap, first, because the Higgsino sector of SUSY naturally has small mass splittings of just a few GeV or less, second, because models of SUSY dark matter often require coannihilation of the dark matter particle with some other species to produce a sufficiently small dark matter density, and this requires a mass gap of order 5 GeV. The ILC, using the advantages already presented for initial state radiation, can fill this gap. For example, simulations of SUSY analyses at the ILC for models with sub-GeV mass gaps are presented in [571].

ILC offers another method to search for dark sector particles using its fixed-target capabilities, as discussed in Sec. 11.3. The ILC will produce an electron beam that combines high intensity and high energy. This beam can be used parasitically, with detectors mounted behind the ILC beam dumps, and directly at dedicated fixed-target interaction halls. Both types of experiments extend the expected reach for dark sector particles both in particle mass and in sensitivity to small couplings.

14.2 ILC and supersymmetry

The ILC can give insight into supersymmetric models of new physics in two different ways, first, through direct searches for supersymmetric particles and, second, through observation of corrections to the Higgs boson couplings induced by loop effects of supersymmetric particles.

14.2.1 Direct SUSY particle production

In the previous section, we have already discussed the ability of the ILC to discover new particles in models with stable neutral particles separated from heavier partners by small mass gaps. This is a general issue, but it has taken on more importance in view of the recent result of the Muon $g - 2$ experiment, which gives a deviation of 4.2σ between the measured result and the theoretical consensus value [676].

There are various more ad hoc models that can explain the muon $g - 2$ deviation, but it is relevant that the anomaly can be explained within the Minimal Supersymmetric Standard Model (MSSM). This has been studied in [677], in the series of papers [552, 678, 679, 680], and in [681, 682]. It is shown that there are MSSM parameter sets that can provide this explanation consistently with LHC SUSY searches by making use of the region of small mass gaps within the chargino-neutralino sector. The points found by this analysis are consistent with the observed cosmic dark matter abundance [683] and constraints from dark matter direct detection experiments [684, 685, 686].

There are five different scenarios, all characterized by a mass region for the lightest SUSY particle M_{LSP} and the mass gap to its heavier partner ΔM . In the first two scenarios, this SUSY sector can supply only a fraction of the total dark matter density. In all of the scenarios, the requirement to explain the $g - 2$ result leads to an upper bound on M_{LSP} .

- (i) higgsino DM : $M_{LSP} \lesssim 500 \text{ GeV}$ with $\Delta M \sim 5 \text{ GeV}$;

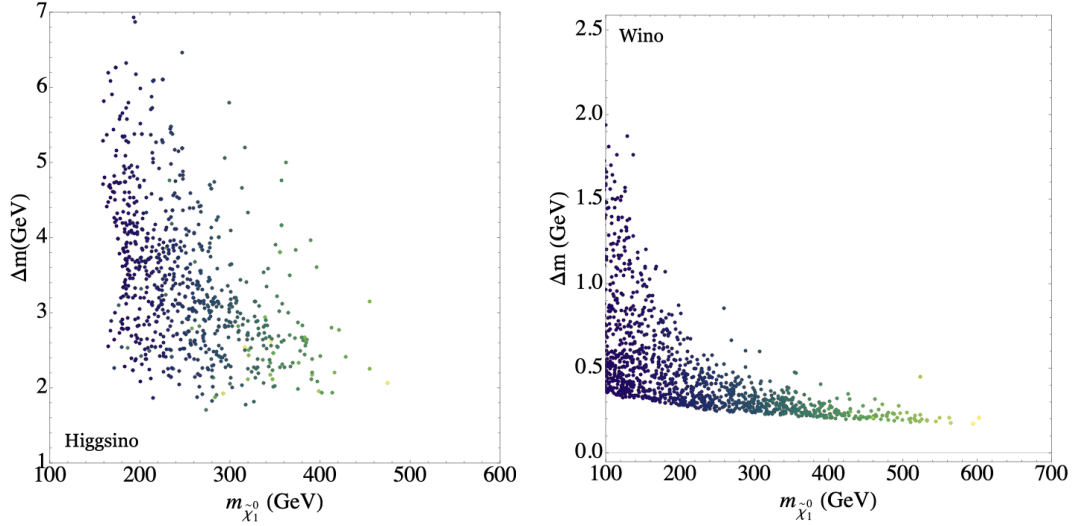


Figure 14.1: Scans over the parameter set of the MSSM giving models that account for the current discrepancy between the observed value of the muon $g - 2$ and the consensus SM prediction, from [680]. Left: Higgsino LSP; Right: Wino LSP. Other scenarios are described in the text. Color encodes the predicted value of the LSP dark matter density, with green indicating a higher value.

- (ii) wino DM : $m_{\text{LSP}} \lesssim 600 \text{ GeV}$ with $\Delta M \sim 0.3 \text{ GeV}$;
- (iii) mixed bino/wino DM with $\tilde{\chi}_1^\pm$ -coannihilation : $m_{\text{LSP}} \lesssim 650 \text{ GeV}$ with $15 \text{ GeV} < \Delta M < 60 \text{ GeV}$;
- (iv) bino DM with $\tilde{\ell}$ -coannihilation with $\tilde{\tau}_L$: $m_{\text{LSP}} \lesssim 650 \text{ GeV}$ with $10 \text{ GeV} < \Delta M < 80 \text{ GeV}$;
- (v) bino DM with $\tilde{\ell}$ -coannihilation with $\tilde{\tau}_R$: $m_{\text{LSP}} \lesssim 650 \text{ GeV}$ with $10 \text{ GeV} < \Delta M < 100 \text{ GeV}$;

The next round of direct detection experiments [687, 688] will give us more information [680]. In the case that no signal is observed, the upper limit on the LSP goes down to $\sim 500 \text{ GeV}$ and the entire parameter region will be covered by the 1 TeV ILC. For certain choices of the signs of the MSSM parameters (in particular, $\mu \times M_1 < 0$) the different contributions to the spin-independent direct detection cross section for a bino-like DM candidate interfere destructively, giving even more space for that solution within the current direct detection constraints [677].

The parameter scans in the first two cases are shown in Fig. 14.1 [680]. These emphasize that the SUSY particles solving the $g - 2$ anomaly may be close at hand and uniquely accessible to an e^+e^- collider. The other cases give substantial opportunity for first discovery of new physics at LHC. However, even in those cases, an e^+e^- collider will be needed to characterize the actual scenario by measuring the quantum numbers and mixing angles of the observed SUSY particles, and to clarify the role of the light SUSY particle in the cosmic dark matter. It has been shown that the e^+e^- studies can measure the masses and mixing angles needed to evaluate the contribution to $(g-2)$ from the new particles and verify that the anomaly indeed has an understood supersymmetric origin [689, 690].

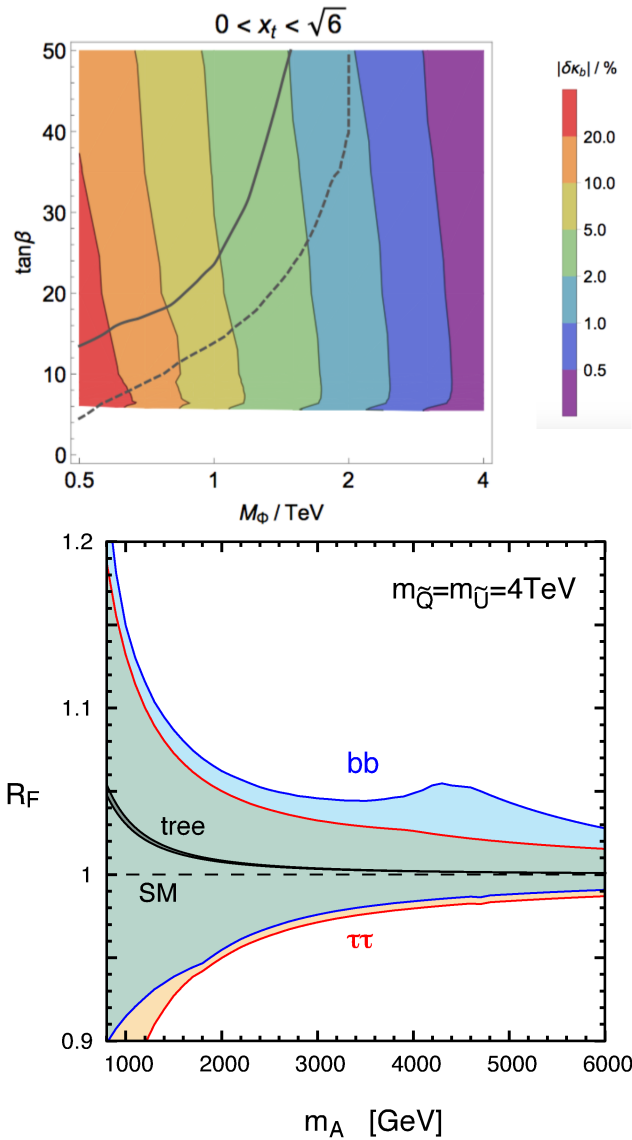


Figure 14.2: Fractional deviations of the Higgs boson couplings from their SM values in supersymmetry models with very heavy SUSY partners: Top: effect on the Hbb couplings in a class of supersymmetry models with b - τ Yukawa unification, from [691]. M_Φ is the mass of a heavy boson in the extended Higgs sector of the model. The extended Higgs sector is excluded by LHC searches above the solid line. The expected exclusion limit at the HL-LHC is shown by the dotted line. Bottom: range of effects on the Hbb and $H\tau\tau$ couplings induced by loop corrections involving heavy SUSY states, from [692]. The black line shows the tree-level prediction due to the 2-Higgs doublet structure, for $\tan\beta = 5 - 50$.

14.2.2 Observation of SUSY effects on the Higgs boson

If the masses of SUSY particles are so large that they cannot be discovered directly at the LHC, it is still possible that their effects can be observed through their effect on the Higgs boson couplings. There are many possible sources of such effects, but two are especially important: (1) the shift of the Higgs boson couplings to $b\bar{b}$ and $\tau^+\tau^-$ coming from the extended Higgs sector required in SUSY, and (2) the shift of the Higgs boson coupling to $b\bar{b}$ due to \tilde{b} -gluino loop diagrams with large \tilde{b}_L - \tilde{b}_R mixing. A broad survey of SUSY effects on the Higgs boson couplings in the parameter region in which the SUSY particles are very heavy is given in Ref. [692]. Further enhancements are possible in the MSSM with general squark generation mixing, as studied in [693]. These can appear both in $\Gamma(H \rightarrow b\bar{b})$ and especially in $\Gamma(H \rightarrow c\bar{c})$, for which the precision measurement is unique to e^+e^- colliders.

Illustrations of these effects are shown in Fig. 14.2. Figure 14.2(a) shows the fractional deviation in the Hbb coupling in a class of SUSY models with b - τ Yukawa unification at the grand unification scale [691]. The models are chosen such that the gluino and stop masses are above 5 TeV, well out of the reach of the LHC. The heavy Higgs sector is excluded by LHC searches in the region above the solid line. The HL-LHC is expected to improve this limit to the dotted line. This still leaves considerable parameter space that can be accessed by precision Higgs boson measurements. Figure 14.2(b) shows the range of values allowed for relative enhancement or depression of the Hbb and $H\tau\tau$ couplings in the MSSM with the squark masses $m_{\tilde{Q}} = m_{\tilde{U}} = m_{\tilde{D}} = 4$ TeV and other sfermion masses greater than 4 TeV [692]. The enhanced range in the Hbb case comes from solutions with large \tilde{b}_L - \tilde{b}_R mixing, respecting the condition of vacuum stability.¹

These figures make a point that is more general. The direct search for new particles and the search for new physics through precision measurement do not compete directly with one another. Instead, they generally access complementary regions of the parameter space. We should make use of both techniques to make the broadest search for new physics.

14.3 ILC and composite Higgs fields

The ILC can give insight into models in which the Higgs field is composite through a number of different measurements. These include direct probes of the Higgs boson properties, as we have already discussed in the section on the ‘‘Higgs size’’ in Sec. 13.4. Because composite Higgs bosons must communicate strongly with the top quark, probes of the top quark also play an important role here.

There is some subtlety to the construction of composite models of the Higgs boson. In such models, the composite scalar sector is parametrized by a mass scale F analogous to the pion decay

¹We caution that the results from public SUSY codes for models with SUSY masses of several TeV are quite unstable with respect to addition of small corrections. The analysis of [692] used FeynHiggs 2.10.2. Using FeynHiggs 2.18.1, the point previously giving the largest deviation in the $b\bar{b}$ coupling for $m_A = 4600$ GeV (5%) now gives a coupling deviation of 2%. However, it is still not difficult to find points with deviations of 3% (6σ for ILC). It would be good to study this issue more systematically.

constant $f_\pi = 93$ MeV in the familiar strong interactions. The first composite models of the Higgs boson, models of “technicolor”, required $F = v = 246$ GeV [694, 695]. These models are now excluded, because such a light compositeness scale generates large corrections to the precision electroweak observables and strong interaction resonances light enough to be observed at the LHC. An attractive picture that move the new binding interactions to higher energies is the idea of the Higgs boson as a Goldstone boson. A lucid review of this idea is given in [696]. Spontaneous symmetry breaking in a new strong interaction theory at a high energy scale generates the Higgs $SU(2)$ doublet as a multiplet of Goldstone bosons, with the associated F parameter related to the high scale of symmetry-breaking. Perturbations of this theory, perhaps generated by coupling to SM particles, break the symmetry weakly and lead to a potential for the Higgs multiplet. This gives a model for the origin of electroweak symmetry breaking.

It is also possible to model the Higgs boson using models with extra space dimensions. Here the Higgs boson appears as the 5th component of a gauge field in the higher-dimensional space. This description can be viewed as dual description of the previous one, with some advantages for calculation [697, 698].

The Goldstone boson origin of the Higgs boson leads to modification of its kinetic energy term and, in particular, generation of a SMEFT correction

$$c_H = av^2/F^2, \quad (14.1)$$

where a is a number of order 1. This leads to a uniform decrease of all Higgs boson partial widths by the factor $(1 - c_H)$. This effect is most visible as a shift of the Higgs boson partial widths to W and Z . At the ILC, this effect can be visible for multi-TeV values of F .

Very often in models, the largest effect that breaks the original strong interaction symmetry is the influence of the top quark and heavy vectorlike top quark partners of that appear as part of the composite model. The heavy partners can also modify the Higgs boson couplings through loop corrections, in particular, modifying the partial width of the Higgs boson into gg [699, 700].

The interplay of the top quark and its partners with the new strong interactions also leads to effects that are visible directly in precision top quark physics. Often, the top quark must acquire some composite structure in order to receive its large mass. This leads to observable effects. The couplings of the top quark to the photon and gluon are fixed by Ward identities, but the couplings to the Z and W bosons can be modified and obtain corrections of order v^2/F^2 . Both positive and negative corrections are possible in models, and the corrections are expected to affect differently the left- and right-handed top quark couplings [491, 490, 535, 536].

The ILC has exceptional sensitivity to modifications of the top quark coupling to the Z boson [499]; see also the discussion of precision top quark physics in Sec. 10.1. At the ILC500, top quarks are pair-produced through s -channel photon and Z exchange. The compositeness corrections appear as interference terms in the production amplitude. Using beam polarization and measuring the polarization of the final top quarks, it is possible separate the various chiral contributions to the production amplitude and to measure these at the parts-per-mil level.

Through these three effects and others, the ILC can give a detailed characterization of the influence of possible composite structure on the Higgs boson and the top quark.

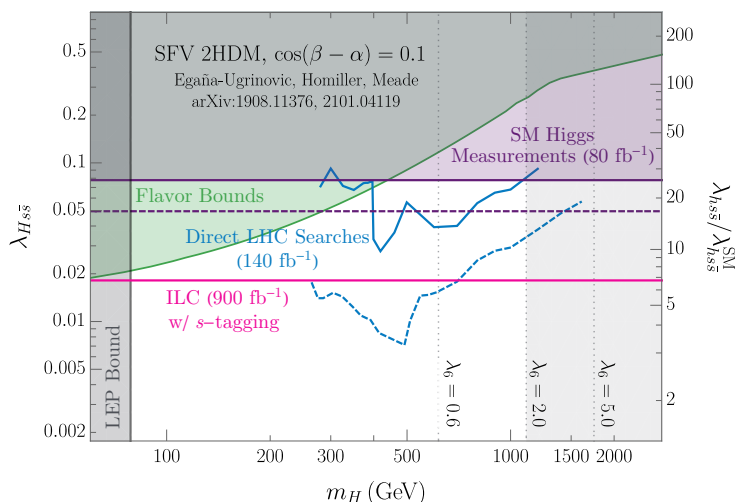


Figure 14.3: LHC bounds on a 2-Higgs-doublet model with specific couplings to the strange quarks as a function of the heavy Higgs mass m_H . The scale on the right-hand side shows the corresponding enhancement of the 125 GeV Higgs Yukawa coupling to strange quarks. From [701], with the ILC expectation from [336] added.

14.4 ILC and flavor

The ILC can give insight into models of flavor-dependence of fermion masses. In the SM, the quark and lepton masses are proportional to the fermion-Higgs Yukawa couplings, which are renormalizable—and therefore freely adjustable—parameters of the model. At this level, there is no explanation for the fermion mass hierarchy.

It is possible that the explanation for the Yukawa couplings comes from physics at a very high mass scale—the grand unification scale or the scale of string compactification—and is inaccessible to foreseen colliders. However, it is also possible that this hierarchy could be generated at the TeV. If the opportunity is there, we should test it.

An approach to the problem of fermion mass generation comes from the idea that there are multiple Higgs bosons, each with a fundamental coupling to one particular generation of fermions. Many models have been proposed that have this general structure [702, 703, 704, 705, 706]. It is possible for additional Higgs bosons coupling differently to fermion generations to be relatively light, with masses below 1 TeV [707, 708, 701]. It is possible to investigate these models through searches at the LHC and, for sufficiently light scalars, at the ILC.

An important feature of these models, offering an alternative search strategy, is that they can lead to values of the Yukawa couplings of the lighter generations that violate the usual SM relation between Yukawa couplings and fermion mass. Both the LHC and ILC can probe the muon Yukawa coupling, but it is a unique feature of e^+e^- colliders that they can probe the charm Yukawa coupling with high precision and also put significant constraints on the strange Yukawa coupling. We have

discussed these analyses at the ILC in Sec. 8.1. Figure 14.3 shows the current constraints on the enhancement of the strange quark Yukawa coupling, from [701], and the improvement currently expected from ILC250 [336].

In addition to the possible enhancement of lighter-generation Yukawa couplings, generation-dependent extended Higgs models predict flavor-off-diagonal Higgs boson couplings. In the SM, it is always possible to redefine fields so that the Higgs boson couplings are diagonal in flavor. However, in SMEFT, when we reach dimension-6 operators, this freedom is already used up, and so, generally, it is not expected that these preserve flavor. Naive estimates of the size of the coefficients would put flavor-violating Higgs decays at the 10^{-3} – 10^{-4} level. This level of Higgs flavor violation is quite compatible with the current strong bounds on $\tau \rightarrow \mu\gamma$ [709]. Within the MSSM with general squark generation mixings, branching ratios for $H \rightarrow bs$ of order 10^{-3} can be generated by loop effects [710, 693]. The LHC will be able to test for $H \rightarrow \tau\mu$, but tests in the quark sector are much more difficult at hadron colliders. At the ILC, though, searches for the exotic decay $H \rightarrow bs$ should reach this level.

14.5 Mass Reach of Precision Higgs Measurements

It is interesting to ask whether the precision measurement of Higgs boson couplings gives access to new physics particles that are outside the range of HL-LHC direct searches. Actually, we have already presented many examples of this in previous sections, but one might ask whether these are special cases or represent more generic situations. In this section, we discuss this question from another point of view.

When the new physics corrections to Higgs couplings can be described by SMEFT, these corrections arise from dimension-6 operators and thus are of the order of v^2/M^2 , where M is the mass scale of new particles that have been integrated out. Naively estimating the size of these corrections by setting $M = 2$ TeV and putting the coefficient 1 in front of the dimensional estimate. This gives the size of these effects as

$$\begin{aligned} \text{tree level effects:} & \quad v^2/M^2 \sim 1\% \\ \text{loop level effects:} & \quad (g^2/4\pi)v^2/M^2 \sim 0.1\% \end{aligned} \tag{14.2}$$

The tree level estimate is roughly the same size as the uncertainties estimated for the ILC. One might conclude from this that the program of precision Higgs measurements can access new particles of mass up to 2 TeV but cannot definitively prove their existence.

However, it is quite possible that the coefficient of the v^2/M^2 dependence is a large dimensionless number. In scenarios with this property, the mass reach of precision Higgs boson measurements can be much larger. The study [711] reviews a number of scenarios that illustrate this using a wide variety of physical mechanisms. The scenarios are presented, not as complete new physics models, but in terms of the dimension-6 SMEFT coefficients that are produced by integrating out specific sections. These scenarios can then appear as elements in a variety of complete models. These scenarios offer discovery sensitivity to new particle masses above 2 TeV and even in the multi-TeV range.

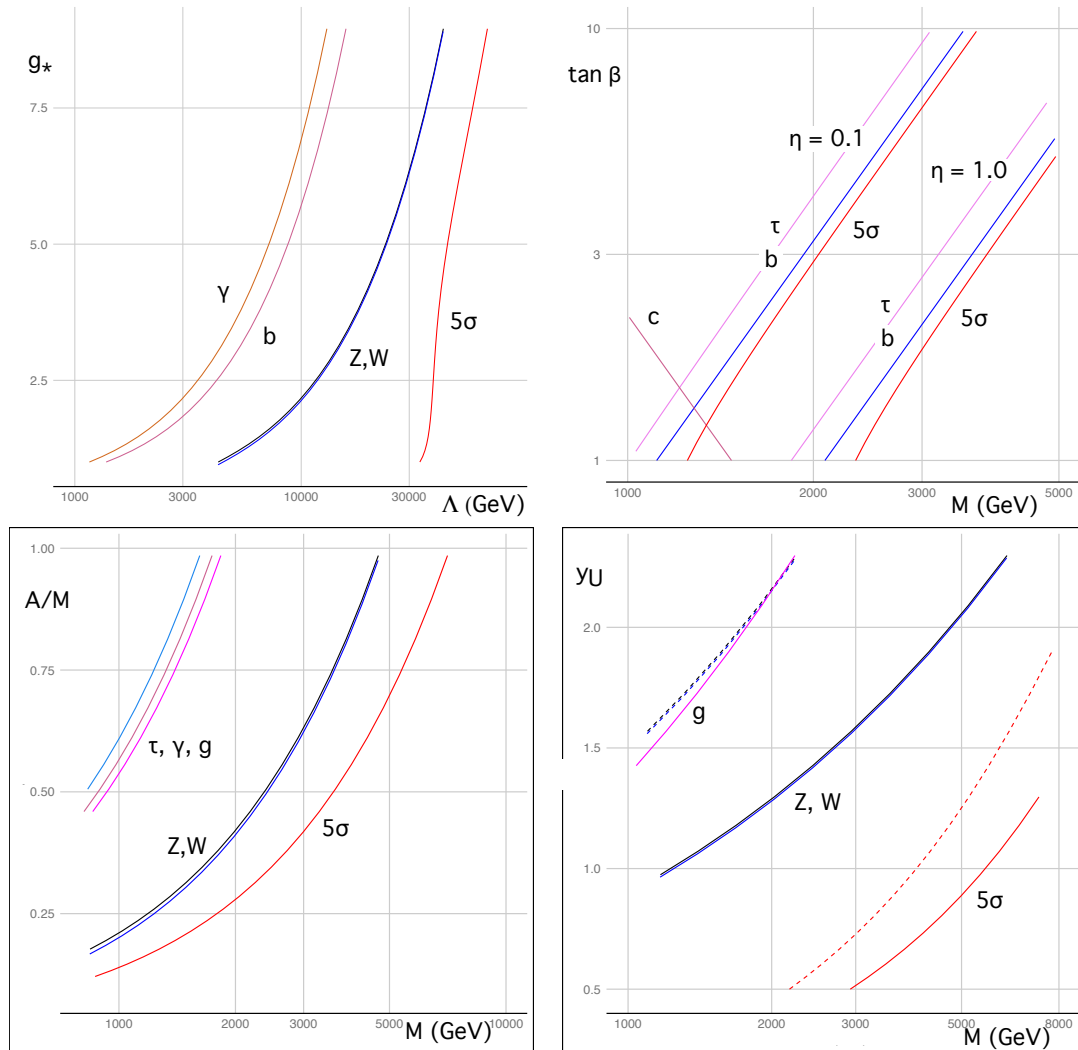


Figure 14.4: Mass reach of Higgs boson coupling deviations in a variety of scenarios reviewed in [711]. The curves give the 3σ sensitivity for particular Higgs boson couplings as a function of the new particle mass and a dimensionless parameter relevant to each scenario. The red curves on the right give the 5σ discovery contour for a fit of the full set of Higgs boson coupling measurements to ILC data. The scenarios are: (upper left) the Strongly Interacting Light Higgs, (upper right) two-Higgs doublet models, (lower left) models with a scalar singlet, (lower right) integration out of a vectorlike quark doublet.

We illustrate the mass reach for four of these scenarios in Fig. 14.4. One way to generate such large coefficients is to consider models in which the Higgs boson is composite, so that higher-dimension operators contain a new strong coupling constant. This is illustrated by the example of the Strongly Interacting Light Higgs (SILH) in which some SMEFT coefficients are multiplied by the strong couplings g_*^2 [712]. In two-Higgs doublet models in the decoupling limit, the tree level v^2/M^2 corrections are proportional to a Lagrangian term that mixes the light (H) and heavy (Φ) Higgs fields,

$$\Delta\mathcal{L} = \eta|H|^2(H^\dagger\Phi + \Phi^\dagger H) . \quad (14.3)$$

Supersymmetric models tend to predict small values of η , but still they lead to sensitivity to heavy Higgs bosons of mass about 1 TeV. For $\tan\beta < 7$, this is beyond the search reach of HL-LHC [713]. In non-supersymmetric models, η can be 1 or larger, leading to mass reach in the 3 TeV region. Mixing of the Higgs boson with a scalar singlet can lead to a significant change in the overall normalization of Higgs couplings. Though the HL-LHC can discover the singlet Higgs up to 2.5 TeV when the mixing angle is of order 10% [509], precision Higgs couplings measurements are sensitive to mixings of 1% and below, with mass reach above 3 TeV. Integrating out a heavy vectorlike quark doublet leads to Wilson coefficients for SMEFT dimension-6 operators depending on the new quark Yukawa couplings as y_U^2 and even y_U^4 . The Yukawa coupling of the top quark is $y_t \sim 1$ or $\alpha_t = 0.08$, and larger Yukawa couplings appear often in models with vectorlike quarks. Then the mass reach for precision measurement can extend above 3 TeV and thus well above HL-LHC search reach for vectorlike quark of about 1.5 TeV [714]. Additional examples, including a specifically supersymmetric effect, are discussed in [711].

It is straightforward, then, to identify scenarios in which the mass sensitivity of Higgs boson coupling measurements extends well above 2 and even 3 TeV. It should be noted that the relevant scenarios are distinct from those in which the lightest new particles are readily discovered at the HL-LHC. As we have emphasized already, precision Higgs measurements do not explore the same windows accessed by the LHC and HL-LHC but rather open new windows that have not been sufficiently explored up to now.

14.6 The Higgs Inverse Problem

In our discussion of the influence of different models on the Higgs boson coupling, we have noted that the various classes of models lead to different effects. This suggests that, by measuring the pattern of deviations of Higgs couplings from their SM values, we can infer properties of the new physics that led to them. These models of new physics are accessed only indirectly, through their effects on precision measurements, but nevertheless we can gain concrete information about their nature.

In the review above, we have pointed out that

- In models with extended Higgs sectors, including in particular supersymmetry, the major effects are on the Higgs boson couplings to b and τ
- In models with new SM singlet scalars and mix with the Higgs boson, and in composite Higgs

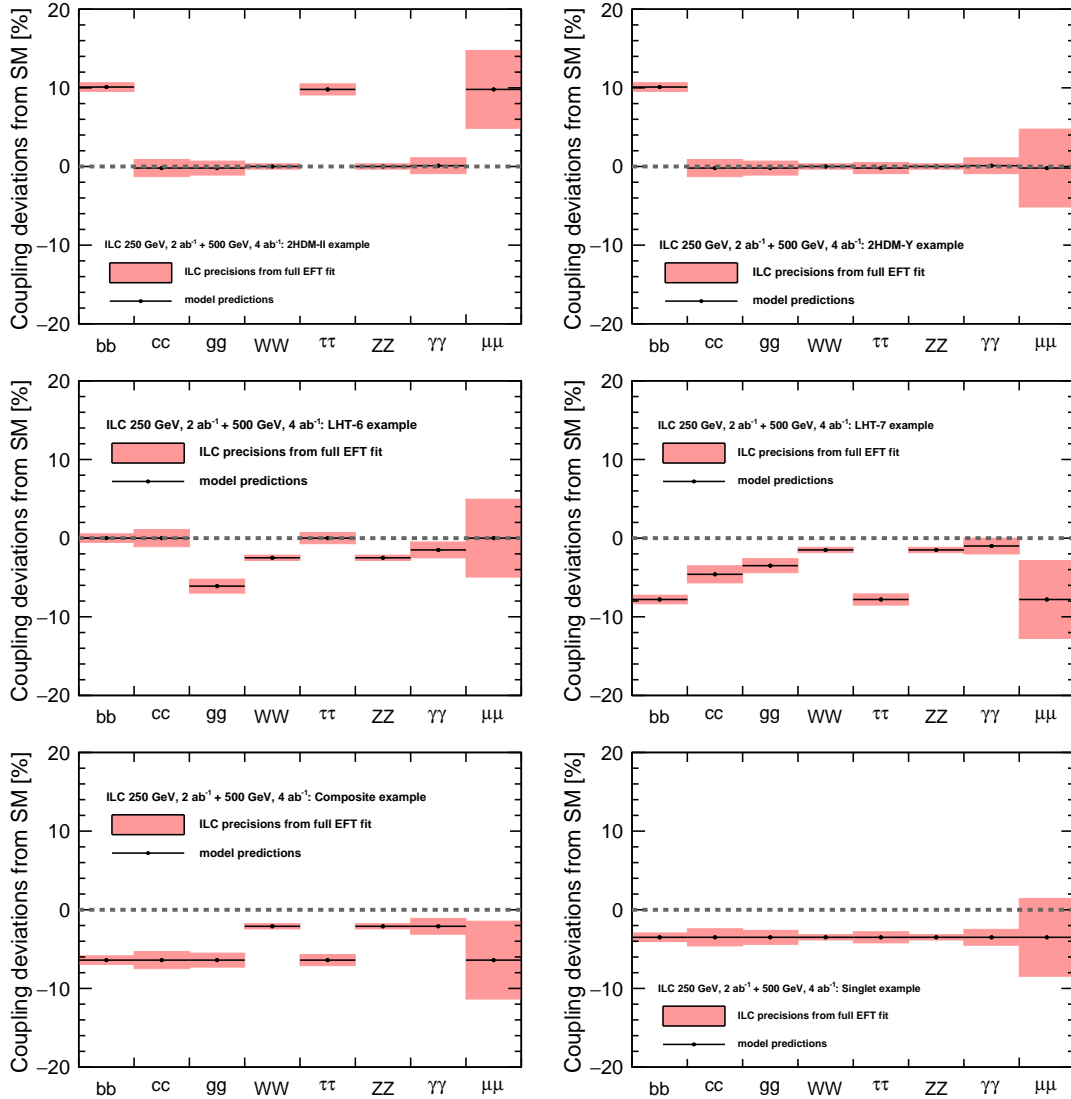


Figure 14.5: Relative deviations of the Higgs boson couplings in six diverse models of new physics. First row: 2-Higgs doublet models; Second row: Little Higgs models; Third row: a Composite Higgs model and a Scalar Singlet model. Error intervals shown are those for the ILC500. From [658]; see this reference for more details.

boson models, there is an overall shift of the scale of the Higgs boson couplings. This shift is especially visible as shifts in the Higgs boson couplings to W and Z , which are expected to be the best measured couplings at the ILC. Models with scalar mixing can also lead to large changes in the Higgs boson self-coupling.

- In models with top quark partners, the Higgs boson coupling to gluons may be shifted, either positively or negatively, depending on the model. This same effect should be seen in models with extra space dimensions. These models generally produce large deviations in the direct Higgs boson coupling to the top quark.
- In models in which the quark and lepton flavor hierarchies originate from extended Higgs sector models with different Higgs bosons coupling to each generation, the Higgs boson couplings to first and second generation fermions can be enhanced. At the ILC, this effect can be seen in the Higgs boson couplings to c , s , and μ .

To illustrate the diversity of expectations for the Higgs boson couplings, we show in Fig. 14.5 the predictions for Higgs coupling deviations from the SM in six specific models of different types, including extended Higgs models, models with composite Higgs bosons, and models with scalar singlets.

The ILC, with its comprehensive, high-precision program of Higgs boson measurements, may well be able to see the overall pattern of Higgs boson couplings. This will be vital information to plan the future stages of exploration with higher energy accelerators.

Chapter 15

Long-Term Future of the ILC Laboratory

The story of the ILC does not end at 500 GeV, or even at 1 TeV. For the studies that we have described in this report, the ILC will create a new international laboratory with substantial capabilities and infrastructure. It will be a major world center for particle physics. If the ILC is constructed in Japan, this laboratory will play a large role in furthering the current rapid growth of physics research in the Asia-Pacific region.

Although we are now proposing only the first stages of this laboratory, it is important that the ILC laboratory should have a longer-term vision that continues the study of particle physics. Especially if the precision study of the Higgs boson and the top quark reveals the existence of new physics at higher energies, it will be imperative to use the resources of the ILC laboratory to go there and fully characterize the interactions that extend the current Standard Model. Any electron accelerator at energies above 500 GeV must be a linear collider. Thus, it is natural to consider extensions of the ILC to meet this goal.

The design of the stages of the ILC up to 500 GeV is mature, well-supported by concrete demonstrations, and ready for construction. We have presented the relevant ideas and supporting R&D in Chapter 4. In contrast, the ideas presented in this section are frankly speculative. However, enough is understood to claim that there is a path from the currently proposed ILC to much higher energies. The routes presented here can be evaluated more concretely and the technologies brought to realization during the construction of the ILC and the course of the experimental program that we have described in the previous chapters.

The layout and geology of the currently favored ILC site allow the construction of linear accelerators as long as 50 km. Still, to reach multi-TeV or higher energies, we will need to develop new accelerating technologies with much higher accelerating gradients. These can be based on superconducting RF, normal-conducting RF, or advanced concepts such as plasma wakefield acceleration.

In this Section, we will describe visions for the long-term future of the ILC Laboratory. We first discuss the physics case. Up to 3 TeV in the center of mass, the physics case for e^+e^- colliders

has been studied in detail as part of the preparations for the CLIC program. We will review the most important items in Sec. 15.1. Less study has been done for e^+e^- above 10 TeV, but there are important reasons to study these energies with lepton collider. We discuss these in Sec. 15.2. We then present possible accelerator technologies to reach these energies. Section 15.3 will discuss designs for superconducting RF accelerators. Section 15.4 will discuss designs based on normal conducting accelerators, both with two-beam acceleration, as in CLIC, and using new advances in direct RF acceleration. Section 15.5 will discuss designs based on advanced acceleration ideas such as plasma wakefield acceleration.

All of these ideas point to a long-term future for the ILC Laboratory, in which this laboratory remains at the forefront of discovery in particle physics.

15.1 Physics opportunities for a multi-TeV collider

In this section, we will describe the physics issues for e^+e^- colliders up to a CM energy of 3 TeV. Multi-TeV collider options open the gates to accessing TeV new physics directly and exploring new physics in a way that is complementary to the lower energy Higgs factory and high energy proton colliders. A multi-TeV lepton collider will shed light on many core puzzles of particle physics. We can probe the Higgs self-coupling, the top quark Yukawa coupling, and electroweak precision observables in di-boson production, adding precision measurements of the SM and testing electroweak symmetry breaking and universal theories. This program can also access flavor physics through measurements of flavor-changing neutral currents and lepton flavor universality violation and through top quark and Higgs boson exotic decays. A multi-TeV collider enables us to directly produce and probe new particles that might be within its energy range, such as top quark partners, dark matter particles, and hidden sector states. The prospects for e^+e^- physics up to E_{CM} of 3 TeV have been studied in detail in for the CLIC program at CERN [509, 715]. In this section, we will select a few representative physics topics that are targeted at these energies.

Higgs Self-Coupling

As we have discussed in Sec. 10.2.2, the Higgs field self-coupling can be measured using the processes of di-Higgs production at e^+e^- colliders. A multi-TeV lepton collider offers two main di-Higgs production modes [526]: double Higgs-strahlung ($e^+e^- \rightarrow Zh h$) and vector boson fusion ($e^+e^- \rightarrow \nu\bar{\nu} h h$). The cross sections for the two channels have different dependences on the center of mass energy of the collider, as shown in the left-hand panel of Fig. 15.1. Double Higgs-strahlung reaches a maximum not far above threshold (at $\sqrt{s} \sim 500$ GeV) and then decreases due to the s -channel Z boson propagator. The vector boson fusion cross section receives a logarithmic enhancement at higher collider energies, giving an advantage for its study at multi-TeV energies. The CLIC study considered measurements at e^+e^- colliders with $\sqrt{s} = 1.4$ and 3 TeV, with 1.5 and 2 ab^{-1} of integrated luminosity, respectively, with unpolarized beams [526].

In the right-hand panel of Fig. 15.1, we show how the trilinear Higgs self-coupling changes the total cross-section in the two leading di-Higgs channels. The result is shown as a function of

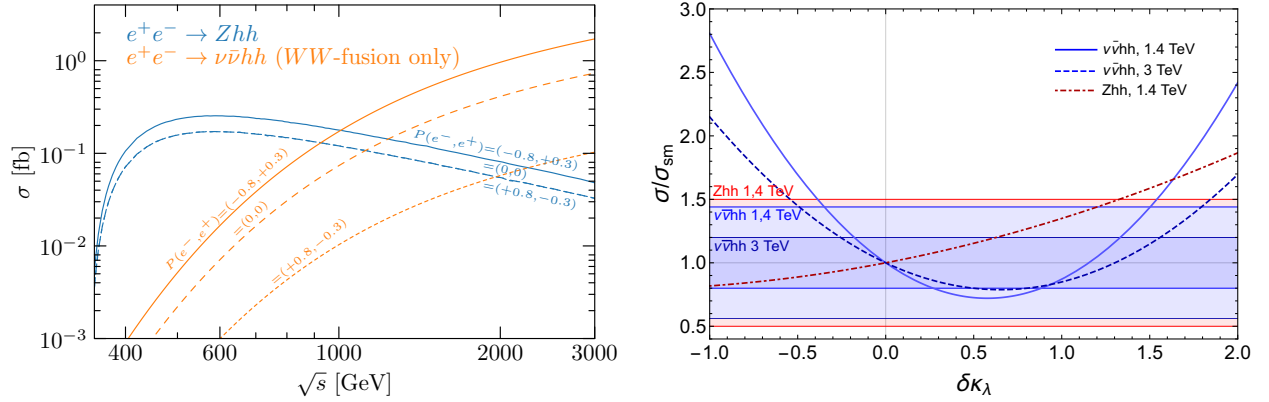


Figure 15.1: Left: Cross section of the two leading diHiggs production modes in a lepton collider as a function of the center-of-mass energy. Right: Dependence of the signal strengths on the trilinear coupling of the Higgs with the horizontal bands showing the estimated sensitivities.

$\delta\kappa_\lambda = \lambda/\lambda_{SM} - 1$, the correction to the Higgs self coupling normalized to its SM value. We can see an interesting complementarity between these two leading di-Higgs production channels. The Zhh cross-section grows for $\delta\kappa_\lambda > 0$ through constructive interference, more sensitive to positive deviations in the trilinear Higgs self-coupling. The $\nu\bar{\nu}hh$ production, instead, is more sensitive to negative shifts of the trilinear coupling. Note, though, that, at high energies, even if the total cross section is insensitive to the presence of $\delta\kappa_\lambda$, the di-Higgs mass distribution shifts toward values closer to $2m_H$ when $\delta\kappa_\lambda$ becomes large [716].

After combining both vector boson fusion and double Higgsstrahlung channels, the two runs at 1.4 TeV and 3 TeV are sufficient to exclude the second fit minimum at $\delta\kappa_\lambda \sim 1$ at 95%CL. We show the results in Table 15.1.

The di-Higgs production is also affected by modifications in other Higgs couplings. To consistently reduce the model dependence, we performed a study comparing single-operator constraints to that of a global fit, shown in Table 15.2. The $\nu\bar{\nu}hh$ production with a differential analysis including 4 bins in the m_{hh} distribution, and the inclusive Zhh cross-section and the $\delta\kappa_\lambda$ dependence of the single-Higgs processes are included in this fit. The 3 TeV run will markedly increase the Higgs self-coupling sensitivity over that for 1.4 TeV due to the increase in statistics allowing access to the differential distributions.

Higgs and Top Compositeness

The Higgs precision program at a multi-TeV lepton collider not only reveals the Higgs trilinear coupling but, more importantly, provides a holistic understanding of the dynamics of the Higgs boson. We illustrate this through an analysis sensitive to the geometric size l_H of the composite Higgs boson. As we have discussed in Sec. 13.4, the size of a composite Higgs boson is measured by the SMEFT coefficient c_H . This and other operator coefficients are enhanced or suppressed by positive or negative powers of the composite coupling parameter g_* [712]. Constraints on the

	$\Delta\chi^2 = 1$	$\Delta\chi^2 = 4$
1.4 TeV	$[-0.22, 0.48]$	$[-0.40, 1.05]$
3 TeV	$[-0.13, 0.16] \cup [1.13, 1.42]$	$[-0.24, 0.42] \cup [0.87, 1.53]$
combined	$[-0.12, 0.14]$	$[-0.21, 0.35]$
5 bins m_H for $\nu\bar{\nu}hh$	$[-0.11, 0.13]$	$[-0.21, 0.29]$

Table 15.1: Single operator constraints on $\delta\kappa_\lambda$ deriving from the measurements of Zhh and $\nu\bar{\nu}hh$ cross sections, with all other parameters fixed to their standard-model values. In the fourth row, a differential m_{hh} measurement in weak boson fusion di-Higgs production at $\sqrt{s} = 3$ TeV is further included.

	68 %CL	95%CL
1.4 TeV, exclusive	$[-0.21, 0.34]$	$[-0.38, 0.89]$
1.4 TeV, global	$[-0.22, 0.40]$	$[-0.39, 1.00]$
1.4 + 3 TeV, exclusive	$[-0.11, 0.12]$	$[-0.20, 0.27]$
1.4 + 3 TeV, global	$[-0.11, 0.13]$	$[-0.21, 0.29]$

Table 15.2: Single and global constraints on $\delta\kappa_\lambda$ after the 1.4 and 3 TeV runs of CLIC. We also show the combined results with the HL-LHC.

SMEFT coefficients can be translated into constraints on g_* and a SMEFT decoupling scale m_* as illustrated in Figure 15.2a [509]. The projected HL-LHC exclusion reach (as opposed to discovery lines shown for CLIC) is also shown in the figures. The improvement achieved by CLIC at small and intermediate g_* is due to the high-energy stages that allow for a very precise determination of the c_H , c_T , c_{WW} and c_{BB} SMEFT coefficients. Single Higgs boson couplings measurements provide the most stringent constraints at large g_* .

Figure 15.2a clarifies the complementarity between precision and high mass searches. Precision measurements of the Higgs boson couplings probe one combination of the two characteristic parameters of this scenario, while the other combination is probed with less copiously produced events at $E_{CM} = 3$ TeV and high invariant mass. We can also consider top quark compositeness in connection with the naturalness puzzle. SMEFT operators in the top sector can be probed by measuring the top Yukawa coupling and as well as $t\bar{t}$ production at high-energy [717]. The reach in the “total t_R compositeness” scenario is displayed on Fig. 15.2b. For further details in the case of “partial top compositeness” see Sec. 2.1 of Ref. [509] and Sec. 10.2 of Refs. [480].

Dark Matter

As we have emphasized in Sec. 14.1, little is known about the particle identity of cosmic dark matter. A general and compelling candidate is the thermal Weakly Interacting Massive Particle (WIMP). WIMPs are in thermal equilibrium in the early universe. From this boundary condition, it is possible to predict the current abundance of these particles. This yields the observed abundance

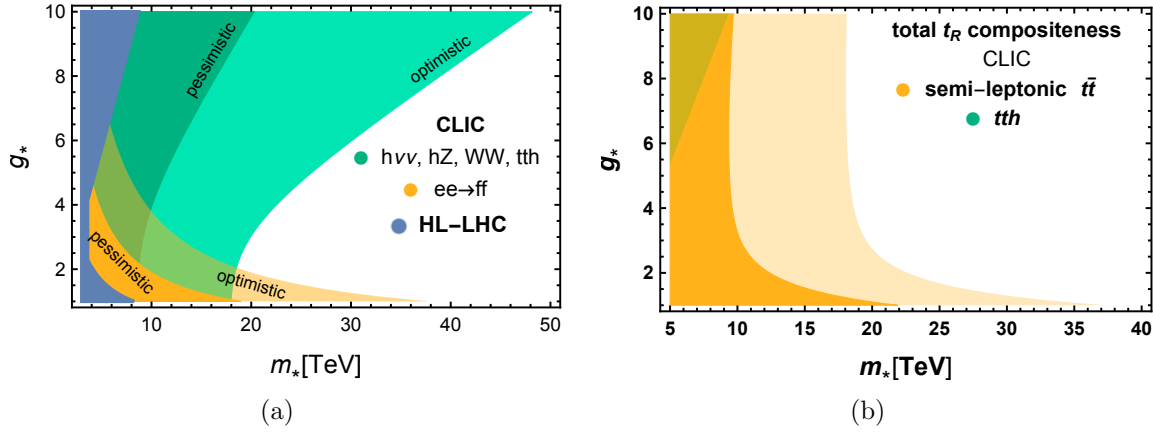


Figure 15.2: Composite Higgs reach from Higgs boson, top quark and Drell-Yan studies taken from Refs. [509] and [480]. Left panel: 5σ discovery contours for Higgs compositeness in the (m_*, g_*) plane, and as well the 2σ projected exclusions from the HL-LHC. Right panel: The 5σ top quark compositeness discovery contours in the (m_*, g_*) planes from studies of $t\bar{t}$ and $t\bar{t}h$ final states. In both panels, darker and lighter shaded areas correspond to the variations of the size of the operators' coefficients by a factor of 2 or 1/2 on top of the baseline expectation from the values of m_* and g_* .

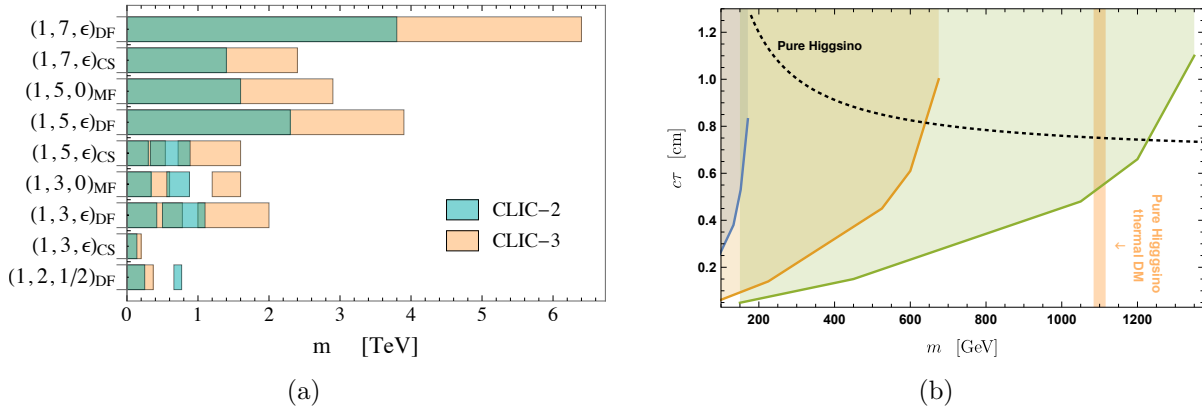


Figure 15.3: Reach of direct searches for Dark Matter. Left panel: 95% excluded masses for new electroweak n -plet states with hypercharge Y . The exclusion results for each state denoted by $(1, n, Y)$ at CLIC Stage2 and Stage3 are presented in green and yellow bar [718]. Right panel: 95% excluded region for pure Higgsino in the mass-lifetime plane. The black dashed line denotes the lifetime of a pure Higgsino. The green, yellow and blue areas correspond to 3 TeV, 1.5 TeV and 380 GeV CLIC expected exclusions, respectively.

of dark matter for masses of order

$$M_{\text{WIMP}} \simeq \text{TeV} (g_{\text{DM}}/g_w)^2, \quad (15.1)$$

where g_{DM} gives the strength of the WIMP coupling in its annihilation reactions and g_w is the SM weak interaction coupling.

In Refs. [509, 719, 717] comprehensive studies are presented to test general WIMPs. WIMPs specified by masses and quantum numbers of new states are dubbed “Minimal DM” [720]. It is shown in these studies that WIMPs can come from many different representations of the SM $SU(2)$ gauge group, even as large as the 7-plet. This whole variety of candidate WIMPs are targets for future colliders. TeV lepton colliders can probe them in different ways, including the ISR photon searches discussed in Sec. 10.5.3 but also in processes involving their charged $SU(2)$ partners. We show the 95% CL sensitivities from of Ref. [718] in Fig. 15.3a. The sensitivity reaches the thermal targets in the case of the Dirac fermion triplet candidate $(1, 3, \epsilon)_{\text{DF}}$. Next, one can exploit the long-lived particle signatures from the charged state in the electroweak multiplet. Its distinctive signature is thus a disappearing track. In figure 15.3b we shows that a 3 TeV e^+e^- collider can discover the thermal Higgsino at 1.1 TeV.

Beyond the minimal dark matter scenarios, thermal WIMPs can show up in different ways at a TeV lepton collider. For instance, in co-annihilation scenarios, two nearly degenerate states can scatter with a larger rate than the DM alone. The Inert Doublet model, discussed earlier in Sec. 10.5.2, can also be thoroughly explored at TeV lepton colliders, extending significantly the domain of the parameters space probed in comparison to the HL-LHC capabilities [580, 583]. Details on these and other models are presented in [509, 719]. Here we are content with stating that, in general, a TeV lepton collider can effectively probe DM models with a sufficient mass-splitting that the DM particles are produced promptly, filling the gap left by the LHC searches.

Hidden Sector

Hidden sector dynamics represents a large class of well-motivated BSM physics that is elusive at hadron colliders. Specialized search strategies are often needed. Here we choose two examples: an RPV electroweakino in connection to baryogenesis, and Higgs decaying into long-lived hadronic particles in connection to neutral naturalness. The first example represents the reach for heavy new states and the second example represents the reach for light states through Higgs decays.

R-parity Violating Long-Lived Wino and Higgsino: We consider a weak scale particle X that decays after thermal freeze-out and has an R-parity violating, baryon number violating decay. The particle freezes out when its annihilation rate falls below the Hubble expansion rate. The temperature at freeze-out, T_{fo} , depends only logarithmically on the annihilation cross-section, such that $T_{\text{fo}} \sim M_X/20$ for annihilation cross-sections $\sim \text{fb}$.

The cosmological condition that X decay out of equilibrium requires that

$$c\tau_X \gtrsim 1 \text{ cm} \left(\frac{100 \text{ GeV}}{M_X} \right)^2. \quad (15.2)$$

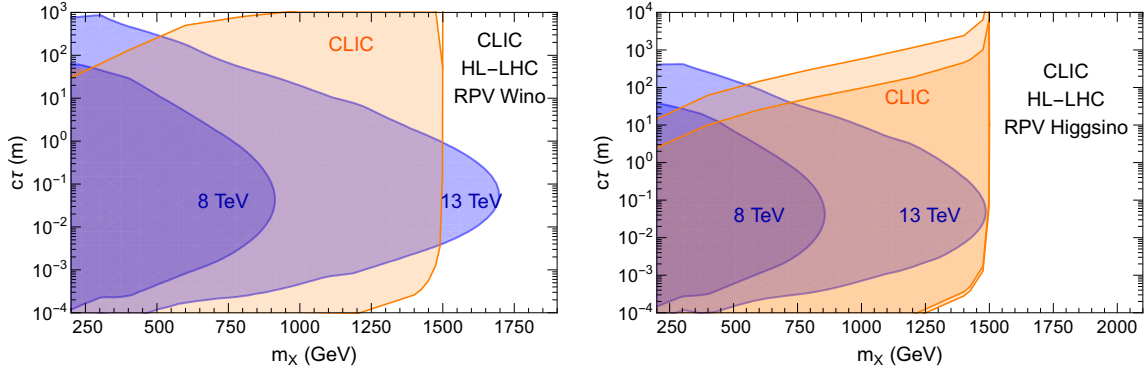


Figure 15.4: Event rates and exclusions for the wino and higgsino signal in the lifetime vs. mass plane. Orange: darker region corresponds to $N > 30$ events in the CLIC acceptance, lighter orange regions corresponds to $N > 3$ events and correspond to a projected 95% C.L. exclusion limit for zero expected background. The left (right) panel refers to the RPV wino (higgsino) signal. Blue region: the recasted current and HL-LHC (3 ab^{-1}) projected 95% C.L. exclusion limit as the function of Wino mass and its lifetime.

Scattering with the SM may keep X in thermal equilibrium down to T_{fo} , in which case the decay length should be somewhat longer. If X decays after the freeze-out, this leads to a final baryon asymmetry proportional the relic abundance that this particle would produce if it did not decay [721]. In any case, This model predicts new particles that can decay with a range of possible lifetimes, visible in various components of a detector at a collider, typically in the displaced vertex regime (or out of the detector as missing energy).

If the decay temperature is less than the freeze-out temperature, $T_{\text{fo}} > T_{\text{d}} > T_{\text{BBN}}$, and assuming that we can neglect washout processes, the baryon asymmetry is given by

$$\Delta_B = \epsilon_{\text{CP}} n_X(T_{\text{fo}}), \quad (15.3)$$

where $\epsilon_{\text{CP}} < 1$ is a measure of CP violation in the decays that can be generated by interference between tree-level and loop-level decay diagrams. Directly measuring such a CP violation effect tied to baryogenesis at collider experiments is exciting yet generally challenging. We will focus on displaced decay signals tied to the other Sakharov condition for baryogenesis.

Note that the lifetime of the parent particle X can be naturally very different from that expected from the couplings that lead to its production. For example, suppose that an approximately conserved Z_2 symmetry is responsible for the long lifetime. In that case, X particles can still be produced in pairs via Z_2 conserving interactions but decay slowly through interactions that violate the symmetry. The TeV lepton collider could copiously produce these particles. An earlier study proposed simplified models for WIMP baryogenesis mechanisms and studies of sensitivity to these models in some searches at ATLAS and CMS [722].

The coverage extends to long and short lifetimes, covering 0.1 millimeters to 500 meters for a 500 GeV wino. These pair-produced winos have low boost factors and therefore move slowly. Further development in using the precision timing for LLPs at the LHC, similar to the GMSB Higgsino

benchmark study in Ref. [362], could improve the HL-LHC sensitivity significantly, especially for the long lifetime regime.

The advantage of high collision energy enables the LHC to cover wino mass up to 1650 GeV in the most sensitive $c\tau$ range (~ 10 cm). 3 TeV CLIC thus cannot compete with LHC in terms of the mass reach of the wino in general. But there is ample parameter space in $c\tau$ at masses below 1.5 TeV that HL-LHC is not sensitive to. This is due to the extensive QCD background at the LHC and the current limit in vertex reconstruction efficiency. In contrast, an e^+e^- collider provides a much cleaner environment for these searches, with almost complete coverage for electroweak states below 1.5 TeV mass. With a much lower background (in particular for hadronic channel) and improved vertex reconstruction techniques, a 3 TeV collider has the potential to close up the region that HL-LHC is not capable of effectively probing, as illustrated in Fig. 15.4.

In Fig. 15.4, the projected exclusion limit for a 3 TeV e^+e^- collider at 95% C.L. for the luminosity of 3 ab^{-1} is indicated by the orange region in the wino mass and $c\tau$ parameter space, overlaid on the blue regions showing the LHC sensitivity. Here we simulated pair production of wino-like charginos at 3 TeV. The charginos almost exclusively decay to wino-like neutralino, and a hefty μ term heavily suppresses a soft pion since the couplings to bino-like neutralino states. The wino-like neutralino decays hadronically via RPV couplings. We make a simplifying assumption for charginos: $c\tau_{\chi^\pm \rightarrow \chi^0} \ll c\tau_{\chi^\pm(\text{RPV})}$, so that tracks contributing to DVs come entirely from wino-like neutralinos and the soft pion track is not associated with any vertex. We assume a nearly perfect vertex reconstruction efficiency in the $c\tau$ range of 0.3 – 100 mm for the analysis. An e^+e^- collider at 3 TeV with 3 ab^{-1} luminosity is sensitive to the large parts of parameter space that LHC is not, below the wino mass of 1500 GeV. It almost entirely covers the open parameter space for $c\tau > 1$ cm and $m_\chi < 1500$ GeV. For lower $c\tau$, this lepton collider can offer up to an order of magnitude improvement in the reach in $c\tau$.

Higgs-portal singlet model: Whether a secluded sector exists in a “hidden world” is an open question. Due to a tiny coupling to Standard Model states, these particles may be secluded to us. Such feeble interactions may be helpful in many contexts to address open issues of the Standard Model, see, e.g., Ref. [723] for a discussion. These searches are very challenging as the properties of the new physics states vary. Consequently, a broad program of searches needs to be put in place to explore this idea effectively. In this context, new physics may manifest itself with light new particles. A TeV lepton collider can make progress on the experimental exploration of this scenario. For example, the clean environment and the absence of triggers allow one to improve significantly over the HL-LHC in the search for Higgs or Higgs-like bosons decay to long-lived particles.

In Fig. 15.5, we compare the 95% C.L. reach of HL-LHC with a 3 TeV e^+e^- collider for this class of models. The LHC sensitivity of various Higgs portal models is studied in [360]. These include Twin Higgs models, Folded SUSY models, quirky little Higgs models, etc. Similar LHC sensitivity is obtained for the Higgs portal singlet model embedded in RPV-NMSSM that decays to SM quarks via RPV couplings as shown by the blue line in Fig. 15.5 for $m_\chi = 30$ GeV.

At an e^+e^- collider, the dominant mode of production is via WW fusion, which has a cross-

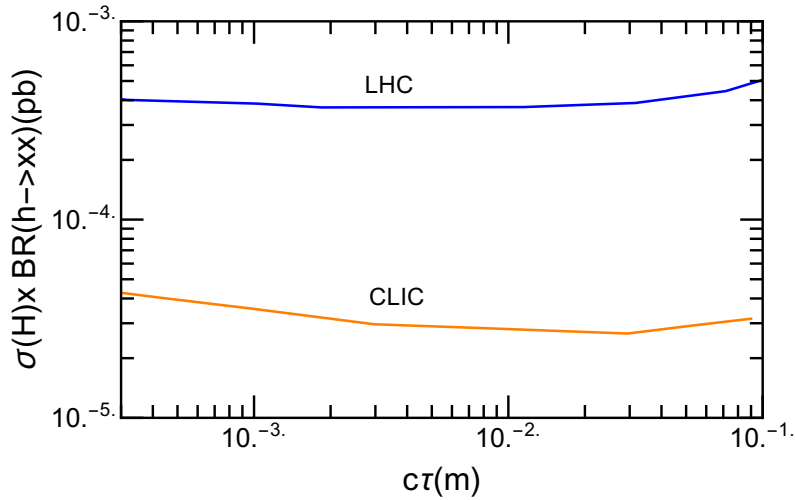


Figure 15.5: Blue line: HL-LHC projected 95% C.L. exclusion limit for the Higgs portal singlet model as the function of $c\tau_\chi$ for $m_\chi = 30$ GeV. Orange line: projection for CLIC with the same model.

section an order of magnitude lower than that at the LHC. Since we are dealing with on-shell production of light states, the cleaner environments and vertex reconstruction efficiencies can enable an e^+e^- collider to have better $c\tau_\chi$ coverage than HL-LHC for a given mass of the exotic particle, similar to the heavier case of RPV wino discussed before. This can be observed in Fig. 15.5. The CLIC sensitivity to $h \rightarrow \chi\chi$ at 3 TeV for 95% C.L. is indicated by the orange line, using the sensitivity given for the Hidden Valley models. This is an order of magnitude better reach in the $c\tau_\chi$ range favored by the WIMP baryogenesis models with light singlets (< 100 GeV).

A TeV lepton collider can also search for relatively heavy Axion-Like Particles motivated by various theoretical contexts. As a high energy collider, it can probe ALPs outside the reach of dedicated low-energy experiments [624]. We can see that for the photo-phobic ALP [724] case, one can improve about one order of magnitude of improvement.

15.2 Physics opportunities for a multi-10 TeV collider

Beyond 3 TeV in the parton-parton CM energy, there are important issues that particle physics must explore. In this section, we will present arguments that call for an advanced collider with parton CM energies of order 10 TeV and discuss some aspects of the experimental program to reach these energies with an electron accelerator.

There are several proposals for such a collider already on the table, including the FCC-hh [725] and a muon collider [726]. The report [727] put forward preliminary designs for a 30 TeV e^+e^- collider (ALIC), based on technologies now under development for advanced electron acceleration. This possibility has also been discussed earlier in this document, in Sec. 15.5. Given the uncertain-

ties in technology and cost and the long time expected to realize such a collider, it is important to continue R&D along all three of these lines. In particular, it would be wonderful if a true highest energy accelerator could also take advantage of the experimental features such as freedom from QCD backgrounds, full event reconstruction, and polarization, that we have stressed for ILC in this report.

We are high-energy physicists, so it is a part of our culture to demand to explore continually higher energies. But it is important for us to enumerate issues that explicitly require colliders with higher CM energies, beyond simply extending search limits to higher mass or precision. In fact, there are three issues that now call for colliders with parton CM energies of 10 TeV and above.

The first motivation for 10 TeV scale experiments is the issue of electroweak symmetry breaking. Before the start of the LHC, most theorists believed that the particles most directly responsible for creating the Higgs field potential had masses near 1 TeV and would be discovered early in the LHC program. This led to optimism that the entire spectrum of supersymmetry partners of SM particles might be accessible at the LHC. Of course, this belief proved not to be correct. New expectations were established, in particular, for models of supersymmetry, based on the idea of “more minimal” or “natural” supersymmetry [728], in which only the Higgs boson partners and the top squarks are light. The paper [729] set out expectations for the masses of supersymmetric particles in this framework, but, today, these are also excluded by LHC searches. Other mechanisms for generating the Higgs boson mass scale discussed in the 2000’s have met similar problems.

There have been three responses to this situation. The first is to dismiss a mechanical explanation for the Higgs boson mass scale, ascribing this to the anthropic principle or other physics that originates from quantum gravity. Unfortunately, there is no specific predictive model of this type. The second is to predict the Higgs mass scale as a consequence of new physics in the process of cosmic inflation, as, for example, in the relaxion [730] or self-organized localization [731] mechanisms.

However, the most concrete models that address this question are those that embed the generation of the Higgs potential in a more general structure. A particular example is given by Little Higgs models [732, 733] where new strong interactions at a very high mass scale Λ drive a spontaneous symmetry breaking that produces a multiplet of Goldstone bosons that includes the Higgs boson. Coupling of this sector to the SM induces some light particles to acquire a masses $M^2 \sim (\alpha_c/4\pi)\Lambda^2$, but the Higgs multiplet escapes obtaining a mass at this level. Then, finally, the Higgs multiplet acquires a potential at the level of $M^2 \sim (\alpha_c/4\pi)^2\Lambda^2$. Putting $\alpha_c \sim \alpha_w \sim 1/30$, we need $M \sim$ few TeV and $\Lambda \sim$ tens of TeV. A similar pattern is found in Randall-Sundrum models with a 5th dimension of space [534]. If the lowest-mass Kaluza-Klein extra-dimensional excitations have masses of a few TeV, these can radiatively generate the Higgs potential [734]. However, much higher energies are needed to discover a series of recurrences of Kaluza-Klein that would give evidence for the 5-dimensional geometry. Within models of supersymmetry, there are also ideas that can extend the range of superparticle masses, including Dirac gauginos and “supersoft” supersymmetry breaking [735, 736, 737, 738, 739].

The second motivation for 10 TeV scale experiments is the flavor problem. In the SM, the quark and lepton masses and mixings are generated from the matrix of Yukawa couplings of the fermions to the Higgs boson. Taking the SM literally, the elements of this matrix are renormalized

parameters that need to be specified externally—that is, they have no explanation. In models of flavor dynamics that extend the SM, new particles are severely constrained if their masses are below 1 TeV. But for particles with masses in the multi-TeV region, more possibilities open up. In particular, models of multi-TeV mass leptoquarks can explain the anomalies in B meson decays suggested by results of the LHCb experiment [740]. Vector leptoquarks have also been proposed to explain the apparent anomaly in the muon $(g - 2)$ [741]. In these models, the lightest leptoquarks are those that involve particular flavor combinations, for example, coupling to μ and b . But if leptoquarks exist, there should be bosons that couple to all combinations of quark and lepton generations. The full explanation of this structure will again take us into the multi-10-TeV regime.

The third motivation for 10 TeV scale experiments comes from the exploration of the space of dark matter candidates. The most attractive candidates for particle dark matter are those whose cosmic density is generated in the early universe as particles in thermal equilibrium that freeze out as the universe cools. For particles with electroweak couplings, the assumption of thermal freeze-out leads to particle masses near 100 GeV. Such models are strongly challenged now by the limits on direct detection cross sections. One way to address this problem is to consider more weakly coupled dark matter candidates such as appear in the dark sector models discussed in Secs. 10.6 and 11.3. But the opposite direction is also possible. For dark matter particle sectors with strong interactions, the condition of thermal freeze-out leads to the prediction of heavier masses. The mass limit from unitarity bounds is in region of 100s of TeV [742]. But this indicates that there is a large range to explore. Given the difficulties discussed earlier for finding even 1 TeV WIMPs at proton-proton colliders, this exploration cannot be done except at an electroweak collider with energies well above the TeV range.

For all of these motivations, evidence for physics beyond the SM can be found in current experiments. The search for this evidence will be extended by particle searches at the HL-LHC and, as we have explained in this report, by precision measurements on the Higgs boson and the top quark at the ILC. To fully explore the consequences of these discoveries, however, we will need accelerators in the 10s of TeV energy range. Access to the electroweak sector at these energies will be essential, and thus a lepton collider will be the instrument of choice.

For an electron-based collider, such a high energy machine must be a linear collider. Then the facilities of a linear collider laboratory such as the ILC Laboratory and the experience of operating a linear collider for high luminosity will be essential to proceed down this road. We now turn to discussion of technologies that could take the ILC Laboratory to energies well above those of the ILC program.

15.3 Very high gradient superconducting RF

In this section we will consider ILC upgrade paths beyond 1 TeV using Superconducting RF cavities with improved performance. We will discuss extensions in energy (1) to 2 TeV and (2) to 3 TeV, depending on the needs of high energy physics.

Cost are quoted in this section for the comparison of options. These are not detailed bottom-up costs as have been presented in Sec. 4.1.7 for the 250 GeV ILC design but rather are extrapolations

based on the costing scheme used there. Absolute cost numbers should be used with caution, especially in comparison to other technologies. As in Sec. 4.1.7, costs are quoted in ILC currency units, 1 ILCU = \$ 1 US using 2012 prices and are capital costs that do not include manpower and detectors.

1. From 1 TeV to 2 TeV, the design will be based one of the paths:
 - (a) Gradient advances of Nb cavities to 55 MV/m anticipated from on-going SRF R&D on Nb structures discussed in Sec. 4.3.
 - (b) Radically new travelling wave (TW) superconducting structures [153, 154, 155] optimized for effective gradients of 70+ MV/m.
2. From 1 TeV to 3 TeV based on one of the paths:
 - (a) Radically new travelling wave (TW) superconducting structures [153, 154, 155] optimized for effective gradients of 70+ MV/m.
 - (b) 80 MV/m gradient potential for Nb₃Sn [157] with a Q of 1×10^{10} . Further, the operating temperature is 4.2 K instead of 2 K.

We will discuss each of these paths in turn and estimate for each the cost increment beyond the 1 TeV ILC and the power requirements.

Cost and power estimates

ILC Energy upgrades beyond 1 TeV (except path 2b) require 300–400 MW AC power for operation. We can expect further reductions in AC power from on-going developments under the Green-ILC program described in Sec. 4.1.6. Efforts under this umbrella are preparing to explore multiple paths to make ILC and its upgrades environmentally sustainable. Wind power is one avenue following the example of ESS in Sweden [743]. A 30–40 unit wind turbine farm is capable of providing 100 MW at a cost of 150 MEuro. Combined heat and power production using bioenergy or solar photovoltaic cells integrated in the buildings are other examples. New ways of recycling low heat water (below 50°C) would also enable agricultural use of recycled heat, such as greenhouse heating.

The 1 TeV upgrade discussion in the TDR does not apply any learning curve cost reduction to cavity, cryomodule or klystrons. Between the baseline ILC at 0.25 TeV and the upgrade options to 2 TeV and 3 TeV the total number of cavities increases by a factor of 5 from 8000 to about 40,000, and the total number of klystrons increases by a factor of 5.6 from 250 to 1500. Accordingly, we apply a 25% cost reduction for cavities and klystrons for 2.5 doublings, using the 90% learning curve in the TDR. We further assume that due to RF power developments, the efficiency of klystrons will improve from 65% (TDR) to 85%. Taking into account modulator and distribution efficiencies of 90% each, we use 65% efficiency for newly installed RF systems for 1 TeV, 2 TeV and 3 TeV upgrades but continue to use 50% efficiency for RF systems installed for the first 0.5 TeV. We expect further cost reductions from several areas of R&D already started. Among the areas under exploration are niobium material cost reduction (25%) for sheet production directly from ingots (large grains),

and/or from seamless cavity manufacturing from tubes with hydroforming or spinning to reduce the number of electron beam welds and weld preparations (15 - 20%). Based on the above ideas, we use an overall cost reduction of 50% in the cost of large productions of SW cavities. After including these reductions, we expect the cost of TW cavities will be 30% higher, leading to 15% increase in the cost of CM for TW structures.

Cost-reducing features for cryomodules [152] are to connect cryomodules in continuous, long strings similar to cryostats for long strings of superconducting magnets, saving the cost for the expensive ends. The elimination of the external cryogenic transfer line by placing all cryogenic supply and return services in the cryomodule also reduce costs, not only directly for the cryogenic components, but also by reducing tunnel space required. We estimate that by this method the filling factor from cavities to “linac tunnel length” will improve from 0.7 to 0.75.

Path 1a: 2 TeV Upgrade with 55 MV/m Nb

Scenario B of the ILC TDR [3] assumes a gradient/ Q of 45 MV/m/ 2×10^{10} for the upgrade from 500 GeV to 1 TeV. This is based on the assumption that improvements in SRF technology discussed in Sec. 4.3 will already be implemented in the design of this upgrade. Recall that the gradient/ Q for the first 500 GeV is 31.5 MV/m/ 1×10^{10} . We expect that R&D in SRF technology will continue in parallel to both construction and operation of the earlier ILC stages to reach 45 MV/m/ 2×10^{10} .

For the 2 TeV upgrade Option 1a we consider advances in SRF performance (as discussed in Sec. 4.3) to gradients/ Q of 55 MV/m/ 2×10^{10} based on the best new treatments applied to advanced shape structures such as the Re-entrant, Low-Loss, or Low-Surface-Field (LSF) candidates. Therefore, applying the best new treatments to the advanced shapes we can optimistically expect gradients from 56–59 MV/m with successful R&D.

The strategy adopted for path 1a is to replace the lowest gradient (31.5 MV/m) 0.5 TeV section of cavities/cryomodules, re-using the tunnel, RF and Refrigeration of this section, keep the 0.5 TeV section with 45 MV/m gradient (11,000 cavities), running with the slightly lower bunch charge (Table 15.4), and add 1.5 TeV with 55 MV/m and $Q = 2 \times 10^{10}$. With this approach it is possible to keep the total linac length to 52 km well below the currently expected 65 km site limit.

Table 15.3 shows high level parameters for the 2 TeV upgrade as compared to 1 TeV in the ILC TDR. Table 15.4 gives more detail parameters for beam and accelerator. The number of particles per bunch is slightly lower than for the 1 TeV case, but the number of bunches and repetition rate are the same. The peak beam current is therefore slightly lower. The total beam power for two beams increases from 27 MW to 47 MW. Other beam parameters are adjusted so that the spot size at collision is reduced to 1.6 nm (from 2.7 nm).

As shown in Table 15.4, the total number of new cavities at 55 MV/m required for 1.5 TeV is 27,000, spanning a linac length of 36 km, of which 22 km can be installed into the empty tunnel (from the removed 0.5 TeV), leaving 14 km of new tunnel to be installed. Adding in the length (16 km) of the 0.5 TeV section remaining with 45 MV/m cavities, the total linac length will be 52 km, below the expected site limit of 65 km. There are savings from cryomodule parts if the tear down and replacement are staged so that some of the removed cryomodules parts are re-used.

From 1600 CM removed from the 0.5 TeV section, we estimate the parts savings to be in the range of 0.5 B provided the removal and production of CMs are properly staged. For the new 1.5 TeV section, the cavity loaded Q is 6.7×10^6 , the input power per cavity will be 365 kW, with RF pulse length 2.0 ms, similar to the RF pulse length for 1 TeV. The total number of klystrons required is 1150 of which 360 klystrons are re-used from the 0.5 TeV removed section, and 65 klystrons are available from the 0.5 TeV remaining section (which operates with the new, lower bunch charge), leaving 725 new klystrons to be added. We use 65% efficiency for RF systems installed for 1 TeV and above, and 50% efficiency for the RF system installed for the first 0.5 TeV, to give an average efficiency of 60%. The total 2 K refrigeration required will be 66 kW, of which 33 kW is re-used, leaving 33 kW new refrigeration to be installed. We assume a cryoload safety factor and RF power overhead of 20% each for the new installations. The damping ring and positron source will be same as for 1 TeV, due to the same number of bunches, but the beam dump cost will increase. Summing all the cost components outlined, the additional cost for the 2 TeV upgrade will be 6.0 B. The AC power to operate 2 TeV will be 345 MW, making ILC with SRF attractive for 2 TeV.

Path 1b: 2 TeV Upgrade from 1 TeV with 70 MV/m TW Nb structures

This is the more attractive option because of the lower AC power and lower capital cost (see Table 15.3), but it depends strongly on the success of the development of the Travelling Wave Nb cavities with 70 MV/m.

As discussed in Sec. 4.3, TW structures offer several advantages compared to standing wave (SW) structures: substantially lower peak magnetic (H_{pk}/E_{acc}) and lower peak electric field (E_{pk}/E_{acc}) ratios, together with substantially higher R/Q (for lower cryogenic losses and lower AC power). We expect that the cost of TW SRF cavities will be 30% higher, leading to 15% increase in the cost of CM for TW structures.

The first strategy adopted in this option is again to remove the lowest gradient (31.5 MV/m) 0.5 TeV section, re-use the tunnel, RF and Refrigeration of this section, keep the 0.5 TeV section (11,000 cavities) with 45 MV/m gradient (running with the slightly lower bunch charge for 2 TeV), and add 1.5 TeV with TW SRF cavities at 70 MV/m/ $Q = 2 \times 10^{10}$ and R/Q 2 times higher than SW Nb cavities. With this approach it is possible to keep the total linac length to 44 km, well below the currently expected 65 km site limit.

As shown in Table 15.4, the total number of new TW cavities at 70 MV/m required is 21,000, spanning a linac length of 28 km, of which 22 km can be installed into the empty tunnel (from the removed 0.5 TeV), requiring 6 km of new tunnel to be installed. For 1600 CMs removed from the 0.5 TeV section, we estimate the savings in re-used parts to be in the range of 0.5B, provided the removal and production of CMs are properly staged. For the new 1.5 TeV section, the cavity loaded Q is 5×10^6 , the input power per cavity will be 460 kW, with RF pulse length 1.76 ms. The total number of klystrons required is 1180, of which 360 klystrons are re-used from the 0.5 TeV removed section, and 65 klystrons are available from the 0.5 TeV remaining section (because it operates with the lower bunch charge than for 1 TeV), leaving 755 new klystrons to be added. The average RF power efficiency of new RF systems will be 65% and the existing RF systems from the first 0.5 TeV installation will be 0.5, giving an overall RF efficiency of 61%. The total 2 K

		ILC 1 TeV TDR	ILC 2 TeV path 1a	ILC 2 TeV 2 TeV path 1b	ILC 3 TeV path 2a	ILC 3 TeV path 2b	CLIC 3 TeV [744]
Energy	TeV	1	2	2	3	3	3
Luminosity	10^{34}	4.9	7.9	7.9	6.1	6.1	5.9
AC Power	MW	< 300	345	315	400	525	590
Cap. Cost	B ILCU	+ 5.5	+11.5	+10.4	+17.3	+16.5	
Gradient (new linac)	MV/m	45	55	70	70	80	72 / 100
Q new linac	10^{10}	2	2	3	3	2 (4.2 K)	
CM unit cost	M ILCU	1.85	1.15	1.32	1.32	1.15	

Table 15.3: High level parameters for ILC energy upgrades. Costs are quoted as estimated additions to the costs from the ILC TDR. These are given in ILC currents units (as in Sec. 4.1.7) and are capital costs not including manpower and detectors. Incremental costs are given relative to the ILC 250 GeV plus 500 GeV upgrade (7.8 B ILCU).

refrigeration required will be 37 kW, of which 33 kW is re-used, leaving 4 kW new refrigeration to be installed. We assume a cryoload safety factor and RF power overhead of 20% each for the new installations. The damping ring and positron source will be same as for 1 TeV, due to the same number of bunches, but the beam dump cost will increase. Summing all the cost components outlined, the additional cost for the 2 TeV upgrade will be 4.9 B. The AC power to operate 2 TeV will be 315 MW, making this path attractive for the improved environmental impact. Note the substantial benefit to the AC power due to the 2 times higher R/Q of the TW cavities. If we follow the alternative path of removing the entire 1 TeV linac, keeping the RF, tunnel and Refrigerator, to install a brand new linac using 70 MV/m TW cavities, we will need to populate the existing 38 km of tunnel with 28,000 TW cavities (no new tunnel needed), and use the existing Refrigeration (no new refrigeration needed), adding 755 klystrons. Savings from re-using CM parts from > 3000 CM from the 1 TeV section is estimated to be 1 B. The additional capital cost for this path will be 5.2 B, comparable to the path above, and the AC power will be 240 MW, less than the path above. The shorter tunnel and lower AC power may dominate the choice of this path.

Path 2a: 3 TeV Upgrade from 1 TeV with 70 MV/m TW Nb structures

The beam bunch charge for the 3 TeV upgrade is chosen to be 3 times lower than the bunch charge for 0.5 TeV stage to obtain a luminosity comparable to CLIC 3TeV [744]. The lower bunch charge helps with wakefields and with IP backgrounds. The number of bunches per RF pulse is doubled to 4900, and the bunch spacing is lowered due to the lower bunch charge (see Table 15.4).

The option adopted here is to remove ALL of the installed cryomodules for 1 TeV and replace them with new 70 MV/m TW cavities/cryomodules, plus add new linac sections to reach 3 TeV energy. We would re-use the existing RF and Refrigeration and CM parts from the removed 1 TeV section. As shown in Table 15.4, a total of 43,000 TW cavities will be required, so that with the

	ILC 1 TeV	ILC 2 TeV	ILC 2 TeV	ILC 3 TeV	ILC 3 TeV	ILC 3 TeV	CLIC 3 TeV
units	TDR	path 1a	path 1b	path 2a	path 2b	path 2b	[744]
Energy	1	2	2	3	3	3	3
particles/bunch	1.74	1.5	1.5	0.65	0.65	0.65	0.37
bunches/train	2450	2450	2450	4900	4900	4900	312
bunch spacing	366	366	366	250	150	150	0.5
pulse current	7.6	6.6	6.6	4.16	4.16	4.16	3
rep. rate	4	4	4	4	4	4	50
RF pulse length (added linac)	1.94	2.0	1.76	2.6	2.6	2.6	0.00024
Beam power (2 beams)	27.2	47	47	61	61	61	28
ϵ_x/ϵ_y	500/3	500/2	500/2	500/2	500/2	500/2	66/2
β_x/β_y	22/0.23	22/0.23	22/0.23	16/0.15	16/0.15	16/0.15	40/1
σ_x/σ_y	335/2.7	237/1.6	237/1.6	165/1.0	165/1.0	165/1.0	0.044
σ_z	0.225	0.225	0.225	0.1	0.1	0.1	5
Ψ (beamstr. parameter)	0.21	0.5	0.5	1/045	1.045	1.045	35
δ (RMS energy spread)	10.5	20	20	16	16	16	35
Luminosity	10^{34}	4.9	7.9	7.9	6.1	6.1	5.9
photons/electron	1.95	2.1	2.1	1.2	1.2	1.2	2.2
coherent pairs	0	2×10^4	2×10^4	7.9×10^5	7.9×10^5	7.9×10^5	6.8×10^8
incoh. pairs	383	49	49	5	5	5	3×10^5
No. of klystrons (new + existing)	460 + 320 = 820	820 + 460 = 1280	755 + 425 = 1180	690 + 820 = 1500	1680 + 820 = 2500	1680 + 820 = 2500	160 (0.25 m)
No. of cavities (new + existing)	11 + 16 = 27	27 + 11 = 38	21 + 11 = 32	43 + 0 = 43	37.5 + 0 = 37.5	37.5 + 0 = 37.5	
Q_L (new cavities)	5.6	8	5	8	10	10	
input power (new cavities)	350	365	460	300	550	550	
linac length (new + existing)	16 + 22 = 38	14 + 38 = 52	6 + 38 = 44	19 + 38 = 57	12 + 38 = 50	12 + 38 = 50	42

Table 15.4: Detailed parameters for the proposed ILC energy upgrades compared with the CLIC 3 TeV design [744].

(cavity to linac tunnel) filling factor of 0.75, the total length of the 3 TeV linac will be 57 km, under the expected site limit of 65 km. 38 km of tunnel would already be present from the 1 TeV removed, requiring 19 km of new linac tunnel. The total number of klystrons required will be 1500, of which 820 are available from the 1 TeV installation. The RF system cost will be higher due to the longer RF pulse length. Also, the existing 820 klystrons and RF system will have to be upgraded to provide longer RF pulses, which will incur a cost of about 0.4 B. The efficiency of the first RF system installed with 360 klystrons for 0.5 TeV is 50%, and for the later installed RF system for the next 0.5 TeV with 460 klystrons it is 65%. Hence the average RF system efficiency used is 61%. The input power per cavity will be 300 kW due to the high gradient. The loaded Q will be 8×10^6 . The total 2 K refrigeration requirement will be 95 kW of which 51 kW is already present, leaving a balance of 44 kW to be installed. Add in the cost of needed damping rings, positron source and beam dump for increasing the number of bunches from 2450 to 4900. The total additional capital cost for 3 TeV (from 1 TeV) will be 11.8 B, shown in Table 15.3 The total AC power to run 3 TeV will be 400 MW, with substantial benefit from the 100% higher R/Q of TW structures.

Table 15.4 gives detailed parameters (for beam and accelerator) for ILC 3 TeV (Option 2a) with 70 MV/m TW structures as compared to CLIC 3 TeV. Note that the backgrounds at the IP for the ILC 3 TeV are much lower than for CLIC, and final beamstrahlung energy spread is 16% compared to 35% for CLIC. To reach the desired luminosity, the beam power is 61 MW with twice the number of bunches (4900) spaced closer together in the linac (250ns instead of 366 for 1 TeV) as allowed by the lower bunch charge. The peak beam current is 4.16 mA. The final vertical spot size is 1 nm, comparable to the CLIC case.

Path 2b: 3 TeV Upgrade with 80 MV/m Nb₃Sn structures at 4.2 K

Option 2b for 3 TeV is to consider 80 MV/m Standing Wave Nb₃Sn TESLA-like structures at 4.2 K with Q values of 1×10^{10} . In this case the challenge is to develop high performance Nb₃Sn. Due to the combined improvement of Carnot and technical efficiency at 4.2 K over 2 K, the comparison of AC power/cryo power improves from a ratio of 730 to 230. We assume that the capital cost of 4.2 K refrigeration will be a factor 3 lower than for 2 K, and that the refrigerator units installed for 1 TeV are designed so that 1 watt of cooling at 2 K would be later equivalent to 3 watts of cooling at 4.2 K when the conversion is made for the 3 TeV upgrade at 4.2 K.

Our plan would be to install Nb₃Sn cavities for 3 TeV, removing all of the cryomodules for 1 TeV and replacing them with new 80 MV/m/ $Q = 1 \times 10^{10}$ cavities/cryomodules, plus install new linac sections to reach 3 TeV energy. We will re-use the RF, Refrigeration and CM parts of the removed 1 TeV section, converting the 2 K refrigeration to remove heat load at 4.2 K. A total of 37,500 Nb₃Sn cavities will be required, so that with the filling factor (cavity to tunnel length) of 0.75, and the total length of the 3 TeV linac will be 50 km, well under the expected Japan site constraint of 65 km. 38 km of tunnel has already been installed for 1 TeV, so that 12 km of new linac will be required. The total number of klystrons required will be 2500, of which 820 are available from the removed 1 TeV installation. The existing klystrons and RF system will have to be upgraded to provide longer RF pulses (2.6 ms), which will incur a cost of about 0.4 B. The number of new klystrons required is 1680. The average efficiency of old and new RF systems will

be 63%. The input power per cavity will be 550 kW, at a loaded Q of 1×10^7 , so couplers will need to be improved. The total 4.2 K refrigeration required will be 352 kW of which 51 kW (at 2 K) is already present for 1 TeV, equivalent to 150 kW at 4.2 K. The balance of 200 kW at 4.2 K needs to be installed. Add in the cost of needed damping rings, positron source and beam dump for increasing the number of bunches from 2450 to 4900. The total additional capital cost for 3 TeV will be 11.0 B, as shown in Table 15.3. The total AC power to run 3 TeV will 525 MW.

15.4 Very high gradient normal conducting accelerators

The infrastructure that will be put in place for the ILC at either the 250 or the 500 GeV center of mass energies provides a unique resource for future experiments after the currently proposed ILC program has been completed. This statement of course applies to superconducting accelerators, but is also true for normal conducting accelerators that could follow the ILC. The ILC civil construction represents a significant investment with tunnels, electrical power distribution, cryogenic systems, *etc.*, that could be re-utilized with modifications for future experiments. The particle sources could also potentially be re-utilized depending on the details of the electron and positron bunch structures required. An advanced accelerator technology could also largely re-utilize parts of the accelerator infrastructure, including the damping rings and elements of the beam delivery system. Given the time required for construction and data collection for the ILC, novel technologies presently under investigation that could be developed into collider concepts will be able to make significant technical progress.

Having discussed in some detail the options for advanced superconducting RF acceleration, we now turn to options based on normal conducting acceleration. In this section, we will discuss possible upgrades of the ILC infrastructure based on two-beam acceleration as studied for CLIC and described in [745, 746], and also on conventional RF distribution in novel structures based either on copper cavities or more advanced materials. An example of the latter approach using copper is the Cool Copper Collider (C^3), for which the concept and the proposed R&D program have been presented in [747]. We will explain both of these concepts as potential examples for reusing the ILC infrastructure, before presenting ideas about more advanced possibilities with even higher gradients.

ILC Energy Upgrade with CLIC Technology

The Compact Linear Collider (CLIC) is a multi-TeV high-luminosity linear e^+e^- collider under development by the CLIC accelerator collaboration [748]. As a standalone proposal the CLIC accelerator has been optimised for three energy stages at centre-of-mass energies 380 GeV, 1.5 TeV and 3 TeV [749]. A future re-use of ILC infrastructure could move directly to a multi-TeV stage. Detailed studies of the CLIC accelerator, detector studies and physics potential are documented in detail at [750].

CLIC layout

A schematic overview of the accelerator configuration for the initially proposed 380 GeV, energy

stage is shown in Figure 15.6. To reach multi-TeV collision energies in an acceptable site length and at affordable cost, the main linacs use normal conducting X-band accelerating structures. These achieve a high accelerating gradient of 100 MV/m. For the first energy stage, a lower gradient of 72 MV/m is the optimum to achieve the luminosity goal, which requires a larger beam current than at higher energies.

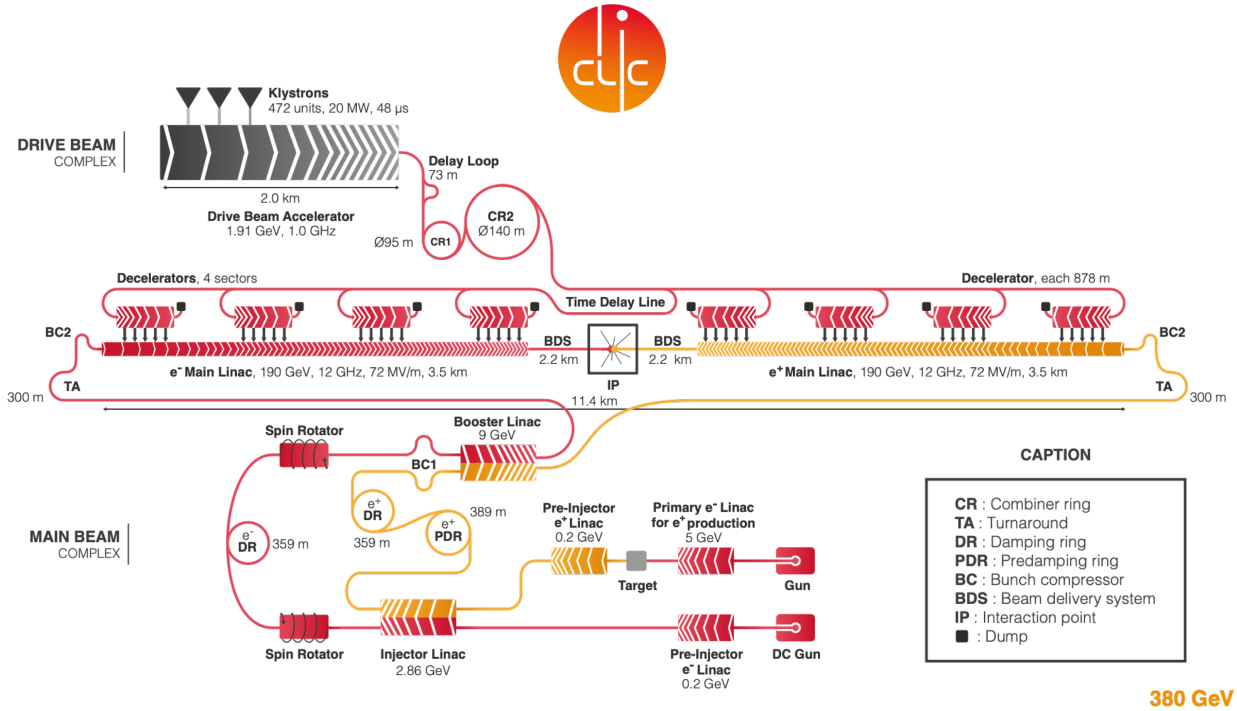


Figure 15.6: Schematic layout of the CLIC complex at 380 GeV.

In order to provide the necessary high peak power, the novel drive-beam scheme uses low-frequency klystrons to efficiently generate long RF pulses and to store their energy in a long, high-current drive-beam pulse. This beam pulse is used to generate many short, even higher intensity pulses that are distributed alongside the main linac, where they release the stored energy in power extraction and transfer structures (PETS) in the form of short RF power pulses, transferred via waveguides into the accelerating structures. This concept strongly reduces the cost and power consumption compared with powering the structures directly by klystrons.

The upgrade to higher energies is done by lengthening the main linacs. While the upgrade to 1.5 TeV can be done by increasing the energy and pulse length of the primary drive-beam, a second drive-beam complex must be added for the upgrade to 3 TeV.

Parameter overview

The parameters for the three energy stages of CLIC are given in Table 15.5. The baseline plan for operating CLIC results in an integrated luminosity per year equivalent to operating at full luminosity for 1.2×10^7 s [751]. With 8, 7 and 8 years of running at 380, 1500 and 3000 GeV respectively, and a luminosity ramp up for the first years at each stage, integrated luminosities of

Table 15.5: Key parameters of the CLIC energy stages.

Parameter	Unit	Stage 1	Stage 2	Stage 3
Centre-of-mass energy	GeV	380	1500	3000
Repetition frequency	Hz	50	50	50
Nb. of bunches per train		352	312	312
Bunch separation	ns	0.5	0.5	0.5
Pulse length	ns	244	244	244
Accelerating gradient	MV/m	72	72/100	72/100
Total luminosity	10^{34}	1.5	3.7	5.9
Lum. above 99% of \sqrt{s}	10^{34}	0.9	1.4	2
Total int. lum. per year	fb^{-1}	180	444	708
Main linac tunnel length	km	11.4	29.0	50.1
Nb. of particles per bunch	10^9	5.2	3.7	3.7
Bunch length	μm	70	44	44
IP beam size	nm	149/2.9	$\sim 60/1.5$	$\sim 40/1$
Norm. emitt. (end linac)	nm	900/20	660/20	660/20
Final RMS energy spread	%	0.35	0.35	0.35
Crossing angle (at IP)	mrاد	16.5	20	20

1.0, 2.5 and 5.0 ab^{-1} are reached for the three stages.

CLIC provides $\pm 80\%$ longitudinal electron polarization and proposes a sharing between the two polarization states at each energy stage for optimal physics reach [752].

Luminosity margins and performance

In order to achieve high luminosity, CLIC requires very small beam sizes at the collision point, as listed in Table 15.5. Recent studies have explored the margins and possibilities for increasing the luminosity, operation at the Z -pole and gamma-gamma collisions [753].

The vertical emittance and consequently the luminosity are to a large extent determined by imperfections in the accelerator complex. Significant margin has been added to the known effects to enhance the robustness of the design; without imperfections a factor three higher luminosity would be reached at 380 GeV [754]. At this energy also the repetition rate of the facility, and consequently luminosity, could be doubled from 50 Hz to 100 Hz without major changes and with relatively little increase in the overall power consumption and cost (at the $\sim 30\%$ and $\sim 5\%$ levels, respectively). This is because a large fraction of the power is used by systems in which the consumption is independent of the repetition rate.

Technical maturity

Accelerating gradients of up to 145 MV/m have been reached with the two-beam concept at the CLIC Test Facility (CTF3). Breakdown rates of the accelerating structures well below the limit of $3 \times 10^{-7}/\text{m}$ per beam pulse are being stably achieved at X-band test platforms.

Substantial progress has been made towards realising the nanometer-sized beams required by CLIC for high luminosities: the low emittances needed for the CLIC damping rings are achieved by modern synchrotron light sources; special alignment procedures for the main linac are now available; and sub-nanometer stabilisation of the final focus quadrupoles has been demonstrated.

The advanced beam-based alignment of the CLIC main linac has successfully been tested at FACET and FERMI [755, 756].

Other technology developments include the main linac modules and their auxiliary sub-systems such as vacuum, stable supports, and instrumentation. Beam instrumentation, including sub-micron level resolution beam-position monitors with time accuracy better than 20 ns and bunch-length monitors with resolution better than 20 fs, have been developed and tested with beam in CTF3.

Recent developments, among others, of high efficiency klystrons have resulted in an improved energy efficiency for the 380 GeV stage, as well as a lower estimated cost.

Schedule, cost estimate, and power consumption

The technology and construction-driven timeline for the CLIC programme as a standalone project is shown in Figure 15.7 [746]. This schedule has seven years of initial construction and commissioning. The 27 years of CLIC data-taking include two intervals of two years between the stages.

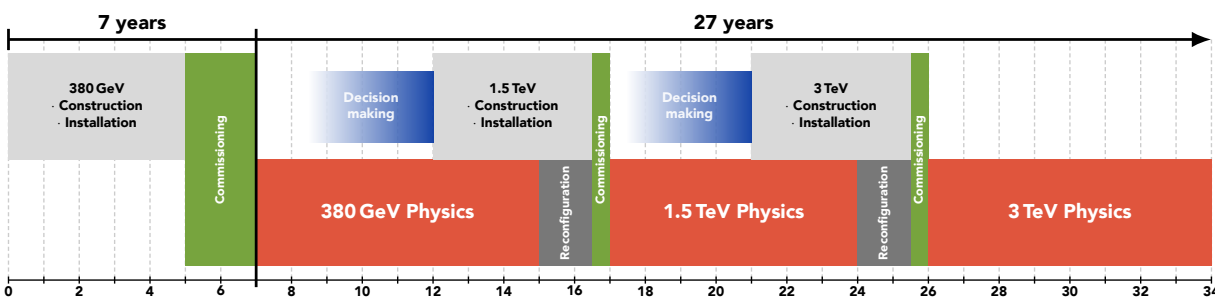


Figure 15.7: Technology and construction-driven CLIC schedule. The time needed for reconfiguration (connection, hardware commissioning) between the stages is also indicated.

The cost estimate of the initial stage as a standalone project is approximately 5.9 billion CHF. The energy upgrade to 1.5 TeV has an estimated cost of approximately 5.1 billion CHF, including the upgrade of the drive-beam RF power. The cost of the further energy upgrade to 3 TeV has been estimated at approximately 7.3 billion CHF, including the construction of a second drive-beam complex.

The nominal power consumption at the 380 GeV stage is approximately 170 MW. Earlier estimates for the 1.5 TeV and 3 TeV stages yield approximately 370 MW and 590 MW, respectively [744], however recent power savings applied to the 380 GeV design have not yet been implemented for these higher energy stages. The annual energy consumption for nominal running at the initial energy stage is estimated to be 0.8 TWh. For comparison, CERN's current energy consumption is approximately 1.2 TWh per year, of which the accelerator complex uses approximately 90%.

Future Programme

The design and implementation studies for the CLIC e^+e^- multi-TeV linear collider are at

an advanced stage. The main technical issues, cost and project timelines have been developed, demonstrated and documented.

During the coming years the focus will remain on core technology development and dissemination, which will capitalise on existing facilities (X-band test stands and the CLEAR beam facility at CERN), as well as optimising X-band components and RF-systems, involving extensive collaborations with laboratories and universities using the technology.

The use of the CLIC technology – primarily X-band RF, associated components and nano-beams – in compact medical, industrial and research linacs has become an increasingly important development and test ground for CLIC, and is destined to grow further [757]. The adoption of CLIC technology for these applications is now providing a significant boost to CLIC, especially through an enlarging commercial supplier base.

On the design side the parameters for running at multi-TeV energies, with X-band or other RF technologies, will be studied further, in particular with energy efficiency guiding the designs.

ILC Energy Upgrade with C³ Technology

C³ is a concept that is aimed at developing normal conducting RF (NCRF) accelerator technology to operate at high gradient with high RF-to-beam efficiency [747, 758]. C³ accelerators are bringing recent advances in the understanding of high-gradient operation [759, 760, 761], cavity design and RF power distribution [762], RF pulse compression [763], and cryogenic operation [764] to improve the performance of normal-conducting RF (NCRF) accelerators for high-gradient, high-brightness and high-luminosity applications. The two principal innovations for the C³ concept are: (1) the use of highly-optimized reentrant cells with distributed coupling to power the linac without cell-to-cell RF coupling, and (2) the operation of the copper accelerating structure at liquid nitrogen temperatures (77 K) to increase the RF efficiency of the structure by a factor of three, while also increasing the strength of the material. This has been found to correlate with the achievable operating gradient. The C³ approach has the potential of operating at extremely high gradients. Prototype structures have been operated with beam up to 160 MeV/m [758, 764] and single cell test cavities have exceeded 200 MeV/m gradients [765, 766]. The C³ cryomodule that is under development for the main linac and the RF sources that accompany it fits comfortably within the existing diameter tunnel that is planned for the ILC main linac tunnel. The nominal operating parameters for C³ technology are 120 MeV/m gradient with ~90% fill factor for the cryomodule that forms the basis of the main linac design. A higher gradient version at 155 MeV/m is also being explored. The proponents of C³ are developing an R&D plan to realize a fully engineered cryomodule and test it with full beam loading over the next decade [767]. During the timescale of this demonstration R&D plan, we will have the opportunity to push the accelerating gradient of the C³ linac well beyond 120 MeV/m, measure the break down rate in realistic operating conditions and make a determination of the physical limit of the installed cryomodules capacity for higher gradient.

For the re-utilization of ILC infrastructure with a C³ energy upgrade we will consider the case of a 30 (20) km tunnel constructed for ILC including the main linac and beam delivery system (BDS).

Parameter	Unit	Value	Value
Center of Mass Energy	GeV	3000	2000
Site Length	km	30	20
Main Linac Length (per side)	km	13	7
Accel. Grad.	MeV/m	120	155
RF Compression for Pre-Pulse		3X	3X
Flat-Top Pulse Length	ns	260	195
Cryogenic Load at 77 K	MW	36.6	24.7
Est. AC Power for RF Sources	MW	322	215
Est. Electrical Power for Cryogenic Cooling	MW	255	170
RF Source efficiency (AC line to linac)	%	80	80
Luminosity	$\times 10^{34} \text{ cm}^{-2}\text{s}^{-1}$	6	4
Single Beam Power	MW	13.5	9
Injection Energy Main Linac	GeV	10	10
Train Rep. Rate	Hz	120	120
Bunch Charge	nC	1	1
Flat-Top RF Pulse Length	ns	260	195
Bunch Spacing	Periods (ns)	20 (3.5)	15 (2.6)
Average Current	μA	9	9
Peak Current	A	0.3	0.385
RF Power for Structure Flat-Top	MW/m	80	140

Table 15.6: Main Linac parameters for C^3 at 3 TeV and 2 TeV center of mass energy.

For e^+e^- collisions, a center of mass energy upgrade to 3 (2) TeV is presently considered the limit for a practical beam delivery system that accounts for beamsstrahlung effects. This BDS would need to be on the order of 2 km per side leaving 13 (7) km of tunnel to reach the colliding beam energy of 1.5 (1) TeV. This main linac length would be achievable with the nominal C^3 operating gradient of 120 (155) MeV/m and a fill factor of $\sim 90\%$. A summary of the parameters is shown in Table 15.6.

Beyond the main linac tunnel, the DC electron gun, polarized positron source and damping ring tunnels could also be re-utilized. The helium cryoplants for the ILC could also be repurposed in part if they use a liquid nitrogen pre-cooler stage for the cryoplant. For C^3 , only the nitrogen pre-cooler would need to be operated. It is likely that additional cryoplants would need to be installed for the required cooling capacity of the main linac.

C^3 R&D for Multi-TeV Operation

Given the high center of mass energy for a C^3 energy upgrade after ILC operation, electrical power consumption will be a key area of concern. This will require RF pulse compression technology and RF source technology to also undergo R&D in order to improve the electrical efficiency to a

practical level at multi-TeV center of mass. These topics are considered for parallel R&D in the C³ development plan [767] as they are essential for multi-TeV operation but not for its utilization as a Higgs factory [747].

Significant electrical power savings are possible with the inclusion of a pulse compressor. This is due to the reduced power loss in the cavity during the long fill time of the cavity, which reduces both the klystron electrical power requirements, as well as the cryogenic cooling requirements. For C³, the extremely high Q-factor of the cryogenic cavities results in a fill time that requires a significant amount of average RF power to be delivered to the accelerating structure when there is no electron beam. It is possible however to reduce the average power loss during the filling of the cavities with appropriate tailoring of the RF pulse to have a very high power pre-pulse. Recent advances in pulse compressors [763] with super-compact spherical cavities has dramatically changed the performance potential for these systems. It has been shown that a chain of spherical cavities can produce tailored pulse formats with extremely high conversion efficiency if the power gain is kept low [768]. A pre-pulse power compression ratio of three can be achieved with >80% conversion efficiency. We have explored the impact of operating with and without a compressed pre-pulse on the thermal and electrical power requirements for the linac and observed a 35% reduction in the electrical power required for the same beam energy if pulse compression is included.

In addition, we have also considered operating with a compressed pulse during the flat-top portion of the RF pulse. This does not prove to be realistic for the power ratios required during the pre-pulse of the system to maintain reasonable power consumption. Increasing the compression for the full pulse by an additional factor of 2 (6X for the pre-pulse) reduces the overall efficiency of the system by a factor of three. This is a startling result considering that pre-pulse compression actually increases the system efficiency by 35% for overall power consumption. In practice this is due to the rather modest requirements of pre-pulse compression becoming excessive in the presence of flat-top compression.

To realize this concept, extensive work on RF source cost and performance is also required. For a normal conducting linear accelerator the cost is dominated by the required RF sources. As we enter the multi-TeV range, RF source cost becomes the dominant factor for the entire normal conducting accelerator complex. While significant progress has been made over the past decade incorporating new concepts in RF sources, significant work remains with key challenges include production, capital cost, lifetime, operating voltage and efficiency all playing key roles. The present state of the art is capable of achieving 65% AC to RF efficiency in klystron RF sources of the power levels that are required. New concepts are being explored to push this up to 80% efficiency [769, 770, 771, 772] which would dramatically reduce the number of sources needed and the electrical power consumed. The techniques that are being developed include core oscillation method, bunch align compress, use of permanent or superconducting solenoids, and implementation of depressed collectors that are externally or self-biased.

Towards GeV/m Accelerating Gradients

Space limitations, significant reductions in RF power cost, or improved accelerator structure shunt impedance (efficiency) may render operation at higher gradient more appealing. Operating beyond

250 MeV/m for an RF accelerator would require a new topology for the linac. One possibility that is actively being researched is the use of shorter RF pulses and higher repetition rates at significantly higher THz frequencies (100-300 GHz). Structures in this frequency range have exceeded GV/m surface fields [773, 773, 774]. High frequency structures made significant progress in recent years and are now being utilized for beam acceleration and beam manipulation [761, 775, 776, 777, 778, 779] but still require significant R&D before formulating a proposal for a high energy facility. Extensive investigations into the beam dynamics of such structures are required to confirm the viability for a high luminosity application such as a linear collider.

Studies of beam transport in these structures with high gradients (500 MeV/m) and pC bunches indicate it is possible to transport the beam while accounting for effects from short and long range wakes [780]. Long range wakefields are particularly challenging at high frequency. One approach to increasing the beam current is to operate with a bunch in every RF period and allow only for excitation of higher order modes that are harmonics at integer multiples of the drive frequency. This would greatly reduce the number of modes which must be damped. With a bunch charge of 1 pC in every cycle, operation at 300 GHz would provide the same peak current during the RF pulse, as shown in Table 15.6 for a C^3 accelerator. Due to the shortened RF pulse, recovering luminosity would require high repetition rates and reduced beam emittance. Powering of such structures would also require very different approach than presently envisioned for RF accelerator based linear colliders. High frequency RF sources can be extremely efficient with fast-wave cyclotron resonance masers and long pulse formats. Matching these RF sources to high luminosity applications requires the development of active quasi-optical pulse compression. R&D on this issue is in progress. Beam-driven (wakefield) RF sources, as envisioned for CLIC, may also be a possible option for such high frequency operation. Finally, it has been discussed since the 1990's that higher frequencies could be preferred for operation with smaller bunches to obtain greater power efficiency at higher gradients (see, for example, [781]). At that time, attempts to realize this approach stumbled on the issue of breakdown. It is now appealing to revisit this program in the light of the advances in THz accelerator technology, to see whether operation at X- or even W-band can give a practical route to very high gradients.

15.5 Plasma, laser, and structure wakefield accelerators

In this section, we will discuss possible upgrades of the ILC infrastructure based on wakefield acceleration. This is an advanced technique capable of extremely high gradient electron acceleration. Today it still very much in the research stage, with many important issues still unanswered. However, this technology has the potential not only to deliver extremely high-energy beams, but do so in a highly efficient manner and to achieve the high luminosities needed for physics at these energies [727]. In this section, we discuss three options for wakefield acceleration; this is not meant to exhaust the possible options.

Status	e^- Source	Drive complex	Interstage coupling	Plasma medium	BDS
Conventional	Damping Ring	Pulsed RF	Warm magnets	Laser-ionized cell	ILC-type
Upgraded	Photoinjector	CW RF	Warm magnets and plasma lenses	Laser-ionized gas jet	CLIC-type
Advanced	Plasma injector	CW High-Q	Combined function plasma	Beam-ionized gas jet	plasma-based

Table 15.7: Envisioned evolution of a plasma-based linear collider.

Beam-Driven Plasma Wakefield Accelerators

Research on beam-driven plasma wakefield acceleration (PWFA) is motivated by the ultimate goal of creating a linear collider that is affordable, highly-efficient, and operates at the highest possible energies. There are many challenges on the path to a plasma-based upgrade to the ILC, but the field has shown steady progress on multiple fronts since the previous Snowmass study in 2013. Among many highlights are the first demonstration of highly-efficient plasma acceleration of electron beams [782], acceleration of positron beams in the non-linear regime [783], proton beam-driven acceleration [784], staged laser-plasma acceleration [785], plasma photocathodes for generating ultralow-emittance beams [786], and emittance preservation in an active plasma lens [787].

The remaining challenges associated with the development of a linear collider based on PWFA have been identified in a variety of papers, workshops, and strategy sessions [788, 789, 790, 791, 792]. We enumerate some of them here:

1. High-efficiency, high-quality acceleration in a single plasma stage.
2. Coupling between plasma stages.
3. Positron acceleration in plasma.
4. Preservation of beam polarization.
5. High repetition-rate plasma acceleration and energy deposition in the plasma source.
6. Final focusing and alignment of beams at the collision point.

Experiments to demonstrate high-efficiency, high-quality electron acceleration in plasma are currently underway at FLASHForward at DESY and preparing to start at FACET-II at SLAC. These experiments will demonstrate the viability of PWFA technology and establish the tolerances for producing high-quality beams. Experiments at FLASHForward will also study high-repetition rate PWFA, while experiments at FACET-II will cover positron acceleration in plasma and beam focusing based on thin plasma lenses. Both FLASHForward and FACET-II need to be modified in order to demonstrate staged PWFA. This is a high priority for the field.

Because of the challenges to the PWFA concept from limitations on power and tolerances, it is important to take a long-term view, going beyond the ideas for the baseline PWFA accelerator to elements that use plasma-based concepts in a more sophisticated way. In Table 15.7, we sketch such upgrade paths for the various elements of a PWFA collider.

Laser Wakefield Accelerators

Laser wakefield accelerators (LWFAs) [793] rely on an intense, ultrashort laser pulses to resonantly excite large amplitude electron plasma waves with relativistic phase velocities. The accelerating fields of the plasma wave, or wakefields, are 1-10 GV/m, orders of magnitude larger than conventional accelerating structures, enabling compact acceleration of charged particle beams. LWFA technology provides an opportunity to upgrade the ILC to higher beam energy using the planned ILC main linac tunnel, site power, and infrastructure. An LWFA-based linac arm would consist of multiple plasma stages, each stage yielding a few GeV/stage energy gain, driven by a multi-J, short pulse laser [790, 794]. Laser drivers are highly flexible, and plasma mirror technology enables compact coupling of the laser driver into the plasma accelerating cells. The multi-Joule-class laser systems, potentially based on fiber laser combination, occupy an area of a few m^2 and both the drive lasers and plasma accelerating stages may be placed in the ILC Main Linac tunnel. LWFAs accelerate short bunches, of order 10 microns, and the resulting beamstrahlung reduction at the IP yields significant power savings for a given target luminosity [795]. To reach $E_{CM} = 1$ TeV, an LWFA-based linac requires potentially only 0.2 km in each linac arm, and 100 MW of power for both beams to reach a luminosity of $10^{34} \text{ cm}^{-2}\text{s}^{-1}$. This could be upgraded to $E_{CM} = 3$ TeV with luminosity of $10^{35} \text{ cm}^{-2}\text{s}^{-1}$, requiring a 0.65 km LWFA linac in each linac arm and 300 MW of power for both beams. The LWFA beam power for 1 TeV and 3 TeV would be 4 MW and 12 MW, respectively, and are within the power rating of the planned ILC beam dump. The unused main linac tunnel length could be employed to extend the BDS system to accommodate $E_{CM} = 3$ TeV, as well as space for linear cooling sections to further reduce the beam emittance. The bunch structure employed is one bunch each 20 μs , and additional bunch compressors would be required to achieve the short, 10-micron-scale, bunch length. Furthermore, achieving high beam energies ($E_{CM} > 3$ TeV) is straightforward by adding additional LWFA stages, although the required increased luminosity would require site power beyond the planned ILC design. This provides a long-term upgrade path to continue realizing new physics reach in realistic stages using the infrastructure of a linear collider. Significant R&D is required to realize an LWFA-based linac, and, in particular, further development of high average power, short-pulse laser systems operating at tens of kHz repetition rates [796].

Structure Wakefield Accelerators

Structure Wakefield Acceleration (SWFA) has been proposed as the backbone for a high-gradient and high-efficiency accelerator for a multi-TeV linear collider [797]. Two separate SWFA schemes, two-beam acceleration (TBA) and collinear wakefield acceleration (CWA) are under consideration. This contribution will explore the application of the relatively mature SWFA schemes (both in the

TBA and CWA implementations) as a possible upgrade path to the ILC. The ILC beam format (a train of 3.2 nC single-bunch with an $\mathcal{O}(\text{MHz})$ micropulse repetition rate) is comparable to the 182-GHz CWA-based XFEL design that is being pursued at Argonne. The challenge for the CWA based linear collider would be to raise the overall efficiency due to its single pulse nature. Alternatively, the TBA technology currently under development at Argonne is a 26 GHz accelerator based on a high charge drive beam. Therefore, a TBA contribution to the ILC application would explore two avenues: either operating ILC with higher charge or raising the TBA operating frequency to operate at lower drive charge. Critical to both the TBA and CWA approaches would be continued development of the SWFA bunch control R&D program. This program develops the bunch shaping technology critical for the main and drive beams. For example, we will explore the possibility of shaping the ILC 3.2nC Gaussian bunch for the CWA scheme with a transformer ratio of 5 to produce a 5 TeV LC in the ILC tunnel at high efficiency. Note that bunch control is critical to both beam-driven wakefield acceleration methods: SWFA and plasma wakefield acceleration (PWFA).

Chapter 16

Conclusions

In this report, we have surveyed all aspects of the International Linear Collider. We have, first of all, explained the importance of this machine for physics. The Higgs boson is at the center of the Standard Model of particle physics, and almost all of the major questions about this model go back to questions about its nature. The ILC will give us a clear and complete view of the properties of this particle, its couplings to all particles of the Standard Model, its self-coupling, and its possible couplings to new particles not yet discovered. At its 500 GeV stage, the ILC will also give us a detailed picture of the top quark that will illuminate its relation to the Higgs boson and the electroweak sector. The ILC will be able to search for weakly coupled particles and the particle of dark matter in a way that is almost free of model assumptions. The ILC also has opportunities for discovery in studies of quark and lepton production, W and Z properties, and high-precision tests of QCD.

We have explained that the ILC will provide an ideal environment for precision studies in particle physics. Electroweak processes at the highest energies dominate the event samples. Individual events can be fully reconstructed, including identification of heavy flavors. Beam polarization can add to the variety of events sampled and offer compelling clues to their interpretation. We have described detector designs that make use of this remarkable physics environment, and also new technologies, some developed from the LHC experiments, that will extend their capabilities further.

We have reviewed the accelerator design of the ILC and shown how it gives a robust solution to deliver electron and positron beams in the energy region of the Higgs boson. This design has been created and refined over more than twenty years. It addresses all of the major technical problems of such beams within a well-understood budget and schedule.

We have discussed how the ILC can be the first step on a road to much higher center of mass energies. We envision the ILC Laboratory as being a major center for particle physics long after the measurements we have presented in this report are completed.

We can look ahead to the future of particle physics and dream of accelerator experiments at very high energies. But the mysteries of the Standard Model are with us today. It is has become clear

that we need a new approach today to gain insight into the key problems of particle physics. The ILC gives us a strategy to address these questions and a technology that is ready for construction. It is time to make the ILC a reality.

ACKNOWLEDGEMENTS

We are grateful to Marina Chadeeva and Alexey Drutskoy (Lebedev Institute) and to Valery Telnov (Budker Institute) for their contributions to this report.

The work of the DESY group is supported by the Deutsche Forschungsgemeinschaft under Germany's Excellence Strategy, EXC 2121 "Quantum Universe", grant 390833306. The work of IFIC is supported by Projects No. PGC2018-094856-B-100 (MCIN/AEI), PROMETEO-2018/060 and CIDEAGENT/2020/21 (Generalitat Valenciana) and iLINK Grant No. LINKB20065 (CSIC). The work of the KEK group is supported in part by JSPS KAKENHI Grant Numbers 16H02173 and 21H01077. The work of the SLAC group is supported by the US Department of Energy, contract DE-AC02-76SF00515. The work of James Brau is supported by the US Department of Energy grant DE-SC0017996. The work of Francesco Giovanni Celiberto is supported by the INFN/NINPHA project. The work of Sven Heinemeyer is supported in part by the grant PID2019-110058GB-C21 funded by MCIN/AEI/10.13039/501100011033 and by "ERDF A way of making Europe", and in part by the grant CEX2020-001007-S funded by MCIN/AEI/10.13039/501100011033. The work of Sunghoon Jung is supported by the National Research Foundation of Korea under grant NRF-2017R1D1A1B03030820. The work of Zhen Liu is supported in part by the U.S. Department of Energy (DOE) under grant No. DE-SC0022345. The work of Nathaniel Craig is supported in part by the U.S. Department of Energy under the grant DE-SC0011702. The work of Alessandro Papa is supported by the INFN/QFTCOLLIDERS project. The work of Junping Tian is supported in part by the Japan Society for the Promotion of Science under the Grant-in-Aid for Science Research 15H02083. The work of Graham Wilson is supported by the US National Science Foundation under award NSF 2013007.

Bibliography

- [1] T. Behnke, J.E. Brau, B. Foster, J. Fuster, M. Harrison, J.M. Paterson et al., eds., *The International Linear Collider Technical Design Report - Volume 1: Executive Summary*, [1306.6327](#).
- [2] H. Baer et al., eds., *The International Linear Collider Technical Design Report - Volume 2: Physics*, [1306.6352](#).
- [3] C. Adolphsen et al., eds., *The International Linear Collider Technical Design Report - Volume 3.I: Accelerator \mathcal{E} in the Technical Design Phase*, [1306.6353](#).
- [4] C. Adolphsen et al., eds., *The International Linear Collider Technical Design Report - Volume 3.II: Accelerator Baseline Design*, [1306.6328](#).
- [5] H. Abramowicz et al., *The International Linear Collider Technical Design Report - Volume 4: Detectors*, [1306.6329](#).
- [6] P. Bambade et al., *The International Linear Collider: A Global Project*, [1903.01629](#).
- [7] LCC PHYSICS WORKING GROUP collaboration, *Tests of the Standard Model at the International Linear Collider*, [1908.11299](#).
- [8] K. Fujii et al., *ILC Study Questions for Snowmass 2021*, [2007.03650](#).
- [9] ICFA, *Linear Collider Activities*, <https://icfa.hep.net/lc/>.
- [10] International Technology Recommendation Panel, *Final Report*, 2004. https://icfa.hep.net/wp-content/uploads/ITRP_Report_Final.pdf.
- [11] Global Design Effort, *emphMission Statement and Documentation*. <https://web.archive.org/web/20130702225429/http://www.linearcollider.org/ILC/GDE>.
- [12] *ILC Technical Design Report*. <https://linearcollider.org/technical-design-report/>.
- [13] “The International Linear Collider Machine Staging Report 2017.” <https://arxiv.org/abs/1711.00568>.
- [14] JAHEP, *Proposal for a Phased Execution of the International Linear Collider*. http://www.jahep.org/office/doc/201210_ILC_staging_e.pdf.

- [15] KEK Press Release, <https://www.interactions.org/press-release/kek-publishes-international-working-groups-recommendations>.
- [16] KEK News, <https://www.kek.jp/en/newsroom/>.
- [17] ICFA 2020 statement, https://icfa.hep.net/wp-content/uploads/ICFA_Statement_August_2020.pdf.
- [18] ILC International Development Team web site: <https://linearcollider.org>.
- [19] ICFA statement on the IDT, <https://www.interactions.org/press-release/icfa-appoints-members-ilc-international-development-team>.
- [20] ILC IDT Working Group 1 web site: <https://linearcollider.org/team/wg1/>.
- [21] ILC IDT Working Group 2 web site: <https://linearcollider.org/team/wg2/>.
- [22] ILC IDT Working Group 3 web site: <https://linearcollider.org/team/wg3/>.
- [23] ILC IDT Working Group 1 Physics Opportunities web site: <https://linearcollider.org/team/wg3/physics/>.
- [24] B. Warmbein, “Thinking outside the Tunnel”, <https://newsline.linearcollider.org/2021/11/26/thinking-outside-the-tunnel/>.
- [25] INTERNATIONAL LINEAR COLLIDER INTERNATIONAL DEVELOPMENT TEAM collaboration, *Proposal for the ILC Preparatory Laboratory (Pre-lab)*, 2106.00602.
- [26] ILC Advisory Panel, *Summary of Discussions on Issues Relating to the International Linear Collider Project*, 2022. https://www.mext.go.jp/content/20220401-mxt_kiso-000020463_9.pdf.
- [27] KEK News, <https://www.kek.jp/en/topics-en/202202251335/>.
- [28] B. Foster *et al.*, “Revised ILC Project Implementation Planning”, 2015. <https://linearcollider.org/files/images/pdf/ProjectImplementationPlanning.pdf>.
- [29] LINEAR COLLIDER COLLABORATION collaboration, *The International Linear Collider Machine Staging Report 2017*, 1711.00568.
- [30] M. Harrison, M. Ross and N. Walker, *Luminosity Upgrades for ILC*, 1308.3726.
- [31] CERN, “Environment report.” <http://cds.cern.ch/record/2737239>, 2020.
- [32] S. Schreiber and B. Faatz, *The free-electron laser FLASH*, *High Power Laser Science and Engineering* **3** (2015) E20.
- [33] M. Vogt *et al.*, *Status of the Superconducting Soft X-Ray Free-Electron Laser FLASH at DESY*, in *Proceedings, 9th International Particle Accelerator Conference (IPAC 2018), Vancouver, BC, Apr 29–May 4, 2018*, pp. 1481–1484 (TUPMF090), 2018, DOI.

- [34] “European XFEL.” <https://www.xfel.eu/>.
- [35] “LCLS-II: A world-class discovery machine.” <https://lcls.slac.stanford.edu/lcls-ii>.
- [36] Z. Zhao, D. Wang, Z.-H. Yang and L. Yin, *SCLF: An 8-GeV CW SCRF Linac-Based X-Ray FEL Facility in Shanghai*, in *Proceedings, 38th International Free Electron Laser Conference, FEL2017*, pp. 182–184 (MOP055), 2018, DOI.
- [37] N. Huang et al., *Features and futures of X-ray free-electron lasers*, *The innovation* **2** (2021) 100097.
- [38] JAHEP SUBCOMMITTEE ON FUTURE PROJECTS OF HIGH ENERGY PHYSICS collaboration, S. Asai et al., “The final report of the subcommittee on future projects of high energy physics.” http://www.jahep.org/office/doc/201202_hecsubc_report.pdf, 2012.
- [39] Japan Association of High Energy Physicists (JAHEP), “A proposal for a phased execution of the International Linear Collider project.” http://www.jahep.org/office/doc/201210_ILC_staging_e.pdf, 2012.
- [40] T. Sanuki, “Overview of the topography and geology of the Kitakami site for the ILC.” Presentation at DESY, Feb. 14, 2017, 2017.
- [41] R.D. Heuer et al., “Parameters for the linear collider.” <https://icfa.fnal.gov/wp-content/uploads/para-Nov20-final.pdf>, 2006.
- [42] G. Dugan, M. Harrison, B. List and N. Walker, “Implications of an energy-phased approach to the realization of the ILC.” <http://edmsdirect.desy.de/item/D00000001046475>, 2014.
- [43] G. White, “Change request ILC-CR-0002: Baseline optics to provide for a single L^* .” <http://edmsdirect.desy.de/item/D00000001119175>, 2014.
- [44] K. Buesser, “Change request ILC-CR-0003: Detector hall with vertical shaft access.” <http://edmsdirect.desy.de/item/D00000001084745>, 2014.
- [45] E. Paterson, V. Kuchler, N. Solyak and T. Sanami, “Change request ILC-CR-0012: Reduction of width of linac shield wall and tunnel cross-section.” <http://edmsdirect.desy.de/item/D00000001127835>, 2015.
- [46] K. Yokoya, B. List and E. Paterson, “Change request ILC-CR-0013: Update of the ILC beam dump specifications.” <http://edmsdirect.desy.de/item/D00000001145035>, 2016.
- [47] K. Yokoya, “Change request ILC-CR-0016: Luminosity improvement at 250 GeV.” <http://edmsdirect.desy.de/item/D00000001159725>, 2017.
- [48] Positron Working Group, “Report on the ILC positron source.” <http://edmsdirect.desy.de/item/D00000001165115>, 2018.
- [49] International Committee for Future Accelerators (ICFA), “ICFA statement on the ILC operating at 250 GeV as a Higgs boson factory.” <https://icfa.fnal.gov/wp-content/uploads/ICFA-Statement-Nov2017.pdf>, 2017.

- [50] “TESLA Technology Collaboration.” <http://tesla-new.desy.de/>.
- [51] C. Adolphsen, “Optimum ML cavity performance: gradient, Q_0 , and other ML parameters.” Presentation at 2011 Linear Collider Workshop of the Americas (ALCPG11), Eugene, OR, Mar 19–23, 2011, <https://agenda.linearcollider.org/event/4572/>, 2011.
- [52] W. Singer et al., *Production of superconducting 1.3 GHz cavities for the European X-ray Free Electron Laser*, *Phys. Rev. Accel. Beams* **19** (2016) 092001.
- [53] D. Reschke et al., *Performance in the vertical test of the 832 nine-cell 1.3 GHz cavities for the European X-ray Free Electron Laser*, *Phys. Rev. Accel. Beams* **20** (2017) 042004.
- [54] N.J. Walker and D. Kostin, “The European XFEL – experience and lessons learned.” Presentation, International Workshop on Future Linear Colliders (LCWS2017), Strasbourg, France, Oct 22–27, 2017, <https://agenda.linearcollider.org/event/7645/>, 2017.
- [55] W. Kaabi et al., *Power couplers for XFEL*, in *Proceedings, 4th International Particle Accelerator Conference (IPAC 2013), Shanghai, China, May 12-17, 2013*, pp. 2310–2312 (WEPWO001), 2013, <https://jacow.org/IPAC2013/papers/wepwo001.pdf>.
- [56] S. Sierra et al., *Status and lesson learned from manufacturing of FPC couplers for the XFEL program*, in *Proceedings, 28th International Linear Accelerator Conference (LINAC16), East Lansing, MI, Sep 25–30, 2016*, pp. 572–574 (TUPLR048), 2017, DOI.
- [57] D. Reschke, W. Decking, N. Walker and H. Weise, *The commissioning of the European XFEL Linac and its performance*, in *Proceedings, 18th International Conference on RF Superconductivity (SRF2017): Lanzhou, China, Jul 17–21, 2017*, pp. 1–5 (MOXA02), 2018, DOI.
- [58] S. Berry and O. Napoly, *Assembly of XFEL cryomodules: lessons and results*, in *Proceedings, 28th International Linear Accelerator Conference (LINAC16): East Lansing, Michigan, September 25-30, 2016*, pp. 646–650 (WE1A02), 2017, DOI.
- [59] T.J. Peterson et al., *A Survey of Pressure Vessel Code Compliance for Superconducting RF Cryomodules*, *AIP Conf. Proc.* **1434** (2011) 1575 [1209.2405].
- [60] D. Kostin, W.-D. Moeller, A. Goessel and K. Jensch, *Superconducting accelerating module tests at DESY*, in *Proceedings, 14th International Conference on RF Superconductivity (SRF2009), Berlin, Sep 20–25, 2009*, pp. 180–184 (TUPPO005), 2009, <https://jacow.org/SRF2009/papers/TUPPO005.PDF>.
- [61] D. Broemmelsiek et al., *Record High-Gradient SRF Beam Acceleration at Fermilab*, *New J. Phys.* **20** (2018) 113018 [1808.03208].
- [62] Y. Yamamoto et al., *Achievement of Stable Pulsed Operation at 36 MV/m in STF-2 Cryomodule at KEK*, in *Proceedings, 18th International Conference on RF Superconductivity (SRF2017), Lanzhou, China, Jul 17–21, 2017*, pp. 722–728 (THYA02), 2018, DOI.

- [63] K. Kasprzak et al., *Test Results of the European XFEL Serial-production Accelerator Modules*, in *Proceedings, 18th International Conference on RF Superconductivity (SRF2017)*, Lanzhou, China, July 17-21, 2017, pp. 312–316 (MOPB106), 2018, DOI.
- [64] S1Global collaboration, “S1Global report.”
<http://edmsdirect.desy.de/item/D00000001005135>, 2012.
- [65] M.A. Kemp et al., *Final design of the SLAC P2 Marx klystron modulator*, in *Proceedings, 18th IEEE International Pulsed Power Conference (PPC11)*, Chicago, IL, Jun 19-23, 2011, pp. 1582–1589, 2011, DOI.
- [66] M.P.J. Gaudreau, N. Silverman, B. Simpson and J. Casey, *ILC-class Marx modulator at KEK*, in *Proceedings, 5th International Particle Accelerator Conference (IPAC 2014)*, Dresden, Germany, Jun 15-20, 2014, pp. 562–563 (MOPME082), 2014,
<https://jacow.org/IPAC2014/papers/mopme082.pdf>.
- [67] I. Syratchev, “Introduction to the High Efficiency International Klystron Activity HEIKA.” Presentation, CLIC workshop 2015, Geneva, Switzerland, Jan 26–30, 2015,
<https://indico.cern.ch/event/336335/>, 2015.
- [68] F. Gerigk, *Status and future strategy for advanced high power microwave sources for accelerators*, in *Proceedings, 9th International Particle Accelerator Conference (IPAC 2018)*, Vancouver, BC, Canada, Apr 29–May 4, 2018, pp. 12–17 (MOYGB1), 2018, DOI.
- [69] I.A. Guzilov, *Bac method of increasing the efficiency in klystrons*, in *Proceedings, 10th International Vacuum Electron Sources Conference (IVESC)*, Jun 30–Jul 4, 2014, p. 6891996, 2013, DOI.
- [70] D. Constable et al., *High efficiency klystron development for particle accelerators*, in *Proceedings, 58th ICFA Advanced Beam Dynamics Workshop on High Luminosity Circular e^+e^- Colliders (eeFACT2016)*, Daresbury, UK, Oct 24–27, 2016, pp. 185–187 (WET3AH2), 2017, DOI.
- [71] A.Y. Baikov, C. Marrelli and I. Syratchev, *Toward high-power klystrons with RF power conversion efficiency on the order of 90 %*, *IEEE Trans. Electron. Dev.* **62** (2015) 3406.
- [72] E. Jensen, “Recent developments towards very high efficiency klystrons.” Presentation, 9th CW and high average RF power workshop, Grenoble, France, Jun 20–24, 2016,
<https://indico.cern.ch/event/472685/>, 2016.
- [73] H. Nakai, “Change request ILC-CR-0014: Cryogenic layout.”
<http://edmsdirect.desy.de/item/D00000001146525>, 2016.
- [74] H. Weise, *How To Produce 100 Superconducting Modules for the European XFEL in Collaboration and with Industry*, in *Proceedings, 5th International Particle Accelerator Conference (IPAC 2014): Dresden, Germany, Jun 15–20, 2014*, pp. 1923–1928 (WEIB03), 2014, <https://jacow.org/IPAC2014/papers/weib03.pdf>.

- [75] R. Alley et al., *The Stanford Linear Accelerator polarized electron source*, *Nucl. Instrum. Meth.* **A365** (1995) 1.
- [76] G. Alexander et al., *Undulator-based production of polarized positrons*, *Nucl. Instrum. Meth.* **A610** (2009) 451 [0905.3066].
- [77] K. Moffeit et al., “Spin rotation schemes at the ILC for two interaction regions and positron polarization with both helicities.” SLAC-TN-05-045, 2005.
- [78] L.I. Malysheva et al., *Design of Pre-Dumping Ring Spin Rotator with a Possibility of Helicity Switching for Polarized Positrons at the ILC*, 1602.09050.
- [79] M.G. Billing et al., *Status of Low Emittance Tuning at CesrTA*, in *Proceedings, 24th Particle accelerator Conference (PAC’11), New York, NY, Mar 28–Apr 1, 2011*, pp. 1540–1542 (WEP022), 2011, <https://jacow.org/PAC2011/papers/WEP022.PDF>.
- [80] J.V. Conway, Y. Li and M.A. Palmer, *The conceptual design of a vacuum system for the ilc damping rings incorporating electron cloud mitigation techniques*, in *Proceedings, 3rd International Conference on Particle accelerator (IPAC 2012), New Orleans, LA, May 2-25, 2012*, pp. 1960–1962 (TUPPR062), 2012, <https://jacow.org/IPAC2012/papers/TUPPR062.PDF>.
- [81] T. Naito et al., *Multi-bunch beam extraction using strip-line kicker at KEK-ATF*, in *Proceedings, 1st International Particle Accelerator Conference (IPAC’10), Kyoto, Japan, May 23–28, 2010*, pp. 2386–2388 (WE0BMH02), 2010, <https://jacow.org/IPAC10/papers/weobmh02.pdf>.
- [82] P. Emma, T. Raubenheimer and F. Zimmermann, *A bunch compressor for the next linear collider*, in *Proceedings, 16th Particle Accelerator Conference and International Conference on High-Energy Accelerators, (HEACC 1995), Dallas, TX, May 1-5, 1995*, pp. 704–706 (RPC03), 1996, <https://jacow.org/p95/ARTICLES/RPC/RPC03.PDF>.
- [83] N. Walker, “Change request ILC-CR-0010: Proposal to include bunch compressor sections into main linac accelerator system.” <http://edmsdirect.desy.de/item/D00000001119175>, 2015.
- [84] P. Raimondi and A. Seryi, *A Novel final focus design for future linear colliders*, *Phys. Rev. Lett.* **86** (2001) 3779.
- [85] ATF2 collaboration, B.I. Grishanov et al., “ATF2 Proposal.” SLAC-R-771, CERN-AB-2005-035, DESY-05-148, KEK-REPORT-2005-2, 2005.
- [86] B.I. Grishanov et al., *ATF2 proposal, Vol. 2*, [physics/0606194](https://jacow.org/p95/ARTICLES/RPC/RPC03.PDF).
- [87] T. Okugi, *Achievement of small beam size at ATF2 beamline*, in *Proceedings, 28th International Linear Accelerator Conference (LINAC16), East Lansing, MI, Sep 25-30, 2016*, pp. 27–31 (MO3A02), 2017, DOI.
- [88] ATF2 collaboration, *Experimental validation of a novel compact focusing scheme for future energy-frontier linear lepton colliders*, *Phys. Rev. Lett.* **112** (2014) 034802.

- [89] R.J. Apsimon et al., *Design and operation of a prototype interaction point beam collision feedback system for the International Linear Collider*, *Phys. Rev. Accel. Beams* **21** (2018) 122802 [[1812.08432](#)].
- [90] R. Ramjiawan et al., *Development of a Low-Latency, High-Precision, Beam-Based Feedback System Based on Cavity BPMs at the KEK ATF2*, in *Proceedings, 9th International Particle Accelerator Conference (IPAC 2018): Vancouver, BC, Ap 29–May 4, 2018*, pp. 2212–2215 (WEPAL025), 2018, [DOI](#).
- [91] A. Latina and A. Faus-Golfe, “ATF2.” Input paper for European Strategy for Particle Physics Update, 2018.
- [92] D.R. Walz, L.R. Lucas, H.A. Weidner, R.J. Vetterlein and E.J. Seppi, *Beam Dumps, Energy Slits and Collimators at SLAC - - Their Final Versions and First Performance Data*, *IEEE Trans. Nucl. Sci.* **14** (1967) 923.
- [93] S. Boogert et al., *Polarimeters and Energy Spectrometers for the ILC Beam Delivery System*, *JINST* **4** (2009) P10015 [[0904.0122](#)].
- [94] V.N. Baier and V.A. Khoze, *Determination of the transverse polarization of high-energy electrons*, *Sov. J. Nucl. Phys.* **9** (1969) 238.
- [95] B. Vormwald, J. List and A. Vauth, *A calibration system for Compton polarimetry at e^+e^- linear colliders*, *JINST* **11** (2016) P01014 [[1509.03178](#)].
- [96] K. Yokoya, K. Kubo and T. Okugi, *Operation of ilc250 at the z-pole*, *arXiv preprint arXiv:1908.08212* (2019) .
- [97] ILC Strategy Council, “Announcement of the results of the ILC candidate site evaluation in Japan.” Press release 28.8.2014, <http://ilc-str.jp/topics/2013/08281826/>, 2014.
- [98] B. Warmbein, “The road to Kitakami.” ILC Newline Feb. 20, 2014, <http://newline.linearcollider.org/2014/02/20/the-road-to-kitakami/>, 2014.
- [99] T. Sanuki, “New developments at the Kitakami site.” Presentation at Linear Collider Workshop 2015 (LCWS15), Whistler, BC, Canada, Nov 1–7, 2015, <https://agenda.linearcollider.org/event/6662/>, 2015.
- [100] T. Sanuki and I. Sekine, “Seismic base isolation for detectors and accelerator.” Presentation at International Workshop on Future Linear Colliders, LCWS2018, Arlington, TX, Oct 22-26, 2018, <https://agenda.linearcollider.org/event/7889/>, 2018.
- [101] T. Sanuki, “Tunnel floor vibration issue.” Presentation at Asian Linear Collider Workshop (ALCW 2018), Fukuoka, Japan, May 28–Jun 2, 2018, <https://agenda.linearcollider.org/event/7826/>, 2018.
- [102] M. Yoshioka. ”Energy Management in Japan, Consequences for Research Infrastructure.”, 2nd Workshop Energy for Sustainable Science at Research Infrastructures (2nd ESSRI WS), October 2013, CERN, Geneva, Switzerland., <https://indico.cern.ch/event/245432/> .

- [103] D. Perret-Gallix. "ILC: an amazing energy transformer from eV to TeV", 2nd Workshop Energy for Sustainable Science at Research Infrastructures (2nd ESSRI WS), October 2013, CERN, Geneva, Switzerland. <https://indico.cern.ch/event/245432> .
- [104] A. Suzuki. "Energy Management at KEK, Strategy on Energy Management, Efficiency, Sustainability", 2nd Workshop Energy for Sustainable Science at Research Infrastructures (2nd ESSRI WS), October 2013, CERN, Geneva, Switzerland. <https://indico.cern.ch/event/245432/> .
- [105] AAA home page. <https://aaa-sentan.org/en/> .
- [106] Green ILC page. <https://green-ilc.in2p3.fr/> .
- [107] Home page of Tohoku ILC Project Development Center. <https://tipdc.org/en> .
- [108] ICFA panel home page. <https://icfa.hep.net/icfa-panel-on-sustainable-accelerators-and-colliders/>.
- [109] Green ILC session, ILCX2021, ILC Workshop on potential experiments. <https://agenda.linearcollider.org/event/9211/>.
- [110] J. Cai and I. Syratchev, "Modelling and Technical Design Study of Two-Stage Multibeam Klystron for CLIC.", *IEEE Transactions on Electron Devices*. No.8 **67** (August 2020) .
- [111] A. Grassellino et al., "Unprecedented quality factors at accelerating gradients up to 45 MV/m in niobium superconducting resonators via low temperature nitrogen infusion.", *Superconducting Science and Technology* **30** (2017) 094004.
- [112] M. Martinello et al., *Advancement in the understanding of the field and frequency dependent microwave surface resistance of niobium*, in *SRF2017, Lanzhou, China.*, p. TUYAA02, 2017, DOI.
- [113] T. Saeki. "Challenge for the Efficient and Sustainable Design of ILC", 4th Workshop Energy for Sustainable Science at Research Infrastructures (4th ESSRI WS), November 2017, Magurele, Romania. <https://indico.eli-np.ro/event/1/timetable/?view=standard> .
- [114] T. Saeki, "study on the international linear collider beam dump by plasma wake-field deceleration, 2016 iee nss/mic conference, nov. 2016, strasbourg, france". <https://ewh.ieee.org/soc/nps/nss-mic/2016/> .
- [115] M. Yoshioka et al., *Study on a sustainable energy management system for the ilc*, in *Proceedings of the 17th Annual Meeting of Particle Accelerator Society of Japan.*, p. WEPP57, 2020, <https://www.pasj.jp/web-publish/pasj2020/proceedings/PDF/WEPP/WEPP57.pdf>.
- [116] OECD, "Prices and purchasing power parities (PPP)." <http://www.oecd.org/sdd/prices-ppp/>, 2018.
- [117] Eurostat, *Eurostat-OECD methodological manual on Purchasing Power Parities*, Luxembourg: Publications Office of the European Union, 2012 ed. (2012).

- [118] ILC Advisory Panel, “Summary of the ILC advisory panel’s discussions to date after revision.” Report, Jul 4, 2018, http://www.mext.go.jp/component/b_menu/shingi/toushin/_icsFiles/afieldfile/2018/09/20/1409220_2_1.pdf, 2018.
- [119] K. Yokoya, K. Kubo and T. Okugi, *Operation of ILC250 at the Z-pole*, [1908.08212](#).
- [120] S. Asai, J. Tanaka, Y. Ushiroda, M. Nakao, J. Tian, S. Kanemura et al., *Report by the Committee on the Scientific Case of the ILC Operating at 250 GeV as a Higgs Factory*, [1710.08639](#).
- [121] A. Grassellino et al., *Accelerating fields up to 49 MV/m in TESLA-shape superconducting RF niobium cavities via 75C vacuum bake*, [1806.09824](#).
- [122] A. Grassellino et al., *Unprecedented quality factors at accelerating gradients up to 45 MV/m in niobium superconducting resonators via low temperature nitrogen infusion*, *Supercond. Sci. Technol.* **30** (2017) 094004 [[1701.06077](#)].
- [123] A. Gurevich, *Enhancement of rf breakdown field of superconductors by multilayer coating*, *Applied Physics Letters* **88** (2006) 012511.
- [124] T. Kubo, *Superheating fields of semi-infinite superconductors and layered superconductors in the diffusive limit: structural optimization based on the microscopic theory*, *Superconductor Science and Technology* **34** (2021) 045006.
- [125] M. Harrison, M. Ross and N. Walker, *Luminosity Upgrades for ILC*, in *Community Summer Study 2013: Snowmass on the Mississippi*, 8, 2013 [[1308.3726](#)].
- [126] T. Sanuki, “Tunnel floor vibration issues.” Presentation, Asian Linear Collider Workshop (ALCW2018), Fukuoka, Japan, May 28–Jun 2, 2018. <https://agenda.linearcollider.org/event/7826/>, 2018.
- [127] K. Yokoya, *Beam-beam interaction in linear collider*, in *AIP Conference Proceedings*, vol. 592, pp. 185–204, American Institute of Physics, 2001.
- [128] L. Evans and S. Michizono, *The international linear collider machine staging report 2017*, [[1711.00568](#)].
- [129] A. Ushakov, G. Moortgat-Pick, S. Riemann, W. Liu and W. Gai, *Positron source simulations for ilc 1 tev upgrade*, [[1301.1222](#)].
- [130] J. Jones and D. Angal-Kalinin, *Beam delivery system dogleg design and integration for the international linear collider*, *EuCARD-CON-2010-032* (2010) .
- [131] A. Yamamoto in *ESPP Symposium 2019*, 2019.
- [132] M. Pekeler, *Superconducting RF Cavity System Production for Particle Accelerators in Scientific and Industrial Applications*, in *Proceedings of ICHEP 2016*, 2016.
- [133] W. Singer et al., *Development of large grain cavities*, *Phys. Rev. ST Accel. Beams* **16** (2013) [012003](#).

- [134] A. Grassellino, *N Doping: Progress in Development and Understanding*, in *17th International Conference on RF Superconductivity*, p. MOBA06, 2015, DOI.
- [135] A. Romanenko and C. Edwardson, *The effect of vacancies on the microwave surface resistance of niobium revealed by positron annihilation spectroscopy*, *Appl. Phys. Lett.* **102** (2013) 232601.
- [136] S. Posen, A. Romanenko, A. Grassellino, O. Melnychuk and D. Sergatskov, *Ultralow Surface Resistance via Vacuum Heat Treatment of Superconducting Radio-Frequency Cavities*, *Phys. Rev. Applied* **13** (2020) 014024 [1907.00147].
- [137] F. He et al., *Medium-temperature furnace bake of Superconducting Radio-Frequency cavities at IHEP*, 2012.04817.
- [138] H. Ito, H. Araki, K. Takahashi and K. Umemori, *Influence of furnace baking on Q - E behavior of superconducting accelerating cavities*, *PTEP* **2021** (2021) 071G01 [2101.11892].
- [139] P. Dhakal, *Nitrogen Doping and Infusion in SRF Cavities: A Review*, *Phys. Open* **5** (2020) 100034 [2005.03149].
- [140] K. Umemori, E. Kako, T. Konomi, S. Michizono, T. Okada, H. Sakai et al., *Study on Nitrogen Infusion using KEK New Furnace*, in *19th International Conference on RF Superconductivity (SRF 2019)*, p. MOP027, 2019, DOI.
- [141] M. Wenskat, C. Bate, A. Jeromin, T. Keller, J. Knobloch, F. Kramer et al., *Cavity Cut-out Studies of a 1.3 GHz Single-cell Cavity After a Failed Nitrogen Infusion Process*, in *19th International Conference on RF Superconductivity (SRF 2019)*, p. MOP025, 2019, DOI.
- [142] V. Shemelin and H. Padamsee, *The optimal shape of cells of a superconducting accelerating section*, *DESY-TESLA-2002-01*.
- [143] V. Shemelin, H. Padamsee and R. Geng, *Optimal cells for TESLA accelerating structure*, *Nucl. Instrum. Meth. A* **496** (2003) 1.
- [144] J. Sekutowicz et al., *Low Loss Cavity for the 12 GeV CEBAF Upgrade*.
- [145] K. Saito, *Strategy for 50 MV/m*, 2004.
- [146] Z. Li and C. Adolphsen, *A New SRF Cavity Shape with Minimized Surface Electric and Magnetic Fields for the ILC*.
- [147] F. Furuta et al., *Experimental comparison at KEK of high gradient performance of different single cell superconducting cavity designs*, *Conf. Proc. C* **060626** (2006) 750.
- [148] G. Ereemeev, R. Geng, H. Padamsee and V. Shemelin, *High Gradient Studies for ILC with Single Cell Reentrant Shape and Elliptical Shape Cavities made of Fine grain and Large grain Niobium*, *Conf. Proc. C* **070625** (2007) 2337.
- [149] R. Geng, A. Seaman, V. Shemelin and H. Padamsee, *World record accelerating gradient achieved in a superconducting niobium RF cavity*, *Conf. Proc. C* **0505161** (2005) 653.

- [150] C.E. Reece and G. Ciovati, *Superconducting Radio-Frequency Technology R&D for Future Accelerator Applications*, *Rev. Accel. Sci. Tech.* **5** (2012) 285 [[1208.1978](#)].
- [151] R.L. Geng et al., *LSF Shape Cavity Development: Recent Results and Future Plan*, in *LCWS 2018*, 2018.
- [152] T. Peterson and J. Weisend II, *TESLA & ILC Cryomodules*, in *Cryostat Design*, pp. 117–145 (2016), [DOI](#).
- [153] A. Avrakhov, P. Kanareykin and N. Solyak, *Traveling wave accelerating structure for a superconducting accelerator*, *Conf. Proc. C* **0505161** (2005) 4296.
- [154] R. Kostin, P. Avrakhov, A. Kanareykin, N. Solyak, V. Yakovlev, S. Kazakov et al., *A high gradient test of a single-cell superconducting radio frequency cavity with a feedback waveguide*, *Supercond. Sci. Technol.* **28** (2015) 095007.
- [155] V. Shemelin, *to be submitted to PRSTAB*, 2021.
- [156] S. Posen and D. Hall, *Nb₃Sn superconducting radiofrequency cavities: fabrication, results, properties, and prospects*, *Supercond. Sci. Technol.* **30** (2017) 033004.
- [157] S. Posen, J. Lee, O. Melnychuk, Y. Pischalnikov, D. Seidman, D. Sergatskov et al., *Nb₃Sn at Fermilab: Exploring Performance*, in *19th International Conference on RF Superconductivity (SRF 2019)*, p. THFUB1, 2019, [DOI](#).
- [158] S. Posen in *TTC2019*, 2019.
- [159] A. Godeke, *A review of the properties of Nb₃Sn and their variation with A15 composition, morphology and strain state*, *Supercond. Sci. Technol.* **19** (2006) R68.
- [160] G. Catelani and J. Sethna, *Temperature dependence of the superheating field for superconductors in the high- κ London limit*, *Phys. Rev.* **B 78** (2008) 224509.
- [161] F.P.-J. Lin and A. Gurevich, *Effect of impurities on the superheating field of type-II superconductors*, *Phys. Rev.* **B 85** (2012) 054513.
- [162] T. Kubo, *Superfluid flow in disordered superconductors with Dynes pair-breaking scattering: depairing current, kinetic inductance, and superheating field*, *Phys. Rev. Res.* **2** (2020) [033203](#) [[2004.00911](#)].
- [163] Becker, C. and Posen, S. and Groll, N. and Cook, R. and Schlepütz, C. M. and Hall, D. L. and Liepe, M. and Pellin, M. and Zasadzinski, J. and Proslir, T., *Analysis of Nb₃Sn surface layers for superconducting radio frequency cavity applications*, *Appl. Phys. Lett.* **106** (2015) 082602.
- [164] D.A. Rudman, *A15 Nb-Sn tunnel junction fabrication and properties*, *J. App. Phys.* **55** (1984) 3544.
- [165] M. Peininger et al., *Work on Nb₃Sn cavities at Wuppertal*, in *Third Workshop on RF Superconductivity*, 1988.

- [166] Lee, J. and Mao, Z. and He, K. and Sung, Z. H. and Spina, T. and Baik, S.-I. and Hall, D. L. and Liepe, M. and Seidman, D. N. and Posen, S., *Grain-boundary structure and segregation in Nb₃Sn coatings on Nb for high-performance superconducting radiofrequency cavity applications*, *Acta Mat.* **188** (2020) 155.
- [167] Hillenbrand, B. and Martens, H. and Pfister, H. and Schnitzke, K. and Ziegler, G. *IEEE Trans. Magn.* **11** (1975) 420.
- [168] Heinrichs, H., and Grundey, T. and Minatti, N and Muller, G. and Peiniger, M. and Piel, H. and Unterborsch, G. and Vogel, H. P. in *Proc. 2nd Workshop on RF Superconductivity (Geneva)*, 1984.
- [169] Peiniger, M. and Piel, H., *Influence of furnace baking on Q–E behavior of superconducting accelerating cavities*, 1985 *IEEE Trans. Nucl. Sci.* **32** (1985) 3610.
- [170] Kneissel, P. and others, *Nb₃Sn Layers on High-Purity Nb Cavities with Very High Quality Factors and Accelerating Gradients*, in *Proc. 5th European Particle Accelerator Conf. (EPAC'96)*, 1997.
- [171] Müller, G. and others in *Proc. 5th European Particle Accelerator Conf. (EPAC'96)*, 1997.
- [172] T. Kubo, Y. Iwashita and T. Saeki, *Radio-frequency electromagnetic field and vortex penetration in multilayered superconductors*, *Appl. Phys. Lett.* **104** (2014) 032603 [[1304.6876](#)].
- [173] T. Kubo, *Multilayer coating for higher accelerating fields in superconducting radio-frequency cavities: a review of theoretical aspects*, *Supercond. Sci. Technol.* **30** (2017) 023001 [[1607.01495](#)].
- [174] S. Posen, M.K. Transtrum, G. Catelani, M.U. Liepe and J.P. Sethna, *Shielding Superconductors with Thin Films as Applied to rf Cavities for Particle Accelerators*, *Phys. Rev. Applied* **4** (2015) 044019 [[1506.08428](#)].
- [175] A. Gurevich, *Theory of RF superconductivity for resonant cavities*, *Supercond. Sci. Technol.* **30** (2017) 034004.
- [176] H. Ito, C.Z. Antoine, H. Hayano, R. Katayama, T. Kubo, T. Saeki et al., *Lower critical field measurement of NbN multilayer thin film superconductor at KEK*, in *19th International Conference on RF Superconductivity (SRF 2019)*, pp. 632–636, 2019, DOI [[1907.03410](#)].
- [177] HIGHFIELD MAGNET PROGRAM collaboration, *Electrochemical Synthesis of Nb₃Sn Coatings on Cu Substrates*, *Mater. Lett.* **161** (2015) 613.
- [178] E. Barzi, G. Bellettini, S. Donati and C. Luongo, *The Science Training Program for Young Italian Physicists and Engineers at Fermilab*, 8, 2019 [[1908.01899](#)].
- [179] Schäfer, N. and Karabas, N. and Palakkal, J. P. and Petzold, S. and Major, M. and Pietralla, N. and Alff, L. , *Kinetically induced low-temperature synthesis of Nb₃Sn thin films*, *J. Appl. Phys.* **128** (2020) 133902.

- [180] HIGH FIELD MAGNET collaboration, *Synthesis of Superconducting Nb₃Sn Coatings on Nb Substrates.*, *Supercond. Sci. Technol.* **29** (2016) 015009.
- [181] E. Barzi et al., *An Impartial Perspective for Superconducting Nb₃Sn coated Copper RF Cavities for Future Linear Accelerators*, in *2022 Snowmass Summer Study*, 3, 2022 [2203.09718].
- [182] ILCIA Panel, *Summary of the ILC advisory panel's discussions to date after revision*, 2018.
- [183] Science Council of Japan, *Assessment of the revised plan of International Linear Collider project*, 2018.
- [184] IIDTWG 2 *Technical preparation and work packages during ILC Pre-Lab*, 2021. <https://zenodo.org/record/4884718> .
- [185] R. Hori. http://www.yk.rim.or.jp/~reyhori/pages/galacc4_e.htm, 2017.
- [186] F. Furuta, D. Bice, A.C. Crawford and T. Ring, *Fermilab EP Facility Improvement*, in *19th International Conference on RF Superconductivity (SRF 2019)*, pp. 453–455, 2019, DOI.
- [187] Y. Pischalnikov, B. Hartman, J. Holzbauer, W. Schappert, S. Smith and J.-C. Yun, *Reliability of the LCLS II SRF Cavity Tuner*, in *17th International Conference on RF Superconductivity*, p. THPB065, 2015, DOI.
- [188] V. Kashikhin, S. Cheban, J. DiMarco, E. Harms, A. Makarov, T. Strauss et al., *Superconducting Magnet Performance in LCLS-II Cryomodules*, in *9th International Particle Accelerator Conference*, p. WEPML009, 2018, DOI.
- [189] M. Doleans, *Ignition and monitoring technique for plasma processing of multicell superconducting radio-frequency cavities*, *J. Appl. Phys.* **120** (2016) 243301.
- [190] P. Berrutti, B. Giaccone, M. Martinello, A. Grassellino, T. Khabiboulline, M. Doleans et al., *Plasma ignition and detection for in-situ cleaning of 1.3 GHz 9-cell cavities*, *J. Appl. Phys.* **126** (2019) 023302 [1902.03172].
- [191] S. Posen, J. Lee, D. Seidman, A. Romanenko, B. Tennis, O. Melnychuk et al., *Advances in Nb₃Sn superconducting radiofrequency cavities towards first practical accelerator applications*, 2008.00599.
- [192] T. Barklow, J. Brau, K. Fujii, J. Gao, J. List, N. Walker et al., *ILC Operating Scenarios*, 1506.07830.
- [193] M. Woods, *The Polarized electron beam for the SLAC linear collider*, in *12th International Symposium on High-energy Spin Physics (SPIN 96)*, pp. 623–627, 10, 1996 [hep-ex/9611006].
- [194] MOLLER collaboration, *The MOLLER Experiment: An Ultra-Precise Measurement of the Weak Mixing Angle Using Moller Scattering*, 1411.4088.

- [195] CREX, PREX collaboration, *New Measurements of the Beam-Normal Single Spin Asymmetry in Elastic Electron Scattering Over a Range of Spin-0 Nuclei*, [2111.04250](#).
- [196] M. Habermehl, *Dark Matter at the International Linear Collider*, Ph.D. thesis, Hamburg U., Hamburg, 2018. 10.3204/PUBDB-2018-05723.
- [197] H. Abramowicz et al., *Performance and Molière radius measurements using a compact prototype of LumiCal in an electron test beam*, *Eur. Phys. J. C* **79** (2019) 579 [[1812.11426](#)].
- [198] I. Božović Jelisavčić, S. Lukić, G. Milutinović Dumbelović, M. Pandurović and I. Smiljanić, *Luminosity measurement at ILC*, *JINST* **8** (2013) P08012 [[1304.4082](#)].
- [199] I. Bozovic-Jelisavcic, S. Lukic, M. Pandurovic and I. Smiljanic, *Precision luminosity measurement at ILC*, in *International Workshop on Future Linear Colliders*, 3, 2014 [[1403.7348](#)].
- [200] C. Grah and A. Saproinov, *Beam parameter determination using beamstrahlung photons and incoherent pairs*, *JINST* **3** (2008) P10004.
- [201] D. Schulte, “Beam-beam simulations with GUINEA-PIG.” weblib.cern.ch/record/382453/files/ps-99-014.pdf, 1999.
- [202] M. Habermehl, M. Berggren and J. List, *WIMP Dark Matter at the International Linear Collider*, *Phys. Rev. D* **101** (2020) 075053 [[2001.03011](#)].
- [203] S. Poss and A. Sailer, *Luminosity Spectrum Reconstruction at Linear Colliders*, *Eur. Phys. J. C* **74** (2014) 2833 [[1309.0372](#)].
- [204] ILD CONCEPT GROUP collaboration, *Precision Electroweak Measurements with ILC250*, *PoS ICHEP2020* (2021) 347.
- [205] B. Madison and G.W. Wilson, *Center-of-mass energy determination using $e^+e^- \rightarrow \mu^+\mu^-(\gamma)$ events at future e^+e^- colliders*, in *2022 Snowmass Summer Study*, 9, 2022 [[2209.03281](#)].
- [206] M. Beckmann, J. List, A. Vauth and B. Vormwald, *Spin Transport and Polarimetry in the Beam Delivery System of the International Linear Collider*, *JINST* **9** (2014) P07003 [[1405.2156](#)].
- [207] I. Marchesini, *Triple gauge couplings and polarization at the ILC and leakage in a highly granular calorimeter*, Ph.D. thesis, Hamburg U., 2011.
- [208] R. Karl, *From the Machine-Detector Interface to Electroweak Precision Measurements at the ILC — Beam-Gas Background, Beam Polarization and Triple Gauge Couplings*, Ph.D. thesis, Hamburg U., Hamburg, 2019. 10.3204/PUBDB-2019-03013.
- [209] LINEAR COLLIDER collaboration, *Polarised Beams at Future e^+e^- Colliders*, *PoS ICHEP2020* (2021) 691 [[2012.11267](#)].
- [210] J. Beyer, *Achieving Electroweak Precision at Future Electron-Positron Colliders*, Ph.D. thesis, Hamburg U. (in preparation), Hamburg, 2022. 10.xxxx/PUBDB-2022-xxxxx.

- [211] J. Beyer and J. List, *Interplay of Beam Polarisation and Systematic Uncertainties in Electroweak Precision Measurements at Future e^+e^- Colliders*, in *24th International Symposium on Spin Physics*, 2, 2022 [2202.07385].
- [212] P.C. Rowson and M. Woods, *Experimental issues for precision electroweak physics at a high luminosity Z factory*, *AIP Conf. Proc.* **578** (2001) 515 [hep-ex/0012055].
- [213] G. Wilkinson, “Requirements for polarization measurements.” https://indico.cern.ch/event/1181966/contributions/5041437/attachments/2512993/4326863/epol_requirements_sep2022_wilkinson.pdf, 2022.
- [214] J. Strube and M. Titov, *Detector Liaison Report v2021.2.2*, *Zenodo* (2021) .
- [215] M. Thomson, *Particle Flow Calorimetry and the PandoraPFA Algorithm*, *Nucl.Instrum.Meth.* **A611** (2009) 25 [0907.3577].
- [216] ILD CONCEPT GROUP collaboration, *International Large Detector: Interim Design Report*, 2003.01116.
- [217] K. Fujii et al., *Physics Case for the 250 GeV Stage of the International Linear Collider*, 1710.07621.
- [218] J. Brau and *et.al.*, “The international linear collider: A global project.” http://ilchome.web.cern.ch/sites/ilchome.web.cern.ch/files/ILC_Global_Project_Final.pdf, 2018.
- [219] B. Parker et al., *Challenges and concepts for design of an interaction region with push-pull arrangement of detectors - an interface document*, *Conf. Proc. C* **0806233** (2008) MOPP031.
- [220] L. Greiner, E. Anderssen, H. Matis, H. Ritter, J. Schambach et al., *A MAPS based vertex detector for the STAR experiment at RHIC*, *Nucl.Instrum.Meth.* **A650** (2011) 68.
- [221] ALICE collaboration, *Technical Design Report for the Upgrade of the ALICE Inner Tracking System*, *J. Phys. G* **41** (2014) 087002.
- [222] DEPFET collaboration, *The ultralight DEPFET pixel detector of the Belle II experiment*, *Nucl. Instrum. Meth.* **A845** (2017) 118.
- [223] S. Murai, A. Ishikawa, T. Sanuki, A. Miyamoto, Y. Sugimoto, C. Constantino et al., *Recent status of FPCCD vertex detector R&D*, in *Proceedings, International Workshop on Future Linear Colliders (LCWS15): Whistler, B.C., Canada, November 02-06, 2015*, 2016 [1603.00009].
- [224] Strube, Jan and Titov, Maxim, “Linear Collider R&D liaison report.” <http://linearcollider.org/physics-detectors/working-group-detector-rd-liaison>, 2018.
- [225] PLUME collaboration, *PLUME collaboration: Ultra-light ladders for linear collider vertex detector*, *Nucl. Instrum. Meth. A* **650** (2011) 208.

- [226] LCTPC collaboration, *Development of a TPC for an ILC Detector*, *Phys. Procedia* **37** (2012) 456 [[1203.2074](#)].
- [227] M. Hauschild, *Particle ID with dE/dx at the TESLA-TPC*, *AIP Conf. Proc.* **578** (2001) 878.
- [228] LCTPC collaboration, *TPC development by the LCTPC collaboration for the ILD Detector at ILC*, in *2011 IEEE Nuclear Science Symposium and Medical Imaging Conference*, pp. 1413–1416, 2011, [DOI](#).
- [229] LCTPC collaboration, *A Time Projection Chamber with GEM-Based Readout*, *Nucl. Instrum. Meth.* **A856** (2017) 109 [[1604.00935](#)].
- [230] J. Bouchez et al., *Bulk micromegas detectors for large TPC applications*, *Nucl. Instrum. Meth.* **A574** (2007) 425.
- [231] F. Sefkow, A. White, K. Kawagoe, R. Pöschl and J. Repond, *Experimental Tests of Particle Flow Calorimetry*, *Rev. Mod. Phys.* **88** (2016) 015003 [[1507.05893](#)].
- [232] CALICE collaboration, *Technological Prototypes and Result Highlights of Highly Granular Calorimeters*, *PoS EPS-HEP2017* (2017) 497.
- [233] CALICE collaboration, *Exploring the structure of hadronic showers and the hadronic energy reconstruction with highly granular calorimeters*, *PoS ICHEP2020* (2021) 862.
- [234] CALICE collaboration, *Beam Test Results with Highly Granular Hadron Calorimeters for the ILC*, *Conf. Proc.* **C0908171** (2009) 539 [[1002.1012](#)].
- [235] G. Baulieu et al., *Construction and commissioning of a technological prototype of a high-granularity semi-digital hadronic calorimeter*, *JINST* **10** (2015) P10039 [[1506.05316](#)].
- [236] I.Laktineh, “Patent: PCT/EP2018/053561.” <https://patentscope.wipo.int/search/en/detail.jsf?docId=W02018149827>, 2018.
- [237] I.Laktineh, “A new concept to readout large detectors.” <https://agenda.linearcollider.org/event/9174/contributions/47747/attachments/36775/57530/Imad%20new%20scheme.pdf>, 2021.
- [238] H. Abramowicz et al., *Forward Instrumentation for ILC Detectors*, *JINST* **5** (2010) P12002 [[1009.2433](#)].
- [239] H. Abramowicz et al., *The International Linear Collider Technical Design Report - Volume 4: Detectors*, [1306.6329](#).
- [240] N. Sinev, J. Brau, D. Strom, C. Baltay, W. Emmet and D. Rabinowitz, *Chronopixel project status*, *PoS VERTEX2015* (2015) 038.
- [241] J. Brau et al., *KPiX - A 1,024 Channel Readout ASIC for the ILC*, in *2012 IEEE Nuclear Science Symposium and Medical Imaging Conference and 19th Workshop on Room-Temperature Semiconductor X-ray and Gamma-ray Detectors*, pp. 1857–1860, 2012, [DOI](#).

- [242] A. Steinhebel and J. Brau, *Studies of the Response of the SiD Silicon-Tungsten ECal*, in *International Workshop on Future Linear Colliders*, 3, 2017 [[1703.08605](#)].
- [243] B. Parker, A. Mikhailichenko, K. Buesser, J. Hauptman, T. Tauchi, P. Burrows et al., *Functional Requirements on the Design of the Detectors and the Interaction Region of an e^+e^- Linear Collider with a Push-Pull Arrangement of Detectors*, in *Particle Accelerator Conference (PAC 09)*, <https://jacow.org/PAC2009/papers/we6pfp078.pdf> .
- [244] K. Buesser, *ILD Machine-Detector Interface and Experimental Hall Issues*, in *International Workshop on Future Linear Colliders (LCWS11)*, 1, 2012 [[1201.5807](#)].
- [245] J. Brau, “The SiD Digital ECal based on Monolithic Active Pixel Sensors.” ILCX2021, (2021). <https://agenda.linearcollider.org/event/9211/contributions/49457/> .
- [246] G. Aglieri, M. Aleksa, D.A. Feito, M. Angeletti, P. Antoszczuk, R. Ballabriga et al., *Strategic R&D Programme on Technologies for Future Experiments*, .
- [247] E.D.R.R.P. Group, *The 2021 ECFA detector research and development roadmap*, *European Strategy report CERN-ESU-017* (2020) .
- [248] *AIDA Innova, European Union’s Horizon 2020 Research and Innovation programme under Grant Agreement No 101004761* (2021) .
- [249] B. Fleming, I. Shipsey, M. Demarteau, J. Fast, S. Golwala, Y.-K. Kim et al., *Basic research needs for high energy physics detector research & development: Report of the office of science workshop on basic research needs for hep detector research and development: December 11-14, 2019* .
- [250] H. Abramowicz et al., *Conceptual design report for the LUXE experiment*, *Eur. Phys. J. ST* **230** (2021) 2445 [[2102.02032](#)].
- [251] DEPFET collaboration, *DEPFET active pixel detectors for a future linear e^+e^- collider*, *IEEE Trans. Nucl. Sci.* **60** (2013) 1457 [[1212.2160](#)].
- [252] P. Fischer et al., *Progress towards a large area, thin DEPFET detector module*, *Nucl. Instrum. Meth. A* **582** (2007) 843.
- [253] BELLE-II collaboration, *Belle II Technical Design Report*, [1011.0352](#).
- [254] J. Baudot et al., *Development of Single- and Double-sided Ladders for the ILD Vertex Detectors*, in *International Workshop on Future Linear Colliders (LCWS11)*, 3, 2012 [[1203.3689](#)].
- [255] MU3E collaboration, *Technical design of the phase I Mu3e experiment*, *Nucl. Instrum. Meth. A* **1014** (2021) 165679 [[2009.11690](#)].
- [256] STAR collaboration, *STAR detector overview*, *Nucl. Instrum. Meth. A* **499** (2003) 624.
- [257] NA62 collaboration, *The Beam and detector of the NA62 experiment at CERN*, *JINST* **12** (2017) P05025 [[1703.08501](#)].

- [258] O.A.D.A. Francisco et al., *Microchannel cooling for the LHCb VELO Upgrade I*, [2112.12763](#).
- [259] L. Andricek, M. Boronat, I. Garcia, P. Gomis, C. Marinas, J. Ninkovic et al., *Integrated cooling channels in position-sensitive silicon detectors*, *JINST* **11** (2016) P06018 [[1604.08776](#)].
- [260] A. Mapelli, P. Petagna and M. Vos, *Micro-channel cooling for collider experiments: review and recommendations*, *AIDA note* **AIDA-2020-NOTE-2020-003** (2020) .
- [261] N. Barchetta, P. Collins and P. Riedler, *Tracking and vertex detectors at FCC-ee*, *Eur. Phys. J. Plus* **137** (2022) 231 [[2112.13019](#)].
- [262] S. Lee, M. Livan and R. Wigmans, *Dual-readout calorimetry*, *Rev. Mod. Phys.* **90** (2018) 025002.
- [263] N. Akchurin et al., *Detection of electron showers in dual-readout crystal calorimeters*, *Nucl. Instrum. Meth. A* **686** (2012) 125.
- [264] N. Akchurin et al., *The electromagnetic performance of the RD52 fiber calorimeter*, *Nucl. Instrum. Meth. A* **686** (2012) 125.
- [265] S. Lee et al., *Hadron detection with a dual-readout fiber calorimeter*, *Nucl. Instrum. Meth. A* **866** (2017) 76.
- [266] N. Akchurin et al., *Lessons from monte carlo simulations of the performance of a dual-readout fiber calorimeter*, *Nucl. Instrum. Meth. A* **762** (2014) 100.
- [267] N. Akchurin et al., *Particle identification in the longitudinally unsegmented RD52 calorimeter*, *Nucl. Instrum. Meth. A* **735** (2014) 120.
- [268] M. Antonello et al., *Tests of a dual-readout fibre calorimeter with sipm light sensors*, *Nucl. Instrum. Meth. A* **899** (2018) 52.
- [269] M. Antonello et al., *Development of a silicon photomultiplier based dual-readout calorimeter: The pathway beyond the proof-of-concept*, *Nucl. Instrum. Meth. A* **963** (2019) 127.
- [270] R. Aly et al., *First test-beam results obtained with idea, a detector concept designed for future lepton colliders*, *Nucl. Instrum. Meth. A* **958** (2020) 162088.
- [271] M. Lucchini, W. Chung, S.C. Eno, Y. Lai, L. Lucchini, M. Nguyen et al., *New perspectives on segmented crystal calorimeters for future colliders*, *Journal of Instrumentation* **15** (2020) P11005.
- [272] M. Aleksa, F. Bedeschi, R. Ferrari, F. Sefkow and C.G. Tully, *Calorimetry at FCC-ee*, *Eur. Phys. J. Plus* **136** (2021) 1066 [[2109.00391](#)].
- [273] M. Antonello, M. Caccia, R. Santoro, R. Ferrari, G. Gaudio, G. Polesello et al., *Dual-readout calorimetry: Present status and perspective*, *Int. J. Mod. Phys. A* **36** (2021) 2142017.

- [274] L3 BGO collaboration, *Results on the calibration of the L3 BGO calorimeter with cosmic rays*, *Nucl. Instrum. Meth. A* **343** (1994) 456.
- [275] CMS collaboration, *Energy Calibration and Resolution of the CMS Electromagnetic Calorimeter in pp Collisions at $\sqrt{s} = 7$ TeV*, *JINST* **8** (2013) P09009 [[1306.2016](#)].
- [276] M.T. Lucchini, W. Chung, S.C. Eno, Y. Lai, L. Lucchini, M.-T. Nguyen et al., *New perspectives on segmented crystal calorimeters for future colliders*, *JINST* **15** (2020) P11005 [[2008.00338](#)].
- [277] M. Aleksa et al., *Calorimeters for the FCC-hh*, [1912.09962](#).
- [278] J.A. Ballin, J.P. Crooks, P.D. Dauncey, A.-M. Magnan, Y. Mikami, O.D. Miller et al., *Monolithic Active Pixel Sensors (MAPS) in a Quadruple Well Technology for Nearly 100% Fill Factor and Full CMOS Pixels*, *Sensors* **8** (2008) 5336.
- [279] J.A. Ballin, P.D. Dauncey, A.M. Magnan, M. Noy, Y. Mikami, O. Miller et al., *A Digital ECAL based on MAPS*, in *International Linear Collider Workshop (LCWS08 and ILC08)*, 1, 2009, <https://arxiv.org/abs/0901.4457> [[0901.4457](#)].
- [280] SPIDER collaboration, *Performance of CMOS sensors for a digital electromagnetic calorimeter*, *PoS ICHEP2010* (2010) 502.
- [281] C. Alice Collaboration, *Letter of Intent: A Forward Calorimeter (FoCal) in the ALICE experiment*, *CERN Document Server* (2020) .
- [282] A.P. de Haas et al., *The FoCal prototype—an extremely fine-grained electromagnetic calorimeter using CMOS pixel sensors*, *JINST* **13** (2018) P01014 [[1708.05164](#)].
- [283] J.-C. Brient and H. Videau, *The Calorimetry at the future e^+e^- linear collider*, *eConf C010630* (2001) E3047 [[hep-ex/0202004](#)].
- [284] IPHC-IRFU collaboration, *Achievements and perspectives of CMOS pixel sensors for charged particle tracking*, *Nucl. Instrum. Meth. A* **623** (2010) 192.
- [285] ALICE collaboration, *The ALPIDE pixel sensor chip for the upgrade of the ALICE Inner Tracking System*, *Nucl. Instrum. Meth. A* **845** (2017) 583.
- [286] J. Alme, G.G. Barnaföldi, R. Barthel, V. Borshchov, T. Bodova, A. van den Brink et al., *A High-Granularity Digital Tracking Calorimeter Optimized for Proton CT*, *Front. Phys.* **0** (2020) .
- [287] G. Pellegrini et al., *Technology developments and first measurements of Low Gain Avalanche Detectors (LGAD) for high energy physics applications*, *Nucl. Instrum. Meth. A* **765** (2014) 12.
- [288] H.F.W. Sadrozinski et al., *Ultra-fast silicon detectors (UFSD)*, *Nucl. Instrum. Meth. A* **831** (2016) 18.

- [289] N. Cartiglia et al., *Beam test results of a 16 ps timing system based on ultra-fast silicon detectors*, *Nucl. Instrum. Meth. A* **850** (2017) 83 [[1608.08681](#)].
- [290] CMS collaboration, *A MIP Timing Detector for the CMS Phase-2 Upgrade*, .
- [291] C. Allaire et al., *Beam test measurements of Low Gain Avalanche Detector single pads and arrays for the ATLAS High Granularity Timing Detector*, *JINST* **13** (2018) P06017 [[1804.00622](#)].
- [292] E. Currás et al., *Inverse Low Gain Avalanche Detectors (iLGADs) for precise tracking and timing applications*, *Nucl. Instrum. Meth. A* **958** (2020) 162545 [[1904.02061](#)].
- [293] G. Paternoster, G. Borghi, M. Boscardin, N. Cartiglia, M. Ferrero, F. Ficorella et al., *Trench-isolated low gain avalanche diodes (ti-lgads)*, *IEEE Electron Device Letters* **PP** (2020) 1.
- [294] M. Mandurrino et al., *First demonstration of 200, 100, and 50 um pitch Resistive AC-Coupled Silicon Detectors (RSD) with 100% fill-factor for 4D particle tracking*, [1907.03314](#).
- [295] O. Karacheban, K. Afanaciev, M. Hempel, H. Henschel, W. Lange, J.L. Leonard et al., *Investigation of a direction sensitive sapphire detector stack at the 5 GeV electron beam at DESY-II*, *JINST* **10** (2015) P08008 [[1504.04023](#)].
- [296] M.R. Hoeferkamp et al., *Novel Sensors for Particle Tracking: a Contribution to the Snowmass Community Planning Exercise of 2021*, [2202.11828](#).
- [297] Parker, S. and Da Viá, C. and Dalla Betta, G.-F., *Radiation Sensors with 3D Electrodes*, CRC Press, Boca Raton (2019).
- [298] J.-W. Tsung, M. Havranek, F. Hugging, H. Kagan, H. Kruger and N. Wermes, *Signal and noise of Diamond Pixel Detectors at High Radiation Fluences*, *JINST* **7** (2012) P09009 [[1206.6795](#)].
- [299] N. Fourches, *Ultimate Pixel based on a Single Transistor with Deep Trapping Gate*, *IEEE Trans. on Electron Devices* **64** (2017) 1619.
- [300] J. Metcalfe, I. Mejia, J. Murphy, M. Quevedo, L. Smith, J. Alvarado et al., *Potential of Thin Films for use in Charged Particle Tracking Detectors*, [1411.1794](#).
- [301] S. Oktyabrsky, M. Yakimov, V. Tokranov and P. Murat, *Integrated Semiconductor Quantum Dot Scintillation Detector: Ultimate Limit for Speed and Light Yield*, *IEEE Trans. Nucl. Sci.* **63** (2016) 656.
- [302] V. Cairo and J. Vavra, *in preparation*, 2022.
- [303] DELPHES 3 collaboration, *DELPHES 3, A modular framework for fast simulation of a generic collider experiment*, *JHEP* **02** (2014) 057 [[1307.6346](#)].

- [304] S. Ovin, X. Rouby and V. Lemaître, *DELPHES, a framework for fast simulation of a generic collider experiment*, [0903.2225](#).
- [305] M. Cacciari, *FastJet: A Code for fast k_t clustering, and more*, in *Deep inelastic scattering. Proceedings, 14th International Workshop, DIS 2006, Tsukuba, Japan, April 20-24, 2006*, pp. 487–490, 2006 [[hep-ph/0607071](#)].
- [306] A. Zarnecki, “Generic ILC detector model for Delphes.” contribution to Snowmass Energy Frontier Preparatory Joint Sessions on “Open questions and News Ideas”, <https://indico.fnal.gov/event/43959/contributions/190778/>, July, 2020.
- [307] Aleksander Filip Zarnecki, “The ILC DELPHES card (IDT-WG3 Software Tutorial).” <https://agenda.linearcollider.org/event/9264/>, 2021.
- [308] Delphes authors, “Delphes Project Page.” <https://github.com/delphes/delphes>, 2009.
- [309] ILD CONCEPT GROUP collaboration, *International Large Detector: Interim Design Report*, [2003.01116](#).
- [310] R. Brun and F. Rademakers, *ROOT: An object oriented data analysis framework*, *Nucl. Instrum. Meth. A* **389** (1997) 81.
- [311] Frank Gaede, “delphes2lcio.” <https://github.com/iLCSoft/LCIO/tree/master/examples/cpp/delphes2lcio>, 2021.
- [312] M. Berggren, *SGV 3.0 - a fast detector simulation*, in *International Workshop on Future Linear Colliders (LCWS11) Granada, Spain, September 26-30, 2011*, 2012 [[1203.0217](#)].
- [313] DELPHI collaboration, *Searches for supersymmetric particles in e^+e^- collisions up to 208-GeV and interpretation of the results within the MSSM*, *Eur. Phys. J.* **C31** (2003) 421 [[hep-ex/0311019](#)].
- [314] “Cholesky decomposition.” https://en.wikipedia.org/wiki/Cholesky_decomposition, 2022.
- [315] iLCSoft authors, “iLCSoft Project Page.” <https://ilcsoft.desy.de/portal>.
- [316] F. Gaede, T. Behnke, N. Graf and T. Johnson, *LCIO: A Persistency framework for linear collider simulation studies*, *eConf* **C0303241** (2003) TUKT001 [[physics/0306114](#)].
- [317] F. Gaede, *Marlin and LCCD: Software tools for the ILC*, *Nucl. Instrum. Meth.* **A559** (2006) 177.
- [318] M. Frank, F. Gaede, C. Grefe and P. Mato, *DD4hep: A Detector Description Toolkit for High Energy Physics Experiments*, *J. Phys. Conf. Ser.* **513** (2014) 022010.
- [319] M. Frank, F. Gaede, N. Nikiforou, M. Petric and A. Sailer, *DDG4 A Simulation Framework based on the DD4hep Detector Description Toolkit*, *J. Phys. Conf. Ser.* **664** (2015) 072017.
- [320] GEANT4 collaboration, *GEANT4: A Simulation toolkit*, *Nucl. Instrum. Meth.* **A506** (2003) 250.

- [321] F. Gaede, S. Aplin, R. Glattauer, C. Rosemann and G. Voutsinas, *Track reconstruction at the ILC: the ILD tracking software*, *J. Phys. Conf. Ser.* **513** (2014) 022011.
- [322] J.S. Marshall and M.A. Thomson, *The Pandora Software Development Kit for Pattern Recognition*, *Eur. Phys. J. C* **75** (2015) 439 [[1506.05348](#)].
- [323] T. Suehara and T. Tanabe, *LCFIPlus: A Framework for Jet Analysis in Linear Collider Studies*, *Nucl. Instrum. Meth.* **A808** (2016) 109 [[1506.08371](#)].
- [324] W. Kilian, T. Ohl and J. Reuter, *WHIZARD: Simulating Multi-Particle Processes at LHC and ILC*, *Eur. Phys. J. C* **71** (2011) 1742 [[0708.4233](#)].
- [325] T. Sjostrand, S. Mrenna and P.Z. Skands, *PYTHIA 6.4 Physics and Manual*, *JHEP* **05** (2006) 026 [[hep-ph/0603175](#)].
- [326] D. Schulte, *Beam-beam simulations with Guinea-Pig*, *eConf* **C980914** (1998) 127.
- [327] P. Chen, T.L. Barklow and M.E. Peskin, *Hadron production in gamma gamma collisions as a background for e^+e^- linear colliders*, *Phys. Rev.* **D49** (1994) 3209 [[hep-ph/9305247](#)].
- [328] A. Schütz, *Pair Background Envelopes in the SiD Detector*, in *Proceedings, International Workshop on Future Linear Colliders 2016 (LCWS2016): Morioka, Iwate, Japan, December 05-09, 2016*, 2017 [[1703.05737](#)].
- [329] Jim Brau et al., “ILC Simulation Resources for Snowmass 2021.” <http://ilcsnowmass.org/>, 2021.
- [330] B.L. Ioffe and V.A. Khoze, *What can be expected from experiments with e^+e^- colliding beams at energy ~ 100 GeV*, *Sov. J. Part. Nucl.* **9** (1978) 50.
- [331] J. Yan, S. Watanuki, K. Fujii, A. Ishikawa, D. Jeans, J. Strube et al., *Measurement of the Higgs boson mass and $e^+e^- \rightarrow ZH$ cross section using $Z \rightarrow \mu^+\mu^-$ and $Z \rightarrow e^+e^-$ at the ILC*, *Phys. Rev. D* **94** (2016) 113002 [[1604.07524](#)].
- [332] J. Tian, *A new method for measuring the Higgs mass at the ILC*, *ILD-PHYS-PUB-2019-001* (2020) .
- [333] G. Wilson, “Complementary Higgs mass measurements at ILC.” <https://agenda.linearcollider.org/event/7645/contributions/40075/>.
- [334] H. Ono and A. Miyamoto, *A study of measurement precision of the Higgs boson branching ratios at the International Linear Collider*, *Eur. Phys. J. C* **73** (2013) 2343 [[1207.0300](#)].
- [335] T. Ogawa, *Sensitivity to anomalous VVH couplings induced by dimension-6 operators at the ILC*, Ph.D. thesis, 2018.
- [336] A. Albert et al., *Strange quark as a probe for new physics in the Higgs sector, in 2022 Snowmass Summer Study*, 3, 2022 [[2203.07535](#)].

- [337] S.-i. Kawada, K. Fujii, T. Suehara, T. Takahashi and T. Tanabe, *A study of the measurement precision of the Higgs boson decaying into tau pairs at the ILC*, *Eur. Phys. J. C* **75** (2015) 617 [[1509.01885](#)].
- [338] S.-i. Kawada, J. List and M. Berggren, *Prospects of measuring the branching fraction of the Higgs boson decaying into muon pairs at the International Linear Collider*, *Eur. Phys. J. C* **80** (2020) 1186 [[2009.04340](#)].
- [339] E. Antonov and A. Drutskoy, *Measurement of $\sigma(e^+e^- \rightarrow HZ) \times \text{Br}(H \rightarrow ZZ^*)$ at the 250 GeV ILC*, [2108.08867](#).
- [340] Y. Aoki, K. Fujii and J. Tian, *Study of the $h\gamma Z$ coupling at the ILC*, in *International Workshop on Future Linear Colliders*, 5, 2021 [[2105.06665](#)].
- [341] ILD CONCEPT GROUP collaboration, *Study of $e^+e^- \rightarrow \gamma h$ at the ILC*, [2203.07202](#).
- [342] D. Jeans and G.W. Wilson, *Measuring the CP state of tau lepton pairs from Higgs decay at the ILC*, *Phys. Rev. D* **98** (2018) 013007 [[1804.01241](#)].
- [343] T. Ogawa, J. Tian and K. Fujii, *Sensitivity to anomalous ZZH couplings at the ILC*, *PoS EPS-HEP2017* (2017) 322 [[1712.09772](#)].
- [344] I. Božović-Jelisavučić, N. Vukausinović and D. Jeans, *Measuring the CP properties of the Higgs sector at electron-positron colliders*, in *2022 Snowmass Summer Study*, 3, 2022 [[2203.06819](#)].
- [345] D. Curtin et al., *Exotic decays of the 125 GeV Higgs boson*, *Phys. Rev. D* **90** (2014) 075004 [[1312.4992](#)].
- [346] ILD collaboration, *Probing the dark sector via searches for invisible decays of the Higgs boson at the ILC*, *PoS EPS-HEP2019* (2020) 358 [[2002.12048](#)].
- [347] C. Potter, A. Steinhebel, J. Brau, A. Pryor and A. White, *Expected Sensitivity to Invisible Higgs Boson Decays at the ILC with the SiD Detector*, [2203.08330](#).
- [348] Z. Liu, L.-T. Wang and H. Zhang, *Exotic decays of the 125 GeV Higgs boson at future e^+e^- lepton colliders*, *Chin. Phys. C* **41** (2017) 063102 [[1612.09284](#)].
- [349] LHC HIGGS CROSS SECTION WORKING GROUP collaboration, *Handbook of LHC Higgs Cross Sections: 4. Deciphering the Nature of the Higgs Sector*, [1610.07922](#).
- [350] M. Cepeda, S. Gori, V.M. Outchoorn and J. Shelton, *Exotic Higgs Decays*, [2111.12751](#).
- [351] J. Alwall, R. Frederix, S. Frixione, V. Hirschi, F. Maltoni et al., *The automated computation of tree-level and next-to-leading order differential cross sections, and their matching to parton shower simulations*, *JHEP* **1407** (2014) 079 [[arXiv:1405.0301](#)].
- [352] Q. Xiu, H. Zhu, X. Lou and T. Yue, *Study of beamstrahlung effects at CEPC*, *Chin. Phys. C* **40** (2016) 053001 [[1505.01270](#)].

- [353] M. Greco, T. Han and Z. Liu, *ISR effects for resonant Higgs production at future lepton colliders*, *Phys. Lett.* **B763** (2016) 409 [[1607.03210](#)].
- [354] Y. Kato, “Search for higgs decaying to exotic scalars at the ilc.” Presentation at The 2021 International Workshop on the high energy Circular Electron-Positron Collider (CEPC), Nov. 8-12, 2021, <https://indico.ihep.ac.cn/event/14938>.
- [355] J. Shelton and D. Xu, *Exotic Higgs Decays to Four Taus at Future Electron-Positron Colliders*, 10, 2021 [[2110.13225](#)].
- [356] M. Carena, Z. Liu and Y. Wang, *Electroweak phase transition with spontaneous Z_2 -breaking*, *JHEP* **08** (2020) 107 [[1911.10206](#)].
- [357] J. Kozaczuk, M.J. Ramsey-Musolf and J. Shelton, *Exotic Higgs boson decays and the electroweak phase transition*, *Phys. Rev. D* **101** (2020) 115035 [[1911.10210](#)].
- [358] S. Alipour-Fard, N. Craig, S. Gori, S. Koren and D. Redigolo, *The second Higgs at the lifetime frontier*, *JHEP* **07** (2020) 029 [[1812.09315](#)].
- [359] Z. Chacko, P.J. Fox, R. Harnik and Z. Liu, *Neutrino Masses from Low Scale Partial Compositeness*, [2012.01443](#).
- [360] N. Craig, A. Katz, M. Strassler and R. Sundrum, *Naturalness in the Dark at the LHC*, *JHEP* **07** (2015) 105 [[1501.05310](#)].
- [361] D. Curtin and C.B. Verhaaren, *Discovering Uncolored Naturalness in Exotic Higgs Decays*, *JHEP* **12** (2015) 072 [[1506.06141](#)].
- [362] J. Liu, Z. Liu and L.-T. Wang, *Enhancing Long-Lived Particles Searches at the LHC with Precision Timing Information*, *Phys. Rev. Lett.* **122** (2019) 131801 [[1805.05957](#)].
- [363] J. Liu, Z. Liu, L.-T. Wang and X.-P. Wang, *Enhancing Sensitivities to Long-lived Particles with High Granularity Calorimeters at the LHC*, *JHEP* **11** (2020) 066 [[2005.10836](#)].
- [364] S. Jung, Z. Liu, L.-T. Wang and K.-P. Xie, *Probing Higgs exotic decay at the LHC with machine learning*, [2109.03294](#).
- [365] N. Arkani-Hamed, T. Cohen, R.T. D’Agnolo, A. Hook, H.D. Kim and D. Pinner, *Solving the Hierarchy Problem at Reheating with a Large Number of Degrees of Freedom*, *Phys. Rev. Lett.* **117** (2016) 251801 [[1607.06821](#)].
- [366] N. Arkani-Hamed, R. Tito D’agnolo and H.D. Kim, *The Weak Scale as a Trigger*, [2012.04652](#).
- [367] P. Meade and H. Ramani, *Unrestored Electroweak Symmetry*, *Phys. Rev. Lett.* **122** (2019) 041802 [[1807.07578](#)].
- [368] I. Baldes and G. Servant, *High scale electroweak phase transition: baryogenesis and symmetry non-restoration*, *JHEP* **10** (2018) 053 [[1807.08770](#)].

- [369] A. Glioti, R. Rattazzi and L. Vecchi, *Electroweak Baryogenesis above the Electroweak Scale*, *JHEP* **04** (2019) 027 [[1811.11740](#)].
- [370] O. Matsedonskyi and G. Servant, *High-Temperature Electroweak Symmetry Non-Restoration from New Fermions and Implications for Baryogenesis*, *JHEP* **09** (2020) 012 [[2002.05174](#)].
- [371] ALEPH, DELPHI, L3, OPAL, LEP ELECTROWEAK collaboration, *Electroweak Measurements in Electron-Positron Collisions at W-Boson-Pair Energies at LEP*, *Phys. Rept.* **532** (2013) 119 [[1302.3415](#)].
- [372] ALEPH collaboration, *Improved measurement of the triple gauge-boson couplings $\gamma W W$ and $Z W W$ in $e^+ e^-$ collisions*, *Phys. Lett. B* **614** (2005) 7.
- [373] DELPHI collaboration, *Measurement of trilinear gauge boson couplings WWV , ($V \equiv Z, \gamma$) in $e^+ e^-$ collisions at 189-GeV*, *Phys. Lett. B* **502** (2001) 9 [[hep-ex/0102041](#)].
- [374] L3 collaboration, *Measurement of triple gauge boson couplings of the W boson at LEP*, *Phys. Lett. B* **586** (2004) 151 [[hep-ex/0402036](#)].
- [375] OPAL collaboration, *Measurement of charged current triple gauge boson couplings using W pairs at LEP*, *Eur. Phys. J. C* **33** (2004) 463 [[hep-ex/0308067](#)].
- [376] CMS collaboration, *Search for anomalous triple gauge couplings in WW and WZ production in lepton + jet events in proton-proton collisions at $\sqrt{s} = 13$ TeV*, *JHEP* **12** (2019) 062 [[1907.08354](#)].
- [377] P. Azzi et al., *Report from Working Group 1: Standard Model Physics at the HL-LHC and HE-LHC*, *CERN Yellow Rep. Monogr.* **7** (2019) 1 [[1902.04070](#)].
- [378] M. Diehl, O. Nachtmann and F. Nagel, *Probing triple gauge couplings with transverse beam polarisation in $e^+ e^- \rightarrow W^+ W^-$* , *Eur. Phys. J. C* **32** (2003) 17 [[hep-ph/0306247](#)].
- [379] M. Diehl, O. Nachtmann and F. Nagel, *Triple gauge couplings in polarized $e^- e^+ \rightarrow W^- W^+$ and their measurement using optimal observables*, *Eur. Phys. J. C* **27** (2003) 375 [[hep-ph/0209229](#)].
- [380] M. Diehl and O. Nachtmann, *Anomalous three gauge couplings in $e^+ e^- \rightarrow W^+ W^-$ and 'optimal' strategies for their measurement*, *Eur. Phys. J. C* **1** (1998) 177 [[hep-ph/9702208](#)].
- [381] J. Beyer, R. Karl and J. List, *Precision measurements of Triple Gauge Couplings at future electron-positron colliders*, in *International Workshop on Future Linear Colliders*, 2, 2020 [[2002.02777](#)].
- [382] J. Beyer and J. List, *Interplay of beam polarisation and systematic uncertainties in electroweak precision measurements at future $e^+ e^-$ colliders*, in *Proceedings of SPIN Conference*, 1, 2022 [[2022.01xyz](#)].
- [383] R. Abbate, M. Fickinger, A.H. Hoang, V. Mateu and I.W. Stewart, *Thrust at N^3LL with Power Corrections and a Precision Global Fit for $\alpha_s(m_Z)$* , *Phys. Rev. D* **83** (2011) 074021 [[1006.3080](#)].

- [384] A.H. Hoang, D.W. Kolodrubetz, V. Mateu and I.W. Stewart, *Precise determination of α_s from the C -parameter distribution*, *Phys. Rev. D* **91** (2015) 094018 [[1501.04111](#)].
- [385] A.J. Larkoski, I. Moult and B. Nachman, *Jet Substructure at the Large Hadron Collider: A Review of Recent Advances in Theory and Machine Learning*, *Phys. Rept.* **841** (2020) 1 [[1709.04464](#)].
- [386] S. Marzani, G. Soyez and M. Spannowsky, *Looking inside jets: an introduction to jet substructure and boosted-object phenomenology*, vol. 958, Springer (2019), [10.1007/978-3-030-15709-8](#), [[1901.10342](#)].
- [387] M. Dasgupta, A. Fregoso, S. Marzani and G.P. Salam, *Towards an understanding of jet substructure*, *JHEP* **09** (2013) 029 [[1307.0007](#)].
- [388] A.J. Larkoski, S. Marzani, G. Soyez and J. Thaler, *Soft Drop*, *JHEP* **05** (2014) 146 [[1402.2657](#)].
- [389] A. Kardos, A.J. Larkoski and Z. Trócsányi, *Groomed jet mass at high precision*, *Phys. Lett. B* **809** (2020) 135704 [[2002.00942](#)].
- [390] D.M. Hofman and J. Maldacena, *Conformal collider physics: Energy and charge correlations*, *JHEP* **05** (2008) 012 [[0803.1467](#)].
- [391] H. Chen, I. Moult, J. Sandor and H.X. Zhu, *Celestial Blocks and Transverse Spin in the Three-Point Energy Correlator*, [2202.04085](#).
- [392] H. Chen, I. Moult and H.X. Zhu, *Spinning Gluons from the QCD Light-Ray OPE*, [2104.00009](#).
- [393] H. Chen, I. Moult and H.X. Zhu, *Quantum Interference in Jet Substructure from Spinning Gluons*, *Phys. Rev. Lett.* **126** (2021) 112003 [[2011.02492](#)].
- [394] H. Chen, M.-X. Luo, I. Moult, T.-Z. Yang, X. Zhang and H.X. Zhu, *Three point energy correlators in the collinear limit: symmetries, dualities and analytic results*, *JHEP* **08** (2020) 028 [[1912.11050](#)].
- [395] H. Chen, I. Moult, X. Zhang and H.X. Zhu, *Rethinking jets with energy correlators: Tracks, resummation, and analytic continuation*, *Phys. Rev. D* **102** (2020) 054012 [[2004.11381](#)].
- [396] J. Holguin, I. Moult, A. Pathak and M. Procura, *A New Paradigm for Precision Top Physics: Weighing the Top with Energy Correlators*, [2201.08393](#).
- [397] P.T. Komiske, I. Moult, J. Thaler and H.X. Zhu, *Analyzing N -point Energy Correlators Inside Jets with CMS Open Data*, [2201.07800](#).
- [398] M. Kologlu, P. Kravchuk, D. Simmons-Duffin and A. Zhiboedov, *The light-ray OPE and conformal colliders*, *JHEP* **01** (2021) 128 [[1905.01311](#)].
- [399] A.H. Hoang, S. Mantry, A. Pathak and I.W. Stewart, *Nonperturbative Corrections to Soft Drop Jet Mass*, *JHEP* **12** (2019) 002 [[1906.11843](#)].

- [400] L.J. Dixon, I. Moult and H.X. Zhu, *Collinear limit of the energy-energy correlator*, *Phys. Rev. D* **100** (2019) 014009 [[1905.01310](#)].
- [401] J. Aparisi et al., *Snowmass White Paper: prospects for measurements of the bottom quark mass*, [2203.16994](#).
- [402] J. Gao, Y. Gong, W.-L. Ju and L.L. Yang, *Thrust distribution in Higgs decays at the next-to-leading order and beyond*, *JHEP* **03** (2019) 030 [[1901.02253](#)].
- [403] J. Mo, F.J. Tackmann and W.J. Waalewijn, *A case study of quark-gluon discrimination at NNLL' in comparison to parton showers*, *Eur. Phys. J. C* **77** (2017) 770 [[1708.00867](#)].
- [404] J. Gao, *Probing light-quark Yukawa couplings via hadronic event shapes at lepton colliders*, *JHEP* **01** (2018) 038 [[1608.01746](#)].
- [405] H.-M. Chang, M. Procura, J. Thaler and W.J. Waalewijn, *Calculating Track-Based Observables for the LHC*, *Phys. Rev. Lett.* **111** (2013) 102002 [[1303.6637](#)].
- [406] H.-M. Chang, M. Procura, J. Thaler and W.J. Waalewijn, *Calculating Track Thrust with Track Functions*, *Phys. Rev. D* **88** (2013) 034030 [[1306.6630](#)].
- [407] M. Jaarsma, Y. Li, I. Moult, W. Waalewijn and H.X. Zhu, *Renormalization Group Flows for Track Function Moments*, [2201.05166](#).
- [408] Y. Li, I. Moult, S.S. van Velzen, W.J. Waalewijn and H.X. Zhu, *Extending Precision Perturbative QCD with Track Functions*, [2108.01674](#).
- [409] V.S. Fadin, E. Kuraev and L. Lipatov, *On the Pomeron Singularity in Asymptotically Free Theories*, *Phys. Lett. B* **60** (1975) 50.
- [410] E.A. Kuraev, L.N. Lipatov and V.S. Fadin, *Multi - Reggeon Processes in the Yang-Mills Theory*, *Sov. Phys. JETP* **44** (1976) 443.
- [411] E. Kuraev, L. Lipatov and V.S. Fadin, *The Pomeron Singularity in Nonabelian Gauge Theories*, *Sov. Phys. JETP* **45** (1977) 199.
- [412] I. Balitsky and L. Lipatov, *The Pomeron Singularity in Quantum Chromodynamics*, *Sov. J. Nucl. Phys.* **28** (1978) 822.
- [413] F.G. Celiberto, *Hunting BFKL in semi-hard reactions at the LHC*, *Eur. Phys. J. C* **81** (2021) 691 [[2008.07378](#)].
- [414] S.J. Brodsky, V.S. Fadin, V.T. Kim, L.N. Lipatov and G.B. Pivovarov, *The QCD pomeron with optimal renormalization*, *JETP Lett.* **70** (1999) 155 [[hep-ph/9901229](#)].
- [415] S.J. Brodsky, V.S. Fadin, V.T. Kim, L.N. Lipatov and G.B. Pivovarov, *High-energy QCD asymptotics of photon-photon collisions*, *JETP Lett.* **76** (2002) 249 [[hep-ph/0207297](#)].
- [416] F. Caporale, D.Y. Ivanov and A. Papa, *BFKL resummation effects in the $\gamma^* \gamma^*$ total hadronic cross section*, *Eur. Phys. J. C* **58** (2008) 1 [[0807.3231](#)].

- [417] X.-C. Zheng, X.-G. Wu, S.-Q. Wang, J.-M. Shen and Q.-L. Zhang, *Reanalysis of the BFKL Pomeron at the next-to-leading logarithmic accuracy*, *JHEP* **10** (2013) 117 [[1308.2381](#)].
- [418] G.A. Chirilli and Y.V. Kovchegov, $\gamma^*\gamma^*$ Cross Section at NLO and Properties of the BFKL Evolution at Higher Orders, *JHEP* **05** (2014) 099 [[1403.3384](#)].
- [419] D.Y. Ivanov, B. Murdaca and A. Papa, *The $\gamma^*\gamma^*$ total cross section in next-to-leading order BFKL and LEP2 data*, *JHEP* **10** (2014) 058 [[1407.8447](#)].
- [420] D.Y. Ivanov and A. Papa, *Electroproduction of two light vector mesons in the next-to-leading approximation*, *Nucl. Phys. B* **732** (2006) 183 [[hep-ph/0508162](#)].
- [421] D.Y. Ivanov and A. Papa, *Electroproduction of two light vector mesons in next-to-leading BFKL: Study of systematic effects*, *Eur. Phys. J. C* **49** (2007) 947 [[hep-ph/0610042](#)].
- [422] R. Enberg, B. Pire, L. Szymanowski and S. Wallon, *BFKL resummation effects in $\gamma^*\gamma^* \rightarrow \rho\rho$* , *Eur. Phys. J. C* **45** (2006) 759 [[hep-ph/0508134](#)].
- [423] J. Kwiecinski and L. Motyka, *Diffraction J/ψ production in high-energy $\gamma\gamma$ collisions as a probe of the QCD pomeron*, *Phys. Lett. B* **438** (1998) 203 [[hep-ph/9806260](#)].
- [424] F.G. Celiberto, D.Y. Ivanov, B. Murdaca and A. Papa, *High-energy resummation in heavy-quark pair photoproduction*, *Phys. Lett. B* **777** (2018) 141 [[1709.10032](#)].
- [425] A.D. Bolognino, A. Szczurek and W. Schäfer, *Exclusive production of ϕ meson in the $\gamma^*p \rightarrow \phi p$ reaction at large photon virtualities within k_T -factorization approach*, *Phys. Rev. D* **101** (2020) 054041 [[1912.06507](#)].
- [426] A.D. Bolognino, F.G. Celiberto, M. Fucilla, D.Y. Ivanov, B. Murdaca and A. Papa, *Inclusive production of two rapidity-separated heavy quarks as a probe of BFKL dynamics*, *PoS DIS2019* (2019) 067 [[1906.05940](#)].
- [427] ALEPH, DELPHI, L3, OPAL, SLD, LEP ELECTROWEAK WORKING GROUP, SLD ELECTROWEAK GROUP, SLD HEAVY FLAVOUR GROUP collaboration, *Precision electroweak measurements on the Z resonance*, *Phys. Rept.* **427** (2006) 257 [[hep-ex/0509008](#)].
- [428] LCC PHYSICS WORKING GROUP collaboration, *Tests of the Standard Model at the International Linear Collider*, [1908.11299](#).
- [429] ALEPH collaboration, *Determination of the LEP center-of-mass energy from Z gamma events: Preliminary*, in *29th International Conference on High-Energy Physics*, 10, 1998 [[hep-ex/9810047](#)].
- [430] T. Ueno, “A simulation study on measurement of the polarisation asymmetry using the initial state radiation at the ilc with center-of-mass energy of 250 gev.” Tohoku University Masters Thesis, 2019.

- [431] T. Mizuno, “Full simulation studies of photon and jet energy scale calibration and precise measurement of left-right asymmetry using $e^+e^- \rightarrow \gamma z$ process at the ilc.” Sokendai PhD Thesis, 2022.
- [432] T. Mizuno, K. Fujii and J. Tian, *Measurement of A_{LR} using radiative return at ILC 250*, in *2022 Snowmass Summer Study*, 3, 2022 [[2203.07944](#)].
- [433] P.C. Rowson, D. Su and S. Willocq, *Highlights of the SLD physics program at the SLAC linear collider*, *Ann. Rev. Nucl. Part. Sci.* **51** (2001) 345 [[hep-ph/0110168](#)].
- [434] S. Bilokin, R. Pöschl and F. Richard, *Measurement of b quark EW couplings at ILC*, [1709.04289](#).
- [435] S. Bilokin, R. Pöschl and F. Richard, *Measurement of c quark EW couplings at ILC*.
- [436] D. Jeans and K. Yumino, *ILD benchmark: a study of $e^-e^+ \rightarrow \tau^-\tau^+$ at 500 GeV*, [1912.08403](#).
- [437] Y. Deguchi, H. Yamashiro, T. Suehara, T. Yoshioka, K. Fujii and K. Kawagoe, *Study of fermion pair events at the 250 GeV ILC*, in *International Workshop on Future Linear Colliders*, 2, 2019 [[1902.05245](#)].
- [438] D.M. Asner et al., *ILC Higgs White Paper*, in *Community Summer Study 2013: Snowmass on the Mississippi*, 10, 2013 [[1310.0763](#)].
- [439] PARTICLE DATA GROUP collaboration, *Review of Particle Physics*, *PTEP* **2020** (2020) [083C01](#).
- [440] A. Djouadi, G. Moreau and F. Richard, *Resolving the $A(FB)^{*}b$ puzzle in an extra dimensional model with an extended gauge structure*, *Nucl.Phys.* **B773** (2007) 43 [[hep-ph/0610173](#)].
- [441] G. Moortgat-Pick, T. Abe, G. Alexander, B. Ananthanarayan, A. Babich et al., *The Role of polarized positrons and electrons in revealing fundamental interactions at the linear collider*, *Phys.Rept.* **460** (2008) 131 [[hep-ph/0507011](#)].
- [442] C.R. Schmidt, *Top quark production and decay at next-to-leading order in e^+e^- annihilation*, *Phys.Rev.* **D54** (1996) 3250 [[hep-ph/9504434](#)].
- [443] R. Hawkings and K. Monig, *Electroweak and CP violation physics at a linear collider Z factory*, *Eur. Phys. J. direct* **1** (1999) 8 [[hep-ex/9910022](#)].
- [444] A. Irlles, “Quark Pair Production at Lepton Colliders: Experimental challenges.”
- [445] M. Baak et al., *Working Group Report: Precision Study of Electroweak Interactions*, in *Community Summer Study 2013: Snowmass on the Mississippi*, 10, 2013 [[1310.6708](#)].
- [446] D0 collaboration, *Measurement of the W Boson Mass with the D0 Detector*, *Phys. Rev. Lett.* **108** (2012) 151804 [[1203.0293](#)].

- [447] ATLAS collaboration, *Measurement of the W -boson mass in pp collisions at $\sqrt{s} = 7$ TeV with the ATLAS detector*, *Eur. Phys. J. C* **78** (2018) 110 [1701.07240].
- [448] CDF collaboration, *High-precision measurement of the W boson mass with the CDF II detector*, *Science* **376** (2022) 170.
- [449] J. Anguiano, *Study of $WW \rightarrow q\bar{q}\ell\nu$ at ILC500 with ILD*, in *International Workshop on Future Linear Colliders*, 11, 2020 [2011.12451].
- [450] K. Hagiwara, R.D. Peccei, D. Zeppenfeld and K. Hikasa, *Probing the Weak Boson Sector in $e^+e^- \rightarrow W^+W^-$* , *Nucl. Phys. B* **282** (1987) 253.
- [451] OPAL collaboration, *Measurement of the mass of the W boson in e^+e^- collisions using the fully leptonic channel*, *Eur. Phys. J. C* **26** (2003) 321 [hep-ex/0203026].
- [452] G.W. Wilson, *Updated Study of a Precision Measurement of the W Mass from a Threshold Scan Using Polarized e^- and e^+ at ILC*, in *International Workshop on Future Linear Colliders*, 3, 2016 [1603.06016].
- [453] Z. Kunszt et al., *Determination of the mass of the W boson*, in *CERN Workshop on LEP2 Physics (followed by 2nd meeting, 15-16 Jun 1995 and 3rd meeting 2-3 Nov 1995)*, 2, 1996 [hep-ph/9602352].
- [454] W.J. Stirling, *The Measurement of m_W from the W^+W^- threshold cross-section at LEP-2*, *Nucl. Phys. B* **456** (1995) 3 [hep-ph/9503320].
- [455] G.W. Wilson, “Exploring W Boson Measurements at ILC250.” Presentation at LCWS 2019, Sendai, Japan, Oct 28–Nov 1, 2019, <https://agenda.linearcollider.org/event/8217/>.
- [456] G.W. Wilson, “Energy calibration and luminosity spectrum using dimuons for precision electroweak measurements at ILC.” Presentation at the ILC IDT-WG3 Physics Open Meeting Seminar, Dec. 16, 2021, <https://agenda.linearcollider.org/event/9352/>.
- [457] G.W. Wilson, “In situ measurements of ILC beam/center-of-mass energy.” Presentation at the ILC MDI-BDS/Physics Topical Meeting, Jan. 13, 2022, <https://agenda.linearcollider.org/event/9401/>.
- [458] ALEPH collaboration, *Measurement of W -pair production in e^+e^- collisions at centre-of-mass energies from 183-GeV to 209-GeV*, *Eur. Phys. J. C* **38** (2004) 147.
- [459] DELPHI collaboration, *Measurement of the W pair production cross-section and W branching ratios in e^+e^- collisions at $\sqrt{s} = 161$ -GeV to 209-GeV*, *Eur. Phys. J. C* **34** (2004) 127 [hep-ex/0403042].
- [460] L3 collaboration, *Measurement of the cross section of W -boson pair production at LEP*, *Phys. Lett. B* **600** (2004) 22 [hep-ex/0409016].
- [461] OPAL collaboration, *Measurement of the $e^+e^- \rightarrow W^+W^-$ cross section and W decay branching fractions at LEP*, *Eur. Phys. J. C* **52** (2007) 767 [0708.1311].

- [462] The ATLAS Collaboration, *Measurement of the top quark mass in the $t\bar{t} \rightarrow \text{lepton+jets}$ channel from $\sqrt{s} = 8$ TeV ATLAS data and combination with previous results*, *Eur. Phys. J. C* **79** (2019) 290 [[1810.01772](#)].
- [463] ATLAS, CDF, CMS, D0 collaboration, *First combination of Tevatron and LHC measurements of the top-quark mass*, [1403.4427](#).
- [464] TEVATRON ELECTOWEAK WORKING GROUP (CDF AND D0 COLLABORATIONS) collaboration, *Combination of CDF and D0 results on the mass of the top quark using up 9.7 fb^{-1} at the Tevatron*, [1608.01881](#).
- [465] PARTICLE DATA GROUP collaboration, *Review of Particle Physics*, *PTEP* **2020** (2020) [083C01](#).
- [466] ATLAS collaboration, *Measurement of the top-quark mass in $t\bar{t} + 1\text{-jet}$ events collected with the ATLAS detector in pp collisions at $\sqrt{s} = 8$ TeV*, *JHEP* **11** (2019) 150 [[1905.02302](#)].
- [467] T. Ježo, J.M. Lindert, P. Nason, C. Oleari and S. Pozzorini, *An NLO+PS generator for $t\bar{t}$ and Wt production and decay including non-resonant and interference effects*, *Eur. Phys. J. C* **76** (2016) 691 [[1607.04538](#)].
- [468] S. Ferrario Ravasio, T. Ježo, P. Nason and C. Oleari, *A theoretical study of top-mass measurements at the LHC using NLO+PS generators of increasing accuracy*, *Eur. Phys. J. C* **78** (2018) 458 [[1906.09166](#)].
- [469] The ATLAS collaboration, *A precise interpretation for the top quark mass parameter in ATLAS Monte Carlo simulation*, *ATL-PHYS-PUB-2021-034* .
- [470] M. Butenschoen, B. Dehnadi, A.H. Hoang, V. Mateu, M. Preisser and I.W. Stewart, *Top Quark Mass Calibration for Monte Carlo Event Generators*, [1608.01318](#).
- [471] J. Kieseler, K. Lipka and S.-O. Moch, *Calibration of the Top-Quark Monte Carlo Mass*, *Phys. Rev. Lett.* **116** (2016) 162001 [[1511.00841](#)].
- [472] A.H. Hoang, *What is the Top Quark Mass?*, *Ann. Rev. Nucl. Part. Sci.* **70** (2020) 225 [[2004.12915](#)].
- [473] P. Marquard, A.V. Smirnov, V.A. Smirnov and M. Steinhauser, *Quark Mass Relations to Four-Loop Order in Perturbative QCD*, *Phys. Rev. Lett.* **114** (2015) 142002 [[1502.01030](#)].
- [474] S. Gusken, J.H. Kuhn and P.M. Zerwas, *Threshold Behavior of Top Production in e^+e^- Annihilation*, *Phys. Lett.* **B155** (1985) 185.
- [475] V.S. Fadin and V.A. Khoze, *Threshold Behavior of Heavy Top Production in e^+e^- Collisions*, *JETP Lett.* **46** (1987) 525.
- [476] V.S. Fadin and V.A. Khoze, *Production of a pair of heavy quarks in e^+e^- annihilation in the threshold region*, *Sov. J. Nucl. Phys.* **48** (1988) 309.

- [477] M.J. Strassler and M.E. Peskin, *The Heavy top quark threshold: QCD and the Higgs*, *Phys. Rev. D* **43** (1991) 1500.
- [478] M. Beneke, Y. Kiyo, P. Marquard, A. Penin, J. Piclum and M. Steinhauser, *Next-to-Next-to-Next-to-Leading Order QCD Prediction for the Top Antitop S-Wave Pair Production Cross Section Near Threshold in e^+e^- Annihilation*, *Phys. Rev. Lett.* **115** (2015) 192001 [[1506.06864](#)].
- [479] A.H. Hoang, A.V. Manohar, I.W. Stewart and T. Teubner, *The Threshold $t\bar{t}$ cross-section at NNLL order*, *Phys. Rev.* **D65** (2002) 014014 [[hep-ph/0107144](#)].
- [480] CLICDP collaboration, *Top-Quark Physics at the CLIC Electron-Positron Linear Collider*, *JHEP* **11** (2019) 003 [[1807.02441](#)].
- [481] K. Seidel, F. Simon, M. Tesar and S.p. Poss, *Top quark mass measurements at and above threshold at CLIC*, *Eur. Phys. J.* **C73** (2013) 2530 [[1303.3758](#)].
- [482] T. Horiguchi, A. Ishikawa, T. Suehara, K. Fujii, Y. Sumino, Y. Kiyo et al., *Study of top quark pair production near threshold at the ILC*, [1310.0563](#).
- [483] M. Martinez and R. Miquel, *Multiparameter fits to the $t\bar{t}$ threshold observables at a future e^+e^- linear collider*, *Eur. Phys. J.* **C27** (2003) 49 [[hep-ph/0207315](#)].
- [484] F. Simon, *A First Look at the Impact of NNNLO Theory Uncertainties on Top Mass Measurements at the ILC*, in *International Workshop on Future Linear Colliders (LCWS15) Whistler, B.C., Canada, November 2-6, 2015*, 2016, <https://inspirehep.net/record/1427722/files/arXiv:1603.04764.pdf> [[1603.04764](#)].
- [485] M. Vos et al., *Top physics at high-energy lepton colliders*, [1604.08122](#).
- [486] F. Simon, *Scanning Strategies at the Top Threshold at ILC*, in *International Workshop on Future Linear Colliders*, 2, 2019 [[1902.07246](#)].
- [487] K. Nowak and A.F. Zarnecki, *Optimising top-quark threshold scan at CLIC using genetic algorithm*, *JHEP* **07** (2021) 070 [[2103.00522](#)].
- [488] M. Boronat, E. Fullana, J. Fuster, P. Gomis, A. Hoang, V. Mateu et al., *Top quark mass measurement in radiative events at electron-positron colliders*, *Phys. Lett. B* **804** (2020) 135353 [[1912.01275](#)].
- [489] B. Bachu, A.H. Hoang, V. Mateu, A. Pathak and I.W. Stewart, *Boosted top quarks in the peak region with NL3L resummation*, *Phys. Rev. D* **104** (2021) 014026 [[2012.12304](#)].
- [490] F. Richard, *Present and future constraints on top EW couplings*, [1403.2893](#).
- [491] C.F. Berger, M. Perelstein and F. Petriello, *Top quark properties in little Higgs models*, in *2005 International Linear Collider Physics and Detector Workshop and 2nd ILC Accelerator Workshop*, 12, 2005 [[hep-ph/0512053](#)].

- [492] C. Grojean, O. Matsedonskyi and G. Panico, *Light top partners and precision physics*, *JHEP* **10** (2013) 160 [[1306.4655](#)].
- [493] G. Durieux and O. Matsedonskyi, *The top-quark window on compositeness at future lepton colliders*, *JHEP* **01** (2019) 072 [[1807.10273](#)].
- [494] V. Miralles, M.M. López, M.M. Llácer, A. Peñuelas, M. Perelló and M. Vos, *The top quark electro-weak couplings after LHC Run 2*, [2107.13917](#).
- [495] T. Martini and M. Schulze, *Electroweak loops as a probe of new physics in $t\bar{t}$ production at the LHC*, *JHEP* **04** (2020) 017 [[1911.11244](#)].
- [496] G. Durieux *et al.* *Snowmass White Paper: prospects for the measurement of top-quark couplings*, [[2205.02140](#)].
- [497] G. Durieux, A. Irlles, V. Miralles, A. Peñuelas, R. Pöschl, M. Perelló *et al.*, *The electro-weak couplings of the top and bottom quarks – Global fit and future prospects*, *JHEP* **12** (2019) 98 [[1907.10619](#)].
- [498] M. Cepeda *et al.*, *Report from Working Group 2: Higgs Physics at the HL-LHC and HE-LHC*, *CERN Yellow Rep. Monogr.* **7** (2019) 221 [[1902.00134](#)].
- [499] M.S. Amjad *et al.*, *A precise characterisation of the top quark electroweak vertices at the ILC*, *Eur. Phys. J. C* **75** (2015) 512 [[1505.06020](#)].
- [500] M.S. Amjad, M. Boronat, T. Frisson, I. Garcia, R. Poschl, E. Ros *et al.*, *A precise determination of top quark electroweak couplings at the ILC operating at $\sqrt{s} = 500$ GeV*, [1307.8102](#).
- [501] G. Durieux, M. Perelló, M. Vos and C. Zhang, *Global and optimal probes for the top-quark effective field theory at future lepton colliders*, *JHEP* **10** (2018) 168 [[1807.02121](#)].
- [502] W. Bernreuther, L. Chen, I. García, M. Perelló, R. Poeschl, F. Richard *et al.*, *CP-violating top quark couplings at future linear e^+e^- colliders*, *Eur. Phys. J. C* **78** (2018) 155 [[1710.06737](#)].
- [503] G. Durieux, J. Gu, E. Vryonidou and C. Zhang, *Probing top-quark couplings indirectly at Higgs factories*, *Chin. Phys. C* **42** (2018) 123107 [[1809.03520](#)].
- [504] S. Jung, J. Lee, M. Perelló, J. Tian and M. Vos, *Higgs, top and electro-weak precision measurements at future e^+e^- colliders; a combined effective field theory analysis with renormalization mixing*, [2006.14631](#).
- [505] The ATLAS collaboration, *Sensitivity of searches for the flavour-changing neutral current decay $t \rightarrow qZ$ using the upgraded ATLAS experiment at the High Luminosity LHC*, *ATL-PHYS-PUB-2019-001* .
- [506] ATLAS COLLABORATION collaboration, *Expected sensitivity of ATLAS to FCNC top quark decays $t \rightarrow Zu$ and $t \rightarrow Hq$ at the High Luminosity LHC*, *ATL-PHYS-PUB-2016-019* .

- [507] G. Durieux, F. Maltoni and C. Zhang, *Global approach to top-quark flavor-changing interactions*, *Phys. Rev. D* **91** (2015) 074017 [[1412.7166](#)].
- [508] L. Shi and C. Zhang, *Probing the top quark flavor-changing couplings at CEPC*, *Chin. Phys. C* **43** (2019) 113104 [[1906.04573](#)].
- [509] J. de Blas et al., *The CLIC Potential for New Physics*, [1812.02093](#).
- [510] H. Hesari, H. Khanpour, M. Khatiri Yanehsari and M. Mohammadi Najafabadi, *Probing the Top Quark Flavour-Changing Neutral Current at a Future Electron-Positron Collider*, *Adv. High Energy Phys.* **2014** (2014) 476490 [[1412.8572](#)].
- [511] J.A. Aguilar-Saavedra and T. Riemann, *Probing top flavor changing neutral couplings at TESLA*, in *2nd Workshop of the 2nd Joint ECFA / DESY Study on Physics and Detectors for a Linear Electron Positron Collider*, pp. 2428–2450, 2, 2001 [[hep-ph/0102197](#)].
- [512] C.F. Dürig, *Measuring the Higgs Self-coupling at the International Linear Collider*, Ph.D. thesis, Hamburg U., Hamburg, 2016. 10.3204/PUBDB-2016-04283.
- [513] J. Tian, *Study of Higgs self-coupling at the ILC based on the full detector simulation at $\sqrt{s} = 500$ GeV and $\sqrt{s} = 1$ TeV*, in *LC Notes*, LC-REP-2013-003, <https://fkc.desy.de/lcnotes/noteslist/>.
- [514] T. Barklow, K. Fujii, S. Jung, M.E. Peskin and J. Tian, *Model-Independent Determination of the Triple Higgs Coupling at e^+e^- Colliders*, *Phys. Rev. D* **97** (2018) 053004 [[1708.09079](#)].
- [515] Y. Radkhorrani and J. List, *Kinematic Fitting for Particle Flow Detectors at Future Higgs Factories*, in *Particles and Nuclei International Conference*, 11, 2021 [[2111.14775](#)].
- [516] K. Goto, T. Suehara, T. Yoshioka, M. Kurata, H. Nagahara, Y. Nakashima et al., *Development of a Vertex Finding Algorithm using Recurrent Neural Network*, [2101.11906](#).
- [517] U. Einhaus, *Charged Hadron Identification with dE/dx and Time-of-Flight at Future Higgs Factories*, in *Particles and Nuclei International Conference*, 12, 2021 [[2112.10009](#)].
- [518] F. Arco, S. Heinemeyer and M.J. Herrero, *Exploring sizable triple Higgs couplings in the 2HDM*, *Eur. Phys. J. C* **80** (2020) 884 [[2005.10576](#)].
- [519] F. Arco, S. Heinemeyer and M.J. Herrero, *Sensitivity to triple Higgs couplings via di-Higgs production in the 2HDM at e^+e^- colliders*, *Eur. Phys. J. C* **81** (2021) 913 [[2106.11105](#)].
- [520] H. Bahl, J. Braathen and G. Weiglein, *New constraints on extended Higgs sectors from the trilinear Higgs coupling*, [2202.03453](#).
- [521] D.E. Morrissey and M.J. Ramsey-Musolf, *Electroweak baryogenesis*, *New J. Phys.* **14** (2012) 125003 [[1206.2942](#)].
- [522] ATLAS collaboration, *Measurement prospects of the pair production and self-coupling of the Higgs boson with the ATLAS experiment at the HL-LHC*, .

- [523] ATLAS collaboration, *Observation of Higgs boson production in association with a top quark pair at the LHC with the ATLAS detector*, *Phys. Lett. B* **784** (2018) 173 [[1806.00425](#)].
- [524] CMS collaboration, *Observation of $t\bar{t}H$ production*, *Phys. Rev. Lett.* **120** (2018) 231801 [[1804.02610](#)].
- [525] R. Yonamine, K. Ikematsu, T. Tanabe, K. Fujii, Y. Kiyo, Y. Sumino et al., *Measuring the top Yukawa coupling at the ILC at $\sqrt{s} = 500$ GeV*, *Phys. Rev. D* **84** (2011) 014033 [[1104.5132](#)].
- [526] H. Abramowicz et al., *Higgs physics at the CLIC electron-positron linear collider*, *Eur. Phys. J. C* **77** (2017) 475 [[1608.07538](#)].
- [527] T. Price, P. Roloff, J. Strube and T. Tanabe, *Full simulation study of the top Yukawa coupling at the ILC at $\sqrt{s} = 1$ TeV*, *Eur. Phys. J. C* **75** (2015) 309 [[1409.7157](#)].
- [528] T. Han, T. Huang, Z.H. Lin, J.X. Wang and X. Zhang, *$e^+e^- \rightarrow t$ anti- t H with nonstandard Higgs boson couplings*, *Phys. Rev. D* **61** (2000) 015006 [[hep-ph/9908236](#)].
- [529] R.M. Godbole, C. Hangst, M. Muhlleitner, S.D. Rindani and P. Sharma, *Model-independent analysis of Higgs spin and CP properties in the process $e^+e^- \rightarrow t\bar{t}\Phi$* , *Eur. Phys. J. C* **71** (2011) 1681 [[1103.5404](#)].
- [530] A. Rosca, *Measurement of the charged triple gauge boson couplings at the ILC*, *Nucl. Part. Phys. Proc.* **273-275** (2016) 2226.
- [531] T. Barklow, private communication to J. List, 2018.
- [532] K. Yumino and D. Jeans, *Measuring the tau polarization at ILC*, in *2022 Snowmass Summer Study*, 3, 2022 [[2203.07668](#)].
- [533] T. Suehara, *Two-fermion final states at International Linear Collider*, in *2022 Snowmass Summer Study*, 3, 2022 [[2203.07272](#)].
- [534] L. Randall and R. Sundrum, *A Large mass hierarchy from a small extra dimension*, *Phys. Rev. Lett.* **83** (1999) 3370 [[hep-ph/9905221](#)].
- [535] S. Funatsu, H. Hatanaka, Y. Hosotani, Y. Orikasa and N. Yamatsu, *Fermion pair production at e^-e^+ linear collider experiments in GUT inspired gauge-Higgs unification*, *Phys. Rev. D* **102** (2020) 015029 [[2006.02157](#)].
- [536] J. Yoon and M.E. Peskin, *Fermion Pair Production in $SO(5) \times U(1)$ Gauge-Higgs Unification Models*, [1811.07877](#).
- [537] S. Funatsu, H. Hatanaka, Y. Hosotani and Y. Orikasa, *Distinct signals of the gauge-Higgs unification in e^+e^- collider experiments*, *Phys. Lett.* **B775** (2017) 297 [[1705.05282](#)].
- [538] S. Matsumoto, S. Shirai and M. Takeuchi, *Indirect Probe of Electroweakly Interacting Particles at the High-Luminosity Large Hadron Collider*, *JHEP* **06** (2018) 049 [[1711.05449](#)].

- [539] K. Harigaya, K. Ichikawa, A. Kundu, S. Matsumoto and S. Shirai, *Indirect Probe of Electroweak-Interacting Particles at Future Lepton Colliders*, *JHEP* **09** (2015) 105 [[1504.03402](#)].
- [540] K. Fujii et al., *The Potential of the ILC for Discovering New Particles*, [1702.05333](#).
- [541] M. Berggren, *What pp SUSY limits mean for future e^+e^- colliders*, in *International Workshop on Future Linear Colliders*, 3, 2020 [[2003.12391](#)].
- [542] G. Karagiorgi, G. Kasieczka, S. Kravitz, B. Nachman and D. Shih, *Machine Learning in the Search for New Fundamental Physics*, [2112.03769](#).
- [543] J. Gonski, J. Lai, B. Nachman and I. Ochoa, *High-dimensional Anomaly Detection with Radiative Return in e^+e^- Collisions*, [2108.13451](#).
- [544] Y.A. Golfand and E.P. Likhtman, *Extension of the Algebra of Poincare Group Generators and Violation of p Invariance*, *JETP Lett.* **13** (1971) 323.
- [545] D.V. Volkov and V.P. Akulov, *Is the Neutrino a Goldstone Particle?*, *Phys. Lett. B* **46** (1973) 109.
- [546] J. Wess and B. Zumino, *Supergauge Transformations in Four-Dimensions*, *Nucl. Phys.* **B70** (1974) 39.
- [547] H.P. Nilles, *Supersymmetry, Supergravity and Particle Physics*, *Phys. Rept.* **110** (1984) 1.
- [548] H.E. Haber and G.L. Kane, *The Search for Supersymmetry: Probing Physics Beyond the Standard Model*, *Phys. Rept.* **117** (1985) 75.
- [549] R. Barbieri, S. Ferrara and C.A. Savoy, *Gauge Models with Spontaneously Broken Local Supersymmetry*, *Phys. Lett.* **119B** (1982) 343.
- [550] MUON G-2 collaboration, *Measurement of the Positive Muon Anomalous Magnetic Moment to 0.46 ppm*, *Phys. Rev. Lett.* **126** (2021) 141801 [[2104.03281](#)].
- [551] E. Bagnaschi et al., *Likelihood Analysis of the pMSSM11 in Light of LHC 13-TeV Data*, *Eur. Phys. J.* **C78** (2018) 256 [[1710.11091](#)].
- [552] M. Chakraborti, S. Heinemeyer and I. Saha, *Improved $(g - 2)_\mu$ Measurements and Supersymmetry*, *Eur. Phys. J. C* **80** (2020) 984 [[2006.15157](#)].
- [553] H. Baer and X. Tata, *Weak scale supersymmetry: From superfields to scattering events*, Cambridge University Press (5, 2006).
- [554] D.P. Roy, *SUSY Search in Future Collider and Dark Matter Experiments*, *AIP Conf. Proc.* **939** (2007) 63 [[0707.1949](#)].
- [555] LEP SUSY WORKING GROUP, ALEPH, DELPHI, L3 AND OPAL COLLABORATIONS collaboration, *Combined lep chargino results, up to 208 gev for large m_0* , Tech. Rep. [LEPSUSYWG/01-03.1](#).

- [556] ALEPH collaboration, *Search for scalar leptons in e^+e^- collisions at center-of-mass energies up to 209-GeV*, *Phys. Lett.* **B526** (2002) 206 [[hep-ex/0112011](#)].
- [557] ALEPH collaboration, *Absolute mass lower limit for the lightest neutralino of the MSSM from e^+e^- data at $s^{*(1/2)}$ up to 209-GeV*, *Phys. Lett.* **B583** (2004) 247.
- [558] ALEPH collaboration, *Search for charginos nearly mass degenerate with the lightest neutralino in e^+e^- collisions at center-of-mass energies up to 209-GeV*, *Phys. Lett.* **B533** (2002) 223 [[hep-ex/0203020](#)].
- [559] L3 collaboration, *Search for scalar leptons and scalar quarks at LEP*, *Phys. Lett.* **B580** (2004) 37 [[hep-ex/0310007](#)].
- [560] OPAL collaboration, *Search for anomalous production of dilepton events with missing transverse momentum in e^+e^- collisions at $s^{*(1/2)} = 183\text{-GeV}$ to 209-GeV*, *Eur. Phys. J.* **C32** (2004) 453 [[hep-ex/0309014](#)].
- [561] M.T. Núñez Pardo de Vera, M. Berggren and J. List, *Chargino production at the ILC*, in *International Workshop on Future Linear Colliders*, 2, 2020 [[2002.01239](#)].
- [562] M.T. Núñez Pardo de Vera, M. Berggren and J. List, *$\tilde{\tau}$ searches at the ILC*, in *International Workshop on Future Linear Colliders*, 5, 2021 [[2105.08616](#)].
- [563] M.T. Núñez Pardo de Vera, M. Berggren and J. List, *Evaluating the ILC SUSY reach in the most challenging scenario: $\tilde{\tau}$ NLSP, low ΔM , lowest cross-section*, in *2022 Snowmass Summer Study*, 3, 2022 [[2203.15729](#)].
- [564] ATLAS collaboration, *Search for electroweak production of supersymmetric particles in final states with two or three leptons at $\sqrt{s} = 13\text{ TeV}$ with the ATLAS detector*, *Eur. Phys. J. C* **78** (2018) 995 [[1803.02762](#)].
- [565] ATLAS collaboration, *Searches for electroweak production of supersymmetric particles with compressed mass spectra in $\sqrt{s} = 13\text{ TeV}$ pp collisions with the ATLAS detector*, *Phys. Rev. D* **101** (2020) 052005 [[1911.12606](#)].
- [566] ATLAS collaboration, *Search for chargino–neutralino pair production in final states with three leptons and missing transverse momentum in $\sqrt{s} = 13\text{ TeV}$ pp collisions with the ATLAS detector*, *Eur. Phys. J. C* **81** (2021) 1118 [[2106.01676](#)].
- [567] ATLAS COLLABORATION collaboration, *Prospects for searches for staus, charginos and neutralinos at the high luminosity LHC with the ATLAS Detector*, Tech. Rep. [ATL-PHYS-PUB-2018-048](#), CERN, Geneva (Dec, 2018).
- [568] LEP SUSY WORKING GROUP, ALEPH, DELPHI, L3 AND OPAL COLLABORATIONS collaboration, *Combined lep chargino results, up to 208 gev for low dm* , Tech. Rep. [LEPSUSYWG/02-04.1](#).
- [569] M. Berggren, A. Cakir, D. Krücker, J. List, I.A. Melzer-Pellmann, B. Safarzadeh Samani et al., *Non-simplified SUSY: $\tilde{\tau}$ -coannihilation at LHC and ILC*, *Eur. Phys. J.* **C76** (2016) 183 [[1508.04383](#)].

- [570] H. Baer, M. Berggren, K. Fujii, J. List, S.-L. Lehtinen, T. Tanabe et al., *The ILC as a natural SUSY discovery machine and precision microscope: from light higgsinos to tests of unification*, [1912.06643](#).
- [571] M. Berggren, F. Brümmer, J. List, G. Moortgat-Pick, T. Robens, K. Rolbiecki et al., *Tackling light higgsinos at the ILC*, *Eur. Phys. J. C* **73** (2013) 2660 [[1307.3566](#)].
- [572] A.F. Zarnecki, J. Kalinowski, J. Klamka, P. Sopicki, W. Kotlarski, T. Robens et al., *Inert Doublet Model Signatures at Future $e+e-$ Colliders*, *PoS ALPS2019* (2020) 010 [[1908.04659](#)].
- [573] D. Sokolowska, J. Kalinowski, J. Klamka, P. Sopicki, A.F. Zarnecki, W. Kotlarski et al., *Inert Doublet Model signatures at future e^+e^- colliders*, *PoS EPS-HEP2019* (2020) 570 [[1911.06254](#)].
- [574] Y. Wang, M. Berggren and J. List, *ILD Benchmark: Search for Extra Scalars Produced in Association with a Z boson at $\sqrt{s} = 500$ GeV*, [2005.06265](#).
- [575] M. Battaglia, *Charged Higgs Boson Physics at Future Linear Colliders*, *PoS CHARGED2010* (2010) 019 [[1102.1892](#)].
- [576] N.G. Deshpande and E. Ma, *Pattern of Symmetry Breaking with Two Higgs Doublets*, *Phys. Rev. D* **18** (1978) 2574.
- [577] Q.-H. Cao, E. Ma and G. Rajasekaran, *Observing the Dark Scalar Doublet and its Impact on the Standard-Model Higgs Boson at Colliders*, *Phys. Rev. D* **76** (2007) 095011 [[0708.2939](#)].
- [578] R. Barbieri, L.J. Hall and V.S. Rychkov, *Improved naturalness with a heavy Higgs: An Alternative road to LHC physics*, *Phys. Rev. D* **74** (2006) 015007 [[hep-ph/0603188](#)].
- [579] A. Ilnicka, M. Krawczyk and T. Robens, *Inert Doublet Model in light of LHC Run I and astrophysical data*, *Phys. Rev. D* **93** (2016) 055026 [[1508.01671](#)].
- [580] J. Kalinowski, W. Kotlarski, T. Robens, D. Sokolowska and A.F. Zarnecki, *Exploring Inert Scalars at CLIC*, *JHEP* **07** (2019) 053 [[1811.06952](#)].
- [581] J. Klamka and A.F. Zarnecki, *Pair-production of the charged IDM scalars at high energy CLIC*, *Eur. Phys. J. C* **82** (2022) 738 [[2201.07146](#)].
- [582] J. Kalinowski, T. Robens and A.F. Zarnecki, *New Physics with missing energy at future lepton colliders - Snowmass White Paper*, in *2022 Snowmass Summer Study*, 3, 2022 [[2203.07913](#)].
- [583] J. Kalinowski, W. Kotlarski, T. Robens, D. Sokolowska and A.F. Zarnecki, *Benchmarking the Inert Doublet Model for e^+e^- colliders*, *JHEP* **12** (2018) 081 [[1809.07712](#)].
- [584] J. Kalinowski, T. Robens, D. Sokolowska and A.F. Zarnecki, *IDM Benchmarks for the LHC and Future Colliders*, *Symmetry* **13** (2021) 991 [[2012.14818](#)].

- [585] T. Robens, *A short overview on low mass scalars at future lepton colliders - Snowmass White Paper*, in *2022 Snowmass Summer Study*, 3, 2022 [[2203.08210](#)].
- [586] T. Robens, *A Short Overview on Low Mass Scalars at Future Lepton Colliders*, *Universe* **8** (2022) 286 [[2205.09687](#)].
- [587] N. Kumar and V. Sahdev, *Alternative signatures of the quintuplet fermions at the LHC and future linear colliders*, [2112.09451](#).
- [588] M. Habermehl, *Dark Matter at the International Linear Collider*, dissertation, Universität Hamburg, Hamburg, 2018. <https://bib-pubdb1.desy.de/record/417605> .
- [589] J. Kalinowski, W. Kotlarski, K. Mekala, P. Sopicki and A.F. Zarnecki, *Sensitivity of future linear e^+e^- colliders to processes of dark matter production with light mediator exchange*, *Eur. Phys. J. C* **81** (2021) 955 [[2107.11194](#)].
- [590] DELPHI collaboration, *Photon events with missing energy in e^+e^- collisions at $s^{*(1/2)} = 130\text{-GeV}$ to 209-GeV* , *Eur. Phys. J.* **C38** (2005) 395 [[hep-ex/0406019](#)].
- [591] DELPHI collaboration, *Search for one large extra dimension with the DELPHI detector at LEP*, *Eur. Phys. J.* **C60** (2009) 17 [[0901.4486](#)].
- [592] P.J. Fox, R. Harnik, J. Kopp and Y. Tsai, *LEP Shines Light on Dark Matter*, *Phys. Rev.* **D84** (2011) 014028 [[1103.0240](#)].
- [593] C. Bartels, M. Berggren and J. List, *Characterising WIMPs at a future e^+e^- Linear Collider*, *Eur. Phys. J.* **C72** (2012) 2213 [[1206.6639](#)].
- [594] J. Kalinowski, W. Kotlarski, K. Mekala, K. Zembaczynski and A.F. Zarnecki, *New approach to DM searches with mono-photon signature*, in *2022 Snowmass Summer Study*, 3, 2022 [[2203.06776](#)].
- [595] J. Kalinowski, W. Kotlarski, P. Sopicki and A.F. Zarnecki, *Simulating hard photon production with WHIZARD*, *Eur. Phys. J. C* **80** (2020) 634 [[2004.14486](#)].
- [596] S. Baum, P. Sandick and P. Stengel, *Hunting for scalar lepton partners at future electron colliders*, *Phys. Rev. D* **102** (2020) 015026 [[2004.02834](#)].
- [597] S.-I. Horigome, T. Katayose, S. Matsumoto and I. Saha, *Leptophilic fermion WIMP: Role of future lepton colliders*, *Phys. Rev. D* **104** (2021) 055001 [[2102.08645](#)].
- [598] S. Weinberg, *Baryon and Lepton Nonconserving Processes*, *Phys. Rev. Lett.* **43** (1979) 1566.
- [599] R. Foot, H. Lew, X.G. He and G.C. Joshi, *Seesaw Neutrino Masses Induced by a Triplet of Leptons*, *Z. Phys. C* **44** (1989) 441.
- [600] E. Ma, *Pathways to naturally small neutrino masses*, *Phys. Rev. Lett.* **81** (1998) 1171 [[hep-ph/9805219](#)].
- [601] A. Abada, C. Biggio, F. Bonnet, M.B. Gavela and T. Hambye, *Low energy effects of neutrino masses*, *JHEP* **12** (2007) 061 [[0707.4058](#)].

- [602] A. Maiezza, M. Nemevšek and F. Nesti, *Lepton Number Violation in Higgs Decay at LHC*, *Phys. Rev. Lett.* **115** (2015) 081802 [[1503.06834](#)].
- [603] S. Antusch, O. Fischer, A. Hammad and C. Scherb, *Low scale type II seesaw: Present constraints and prospects for displaced vertex searches*, *JHEP* **02** (2019) 157 [[1811.03476](#)].
- [604] A. Das, S. Mandal and T. Modak, *Testing triplet fermions at the electron-positron and electron-proton colliders using fat jet signatures*, *Phys. Rev. D* **102** (2020) 033001 [[2005.02267](#)].
- [605] F. del Aguila, J. de Blas and M. Perez-Victoria, *Effects of new leptons in Electroweak Precision Data*, *Phys. Rev. D* **78** (2008) 013010 [[0803.4008](#)].
- [606] A. Das and S. Mandal, *Bounds on the triplet fermions in type-III seesaw and implications for collider searches*, *Nucl. Phys. B* **966** (2021) 115374 [[2006.04123](#)].
- [607] CMS collaboration, *Search for physics beyond the standard model in multilepton final states in proton-proton collisions at $\sqrt{s} = 13$ TeV*, *JHEP* **03** (2020) 051 [[1911.04968](#)].
- [608] ATLAS collaboration, *Search for type-III seesaw heavy leptons in dilepton final states in pp collisions at $\sqrt{s} = 13$ TeV with the ATLAS detector*, *Eur. Phys. J. C* **81** (2021) 218 [[2008.07949](#)].
- [609] G. Aad et al. [ATLAS], *Search for type-III seesaw heavy leptons in leptonic final states in pp collisions at $\sqrt{s} = 13$ TeV with the ATLAS detector*, *Eur. Phys. J. C* **82** (2022) 988 [[2202.02039](#)].
- [610] CMS collaboration, *Search for heavy neutral leptons in events with three charged leptons in proton-proton collisions at $\sqrt{s} = 13$ TeV*, *Phys. Rev. Lett.* **120** (2018) 221801 [[1802.02965](#)].
- [611] S. Pascoli, R. Ruiz and C. Weiland, *Heavy neutrinos with dynamic jet vetoes: multilepton searches at $\sqrt{s} = 14$, 27, and 100 TeV*, *JHEP* **06** (2019) 049 [[1812.08750](#)].
- [612] K. Mekala, J. Reuter and A.F. Żarnecki, *Heavy neutrinos at future linear e^+e^- colliders*, *JHEP* **06** (2022) 010 [[2202.06703](#)].
- [613] B. Vormwald and J. List, *Bilinear R parity violation at the ILC: neutrino physics at colliders*, *Eur. Phys. J. C* **74** (2014) 2720 [[1307.4074](#)].
- [614] A. Das, N. Okada, S. Okada and D. Raut, *Probing the seesaw mechanism at the 250 GeV ILC*, *Phys. Lett. B* **797** (2019) 134849 [[1812.11931](#)].
- [615] J. Nakajima, A. Das, K. Fujii, D. Jeans, N. Okada, S. Okada et al., *Probing heavy Majorana neutrino pair production at ILC in a $U(1)_{B-L}$ extension of the Standard Model*, in *2022 Snowmass Summer Study*, 3, 2022 [[2203.06929](#)].
- [616] J.C. Romao and J.W.F. Valle, *Neutrino masses in supersymmetry with spontaneously broken R parity*, *Nucl. Phys. B* **381** (1992) 87.

- [617] M. Hirsch and W. Porod, *Neutrino properties and the decay of the lightest supersymmetric particle*, *Phys. Rev. D* **68** (2003) 115007 [[hep-ph/0307364](#)].
- [618] R.K. Ellis et al., *Physics Briefing Book: Input for the European Strategy for Particle Physics Update 2020*, [1910.11775](#).
- [619] ILC CONCEPT GROUP collaboration, *New physics searches with the International Large Detector at the ILC*, in *Particles and Nuclei International Conference*, 11, 2021 [[2111.09928](#)].
- [620] S. Snyder, C. Weber and D. Zhang, *Prospects for searches for Higgs boson decays to dark photons at the ILC*, in *2022 Snowmass Summer Study*, 3, 2022 [[2203.08270](#)].
- [621] Y.C. San, M. Perelstein and P. Tanedo, *Dark Z at the International Linear Collider*, *Phys. Rev. D* **106** (2022) 015027 [[2205.10304](#)].
- [622] N. Craig, C. Englert and M. McCullough, *New Probe of Naturalness*, *Phys. Rev. Lett.* **111** (2013) 121803 [[1305.5251](#)].
- [623] M. Bauer, M. Neubert and A. Thamm, *Collider Probes of Axion-Like Particles*, *JHEP* **12** (2017) 044 [[1708.00443](#)].
- [624] M. Bauer, M. Heiles, M. Neubert and A. Thamm, *Axion-Like Particles at Future Colliders*, *Eur. Phys. J. C* **79** (2019) 74 [[1808.10323](#)].
- [625] R. Schäfer, F. Tillinger and S. Westhoff, *Near or Far Detectors? Optimizing Long-Lived Particle Searches at Electron-Positron Colliders*, [2202.11714](#).
- [626] L. Jeanty, L. Nosler and C. Potter, *Sensitivity to decays of long-lived dark photons at the ILC*, [2203.08347](#).
- [627] S. Kanemura, T. Moroi and T. Tanabe, *Beam dump experiment at future electron-positron colliders*, *Phys. Lett. B* **751** (2015) 25 [[1507.02809](#)].
- [628] BDX collaboration, *Dark Matter Search in a Beam-Dump eXperiment (BDX) at Jefferson Lab*, [1607.01390](#).
- [629] K. Asai, S. Iwamoto, Y. Sakaki and D. Ueda, *New physics searches at the ILC positron and electron beam dumps*, *JHEP* **09** (2021) 183 [[2105.13768](#)].
- [630] Y. Sakaki and D. Ueda, *Searching for new light particles at the international linear collider main beam dump*, *Phys. Rev. D* **103** (2021) 035024 [[2009.13790](#)].
- [631] K. Asai, T. Moroi and A. Niki, *Leptophilic Gauge Bosons at ILC Beam Dump Experiment*, *Phys. Lett. B* **818** (2021) 136374 [[2104.00888](#)].
- [632] M.M. Nojiri, Y. Sakaki, K. Tobioka and D. Ueda, *First Evaluation of Meson and τ lepton Spectra and Search for Heavy Neutral Leptons at ILC Beam Dump*, [2206.13523](#).
- [633] P. Giffin, S. Gori, Y.-D. Tsai and D. Tuckler, *Heavy Neutral Leptons at Beam Dump Experiments of Future Lepton Colliders*, [2206.13745](#).

- [634] Z. Bai et al., *LUXE-NPOD: new physics searches with an optical dump at LUXE*, [2107.13554](#).
- [635] A. Fedotov, A. Ilderton, F. Karbstein, B. King, D. Seipt, H. Taya et al., *Advances in QED with intense background fields*, [2203.00019](#).
- [636] E144 collaboration, *Observation of nonlinear effects in Compton scattering*, *Phys. Rev. Lett.* **76** (1996) 3116.
- [637] D.L. Burke et al., *Positron production in multi - photon light by light scattering*, *Phys. Rev. Lett.* **79** (1997) 1626.
- [638] C. Bamber et al., *Studies of nonlinear QED in collisions of 46.6-GeV electrons with intense laser pulses*, *Phys. Rev. D* **60** (1999) 092004.
- [639] S. Meuren, “Probing strong-field QED at FACET-II (SLAC E-320) .”
- [640] F.C. Salgado et al., *Single Particle Detection System for Strong-Field QED Experiments*, [2107.03697](#).
- [641] H. Abramowicz et al., *Letter of Intent for the LUXE Experiment*, [1909.00860](#).
- [642] K. Qu, S. Meuren and N.J. Fisch, *Signature of Collective Plasma Effects in Beam-Driven QED Cascades*, *Phys. Rev. Lett.* **127** (2021) 095001 [[2001.02590](#)].
- [643] A. Freitas et al., *Theoretical uncertainties for electroweak and Higgs-boson precision measurements at FCC-ee*, [1906.05379](#).
- [644] S. Jadach and M. Skrzypek, *QED challenges at FCC-ee precision measurements*, *Eur. Phys. J. C* **79** (2019) 756 [[1903.09895](#)].
- [645] Y. Aoki et al., *FLAG Review 2021*, [2111.09849](#).
- [646] A. Verbytskyi, A. Banfi, A. Kardos, P.F. Monni, S. Kluth, G. Somogyi et al., *High precision determination of α_s from a global fit of jet rates*, *JHEP* **08** (2019) 129 [[1902.08158](#)].
- [647] S. Marzani, D. Reichelt, S. Schumann, G. Soyez and V. Theeuwes, *Fitting the Strong Coupling Constant with Soft-Drop Thrust*, *JHEP* **11** (2019) 179 [[1906.10504](#)].
- [648] J. Ablinger, J. Blümlein, A. De Freitas and K. Schönwald, *Subleading Logarithmic QED Initial State Corrections to $e^+e^- \rightarrow \gamma^*/Z^{0*}$ to $O(\alpha^6 L^5)$* , *Nucl. Phys. B* **955** (2020) 115045 [[2004.04287](#)].
- [649] LHC HIGGS CROSS SECTION WORKING GROUP collaboration, *LHC HXSWG interim recommendations to explore the coupling structure of a Higgs-like particle*, [1209.0040](#).
- [650] G. Buchalla, O. Catà and C. Krause, *Complete Electroweak Chiral Lagrangian with a Light Higgs at NLO*, *Nucl. Phys. B* **880** (2014) 552 [[1307.5017](#)].
- [651] G. Buchalla, O. Cata, A. Celis and C. Krause, *Note on Anomalous Higgs-Boson Couplings in Effective Field Theory*, *Phys. Lett. B* **750** (2015) 298 [[1504.01707](#)].

- [652] R. Alonso, E.E. Jenkins and A.V. Manohar, *Geometry of the Scalar Sector*, *JHEP* **08** (2016) 101 [[1605.03602](#)].
- [653] A. Helset, A. Martin and M. Trott, *The Geometric Standard Model Effective Field Theory*, *JHEP* **03** (2020) 163 [[2001.01453](#)].
- [654] T. Cohen, N. Craig, X. Lu and D. Sutherland, *Unitarity violation and the geometry of Higgs EFTs*, *JHEP* **12** (2021) 003 [[2108.03240](#)].
- [655] J. De Blas, G. Durieux, C. Grojean, J. Gu and A. Paul, *On the future of Higgs, electroweak and diboson measurements at lepton colliders*, *JHEP* **12** (2019) 117 [[1907.04311](#)].
- [656] J. de Blas et al., *Higgs Boson Studies at Future Particle Colliders*, *JHEP* **01** (2020) 139 [[1905.03764](#)].
- [657] J. de Blas, Y. Du, C. Grojean, J. Gu, V. Miralles, M.E. Peskin et al., *Global SMEFT Fits at Future Colliders*, in *2022 Snowmass Summer Study*, 6, 2022 [[2206.08326](#)].
- [658] T. Barklow, K. Fujii, S. Jung, R. Karl, J. List, T. Ogawa et al., *Improved Formalism for Precision Higgs Coupling Fits*, *Phys. Rev.* **D97** (2018) 053003 [[1708.08912](#)].
- [659] M.E. Peskin, *Higgs/EW fit at future $e+e-$ colliders*, presentation at the 2022 Snowmass CSS Meeting, <https://indico.fnal.gov/event/22303/contributions/245703/attachments/157669/206487/SMEFTate%2Be-.pdf> .
- [660] B. Grzadkowski, M. Iskrzynski, M. Misiak and J. Rosiek, *Dimension-Six Terms in the Standard Model Lagrangian*, *JHEP* **10** (2010) 085 [[1008.4884](#)].
- [661] FCC collaboration, *FCC Physics Opportunities: Future Circular Collider Conceptual Design Report Volume 1*, *Eur. Phys. J. C* **79** (2019) 474.
- [662] M. McCullough, *An Indirect Model-Dependent Probe of the Higgs Self-Coupling*, *Phys. Rev. D* **90** (2014) 015001 [[1312.3322](#)].
- [663] G. Degrandi, S. Di Vita, J. Elias-Miro, J.R. Espinosa, G.F. Giudice, G. Isidori et al., *Higgs mass and vacuum stability in the Standard Model at NNLO*, *JHEP* **08** (2012) 098 [[1205.6497](#)].
- [664] S. Chigusa, T. Moroi and Y. Shoji, *Decay Rate of Electroweak Vacuum in the Standard Model and Beyond*, *Phys. Rev. D* **97** (2018) 116012 [[1803.03902](#)].
- [665] S. Chigusa, T. Moroi and Y. Shoji, *State-of-the-Art Calculation of the Decay Rate of Electroweak Vacuum in the Standard Model*, *Phys. Rev. Lett.* **119** (2017) 211801 [[1707.09301](#)].
- [666] F.L. Bezrukov and M. Shaposhnikov, *The Standard Model Higgs boson as the inflaton*, *Phys. Lett. B* **659** (2008) 703 [[0710.3755](#)].
- [667] F. Bezrukov and M. Shaposhnikov, *Standard Model Higgs boson mass from inflation: Two loop analysis*, *JHEP* **07** (2009) 089 [[0904.1537](#)].

- [668] P. Huang, A.J. Long and L.-T. Wang, *Probing the Electroweak Phase Transition with Higgs Factories and Gravitational Waves*, *Phys. Rev. D* **94** (2016) 075008 [[1608.06619](#)].
- [669] A. Adams, N. Arkani-Hamed, S. Dubovsky, A. Nicolis and R. Rattazzi, *Causality, analyticity and an IR obstruction to UV completion*, *JHEP* **10** (2006) 014 [[hep-th/0602178](#)].
- [670] G.N. Remmen and N.L. Rodd, *Consistency of the Standard Model Effective Field Theory*, *JHEP* **12** (2019) 032 [[1908.09845](#)].
- [671] B. Bellazzini and F. Riva, *New phenomenological and theoretical perspective on anomalous ZZ and Z γ processes*, *Phys. Rev. D* **98** (2018) 095021 [[1806.09640](#)].
- [672] Q. Bi, C. Zhang and S.-Y. Zhou, *Positivity constraints on aQGC: carving out the physical parameter space*, *JHEP* **06** (2019) 137 [[1902.08977](#)].
- [673] J. Gu, L.-T. Wang and C. Zhang, *An unambiguous test of positivity at lepton colliders*, [2011.03055](#).
- [674] B. Fuks, Y. Liu, C. Zhang and S.-Y. Zhou, *Positivity in electron-positron scattering: testing the axiomatic quantum field theory principles and probing the existence of UV states*, *Chin. Phys. C* **45** (2021) 023108 [[2009.02212](#)].
- [675] I. Low, J. Lykken and G. Shaughnessy, *Have We Observed the Higgs (Imposter)?*, *Phys. Rev. D* **86** (2012) 093012 [[1207.1093](#)].
- [676] MUON G-2 collaboration, *Measurement of the Positive Muon Anomalous Magnetic Moment to 0.46 ppm*, *Phys. Rev. Lett.* **126** (2021) 141801 [[2104.03281](#)].
- [677] S. Baum, M. Carena, N.R. Shah and C.E.M. Wagner, *The tiny ($g-2$) muon wobble from small- μ supersymmetry*, *JHEP* **01** (2022) 025 [[2104.03302](#)].
- [678] M. Chakraborti, S. Heinemeyer and I. Saha, *Improved $(g-2)_\mu$ measurements and wino/higgsino dark matter*, *Eur. Phys. J. C* **81** (2021) 1069 [[2103.13403](#)].
- [679] M. Chakraborti, S. Heinemeyer and I. Saha, *The new “MUON G-2” result and supersymmetry*, *Eur. Phys. J. C* **81** (2021) 1114 [[2104.03287](#)].
- [680] M. Chakraborti, S. Heinemeyer, I. Saha and C. Schappacher, *$(g-2)_\mu$ and SUSY Dark Matter: Direct Detection and Collider Search Complementarity*, [2112.01389](#).
- [681] M. Endo, K. Hamaguchi, S. Iwamoto and T. Kitahara, *Muon $g-2$ vs LHC Run 2 in Supersymmetric Models*, *JHEP* **04** (2020) 165 [[2001.11025](#)].
- [682] M. Endo, K. Hamaguchi, S. Iwamoto and T. Kitahara, *Supersymmetric interpretation of the muon $g-2$ anomaly*, *JHEP* **07** (2021) 075 [[2104.03217](#)].
- [683] PLANCK collaboration, *Planck 2018 results. VI. Cosmological parameters*, *Astron. Astrophys.* **641** (2020) A6 [[1807.06209](#)].

- [684] XENON collaboration, *Dark Matter Search Results from a One Ton-Year Exposure of XENON1T*, *Phys. Rev. Lett.* **121** (2018) 111302 [[1805.12562](#)].
- [685] LUX collaboration, *Results from a search for dark matter in the complete LUX exposure*, *Phys. Rev. Lett.* **118** (2017) 021303 [[1608.07648](#)].
- [686] PANDAX-II collaboration, *Dark Matter Results From 54-Ton-Day Exposure of PandaX-II Experiment*, *Phys. Rev. Lett.* **119** (2017) 181302 [[1708.06917](#)].
- [687] XENON collaboration, *Projected WIMP sensitivity of the XENONnT dark matter experiment*, *JCAP* **11** (2020) 031 [[2007.08796](#)].
- [688] LUX-ZEPLIN collaboration, *Projected WIMP sensitivity of the LUX-ZEPLIN dark matter experiment*, *Phys. Rev. D* **101** (2020) 052002 [[1802.06039](#)].
- [689] M. Endo, K. Hamaguchi, S. Iwamoto, T. Kitahara and T. Moroi, *Reconstructing Supersymmetric Contribution to Muon Anomalous Magnetic Dipole Moment at ILC*, *Phys. Lett. B* **728** (2014) 274 [[1310.4496](#)].
- [690] M. Endo, K. Hamaguchi, S. Iwamoto, S.-i. Kawada, T. Kitahara, T. Moroi et al., *Stau study at the ILC and its implication for the muon $g-2$ anomaly*, in *2022 Snowmass Summer Study*, 3, 2022 [[2203.07056](#)].
- [691] J.D. Wells and Z. Zhang, *Effective field theory approach to trans-TeV supersymmetry: covariant matching, Yukawa unification and Higgs couplings*, *JHEP* **05** (2018) 182 [[1711.04774](#)].
- [692] M. Endo, T. Moroi and M.M. Nojiri, *Footprints of Supersymmetry on Higgs Decay*, *JHEP* **04** (2015) 176 [[1502.03959](#)].
- [693] K. Hidaka, H. Eberl and E. Ginina, *The $h(125)$ decays to $c\bar{c}$, $b\bar{b}$, $b\bar{s}$, $\gamma\gamma$ and gg in the light of the MSSM with quark flavor violation*, in *European Physical Society Conference on High Energy Physics 2021, PoS EPS-HEP2021 (2022)* 594 [[2111.02713](#)].
- [694] S. Weinberg, *Implications of Dynamical Symmetry Breaking*, *Phys. Rev. D* **13** (1976) 974.
- [695] L. Susskind, *Dynamics of Spontaneous Symmetry Breaking in the Weinberg-Salam Theory*, *Phys. Rev. D* **20** (1979) 2619.
- [696] R. Contino, *The Higgs as a Composite Nambu-Goldstone Boson*, in *Theoretical Advanced Study Institute in Elementary Particle Physics: Physics of the Large and the Small*, pp. 235–306, 2011, DOI [[1005.4269](#)].
- [697] N. Arkani-Hamed, M. Porrati and L. Randall, *Holography and phenomenology*, *JHEP* **08** (2001) 017 [[hep-th/0012148](#)].
- [698] R. Contino, Y. Nomura and A. Pomarol, *Higgs as a holographic pseudoGoldstone boson*, *Nucl. Phys. B* **671** (2003) 148 [[hep-ph/0306259](#)].

- [699] T. Han, H.E. Logan, B. McElrath and L.-T. Wang, *Phenomenology of the little Higgs model*, *Phys. Rev. D* **67** (2003) 095004 [[hep-ph/0301040](#)].
- [700] T. Han, H.E. Logan, B. McElrath and L.-T. Wang, *Loop induced decays of the Little Higgs: $H \rightarrow gg, \gamma\gamma$* , *Phys. Lett. B* **563** (2003) 191 [[hep-ph/0302188](#)].
- [701] D. Egana-Ugrinovic, S. Homiller and P. Meade, *Multi-Higgs Production Probes Higgs Flavor*, *Phys. Rev. D* **103** (2021) 115005 [[2101.04119](#)].
- [702] A.K. Das and C. Kao, *A Two Higgs doublet model for the top quark*, *Phys. Lett. B* **372** (1996) 106 [[hep-ph/9511329](#)].
- [703] A.E. Blechman, A.A. Petrov and G. Yeghiyan, *The Flavor puzzle in multi-Higgs models*, *JHEP* **11** (2010) 075 [[1009.1612](#)].
- [704] W. Altmannshofer, S. Gori, A.L. Kagan, L. Silvestrini and J. Zupan, *Uncovering Mass Generation Through Higgs Flavor Violation*, *Phys. Rev. D* **93** (2016) 031301 [[1507.07927](#)].
- [705] D. Ghosh, R.S. Gupta and G. Perez, *Is the Higgs Mechanism of Fermion Mass Generation a Fact? A Yukawa-less First-Two-Generation Model*, *Phys. Lett. B* **755** (2016) 504 [[1508.01501](#)].
- [706] F.J. Botella, G.C. Branco, M.N. Rebelo and J.I. Silva-Marcos, *What if the masses of the first two quark families are not generated by the standard model Higgs boson?*, *Phys. Rev. D* **94** (2016) 115031 [[1602.08011](#)].
- [707] W. Altmannshofer, J. Eby, S. Gori, M. Lotito, M. Martone and D. Tuckler, *Collider Signatures of Flavorful Higgs Bosons*, *Phys. Rev. D* **94** (2016) 115032 [[1610.02398](#)].
- [708] D. Egana-Ugrinovic, S. Homiller and P.R. Meade, *Higgs bosons with large couplings to light quarks*, *Phys. Rev. D* **100** (2019) 115041 [[1908.11376](#)].
- [709] A. Vicente, *Higgs lepton flavor violating decays in Two Higgs Doublet Models*, *Front. in Phys.* **7** (2019) 174 [[1908.07759](#)].
- [710] M.E. Gómez, S. Heinemeyer and M. Rehman, *Quark flavor violating Higgs boson decay $h \rightarrow \bar{b}s + b\bar{s}$ in the MSSM*, *Phys. Rev. D* **93** (2016) 095021 [[1511.04342](#)].
- [711] M.E. Peskin, *Model-Agnostic Exploration of the Mass Reach of Precision Higgs Boson Coupling Measurements*, in *2022 Snowmass Summer Study*, 9, 2022 [[2209.03303](#)].
- [712] G.F. Giudice, C. Grojean, A. Pomarol and R. Rattazzi, *The Strongly-Interacting Light Higgs*, *JHEP* **06** (2007) 045 [[hep-ph/0703164](#)].
- [713] CMS collaboration, *Search for a new scalar resonance decaying to a pair of Z bosons at the High-Luminosity LHC*, .
- [714] X. Cid Vidal et al., *Report from Working Group 3: Beyond the Standard Model physics at the HL-LHC and HE-LHC*, *CERN Yellow Rep. Monogr.* **7** (2019) 585 [[1812.07831](#)].

- [715] R. Franceschini, *Beyond the Standard Model Physics at CLIC*, *Int. J. Mod. Phys. A* **35** (2020) 2041015 [[1902.10125](#)].
- [716] CLICDP collaboration, *Double Higgs boson production and Higgs self-coupling extraction at CLIC*, *Eur. Phys. J. C* **80** (2020) 1010 [[1901.05897](#)].
- [717] H. Al Ali et al., *The Muon Smasher's Guide*, [2103.14043](#).
- [718] L. Di Luzio, R. Gröber and G. Panico, *Probing new electroweak states via precision measurements at the LHC and future colliders*, *JHEP* **01** (2019) 011 [[1810.10993](#)].
- [719] T. Han, Z. Liu, L.-T. Wang and X. Wang, *WIMPs at High Energy Muon Colliders*, *Phys. Rev. D* **103** (2021) 075004 [[2009.11287](#)].
- [720] M. Cirelli, N. Fornengo and A. Strumia, *Minimal dark matter*, *Nucl. Phys. B* **753** (2006) 178 [[hep-ph/0512090](#)].
- [721] Y. Cui and R. Sundrum, *Baryogenesis for weakly interacting massive particles*, *Phys. Rev. D* **87** (2013) 116013 [[1212.2973](#)].
- [722] Y. Cui and B. Shuve, *Probing Baryogenesis with Displaced Vertices at the LHC*, *JHEP* **02** (2015) 049 [[1409.6729](#)].
- [723] J. Alexander et al., *Dark Sectors 2016 Workshop: Community Report*, 8, 2016 [[1608.08632](#)].
- [724] N. Craig, A. Hook and S. Kasko, *The Photophobic ALP*, *JHEP* **09** (2018) 028 [[1805.06538](#)].
- [725] FCC collaboration, *FCC-hh: The Hadron Collider: Future Circular Collider Conceptual Design Report Volume 3*, *Eur. Phys. J. ST* **228** (2019) 755.
- [726] D. Schulte, J.-P. Delahaye, M. Diemoz, K. Long, B. Mansoulié, N. Patrone et al., *Muon Collider. A Path to the Future?*, *PoS EPS-HEP2019* (2020) 004.
- [727] ALEGRO collaboration, *Towards an Advanced Linear International Collider*, [1901.10370](#).
- [728] A.G. Cohen, D.B. Kaplan and A.E. Nelson, *The More Minimal Supersymmetric Standard Model*, *Phys. Lett. B* **388** (1996) 588 [[hep-ph/9607394](#)].
- [729] M. Papucci, J.T. Ruderman and A. Weiler, *Natural SUSY Endures*, *JHEP* **09** (2012) 035 [[1110.6926](#)].
- [730] P.W. Graham, D.E. Kaplan and S. Rajendran, *Cosmological Relaxation of the Electroweak Scale*, *Phys. Rev. Lett.* **115** (2015) 221801 [[1504.07551](#)].
- [731] G.F. Giudice, M. McCullough and T. You, *Self-organised localisation*, *JHEP* **10** (2021) 093 [[2105.08617](#)].
- [732] N. Arkani-Hamed, A.G. Cohen and H. Georgi, *Electroweak symmetry breaking from dimensional deconstruction*, *Phys. Lett. B* **513** (2001) 232 [[hep-ph/0105239](#)].

- [733] N. Arkani-Hamed, A.G. Cohen, E. Katz and A.E. Nelson, *The Littlest Higgs*, *JHEP* **07** (2002) 034 [[hep-ph/0206021](#)].
- [734] K. Agashe, R. Contino and A. Pomarol, *The Minimal composite Higgs model*, *Nucl. Phys. B* **719** (2005) 165 [[hep-ph/0412089](#)].
- [735] G.D. Kribs and A. Martin, *Supersoft Supersymmetry is Super-Safe*, *Phys. Rev. D* **85** (2012) 115014 [[1203.4821](#)].
- [736] A.E. Nelson and T.S. Roy, *New Supersoft Supersymmetry Breaking Operators and a Solution to the μ Problem*, *Phys. Rev. Lett.* **114** (2015) 201802 [[1501.03251](#)].
- [737] L.M. Carpenter, *Antisplit Supersymmetry*, *JHEP* **10** (2017) 205 [[1612.09255](#)].
- [738] H. Baer, V. Barger, J.S. Gainer, P. Huang, M. Savoy, H. Serce et al., *What hadron collider is required to discover or falsify natural supersymmetry?*, *Phys. Lett. B* **774** (2017) 451 [[1702.06588](#)].
- [739] S. Chakraborty, A. Martin and T.S. Roy, *Charting generalized supersoft supersymmetry*, *JHEP* **05** (2018) 176 [[1802.03411](#)].
- [740] J. Aebischer, W. Altmannshofer, D. Guadagnoli, M. Reboud, P. Stangl and D.M. Straub, *B-decay discrepancies after Moriond 2019*, *Eur. Phys. J. C* **80** (2020) 252 [[1903.10434](#)].
- [741] K. Ban, Y. Jho, Y. Kwon, S.C. Park, S. Park and P.-Y. Tseng, *A comprehensive study of vector leptoquark with $U(1)_{B_3-L_2}$ on the B-meson and Muon $g-2$ anomalies*, [2104.06656](#).
- [742] K. Griest and M. Kamionkowski, *Unitarity Limits on the Mass and Radius of Dark Matter Particles*, *Phys. Rev. Lett.* **64** (1990) 615.
- [743] “How ESS will become sustainable.” <https://europeanspallationsource.se/how-ess-will-become-sustainable>, 2021.
- [744] M. Aicheler, P. Burrows, M. Draper, T. Garvey, P. Lebrun, K. Peach et al., *A Multi-TeV Linear Collider Based on CLIC Technology*, .
- [745] CLICDP, CLIC collaboration, *The Compact Linear Collider (CLIC) - 2018 Summary Report*, [1812.06018](#).
- [746] CLIC ACCELERATOR collaboration, M. Aicheler, P.N. Burrows, N. Catalan Lasheras, R. Corsini, M. Draper, J. Osborne et al., eds., *The Compact Linear Collider (CLIC) - Project Implementation Plan*, [1903.08655](#).
- [747] M. Bai et al., *C^3 : A “Cool” Route to the Higgs Boson and Beyond*, 10, 2021 [[2110.15800](#)].
- [748] “Compact Linear Collider (CLIC).” <http://clic.cern/>.
- [749] CLIC, CLICDP collaboration, *Updated baseline for a staged Compact Linear Collider*, [1608.07537](#).

- [750] “Compact Linear Collider (CLIC) papers for the European Strategy for Particle Physics.” <http://clic.cern/european-strategy>.
- [751] F. Bordry et al., *Machine Parameters and Projected Luminosity Performance of Proposed Future Colliders at CERN*, 2018.
- [752] CLIC, CLICDP collaboration, P. Roloff, R. Franceschini, U. Schnoor and A. Wulzer, eds., *The Compact Linear e^+e^- Collider (CLIC): Physics Potential*, [1812.07986](#).
- [753] C. Gohil, A. Latina, D. Schulte and S. Stapnes, *High-Luminosity CLIC Studies*, Aug, 2020.
- [754] C. Gohil, P.N. Burrows, N. Blaskovic Kraljevic, A. Latina, J. Ögren and D. Schulte, *Luminosity performance of the Compact Linear Collider at 380 GeV with static and dynamic imperfections*, *Phys. Rev. Accel. Beams* **23** (2020) 101001 [[2009.01184](#)].
- [755] “FACET Facility for Advanced Accelerator Experimental Tests.” http://portal.slac.stanford.edu/sites/ard_public/facet/Pages/default.aspx.
- [756] “FERMI Free Electron laser Radiation for Multidisciplinary Investigations.” <https://www.elettra.trieste.it/lightsources/fermi.html>.
- [757] G. D’Auria et al., “Status of the CompactLight Design Study.” <https://doi.org/10.18429/JACoW-FEL2019-THP078>, 2019.
- [758] K.L. Bane, T.L. Barklow, M. Breidenbach, C.P. Burkhardt, E.A. Fauve, A.R. Gold et al., *An advanced ncrf linac concept for a high energy e^+e^- linear collider*, 2018. [[1807.10195](#)].
- [759] A. Grudiev, S. Calatroni and W. Wuensch, *New local field quantity describing the high gradient limit of accelerating structures*, *Physical Review Special Topics-Accelerators and Beams* **12** (2009) 102001.
- [760] E.I. Simakov, V.A. Dolgashev and S.G. Tantawi, *Advances in high gradient normal conducting accelerator structures*, *Nuclear Instruments and Methods in Physics Research Section A: Accelerators, Spectrometers, Detectors and Associated Equipment* **907** (2018) 221.
- [761] M.A. Othman, J. Picard, S. Schaub, V.A. Dolgashev, S.M. Lewis, J. Neilson et al., *Experimental demonstration of externally driven millimeter-wave particle accelerator structure*, *Applied Physics Letters* **117** (2020) 073502.
- [762] S. Tantawi, M. Nasr, Z. Li, C. Limborg and P. Borchard, *Design and demonstration of a distributed-coupling linear accelerator structure*, *Physical Review Accelerators and Beams* **23** (2020) 092001.
- [763] J.W. Wang, S.G. Tantawi, C. Xu, M. Franzi, P. Krejcik, G. Bowden et al., *Development for a supercompact X-band pulse compression system and its application at slac*, *Physical Review Accelerators and Beams* **20** (2017) 110401.

- [764] M. Nasr, E. Nanni, M. Breidenbach, S. Weathersby, M. Oriunno and S. Tantawi, *Experimental demonstration of particle acceleration with normal conducting accelerating structure at cryogenic temperature*, *Physical Review Accelerators and Beams* **24** (2021) 093201.
- [765] A. Cahill, J. Rosenzweig, V.A. Dolgashev, S.G. Tantawi and S. Weathersby, *High gradient experiments with X-band cryogenic copper accelerating cavities*, *Physical Review Accelerators and Beams* **21** (2018) 102002.
- [766] E. Simakov et al., *First C-Band High Gradient Cavity Testing Results at LANL*, [JACoW IPAC2021 \(2021\) MOPAB341](#).
- [767] E.A. Nanni et al., *C⁸ Demonstration Research and Development Plan*, in *2022 Snowmass Summer Study*, 3, 2022 [[2203.09076](#)].
- [768] P. Wang, H. Zha, I. Syratchev, J. Shi and H. Chen, *rf design of a pulse compressor with correction cavity chain for klystron-based compact linear collider*, *Physical Review Accelerators and Beams* **20** (2017) 112001.
- [769] A.Y. Baikov, C. Marrelli and I. Syratchev, *Toward high-power klystrons with rf power conversion efficiency on the order of 90%*, *IEEE Transactions on Electron devices* **62** (2015) 3406.
- [770] D.A. Constable, C. Lingwood, G. Burt, A.Y. Baikov, I. Syratchev and R. Kowalczyk, *Magic2-d simulations of high efficiency klystrons using the core oscillation method*, in *2017 Eighteenth International Vacuum Electronics Conference (IVEC)*, pp. 1–2, IEEE, 2017.
- [771] B. Weatherford, V. Dolgashev, J. Neilson and A. Jensen, *High efficiency X-band 50mw klystron study* .
- [772] B. Weatherford, M. Kemp, X. Lu, J. Merrick, E. Nanni, J. Neilson et al., *Modular high power rf sources for compact linear accelerator systems*, in *2020 IEEE 21st International Conference on Vacuum Electronics (IVEC)*, pp. 55–56, IEEE, 2020.
- [773] M. Dal Forno, V. Dolgashev, G. Bowden, C. Clarke, M. Hogan, D. McCormick et al., *Rf breakdown measurements in electron beam driven 200 ghz copper and copper-silver accelerating structures*, *Physical Review Accelerators and Beams* **19** (2016) 111301.
- [774] M.D. Forno, V. Dolgashev, G. Bowden, C. Clarke, M. Hogan, D. McCormick et al., *High gradient mm-wave metallic accelerating structures*, in *AIP Conference Proceedings*, vol. 1812, p. 060011, AIP Publishing LLC, 2017.
- [775] R. Li, M. Hoffmann, E. Nanni, S. Glenzer, M. Kozina, A. Lindenberg et al., *Terahertz-based subfemtosecond metrology of relativistic electron beams*, *Physical Review Accelerators and Beams* **22** (2019) 012803.
- [776] M.A. Othman, E.C. Snively, A.E. Gabriel, M.E. Kozina, X. Shen, F. Ji et al., *Visualizing femtosecond dynamics with ultrafast electron probes through terahertz compression and time-stamping*, 2021. [[2104.05691](#)].

- [777] E. Snively, M. Othman, M. Kozina, B. Ofori-Okai, S. Weathersby, S. Park et al., *Femtosecond compression dynamics and timing jitter suppression in a thz-driven electron bunch compressor*, *Physical Review Letters* **124** (2020) 054801.
- [778] H. Tang, L. Zhao, P. Zhu, X. Zou, J. Qi, Y. Cheng et al., *Stable and scalable multistage terahertz-driven particle accelerator*, *Physical Review Letters* **127** (2021) 074801.
- [779] D. Zhang, M. Fakhari, H. Cankaya, A.-L. Calendron, N.H. Matlis and F.X. Kärtner, *Cascaded multicycle terahertz-driven ultrafast electron acceleration and manipulation*, *Physical Review X* **10** (2020) 011067.
- [780] E. Nanni et al., *High-gradient accelerators at THz frequencies, in preparation*, 2022.
- [781] F. Zimmermann and D. Whittum, *Final-focus system and collision schemes for a 5-TeV W-band linear collider*, *International Journal of Modern Physics A* **13** (1998) 2525.
- [782] M. Litos et al., *High-efficiency acceleration of an electron beam in a plasma wakefield accelerator*, *Nature* **515** (2014) 92.
- [783] S. Corde et al., *Multi-gigaelectronvolt acceleration of positrons in a self-loaded plasma wakefield*, *Nature* **524** (2015) 442.
- [784] AWAKE collaboration, *Acceleration of electrons in the plasma wakefield of a proton bunch*, *Nature* **561** (2018) 363 [[1808.09759](https://doi.org/10.1038/1808.09759)].
- [785] S. Steinke et al., *Multistage coupling of independent laser-plasma accelerators*, *Nature* **530** (2016) 190.
- [786] A. Deng et al., *Generation and acceleration of electron bunches from a plasma photocathode*, *Nature Phys.* **15** (2019) 1156.
- [787] C.A. Lindström et al., *Emittance Preservation in an Aberration-Free Active Plasma Lens*, *Phys. Rev. Lett.* **121** (2018) 194801 [[1808.03691](https://doi.org/10.1103/PhysRevLett.121.194801)].
- [788] J.B. Rosenzweig, N. Barov, A. Murokh, E. Colby and P. Colestock, *Towards a plasma wake field acceleration-based linear collider*, *Nucl. Instrum. Meth. A* **410** (1998) 532.
- [789] A. Seryi, M. Hogan, S. Pei, T. Raubenheimer, P. Tenenbaum, T. Katsouleas et al., *A Concept of Plasma Wake Field Acceleration Linear Collider (PWFA-LC)*, in in *Particle Accelerator Conference (PAC 09)*, <https://jacow.org/PAC2009/papers/we6pfp081.pdf> .
- [790] C.B. Schroeder, E. Esarey, C.G.R. Geddes, C. Benedetti and W.P. Leemans, *Physics considerations for laser-plasma linear colliders*, *Phys. Rev. ST Accel. Beams* **13** (2010) 101301.
- [791] E. Adli, J.-P. Delahaye, S.J. Gessner, M.J. Hogan, T. Raubenheimer, W. An et al., *A Beam Driven Plasma-Wakefield Linear Collider: From Higgs Factory to Multi-TeV*, in *Community Summer Study 2013: Snowmass on the Mississippi*, 8, 2013 [[1308.1145](https://doi.org/10.1145/1308.1145)].

- [792] ALEGRO collaboration, *ALEGRO input for the 2020 update of the European Strategy*, [1901.08436](#).
- [793] E. Esarey, C.B. Schroeder and W.P. Leemans, *Physics of laser-driven plasma-based electron accelerators*, *Rev. Mod. Phys.* **81** (2009) 1229.
- [794] C.B. Schroeder, C. Benedetti, E. Esarey and W.P. Leemans, *Laser-plasma-based linear collider using hollow plasma channels*, *Nucl. Instrum. Meth. A* **829** (2016) 113.
- [795] V. Yakimenko et al., *Prospect of Studying Nonperturbative QED with Beam-Beam Collisions*, *Phys. Rev. Lett.* **122** (2019) 190404 [[1807.09271](#)].
- [796] W. Leemans, ed., *Report of the Workshop on Laser Technology for k-BELLA and Beyond*. https://www2.lbl.gov/LBL-Programs/atap/Report_Workshop_k-BELLA_laser_tech_final.pdf .
- [797] W. Gai, J.G. Power and C. Jing, *Short-pulse dielectric two-beam acceleration*, *J. Plasma Phys.* **78** (2012) 339.